PROCEEDINGS
TWELFTH WORKSHOP
GEOTHERMAL RESERVOIR ENGINEERING

January 20-22, 1987



Henry J. Ramey, Jr., Paul Kruger, Frank G. Miller,
Roland N. Horne, William E. Brigham,
Jesus Rivera
Stanford Geothermal Program
Workshop Report SGP-TR-109*

*Sponsored by the Geothermal and Hydropower Technologies Division of the U.S. Department of Energy, Stanford-DOE Contract No. DE-AT03-80SF11459 and Contract No. DE-AS07-84ID12529

Library of Congress Catalog Card No. 87-062306

TABLE OF CONTENTS

Page

Preface ..... -ix-

Introduction

The U.S. Department of Energy's Geothermal Reservoir Technology Program
J. E. Mock and R. E. Blackett 1

The U.S. Hot Dry Rock Project
R. H. Hendron 7

Magma Energy Extraction
J. C. Dunn et al 13

Potential Impact of Reservoir Engineering R&D on Geothermal
Energy Costs - R.K. Traeger and D. Entingh 21

The Geysers Geothermal Development

Decline Curve Analysis of Production Data from The Geysers
Geothermal Field - M. Ripperda and G. S. Bodvarsson 23

Applying Flowrate Type Curves to Geysers Steam Wells
S. Enedy 29

Well Testing

Long-Term Testing of Geothermal Wells in the Coso Hot Springs KGRA
S. Sanyal et al 37

A New Derivative Type-Curve for Pressure Buildup Analysis with Boundary
Effects - S. Mishra and H. J. Ramey, Jr. 45

Tracer Breakthrough Time for the Rate-Pressure Doublet
W. Menninger and A. Sageev 49

Analysis of Thermally Induced Permeability Enhancement in
Geothermal Injection Wells - S. M. Benson et al 57

Reservoir Modelling (Field Studies)

Reservoir Studies of the Seltjarnarnes Geothermal Field, Iceland
H. Tulinius et al 67

Conceptual Model of the Klamath Falls, Oregon Geothermal Area
R. H. Prucha et al 77

On Fluid and Heat Transfer in Deep Zones of Vapor-Dominated Geothermal Reservoirs - K. Pruess et al 89

Heat Sweep Analysis of Thermal Breakthrough at Los Humeros and La Primavera Fields, Mexico - P. Kruger et al 97

Reservoir Modelling II

Pressure Depletion Calculations for Liquid Geothermal Reservoirs R. C. Schroeder 103

Linear Water Influx of an Infinite Aquifer Through a Partially Communicating Fault - A. K. Ambastha and A. Sageev 109

Multiphase, Multicomponent Compressibility in Geothermal Reservoir Engineering - L. Macias-Chapa and H. J. Ramey, Jr. 119

Radial Dispersion in a Double-Porosity System with Fracture Skin A. F. Moench 125

Measurement Technology

Active Seismics to Determine Reservoir Characteristics of a Hot Dry Rock Geothermal System - A. S. P. Green, R. Baria 131

Sensitivity Analysis of Dual-Permeability Systems L. C. Hull and T. M. Clemo 139

Two Phase Streaming Potentials S. S. Marsden and M. W. Wheatall 147

Cerro Prieto - Contents of the Technical Information Files Generated at the Field - M. A. Ayuso 153

Field Development I

Development Drilling, Testing and Initial Production of the Beowawe Geothermal Field - V. T. Hoang et al 159

Geochemistry and Tracer Behavior During a Thirty Day Flow Test of the Fenton Hill HDR Reservoir - B. A. Robinson et al 163

Interference Tests at Kawerau, New Zealand J. G. Burnell and M. J. McGuinness 173

Field Development II

Response of the Los Azufres Geothermal Field to Four Years of 25 MW Wellhead Generation - P. Kruger et al 181

Pressure Buildup Testing of Well 18 in Los Azufres Field, Mexico
P. Sanchez Upton and J. S. Gudmundsson 189

Petrophysical Properties of Twenty Drill Cores from the Los Azufres,
Mexico, Geothermal Field - E. R. Iglesias et al 195

Development and Exploitation of Low Enthalpy Geothermal Systems:
Example of "The Dogger" in the Paris Basin, France - J. Rojas et al 203

Tracer Flow

Tracer Flow in a Fractured Geothermal Reservoir Model
M. Bayar and E. Okandan 213

The Theory and Selection of Chemically Reactive Tracers for Reservoir
Thermal Capacity Production - J. W. Tester et al 219

Parallel Fractures Model for Tracer Flow Through Geothermal Reservoirs -
Preliminary Results - J. R. Rivera et al 229

Analysis of Injection-Backflow Tracer Tests in Fractured Geothermal
Reservoirs - I. Kocabas and R. N. Horne 233

Geochemistry

Fieldwide Chemical and Isotopic Gradients in Steam from The Geysers
A. H. Truesdell et al 241

Gas Geothermometry Based on CO Content - Application in Italian
Geothermal Fields - F. D'Amore et al 247

Chemical and Isotopic Evidence of Steam Upflow and Partial Condensation
in Los Azufres Reservoir - D. Nieva et al 253

Geochemistry and the Exploration of the Ngawha Geothermal System,
New Zealand - D. S. Sheppard 261

Geoscience

Structure, Permeability and Production Characteristics of the Heber,
California Geothermal Reservoir - E. D. James et al 267

Results of Deep Drilling in the Western Moat of Long Valley California
G. Suemnicht 273

Geothermal Well Stimulated Using High Energy Gas Fracturing
T. Y. Chu et al 279

The Electrokinetic Mechanism of Hydrothermal-Circulation-Related and
Production-Induced Self-Potentials - T. Ishido et al 285

Papers Not Presented

Vapor-Dominated Zones within Hydrothermal Convection Systems
S. E. Ingebritsen 291

Bleeding Characteristics of Geothermal Wells
R. James and T. Goulda 297

Discharging Through an Orifice Determines Steam-Water Enthalpy
R. James 301

Fracture Detection in Geothermal Wells Drilled in Volcanic Rocks
M. Gonfalini et al 305

Analysis of Transient Pressure Tests for Olkaria Exploration Wells
C. B. Haukwa 315

Gas Geochemistry of the Dogger Geothermal Aquifer (Paris, Basin, France)
A. Criaud et al 321

A Practical Approach to Producing Vapor-Dominated Reservoirs
M. K. Kumataka 327

Geothermal Energy - An Emerging Resource (Talk from the dinner session)
J. R. Berg 333

List of Participants 337

Subject Index Volumes 1-12 349

Author Index Volumes 1-12 361

Preface

The Twelfth Workshop on Geothermal Reservoir Engineering was held at Stanford University on January 20-22, 1987. The year ending December 1986 was very difficult for the domestic geothermal industry. Low oil prices caused a sharp drop in geothermal steam prices. We expected to see some effect upon attendance at the Twelfth Workshop. To our surprise, the attendance was up by thirteen from previous years, with one hundred and fifty-seven registered participants. Eight foreign countries were represented: England, France, Iceland, Italy, Japan, Mexico, New Zealand, and Turkey. Despite a worldwide surplus of oil, international geothermal interest and development is growing at a remarkable pace.

There were forty-one technical presentations at the Workshop. All of these are published as papers in this Proceedings volume. Seven technical papers not presented at the Workshop are also published; they concern geothermal developments and research in Iceland, Italy, and New Zealand. In addition to these forty-eight technical presentations or papers, the introductory address was given by Henry J. Ramey, Jr. from the Stanford Geothermal Program.

The Workshop Banquet speaker was John R. Berg from the Department of Energy. We thank him for sharing with the Workshop participants his thoughts on the expectations of this agency in the role of alternative energy resources, specifically geothermal, within the country's energy framework. His talk is represented as a paper in the back of this volume.

The chairmen of the technical sessions made an important contribution to the workshop. Other than Stanford faculty members they included: M. Gulati, K. Goyal, G.S. Bodvarsson, A.S. Batchelor, H. Dykstra, M.J. Reed, A. Truesdell, J.S. Gudmundsson, and J.R. Counsil.

The Workshop was organized by the Stanford Geothermal Program faculty, staff, and students. We would like to thank Jean Cook, Marilyn King, Amy Osugi, Terri Ramey, and Rosalee Benelli for their valued help with the meeting arrangements and preparing the Proceedings. We also owe great thanks to our students who arranged and operated the audio-visual equipment, specially Jim Lovekin.

The Twelfth Workshop was supported by the Geothermal Technology Division of the U. S. Department of Energy through Contract Nos. DE-AS03-80SF11459 and DE-AS07-84ID12529. We deeply appreciate this continued support.

January 1987

Henry J. Ramey, Jr.
Paul Kruger
Roland N. Horne
William E. Brigham
Frank G. Miller
Jesus Rivera

PROCEEDINGS, Twelfth Workshop on Geothermal Reservoir Engineering
Stanford University, Stanford, California, January 20-22, 1987
SGP-TR-109

THE U.S. DEPARTMENT OF ENERGY'S GEOTHERMAL RESERVOIR TECHNOLOGY PROGRAM

Dr. John E. Mock
Mr. Robert E. Blackett*

U.S. Department of Energy, Geothermal Technology Division, Washingon, D.C.
*Meridian Corporation, Falls Church, VA

ABSTRACT

Geothermal reservoir engineering is an important aspect of the Department of Energy's Geothermal Technology Division, geothermal research and development program. Reservoir engineering-related research, a component of all geosciences activities, is of particular importance in the context of Hydrothermal Reservoir Research. Three closely related research activities (Brine Injection, Reservoir Definition, and Caldera Reservoir Investigations) are now combined under the more general heading of Reservoir Technology. Scientific investigations, as part of the Salton Sea Scientific Drilling Program, also contribute greatly to the understanding of the behavior of high-temperature hydrothermal convection systems. With the creation of the Geothermal Technology Organization, where geothermal research will be cost-shared with industry, it is anticipated that a number of research topics will be brought to the point where the geothermal industry can rapidly put new technology into use.

OVERVIEW

Program Objectives

The U.S. Department of Energy's (DOE) geothermal research and development programs, administered through the Geothermal Technology Division (GTD), have been organized to achieve two major objectives. First, is to advance the state of the art of the technology to exploit hydrothermal resources. The current emphasis is on geoscience and energy conversion technology R & D that will increase the effectiveness of second generation flash and binary electric systems. The performance goals to meet this objective are:

1. Expand the current knowledge of hydrothermal reservoirs and improve reservoir analysis techniques to reduce the uncertainty of predicting reservoir performance by a factor of 5.

2. Develop techniques for monitoring fluid migration to enable better management of the recharging of hydrothermal reservoirs so as to increase reservoir lifetimes by a factor of 2.

3. Continue laboratory research and field testing of improved drilling components that will reduce the cost of geothermal wells by 20 percent.

4. Continue research to improve the efficiency of binary cycle systems by 30 percent.

The second major objective is to provide the technical basis that will allow industry to make investment decisions in the future regarding the development of unconventional geothermal energy resources -- geopressured Gulf Coast strata containing hot brine and dissolved methane, hot low-permeability rock (hot dry rock), and high-level silicic magma bodies in the western U.S. These "advanced" resource types have the potential for contributing significantly to the regional and national energy picture. The DOE/GTD is pursuing research of these more advanced forms of geothermal energy, ahead of industry, due to the high risks and uncertainty involved with initial development work. The performance goals set for the advanced resources programs are:

1. Geopressured-Geothermal - Development of accurate reservoir performance models and energy extraction technologies capable of 20 percent thermal efficiency.

2. Hot Dry Rock - Develop the necessary technology to extract energy from hot low-permeability rock through a man-made fractured reservoir and maintain the thermal drawdown at less than 10 percent over a 10-year period.

3. Magma - Develop technology to accurately locate and outline a magma body, and extract thermal energy to provide multi-year thermal recovery data.

Organization and FY 1987 Budget

The DOE/GTD geothermal program has been organized functionally into two sub-programs -- Geothermal Geosciences Technology and Geothermal Conversion Technology. The

GEOTHERMAL GEOSCIENCES TECHNOLOGY	GEOTHERMAL CONVERSION TECHNOLOGY
• Hydrothermal Reservoir Research	• Hard Rock Penetration
• Geopressured Resources Research	• Permeability Enhancement
• Hot Dry Rock Reservoir Research	• Hydrothermal Conversion
• Magma Energy Research	• Geopressured Conversion Research
	• Hot Dry Rock Conversion Research
	• Magma Conversion Research

Table 1: DOE/GTD Geothermal Research Programs

Geothermal Geosciences Technology sub-program concerns the technologies used to locate and predict subsurface characteristics of geothermal resources. Conversion Technology includes the technologies dealing with providing access to reservoirs, production and energy conversion. The various component parts of the Geothermal Geosciences Technology sub-program and the Geothermal Conversion Technology sub-program are listed in Table 1, while the FY 1987 budget for all GTD programs is summarized in Table 2.

RESERVOIR ENGINEERING-RELATED RESEARCH

Reservoir Technology

Within the context of the Geothermal Geosciences Technology sub-program, Reservoir Technology, a subset of Hydrothermal Reservoir Research, combines three closely-related research efforts -- Brine Injection, Reservoir Definition, and Caldera Reservoir Investigations. The three are closely coordinated and maintain well-defined goals.

Historically, reservoir analysis procedures from the petroleum industry have been adapted to geothermal resource investigations, and have been successfully applied to reservoirs with intergranular permeability. Use of these same techniques has been less successful in defining geothermal fields dominated by fracture permeability -- the condition that exists in most high-temperature geothermal fields. Experience suggests that the high flow rates required for a successful geothermal project must come from fracture permeability.

The attention given to geothermal reservoir analysis then is to create the necessary "tools" to determine reservoir size and the nature of fluid flow. Today, geothermal reservoirs are better understood, but there are still important areas that need to be investigated. The two most important areas of attention are (1) determining production capabilities of reservoirs, and (2) interpreting the geophysical signature of reservoirs.

In cooperation with industry, new experimental well testing methods have been devised for production and injection modes under the Reservoir Technology Program by researchers at Stanford University, Lawrence Berkeley Laboratory (LBL) and Idaho National Engineering Laboratory (INEL). Flow in fracture networks is being investigated by using laboratory and theoretical models of discrete fractures and stochastically distributed fractures. This work is necessary in order to predict more accurately reservoir longevity and maximum energy recovery.

New geophysical methods and new interpretations of old methods used by the petroleum and mining industries have proven to be useful in characterizing geothermal reservoirs. In addition to the aforementioned organizations, other institutions involved in the development of geophysical methods and interpretation include the U.S. Geological Survey (USGS), Lawrence Livermore National Laboratory (LLNL), and the University of Utah Research Institute (UURI). Emphasis on analyzing geophysical data is directed at producing two- and three-dimensional models of reservoirs, and surveying to locate fractures from the surface and within wells. Experimental methods that are currently being investigated are:

- Passive Seismic Monitoring of Injected Fluid (LLNL)
- Vertical Seismic Profiling (LBL)

VALUE IN $ X 1000	FY 1987 BUDGET
HYDROTHERMAL INDUSTRIALIZATION	2,000
GEOPRESSURED	4,000
GEOTHERMAL TECHNOLOGY DEVELOPMENT	14,150
Hot Dry Rock Research	8,000
Hydrothermal Research	2,950
Hard Rock Penetration Research	1,400
Magma Energy Extraction Research	500
Salton Sea Scientific Drilling Program	1,300
PROGRAM DIRECTION	780
GEOTHERMAL LOAN PROGRAM	72
TOTAL	21,002

Table 2: GTD Program Budget - FY 1987

- Time-Domain Electromagnetic Surveys (USGS & LBL)
- Controlled-Source Audio Magnetotellurics (UURI)
- Deep Magnetotelluric Surveys (UURI & LBL)

Using these geophysical studies in conjunction with structural models, researchers are focusing on determining the location, orientation, extent, and aperture of fractures in reservoirs.

The consequences of injection of spent brine is important to geothermal development because injection must take place in order that adequate reservoir pressures be maintained for production. The resultant pressure pulse is desirable; however, the reduction of reservoir temperature produced by the thermal pulse, and the chemical effects of the injected fluid within the reservoir rock can be detrimental since they reduce the amount of thermal energy recoverable.

In order to better predict the effects of the injection of spent brine, research is being performed on the use of soluble tracers to track injected fluid through the reservoir to the production wells. The research emphasis has been to develop tracers that will (1) maintain thermal and chemical stability at high temperatures, and (2) be detectable in minute quantities in large volumes of fluid. Synthesis and testing of fluorinated hydrocarbons is underway at UURI, and research on activable tracers (excitation by neutron activation) is being done at Stanford.

Numerical modeling of tracer transport in fractures is being carried out at INEL and at Stanford.

All research carried out as part of the Reservoir Definition and Brine Injection program elements is being synthesized into structural geologic models which will be refined by considerations for local geology. Geologic modeling provides a check on the agreement between geophysical and hydrologic data sets. Structural models, which will be necessary for industry engineers to develop strategies for resource development, are being formulated by scientists at LBL and UURI.

Within the program element of Caldera Reservoir Investigations, DOE/GTD is cost-sharing with industry participants several deep thermal gradient test wells within the Cascades volcanic region of the Pacific Northwest. The approximately 4,000 foot wells are intended to provide relevant data concerning the deep thermal regime of the region below the prevailing shallow, cold groundwater system. Recently, three wells were drilled with reported success (Figure 1). Two of the wells, completed near the Newberry Caldera in west-central Oregon, were drilled to depths of 4,000 ft and 4,500 ft. Another well, drilled near Breitenbush Hot Springs, Oregon, was completed to a depth of 4,800 ft. All of the wells have provided the opportunity to obtain meaningful heat flow and temperature gradient information from below the level of influence of the shallow groundwater system. This system has been found to extend downward to depths of roughly 2,000 ft. Drilling at a fourth location, near Crater Lake, Oregon, was suspended due

to loss of circulation and certain requirements imposed by the U.S. Forest Service. Drilling may be resumed at the site next year following treatment of the lost circulation problem.

Downhole studies in the research wells have confirmed the usefulness of Time-Domain EM surveys. The TDEM survey, performed by the USGS, is likely to be a useful technique for determining the subsurface location of the base of the shallow groundwater system in the Cascades region.

Evaluation of the geophysical logs in conjunction with alteration studies of core and cuttings is underway at UURI in an effort to develop log interpretation methods. Emphasis is placed upon (1) formulation of a model for magmatic heat sources in the Cascades; (2) formulation of a model for fracture permeability in the Cascades; and (3) determination of methodologies that can lead to the discovery of buried geothermal systems in the Cascades.

Within the overall scheme of Reservoir Technology, it is essential that communication be maintained with the geothermal industry. Workshops are held to provide a forum for discussions with industry on current field development-related problems. The direction of future Federal cost-shared research is greatly influenced by the results of these discussions.

Salton Sea Scientific Drilling Program (SSSDP)

The SSSDP is a program involving the sampling and testing of a scientific geothermal well that was drilled in the Salton Sea Geothermal Field (SSGF) of California's Imperial Valley (Figure 2). The program is jointly sponsored by the U.S. Department of Energy, the U.S. Geological Survey and the National Science Foundation, and involves Bechtel National, Inc. as the principal contractor, Kennecott Corporation as the resource owner, other industry participants and numerous research institutions. The original objective of the project was to penetrate the "roots" of a known hydrothermal system to obtain fluid and rock samples to be made available to government, academic and industry researchers; test the deeper geothermal zones to evaluate energy potential; and provide for a better understanding of heat and mass transfer processes within a magma-driven hydrothermal system. More than 30 scientific investigations have been funded by the participating agencies.

The well was drilled to depth of 10,564 ft in March 1986, and a reservoir temperature of more than 350°C was measured. During and shortly after the drilling phase, two short-duration flow testing and fluid sampling sessions were conducted and several suites of

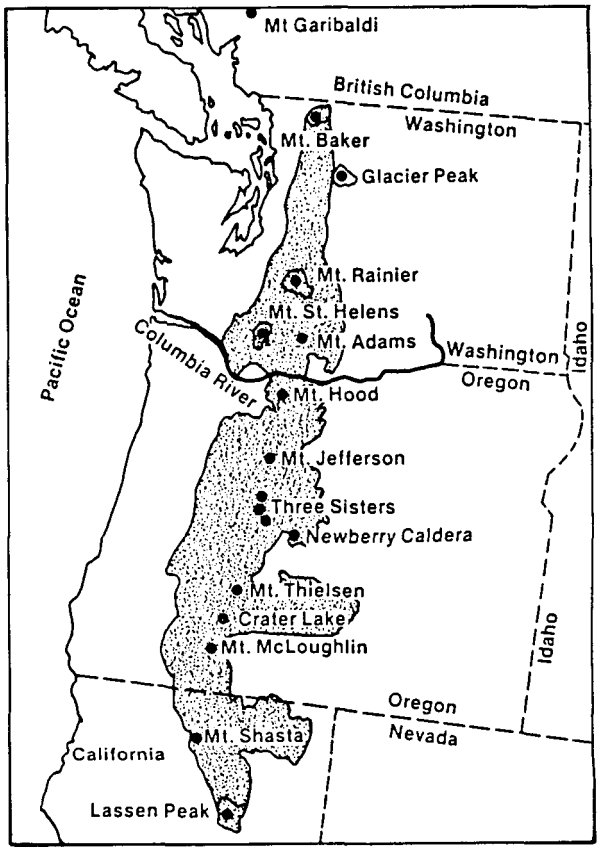


Figure 1: Cascades Regional Setting

commercial and research geophysical well logs were obtained. More than 725 feet of core was recovered and cutting samples were retrieved throughout the drilling process.

Plans for continued studies include the requirement to repair a damaged liner within the well, obtain equilibrium temperature and pressure profiles, and perform a long-term (30-day) flow test in cooperation with Kennecott Corporation. As part of the long-term flow test, the deepest reservoir would be isolated and tested, and high quality fluid samples would be collected an analyzed.

Technological "fall out" from the project has already occurred through the commercial availability of some of the high-temperature (dewared) slickline logging tools. Developed cooperatively by scientists and engineers at Sandia National Laboratories and Los Alamos National Laboratory, the tools include (1) dewared mechanical, pressure, temperature and flow probes designed by Sandia and built by the Kuster Company; (2) an electronic-memory pressure and temperature probe developed by Sandia; and (3) a 2-liter downhole fluid sampler developed by Los Alamos, that may be coupled to a Sandia-built power pack and control unit for non-conducting wireline operation.

Preliminary indications are that the deep hydrothermal system of the SSGF was not fully penetrated by drilling. The fractured, hydrothermal convection system could extend several thousand feet below the bottom of the well.

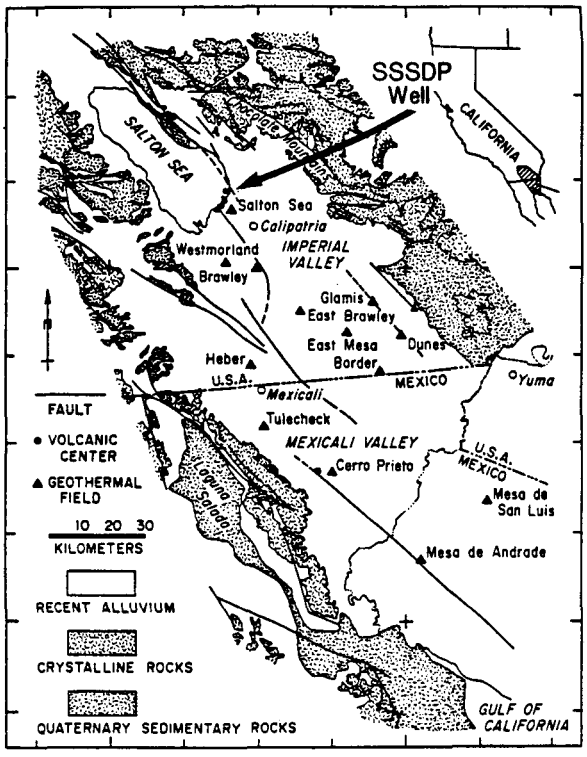


Figure 2: Salton Sea Geothermal Field Regional Setting

Geothermal Technology Organization

As part of DOE's continuation of cooperative research with industry, the objective of a newly established Geothermal Technology Organization, or GTO, will be to foster cost-shared technology development in the areas of geothermal reservoir research and geothermal conversion research. Through the formation and operation of the GTO, non-profit funding arrangements will be made between DOE (represented by INEL) and industry partners to conduct research in all aspects of geothermal energy, exclusive of drilling research.

GTO-funded projects will address research to improve technology for locating, characterizing, developing, and utilizing geothermal resources. Areas of research may include high-temperature instrumentation, reservoir modeling, analysis and interpretation of geophysical data, reservoir stimulation, materials testing, well field design, fluid treatment, and materials compatibility.

In initial meetings with industry representatives, a favorable response has been indicated. The establishment of the GTO will follow the approach taken in establishing the Geothermal Drilling Organization (GDO). A charter and agreement will be established between DOE and the GTO, using GDO documentation as the framework. Projects will be identified, GTO participants determined, and requests for proposals will be issued, selected, and awarded on a cost-shared basis (49% DOE, 51% industry partners). Participation in GTO projects will be required by at least two member companies.

CONCLUSIONS

The DOE/GTD Reservoir Technology Program, the Salton Sea Scientific Drilling Program, and the establishment of the Geothermal Technology Organization are critical Federal efforts to assist U.S. industry in geothermal resource development. The Reservoir Technology Program is assisting industry in developing technology to more effectively locate hydrothermal systems and characterize the commercial developability of those systems. Specific efforts to better understand the nature of high-temperature hydrothermal systems are flow testing and sampling of fluids and rock, and geophysical logging in the SSSDP. The GTO, through cost-shared participation by industry, will provide a means to focus more attention on specific problems hampering field developers. All of these efforts combined result in an improving economic picture for geothermal energy and make U.S. geothermal technology and expertise more attractive in the world marketplace.

PROCEEDINGS, Twelfth Workshop on Geothermal Reservoir Engineering
Stanford University, Stanford, California, January 20-22, 1987
SGP-TR-109

THE U.S. HOT DRY ROCK PROJECT

Robert H. Hendron

Los Aamos National Laboratory
P.O. Box 1663, Mail Stop J979
Los Alamos, New Mexico 87545

ABSTRACT

The Hot Dry Rock geothermal energy project began in the early 1970's with the objective of developing a technology to make economically available the large ubiquitous thermal energy of the upper earth crust. The program has been funded by the Department of Energy (and its predecessors) and for a few years with participation by West Germany and Japan. An energy reservoir was accessed by drilling and hydraulically fracturing in the precambrian basement rock outside the Valles Caldera of north-central New Mexico. Water was circulated through the reservoir (Phase I, 1978-1980) producing up to 5 MWt at 132°C. A second (Phase II) reservoir has been established with a deeper pair of holes and an initial flow test completed producing about 10 MWt at 190°C. These accomplishments have been supported and paralleled by developments in drilling, well completion and instrumentation hardware. Acoustic or microseismic fracture mapping and geochemistry studies in addition to hydraulic and thermal data contribute to reservoir analyses. Studies of some of the estimated 430,000 quads of HDR resources in the United States have been made with special attention focused on sites most advantageous for early development.

INTRODUCTION

The primary objective of the U.S. Hot Dry Rock Program is to develop and demonstrate an economical, commercially usable technology for recovering thermal energy from naturally heated rock at accessible depths in the earth's crust. While other methods are possible in different geologic environments, the Program has so far concentrated on hot crystalline rock of low initial permeability; the use of fluid pressure (hydraulic fracturing) to create flow passages and heat-transfer surface in that rock; and operation of a closed, recirculating, pressurized-water loop to extract heat from the rock and transport it to the earth's surface. Large-scale field experiments are conducted at Fenton Hill in the Jemez Mountains of northern New Mexico, and supporting activities are primarily at Los Alamos National Laboratory. The latter include development of new or improved downhole equipment and instruments, field and laboratory experimental and observational techniques, and analytical and numerical data analyses and modeling procedures. Many of these developments have been found useful in other experimental programs and in a variety of industrial applications.

The technical issues faced in HDR development are challenging. Wells must be drilled to depths where temperatures range from 200 to 350°C, suitable for electricity generation. In regions with favorable geothermal gradients such temperatures are found at depths, of 3 to 5 km, where the minimum component of the in-situ earth stress is likely to be 35 to 100 MPa. One must then fracture the rock formation, and open the fractures so that the permeability remains high and flow resistance is low. Furthermore, large areas of hot rock must be adequately bathed to result in high heat production. At the same time, since all water must be provided extraneously, one must avoid excessive water losses to the country rock surrounding the fractured reservoir. Furthermore, the technology development must assure that potentially damaging earthquakes will not be caused by down hole accumulation of this water. One must also avoid potential geochemical problems, such as scaling of surface equipment with precipitated products of aqueous rock dissolution and corrosion of surface and downhole piping.

The incentive for meeting these challenges is the enormous resource base that HDR energy provides. Unlike hydrothermal reservoirs, which are rarely found, potential HDR reservoirs underlie much of the world. Even if one considers just the high grade resources, i.e., regions with geothermal gradients greater than 40°C/km, the HDR resource base in the U.S. alone represents a thermal energy equivalent to nearly 100 million Megawatt-centuries, about ten times that of coal deposits.

An International Energy Agency Implementing Agreement adopted in 1979 provided for participation by other countries in the Fenton Hill Project of the U.S. Hot Dry Rock Geothermal Energy Development Program which, until then, had been sponsored solely by the U.S. Department of Energy and its predecessor agencies. Under the IEA Agreement, Kernforschungsanlage - Julich GmbH (representing the Federal Republic of Germany) and the New Energy Development Organization (rep-

resenting the Government of Japan) have participated in the Project since 1980. Their participation included partial financial support of the Project, membership in its International Steering Committee, and assignment of scientists and engineers who worked as Staff Members at Los Alamos National Laboratory. German participation in the Fenton Hill Project ended in 1985 and Japanese participation ended in 1986. Informal cooperation as exchange of information continues.

EARLY ACCOMPLISHMENTS

The world's first hot dry rock geothermal energy system was completed at Fenton Hill in 1977, enlarged in 1979 by additional hydraulic fracturing, and operated successfully for more than a year. It was constructed by drilling a hole from the surface to a depth of approximately 3000 m, into granitic rock at about 185°C; producing large hydraulic fractures centered at about 2600 m depth; and directionally redrilling to intersect those fractures. Results of reservoir testing are provided by Dash et al. (1983).

To extend the technology to the temperatures and rates of heat production required to support a commercial power plant, construction of a larger, hotter, system was initiated at Fenton Hill in 1979. This is often referred to as our Phase II system. Two new holes, about 50 m apart at the surface, were drilled directionally, the deeper one to a vertical depth of 4.66 km -- where the rock temperature was 327°C. As was the case in the shallower system described above, it was expected that planar hydraulic fractures produced from these holes would be substantially vertical, with an approximately north-northwest strike. To provide the horizontal separation required to thermally isolate a series of such fractures, the bottom 1000 m of each hole was drilled toward the east-northeast and inclined 35° from the vertical. Figure 1 shows a perspective view. The upper well, EE-3, lies 300 m above the lower well, EE-2, in the slanted interval. Also shown in Figure 1 is a Phase I reservoir well which contains a geophone sonde. This sonde, and similar seismic sensors emplaced in other boreholes, detect and locate the microearthquakes triggered during hydraulic fracturing (House, Keppler and Kaieda, 1985).

FRACTURING THE NEW RESERVOIR

In 1982, hydraulic fracturing experiments were conducted at the deepest depths in the two new wells. Unexpectedly, the stimulated zones produced were three-dimensional rather than planar, inclined rather than vertical, according to location of microseismic events, and did not meet each other or connect the two wells hydraulically. The unexpected non-vertical inclination of the microseismic zone is believed to be related to the presence of a cooling magma body beneath a volcanic

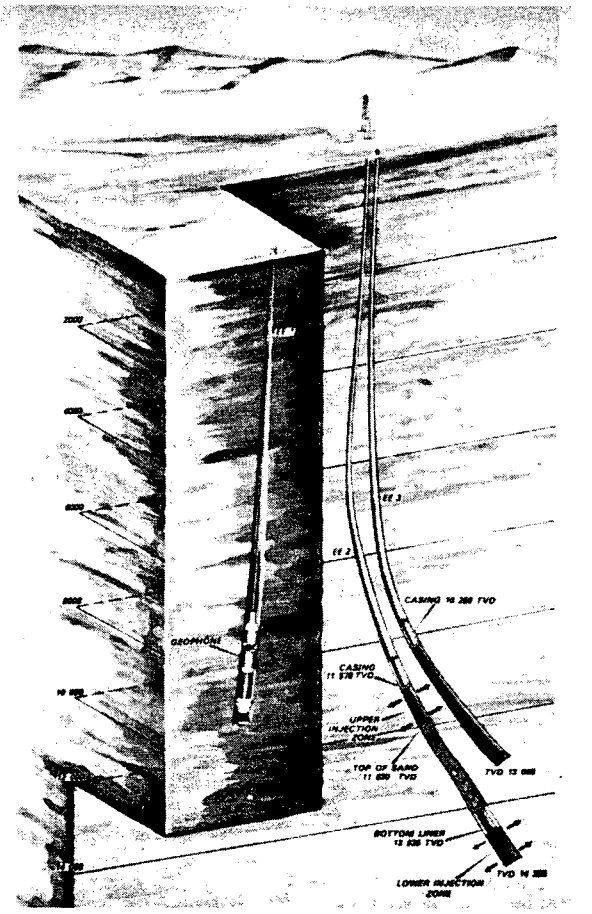


Figure 1. Perspective view of Phase II boreholes and geophone emplaced for microearthquake monitoring during fracturing.

caldera a few kilometers east of Fenton Hill which altered the earth stresses.

In December 1983 a massive hydraulic fracturing operation was conducted in which 21,000 cubic meters of water were injected at 3.5 km in the lower well at downhole pressure and average flow rate of 83 MPa and 100 l/s. Details are provided by Dreesen and Nicholson (1985), and House, Keppler and Kaieda (1985). Figure 2 shows the locations of the microearthquakes induced. The sensitivity of the downhole seismic sensors enabled detection of events with body wave magnitudes as low as -5, on an extrapolation of the relative Richter scale, but Figure 2 shows only 850 high quality events with magnitudes from -3 to 0. Note that seismicity is induced over a rock volume that is about 0.8 km high, 0.8 km wide in the N-S direction, and about 0.15 km thick, or about 0.05 km^3 of stimulated rock volume. This rock volume is 3000 times greater than the water volume injected. House et al. (1985) concluded that:

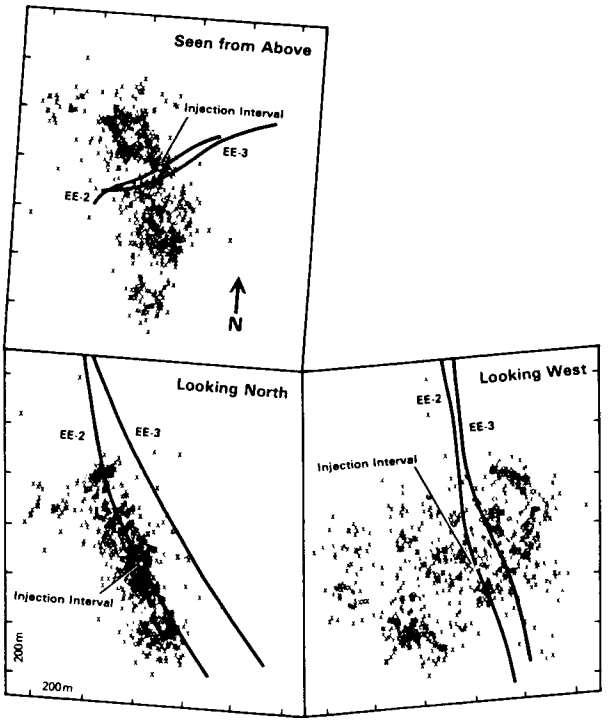


Figure 2. Hypocentral locations of microearthquakes induced by massive hydraulic fracturing in injection well EE-2

1. First motions of the microearthquakes and the fault plane solutions determined from the surface array of seismometers indicated a shear-slip motion, probably along existing rock joints. This suggests that any tensile or oscillatory source mechanism may generate only very weak seismic signals.

2. The finite thickness, 0.15 km, of the zone of seismicity and its spatial growth imply the creation of a zone of joint stimulation, rather than a single fracture.

Fehler (1984) performed spectral analysis of many of the microearthquake coda, and found power spectral densities consistent with usual earthquake mechanics, i.e., shear slippage. Corner frequencies were of the order of 300 Hz, and based upon the work of Brune (1970), Fehler found that the characteristic dimension of the rock surface mobilized for each shear-slip event was of the order of 10 m, comparable to the spacing of the major joints observed in well surveys.

The above results indicate a fracturing mechanism which is inconsistent with conventional theories of hydraulic fracturing (Hubbert and Willis, 1957; Daneshy, 1973) which predict the propagation of a single fracture caused by tensile failure of the rock. However, the HDR results are consistent with Lockner and Byerlee (1977), who observed a transition from tensile to shear fracturing when low flow rates were injected into laboratory rock specimens; and our observations were confirmed at the British Hot Dry Rock reservoir in Cornwall where it was observed (Pine and Batchelor, 1984) that fracturing occurred as a zone of multiple fractures, and that shear slippage along existing joints was the dominant mechanism. Because these joints are pre-existing natural fractures, it is perhaps inappropriate to refer to the process of forcing water into them as "fracturing;" "stimulation" is used instead in the remainder of this report.

The stimulation results just discussed, and the important role played by shear, rather than tension, have important implications not only for HDR programs, but also for stimulation of oil and gas reservoirs. So important is "shear stimulation" that it is a key research issue in the U.S. and HDR projects, and serves as an important basis for collaborative research. For example, the FRIP code (Fluid Rock Interaction Program), developed for the British HDR project by Peter Cundall, is also used at Los Alamos, and recent improvements have been cost-shared by both HDR projects.

ACHIEVING HYDRAULIC COMMUNICATION

Despite the huge volume of water injected in the lower well during the 1983 massive hydraulic fracturing, the stimulated zone did not propagate into the vicinity of the upper well, as shown in Figure 2, and no hydraulic communication between the two wells was observed. Another large fracturing operation was conducted, this time in the upper well, but the two stimulated zones did not overlap and again no communication was observed. Consequently, in March of 1985 the upper well was sidetracked at a depth of 2.9 km, and directionally drilled as shown in Figure 3 through the fracture zone associated with the lower well. This redrilled well is referred to as EE-3A.

Precursor signs of an impending connection were observed when water flowed into the redrilled well when the other well was pressurized to 12 MPa. It was decided to improve the hydraulic communication quality of joints near 3.6 km by stimulating them with high pressure. This was accomplished by setting a specially developed, high temperature packer (Dreesen and Miller, 1985) at a depth of 3.52 km, where the drill hole was reasonably smooth, and then pumping water into the entire open hole interval between the packer and the bottom of the hole, which was located at 3.72 km at this time. The physical situation is depicted in Figure 3. A volume of 1,670 m^3 was injected, primarily at rates of 15 to 27 l/s, and at downhole pressures ranging from 66 to 75 MPa. A rapid rise in pressure occurred at EE-2, and two hours after the commencement of pumping in EE-3A, EE-2 was put on

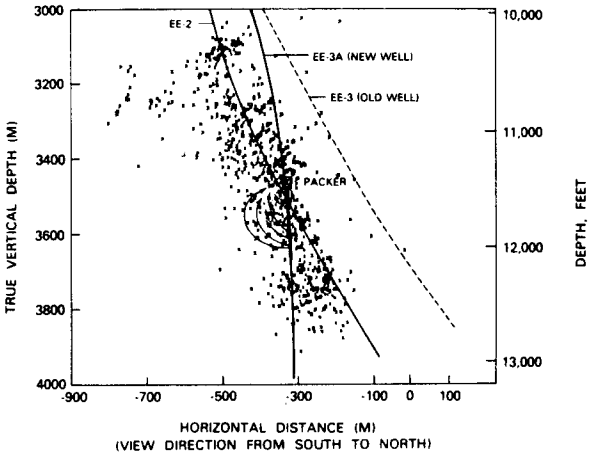


Figure 3. Elevation view of reservoir, looking North. Packer shown allowed supplementary stimulation of EE-3A, which resulted in low flow resistance connection between EE-2 and EE-3A. The flow paths indicated are inferred from joint locations determined from a temperature survey in EE-3A.

production and water flowed out. At first the outflow rate was small, but by repetitively surging the well i.e., by shutting it in for a while, then quickly venting it, the outflow rate was steadily increased, and at the end of the test it attained a value of 10 l/s. A post-connection temperature survey taken in EE-3A on May 30 showed that several new joints had been stimulated which served as flow entries from EE-3A to the reservoir. Figure 3 portrays the potential flow paths, which appear short in this elevation view, but bear in mind that EE-2 and EE-3A are horizontally separated by 150 m at the depth at which the two wells appear to intersect.

Following this successful connection the redrilling continued and three additional stimulations were conducted with open hole packers. The second stimulation was conducted very deep, at 3.83 km, and failed to result in additional hydraulic communication and with flow indicated going down from the bottom of the borehole. The third stimulation occurred at 3.65 km, a depth about midway between the successful and unsuccessful ones, and another hydraulic connection was achieved. In February 1986 the final stimulation was attempted, at 3.76 km, but little evidence of hydraulic communication was observed.

In summary, the two shallower, and successful, stimulations were more centrally located within the zone of seismicity induced during the 1983 massive stimulation of EE-2. The injection depths of the two deeper, unsuccessful, stimulations were still within, but closer to the perimeter of, the 1983 seismic zone. While the seismic zone induced by these two unsuccessful stimulations tended to grow down and away from the 1983 seismic zone, nevertheless there was sufficient overlap of the zones that hydraulic connection of the wells would have been expected. This illustrates the complex nature of stimulation of jointed rock - one cannot expect to encounter high permeability stimulated rock everywhere in the seismic zone. Instead, discrete, and often well spaced, natural joints are stimulated. Hence, one needs to examine carefully the complete three dimensional nature of the seismic zone, and track its development with time. Of particular promise are the recent developments at both the British and US HDR programs of techniques for detecting lineaments in the seismic zones which may reveal the presence of those natural fractures most successfully stimulated.

TESTING THE NEW RESERVOIR

In March and April of 1986 the new reservoir was readied for preliminary testing by cementing-in a liner in well EE-3A; finishing the surface piping system; readying the water-to-air heat exchanger used previously for the Phase I reservoir; and hiring a service company to pump water (injection capability of 30 l/s and 35 MPa).

The Initial Closed-loop flow test was begun May 19, 1986 and completed June 18, 1986. Cold water was injected into EE-3A, and hot water produced from EE-2. The hot water was cooled to 20°C in the heat exchanger before being reinjected. Major flow parameters are presented in Table I, and these are compared with values measured in the enlarged, earlier Phase I reservoir and the British program.

COMPARISON OF THREE HDR RESERVOIRS AFTER ONE MONTH OF OPERATION

	FENTON HILL		
	ENLARGED PHASE I RESERVOIR	CURRENT PHASE II RESERVOIR	ROSEMANOWES CORNWALL, U.K.
DEPTH OF RESERVOIR (m)	2,800	3,560	2,400
TEMPERATURE OF RESERVOIR (°C)	195	240	85
MODAL VOLUME (m^3)	160	350	270
SURFACE TEMPERATURE (°C)	135	191	76
THERMAL POWER (MW)	3	9	1
PRODUCTION FLOW RATE (l/s)	7	13	4
INJECTION WELL PRESSURE (MPa)	10	30	4
CORRECTED IMPEDANCE (GPa s/m^3)	1.7	2.2	1.0
WATER LOSS RATE AT 30 DAYS (l/s)	1.1 (16%)	6.0 (33%)	0.4 (10%)

During the course of the 30 day test the flow impedance of the reservoir declined, and at the end was about half its initial value.

Furthermore, the final impedance was nearly equal to that measured in the Phase I reservoir after a comparable period of time, despite the fact that, on average, the effective confining stress acting to close joints is over three times higher in the new reservoir. Two tracer experiments were conducted during the 30 days, and the modal volume, a Table I characteristic measure of the void volume of major fractures and joints, increased from 270 to 350 m^3. This is quite promising, as a reduction of impedance could be the result of flow channeling, i.e., the tendency for the water to sweep through fewer fractures of larger aperture, resulting in smaller modal volumes and heat production, rather than the increased modal volume actually observed.

The water loss rate, expressed as a fraction of the injected flow rate, was higher than the Phase I value after a comparable period, but this may be an artifact of our constant experimentation during the 30 days of testing. Many shut-in experiments were conducted, as well as changes of injection flow rate and production well pressure, thus precluding the attainment of quasi-steady state water losses. In addition we attribute this short-term loss rate to the large highly fractured volume of the several fracture and stimulation efforts and the increasing volume due to high injection pressures maintained and evidenced by microseismic activity.

Seismicity during this experiment was quite low, and the largest event registered about 0.4 on the extrapolated Richter body wave scale. Observation of coupon test specimens indicate very low corrosion (15 mils per year or 0.38 mm/yr). Finally, this short test was designed to measure hydrological and volume properties, and so was never intended to be run long enough to measure potential thermal drawdown. A test of about one year duration is presently scheduled to begin in 1988.

SUPPORTING ACTIVITIES

In addition to the drilling and stimulation activities described above, the following activities have continued. These activities are expected to have significant impact on the continuing development of HDR technology.

1. In a cooperative program with Westfalische Berggewerkschaftskasse of Bochum, FRG, a high-temperature borehole acoustic televiewer has been designed and fabricated, and will be field tested at the end of February 1987. A televiewer measures the travel time of ultrasonic pulses reflected from the borehole wall to map irregularities in the reflecting surface -- such as natural or hydraulic fractures -- with a high degree of resolution. In addition to a number of acoustic and thermal design improvements, this new instrument is of modular construction to facilitate field assembly and maintenance, and incorporates a downhole microprocessor to control data collection and produce a digital signal for transmission to the surface.

2. In addition to conventional analyses of microseismic data collected during pressurization tests, special studies have been made of low-frequency, long-period events that occur early in pressurization, which may represent tensile fractures. Downhole-tool coupling phenomena are being investigated to improve design of geophone sondes. There has been further improvement of the hodogram technique of seismic-event location, and software has been developed for a Masscomp computer that has greatly increased the speed and accuracy of on-line event location during stimulation and flow experiments. This system will be employed for a more comprehensive look at earlier data. Good progress has been made in correlating fault-plane solutions with the locations of seismic events.

3. An active seismic interrogation method has been developed that uses an acoustic source transmitter that "scans" a section of one wellbore, while a receiver is stationed in the adjacent wellbore. The transmitter houses a 3J magnetostrictive source that operates at the frequency of 8.5 kHz. The transmitter can be triggered at rates of up to 5 pulses per second. An accelerometer, mounted coaxially with the magnetostrictive source, provides a zero time for each pulse. The receiver consists of a piezoelectric transducer that is tuned for maximum response at the transmission frequency. The receiver gain can be controlled automatically downhole or manually from the surface control unit. The characteristics of the medium through which the acoustic vibrations pass are deduced from the character of the received signals and from their arrival times at the detector. The distance between two boreholes can be measured with considerable accuracy, and the presence of fluid-filled fractures in the formation can be determined.

4. Recent reservoir-engineering activities have included numerical and analytical studies of fluid flow in deformable joints; estimations of fracture apertures from hydraulic data and of fractured-reservoir size from the results of hydraulic-fracturing experiments; and modeling of thermal effects during a variety of pressure-transient tests.

5. Geochemical studies have included investigations of the degradation of sepiolite drilling muds at high temperatures, corrosion and calcite deposition in surface-system components, a variety of chemically reactive tracers, and the adsorption of such tracers on rock surfaces. The reactive tracer technique will use the extreme temperature dependence of chemical reaction rates to map the progress of the thermal front in an HDR reservoir during long term energy extraction. Derivatives of bromobenzene are excellent candidates for re-

active tracers in high temperature geothermal reservoirs from 200-300°C.

6. Corrosion resistance of the logging cable accounts for many of the limitations to work in geothermal boreholes. Tests are in progress to determine effects of brines where sulfides and chlorides are present. Tests are also planned to determine work hardening of tubular cores used in available magnesium oxide-insulated cables. More studies are needed to determine cooling methods when retrieving cables from very hot wellbores. In addition, development of high-temperature electronics using special devices such as integrated thermionic circuits will contribute to reliable operation of logging tools up to temperatures of 500°C.

7. The Electric Power Research Institute has undertaken an independent study of the economic potential of commercial hot dry rock energy systems.

CONCLUSIONS

Seismic monitoring provides a view of fracture systems which is unobtainable by any other means at the depths of interest here. These seismic observations, supported by results in Britain as well as from the rock mechanics lab, indicate that injecting low viscosity fluid, like water, into jointed rock results in multiple joint stimulation caused by shear-slippage, not the single tensile fracture of conventional theory. Guided by microearthquake maps, an existing well was sidetracked and redrilled into the 0.05 km^3 stimulated zone created by earlier massive hydraulic injections at EE-2. The redrilled well encountered zones of permeability induced by the early stimulation but it required supplementary stimulation before good flow communication could be established between the two wells. Two of the four supplementary stimulations were successful in making hydraulic connections, and the new reservoir appears promising. In May and June of 1986 we completed an initial closed-loop flow test to acquire preliminary information on reservoir behavior, and as shown in Table I, the new reservoir represents a considerable improvement over the old Phase I reservoir. A long term test is planned. Armed with these results, as well as complementary results in Europe and Japan, the stage should be set for successful commercial adaptation of HDR technology.

REFERENCES

1) Brune, J.N., Tectonic Stress and the Spectra of Seismic Shear Waves from Earthquakes, J. Geophys. Res., 75, 4997-5009, 1970.

2) Dash, Z.V., H.D. Murphy, R.L. Aamodt, R.G. Aguilar, D.W. Brown, D.A. Counce, H.N. Fisher, C.O. Grigsby, H. Keppler, A.W. Laughlin, R.M. Potter, J.W. Tester, P.E. Trujillo, and G.A. Zyvoloski, Hot Dry Rock Geothermal Reservoir Testing: 1978 to 1980, J. Volcan. Geotherm. Res., 15, 59-99, 1983.

3) Dash, Z.V., D.S. Dreesen, F. Walter, and L. House, The Massive Hydraulic Fracture of Fenton Hill HDR Well EE-3, Geothermal Resources Council Annual Meeting, Kona, HA, August 26-30, 1985.

4) Dreesen, D.S. and J.R. Miller, Open Hole Packer/Running Procedure for Hot Dry Rock Reservoir Testing, these proceedings.

5) Dreesen, D.S. and R.W. Nicholson, Well Completion and Operation for MHF of Fenton Hill HDR Well EE-2, Geothermal Resources Council Annual Meeting, Kona, HA, August 26-30, 1985.

6) Daneshy, A.A., On the Design of Vertical Hydraulic Fractures, J. Petr Tech, Jan., 1973.

7) Fehler, M., "Source Properties of Microearthquakes Accompanying Hydraulic Fracturing" EOS, (Trans. of Amer. Geophys. Union), 65, 1011, 1984.

8) House, L., H. Keppler and H. Kaieda , Seismic Studies of a Massive Hydraulic Fracturing Experiment, Geothermal Resources Council Annual Meeting, Kona, HA, August 26-30, 1985.

9) Hubbert, M.K. and D.G. Willis, Mechanics of Hydraulic Fracturing, Trans. A.I.M.E., 210, 153-168, 1957.

10) Lockner, D., and Byerlee, J.D., Hydrofracture in Weber Sandstone at High Confining Pressure and Differential Stress, J. Geophys. Res., 82, 2018-2026, 1977.

11) Nicholson, R.W., D.S. Dreesen and W.C. Turner, Improvement of Tubulars Used for Fracturing in Hot Dry Rock Wells, Geothermal Resources Council Annual Meeting, Reno, NV, August 26-29, 1984.

12) Pine, R.J. And A.S Batchelor, Downward Growth of Hydraulic Stimulation by Shearing in Jointed Rock, Int. J. Rock Mech. Min. Sci and Geomech., 1984.

PROCEEDINGS, Twelfth Workshop on Geothermal Reservoir Engineering
Stanford University, Stanford, California, January 20-22, 1987
SGP-TR-109

MAGMA ENERGY EXTRACTION

J. C. Dunn, A. Ortega, C. E. Hickox, T. Y. Chu, R. P. Wemple
Sandia National Laboratories
Albuquerque, NM 87185

R. F. Boehm
University of Utah
Salt Lake City, UT 84112

ABSTRACT

The rate at which energy can be extracted from crustal magma bodies has an important influence on the economic viability of the magma energy concept. Open heat exchanger systems where fluid is circulated through solidified magma offer the promise of high energy extraction rates. This concept was successfully demonstrated during experiments in the molten zone of Kilauea Iki lava lake. Ongoing research is directed at developing a fundamental understanding of the establishment and long term operation of open systems in a crustal magma body. These studies show that magma solidifying around a cooled borehole will be extensively fractured and form a permeable medium through which fluid can be circulated. Numerical modeling of the complete magma energy extraction process predicts that high quality thermal energy can be delivered to the wellhead at rates that will produce from 25 to 30 MW electric.

INTRODUCTION

Magma is a huge potential resource. The work of Smith and Shaw (1978) resulted in an estimate for the U. S. of 50,000 to 500,000 quads contained in magma at temperatures above 600°C and at depths shallower than 10 km. Before industry can evaluate the future economic viability of magma energy, several key areas require further study and technology development.

The Magma Energy Extraction Project, initiated by the Geothermal Technology Division of DOE during FY 84, is assessing the engineering feasibility of extracting high quality thermal energy directly from crustal magma bodies. This program follows a seven year study that demonstrated the scientific feasibility of the magma energy concept [Colp (1982)]. At the conclusion of the previous project, many of the energy extraction concepts were demonstrated by drilling into the molten zone of Kilauea Iki lava lake, emplacing energy extraction hardware, and operating the system for a period of five days [Hardee et al. (1981)].

The magma project is organized to address: (1) resource location and definition, (2) drilling, (3) magma characterization and materials compatibility, and (4) energy extraction. We have an ultimate objective of drilling into an active crustal magma body and conducting an energy extraction experiment. The location for this experiment has been selected in Long Valley caldera, California, where magma drilling targets have been identified.

A magma energy technology of interest to this conference is energy extraction due to its similarities with reservoir engineering in that both must treat fluid flow and heat transfer in fractured media. The rate at which electricity can be generated from a magma well is a major factor in determining its economic viability. However, determination of such rates is complex because of the uncertainties in the nature and properties of in situ magma bodies, and the complexity of potential heat exchange processes within the magma. Our approach has been to perform fundamental engineering analyses in conjunction with phenomenological experiments in order to develop conceptual models of the magma heat exchanger and obtain estimates of potential rates of energy extraction. In this paper, we briefly summarize past and recent research in the area of energy extraction.

PRIOR ANALYSES

Magma is a multicomponent material that usually resides in the crust at temperatures near or below its liquidus. At these temperatures, the material is a mixture of liquid and crystalline phases and behaves like a high Prandtl number, non-Newtonian fluid. Much of the early work was directed at evaluating natural convection heat transfer rates in magma, both analytically and experimentally. Heat flux measurements were made in degassed basaltic lava at temperatures near and below the liquidus and were in excellent agreement with

This work was supported by the U. S. Department of Energy at Sandia National Laboratories under Contract DE-AC04-76DP00789.

calculations based on a boundary-layer analysis for a high Prandtl number, non-Newtonian fluid. [Hardee and Dunn (1981)]. Experiments were also performed at in situ conditions of temperature, pressure, and volatile content, [Dunn et al. (1983)], and confirmed predictions that significantly higher heat transfer rates are obtained at in situ conditions where volatiles have an important effect on viscosity.

Hardee (1981) used boundary-layer analysis to predict thermal energy extraction rates for several magma compositions assuming a "closed" heat exchanger system where fluid is contained within a pipe and does not directly contact magma. Hardee's calculations show very high heat transfer rates (resulting in 20 to 80 MWth/well) for basaltic magma which has relatively low viscosity. Rhyolitic magma, with much higher viscosity, was predicted to offer lower energy extraction rates, on the order of 4 to 19 MWth per well.

An alternative "open heat exchanger" concept for magma energy extraction uses direct fluid/magma contact. Analyses by Dunn (1983) showed that thermal stresses created in magma solidifying around a cooled borehole would be sufficient to cause fracturing. By circulating a heat transfer fluid through the solidified and fractured magma, greatly increased surface area and energy extraction rates could be achieved. The concept was tested in the 1981 Kilauea Iki experiments. During a five day period, energy extraction rates were found to increase with time (indicating growth of the fractured region) reaching a value more than 10 times the expected value for a closed heat exchanger in the same borehole [Dunn (1983)].

The present magma energy program is focused on silicic magma systems which are most representative of high-level magma bodies in the crust and the type expected at most western U. S. sites. An economic analysis of magma power generation [Carson and Haraden (1985)] indicates that closed heat exchangers can have only limited application in silicic magmas. However, open, direct contact heat exchanger systems operating at depths up to 6 km are shown to be roughly competitive with existing sources of energy for power generation. As a result, our recent work in energy extraction is concentrated on extraction processes using fluid circulation through solidified/fractured magma.

THE OPEN HEAT EXCHANGER

Figure 1 shows our current conceptual representation of a single well during steady operation in an open heat exchanger mode. The well is cased above the magma chamber and the injection tube is surrounded by a fractured, solidified region whose radial extent is determined by the rate of energy extraction. There is an intermediate transition zone which behaves as a plastic solid and does not support fracturing. Because of heat transfer to the exchanger, large scale natural convection is induced within the chamber with magma flowing down the outer solidification boundary.

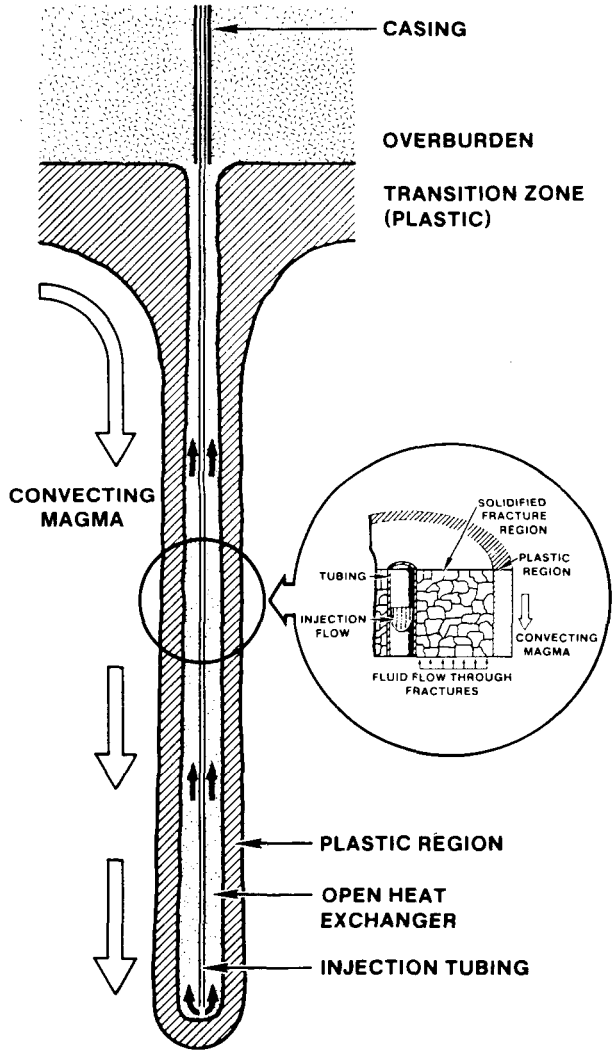


Figure 1. Conceptual representation of open heat exchanger with fluid flow through fractured, solidified magma.

The formation and operation of an open heat exchanger, as presently envisioned, involves numerous complex processes. Our current research approach follows two paths: one, research into the formation of a fractured, solidified region suitable for heat exchange, and two, analysis of the local heat exchange processes within the fractured mass and in the external convecting magma. The remainder of this paper summarizes recent activities in these two areas.

Thermal Fracturing of Solidfying Magma

Dunn (1983) and Wemple and Longcope (1986) developed theoretical models to describe thermal stress fracturing in a solidified magma region surrounding a borehole. The models only consider stresses caused by temperature gradients in a solid annulus. Secondary fracturing due to flow in the initial fractures or pressure driven hydraulic-type fracturing are not included. The analyses predicts vertical and horizontal fractures even for large overburden pressure. Wemple and Longcope (1986) show that horizontal fractures should predominate and give estimates for their spacing and aperture. For a basaltic lava and wellbore parameters typical of those for the Kilauea Iki experiment, a fracture spacing of 1 cm with aperture of 0.1 mm is obtained. The analysis also predicts that the fractures will extend almost to the outer limit of the solidified region.

An experimental program was recently begun to examine the qualitative and semi-quantitative features of the initiation and propagation of thermal-stress fractures in solidifying magma simulant materials. Initial thermal stress fracturing experiments were performed in thick-walled Sandia "S" glass cylinders (6.35 cm OD x 10.16 cm L) which were cast, annealed, and axially cored. The cylinders were fitted with a 304 SS tube to allow injection of air or water into the center bore after preheating the cylinders to initial temperatures ranging from 200 to 400°C. Figure 2 illustrates a typical fractured thick-walled cylinder which was preheated to 200°C then cooled at the inner bore with water at 20°C. Extensive fracturing of the specimen occurs within seconds after cooling is initiated. The fracture distribution is in general agreement with theoretical predictions. In accordance with the theory, both horizontal and vertical fractures were produced and no cylindrical fractures occurred. At both 200 and 400°C, there were substantially more horizontal than vertical fractures.

Several laboratory experiments have been performed to qualitatively evaluate the processes by which a simulant glass solidifies and fractures from an initially molten state under the influence of a cooled inner boundary. The phase change from a molten to solid state will occur at a rate which is governed by the rate at which heat is removed from the inner boundary. Solidification will be slow compared to the speed at which fractures propagate through the solid, hence, fractures will initiate and propagate rapidly into the solid phase until thermal stresses are relieved. In the melt solidification experiments, an axial cooling flow tube was pre-cast in an "S" glass cylinder which was then re-melted in an induction furnace at approximately 750°C. Water at room temperature was allowed to flow through the center tube to chill the melt at a controlled rate. Figure 3 shows a cross-section of a sample that was chilled rapidly. The rapid cooling of the tube resulted in a glassy phase nearest the tube surrounded by a region of mixed glass and crystalline phases. The inner glass phase is extensively fractured but its radial extent is limited. The outer region has fewer fractures, but extensive interconnection between fractures was observed. In this experiment the outer melt zone was maintained at 1000°C and the cooling tube wall was calculated to be no greater than 150°C.

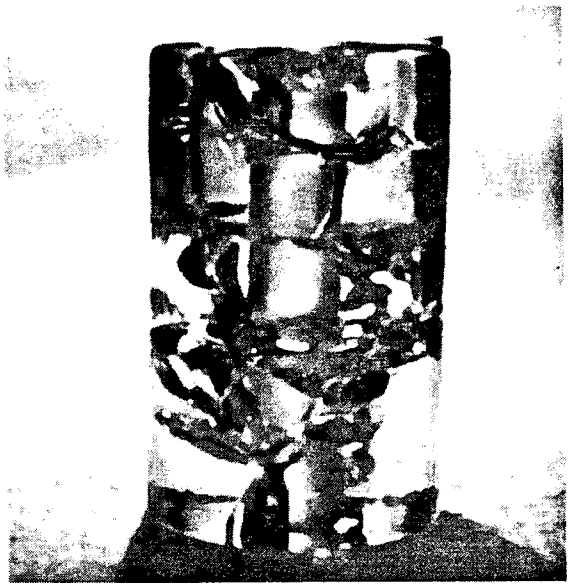


Figure 2. Thick walled glass cylinder thermally fractured at 200°C.



Figure 3. Cross-section of pre-melted glass cylinder after solidification induced by cooling flow through center tube.

Secondary fracturing processes, not yet evaluated, may play a significant role in the formation of the fractured region. Fluid in direct contact with the cooled inner surface will flow into the primary fractures as long as new fractures are propagated. Fluid flow will have two effects on the rate and extent of fracturing. First, heat transfer from the primary fracture walls to the flow will introduce temperature gradients that tend to produce secondary fractures normal to the principal fractures. Second, fluid pressure in the primary fracture may exceed the confining pressure on the solidified region such that the fluid will exert a net hydraulic pressure on the fracture walls and enhance the propagation. Our present approach is to first clarify understanding of the fracture mechanics in a homogeneous medium using simulant materials, then introduce secondary effects one at a time and assess their importance.

Heat Transfer in the Open Heat Exchanger

As a first approximation to heat transfer within the open direct contact heat exchanger, the solidified and fractured region surrounding the borehole is modeled as a porous medium with local thermal equilibrium between the solid and fluid phases. The porous medium can be completely characterized by specification of its effective permeability, K, and the effective saturated thermal conductivity, k. Order of magnitude estimates for the permeability were obtained using the cubic fracture model of Snow (1968) with the fracture geometry predictions of Wemple and Longcope (1986). Due to the small volume of interstitial fluid, the effective thermal conductivity was taken as that for solidified magma. Hardee (1981) presents data showing typical values on the order of 3 W/m-K for rhyolitic magmas.

Flow and heat transfer within the porous annular region is, at this level of approximation, described by the standard Darcy formulation for porous media. The conservation equations in differential form are given as:

$$\text{mass:}\quad \frac{1}{r}\frac{\partial}{\partial r}(rv_r) = \frac{\partial}{\partial z}(v_z) = 0 \qquad (1)$$

$$\text{momentum:}\quad v_r = -\frac{K}{\mu}\frac{\partial}{\partial r}(p + \rho gz) \qquad (2)$$

$$v_z = -\frac{K}{\mu}\frac{\partial}{\partial z}(p + \rho gz) \qquad (3)$$

$$\text{energy:}\quad v_z\frac{\partial T}{\partial z} + v_r\frac{\partial T}{\partial r} = \alpha\nabla^2 T \qquad (4)$$

where r and z are the radial and axial directions, respectively, K is the permeability, μ is the fluid viscosity, α is the effective thermal diffusivity and ρ is the fluid density.

For an annular porous region the lower limit on the local mixed mean Nusselt number is found under the conditions of fully-developed slug flow, and fully-developed temperature profiles. For an annulus in which the outer wall temperature is held constant at T_o and the inner wall temperature at T_i, the fully-developed temperature profile is the same as the conduction profile, and the mixed mean Nusselt number is given by:

$$Nu_i = \frac{2(1-r^*)}{r^*\ln r^*\left(\frac{1}{1-r^{*2}} + \frac{1}{2\ln r^*}\right)} \qquad (5)$$

$$Nu_o = \frac{2(1-r^*)}{\ln r^*\left(1 - \frac{1}{1-r^{*2}}\right) - \frac{1}{2}} \qquad (6)$$

where $r^* = r_i/r_o$. Similar expressions may be found for the case of uniform heat flux walls by using linear superposition of partial solutions for heating on one wall. These are omitted here for brevity.

Various effects can alter the heat transfer within the porous annulus and significantly affect the net energy extraction. Among the most important considerations are developing flow effects and local buoyancy. The developing thermal field for fully-developed slug flow in an annular region, may be found by direct analogy to the problem of transient cooling of an annular-shaped billet. For the case of an insulated inner boundary and a constant temperature outer boundary, the solution for the temperature field is shown by Carslaw and Jaeger (1959). Two results from this analysis are of interest. First, the mixed mean Nusselt number in the entry region is much higher than its asymptotic value. Second, preliminary calculations indicate that fully-developed thermal conditions may not be attained for the range of Peclet number and annulus aspect ratios of current interest. The net result is that the overall heat transfer coefficient for the annulus may be from two to five times higher than the conservative fully-developed estimate.

Local buoyancy effects can become important in determining the overall heat transfer if temperature gradients within the annulus are severe. The relative importance of the two mechanisms can be found by inspection of the ratio of the local forced flow Peclet number, Pe, and the local Rayleigh number, Ra, which is indicative of the local buoyancy. Using geometry and property data expected for operation of an open direct contact heat exchanger in magma, the above dimensionless groups lie within the range: $0.18 < Ra/Pe < 4.0$. At the low end, buoyancy effects are negligible, but for Ra/Pe on the order of 1.0, local buoyancy effects may substantially affect the heat transfer. To evaluate this effect, we are currently performing full

numerical solution of equations [1-4] using the finite element code MARIAH [Gartling and Hickox (1982)] in a cylindrical annulus with both constant temperature and constant heat flux boundary conditions. An example of this effect can be seen in Figures 4 and 5 which give calculated results for an experimental facility at the University of Utah. Figures 4(a) and 4(b) show streamlines in the annular region with the outer boundary at constant temperature, and an insulated inner boundary. Figure 4(a) is for pure forced convection and the flow is very nearly a uniform slug flow. For non-negligible local buoyancy effects, Fig. 4(b), flow is entrained towards the heated

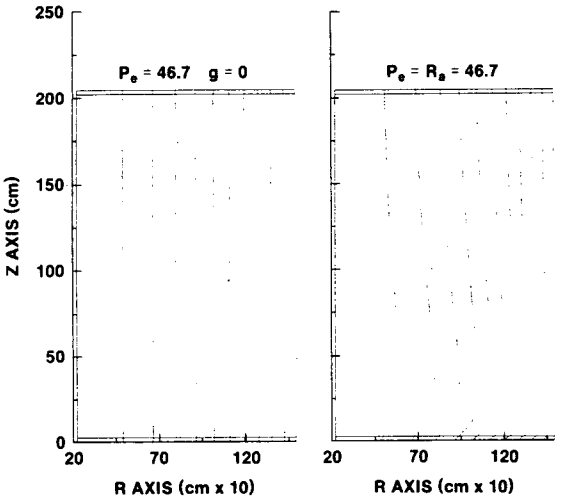


Figure 4. Streamlines--U. of Utah experiment simulation: (a) Forced slug flow, (b) buoyancy-assisted flow.

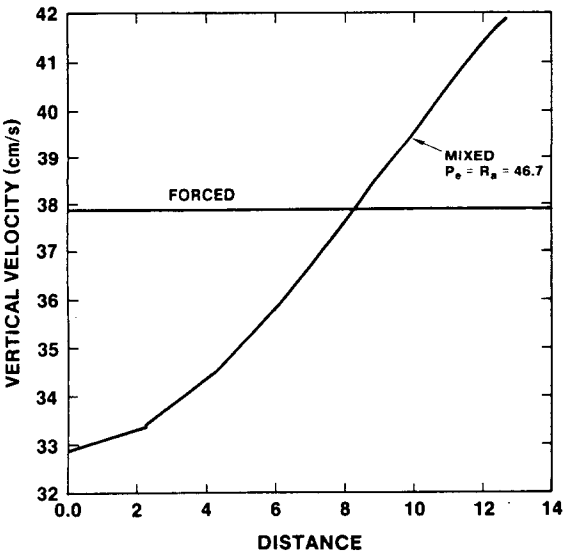


Figure 5. Vertical velocity profiles at horizontal midplane--U. of Utah experiment simulation.

boundary in the lower part of the annulus resulting in increased mass flow within the thermal boundary layer. The upward velocity through the annulus at the horizontal midplane is shown in Fig. 5. The net result of this buoyancy-assistance is that convection near the heated boundary may be enhanced above that for forced slug flow. The degree of enhancement depends on the boundary conditions, the ratio of Ra/Pe, and the annulus geometry.

To complement the numerical studies of the porous open heat exchanger R. F. Boehm is conducting experiments in buoyancy-assisted porous media flows at the University of Utah. The experimental apparatus uses an annular space formed between two concentric pipes having diameters of 1.25 and 11.5 inches. The space is filled with 1mm ceramic microshperes to form a porous bed. Water can be injected at the base either in a uniform slug flow from a supply header, or as a source flow at the base of the center tube. The outer walls are maintained at uniform temperature. The temperature distribution in the bed is measured at seven axial locations. Experiments are currently underway which will cover a wide range of conditions in both forced and buoyancy-affected flows.

NUMERICAL SIMULATION OF SINGLE WELL ENERGY EXTRACTION

Hickox and Dunn (1985) used simplified models to obtain first order estimates of the complete energy extraction process including heat transfer in counterflowing fluids from the surface to the magma zone, with possible heat loss to the overlying formation. They made several important observations. Reasonable hole diameters, on the order of 0.194 m in the magma zone were shown to be sufficient for large energy extraction rates. Using concentric pipes with fluid flow down the annulus and return through an insulated core, the fluid receives a net heat gain from (not a loss to) the formation above a magma body. A relatively modest insulation thickness, on the order of 1.5 cm, was found to provide good isolation between the hot return fluid and cold injection fluid. Finally, it was observed that for a given magma heat transfer coefficient, an optimum flow rate exists that maximizes electric power production. For the open heat exchanger, which was assumed to have an overall heat transfer coefficient ten times that for the closed exchanger, optimum flow rates lead to predicted energy extraction rates of about 25 MW electric.

A numerical code called MAGMAXT has recently been developed to simulate the flow of compressible, homogeneous water/vapor within the well and heat exchanger with heat transfer to and from

the convecting magma and the overlying formation. The code allows arbitrary specification of a contiguous flow path through regions such as tubing, concentric pipe annulus, or heat exchanger. Heat transfer to or from the fluid stream is allowed through the specification of overall heat transfer coefficients between the counterflowing flow streams and between the fluid and formation or magma. Heat transfer is assumed to occur in the radial direction only. Convective heat transfer coefficients within the tube or annulus are evaluated assuming fully-developed turbulent flow using commonly available correlations for single or two-phase flow. Separate correlations are used in the sub-cooled, saturated, super-heated and supercritical regions. The overlying formation is assumed to be homogeneous, with constant properties, and conduction to the formation is modeled using the quasi-steady assumption of Ramey (1962).

MAGMAXT has been used to simulate the flow and energy extraction rate in the base case geometry which was previously investigated by Hickox and Dunn (1985). The well depth is 5 km followed by a 1 km heat exchanger in magma. The open heat exchanger is assumed to be a porous annulus whose outer diameter can vary depending on the heat exchange rate. Results shown in Figures 6 through 10 are found using the fully-developed slug flow Nusselt numbers given by Eqns. [5] and [6]. The fully-developed values of the Nusselt number are the most conservative, i.e. lowest, values which can be attained. As discussed in the previous section, the heat transfer can be considerably higher than this value due to the effects of developing flow and buoyancy. The present results provide a realistic lower limit on expected energy extraction rates and point out various important characteristics in the single well energy extraction process.

By specification of the injection pressure and mass flow rate, the flow state throughout the circulation path can be computed in an iterative marching procedure by MAGMAXT. Specification of a wellhead back-pressure is optional. For a specified mass flow rate, the injection pressure specified is acceptable if the exit pressure is equal to the specified wellhead pressure or is greater than ambient if a wellhead pressure is not specified.

Figure 6 shows the temperature of the circulating water at a flow rate of 50 kg/s (800 gal/min). The flow path is specified as down the wellbore annulus (A-B), down the insulated tubing in the heat exchange region (B-C), up the porous annulus (C-D), and up the insulated wellbore tubing (D-E). At this relatively high flow rate, there is little temperature change in the wellbore in both the injection and return directions. Within the heat exchanger, the temperature increases from 100 to 300°C. The temperature of the plastic zone around the heat exchanger is maintained at a constant 900°C, and the available heat flux is specified as 1 kW/m^2.

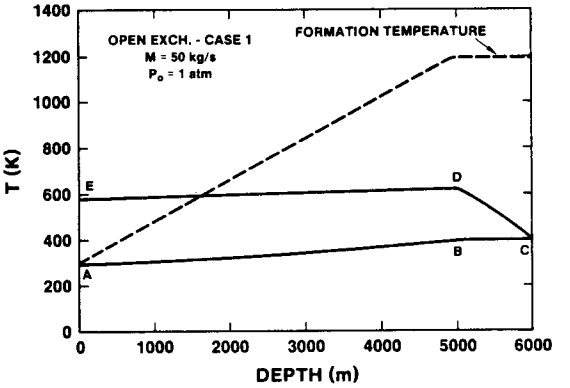


Figure 6. Flow temperature for M=50 kg/s; open heat exchanger base case.

As seen in Fig. 7, the pressure increase in the injection path is due almost entirely to the hydrostatic pressure of the fluid in the subcooled state. As the fluid is heated in the heat exchange region, its density decreases, hence, the pressure in the return path decreases less rapidly than in the injection path. Because of the net density imbalance between the two flow paths, the flow loop has the capacity for natural thermosyphoning. In the current example, the inlet pressure was specified as ambient, hence the well is self-flowing at a flow rate of 50 kg/s with a back-pressure of roughly 15 MPa.

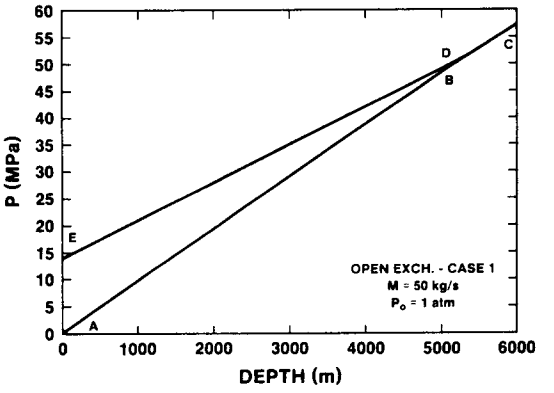


Figure 7. Flow pressure for M=50 kg/s; open heat exchanger base case.

The P-h diagram for the flow, Fig. 8, illustrates the fluid phase in the loop. The hydro- static pressure increase in the injection path results in pressures well above the critical pressure at the inlet to the heat exchanger. Because of the large

flow area in the open heat exhanger annulus, the fluid is heated with very little pressure drop but with an accompanying density decrease. Depending on the flow rate and the specified wellhead back-pressure, the exiting fluid state may be superheated vapor, supercritical, or highly-pressurized, hot water, as in the current example. No realistic operating conditions have been found in which the return state is saturated vapor, hence, two-phase choking in the return tubing does not limit the available flow rate as is commonly the case in vapor producing geothermal wells.

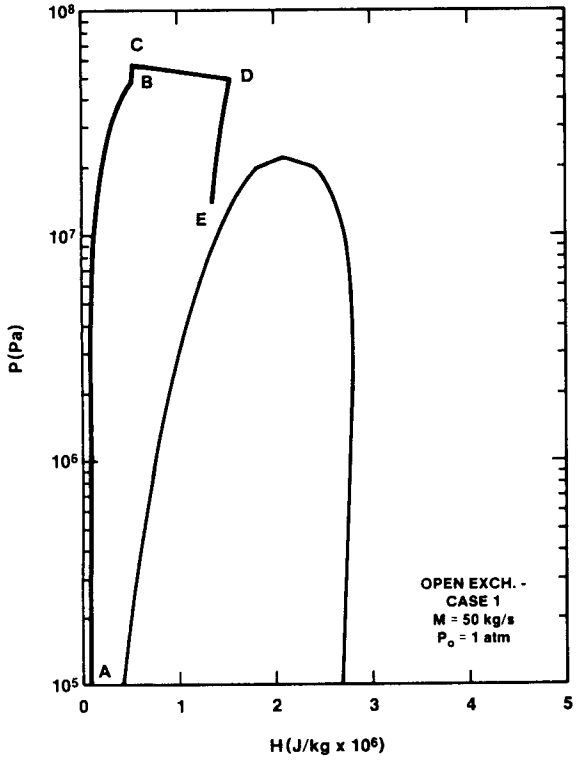


Figure 8. Pressure-enthalpy characteristics for M=50 kg/s; open heat exchanger base case.

The solidification diameter of the open heat exchanger depends directly on the rate of cooling since the energy convected by the fluid must equal the energy convected by the magma to the outer boundary of the heat exchanger. Figure 9 shows the resulting diameter of the exchanger as a function of depth for flow rates of 10, 70, and 100 kg/s. For low flow rates, the diameter changes rapidly since the fluid temperature increases rapidly and the cooling rate decreases. For increasing flow rates, the initial diameter increases, and the diameter decreases less rapidly, consistent with the increased rate of cooling. For optimum conditions, the average diameter is from 10 to 20 m.

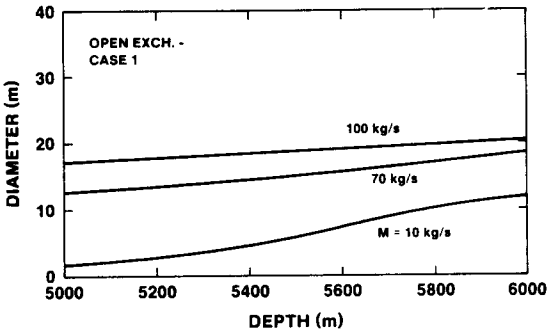


Figure 9. Open heat exchanger diameter for various flow rates; base case.

The optimum operating flow rate for the well is the flow that maximizes the rate at which thermal energy is extracted and converted to useful electric power. Following the approach of Hickox and Dunn (1985), we take the energy conversion efficiency as a first approximation to be the Carnot efficiency, given by:

$$\eta = 1 - \frac{T_{ambient}}{T_{well\ exit}} \qquad (7)$$

The net useful power is thus given by

$$Q_e = \eta\, Q_{thermal} \qquad (8)$$

Figure 10 shows the net useful power in MWe for a single well as a function of flow rate. Three cases are shown: (1) a closed heat exchanger consisting of closed concentric pipes surrounded by solidified magma, (2) an open heat exhanger which is assumed to operate with slug flow and the fully-developed heat transfer model discussed previously, and (3) an open heat exchanger in which the effective thermal conductivity has been taken as twice the nominal value used in the fully-developed model. This latter case represents to some degree the enhancements which may be possible due to entry length and buoyancy effects. An order of magnitude increase in the available power is found between the closed exchanger and the enhanced open exchanger. The open exchanger has a very broad optimum region in which a rate of 30 MWe net power is conservatively estimated. Reasonable enhancements may easily increase this rate by a factor of two or more.

SUMMARY

The open direct contact heat exchanger has the most promise for high rates of energy extraction from crustal magma bodies. The field experiments in the molten zone of Kilauea Iki lava lake demonstrated the validity of this concept at shallow depth and showed that very high rates of energy extraction could be achieved.

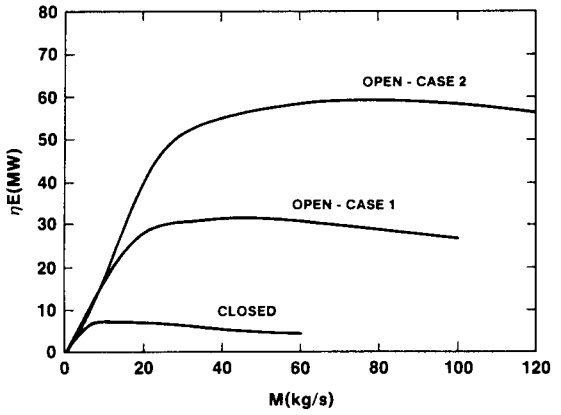


Figure 10. Net converted power for a single heat exchanger.

Experimental and analytical studies show that thermal-stress fracturing will occur in a solidifying magma around a cooled borehole. We predict that large primary fractures will propagate from initial micro-fractures in a glass phase, and that secondary interconnecting fractures will arise under the combined influence of fracture wall cooling, hydraulic pressure within the fracture, and weak intergranular boundaries in the crystalline phases. Current estimates of the extent of fracturing lead to permeabilities which favor the flow of heat exchange fluid through the medium.

Numerical simulation of the energy extraction process from a single well open heat exchanger elucidates several important features. For expected well depths, the fluid pressure in the heat exchanger will be well in excess of the critical pressure of water. Because of the large flow area, heat transfer to the fluid will occur essentially isobarically but with substantial volumetric expansion. The resulting density imbalance between the injection and return flow paths will allow the well to self-flow as an open thermosyphon with the flow rate limited only by the wellhead pressure. In all cases currently anticipated, neither flashing to two-phase flow nor two-phase choking will occur as is commonly the case in vapor producing geothermal wells. The extent of solidification and fracturing of the magma is greatly dependent on the rate of cooling. Our estimates show that magma can be solidified to a diameter on the order of 20 m, resulting in net energy extraction rates of 30 MWe. Reasonable enhancements due to secondary effects not included in the conservative analysis are expected to increase this rate by a factor of two or more.

The ultimate tests of magma energy extraction processes will be carried out by drilling into an active crustal magma body. The current experimental and analytical investigations will guide the planning of these field experiments and be used for data interpretation and evaluation.

REFERENCES

Carslaw, H. S. and Jaeger, J. C. (1959), Conduction of Heat in Solids, 2nd edition, Clarendon Press, Oxford.

Carson, C. C. and Haraden, J. (1985), The Economics of Magma Power Generation, GRC Trans., Vol. 9, Part I, pp. 171-175.

Colp, J. L. (1982), Final Report - Magma Energy Research Project, Sandia Report SAND82-2377, Sandia National Laboratories, Albuquerque, NM 87185.

Dunn, J. C. (1983), Energy Extraction from Crustal Magma Bodies, ASME/JSME Thermal Engineering Joint Conference Proceedings, Vol. II, pp. 93-100.

Dunn, J. C., Carrigan, C. R., and Wemple, R. P. (1983), Heat Transfer in Magma in Situ, Science, V. 12, pp. 3-8.

Gartling, D. K. and Hickox, C. E. (1982), MARIAH-A Finite Element Computer Program for Incompressible Porous Flow Problems, Sandia Natl. Labs. Report SAND-1623, Albuquerque, NM.

Hardee, H. C. (1981), Convective Heat Extraction From Molten Magma, J. Volcanol. Geotherm. Res., V. 10, p. 175-193.

Hardee, H. C., Dunn, J. C., Hills, R. G., and Ward, R. W. (1981), Probing the Melt Zone of Kilauea Iki Lava Lake, Kilauea Volcano, Hawaii, Geophy. Res. Lett., V. 8, pp. 1211-1214.

Hickox, C. E. and Dunn, J. C. (1985), Preliminary Considerations for Extraction of Thermal Energy from Magma, GRC Trans., V. 9, Part II, pp. 319-324.

Ramey, H. J. (1962), Wellbore Heat Transmission, J. Petr. Tech., April, pp. 427-435.

PROCEEDINGS, Twelfth Workshop on Geothermal Reservoir Engineering
Stanford University, Stanford, California, January 20-22, 1987
SGP-TR-109

Potential Impact of Reservoir Engineering R&D on Geothermal Energy Costs*

Richard K. Traeger
Sandia National Laboratories
Albuquerque, NM 87185

Daniel Entingh
Meridian Corporation
Falls Church, VA 22041

Abstract

A tutorial program for use on personal computers is being developed to evaluate the sensitivity of geothermal energy costs to potential technological improvements. Reservoir engineering R&D will reduce risk to the funding organization and in turn reduce the risk premium paid on a loan. The use of a risk premium was described as an investment banker's option at the November 1986 "Future of Geothermal Energy Conference" in San Diego, California.

In the sensitivity analysis, we propose to calculate an energy cost: (1) at the predicted production parameters of temperature, drawdown rate, etc., and (2) at the most likely worse case values. The differential higher cost of the worse case over the predicted case is the risk premium. Thus R&D that improves reservoir definition will reduce the worse-case-minus-predicted-case difference and the financial risk premium. Improvements in reservoir engineering can then be quantified in terms of reduced energy costs.

This paper will discuss the proposed approach to obtain critique of the procedure and provide the best logic for use in evaluating the potential impact of reservoir engineering R&D.

* This work was supported by the U.S. Department of Energy at Sandia National Laboratories under Contract DE-AC04-76DP00789.

(This paper was presented at the workshop, but not written for publication.)

PROCEEDINGS, Twelfth Workshop on Geothermal Reservoir Engineering
Stanford University, Stanford, California, January 20-22, 1987
SGP-TR-109

DECLINE CURVE ANALYSIS OF PRODUCTION DATA FROM THE GEYSERS GEOTHERMAL FIELD

M. Ripperda and G. S. Bodvarsson

Earth Sciences Division
Lawrence Berkeley Laboratory
University of California
Berkeley, CA 94720

ABSTRACT

Production data for over two hundred wells at The Geysers geothermal field were compiled and analysed. Decline curves for groups of wells with 5, 10, and 40 acre spacing are presented and compared to curves published previously by Budd (1972) and Dykstra (1981). Decline curves for several individual wells and leases are discussed to illustrate the effects of well spacing and location, as well as the heterogeneous nature of the reservoir.

INTRODUCTION

Production rate decline curves are widely used in the petroleum and geothermal industries to assess individual well or field performance and to predict future production. The primary purpose of decline analysis at The Geysers is to determine the infill drilling requirements for maintaining a constant supply of steam to the power plants. Unfortunately, much of the data from The Geysers are of a proprietary nature, and thus, only two sets of decline curves have been published in the open literature. Budd presented three curves illustrating the effects of well spacing on production decline. However, his curves are the results of a computer simulation using average reservoir characteristics for The Geysers and do not necessarily represent actual production behavior. Dykstra published a curve based on production from 18 wells, which suggested that after 8 years, production rate from an average well had declined by 50 percent. However, due to the small number of wells included in the analysis, Dykstra's results do not discriminate between various well spacings or locations within the field.

The Earth Sciences Division of the Lawrence Berkeley Laboratory (LBL) has started a project with the California State Lands Commision (CSLC) to research fluid and heat flow behavior at The Geysers. As a part of this work, a data base for The Geysers field has been developed (Bodvarsson et al., 1986) and various reservoir engineering studies performed. This work has laid the necessary background for research into field conditions and behavior during exploitation.

This paper describes the results of decline curve analysis performed on over 150 open file wells at The Geysers.

PRODUCTION BACKGROUND

Several hundred wells have been completed at The Geysers since drilling commenced in the 1920s. Large amounts of reservoir engineering data have been collected, especially since the late 1960s, when large-scale power production began. These data include temperature/pressure surveys, rig test data, wellhead data, production/injection histories and pressure transient test data. Many of the wells have been producing for over a decade, yielding flow rate and shut-in pressure histories that reflect changes in reservoir conditions. Much of the reservoir engineering data from The Geysers field are proprietary and not available in the open literature. However, papers and reports have been published that describe in general terms the reservoir behavior prior to and during exploitation. The most comprehensive reviews include those of Ramey (1970), Lipman et al. (1977) and Dykstra. Mogen and Maney (1985) give a very detailed description of the characteristics and behavior of the Thermal shallow reservoir. There are also data available from the California Division of Oil and Gas for over 150 open file wells (a well is put on open file after 5 years of production). The data for these open file wells include flow rates, wellhead pressures, wellhead temperatures, and drilling information.

It is estimated that over 1400 billion lbs (640 billion kg) of steam have been produced at The Geysers since 1968 (modified from California Division of Oil and Gas, 1985). Although initially it was believed that steam production would remain fairly constant with time and no significant pressure decline would occur at The Geysers, it is now well established that the wells decline in productivity with time and that significant pressure drop has occurred (Ramey, 1970; Lipman et al., 1977; Dykstra, 1981). The well flow rate decline is offset by infill drilling or expansion of the wellfield feeding a given power plant. Lipman et al. (1977) state

that on the average, one make-up well per year must be drilled for each 100 MW_e unit.

DECLINE CURVE ANALYSIS

A very brief description of the decline curve equations will be presented here; a complete derivation and detailed explanation may be found in Arps (1945), Zais and Bodvarsson (1981), or Fetcovich (1980). The three equations generally used for analyzing flow rate decline are the so called exponential, hyperbolic, and harmonic equations. These equations stem from the empirical assumption that the decline rate is proportional to the production rate raised to some exponent, i.e.,

$$(\frac{1}{q})\frac{dq}{dt} = -D^*q^b. \quad (1)$$

Integration of this equation yields the hyperbolic rate-time equation

$$\frac{q(t)}{q_i} = \frac{1}{(1 + bDt)^{1/b}}. \quad (2)$$

The special cases of b = 0.0 and b = 1.0 yield the following equations:

$$\frac{q(t)}{q_i} = \frac{1}{e^{Dt}} \quad (3)$$

$$\frac{q(t)}{q_i} = \frac{1}{(1 + Dt)}, \quad (4)$$

which are called the exponential and harmonic equations, respectively. The exponential equation leads to conservative estimates of future recovery because the decline rate does not decrease as the flow rate decreases with time. An harmonic equation, on the other hand, leads to more optimistic estimates of recovery because the decline rate decreases as the flow rate decreases. The hyperbolic equation usually has an exponent between zero and one, though Gentry and McCray (1978) have shown that in special cases it can be greater than one.

The decline curves may be calculated statistically using a nonlinear least squares type approach, or they may be found from type curves such as those presented by Fetcovich. A stastistical computer program provides unbiased determination of the coefficients for the decline curve equations, but offers little physical insight and does not allow the application of engineering judgement. Type curves, on the other hand, allows one to see the effects of various parameters, as well as providing reasonable estimates of the formation permeability-thickness product (Enedy, 1987). Another important feature of type curves is the determination of the minimum production history necessary for distingishing the type of behavior for each well. This is necessary because the results from the three different equations are very similar at early times, while their projections may differ by up to 50 percent after 10 years. We used both methods in our analysis and found that, in general, the type curve method provided more reliable results.

Causes of Flow Rate Decline

Wells at The Geysers show flow rate decline with time, due to pressure reduction in the reservoir in response to fluid extraction (Budd, 1972). Ramey (1970) noted that all of the wells available in 1968 showed measureable pressure decline. The rate of production decline varies greatly between wells and also from region to region within The Geysers area. Budd published decline curves for various well spacings based upon a theoretical model and estimated that a 50% flow rate decline would occur in 5, 15 and 25 years for well spacings of 5, 20 and 45 acres, respectively. Dykstra used actual flow histories from 18 wells at The Geysers and concluded that, on the average, a 50% decline in flow rate occurs after about 8 years of production. He also concluded that an harmonic-type model best represented the observed flow rate decline. However, one must be aware that the wells used by Dykstra were completed in areas with different well spacings, varying from 40 acres to about 5 acres.

In addition to well spacing, many other factors affect the flow rate decline. Using a fracture model proposed by Pruess and Narasimhan (1982) that assumes significant fluid reserves in the rock matrix, Bodvarsson and Witherspoon (1985) evaluated the effects of various parameters on the flow rate decline. They concluded that the main parameter controlling the flow rate decline is k_m/D^2, where k_m is the matrix permeability and D is the average fracture spacing. Brigham and Dee (1985), on the other hand, used a model that assumes that the fluid reserves are primarily associated with a deep water table. They found that the long term flow rate decline depends primarily on the flow resistance in the primary pathways from deep water table to the steam entries table, hence, the fracture permeabilities.

Individual Well Rates and Decline

Well productivity varies greatly from one well to another, which is to be expected given the heterogeneous, fractured nature of the reservoir. The variability of initial flow rates is illustrated in Figure 1, which shows the number of wells with a given initial steam flow rate. A typical well produces some 150,000 lbs/hr (19 kg/s), but the productivity is highly dependent upon characteristics such as the reservoir pressure, the fracture spacing and permeability. Steam rates in excess of 300,000 lbs/hr (38 kg/s) have been reported for some of the best producers at The Geysers.

Most of the wells for which we have data show a near-harmonic flow rate decline, which is in

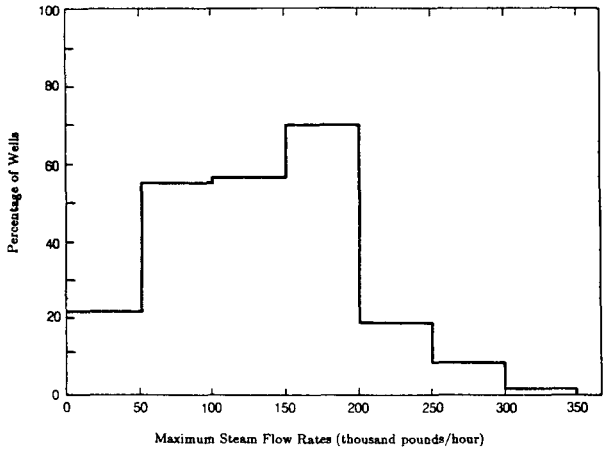


Figure 1. Number of wells with a given maximum flow rate.

agreement with earlier results (Dykstra, 1981). Also, Gentry and McCray (1978) have shown that the hyperbolic constant increases with reservoir heterogeneity, which implies that the flow behavoir in a highly fractured reservoir such as The Geysers should be either harmonic or hyperbolic with an high exponent. A determination of the proper decline behavior is important for making predictions of future flow rates. This is illustrated by Figure 2, which is a type curve match for a well on the Sulphur Bank lease. The flow rate for this well appears to exhibit a hyperbolic decline with b = 0.8. An extrapolation based on b = 0.8 predicts a flow rate of 29,000 kg/hr after 20 years, while a standard semi-log (b = 0) extrapolation predicts a flow rate of only 16,000 kg/hr after an equal amount of time.

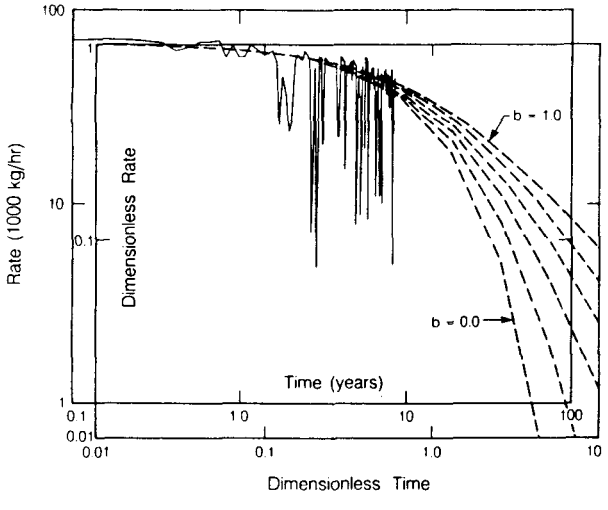


Figure 2. Flow rate decline type curve match for a well located on the Sulphur Bank lease.

Any extrapolations of flow rates, however, are valid only as long as operating conditions remain constant. Figure 3 is a decline curve for a well on State Lands lease PRC 4596. The flow rate from this well exhibits a near-harmonic decline for the first 6 to 8 years of its production history, but then experiences a drastic change, with the decline rate becoming much slower. This behavior is shown by other wells in the immediate vicinity and is probably due to injection which was begun in that area just prior to the change in flow behavior. Figure 4 shows an opposite behavior for a well on State Lands lease PRC 4597. The flow rate for this well has a significant increase in decline rate after about 8 years of production, which is usually indicative of problems in the wellbore. However, because the change in decline rate for this well is rather small and many wells on this lease exhibit a similar change in their flow rates, this case may be due to a change in reservoir conditions. Several power plants have been brought on line over the past 6 years in the areas surrounding this lease, thus reducing the reservoir pressure and the available fluid recharge. It has been seen in other areas of The Geysers that there is an initial transition period with a rapid decrease in pressure when a new power plant is brought on line, but that eventually a psuedo-equilibrium is reached with the available recharge and the pressure declines at a much slower rate. Thus, when the areas around this lease are fully developed, the flow rates should resume a harmonic type decline, but at reduced rates.

Average Decline Curves

To investigate the effects of well spacing, average decline curves were computed for 40-, 10-, and 5-acre spacings. Production rates from 14 wells in SLC lease PRC 4597 and 16 wells in SLC lease PRC 4956 were combined to compute a decline

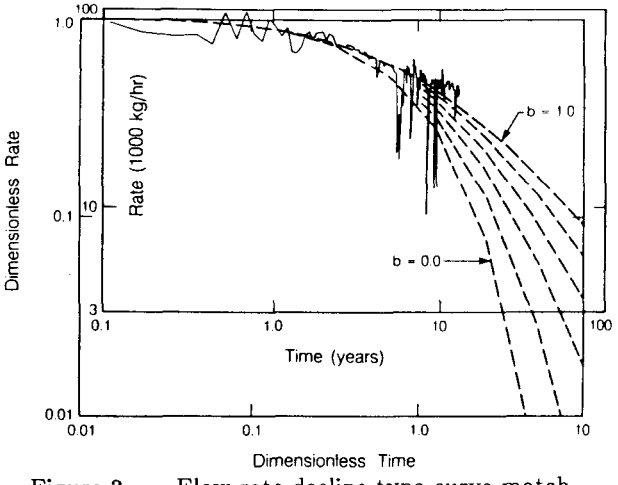


Figure 3. Flow rate decline type curve match for a well located on State lease PRC 4596.

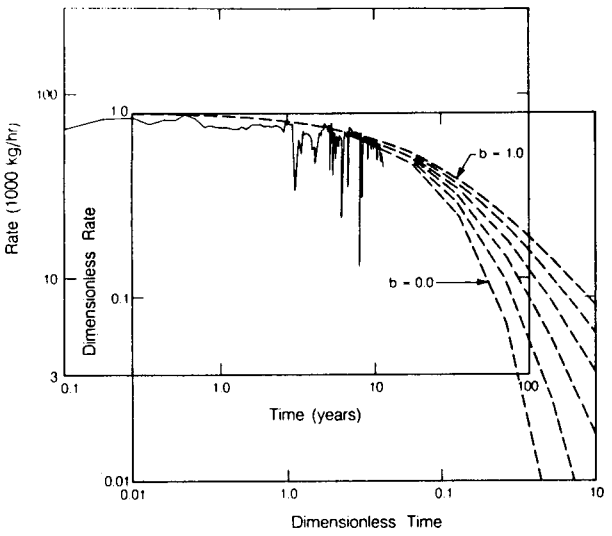


Figure 4. Flow rate decline type curve match for a well located on State lease PRC 4597.

curve for 40-acre spacing. Rates from 23 wells from the Sulphur Bank lease and 10 wells from the Happy Jack lease were used to compute a curve for 5-acre spacing, and 9 wells from the Rorabaugh lease were used to compute a curve for 10-acre spacing. The Rorabaugh wells had production histories of 5 to 7 years , while the rest of the wells had been flowing for at least 7 years. Production data for all the wells were included only up to the time that infill drilling significantly changed the well spacing.

The averaged, normalized decline curves for the five leases are plotted in Figure 5 and the combined values for 40-, 10-, and 5-acre spacing are summarized in Table 1. The leases with 40- and 5-acre spacings behave as expected, with production declining to 50 percent in approximately 8 years for the wells with 5-acre spacing, and 12 years for the wells with 40-acre spacing. However, the wells in the Rorabough lease with 10-acre spacing show a more rapid production rate decline. Several reasons could account for this. The Rorabaugh lease is in the far western edge of the developed field and is bordered to the east by older producing leases such as Sulphur Bank, Happy Jack, and Thermal, and bounded to the west by the edge of the field. This could limit the amount of recharge available to the Rorabaugh wells, decrease the static reservoir pressure and increase the rate at which their production declines. Thus, the flowrate decline in the Rorabaugh lease illustrates the importance of accounting for location with respect to the field boundaries and other producing areas.

A comparison of Budd's, Dykstra's, and our curves is presented in Figure 6. Our 5-acre curve is very similar to Dykstra's curve, which is to be expected, since his curve is primarily based on wells in densely drilled areas. Budd's curves exhibit a much greater dependence on well spacing than is indicated by our data. The dependence of the flow rate decline on well spacing may be smaller than expected because of the significant and rapid communication that exists within the reservoir due to its extensive fracture network. This communication may also be seen in pressure maps of The Geysers reservoir (Lipman, 1977), showing reduced pressures in areas distant from regions with significant production.

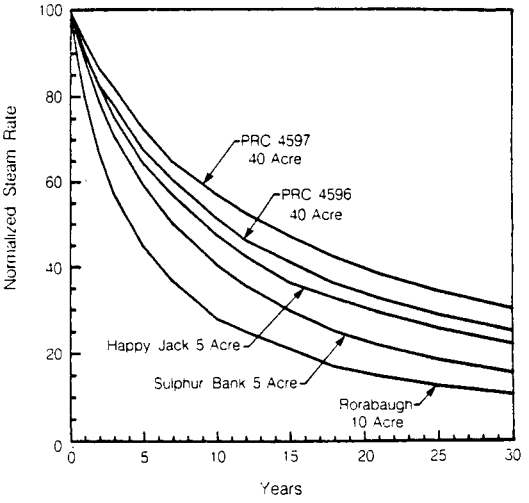


Figure 5. Normalized flow rate decline curves for leases with 5, 10, and 40 acre spacing.

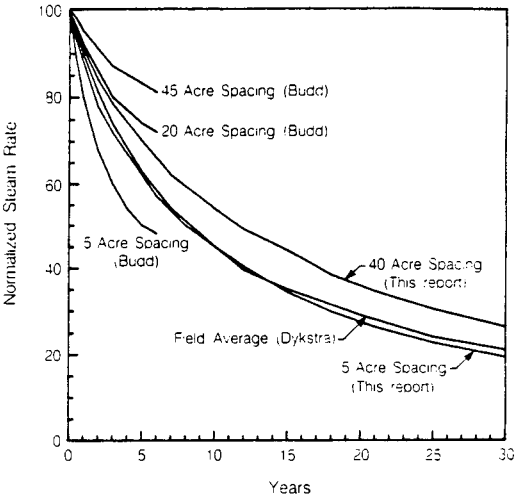


Figure 6. Comparison of normalized flow rate decline curves from Budd (1972), Dykstra (1981), and this report.

Table 1.
Normalized production rates for three different well spacings.

Number of Years	Well Spacing 40-acre	10-acre	5-acre
0.0	100.0	100.0	100.0
1.0	92.5	80.2	89.7
5.0	70.7	43.9	62.6
8.0	59.6	32.4	50.5
12.0	49.1	23.8	39.8
20.0	35.7	15.4	27.4
30.0	26.2	10.5	19.3

CONCLUSIONS

A preliminary investigation of flow rate behavior for wells from The Geysers field has been presented. Steam rates from production wells at The Geysers vary from 30,000 to over 300,000 lbs/hour, with a typical well producing at a rate of about 150,000 lbs/hour. The flow rate decline in these production wells depends on many factors including reservoir heterogeneities (primarily matrix permeability and fracture spacing), well density, and well location with respect to field boundaries and major producing areas. The flow rate decline is usually near-harmonic and a minimum production history of 5 years is required to determine an accurate value for b. On the average, the flow rate declines by 50% in 8 and 12 years for wells with 5- and 40-acre spacing, respectively. This somewhat small dependence on well spacing is explained by the high fracture permeabilities and the resulting near uniform pressure decline over large areas.

REFERENCES

Arps, J., Analysis of Decline Curves, Trans. AIME, 1945.

Budd, C. F., Jr., Producing Geothermal Steam at The Geysers Field, SPE paper 4178, Bakersfield, California, November 8-10, 1972.

California Division of Oil and Gas, Geothermal Hot Line, vol. 15, no. 1, p. 7, July 1985.

Dykstra, H., in A Reservoir Assesment of The Geysers Steam Field, A. D. Stockton, Principal Investigator, California Division of Oil and Gas, Sacremento, California, 1981.

Enedy, S., Applying Flowrate Type Curves to Geysers Steam Wells, Proceedings of the Twelth Workshop on Geothermal Reservoir Engineering, Stanford University, 1987.

Fetcovich, M.J., Decline Curve Analysis Using Type Curves, J. of Pet. Tech., pp. 1065-1077, June 1980.

Lipman, S. C., C. J. Strobel, and M. S. Gulati, Reservoir Performance of The Geysers Field, in Proceedings of the Larderello Workshop on Geothermal Resource Assessment and Reservoir Engineering, Geothermics, Vol. 7, pp. 209-219, 1977.

Mogen P., and J. Maney, The Thermal 15 Relief Well and Production Performance of the Thermal Shallow Reservoir, Proceedings of the Tenth Workshop on Geothermal Reservoir Engineering, Stanford University, pp. 141-144, 1985.

Ramey, H. J., A Reservoir Engineering Study of The Geysers Geothermal Field, Reich and Reich, Petitioners, vs. Commissioner of Internal Review, 1969 Tax Court of the United States, 52, T.C. No. 74, 1970.

Zais, E. J., and G. Bodvarsson, Analysis of Production Decline in Geothermal Reservoirs, Geothermal Reservoir Engineering Management #4503010, Sept. 1980.

PROCEEDINGS, Twelfth Workshop on Geothermal Reservoir Engineering
Stanford University, Stanford, California, January 20-22, 1987
SGP-TR-109

APPLYING FLOWRATE TYPE CURVES TO GEYSERS STEAM WELLS

Steve Enedy

Northern California Power Agency
Bear Ridge Road
The Geysers

ABSTRACT

Dimensionless flowrate type curves were applied to steam wells at The Geysers in an attempt to quantify reservoir properties and to predict flowrate decline. Although data scatter was a problem, the flowrate data was smoothed by a normalization routine based on the back-pressure equation and the wells were modeled by dimensionless functions for a radial system with a infinite or finite outer boundary and a constant pressure inner boundary (composite analytical-empirical type curve).

The "match" resulted in a unique D_i value for use in Arps' equation and a permeability-thickness product (kh) comparable to kh values obtained from pressure buildup analysis. Finally, it was shown that at least four years of data is required to obtain a unique b value.

INTRODUCTION AND BACKGROUND

Decline type curves have been applied to geothermal wells to model flowrate decline by several authors [1,2]. The purpose of this study was to determine if type curves could be applied to Northern California Power Agency's (NCPA's) wells at The Geysers. In particular, those used to start-up NCPA Geothermal Plant No. 1. These wells are exhibiting a hyperbolic or harmonic decline which complicates standard (semi-log) rate-time analysis.

NCPA's steam supply area is on the Sonoma/Lake County border near the southeastern edge of the field (Figure 1).

NCPA Activities at The Geysers

NCPA Geothermal Plant No. 1, rated at 124 megawatts (MW), and NCPA Geothermal Plant No. 2, rated at 114 MW, provide baseload power for the NCPA's 14 member utilities. Plant No. 1 was completed in 1983, Plant No. 2 was dedicated in 1986.

Steam for NCPA's two geothermal plants at The Geysers is provided by wells located on ten (10) drilling pads within federal leases CA-949 and CA-950 (Figure 1). In September of 1986, eight and one half miles of pipeline connected the thirty five producing wells to the plants. The combined electrical output of both plants is normally 238 MW gross.

In September of 1985, NCPA purchased the steam field from Grace Geothermal Company to become the operator of the largest combined power plant-steam field complex at The Geysers. Originally, NCPA had contracts with Shell Oil Company and later with Grace Geothermal Company to supply steam.

DECLINE ANALYSIS METHODOLOGY AND EQUATIONS

Arps' work forms the basis for many of the decline curve equations used for modeling apparent hyperbolic or harmonic decline[3].

$$q(t) = q_i (1 + bD_i t)^{-1/b} \qquad (1)$$

Fetkovich [4,5,6] recommends fitting Arps' equation only to the pseudo-steady state (non-transient) portion of the rate time data. A forced fit of transient data results in apparent b values greater that 1. Fetkovich also states that log rate-log time plots should be made to identify "transient data" and/or "depletion" data. This plot should be reinitialized in time to eliminate any constant rate production period.

Study Methodology

The above recommendations from the basis for this study. The methodology consists of the following steps:

1) Normalizing the flow data to a constant (nominal) back-pressure using the back-pressure equation.

2) Modeling the log rate-log time plots versus available decline type curves.

3) Calculating values of Di, b and kh from the type curve match.

The type curves which best fit the normalized data were the composite of the analytical constant wellbore pressure solutions and the Arps' exponential, hyperbolic and harmonic decline curve solutions (Figure 2).

Decline curve dimensionless rate and dimensionless time in terms of reservoir variables and standard geothermal steam units are defined as:

$$q_{Dd} = \frac{q_t}{\frac{kh(Pi - P_{wf})}{1207\bar{v}u\bar{p}[\ln(r_e/r_w) - 1/2]}} \quad (2)$$

and

$$t_{Dd} = \frac{.00634\ kh\ t}{\phi h(uc_t)_i r_w^2} \times \frac{1}{1/2[(r_e/r_w)^2 - 1][\ln(r_e/r_w) - 1/2]} \quad (3)$$

The boundary conditions are described in detail in References 4, 5 and 6 and are summarized in Figure 3. It is important to note that a constant wellbore pressure is assumed in the analytical solution. Since NCPA's pressure data exhibited a high degree of fluctuation, a normalization routine was required.

Finally, from Arps' empirical decline curve solutions, the factor Di can be calculated from any matchpoint using Equation 4.

$$t_{Dd} = Di\ t \quad (4)$$

BASIC WELL AND RESERVOIR DATA

Source of Basic Flow Data

All wells producing to NCPA Geothermal Plants 1 and 2 are controlled by a supervisory system driven by two HP-1000 "E" Series mini-computers. An annubar (Dieterich Standard Corporation) is the primary flow sensor installed near the wellhead. Pressure, temperature and differential pressure are recorded every five seconds. Flowrate and pressure values are averaged every two minutes and stored for one month.

Following the purchase of the steam field by NCPA, instantaneous flowrates and pressures were recorded as often as requested (currently once per shift) then exported to an IBM-PC for further manipulation by a data-base (DB) manager program.

The DB manager verifies then sorts the data, performs all normalization calculations and outputs a file suitable for graphing.

Prior to the installation of the automated data collection system, instantaneous flowrates were recorded by the field operators. All available data was collected by GeothermEx for NCPA and input to a DB manager then combined with the data currently being stored by the supervisory system.

Both the quantity and quality of the basic flow data was acceptable for basic decline curve analysis following a normalization to a constant surface pressure. Ordinarily, flowrate, pressure and temperature values were available for each day the well produced. A general problem with the instrumentation was a lack of historical calibration checks on the pressure and temperature transmitters. NCPA currently checks calibration once per month.

The lack of stabilized (constant pressure) flow periods posed a problem with the rate data. The degree of fluctuations in the back-pressure required that all the rate-data be "normalized" to a constant "nominal" back-pressure. Flow tests are now conducted at a constant nominal back-pressure to determine a stabilized (constant pressure) flowrate. However, all historic data must be normalized.

Normalization Routine

Generally, only the surface normalization routine was warranted as the match was not improved using bottom-hole data. The normalization routine is a two-step process:

1) Adjust all rates to a nominal surface pressure using surface data.

2) Convert the adjusted flowrates to a constant bottom-hole pressure (if necessary).

The basis for the normalization calculations[7,8] is the back-pressure equation:

$$q = C(P_{ts}^2 - P_{tf}^2)^n \qquad (5)$$

The equation is sufficiently accurate for normalizing data provided the parameters Pts and n are adequately measured. These values are often calculated with special reservoir flow and buildup tests.

Source of Reservoir Data

Prior to the start-up of NCPA Plant No. 1, Shell Oil Company conducted isochronal type flow tests and pressure buildup tests[9]. From these tests, the initial reservoir pressure (Pi), kh and n factors were calculated then input into the DB manager. The Shell data was combined with subsequent flow and pressure buildup data for use in the normalization routine.

The reservoir pressure was modeled with a cubic regression equation:

$$P_{ts} = A + BX + CX^2 + DX^3 \qquad (6)$$

where X was either the days since start-up or the cumulative production since start-up at the time the pressure was recorded. This model allows the DB manager to quickly calculate a reservoir pressure for each flowrate to be normalized.

For the most part, P_{ts} and n factor data were limited in both quantity and quality. As a rule, operating companies cannot afford to shut-in a well for special well tests. The main reason Shell Oil Company conducted the special well tests prior to plant start-up was to quantify reservoir characteristics for a pending sale.

CONVERTING RATES FROM CONSTANT SURFACE TO CONSTANT BOTTOM-HOLE PRESSURE

A cubic regression equation was developed for each well to model the head and friction loss:

$$P_{wf} = A + B(Wnom) + C(Wnom)^2 + D(Wnom)^3 \qquad (7)$$

Wnom is the surface normalized flowrate. The relationship between bottom-hole pressure and flowrate is based on the equations developed by Cullender and Smith[10]. Also, the surface shut-in pressure was adjusted to bottom-hole using the equation[11]:

$$P_{ws} = -6 + (6 + P_{ts})e^{.000015H} \qquad (8)$$

where H is the vertical depth to the mid point of steam. The major advantage of Equations 7 and 8 is the direct calculation of bottom-hole conditions without using an iterative procedure.

Finally, the back-pressure equation (Equation 5) is solved for a normalized flowrate assuming a constant (nominal) bottom-hole pressure.

Although the constant bottom-hole pressure normalization routine was run on all wells, the data scatter always increased (probably due to the lack of quality bottom-hole measurements). Therefore, all decline type curve matches are based on constant surface pressure data.

LOG-LOG DECLINE CURVES (CONSTANT SURFACE PRESSURE)

Log rate - log time plots were generated from the normalized flowrates to the same scale as the decline type curve plots. A graphical match was attempted with several families of decline curves including 1) the infinite conductivity vertical fracture constant pressure solution, 2) naturally fractured reservoir and 3) the composite analytical-empirical solution.

The best match was obtained with the composite type curve. Although data scatter was still a problem, a general decline trend could be determined. A unique t_{Dd} match (therefore Di) was obtained on each well. However, the majority of the wells did not have a sufficient flow period to establish a unique match for b on the empirical hyperbolic and harmonic decline curve solution.

Individual Well Decline Curves

The type curve match for Well #3 was determined graphically and is shown as Figure 4. A match using the composite $q_{Dd} - t_{Dd}$ type curve (Figure 2), at a real time of ten days, indicated t_{Dd} value of .0048. Table 1 lists the t_{Dd} value at a real time of ten days for all the study wells. Well #3 is a typical match and is illustrative of the usefulness of the type curve to quantify Di but not necessarily b. The limiting factor is the flow time. Apparently, at least four years of rate data is necessary to establish a unique b value.

The type curve matches for Wells #8 and #1 are shown as Figures 5 and 6. The late time data exhibits increased scatter. Because the parameters for the back-pressure equation were not well known, the normalization routine was affected. In addition, the unit demand fluctuates due to overhauls, hydro-curtailments, etc. which effects flowrates.

Although a unique b could not be determined for the above wells, a range of b values was found which aided in the steam supply forecast. Also, a unique b value was determined for several wells.

Figure 7 is the log-log plot of daily production for Well #12. The b=1.0 stem of the composite curve best models the data beyond t_{Dd} =.3.

The well with the lowest flowrate and the highest overall decline rate is Well #10 shown as Figure 8. The best fit of the empirical data is as exponential decline (b=0).

Once the average log rate - log time decline curve characteristics are established, exceptions to the average (Well #10) or problem wells (Well #11) are easily determined.

A wellbore problem was found in Well #11 (Figure 9) using type curves. The rate curve diverges from the type-curve match at the late time (>1000 days). A restriction was subsequently confirmed using a wireline survey.

MATCH RESULTS

The value of dimensionless time (t_{Dd}) at a real time of ten days was plotted at the mid-point of steam. An areal distribution is shown as Figure 10. The results are also listed in Table 1.

Based on the match of dimensionless time, the wells were divided into two groups:

$$\text{Group A} \quad .0015 < t_{Dd} < .0048$$
$$\text{Group B} \quad .0060 < t_{Dd} < .0094$$

The grouping is arbitrary as half of the wells were placed in each group. Figure 10 illustrates that the calculated value of Di (Equation 8) is a function of location within the reservoir and controlled by reservoir parameters.

It can be inferred that makeup wells drilled into each area will behave similarly to other wells in the group. Predicting the decline characteristic of a makeup well is useful in forecasting future steam supply.

Since the Group A wells behave in a similar manner, those wells could be combined to form a composite decline curve.

Figure 11 is a four well composite of the normalized rate data. The composite flowrate was calculated by adding the individual well flowrates on four wells within Group A. Although not demonstrated in this paper the advantage of the composite plot is that an overall average decline can be calculated on wells with a high degree of interference.

Calculated kh Values

Given a unique match of the analytical-empirical type curve, a permeability-thickness product can be calculated from Equation 2 if a value for ln re/rw can be either assumed or determined from the match.

Table 2 lists the calculated kh products obtained from the type curve match assuming the value for [ln re/rw - 1/2] is 9. The kh products obtained from pressure buildup tests conducted by Shell Oil Company prior to plant start-up are also listed. Although the absolute kh values obtained by the two methods are not exact, the general

trend is similar (e.g. the high kh values are high by both methods).

For the most part, the kh products obtained from surface normalized decline curve matches are not as reliable as the kh products obtained from a pressure buildup test because a unique value of [ln re/rw - 1/2] could not be obtained by type curve matching or other tests.

An unsuccessful attempt to normalize the data to a constant bottom-hole pressure was made to determine if a unique match on the re/rw stem could be obtained.

LOG-LOG RATE-TIME PLOTS (CONSTANT BOTTOM-HOLE PRESSURE)

Log rate-log time graphs of rates normalized to a constant bottom-hole pressure were prepared and compared to surface normalized graphs. Figure 12 is such a graph for Well #1. It was found that the general characteristics of the early-time data (<100 days) of the high flowrate wells (>150,000 pph) was different enough to require a new match on the re/rw stem. However, the matchpoint results of Di and b did not change. Regardless of the re/rw stem modeled, once the well passes from the transient region to the depletion region the value for Di (obtained from Equation 8) does not change. Also, the overall data scatter increased. This decreased the confidence of the type curve fit.

The increased data scatter is probably due to the lack of reliable downhole data (P_{wf} and n). Even though the bottom-hole normalization routine should (theoretically) smooth the data, error was introduced.

Consequently, all flowrate projections were based on results of type curve matches (eg. b, Di) derived from surface pressure normalized data.

CONCLUSIONS

1. Steam wells (located at The Geysers) used to start-up NCPA Geothermal Plant No.1 exhibited hyperbolic or harmonic decline.

2. The log rate - log time curves for these wells were best modeled using composite analytical-empirical type curves after the data was normalized to a constant pressure.

3. The flow period of nearly four years was sufficient to determine a unique value of Di but not usually of b for use in Arps' equation. Overall, the type curve match was an aid to standard semi-log analysis.

4. Grouping wells with similar type curve matches and creating composite or average decline curves is a useful forecasting tool.

5. Normalizing the rate-time data to a constant bottom-hole pressure introduced increased data scatter and did not improve the match for Di or b.

6. Permeability-thickness products obtained from decline type curve matches cannot replace kh products obtained from pressure buildup tests unless an accurate re/rw value is known.

TABLE 1

DIMENSIONLESS TIME RESULTING FROM A MATCH AT REAL TIME = 10 DAYS

WELL	t_{Dd} @ Dt=TEN DAYS	Comparative Rank of t_{Dd}	GROUP
1	.0048	5	A
2	.0072	8	B
3	.0015	1	A
4	.0048	6	A
5	.0090	10	B
6	.0036	3	A
7	.0060	7	B
8	.0026	2	A
9	.0090	9	B
10	.0061	12	B
11	.0041	4	A
12	.0094	11	B

TABLE 2. COMPARISON OF KH PRODUCTS OBTAINED FROM PBU TESTS AND DECLINE CURVE MATCHES

WELL	PBU (D-FT)	DECLINE TYPE CURVE MATCH (D-FT)
1	175	162
2	250	148
3	18	69
4	17	42
5	13	34

NOMENCLATURE

A	coefficient of cubic regression equation
B	coefficient of cubic regression equation
b	reciprocal of decline curve exponent
C	coefficient of cubic regression equation or coefficient of back-pressure equation
c_t	compressibility, psi^{-1}
D	coefficient of cubic regression equation
D_i	initial decline rate, t^{-1} (eg. day^{-1})
H	vertical depth to mid-point of steam, ft
kh	effective permeability-thickness, md-ft
n	exponent of back-pressure equation
P_i	initial pressure at start of decline, psia
P_{ts}	surface shut-in pressure, psia
P_{tf}	surface flowing pressure, psia
P_{ws}	bottom-hole shut-in pressure, psia
P_{wf}	bottom-hole flowing pressure, psia
$\overline{p}$	average reservoir pressure, psia
q_{Dd}	decline curve dimensionless rate
q_t	mass rate of flow at time t, lbs/hour
q_i	mass rate of flow at time 0, lbs/hour
re	external boundary radius, ft
rw	effective wellbore radius, ft
t	real time, days
t_{Dd}	dimensionless time
u	viscosity, cp
$\overline{v}$	specific volume at $\overline{p}$ (lbm/ft3)
ϕh	porosity-thickness product, ft
Wnom	normalized flowrate, lbs/hour

REFERENCES

1. Zais, E. J.: "Analysis of Production Decline In Geothermal Reservoirs" LBL-11215, GREMP-10, UC-66d, September, 1980.

2. Ramey, H.J. (editor): "Reservoir Engineering Assessment of Geothermal Systems". Dept. of Petroleum Engineering Stanford University. October, 1981.

3. Arps, J.J.: "Analysis of Decline Curves," TRANS, AIME (1945) 160, 228-247

4. Fetkovich, M.J.: "Decline Curve Analysis Using Type Curves', J. Pet. tech (June 1980) 1065-1077 SPE 4629 first presented at SPE 48th Fall Meeting Sept. 30, 1973.

5. Fetkovich, M.J.: "Decline Curve Analysis Using Type Curves: Case Histories" SPE 13169 presented at the 59th Annual Technical Conference and Exhibition, Houston, TX September 16, 1984.

6. Fetkovich, M.J.: "Case Study of a Low-Permeability Volatile Oil Field Using Individual Well Advanced Decline Curve Analysis". SPE 14237 Presented at the 60th Annual Technical Conference and Exhibition. Las Vegas, Sept. 22-25 1985.

7. Budd, C.F.Jr.: "Producing Geothermal Steam at The Geysers Field: SPE paper 4178, Bakersfield CA. Nov. 8-10, 1972.

8. Rawlins, E.L. and Schellhardt, M.A.: "Back-Pressure Data on Natural Gas Wells and Their Application to Production Prodices, " Monograph 7, U.S. Bureau of Mines (1936).

9. Economides, M.J.: "Two Short-Time Buildup Test Analysis for Shell's Geysers Well D-6, A Year Apart: Fifth Workshop Geothermal Reservoir Engineering, Stanford University 1979.

10. Cullender, M.H. and Smith, R.V.: "Practical Solution of Gas Flow Equations for wells and Pipelines with Large Temperature Gradients," TRANS A.I.M.F., V.207 (1956), pp 281-287.

11. Economides, M.J.: "Shut-In and Flowing Bottom-Hole Pressure Calculation for Geothermal Steam Well," Presented at Fifth Workshop Geothermal Reservoir Engineering Dec. 12-14, 1979.

12. Stockton A.D., et. al.: "A Reservoir Assessment of The Geysers Geothermal Field" Publication No. TR 27, 1981.

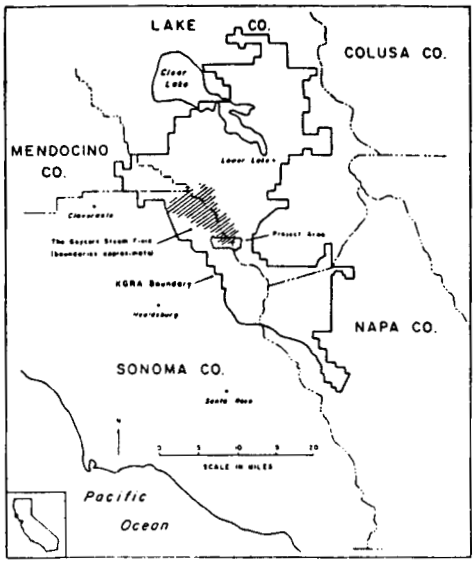


Figure 1. The Geysers - Calistoga KGRA and the Steam Supply Area.

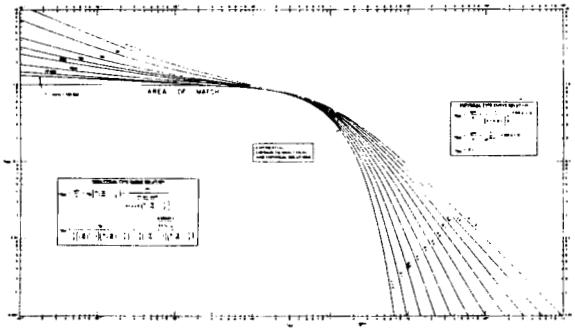


Figure 2. Composite of Analytical and Empirical Type Curves (Fetkovich)

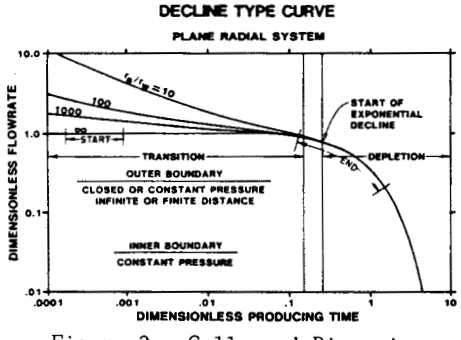


Figure 3. Collapsed Dimensionless Flowrate Functions with Boundary Conditions.

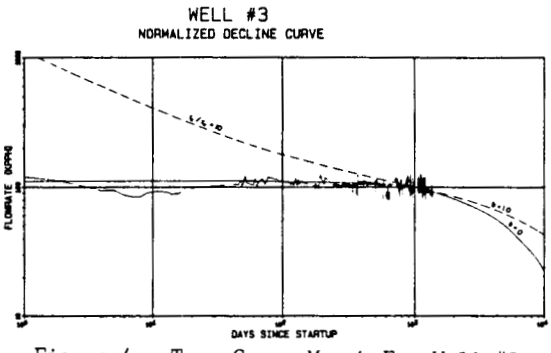


Figure 4. Type Curve Match For Well #3.

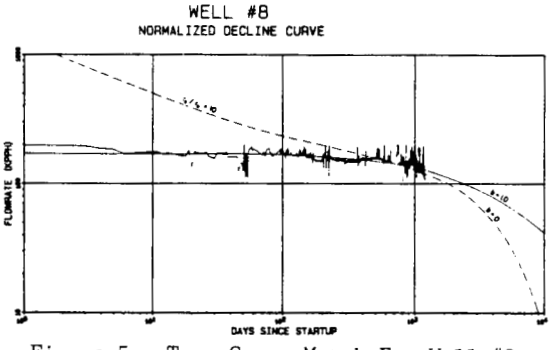


Figure 5. Type Curve Match For Well #8.

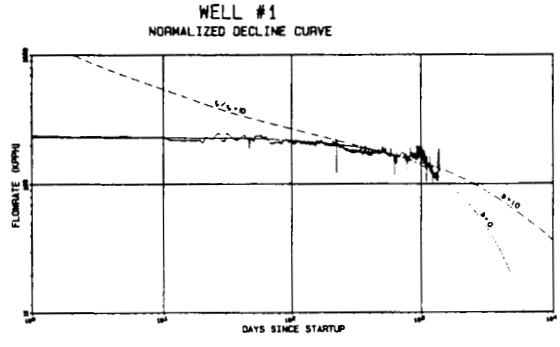


Figure 6. Type Curve Match For Well #1.

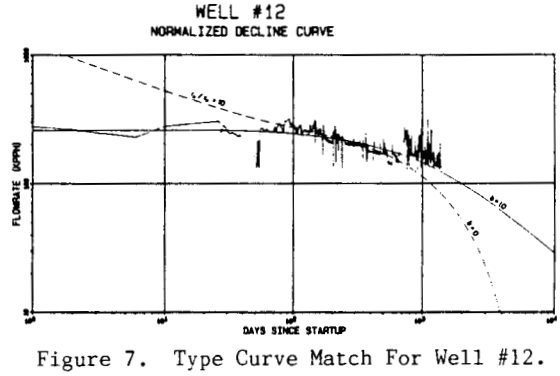


Figure 7. Type Curve Match For Well #12.

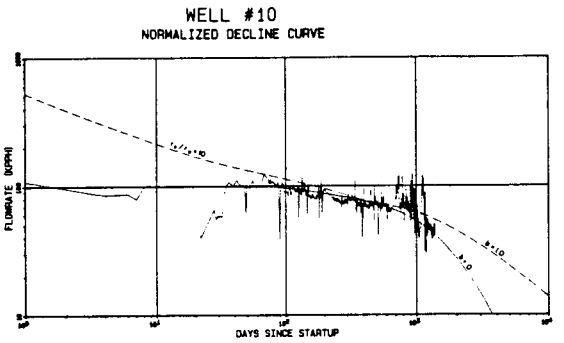


Figure 8. Type Curve Match For Well #10.

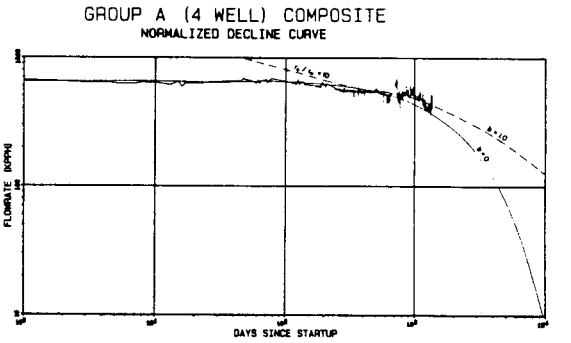


Figure 11. Type Curve Match For Group A (4 Well) Composite.

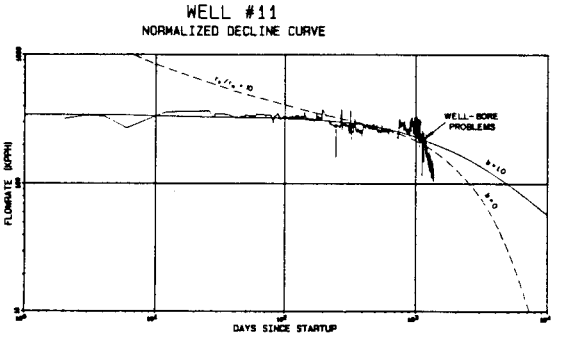


Figure 9. Type Curve Match For Well #11.

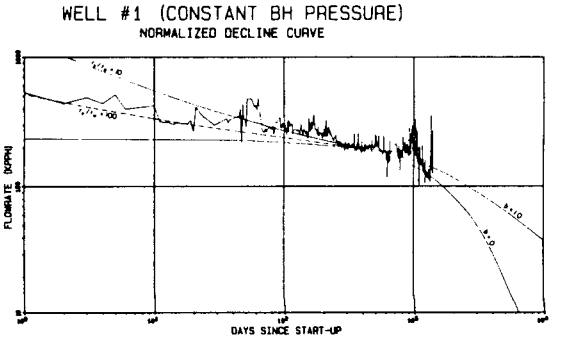


Figure 12. Type Curve Match for Well #1.

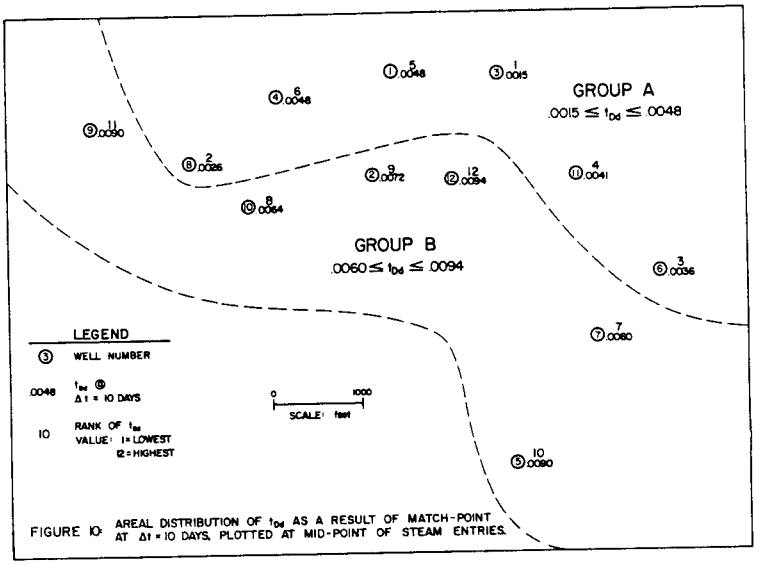


FIGURE 10- AREAL DISTRIBUTION OF t_{Dd} AS A RESULT OF MATCH-POINT AT Δt = 10 DAYS, PLOTTED AT MID-POINT OF STEAM ENTRIES.

PROCEEDINGS, Twelfth Workshop on Geothermal Reservoir Engineering
Stanford University, Stanford, California, January 20-22, 1987
SGP-TR-109

LONG-TERM TESTING OF GEOTHERMAL WELLS IN THE COSO HOT SPRINGS KGRA

S. Sanyal, A. Menzies, E. Granados, S. Sugine* and R. Gentner*

GeothermEx, Inc., Richmond, CA
*Los Angeles Department of Water and Power, Los Angeles, CA

ABSTRACT

Three wells have been drilled by the Los Angeles Department of Water and Power at the Coso Hot Springs KGRA. A long-term flow test was conducted involving one producing well (well 43-7), one injector (well 88-1), and two observation wells (well 66-6 and California Energy Co's well 71A-7).

This paper presents the equipment and techniques involved and the results from the long-term test conducted between December 1985 and February 1986.

INTRODUCTION

A long-term flow test was conducted in the Coso Hot Springs KGRA, California, during the period December 1985 to March 1986. The flow test involved wells 43-7, 88-1 and 66-6 on the leases of Los Angeles Department of Water and Power (LADWP) and well 71A-7 on the leasehold of California Energy Company (CEC). The well locations are shown on figure 1.

The long-term flow test involved flowing LADWP 43-7 through a 10-inch pipeline to a vertical flash cyclonic separator. The water and steam phases were metered separately and then recombined before being discharged to the atmosphere through an atmospheric separator/muffler. The separated waste water was allowed to cool in a settling pond to precipitate the majority of the dissolved silica and then pumped to LADWP 88-1 where the water was first filtered and then injected back into the reservoir. Wells LADWP 66-6 and CEC 71A-7 were used to monitor for any interference effects caused by production from LADWP 43-7 or injection to LADWP 88-1. Downhole pressures were also monitored in both the production and injection wells.

The production well, LADWP 43-7, was completed on February 28, 1985 to a total depth of 2,976 feet. The well profile, including casing shoe depths and fluid entries recorded during air drilling, is shown in figure 2. The well was flow tested for a period of 37 hours during March 1 and 2, 1985 and was found to produce 5.5 MW (mass flow = 390,000 lbs/hr; enthalpy = 490 BTU/lb) at a wellhead pressure of 130 psia. The well encountered a maximum reservoir temperature of 468°F (figure 3) which has a corresponding saturation enthalpy of 450 BTU/lb; hence the well was producing some free steam from the reservoir.

After the short-term test, the well was shut-in until the start of the long-term test.

TEST EQUIPMENT

The equipment involved in the long-term flow test can be divided into 3 main components:

(1) well production metering system,
(2) water injection metering system, and
(3) downhole pressure monitoring system.

The well production metering system was used to measure the wellhead pressure and determine the production rate, enthalpy and chemical charateristics of the produced steam and water from LADWP 43-7. The two-phase fluid produced at the well was conducted through a 10-inch pipe to a vertical flash cyclonic separator rated for 175 psi at 371°F. After separation, the water and steam phases were metered separately and remixed downstream of the separator control valves. The mixture was then conducted through a 12-inch pipe to an atmospheric separator/muffler which served the purpose of reducing the noise level at the exhaust.

The separated waste water was collected in a setting pond and then pumped through a 6-inch aluminum pipeline to the injection well, LADWP 88-1. Both direct reading and recording equipment were used to monitor the injection rate. Injection water temperature and wellhead pressure (vacuum) were also monitored at LADWP 88-1. A double body filtering unit with a capacity of 1000 gpm utilizing 28 filtering elements (20 microns) was installed before the liquid inlet to LADWP 88-1.

The downhole pressure monitoring equipment for each well included a stainless steel pressure chamber attached to 0.125 inch O.D.

stainless steel capillary tubing. The surface end of the capillary tubing was connected to a Paroscientific quartz pressure transducer. Any change in downhole pressure would be transmitted to the transducer by helium gas contained in the chamber and the tubing. The transducer signals were amplified and sent via a multiple conductor cable to a central data logger equipped with a portable computer. Pressure transducers were also used to monitor the wellhead presure of LADWP 43-7 and to monitor atmospheric pressure. Wellhead and ambient temperature were also recorded.

TEST SCHEDULE

Well LADWP 43-7 was stimulated to flow on December 11, 1985 after compressing the well with air to approximately 350 psig and allowing the well to heat up for 24 hours. The flow was then bypassed to the separator and the well continued to flow until February 27, 1986 when it died due to hole collapse. During the last month of the test, sudden changes in the flowing parameters and downhole presssure were noted on 2 occasions, accompanied by drops in flow rate and enthalpy.

After the well died, monitoring of downhole pressures in the observation wells continued until March 28, 1986.

ANALYSIS OF TEST DATA

Well LADWP 43-7 Flow Data

Figure 4 presents plots of the downhole pressure data, production rate and total fluid enthalpy as functions of time for well LADWP 43-7. The data covers the time period 70 to 160 days, based on September 27, 1985, as the starting data. The zero time was chosen as it coincided with the start of monitoring of downhole pressures in the wells. Several important observations can be made based on the flow metering data and downhole pressure data collected from well LADWP 43-7:

1. The well produced a small amount of free steam during most of the flow period, with the downhole steam quality declining from about 3% at the start of the flow test to nearly 0% after day 137 (that is, after 61 days of flow). Under static conditions, the reservoir is at saturation condition but has no free steam.

2. The well's flow characteristics changed abruptly on days 119-120 (24-25 January 1986), as evidenced by sharp reductions in both wellhead and downhole pressures and mass flow rate. The enthalpy also showed a slight rise, but the change is not as significant as noted in the other parameters. This abrupt change was believed to be caused by a sudden fill-up of the lower part of the well by rock debris.

3. The well characteristics continued to deteriorate after the first abrupt change. This deterioration is believed to result from continued fill-up of the well with rock debris.

Table 1 summarizes the observed characteristics of well LADWP 43-7 after it stabilized (and before it deteriorated because of hole fill-up).

Drawdown Data

The downhole pressure data from well LADWP 43-7 were analyzed using a mathematical model based on the line source solution for radial flow in a homogenous and isotopic porous medium of uniform-thickness with pressure-independent rock and fluid properties, small pressure gradients and negligible gravity forces. As we are analyzing the response in the producing well, it is also necessary to include the skin factor of the well in the calculations.

The line source solution is generally only applicable when the active well is producing at a constant flow rate. However, by using the principle of superposition in time, it is possible to account for a variable flow rate history.

The procedure used in the model calculations was to input the measured production schedule (figure 4) and the pressure behavior of the well was then calculated as a function of time for a series of reservoir and well characteristics input to the model: specific volume of the reservoir fluid; wellbore diameter and skin factor; reservoir flow capacity (kh) and storage capacity; reservoir temperature and initial pressure; initial static water level in the well; concentration of dissolved solids and gases in the reservoir fluid; etc. Reservoir properties were assumed to be isotropic.

The calculated pressure behavior was then compared with the observed pressure behavior. If the two agreed within a chosen tolerance, the test data for the well were assumed to be "matched"; that is, the assumed model with the chosen parameters was supposed to be "calibrated".

If the calculated and observed pressure behaviors did not match, one or more of the flow capacity, storage capacity or skin factor were changed and the pressure behavior recalculated. This trial-and-error process was continued until the calculated pressure behavior matched with the observed within the chosen tolerance. Although it is theoretically possible that this process may not give a unique solution, in practice it is generally found that the overall shape of such a measured pressure response can only be matched by a unique set of parameters.

For well LADWP 43-7, attempts were made to match the measured response as outlined in the above discussion. However, it was found that the downhole pressure was not responding to production as expected; the pressure was dropping as the flow rate decreased from 90 to 116 days instead of rising as would be predicted by the above model. This suggested that the response could not be adequately matched by assuming that the input parameters remained constant.

It was decided to match the measured response in well LADWP 43-7 by assuming the reservoir flow capacity and storage capacity had the same values as calculated from the short term flow test in March 1985 (kh = 8000 md·ft, S=0.004 ft/psi, S=0.004 ft/psi) and by allowing the skin factor to vary as a function of time. The resulting match to the measured data is shown in figure 5 while the calculated variation in apparent skin factor is shown in figure 6. The apparent skin factor history provides a method of illustrating the changes in well performance with time.

The plot in figure 6 shows that the well initially had an apparent skin factor of approximately -3.5. The skin factor increased gradually from -3.5 to -2.6 by day 120 (25 January 1986) when the sharp deterioration in well characteristics was noted as discussed before. This gradual increase may have been due to changes in apparent flow capacity caused by two phase conditions in the reservoir but the change is not considered to be particularly significant. After day 120, the skin factor jumped from -2.6 to -0.8 within 3 days implying a significant deterioration in well characteristics. The skin factor remained reasonably stable until day 140 (14 February 1986), when it began increasing rapidly again. The well had reached an apparent skin factor of 2.6 on day 153, just before the well stopped flowing.

Observation and Injection Well Data

From a preliminary analysis of the observation and injection well data, we have concluded the following:

1. The downhole pressure in well LADWP 66-6 did not respond when well LADWP 43-7 started producing but started to rise once injection began to well LADWP 88-1. Similarly, the pressures began to fall as soon as injection to well LADWP 88-1 was stopped. It is therefore concluded that well LADWP 66-6 was only responding to injection in well LADWP 88-1 and not to production from well LADWP 43-7.

2. Considering that well LADWP 66-6 is responding to injection even though it is closer to the production well LADWP 43-7 than the injection well LADWP 88-1, and that both wells LADWP 88-1 and LADWP 66-6 have deeper casing and deeper production zones than does well LADWP 43-7, we conclude that wells LADWP 88-1 and LADWP 66-6 are communicating through a deeper part of the reservoir than the level from which LADWP 43-7 is producing.

3. The downhole pressure in well LADWP 88-1 declined considerably during the test even though the injection rate remained nearly constant. This implies that the well was improving in injectivity, possibly due to cleaning up of existing fractures and/or opening up of new fractures.

4. Well CEC 71A-7 had a very "noisy" pressure response, when compared to the response measured in well LADWP 66-6. This is believed to be due to the well being on bleed during the test.

The pressure response of well LADWP 66-6 was analyzed using the mathematical model described above, assuming that the well was responding to injection to well LADWP 88-1. In this case, the response in an observation well was being matched and hence it was not necessary to know the skin factor. With observation well data, it is also possible to directly calculate both the flow capacity and the storage capacity.

Figure 7 shows the match obtained between the observed (continuous line) and calculated (small squares) pressure responses at well LADWP 66-6. The match is excellent, the difference between the calculated and observed pressure values being always less than the resolution of the pressure data obtained. The reservoir flow capacity required to obtain the match was 108,000 md·ft, indicating that the "lower" reservoir with which LADWP 66-6 communicates has a very good flow capacity. The storage capacity value required to match the pressure data of LADWP 66-6 was 0.0012 ft/psi. Assuming typical values of 10^{-5} psi^{-1} for total reservoir compressibility and 0.05 to 0.10 for porosity, this storativity value implies a reservoir thickness of 1,200 to 2,400 feet. This range of reservoir thickness appears reasonable.

The value of flow capacity calculated from the analysis of the interference response of well LADWP 66-6 is an order of magnitude higher than the values calculated from short term flow test data for wells LADWP 43-7 (March 1985) and LADWP 66-6 (June 1985). This difference between parameters calculated from single well tests and interference tests has been seen in a number of geothermal fields. It is believed, however, that the parameters calculated from interference data better reflect how the reservoir will respond to exploitation.

It is believed that well CEC 71A-7 did not respond to the discharge of well LADWP 43-7 and the pressure variations can be satisfactorily explained by leaks in the capillary tubing and the bleeding of the well. A possible reason for the lack of response is the high compressibility of the two-phase steam/water mixture which is known to exist around well CEC 71A-7. Fluid with high compressibility acts like a barrier to pressure transients.

The pressure response of well LADWP 88-1 was also analyzed using the same approach as used for LADWP 43-7 and LADWP 66-6. As with well LADWP 43-7, it was found that the measured pressure response could not be adequately matched if it was assumed that the reservoir parameters remained constant during the test. It was noted that the measured pressures were declining at a faster rate after 120 days than would be expected by the drop in injection rate caused by the hole collapse in well LADWP 43-7.

The decline in pressure noted in well LADWP 88-1 may have been caused by:

1. reservoir pressure drawdown related to the discharge of well LADWP 43-7; or
2. improvement in the injectivity of well LADWP 88-1.

The most likely explanation is the improvement in injectivity of well LADWP 88-1. If the change was due to interference from well LADWP 43-7, it would have started to occur nearer the start of the flow test.

To model the improvement in injectivity, the skin factor was allowed to vary as a function of time. For practical purposes it is found that the skin factor generally falls within the range from -8 to 20 for the vast majority of geothermal wells. The possible range of skin factor values therefore provided a constraint on the value of flow capacity that could be used in the model. The storage capacity used in the model was assumed to be the same as calculated from the pressure response measured in well LADWP 66-6 (0.0012 psi/ft).

After numerous trials it was found that a flow capacity of 50,000 md·ft gave a good match to the measured pressure response, with calculated skin factors remaining within the required range. The match to the observed pressure response is shown in figure 8. Figure 9 shows the calculated skin factor history as a function of time. The well had a high apparent well damage (skin factor of 16) until day 120, after which the general trend shows the skin factor gradually dropping until it reached -8 at the end of the test. These changes in skin factor are believed to indicate that the well showed improved injectivity either due to clean up of drill cuttings or opening of more fractures due to the thermal shock of cold water injection.

CONCLUSIONS

In summary, it can be concluded that the long-term test program has been quite successful in assessing the LADWP wells and the reservoir. The following important information relating to the development aspects of the field were learned from the test:

1. Well LADWP 43-7 has a sustained capacity of approximately 4 MW at a wellhead pressure of 80 psia.
2. The test indicated that there are probably two different production levels in the reservoir. The shallower level, in the depth range 2,000 to 3,000 feet, is tapped by LADWP 43-7, while the deeper level (below 3,500 feet) is tapped by wells LADWP 88-1 and LADWP 66-6.
3. The lower level is believed to be a better exploration target because it is probably the source of fluid for the upper level and it has a higher reservoir pressure. Although wells LADWP 88-1 and LADWP 66-6 proved to be cooler and therefore less productive than LADWP 43-7, the upflow zone appears to underlie most of the LADWP leasehold. Therefore, hotter deeper production may be discovered on the LADWP leasehold in the future.
4. The test clearly indicated that the production wells should be lined with slotted liner to prevent accumulation of rock debris in the well.

Table 1 Stabilized Characteristics of Well LADWP 43-7

Flowing wellhead pressure = 126.35 psia

Total mass flow rate = 295,000 lbs/hour

Wellhead steam quality = 16.4%

Enthalpy of total fluid = 460 BTU/lb

Static reservoir pressure = 541 psia

Static reservoir temperature = 470°F

Reservoir steam saturation at static condition = 0%

Flowing downhole pressure = 225.37 psia

Flowing downhole temperature = 392°F

Downhole steam quality = 0.8%

Productivity Index = 0.012 MW per psi

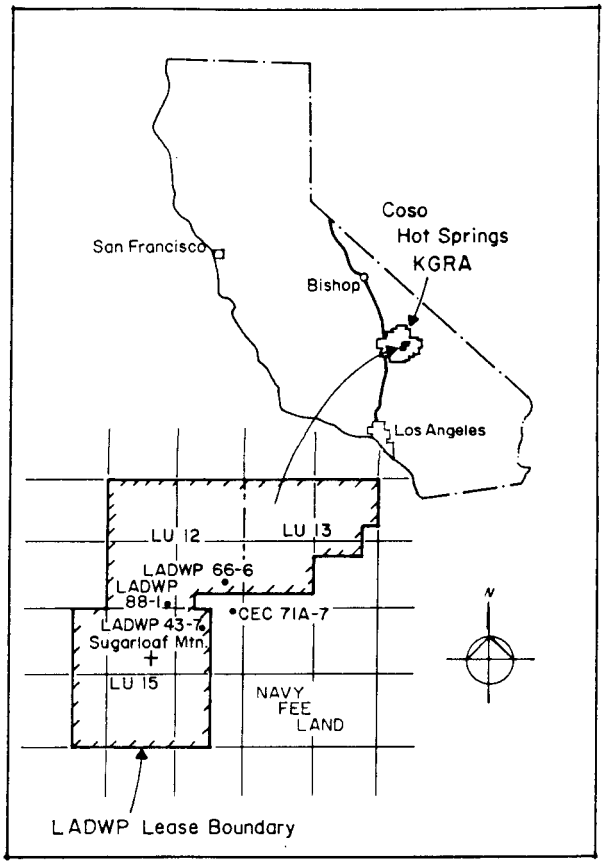


Figure 1. Location Map

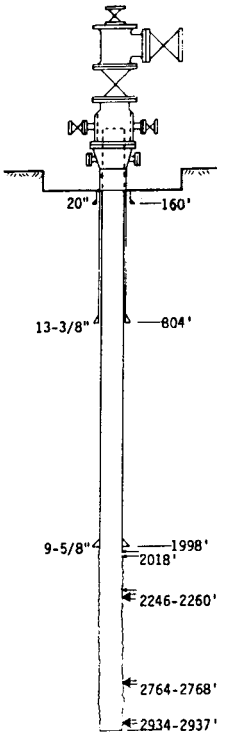


Figure 2: Well 43-7 Drilling Breaks

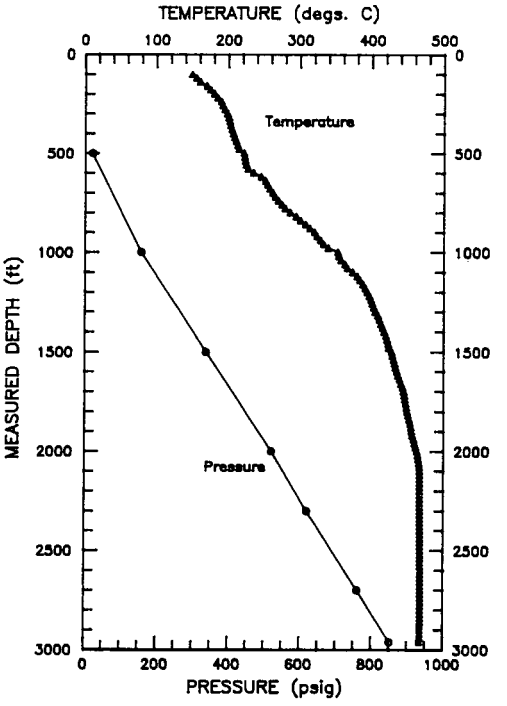


Figure 3: Downhole Surveys, Well 43-7

Figure 4: Downhole Pressure, Flow rate and Enthalpy Data, Well 43-7

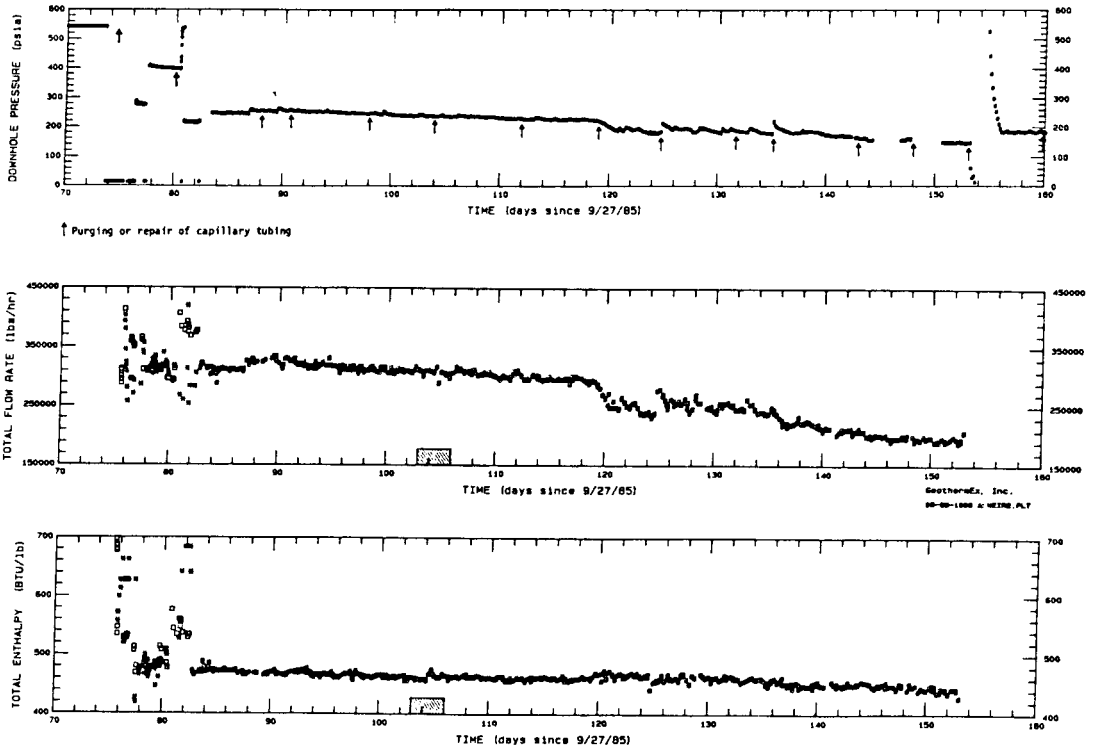


Figure 5: Drawdown Data Analysis, Well 43-7

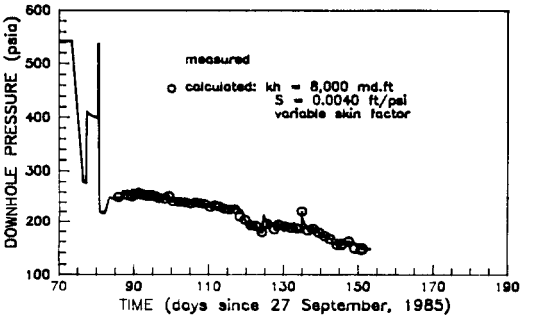


Figure 6: Calculated Skin Factor, Well 43-7

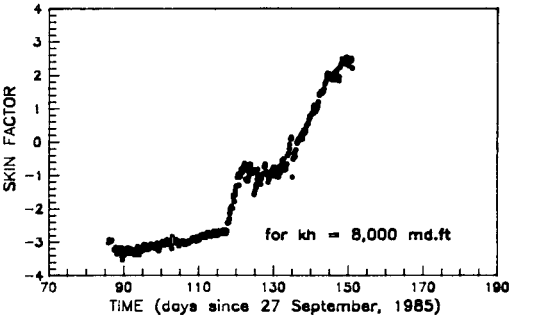


Figure 7: Interference Test Data, Well 66–6

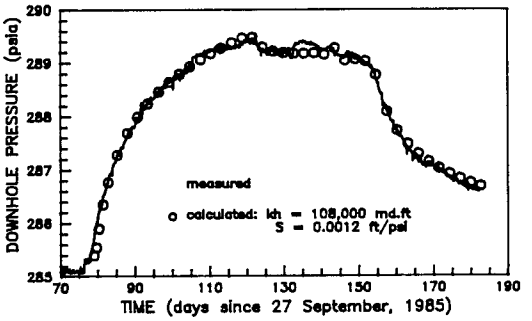


Figure 8: Injection Data Analysis, Well 88–1

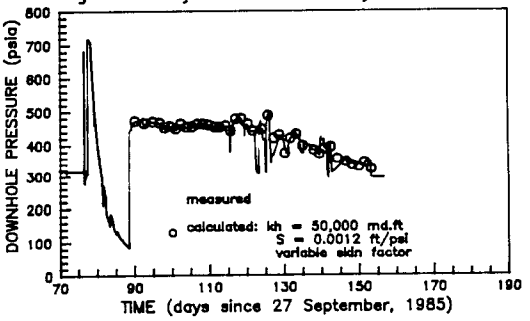
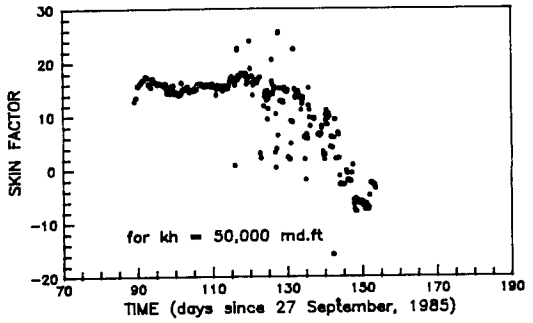


Figure 9: Calculated Skin Factor, Well 88–1



PROCEEDINGS, Twelfth Workshop on Geothermal Reservoir Engineering
Stanford University, Stanford, California, January 20-22, 1987
SGP-TR-109

A New Derivative Type-Curve for Pressure Buildup Analysis with Boundary Effects

S. Mishra and H. J. Ramey, Jr.

Department of Petroleum Engineering
Stanford University

ABSTRACT

This study investigates pressure buildup behavior of wells with wellbore storage and skin in bounded circular reservoirs, when inner and outer boundary effects interact to fully or partially dominate the well pressure response. Using dimensionless pressure derivative as the dependent variable, we show that early time response is governed by C_De^{2S} and late time response by r_{eD}^2/C_D. Equations are provided to estimate the limits of the intermediate time period, which corresponds to infinite acting radial flow and a semi-log straight line on a pressure-time graph. We present a new buildup derivative type curve, incorporating inner boundary (early-time) and outer boundary (late-time) effects. Applications of this type curve in buildup test design and interpretation are discussed.

INTRODUCTION

For a well with wellbore storage and skin and producing from a bounded reservoir, it is possible for inner and outer boundary effects to interact and dominate the well pressure response. *Chen and Brigham* (1978) investigated conditions under which such interference might obscure the semi-log straight line, corresponding to infinite acting radial flow, on a Horner buildup graph (*Horner*, 1951). It was found that this could occur even for small values of wellbore storage coefficient in reasonably sized drainage areas. However, they observed that a semi-log straight line with 5-10% error in slope could be found in almost all cases.

In this study, we expand upon the work of *Chen and Brigham* (1978) to identify conditions under which the inner and outer boundary combine to dominate the well pressure response. A second objective is to develop a general buildup type curve incorporating inner and outer boundary effects.

THEORY

The dimensionless wellbore pressure response for a well with storage and damage may be expressed using the convolution theorem as (*van Everdingen and Hurst*, 1949)

$$p_{wD}(t_D) = \frac{2\pi kh}{q\mu}\left[p_i - p_{wf}\right] = L^{-1}\left[\frac{1}{C_D l^2 + \dfrac{l}{S + l\bar{p}_D}}\right] \quad (1)$$

Here, L^{-1} is the inverse Laplace transform operator, l the Laplace space variable, S the skin factor, t_D the dimensionless time defined as

$$t_D = \frac{kt}{\phi\mu c_t r_w^2} \quad (2)$$

and C_D the dimensionless wellbore storage coefficient defined by

$$C_D = \frac{C}{2\pi\phi c_t h r_w^2} \quad (3)$$

In eqn. (1), $\bar{p}_D$ is the appropriate reservoir model in Laplace space, and for the case of a well draining from the center of a closed circle, it is given as (*van Everdingen and Hurst*, 1949)

$$\bar{p}_D = \frac{1}{l^{3/2}}\left\{\frac{K_0(\sqrt{l})\,I_1(r_{eD}\sqrt{l}) + I_0(\sqrt{l})\,K_1(r_{eD}\sqrt{l})}{K_1(\sqrt{l})\,I_1(r_{eD}\sqrt{l}) - I_1(\sqrt{l})\,K_1(r_{eD}\sqrt{l})}\right\} \quad (4)$$

where I_n and K_n are modified Bessel functions, of order n, of the first and second kind respectively, and r_{eD} is the dimensionless outer radius r_e/r_w.

Defining the dimensionless buildup pressure as

$$p_{Ds}(\Delta t_D) = \frac{2\pi kh}{q\mu}\left[p_{ws} - p_{wf}\right] \quad (5)$$

we obtain, from eqn. (1), by superposition

$$p_{Ds}(\Delta t_D) = p_{wD}(t_{pD}) + p_{wD}(\Delta t_D) - p_{wD}(t_{pD} + \Delta t_D) \quad (6)$$

where Δt_D is the dimensionless shut-in time and t_{pD} the dimensionless producing time. Eqn. (6) is used for computing buildup pressure response. Appropriate p_{wD} terms are calculated by substituting eqn. (4) in eqn. (1), and then numerically inverting the Laplace space solution with the algorithm of *Stehfest* (1970).

In the recent literature, use of the pressure derivative has been shown to enhance the pressure response signal (e.g. *Bourdet et al.*, 1984). Hence, pressure derivative, rather than pressure, is chosen as

the dependent variable in this work. The dimensionless buildup derivative group is defined as

$$p'_{Ds} = \frac{dp_{Ds}}{d\ln(\Delta t_D)} = \frac{2\pi kh}{q\mu} \frac{d(p_{ws} - p_{wf})}{d\ln(\Delta t)} \qquad (7)$$

and is easily seen to be the slope of a dimensionless MDH buildup graph (*Miller, Dyes and Hutchinson*, 1950).

CORRELATIONS

For large producing times such that $t_{pD} > t_{Dpss}$, *Ramey and Cobb* (1971) show that, for a given system, all dimensionless MDH buildup graphs are identical. This observation facilitates eliminating producing time effects from our analysis. Under these conditions, we examined dimensionless buildup behavior for several combinations of C_D, S and r_{eD} and found that two parameters are sufficient to correlate the buildup response when p'_{Ds} is graphed as a function of $\Delta t_D/C_D$. The early-time behavior, reflecting inner boundary (wellbore storage and skin) effects, is controlled by the group C_De^{2S}. Late-time data, influenced by outer boundary effects, are correlatable with r_{eD}^2/C_D. Fig. 1 demonstrates the appropriateness of these correlating parameters for a variety of conditions.

Such behavior suggests that the overall pressure response may be approximated by superposing the independent effects of (a) a well with storage and skin in an infinte system, (b) a well without storage and skin in a finite system. This logic is similar to that used by *Bourdet and Gringarten* (1980) in generating their double-porosity system type-curves, and forms the basis for developing the new type-curve.

It should be pointed out that the use of C_De^{2S} as a correlating parameter for wellbore storage dominated *pressure* data was first theoretically justified by *Bourdet and Gringarten* (1980). Moreover, since the onset of outer boundary effects can be correlated with t_D/r_{eD}^2 for drawdown data, the use of $\Delta t_D/C_D$ as the time group intuitively suggests r_{eD}^2/C_D as the late-time correlating parameter for buildup data. These choices have been validated for buildup derivative data in Fig.1.

A NEW TYPE-CURVE

Fig. 2 shows the buildup derivative type-curve developed in this study. The dimensionless derivative group p'_{Ds} is graphed as a function of the time group $\Delta t_D/C_D$ on log-log coordinates. As mentioned earlier, the early and late time correlating parameters are C_De^{2S} and r_{eD}^2/C_D respectively. The intermediate time period reflects the degree of interference between inner and outer boundary effects, which determines whether the semi-log straight line will develop or not on a pressure-time graph. On the type-curve of fig. (2), the semi-log straight line is equivalent to a p'_{Ds} value of 0.50 .

Since the semi-log straight line is integral to conventional analysis of buildup pressure data, it is

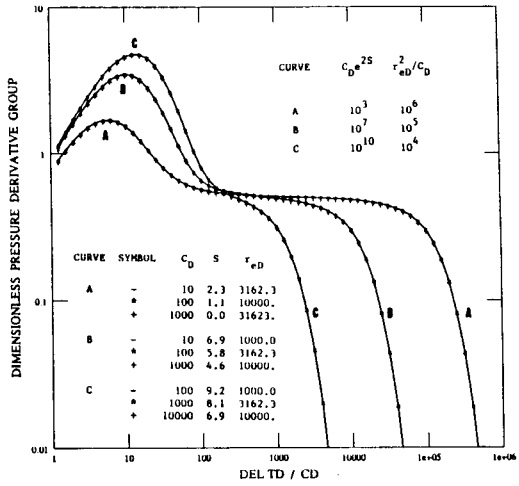


Fig. 1. Validation of C_De^{2s} and r^{2eD}/C_D as correlating parameters.

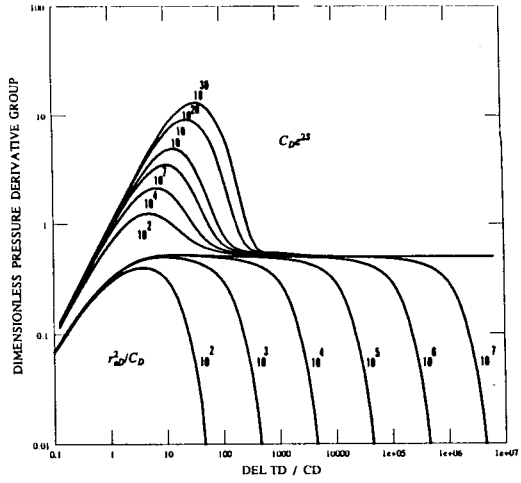


Fig. 2. New buildup derivative type-curve.

useful to specify its limits. By examining the behavior of p'_{Ds} as it approaches (and deviates from) the value of 0.50 , we find that

$$\left.\frac{\Delta t_D}{C_D}\right|_{begin} \approx 30 \log(C_De^{2S}) \qquad (8)$$

$$\left.\frac{\Delta t_D}{C_D}\right|_{end} \approx \frac{r_{eD}^2}{100\, C_D} \qquad (9)$$

Conditions under which boundary effects might dominate the well pressure response can also be quantitatively established. Defining interference between inner and outer boundary to be such that less than half a log-cycle of semi-log straight line is present, we have

$$\left.\frac{\Delta t_D}{C_D}\right|_{end} < 10^{0.5} \left.\frac{\Delta t_D}{C_D}\right|_{begin} \qquad (10)$$

Substitution from eqn. (8) and (9) then yields

$$\frac{r_{eD}^2/C_D}{\log(C_De^{2S})} > 10000 \qquad (11)$$

as the limiting condition for a semi-log straight line to develop on an MDH buildup graph.

APPLICATIONS

The type-curve presented in fig. 2 can be used for buildup test design and interpretation. In test design, an often sought information is the duration of the semi-log straight line. Based on *a priori* estimates of wellbore/reservoir parameters, this can be calculated using eqn. (8) and (9).

For interpretation, field data is plotted on log-log paper with $d(p_{ws}-p_{wf}) / d(\log \Delta t)$ on the y-axis and Δt on the x-axis. This is then overlain on fig. (2) and a match is obtained for the entire curve. C_De^{2S} and r_{eD}^2/C_D are read-off as the parameters of the early and late time match respectively. Permeability-thickness is obtained from the pressure match. C_D can be calculated from the early-time line of unit-slope on the log-log graph, and then both r_{eD} and S can be estimated.

This procedure can be useful when the semi-log straight line has been obscured by interference between inner and outer boundary effects, in which case a conventional semi-log analysis or a type-curve analysis based on existing storage and skin type-curves may not work.

SUMMARY

We have presented a new buildup derivative type curve for wells with storage and damage in bounded circular reservoirs. Equations for estimating the beginning and end of the proper semi-log straight line on an MDH buildup graph are provided. The type-curve should be useful in buildup test design and interpretation for situtations when inner and outer boundary effects interact to fully or partially dominate the well pressure response.

NOMENCLATURE

c_t	total system compressibility
C	wellbore storage coefficient
h	formation thickness
k	formation permeability
p_{wf}	flowing sandface pressure
p_{ws}	shut-in sandface pressure
p_i	initial pressure
q	well flow rate
r_w	well bore radius
r_e	external radius
t	time
t_p	producing time
Δt	shut-in time
t_{Dpss}	dimensionless time to pseudo-steady state
ϕ	porosity
μ	viscosity

ACKNOWLEDGEMENTS

We thank Stanford University, Stanford Center for Reservoir Forecasting and Stanford Geothermal Program (DOE Contract No. DE-ATO3-80SF11459) for funding this study.

REFERENCES

Bourdet, D., Ayoub, J.A. and Pirard, Y.M. (1984) : "Use of Pressure Derivative in Well Test Interpretation," paper SPE 12777 presented at the California Regional Meeting, Long Beach, April 11-13.

Bourdet, D. and Gringarten, A.C. (1980) : "Determination of Fissure Volume and Block Size in Fractured Reservoirs by Type Curve Analysis," paper SPE 9293 presented at the SPE 55th Annual Fall Technical Conference and Exhibition, Dallas, Sept. 21-24.

Chen, H.K. and Brigham, W.E. (1978) : "Pressure Buildup for a Well with Storage and Skin in a Closed Square," *J. Pet. Tech.* (Jan.), 141-146.

Horner, D.R. (1951) : "Pressure Buildup in Wells," *Proc.* Third World Pet. Cong., The Hague, **II**, 503-523.

Miller, C.C., Dyes, A.B. and Hutchinson, C.A. (1950) : "The Estimation of Permeability and Reservoir Pressure from Bottom-hole Pressure Buildup Characteristics," *Trans.*, AIME, **189**, 91-100.

Ramey, H.J., Jr. and Cobb, W.M. (1971) : "A General Pressure Buildup Theory for a Well in a Closed Drainage Area," *J. Pet. Tech.* (Dec.), 1493-1505.

Stehfest, H. (1970) : "Numerical Inversion of Laplace Transforms," Algorithm 368, *Communications of the ACM*, **13**, 47.

van Everdingen, A.F. and Hurst, W. (1949) : "The Application of the Laplace Transformation to Flow Problems in Reservoirs," *Trans.*, AIME, **186**, 305-324.

PROCEEDINGS, Twelfth Workshop on Geothermal Reservoir Engineering
Stanford University, Stanford, California, January 20-22, 1987
SGP-TR-109

TRACER BREAKTHROUGH TIME FOR THE RATE-PRESSURE DOUBLET

Will Menninger and Abraham Sageev

Stanford University

Stanford CA 94305

ABSTRACT

A pressure transient analysis method is presented for interpreting breakthrough time between a constant rate well and a constant pressure well. The wells are modeled as two line sources in an infinite reservoir where the first well injects at a constant pressure and the second well produces at a constant rate. The effects of transient pressure conditions, the distance between the wells, the flowrate, and the tracer injection time on breakthrough time are examined. The first arrival of injected fluid at the production well is significantly longer under transient condition than under steady state condition for the rate-pressure model when the injection pressure is equal to initial reservoir pressure. An injection pressure larger than initial reservoir pressure significantly reduces the breakthrough time, and may yield a breakthrough time significantly smaller than the breakthrough time for the steady state case.

INTRODUCTION

Pressure transient analysis methods are used to estimate reservoir properties so that exploitation schemes may be evaluated. Well-to-well tracer tests yield information about preferential flow paths and about reservoir heterogeneity. One of the important parameters in a well-to-well tracer test is the time of first arrival of the tracer at the production well, or the breakthrough time. The method presented in this paper permits the interpretation and design of a special case, which will be referred to as the rate-pressure doublet. In this two-well system, one well produces at a constant rate and the other well injects at a constant pressure. The two time dependent parameters in the rate-pressure doublet model are the pressure response of the producing well and the rate response of the injecting well. These parameters and ensuing equations will be described further in the Theory section.

A constant rate well is approximated as a line source, since the reservoir and the interwell distance are much larger than the finite radius of the well. The constant rate production or injection line source well has been used as a building block for calculating the response of various reservoir systems. *Theis* (1935) presented the line source pressure solution in an infinite domain. *Carslaw and Jaeger* (1960) and *Van Everdingen and Hurst* (1949) presented the pressure solution for a finite radius well in an infinite system. *Mueller and Witherspoon* (1965) showed the geometrical and time conditions under which the line source and the finite radius solutions are practically identical. They concluded that for observation wells located at a distance twenty times the wellbore radius the line source approximation is applicable. Also, this approximation is applicable for any observation well after a dimensionless time of ten.

Since the diffusivity equation describing the flow in the system is linear, superposition in space of constant rate line sources may be used. *Stallman* (1952) presented the superposition of two constant rate line sources replicating the effects of constant pressure or impermeable linear boundaries. In the same way, superposition of arrays of rate sources (*Kruseman and De Ridder* 1970, and *Ramey et al* 1973) were used to generate the effects of combinations of rectangular boundaries around a well. By using the method of superposition, the line source approximation, and fluid flow particle tracking, transient breakthrough time from the injecting well to the producing well is calculated for the rate-pressure well doublet. This transient breakthrough time is then compared to the analytical steady state solution for breakthrough time, and to the transient rate-rate solution for transient breakthrough time presented by *Menninger and Sageev* (1986).

THEORY

In the case of the steady state rate-rate well doublet, the velocity map is only a function of space, and is constant with respect to time. In the case of the transient rate-rate model, the velocity map is a function of space and time. This is true for the rate-pressure well doublet as well. In this section we present a summary of the various methods used for computing the velocity along the shortest stream line between the two wells (See Figure 1.) In the following derivations, we assume that the pressure behavior in the reservoir is governed by the diffusivity equation, and that the reservoir is homogeneous with isotropic properties. Also, we assume a unit mobility ratio and piston-like displacement.

We consider two independent well configurations in this section. In the first configuration, we have a well producing at a constant rate and an injection well that maintains a constant pressure equal to the initial pressure of the system, p_i. This configuration is termed the rate-pressure model, and was developed by *Sageev and Horne* (1983), and *Sageev and Horne* (1985a). The Second configuration includes a constant pressure injection well in an infinite reservoir, and is termed the constant pressure model. This configuration was described by *Carslaw and Jaeger* (1960), *Van Everdingen and Hurst* (1949), and by *Fetkovich* (1980). The superposition of the rate-pressure and the constant pressure models is presented in Figure 2, and was discussed by *Sageev and Horne* (1985b). The results of this superposition are presented in the Results section.

Velocity for the Rate-Pressure Model

The velocity for the rate-pressure model is a function of space and time. *Sageev and Horne* (1985a) presented the interference dimensionless pressure solution in Laplace

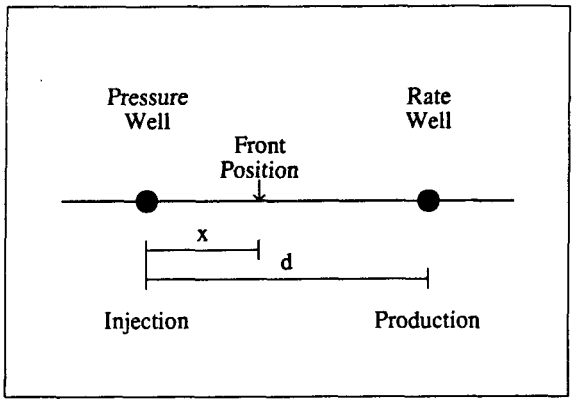


Figure 1: Schematic of a rate-pressure well doublet.

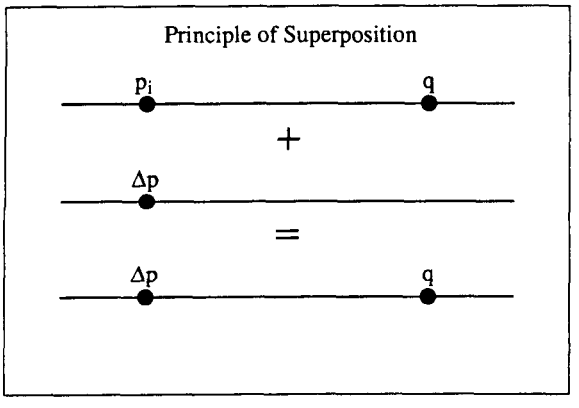


Figure 2: Schematic of the superposition for the rate-pressure well doublet.

space. Along the line between the two wells, the dimensionless Laplace pressure solution is:

$$\bar{p}_D = \frac{1}{s} \sum_{n=0}^{\infty} \varepsilon_n \left[I_n(x_D\sqrt{s})\, K_n(d_D\sqrt{s}) - \frac{I_n(\sqrt{s})\, K_n(d_D\sqrt{s})}{K_n(\sqrt{s})} K_n(x_D\sqrt{s}) \right] \quad (1)$$

where:
n = 0,1,2,3,.....
$\varepsilon_n = 1$ for n = 0
$\varepsilon_n = 2$ for n > 0
The variables are defined in the Nomenclature. The dimensionless Laplace spatial derivative of the pressure along the line between the two wells is:

$$\frac{\partial \bar{p}_D}{\partial x_D} = \frac{\sqrt{s}}{s} \sum_{n=0}^{\infty} \varepsilon_n \left[I_{n+1}(x_D\sqrt{s})\, K_n(d_D\sqrt{s}) + \frac{I_n(\sqrt{s})\, K_n(d_D\sqrt{s})}{K_n(\sqrt{s})} K_{n+1}(x_D\sqrt{s}) \right] \quad (2)$$

Finally, the velocity along the line between the two wells is:

$$V_x = \frac{-q}{2\pi\phi h r_w} \frac{\partial p_D}{\partial x_D} = \frac{-q}{2\pi\phi h r_w} L^{-1} \left\{ \frac{\partial \bar{p}_D}{\partial x_D} \right\} \quad (3)$$

Equation (2) involves an infinite summation on the order of modified Bessel functions, and is not readily inverted numerically to real time. Instead of using the Laplace velocity of Equation (3), we discretize the rate history at the constant pressure well, and use the superposition of constant rate line sources. This is described in the next two sections.

Velocity for the Constant Rate Case

The radial velocity field created by a constant rate well in an infinite reservoir is related to the derivative of pressure with respect to radius. In this study, the constant rate well is approximated by the *Theis* (1935) line source model. The dimensionless pressure solution for this model is:

$$p_D = -\frac{1}{2} E_i(-X) \quad (4)$$

where a positive dimensionless pressure is associated with pressures below the initial pressure p_i, and

$$X = \frac{r_D^2}{4t_D} \quad (5)$$

and the dimensionless terms are defined as:

$$t_D = \frac{kt}{\phi\mu c_t r_w^2} \quad (6)$$

and

$$r_D = \frac{r}{r_w} \quad (7)$$

The rest of the terms are defined in the Nomenclature. We are interested in computing the breakthrough time for the well doublet presented in Figure 1. The origin of the coordinate system is located at the injection well, hence, the tracer front moves along the straight line between the two wells. The distance between the two wells is denoted by d, and the distance between the location of the tracer front and the injection well is denoted by x. The Darcy velocity at a point x away from the injector caused by the constant rate production well is given by:

$$V_x = -\frac{k}{\mu} \frac{q\mu}{2\pi\phi k h r_w} \frac{\partial p_D}{\partial x_D} = \frac{-q}{2\pi\phi h r_w} \frac{\partial p_D}{\partial x_D} \quad (8)$$

The calculation of $\frac{\partial p_D}{\partial x_D}$ is performed using the formula for the derivative of the exponential integral:

$$\frac{dE_i(u)}{du} = \frac{1}{u} e^u \quad (9)$$

In terms of the coordinate system centered at the injection well, the dimensionless pressure and the spatial derivative of the dimensionless pressure are:

$$p_D = -\frac{1}{2} E_i \left[-\frac{\left[\frac{d-x}{r_w}\right]^2}{4t_D} \right] \quad (10)$$

$$\frac{\partial p_D}{\partial x_D} = \left[\frac{1}{\frac{d-x}{r_w}}\right] e^{-\frac{\left[\frac{d-x}{r_w}\right]^2}{4t_D}} \qquad (11)$$

The particle velocity, V_x, is calculated using Equations (8) and (11).

Velocity for the Constant Initial Pressure Well

Since the pressure at the injection well is constant and is equal to the initial pressure p_i, the time dependent variable is the injection rate. *Sageev and Horne* (1985b) presented the dimensionless Laplace rate solution for the injection well:

$$\bar{q}_D = \frac{-1}{\sqrt{s}}\left[I_1(\sqrt{s})K_0(d_D\sqrt{s}) + \frac{I_0(\sqrt{s})K_0(d_D\sqrt{s})}{K_0(\sqrt{s})} K_1(\sqrt{s})\right] \qquad (12)$$

where q_D is defined as:

$$q_D = \frac{q_{injection}}{q_{production}} \qquad (13)$$

The dimensionless rate at the injector starts with a value of zero and increases with time. At late time, the injection rate approaches the production rate and the dimensionless rate approaches unity. Figure 3, after *Sageev and Horne* (1985a), shows the rate response for various distances between the two wells. It takes a long time for the rate response at the constant pressure well to increase. The curves in Figure 3 were generated by numerically inverting Equation (12) using an algorithm developed by *Stehfest* (1970).

For a given system, we can generate the rate response of the constant pressure well using Equation (12). We discretize the time domain and assume that during a given time step, the injection rate is constant. Hence, after n time steps, we have n flow rates and we apply the method of superposition of constant rate line sources. The dimensionless pressure derivative at point x_D is related to the dimensionless rate by:

$$\frac{\partial p_D}{\partial x_D}(x_D,t_D) = \sum_i^n \frac{\Delta q_{Di}}{x_D} e^{-\frac{x_D^2}{4t_D - t_{Di}}} \qquad (14)$$

where Δq_{Di} and t_{Di} are the rates and beginning injection times of each hypothetical new well, respectively, and $x_D = x/r_w$. This method is visualized in Figure 4, where only two different Δq_i's are used. A Δq_i of 0.08 is used before tracer injection, and a Δq_i of 0.05 is used after tracer injection. With such a method for discretizing the injection rate into a set of constant rate changes, we can now calculate the velocity, $v(x,t)$, of any fluid particle. Combining this result with the one for the constant rate well, we can use superposition to calculate the velocity of any particle on the straight line path between the two wells, and thus we can use fluid flow front tracking to calculate the breakthrough time for the rate-pressure model.

Velocity for a Constant Pressure Well

In this section we present the velocity as a function of space and time caused by a constant pressure well in an

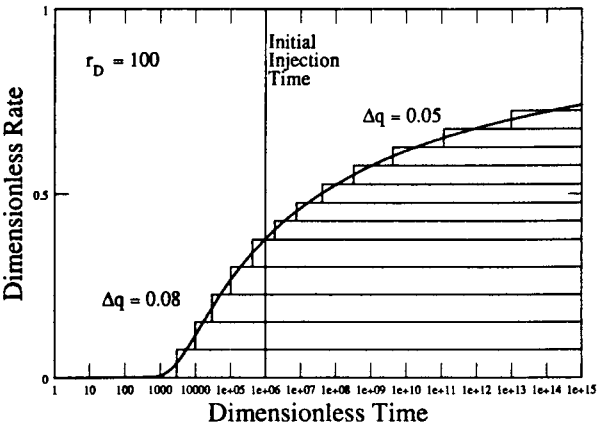


Figure 3: The dimensionless injection rate for various interwell distances. After *Sageev and Horne* (1985a).

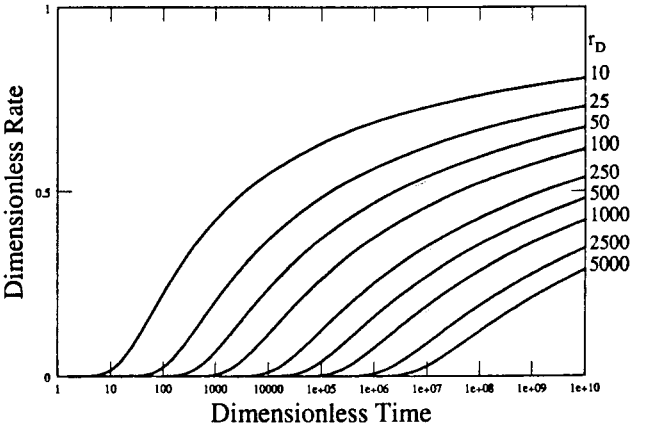


Figure 4: Discretized dimensionless rate curve, using different values of Δq before and after initial injection time.

infinite reservoir. The Laplace space solution, that was presented by *Carslaw and Jaeger* (1960), *Van Everdingen and Hurst* (1949), or by *Fetkovich* (1980) is:

$$\bar{p}_D = \frac{K_0(r_D\sqrt{s})}{sK_0(\sqrt{s})} \qquad (15)$$

where r_D is the dimensionless distance from the constant pressure source, and p_D is the dimensionless pressure, defined by

$$p_D = \frac{p - p_i}{\Delta p} \qquad (16)$$

where p_i is the initial reservoir pressure. Differentiating Equation (15) with respect to r_D yields:

$$\frac{\partial \bar{p}_D}{\partial r_D} = \frac{-\sqrt{s}K_1(r_D\sqrt{s})}{sK_0(\sqrt{s})} \qquad (17)$$

Equation (17) is numerically inverted to real space using the inversion algorithm developed by *Stehfest* (1970).

Hence, the velocity caused by the constant pressure well is:

$$V_x = -\frac{k\Delta p}{\mu r_w}\frac{\partial p_D}{\partial x_D} = -\frac{k\Delta p}{\mu r_w} L^{-1}\left\{\frac{\partial \bar{p}_D}{\partial x_D}\right\} \quad (18)$$

The Steady State Solution

The steady state solution to a rate-pressure well doublet is just the same as that for a rate-rate well doublet, however, approaching steady state is a much slower process for the rate-pressure configurations. This slow approach to steady state is due to the slow rate at which the constant pressure well approaches a steady state injection rate. From *Menninger and Sageev* (1986), the solution to the steady state breakthrough time for either rate-rate or rate-pressure doublets is:

$$t_{bt} = \frac{2\pi h\phi d^2}{6q} \quad (19)$$

This resulting breakthrough time for the steady state well doublet can now be compared to transient breakthrough times.

RESULTS

In this section, we describe the effects of the distance between the two wells, the rate of injection, the time of tracer injection, and the additional pressure drop at the injection well on the transient breakthrough time. In the first portion of the discussion, we concentrate on the rate-pressure model, where the injection well remains at the initial reservoir pressure p_i. In the second portion of the discussion, we consider the effects of the additional pressure rise at the injection well on the breakthrough time.

The Rate-Pressure Model

Consider a rate-pressure model with the following properties: $c_t = 6 \times 10^{-6}\ psi^{-1}$, $h = 20\ ft$, $k = 100\ md$, $\phi = 0.15$, $r_w = 0.5\ ft$, and $\mu = 1\ cp$. The effects of the rate of injection, q, the distance between the wells, d, and the initial tracer injection time, t_i, are examined in the next few figures. Figure 5 presents the effects of tracer injection time. Here, the time from tracer injection is graphed as a function of the position of the leading front of the tracer. The plot is cartesian. The top curve represents front tracking of a single constant rate producing well in an infinite reservoir, and the bottom curve represents a steady state doublet system. These extreme cases are used for comparison. We note that breakthrough time for the steady state case is at 120 days, and is much shorter than the breakthrough time for just a single constant rate producing well, that is 330 days. The second curve from the top represents a case where the tracer is injected at time zero into the rate-pressure doublet system with a breakthrough time of 160 days. As the the tracer injection time is delayed, the injection rate at the constant pressure well increases, and the breakthrough time decreases. However, even waiting for 10^{18} days before injecting the tracer, does not reduce the tracer breakthrough time to the steady state case (See Figure 5).

The top curve in Figure 5, representing the front position between the two wells caused by only the production well has an ever reducing slope. Hence, the velocity of the front increases with time along the particle flow path. The curves for the rate-pressure doublet have an inflection point. At short times after tracer injection, the slope of the curves is small, indicating a high velocity caused by the injection well. As the front moves away from the injector, the velocity decreases, and goes through a minimum about midway between the wells. As the front approaches the production well, the front velocity increases. The high front velocity at late time is caused by the large pressure gradients caused by the production well.

In Figure 6, we have the breakthrough times graphed as a function of the initial injection time in a semi-log format for the same example previously considered. As the tracer injection time is delayed, the breakthrough time decreases. The bars extending from the breakthrough time curve represent the time span for which the tracer front moves from the injection well to the production well along

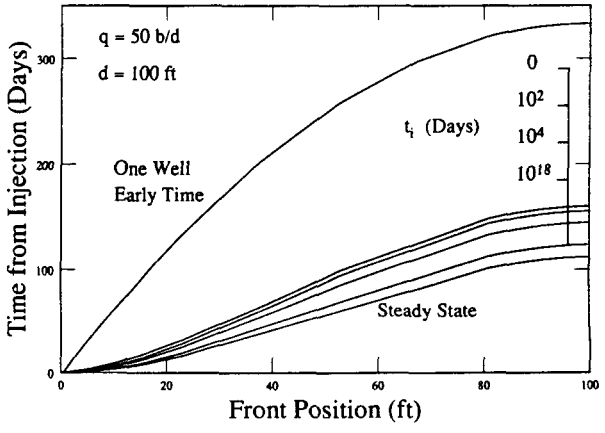


Figure 5: Front position for a rate-pressure doublet as a function of time for different tracer injection times. Reservoir parameters are: $\phi = 0.15$, $\mu = 1cp$, $c_t = 6\times10^{-6}\ psi^{-1}$, $h = 20\ ft$, $k = 100\ md$, $r_w = 0.5\ ft$.

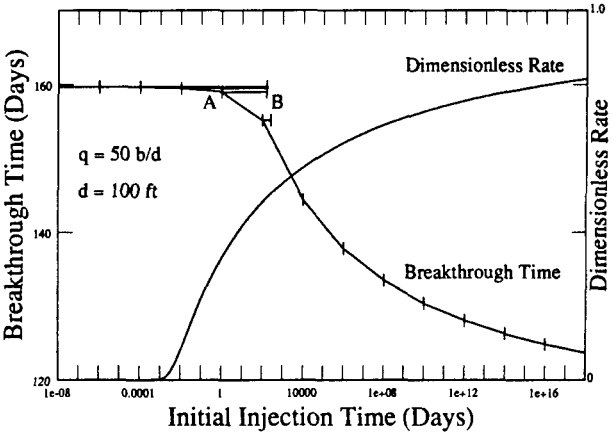


Figure 6: Breakthrough times and the dimensionless rate as a function of initial injection time. The bars represent the duration of the breakthrough time. Reservoir parameters are: $\phi = 0.15$, $\mu = 1cp$, $c_t = 6\times10^{-6}\ psi^{-1}$, $h = 20\ ft$, $k = 100\ md$, $r_w = 0.5\ ft$.

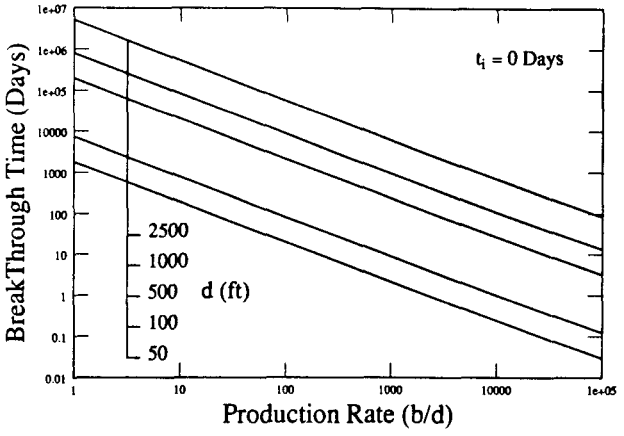


Figure 7: Breakthrough times as a function of production rate for various interwell distances with a zero tracer injection time. Reservoir parameters are: $\phi = 0.15$, $\mu = 1cp$, $c_t = 6\times10^{-6}\ psi^{-1}$, $h = 20\ ft$, $k = 100\ md$, $r_w = 0.5\ ft$.

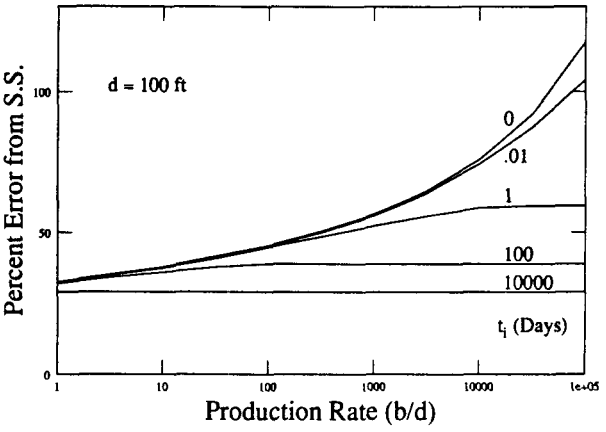


Figure 9: Percent error of the breakthrough times as a function of production rate for various tracer injection time and an interwell distance $d = 100\ ft$. Reservoir parameters are: $\phi = 0.15$, $\mu = 1cp$, $c_t = 6\times10^{-6}\ psi^{-1}$, $h = 20\ ft$, $k = 100\ md$, $r_w = 0.5\ ft$.

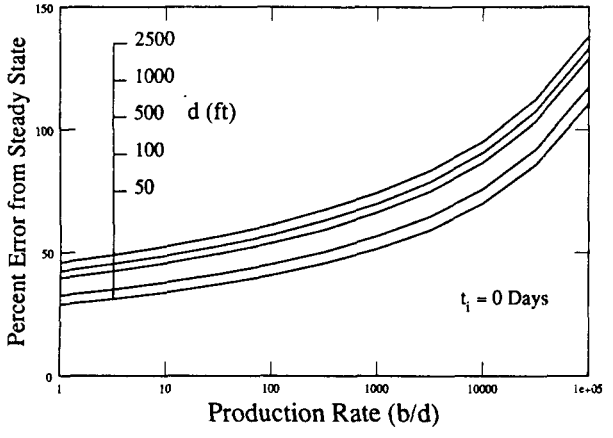


Figure 8: Percent error of the breakthrough times as a function of production rate for various interwell distances with a zero tracer injection time. Reservoir parameters are: $\phi = 0.15$, $\mu = 1cp$, $c_t = 6\times10^{-6}\ psi^{-1}$, $h = 20\ ft$, $k = 100\ md$, $r_w = 0.5\ ft$.

the straight line between them. Also the dimensionless rate of the constant pressure well is graphed in Figure 6. Points A and B represent the injection time and the arrival time respectively, for an initial tracer injection time of one day. As the initial tracer injection time increases, the average value of q_D under the bars representing the duration of the tracer test increases, and we get a corresponding reduction in breakthrough time. Hence, the time of tracer injection has a significant effect on tracer breakthrough time.

Figure 7 is a log-log presentation of the breakthrough time as a function of production rate for various values of the interwell distance. All the responses presented in Figure 7 are for the case where the tracer is injected at time zero, for the same reservoir properties discussed before. The lowermost curve in Figure 7 is for $d = 50\ ft$. As the production rate increases, the breakthrough time decreases. For a fixed production rate, the breakthrough time increases as the interwell distance increases.

In Figure 8, we see that the early time percent error from the steady state breakthrough times depends both on d and on q. We define the percent error as:

$$\%Error = \frac{t_{bt} - t_{bt,ss}}{t_{bt,ss}} \times 100 \qquad (20)$$

As the production rate increases or as the interwell distance increases, the deviation from the steady state solution increases. Figure 9 presents the combined effects of the production rate and the tracer injection time with a constant distance between the wells, $d = 100\ ft$. The dependence of the precent error on the flowrate q reduces as the initial injection time increases. As initial injection time increases, the rate of the constant pressure well changes less during the time that the tracer moves from the injector to the producer as demonstrated in Figure 6. For example, at $t_i = 100\ days$ (about where point B is in Figure 6), q_D changes less and less over the length of the bars, until the bars become so short that they look like a point on the dimensionless rate curve, and the rate of the constant pressure well can be considered constant over the duration of the breakthrough time. When $t_i = 10000\ days$, as Figure 9 shows, the precent error from the steady state case does not depend on the production rate.

since the shape of the dimensionless rate curves varies for each interwell distance, as shown in Figure 3, the error dependence on d does not disappear as t_i increases. As Figure 10 shows, the error curves change shape, but do not become horizontal, for the error depends on where t_i crosses each dimensionless rate curve (See Figure 3). For larger d, a constant t_i line crosses the rate curves in Figure 3 at lower rate values, yielding a transitionary flow period. Hence, the injection rate varies significantly during the tracer test, and the precent error from the steady state case increases. This is also demonstrated in Figure 11, that is a semi-log graph showing error dependence on initial injection time for varying d. The error levels off as t_i gets larger, and, as explained before, the injection rate varies less during the breakthrough process.

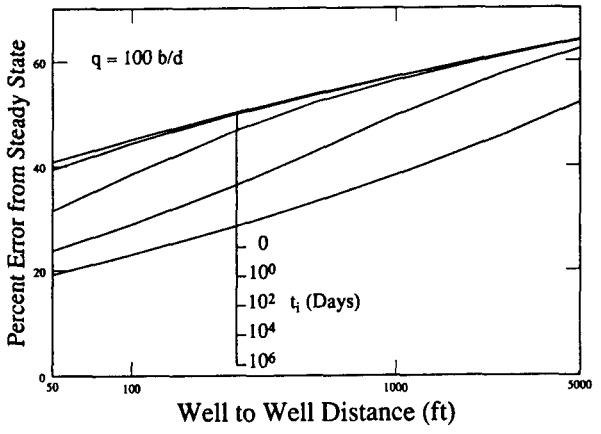


Figure 10: Percent error of the breakthrough times as a function of interwell distance and tracer injection time for a constant production rate $q = 100$ *b/d*. Reservoir parameters are: $\phi = 0.15$, $\mu = 1cp$, $c_t = 6\times10^{-6}\ psi^{-1}$, $h = 20\ ft$, $k = 100\ md$, $r_w = 0.5\ ft$.

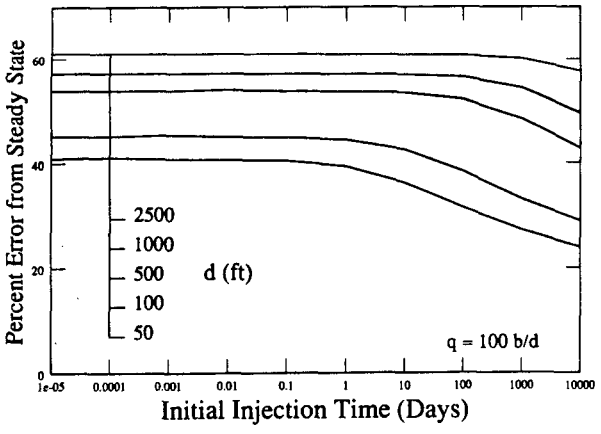


Figure 11: Percent error of the breakthrough times as a function of tracer injection time for various interwell distances and for a constant production rate $q = 100$ *b/d*. Reservoir parameters are: $\phi = 0.15$, $\mu = 1cp$, $c_t = 6\times10^{-6}\ psi^{-1}$, $h = 20\ ft$, $k = 100\ md$, $r_w = 0.5\ ft$.

The deviation of the breakthrough time for the rate-pressure model from the steady state breakthrough time is significant. This deviation is mainly attributed to the transient flow conditions around the production well, and to the slow response of the injection rate at the constant pressure well. Hence, the first injected tracer particle at the constant pressure well starts moving in the direction of the production well at a lower velocity in comparison to the steady state case, yielding a longer breakthrough time. One way in which to increase particle throughput and decrease breakthrough times in a rate-pressure doublet system is to create a pressure rise at the constant pressure well. This is described in the next section.

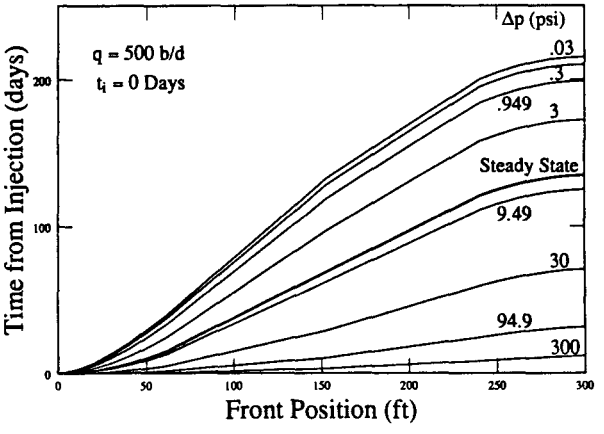


Figure 12: Front position for rate-pressure doublet as a function of pressure rise at the injection well for $q = 500$ *b/d* and zero tracer injection time. Reservoir parameters are: $\phi = 0.2$, $\mu = 0.5cp$, $c_t = 5\times10^{-6}\ psi^{-1}$, $h = 20\ ft$, $k = 50\ md$, $r_w = 0.3\ ft$.

The Rate-Pressure Doublet

The rate-pressure doublet differs from the rate-pressure model in the boundary condition at the constant pressure well. In the rate-pressure doublet, we impose a sudden pressure rise at the constant pressure well. Hence, the rate of injection at the constant pressure well is a function of the magnitude of the pressure rise imposed at the well, and of the response to the constant rate production well. The rate of injection caused by a constant pressure well in an infinite reservoir decreases with time, and was described by *Fetkovich* (1980). The rate of injection caused by the constant rate production well increases with time, as shown in Figure 3.

Figure 12 presents the time from tracer injection as a function of the tracer front position between the two wells for various pressure increases at the injection well, denoted by Δp. The reservoir parameters for the responses presented in Figure 12 are: $c_t = 5x10^{-6}\ psi^{-1}$, $h = 20ft$, $k = 50\ md$, $\phi = 0.2$, $r_w = 0.3\ ft$, $q = 500\ b/d$, $d = 100\ ft$, and $\mu = 0.5\ cp$. All the curves in Figure 12 are for a tracer injection time of zero. The highlighted curve in the middle represents the steady state rate-rate doublet case. The uppermost curve is for a small pressure rise at the injector of 0.03 psi, yielding a breakthrough time of about 60% larger than the steady state case. As the initial pressure rise at the injection well increases, the breakthrough time decreases significantly. For a Δp of 9.49 psi, the breakthrough time is just under the steady state case. For a Δp of 94.9 psi, the breakthrough time is mainly controlled by the injection well, and is about 20% of the steady state case.

Figure 13 presents similar curves as presented in Figure 12, with the tracer injection time at 10 days. The breakthrough times are slightly lower than the breakthrough times presented in Figure 12, and the main controlling parameter remains the magnitude of the pressure rise at the injection well.

The effects of the initial injection pressure rise at the injection well is summarized in Figure 14. In this figure, breakthrough times as a function of the injection pressure

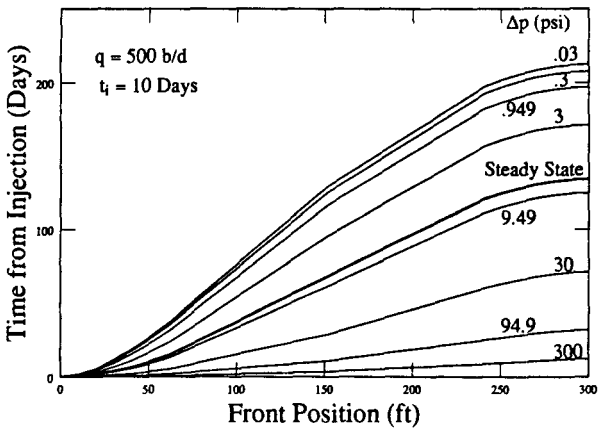


Figure 13: Front position for rate-pressure doublet as a function of pressure rise at the injection well for $q = 500$ *b/d* and for a tracer injection time of 10 days. Reservoir parameters are: $\phi = 0.2$, $\mu = 0.5cp$, $c_t = 5\times10^{-6}\ psi^{-1}$, $h = 20\ ft$, $k = 50\ md$, $r_w = 0.3\ ft$.

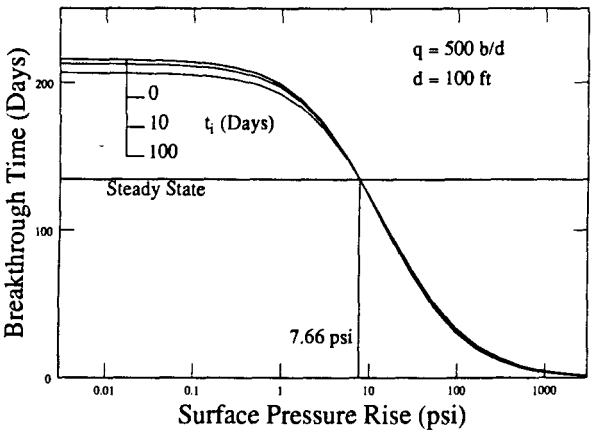


Figure 14: Breakthrough time as a function of pressure rise at the injection well for various tracer injection times, and $q = 500\ b/d$ and $d = 100\ ft$. Reservoir parameters are: $\phi = 0.2$, $\mu = 0.5cp$, $c_t = 5\times10^{-6}\ psi^{-1}$, $h = 20\ ft$, $k = 50\ md$, $r_w = 0.3\ ft$.

rise for various tracer injection times are presented. The horizontal line represents the steady state breakthrough time. For pressure rises smaller than 7.66 psi (for reservoir properties described in this section) breakthrough times are larger than the steady state breakthrough time by about 60%. The effects of the tracer injection time up to 100 days from the start of production is not significant. For pressure rises greater than 7.66 psi the breakthrough times for the rate-pressure doublet are smaller than for the steady state case. Large imposed pressure rises at the injection well dominate the tracer movement along the line between the two wells.

CONCLUSIONS

In the following conclusions we consider two well configurations: the rate-pressure model and the rate-pressure doublet. These two configurations differ in the imposed constant pressure, Δp, at the injection well. For the rate-pressure model $\Delta p = 0$ and for the rate-pressure doublet $\Delta p > 0$. In general, the rate-pressure model yields a breakthrough time larger than the steady state case. In the examples considered in this study, we observed that the breakthrough time may be 50%-100% larger than for the steady state case. The rate-pressure doublet may yield breakthrough times that are smaller or larger than the steady state case depending on the magnitude of the imposed pressure rise at the injection well. In the examples considered in this study, we found that the breakthrough time may be as low as 1/5 of the breakthrough time for the steady state case.

Rate-Pressure Model:

1. The breakthrough time reduces as the tracer injection time, and the production rate increase.
2. The percent error of the breakthrough time from the steady state case increases as the production rate and the interwell distance increase.
3. The percent error of the breakthrough time from the steady state case decreases as the tracer injection time increases.
4. The percent error of the breakthrough time from the steady state case for the rate-pressure model can be as high as 50%-100% for practical cases.

Rate-Pressure Doublet:

5. Small imposed pressure rises at the injection well yield breakthrough times similar to the breakthrough times for the rate-pressure model.
6. For small imposed pressure rises at the injection well, the breakthrough times are affected by the tracer injection time. As tracer injection time is increased, the breakthrough time decreases.
7. Large imposed pressure rises at the injection well dominate the space-time velocity of the tracer, and yield significantly smaller breakthrough times than the breakthrough times for the steady state model.
8. The effect of the tracer injection time is not significant when the imposed pressure rise at the injection well is large in comparison to the steady state pressure rise.

ACKNOWLEDGEMENTS

Financial support was provided by the Stanford Geothermal Program, DOE Contract No. DE-AT02-80SF11459, and by Stanford University.

NOMENCLATURE

E_i = Exponential Integral
I_n = Modified Bessel function, first kind, n'th order
K_n = Modified Bessel function, second kind, n'th order
V_x = Velocity in the x direction
X = Exponential Integral argument

c_t = total system compressibility
h = Formation thickness

k = Permeability
p = Pressure
p_D = Dimensionless pressure, $2\pi kh(p_i-p)/q\mu$
$\bar{p}_D$ = Laplace transformation of p_D
p_i = Initial pressure
Δp = Imposed injection well pressure rise
q = Volumetric rate
q_D = Dimensionless rate, $q(t)/q_{source}$
$\bar{q}_D$ = Laplace transformation of q_D
r = Radius
r_D = Dimensionless radius, r/r_w
r_w = Wellbore radius
s = Laplace variable
t = Time
t_{bt} = Breakthrough time
$t_{bt,ss}$ = Steady state breakthrough time
t_D = Dimensionless time, $kt/\phi\mu c_t r_w^2$
x = Distance from injector
x_D = Dimensionless distance, x/r_w

μ = Viscosity
ϕ = Porosity

REFERENCES

Carslaw, H.S. and Jaeger, J.C.:*Conduction of Heat in Solids*, 2nd ed. Oxford University Press, 1960.

Fetkovich, M.J.: "Decline Curve Analysis Using Type Curves," *J. Pet. Tech* (June 1980) 1065-1077.

Kruseman, G.P., and De Ridder, N.A.: "Analysis and Evaluation of Pumping Test Data," International Institute of Land Reclamation and Improvement, Wageningen, The Netherlands (1970).

Menninger, W., and Sageev, A.: "Breakthrough Time for the Source-Sink Well Doublet," Presented at the 11th Workshop on Geothermal Reservoir Engineering, Stanford, CA. (1986).

Mueller, T.D., and Witherspoon, P.A.: "Interference Effects Within Reservoirs and Aquifers," *J. Pet. Tech.* (Oct. 1965) 1803-1812.

Ramey, H.J., Jr., Kumar, A. and Gulati, M.S., *Gas Well Test Analysis Under Water Drive Conditions*, American Gas Association, Arlington, VA, (1973).

Sageev, A., and Horne, R.N.: "Pressure Transient Analysis of Reservoirs with Linear or Internal Linear Boundaries," SPE 12076, Presented at the 58th Annual Technical Conference and Exhibition, San Francisco, California (Oct. 1983).

Sageev, A., and Horne, R.N.: "Interference Between Constant Rate and Constant Pressure Wells," Geothermal Resources Council, *Transactions*, v. 9, Part II, 573-577. (1985a).

Sageev, A., and Horne, R.N.: "Interference Between Constant Rate and Constant Pressure Reservoirs Sharing a Common Aquifer," *Soc. Pet. Eng. J.*, 419-426 (1985b)

Stallman, R.W., "Nonequilibrium Type Curves Modified for Two-Well Systems", U.S. Geol. Surv., Groundwater Note 3, (1952).

Stehfest, H.: "Algorithm 368, Numerical Inversion of Laplace Transforms," *Communications of the ACM*, D-5 13, No. 1, 47-49, (Jan. 1970).

Theis, C.V., "The Relationship Between the Lowering of Piezometric Surface and Rate and Duration of Discharge of Wells using Groundwater Storage," Trans., AGU, 2, 519, (1935).

Van Everdingen, A.F. and Hurst, W.: "The Application of the Laplace Transformation Flow Problems in Reservoirs," *Trans.*, AIME (Dec. 1949) 186, 305-324.

PROCEEDINGS, Twelfth Workshop on Geothermal Reservoir Engineering
Stanford University, Stanford, California, January 20-22, 1987
SGP-TR-109

Analysis of Thermally Induced Permeability Enhancement in Geothermal Injection Wells

S. M. Benson and J.S. Daggett

Earth Sciences Division
Lawrence Berkeley Laboratory
Berkeley, California 94720

E. Iglesias, V. Arellano, and J. Ortiz-Ramirez

Instituto De Investigaciones Electricas
Departamento De Geotermia
Cuernavaca, Morelos, Mexico

ABSTRACT

Reinjection of spent geothermal brine is a common means of disposing of geothermal effluents and maintaining reservoir pressures. Contrary to the predictions of two-fluid models (two-viscosity) of nonisothermal injection, an increase of injectivity, with continued injection, is often observed. Injectivity enhancement and thermally-affected pressure transients are particularly apparent in short-term injection tests at the Los Azufres Geothermal Field, Mexico. During an injection test, it is not uncommon to observe that after an initial pressure increase, the pressure decreases with time. As this typically occurs far below the pressure at which hydraulic fracturing is expected, some other mechanism for increasing the near-bore permeability must explain the observed behavior. This paper focuses on calculating the magnitude of the near-bore permeability changes observed in several nonisothermal injection tests conducted at the Los Azufres Geothermal Field. In order to evaluate the pressure transient data and calculate the magnitude of the thermally induced permeability changes, a new analytic solution for calculating pressure transients with time-varying sandface flowrates and temperatures has been developed. The effects of temperature-dependent fluid and rock properties, as well as a moving thermal front, are explicitly included in the calculations. Based on this new solution, a technique is developed for calculating the reservoir permeability, skin factor of the well, and near-bore permeability increases. The results of these calculations indicate that the permeability increases by a factor of 5 in the near-bore region during the 2 to 3 hour injection tests. A good correlation between the permeability increase and the sandface injection temperature indicates that the permeability increase is caused by cooling the formation.

INTRODUCTION

Injecting cold water is a common technique for estimating the permeability, productivity, and injectivity of geothermal wells. In addition to providing a measure of these parameters, there is some evidence that this practice stimulates the well (Bodvarsson et al., 1984). This is contrary to the predictions of physical and mathematical models that consider only the temperature dependent fluid properties (Benson, 1984; Benson and Bodvarsson, 1986).

This intriguing phenomena is particularly apparent in geothermal wells in the Los Azufres Geothermal Field in Mexico, where a large set of pressure transient data exhibit unusual characteristics. As shown by pressure buildup curves for three wells in Figure 1, it is not uncommon to observe that after an initial period during which the pressure increases as expected, the pressure stabilizes and then begins to drop, even though injection continues at a steady rate. This unusual behavior is attributed to progressive increases in the near-bore permeability. Several physical mechanisms can increase the near-bore permeability, including; hydraulic fracturing, pushing drilling mud and formation fines away from the well-bore and into the formation, thermal contraction and thermal stress cracking of the rock, and dissolution of fracture filling minerals. As these tests were conducted well below the fracture gradient, hydraulic fracturing has been eliminated as a possible cause for the permeability increase, leaving one or more of the other mechanisms to account for the observed behavior.

The goal of this investigation is two-fold. First we attempt to quantify the magnitude of the permeability increase needed to explain the observed pressure behavior. Next, we investigate correlations between temperature and the permeability increase in an effort to provide insight into the physical mechanism governing this occurrence.

BACKGROUND

It is worthwhile to spend a moment reviewing the physical processes that occur as cold water is injected into a hot geothermal reservoir. First, injection causes the pressure to increase due to the formation's resistance to flow. For horizontal flow in a liquid saturated rock, the pressure buildup is governed by Equation 1

$$\nabla\cdot(\frac{k\,\rho}{\mu}\nabla p\,) = \frac{\partial(\rho\phi)}{\partial p}\frac{\partial p}{\partial t} \qquad (1)$$

where k is the formation permeability, ρ is the fluid density, μ is the fluid viscosity, p is the fluid

pressure, and ϕ is the porosity of the formation. Second, as fluid is injected into the well, an interface (called the hydrodynamic front) between the undisturbed reservoir fluids and the injected fluid moves away from the injection well. The thermal front (defined as the surface where the temperature is midway between the temperature of the reservoir and injected fluids) lags some distance behind the hydrodynamic front due to a transfer of heat from the reservoir rock to the injected fluid. The distance to these fronts (r_f) and the rate at which they move away from the injection well depend on the relevant mass and energy conservation equations and the geometry of the system. In the region behind the fronts, the composition, temperature, compressibility (c_f) and density of the fluid may be different than the in-situ fluid. In addition, if the permeability, porosity, and pore-volume compressibility (c_{pv}) are temperature, stress, or composition sensitive, they too may vary in the region behind the front.

The wellbore also influences the pressure changes caused by injection. In deep geothermal systems the typically large wellbores create significant wellbore storage effects, resulting in a long time period before the surface and sandface injection rates are equal. Second, the wellbore acts like a large heat exchanger, transferring heat from the formation to the injected fluid before in is injected into the open interval of the well. This results in a time-varying sand-face injection temperature. At moderate injection rates it may take several hours for the sandface injection temperature to stabilize.

MATHEMATICAL MODEL

Having reviewed the range of physical processes controlling the pressure buildup during injection, we are ready to choose a mathematical model for interpreting the data. There is a small but relevant collection of papers devoted to the interpretation of injection tests. However, all of these models consider only that the properties of the injected fluid are different from the properties of the in situ fluid. Nevertheless, they provide valuable insight into the pressure transient behavior. Consequently, they are reviewed briefly below.

A closed form analytical solution for Equation 1 has been derived for the special case where the volumetric injection rate (Q) is constant and

$$r_f(t) = \left[\frac{bQt}{\pi h}\right]^{1/2} \tag{2}$$

where b is a constant that depends on the relevant mass and/or energy balances and h is the thickness of the formation, provided that the properties of the fluid and formation behind the front are uniform and constant (Ramey, 1970). For nonisothermal injection

$$b = \frac{\rho_w C_w}{\rho_a C_a} \tag{3}$$

where C_w and C_a are the heat capacity of the injected water and reservoir, and ρ_w and ρ_a are the density of water and the reservoir, respectively. Although, this solution can be extended to consider the effects of increasing near-bore permeability, several other important factors, such as varying

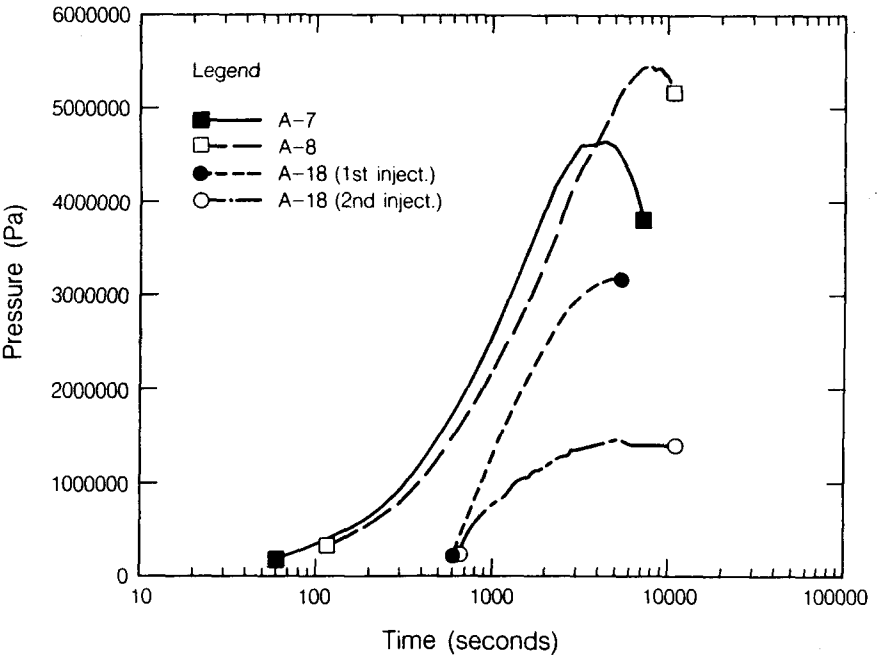


Figure 1. Pressure transient data from four injection tests at the Los Azufres Geothermal Field.

flowrates and time-dependent sandface injection temperatures can not be included.

Numerical solutions of Equation 1 have also provided insightful descriptions of pressure transient behavior during nonisothermal and multicomponent injection. An extensive study of the influence of temperature dependent fluid viscosity and density on the pressure transient behavior, resulted in developing injection test analysis methods and front tracking techniques under certain idealized conditions (Benson, 1984; Benson and Bodvarsson, 1986). Additional studies by Cox and Bodvarsson (1985) investigate pressure transients during nonisothermal injection into a horizontally and vertically fractured formation.

A review of the literature shows that although Equation 1 has been solved for some special cases where the properties of the injected fluid differ from the injected system, in general, we are still restricted to a two-fluid model, where the properties are uniform within each of the two regions. Furthermore, using currently available solutions, we are restricted to studying systems where the movement of the front is described by Equation 2. Other restrictive factors include requiring that the rock properties remain constant, that the injection rate remains constant or is a series of step rates, and the properties of the fluid remain constant during injection. As discussed above in actual field tests, many of these conditions are violated, rendering the currently available solutions inadequate.

New Solution

To circumvent the restrictive assumptions required to develop a closed form analytic solution to Equation 1, an alternative approximate solution of the form

$$\Delta p\,(r_w\,,t\,) = \Delta p_{ss}\,(r_w\,,t\,)+\Delta p_t\,(r_f\,,t\,) \qquad (4)$$

is proposed, where $\Delta p\,(r_w\,,t\,)$ is the pressure change at the injection well, $\Delta p_{ss}\,(r_w\,,t\,)$ is the steady-state pressure change across the invaded region at time t, and $\Delta p_t\,(r_f\,,t\,)$ is the transient pressure response in the uninvaded formation. The mathematical advantages of this form of the solution are twofold. First, all of the non-linear terms associated with the region behind the front in Equation 1 are incorporated into the first term of Equation 4, which for a slightly-compressible single component fluid flowing through a radially symmetric system is calculated by

$$\Delta p_{ss}\,(t\,) = \frac{q}{2\pi h}\int_{r_w}^{r_f\,(t\,)} \frac{\mu(r\,,t\,)}{k\,(r\,,t\,)\,\rho(r\,,t\,)}\,\frac{dr}{r} \qquad (5)$$

where q is the mass injection rate and the other terms are defined as before. Second, the term $\Delta p_t\,(r_f\,,t\,)$ can easily be evaluated from well established solutions such as the exponential integral solution, convolution of the instantaneous line source solution for variable flow rates, or any one of a number of relevant solutions that satisfy the desired outer boundary conditions.

With the utility of Equation 4 established, it becomes important to determine the range of conditions under which it is valid. The condition that pseudo-steady flow conditions exist within the invaded region is implicit in Equation 4. This condition is approximately satisfied for

$$t > \frac{25\,r_f^{\,2}}{\eta_1} \qquad (6)$$

where η_1 is the diffusivity $(k\,/\phi\mu c_t\,)$ of the inner region. Evaluation of Equation 6 for a wide range of formation parameters and fluid properties shows that Equation 4 is valid within several seconds after injection begins if r_f (at $t=0$)$=r_w$.

Verification

As an example how Equation 4 is applied in a typical situation, it will be compared to the closed form analytical solution for nonisothermal injection of a fluid at a temperature of T_i (with properties μ_i and ρ_i) into a uniform, areally infinite, porous media with constant rock properties, that is originally at temperature of T_r (with properties μ_r and ρ_r). In this case, the radial distance to the thermal front is given by

$$r_f\,(t\,)=\left[\frac{\rho_w\,C_w\,Qt}{\rho_a\,C_a\,\pi h}+r_w^{\,2}\right]^{1/2} \qquad (7)$$

For uniform fluid properties, and constant rock properties behind the front, the first term in Equation 4 (evaluated by integrating Equation 5) is given by

$$\Delta p_{ss}\,(r_w\,,t\,) = \frac{q\,\mu_i}{2\pi\rho_i\,kh}\ln\left(\frac{r_f}{r_w}\right) \qquad (8)$$

The second term in Equation 4 is evaluated with the exponential integral solution (Ei) and is given by

$$\Delta p_t\,(r_f\,,t\,)=\frac{q\,\mu_r}{4\pi\rho_r\,kh}Ei\left(\frac{r_f^{\,2}}{4\eta_r\,t}\right) \qquad (9)$$

Adding Equations 8 and 9 together, and recognizing that the asymptotic expression for the exponential integral (Ei) is appropriate in this case, we see

$$\Delta p\,(r_w\,,t\,) = \frac{q\,\mu_r}{4\pi\rho_r\,kh}\left[\frac{\mu_r\,\rho_i}{\mu_i\,\rho_r}\ln\left(\frac{r_f}{r_w}\right)^2+\ln t\right.$$

$$\left.+\ln\left(\frac{\eta_r}{r_f^{\,2}}\right)+0.80907\right] \qquad (10)$$

The closed form analytic solution for the same problem is given by

$$\Delta p\,(r_w, t) = \frac{q\,\mu_i}{4\pi\rho_i\,kh}\left[Ei\left(\frac{r_w{}^2}{4\eta_i\,t}\right) - Ei\left(\frac{r_f{}^2}{4\eta_i\,t}\right)\right] + \frac{q\,\mu_r}{4\pi\rho_r\,kh}\,e^{\frac{-r_f{}^2}{4\eta_i}\left(1-\frac{\eta_i}{\eta_r}\right)}\,Ei\left(\frac{r_f{}^2}{4\eta_r\,t}\right) \qquad (11)$$

For a slightly compressible fluid, the exponential expression in the second term of Equation 11 is within 1% of unity within several seconds after injection begins. Also, as in the above case, the asymptotic approximation for the Ei function is appropriate. Under these conditions, the sum of the two terms inside the brackets is equal to $\ln(r_f/r_w)^2$ and Equation 11 can be rearranged to produce a result that is identical to Equation 10.

In addition to comparing Equation 4 to the closed form analytical solution for a two-fluid system, mathematical solutions generated with Equation 4 have been verified by comparison to numerically simulated pressure transients during nonisothermal injection in geothermal reservoirs. Results have been compared for variable and steady injection rates in porous systems, as well as for steady injection rates in horizontally and vertically fractured geothermal reservoirs. In all cases, agreement between the two methods is excellent, as long as Equation 6 is satisfied.

ANALYSIS METHOD

Before analyzing the pressure transient data from any injection test, it is necessary to carefully assess all of the salient features of the test data. Once these have been established, a mathematical solution tailored to the problem at hand, can be developed by applying Equations 4 and 5.

The Los Azufres geothermal system occurs in fractured volcanic deposits, at a depth of 1000 to 2000 m. Reservoir temperatures range from 220 to 280 ° C in the wells from which injection test data are available. Geothermal fluids are produced from fractured horizons within andesitic rocks. The injection tests consisted of injecting 20 ° C water into the formation at a constant wellhead injection rate for 2 to 3 hours. During injection, the formation pressure was measured with an Amerada pressure gauge positioned adjacent to the production zone in the well.

Log(pressure) vs. log(time) graphs (not shown here) of the pressure buildup data shown in Figure 1 indicate that wellbore storage effects persist throughout the entire 2 to 3 hour test. This is illustrated in Figure 2, which shows the sandface injection rate as a function of time for well A-7. For the first half of the test, the sandface injection rate gradually increases to the surface injection rate. During the latter half of the test, the sandface injection rate is greater than the surface

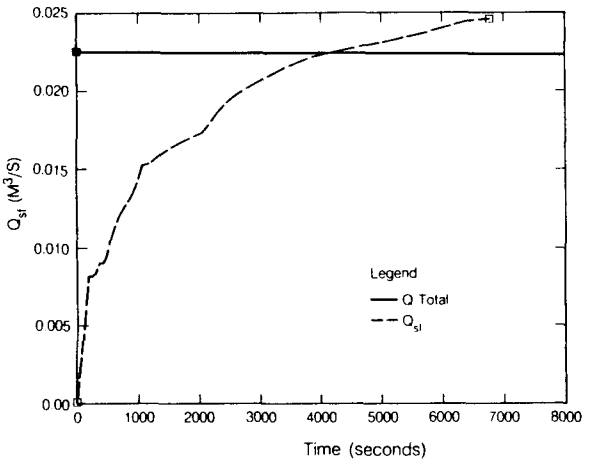


Figure 2. Sandface flowrate during the well A-7 injection test.

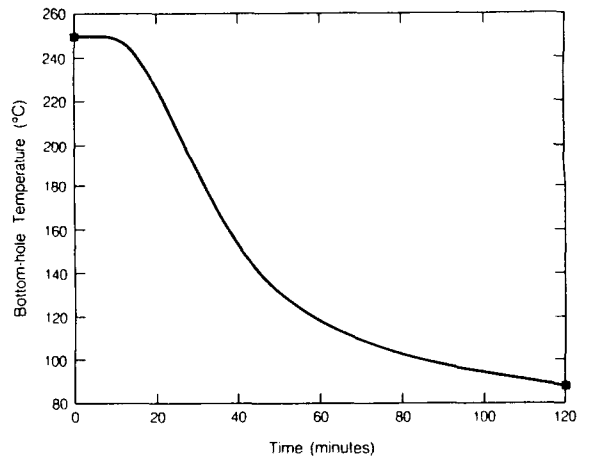


Figure 3. Simulated sandface temperature during the well A-7 injection test.

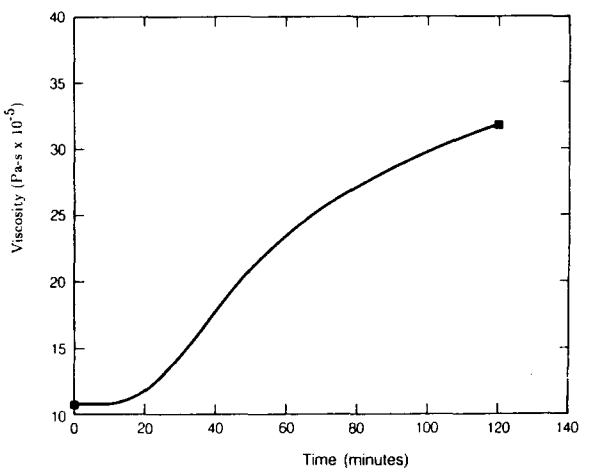


Figure 4. Sandface fluid viscosity during the well A-7 injection test.

injection rate because the pressure (waterlevel) is dropping in the wellbore.

Another factor that must be considered is that although the temperature of the injected water is constant at the wellhead, it is not constant at the formation face. As shown by the simulated sandface injection temperature in Figure 3, the sandface temperature decreases throughout the test. By the end of the test, the temperature is still nearly 70 °C above the surface temperature. The time-varying injection temperature causes the fluid viscosity (see Figure 4) and density to vary throughout the test. This creates a non-uniform distribution of the fluid properties in the region behind the front.

In light of these complications, one might deduce that there is little chance of obtaining any valuable information from this test data. However, by making a few assumptions, which will be discussed below, and applying a solution generated from Equation 4, we are able to determine the formation permeability, and estimate the magnitude of the thermally-induced permeability enhancement that causes the unusual pressure transient response.

To develop a mathematical solution for calculating the pressure buildup, we must first describe how the front moves with time. For the purposes of this analysis, the distance to the front, based on an energy balance between the heat lost from the rock and that gained by the injected fluid, is assumed to be given by

$$r_f^{\,2} = \frac{\rho_w C_w}{\rho_a C_a} \frac{1}{\pi h} \int_0^t Q(t)\,dt \qquad (12)$$

where C_w and C_a are the heat capacities of water and the formation, respectively and the other terms are as defined previously. Note that this formulation assumes that there is no heat transfer between the low permeability rock formation and the permeable layers into which fluid is injected. Although this is not generally true for fractured reservoirs, this assumption is justified in light of the short duration of the tests and that fluid is injected into a "fracture zone" that is much thicker than the apertures of individual fractures. If the fluid is injected into very thin strata, separated by much thicker strata, the effects of heat conduction to the surrounding strata must be considered (Bodvarsson and Tsang, 1982).

It is also necessary to describe how the fluid properties vary behind the front. For this study we assume that the fluid viscosity and density, as well as, the formation permeability vary linearly in the region behind the front

$$\mu_i(r,t) = \mu_i(r_w,t) + \frac{\mu_r - \mu_i(r_w,t)}{r_f - r_w}(r - r_w)$$

$$\rho_i(r,t) = \rho_i(r_w,t) + \frac{\rho_r - \rho_i(r_w,t)}{r_f - r_w}(r - r_w)$$

$$k_i(r,t) = k_i(r_w,t) + \frac{k_r - k_i(r_w,t)}{r_f - r_w}(r - r_w) \qquad (13a, b, c)$$

We could equally well choose some other functional form for describing how these properties vary behind the front. These ones are chosen for simplicity and lack of data suggesting that some other form is more appropriate. By substituting Equations 13a to 13c into Equation 5, we can calculate the steady-state pressure buildup in the region behind the front from

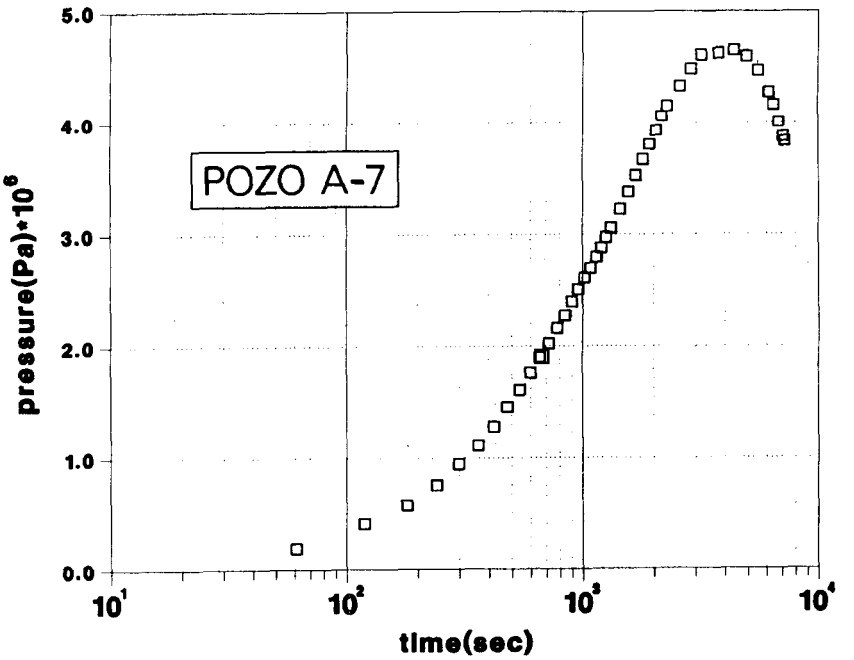


Figure 5. Pressure transient data from the well A-7 injection test.

$$\Delta p_{ss}(t) = \frac{q(t)}{2\pi h}\left[\frac{\mu_i(r_w,t)}{k_i(r_w,t)\rho_i(r_w,t)}\ln\frac{r_f}{r_w} + \left(\frac{\mu_r}{k_r\rho_r} - \frac{\mu_i(r_w,t)}{k_i(r_w,t)\rho_i(r_w,t)}\right)\left[1 - \frac{r_w}{r_f - r_w}\ln\frac{r_f}{r_w}\right]\right] \quad (14)$$

To develop a full solution to Equation 4 we also need an expression for calculating the transient pressure response in the uninvaded region of the reservoir. For this study we assume that the reservoir is approximately described as a uniform porous media, of infinite areal extent, and bounded above and below by impermeable strata. For this type of system, the second term of Equation 4 can be evaluated easily if the time-varying flow rate is represented by a sequence of straight line segments, each of the proper duration and slope (McEdwards and Benson, 1981). The full solution to Equation 4 is calculated by adding Equation 14 to the pressure transient response in the outer region. A computer program that performs the necessary calculations has been written.

Three primary variables must be determined to analyze the pressure buildup tests. These include the permeability-thickness product (kh) of the fracture zones, the mechanical skin factor of the well (s_m), and the magnitude of the near-bore permeability enhancement. A two-stage analysis method is required for evaluating all of these parameters. First, kh and s_m are calculated from the early part of the pressure buildup data when the nonisothermal effects are small. As shown by Figures 3 and 4, this period lasts approximately for 15 minutes. Although this early time data is strongly influenced by wellbore storage, a history-match of the data can be used to calculate kh and s_m by using the variable flowrate algorithm described above (McEdwards and Benson, 1981; and Bodvarsson et al., 1984). Once these two parameters are established, the remainder of the test data are used to calculate the magnitude of the near-bore permeability changes that occur as the progressively colder water is injected into the formation.

The procedure for doing this is as follows. First, the pressure buildup ($\Delta p_i(r_w,t)$) for an isothermal injection test (at the formation temperature) is calculated using the formation parameters obtained from the initial step of the analysis. Next, the difference between $\Delta p_i(r_w,t)$ and the actual pressure response is used to calculate the near-bore permeability change from the following expression

$$\frac{k_r}{k_i(r_w,t)} = \frac{\mu_r\,\rho_i(r_w,t)}{\mu_i(r_w,t)\rho_r}\left\{\frac{\frac{2\pi k_r\rho_r h}{q\mu_r}\left(\Delta p(r_w,t) - \Delta p_i(r_w,t)\right) - s_{ma} + s_m}{\left[\left(1+\frac{r_w}{r_f - r_w}\right)\ln\frac{r_r}{r_w} - 1\right]} + 1\right\} \quad (15)$$

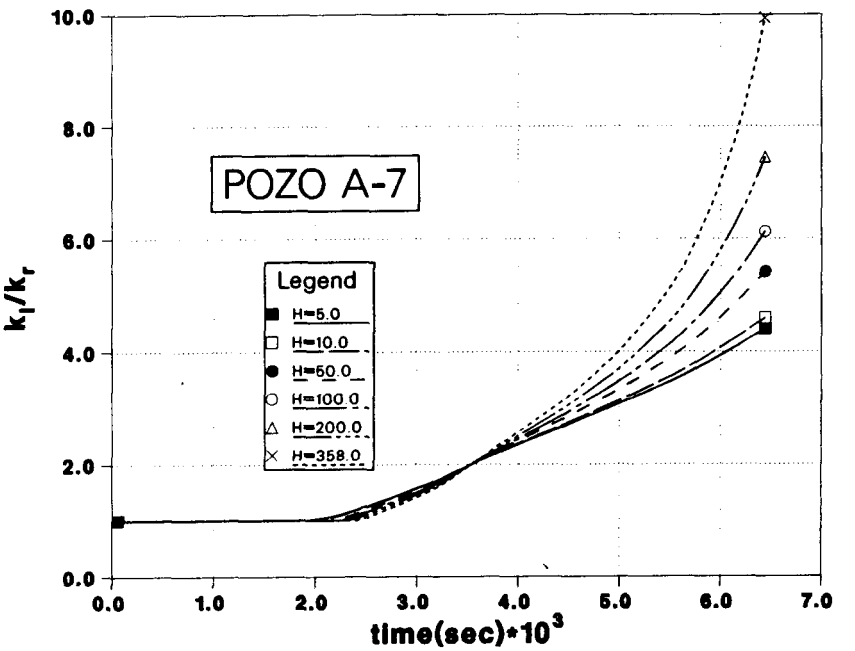


Figure 6. Calculated permeability enhancement during the well A-7 injection test for a range of assumed values for the formation thickness.

where s_{ma} is the apparent-mechanical skin factor of the well. For $s_m > 0$

$$s_{ma} = \frac{\mu_i(r_w, t)\rho_r}{\mu_r \rho_i(r_w, t)} s_m \qquad (16a)$$

and for $s_m << 0$

$$s_{ma} = s_m \qquad (16b)$$

(Benson, 1984).

Each of the four injections tests shown in Figure 1 have been analyzed using the above procedure. The analysis of the data from well A-7 is reviewed in detail.

Well A-7 Analysis

The injection test data for well A-7 are shown in Figure 5. The sandface injection rate, temperature, and fluid viscosity are shown in Figures 2 through 4, respectively. For the first 15 minutes of the test, the bottomhole temperature remained at approximately 250 °C. A history match of this data yields a kh of $3x\ 10^{-13}$ m^3 and a mechanical skin factor of -2. After the first fifteen minutes, the temperature sensitive rock and fluid properties begin to influence the data. Using the procedure outlined above, the ratio of the undisturbed formation permeability to the permeability of the invaded region immediately adjacent to the wellbore is calculated for the rest of the test period. The results of these calculations are shown in Figure 6, where the ratio of $k_i(r_w, t)/k_r$ is plotted as a function of time from the beginning of the injection test. The ratio is plotted for a range of values for the formation thickness because we do not have an accurate measure of the thickness of the zone(s) into which the fluid is injected. The figure shows that the permeability of the near-bore region must increase by a factor ranging from 4 to 10 over the 2 hour test, depending on the actual thickness of the formation. Figure 6 also demonstrates that if the formation thickness is less than 50 m, the results of the calculation are relatively insensitive to the actual value of the formation thickness. The fractured nature of the producing formation and the occurrence of discrete loss-of-circulation zones encountered while drilling these wells suggests that the actual thickness is in the range of 5 to 10 m. Thus, the permeability appears to increase by a factor of 5 over the test period.

Once the formation parameters and the magnitude of the near-bore permeability increases are determined, these calculations can be double-checked by comparing the measured pressure response to the calculated response. Figure 7 shows the comparison for well A-7.

Another source of uncertainty in this analysis is the actual distribution of the fluid and rock properties within the invaded region. As mentioned above, we assume that these vary linearly. To test the restraints imposed on the analysis by this assumption, we repeated these calculations for the case where the fluid and rock properties are constant throughout the invaded region. The results of these calculations are shown in Figure 8, where $k_i(r_w, t)/k_r$ is calculated for formation thicknesses of 5 and 10 m. These calculations show the results are relatively insensitive to the presumed distribution of the various parameters. This is explained in light of the dominating influence of the very near-well region on the pressure response, which is nearly the same, regardless of how the properties are distributed farther away from the well.

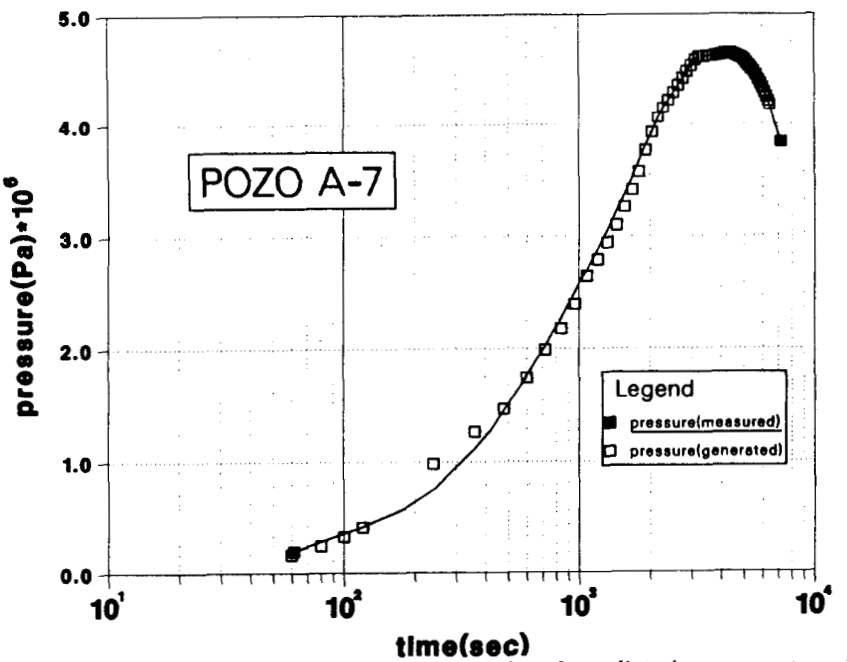


Figure 7. Match between the measured and predicted pressure transient response during the well A-7 injection test.

RESULTS

The magnitude of the near-bore permeability enhancement in each of the 3 test wells (A-7, A-8, and A-18) is plotted as a function of the sandface injection temperature in Figure 9. For the well A-18, the permeability increase during a second injection test is also plotted. The calculated permeability increases for wells A-7, A-8, and the first test of A-18 are remarkably similar, suggesting that the correlation between the sandface injection temperature and the permeability increase is attributable to the thermal characteristics of the rock mass. On the other hand, the larger increase in the permeability calculated from the second test in well A-18 suggests that the effects of heating and cooling are cumulative. This suggests that stress changes occurring during injection also influence the permeability increase. The readjustments of the contact points between the opposing walls of the frac-

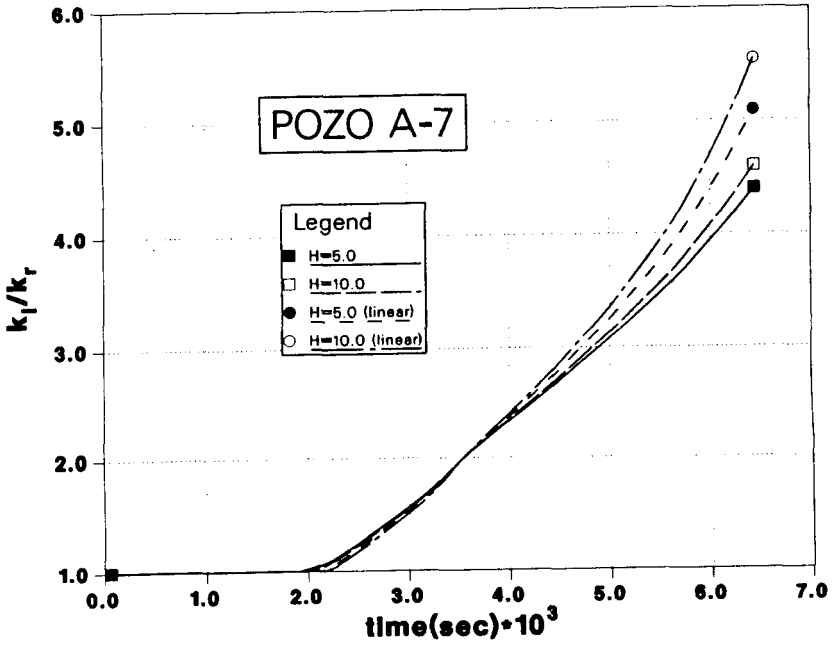


Figure 8. Comparison between the calculated permeability enhancement for a linear and a uniform distribution of fluid and rock properties in the region behind the front.

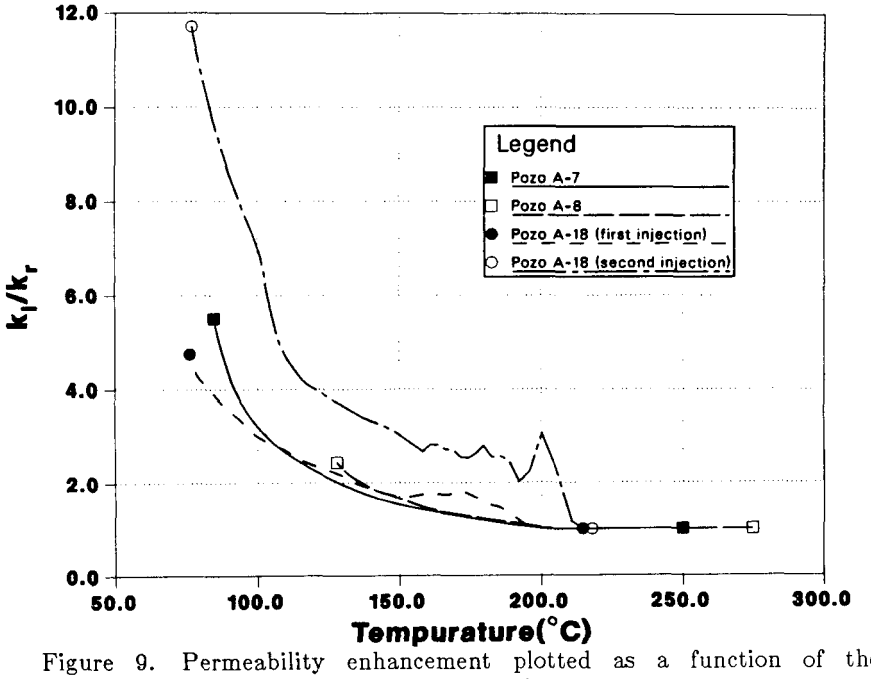


Figure 9. Permeability enhancement plotted as a function of the sandface injection temperature for four injection tests.

tures that take place in response to pore pressure increases and thermal contraction of the rock may result in permanent increases in the near-bore permeability as the result of injecting cold water into a geothermal formation.

There are several possible explanations for the observed temperature versus permeability relationship, including; thermal stress cracking, dissolution of the formation, and thermal contraction of the rock matrix. In the absence of additional information, we can not decide which amongst these possibilities is the correct one, nor if a single mechanism is responsible for the observed behavior. Recent laboratory studies of thermal stress cracking indicate that both intragranular and grain-boundary stress cracks can develop in the thermal regime in which these tests are conducted (Fredrich and Wong, 1986). Analysis of field experiments at the hot-dry-rock site at Fenton Hill indicate that "reservoir growth" can be at least partially attributed to thermally induced stress cracks (Tester et al., 1986). It is likely that a similar mechanism is responsible for the permeability enhancement observed in the data described here.

The analysis presented here is just the beginning of a series of studies that must be conducted if we are to improve our understanding of the physical phenomena that accompany reinjection into geothermal reservoirs. To date, we do not have an adequate physical understanding of the physical mechanisms causing the unusual pressure transients responses nor the observations that well injectivity is often better than anticipated. The possibility that the observed permeability increases may be permanent or semi-permanent is also intriguing. If so, cold water injection may come to be considered as a bona fide stimulation treatment for geothermal wells.

CONCLUSION

Analysis of injection test data from three wells at the Los Azufres geothermal field in Mexico indicate that the permeability of the near-bore region increases during cold water injection. Careful examination of the data reveal that an accurate analysis of the data is impossible if wellbore storage effects and thermal transients in the wellbore are not accounted for in the analysis. By using a new analysis method that is outlined in this paper, the magnitude of the permeability increase that is required to match the observed pressure transient data is calculated for each of the wells. These analyses indicate that the permeability increases by approximately a factor of 5 in the near-bore region during the 2 to 3 hour period when cold water is injected into the formation. A good correlation between the permeability increase and the sandface injection temperature indicates that the permeability increase is caused by cooling the formation. Thermal contraction and thermal stress cracking of the formation are the most probable cause of the near-bore permeability increase.

ACKNOWLEDGEMENTS

This work is supported through the U.S. Department of Energy Contract No. DE-AC03-76SF00098 by the Assistant Secretary for Conservation and Renewable Energy, Office of Renewable Technology, Division of Geothermal Technology.

REFERENCES

Benson, S.M., 1984. Analysis of Injection Tests in Liquid Dominated Geothermal Reservoirs. M.S. Thesis, University of California, Berkeley, California, Lawrence Berkeley Laboratory Report, LBL-17953, Berkeley, California.

Benson, S.M. and Bodvarsson, G.S., 1986. Non-isothermal Effects During Injection and Falloff Tests, Society of Petroleum Engineers Formation Evaluation, February, 1986, pp. 53-63.

Bodvarsson, G.S., Benson, S.M., Sigurdsson, O., Stefansson, V., and Eliasson, E.T., 1984. The Krafla Geothermal Field, Iceland: 1. Analysis of Well Test Data, Water Resources Research, Vol 20, No. 11, pp. 1515-1530.

Bodvarsson, G.S. and Tsang, C.F., 1982. Injection and Thermal Breakthrough in Fractured Geothermal Reservoirs, Journal of Geophysical Research, Vol. 84, No. B2, pp. 1031-1048.

Cox, B.L., and Bodvarsson, G.S., 1985. Nonisothermal Injection Tests in Fractured Reservoirs, Proceedings, Tenth Workshop on Geothermal Reservoir Engineering, Stanford University, Stanford, California, pp. 151-162.

Fredrich, J.T., and Wong, T., 1986. Micromechanics of Thermally Induced Cracking in Three Crustal Rock, Journal of Geophysical Research, V. 91, No. B12, pp. 12743-12764.

McEdwards, D.G. and Benson, S.M., 1981. User's Manual for ANALYZE-- A Variable-Rate, Multiple Well, Least Squares Matching Routine for Well Test Analysis, Lawrence Berkeley Laboratory Report, LBL-10907, Berkeley, California.

Ramey, H.J. Jr., 1970. Approximate Solutions for Unsteady Liquid Flow in a Composite Reservoir, Journal of Canadian Petroleum Technology, March, 1970, pp. 32-37.

Tester, J.M., Murphy, H.D., Potter, R.M., and Robinson, B.A., 1986. Fractured Geothermal Reservoir Growth Induced By Heat Extraction. Society of Petroleum Engineers Paper SPE-15124. Presented at the 56th California Regional Meeting of the Society of Petroleum Engineers, Oakland, California, April 2-4, 1986.

PROCEEDINGS, Twelfth Workshop on Geothermal Reservoir Engineering
Stanford University, Stanford, California, January 20-22, 1987
SGP-TR-109

RESERVOIR STUDIES OF THE SELTJARNARNES GEOTHERMAL FIELD, ICELAND

H. Tulinius, A. L. Spencer,** G. S. Bodvarsson,***
H. Kristmannsdottir, T. Thorsteinsson,* A. E.*
Sveinbjornsdottir,+

* Iceland National Energy Authority, Orkustofnun, Geothermal Division
Grensasvegur 9, 108 Reykjavik, Iceland

** Lawrence Berkeley Laboratory, Earth Science Divisions
University of California, Berkeley, California 94720

+ Science Institute, University of Iceland
Dunhagi 3, 107 Reykjavik, Iceland

ABSTRACT

The Seltjarnarnes geothermal field in Iceland has been exploited for space heating for the last 16 years. A model of the field has been developed that integrates all available data. The model has been calibrated against the flow rate and pressure decline histories of the wells and the temperature and chemical changes of the produced fluids. This has allowed for the estimation of the permeability and porosity distribution of the system, and the volume of the hot reservoir. Predictions of future reservoir behavior using the model suggest small pressure and temperature changes, but a continuous increase in the salinity of the fluids produced.

INTRODUCTION

The Seltjarnarnes geothermal area is located in Seltjarnarnes, a suburb of Reykjavik, the capital city of Iceland (Figure 1). The field has been exploited for the past 16 years to provide hot fluids for the central heating of Seltjarnarnes. In the typical low temperature field, temperatures of about 100 °C at have been encountered at 1000 m depth, and over 140 °C at 2700 m depth. Drilling in the region started in 1965; a total of six wells had been drilled by 1985. Four of these wells are being produced with maximum capacity of 110 l/s, while the remaining two are used for observation.

During the sixteen years of production (1970 to 1986), the salinity within the system has increased. Although the salinity changes were relatively slow initially, an increase in production in 1972 (by 35 l/s), and again in 1981 (by 30 l/s), accelerated the increase. Changes in the average temperature of the produced fluids have been very small (<2 °C) throughout the production period. The pressure changes induced by production have also been small.

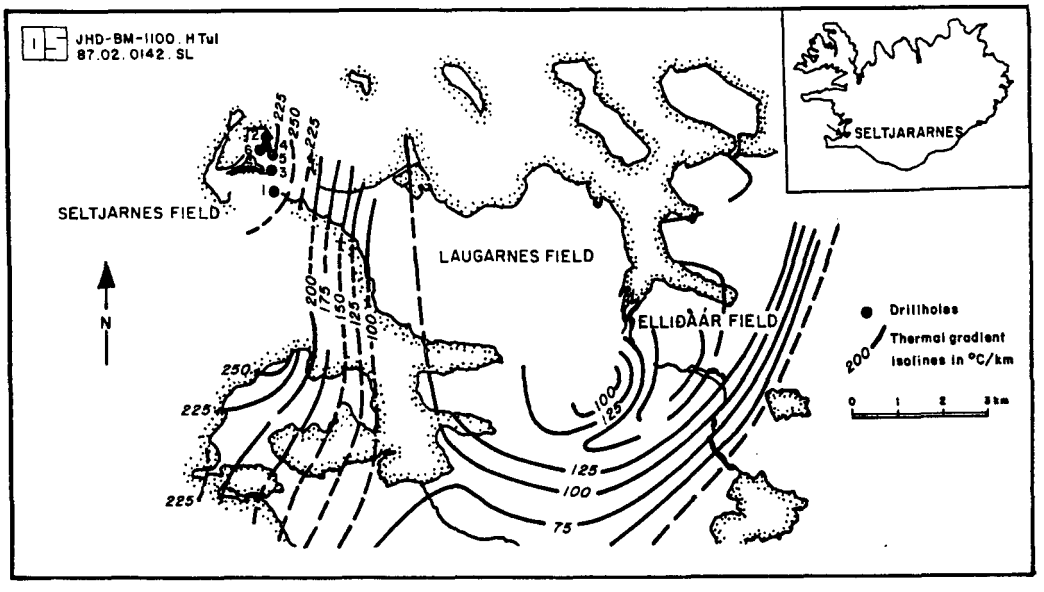


Figure 1. Low-temperature geothermal fields in Reykjavik, showing the locations of the wells in the Seltjarnarnes field. Contours of the thermal gradient in the region are shown on the map.

In the summer of 1986, all available data on the Seltjarnarnes field (geological, geophysical and geochemical) were compiled and integrated into a conceptual model for reservoir simulation studies. The main objective of this work was to develop a numerical model of the field that was calibrated against the production history, interference test data and observed thermal and chemical changes. The model was then used to predict changes in pressure, temperature, and chemical composition with future production. This paper summerizes the work done; a detailed description is given in Tulinius et al. (1987).

BACKGROUND

Since the drilling of the first well in 1965, considerable amounts of data have been collected and several reports have been published describing the field (Tomasson et al., 1977; Palmason et al., 1983; Sigurdsson et al., 1985 and Kristmannsdottir, 1986). Other, more specific reports on well drilling, fracturing, pressure testing, well tests, fluid chemistry and other aspects of the Seltjarnarnes field include Sveinbjornsdottir et al., 1984a,b; Kristmannsdottir, 1983 and 1984; Kristmannsdottir and Tulinius, 1984; Kristmannsdottir et al., 1984; Tomasson and Saemundsson, 1970; Haraldsdottir, 1984; Thorsteinsson, 1970, 1980 - 1985; Thorsteinsson and Tomasson, 1972; and Thorsteinsson et al., 1985).

The Seltjarnarnes field is located in the Kjalarnes caldera. The main reservoir rocks are Quanternary (1.8 - 2.8 m.y.b.p.), and become younger towards the southeast. A simplified geological cross-section including all six wells is shown in Figure 2. The cross-section, which extends from well SN-01 in the southeast to well SN-02 in the northeast, is based on analyses of drill cuttings. The rocks can be divided into 7 main groups (8 for well SN-06) of Quaternary basalt lavas and hyaloclastites interbedded with a few small sedimentary beds and igneous intrusions that increase in frequency with depth.

Several aquifers have been identified in each of the wells from water losses/gains during drilling, or from temperature logs during the heating period. The main feed zones are shown in Figure 2. All of the wells have at least three feed zones, and some as many as nine (well SN-06). Well SN-01 intersects five aquifers, although it is not productive. The four production wells all encounter an aquifer at around 400 m (see Figure 2). This aquifer probably contains very saline water with an average temperature of 75 °C - 80 °C. The most productive aquifer in all of the wells is located below a depth of 1700 m and has a temperature of approximately 125 °C. About 40% of the water produced from wells SN-03 and SN-05 comes from this aquifer, and up to 80% in wells SN-04 and SN-06.

Several downhole temperature surveys have been obtained for each of the wells. Figure 3 shows the estimated formation temperature profiles for all of the wells. All of the profiles show an increase in temperature with depth with an approximate 300 °C/km gradient in the uppermost 200 m. Below a depth of 600 m, the thermal gradient is about 35 °C/km. The highest measured temperature (>140 °C) is in well SN-06 at 2700 m

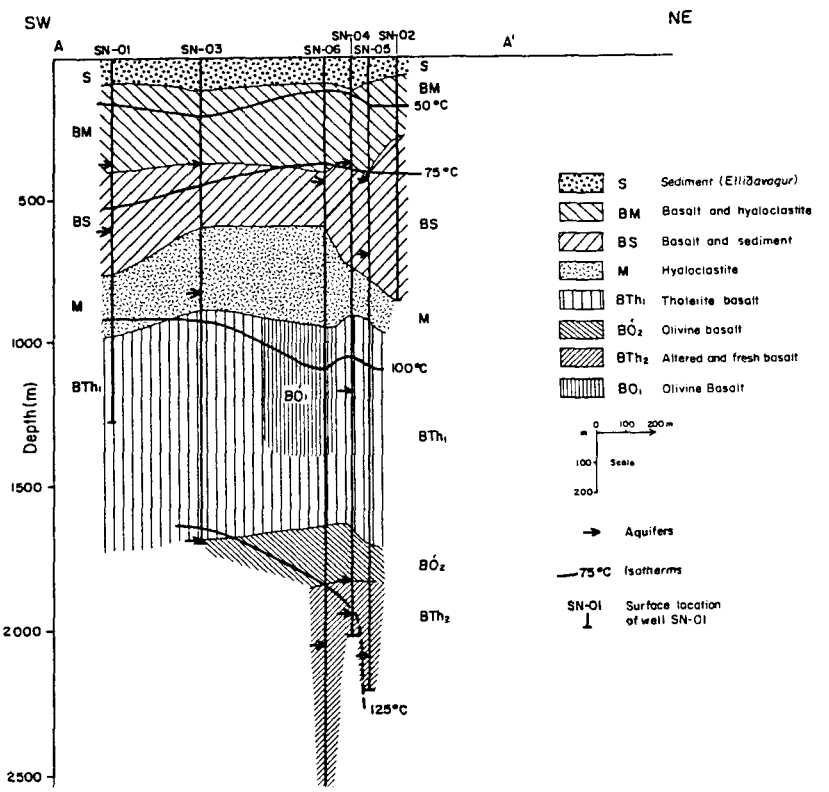


Figure 2. Cross-section A-A' of the Seltjarnarnes field.

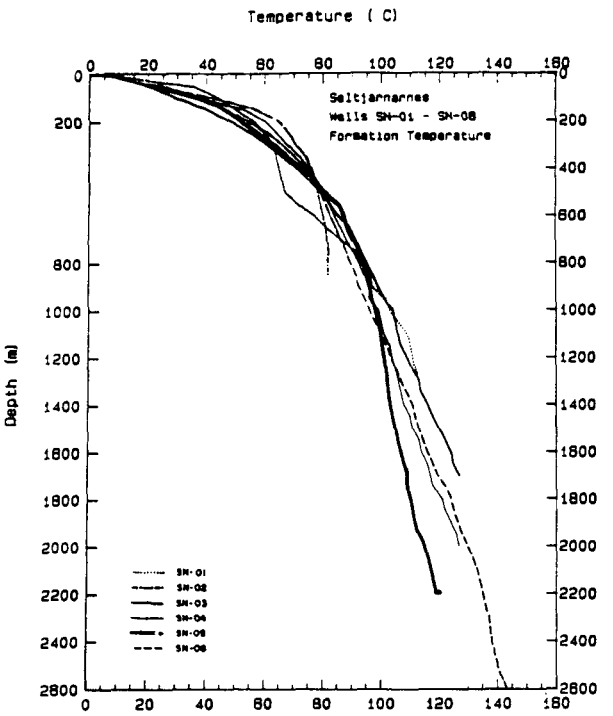


Figure 3. Estimated formation temperature profiles for all six wells.

depth. Temperatures average 110 °C in the 400 - 2200 m interval, where most of the aquifers are encountered. Isotherms plotted along the cross-section AA' (see Figure 2) indicate that temperatures are fairly uniform over the entire wellfield above 1500 m. Well SN-05 is somewhat colder than the other wells below 2000 m depth. This could indicate that hot water recharges the reservoir from the south-east or that colder waters are present close to well SN-05.

Chemical monitoring of the geothermal water has been carried out since 1968. Several downhole samples collected early in the production period indicate that the initial concentrations of the total dissolved solids, chloride, and sodium were fairly uniform throughout the wellfield. The produced water was relatively saline in the beginning of production (1300 ppm total dissolved solids). The salinity increased slowly for the first ten years of production, as the rate of production has increased, so has the rate of increase in salinity. The total dissolved solids has increased from about 1300 ppm in 1966 to 3000 ppm in 1986. The chloride concentration is now 1000 - 1400 ppm, up from around 500 ppm in 1966. Likewise, the concentration of sodium has increased from approximately 300 ppm in 1966 to 600 - 800 ppm in 1986. The stable isotope ratio oxygen-18/oxygen-16 has not changed significantly with time. The near-constant concentration of oxygen-18 suggests recharge of meteoric water, whereas the increase in the chloride and sodium suggests an influx of seawater.

While continuous chemical monitoring of wells SN-02 through SN-06 shows a significant increase in salinity, downhole samples taken from well SN-01 in 1984 show that no changes in the salinity have occurred in the vicinity of this well. This suggests that this well is outside the main reservoir. Samples taken from wells SN-02 through SN-06 at different depths also indicate that the salinity has increased most in the shallow aquifers.

Water level monitoring in the area started in 1966 with the objective of determining if production in the Laugarnes field was causing drawdown in the Seltjarnarnes field 5 - 6 km away (Thorsteinsson and Eliasson, 1970). As no significant changes were observed, it was concluded that these two fields are separated by an impermeable barrier. The water level monitoring continued, using wells SN-01 and SN-02, after production in the field started.

Several interference tests have been performed at the Seltjarnarnes field. A test performed in August - September 1970 involved production of 17 l/s from well SN-03 for 14 days, while water levels were monitored in wells SN-01 and SN-02. The drawdown over the 14 day period was only 4 m in well SN-01 and 6 m in well SN-02. Although well SN-01 is closer than SN-02 to well SN-03, the well experienced less drawdown. This indicates higher permeability between SN-02 and SN-03 than between wells SN-01 and SN-03. It should be noted that well SN-02 was flowing prior to the interference test, which means that part of the drawdown in SN-02 could be due to cooling in the upper part of the well.

CONCEPTUAL MODEL

All available data were integrated to form a conceptual model of the field. The thermal gradient low between Seltjarnarnes and the Laugarnes and Ellidaar fields and the fact that no pressure changes were detected in the Seltjarnarnes field due to production in the Laugarnes field, indicate the presence of low permeability rocks (faults?) between these fields. Tests on shallow wells indicate that the top 100 m of the subsurface rocks are nearly impermeable. Most of the aquifers are located in the interval from about 400 m to 2200 m depth (see Figure 2).

The low oxygen-18 content of the fluid indicates that the water originated from a meteoric source, most likely infiltrating in the highlands tens of kilometers to the north (Arnason, 1976, 1986). The water percolates down to about 3 - 4 km depth, and heats up due to the anomalous thermal conditions in the subsurface rocks. The water flows to the south and ascends under the Seltjarnarnes field through fissures that extend to considerable depths and are more permeable than in the surrounding areas. The small amount of change in the oxygen-18 suggests that a large portion of the fluids recharging the field during exploitation is meteoric. The increase in most of the other chemical components is large, indicating that a portion of the recharge fluids consists of highly saline water. The source is most likely seawater recharging the reservoir at shallow depths (above 400 m). From the observed changes in the chemical composition of individual wells, it appears that the seawater is recharging from the southwest.

Figure 4 shows a topview of the conceptual model for the Seltjarnarnes area. Lines with equal thermal gradient in the uppermost 200 - 300 m are plotted on the figure (Tulinius et al., 1986), along with suggested flow directions for the recharge water (plotted as arrows).

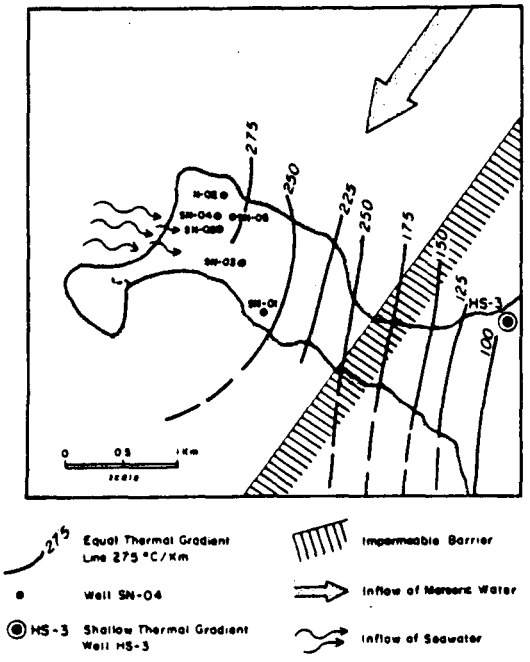


Figure 4. Conceptual model of the Seltjarnarnes geothermal field.

NUMERICAL SIMULATION

The single-phase three-dimensional numerical code PT (Bodvarsson, 1982) was used to simulate the interference tests and the production history. The simulator solves the mass and energy transport equations for liquid-saturated, heterogeneous, porous and/or fractured media using an integrated finite-difference method. The density of the fluid is calculated as a function of pressure and temperature; fluid viscosity is calculated as a function of temperature. A modified version of PT (Spencer, 1986), which allows for chemical transport modeling, was used to model the changes in the chloride, sodium, silica and oxygen-18 concentrations. The modified program is capable of modeling the convective transport of up to ten conservative (non-reactive) chemical species, as well as the kinetic reactions and convective transport of silica and oxygen-18.

In the first attempt to match the interference and production data, a single layer, two-dimensional model was used. Isothermal conditions were assumed initially, with temperature held constant at 110 ° C. This allowed very economical compilations to be achieved, as only the mass balance equation was solved. The model used a 1800 m recharge layer representing the depth interval 400 - 2200 m. The mesh consisted of squares 50 x 50 m in size around the wells and increasing rapidly in size away from the wellfield. The grid extended far enough in all directions so that boundary conditions were not felt during the simulation (infinite reservoir system). The total number of elements was 316. The initial average pressure was estimated to be 123 bars, using the average depth of 1300 m, density of water at 110 ° C, and the initial wellhead pressure in well SN-02 of 13 m.a.s.l. The interference tests from 1970 involving wells SN-01, SN-02 and SN-03 and the production history were simulated. Trial and error simulations were carried out using the permeability (k) and porosity (ϕ) as adjustable parameters. The compressibility of the rock (C) was held constant at 5 x 10^{-10} Pa^{-1}.

RESULTS

The best model derived from the match using the interference test data consisted of six regions with different porosities and permeabilities. Figure 5 shows the central portion of the grid and the locations of the six regions; the match between the calculated and observed data is shown in Figure 6. The area around all the wells except SN-01 (region 5) was found to have the

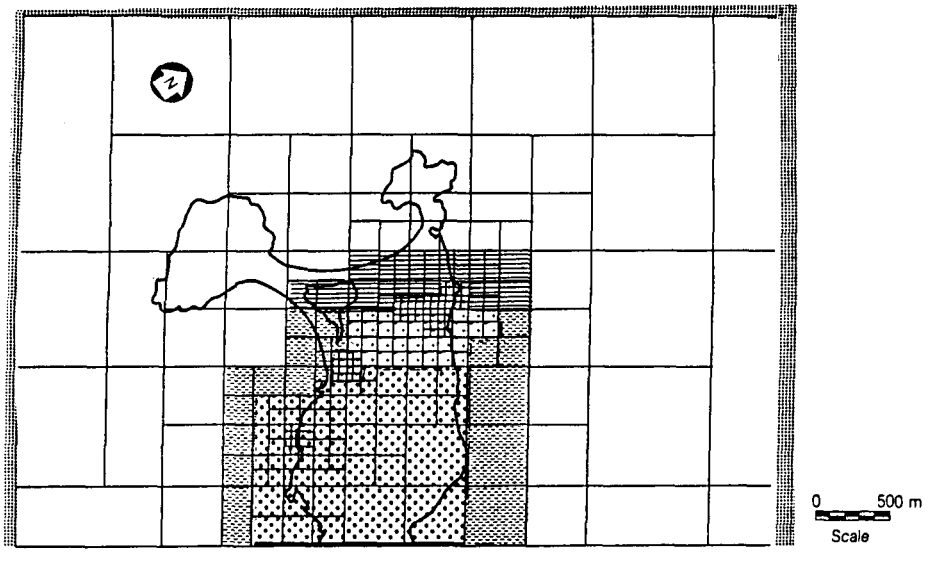


Figure 5. Central part of the mesh showing the location of the six regions of different permeabilities and porosities. Large dots = Region 1; unshaded area = Region 2; dashes = Region 3; small dots = Region 4 (outside mesh region shown); crosses = Region 5; stripes = Reigon 6.

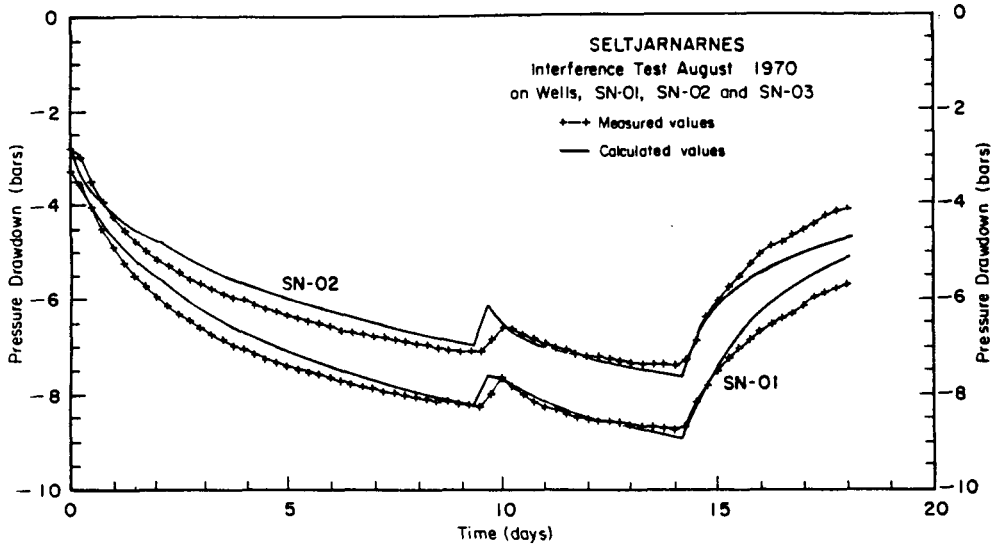


Figure 6. Match between calculated and observed data for the 1970 interference test.

largest permeability (80 md) and a porosity of 2%. The total volume of this region is about 0.8 km^3. The area around well SN-01 (region 1) has the lowest porosity (<0.1%), and a permeability of 7 md. The porosity seems to increase away from the well field with a value of 15% 4 km from the wellfield (region 4); the permeability of this region is about 10 - 15 md. The porosity and permeability near the wellfield are estimated to be 3% and 10 md, respectively (region 2). To achieve a reasonable match with the pressure transients for both wells SN-01 and SN-02, a third region between region 1 (well SN-01) and region 2 with a porosity of 0.3%, and a permeability of 10 md was necessary. Region 6 has a porosity of 4%, and a permeability of 10 md.

After matching the interference data the model had to be modified slightly to get a good match for the production history (Figure 7). The permeability away from the wellfield (regions 2, 4 and 6) had to be increased to 17 md and the porosity in the regions next to the wellfield (region 6) was increased from 3 to 4%. All other parameters remained the same.

The fact that somewhat different models were needed to achieve a good match with both the interference test data and the production history suggest that the effects of fractures may be important. Due to the short duration of the interference test, the overall permeability was most likely dominated by the fracture permeability. However, during the long term production period the matrix permeability becomes more important.

TEMPERATURE AND CHEMISTRY MATCH

After obtaining a match using only the pressure data the temperature was taken into account. The same grid was used, dividing the volume into two regions, a

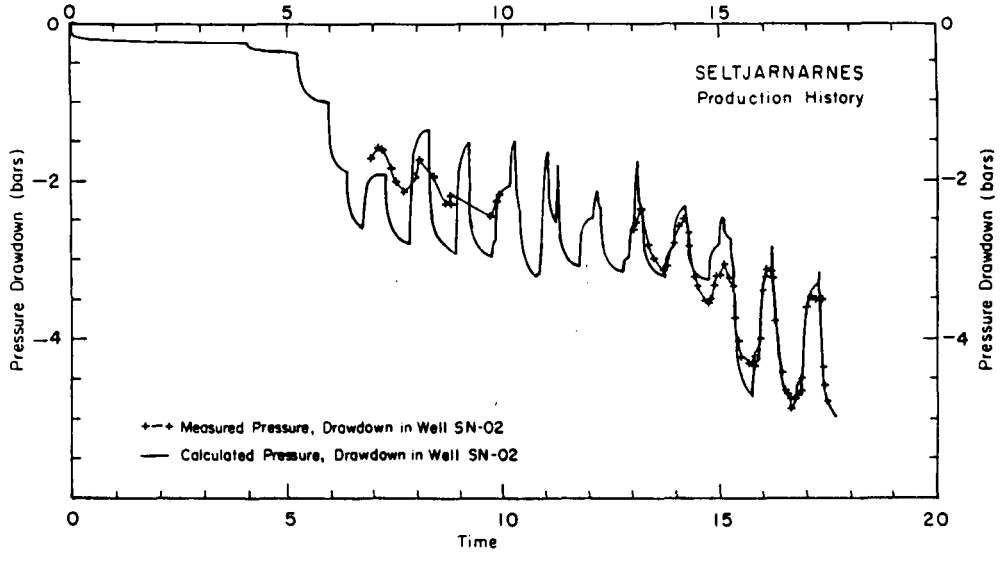


Figure 7. Match between calculated and observed data for the production history.

high temperature region with an initial temperature of 110 ° C, and a low temperature region with a temperature of 75 ° C. The high temperature region includes the wellfield (region 5) and well SN-01. Using this temperature distribution, very little cooling was detected in the field (<1 ° C) over the production history, which is in agreement with the observed data.

To aid in confirming the permeability and porosity of the wellfield, a match with the changes in the fluid chemistry over time was attempted. A very simple two layer model was used, with the entire wellfield contained in one element on the bottom layer. The initial values for temperatures and chemistry were determined from well data. The regions directly above and adjacent to the wellfield were assumed to have fluid of the same composition as that initially present in the field (Cl^- = 500 ppm, Na^{+2} = 300ppm; δO^{18} = -10.5 per mil); silica was in equilibrium with the field temperatures (130 ppm at 110 ° C in the well field; 80 ppm at 75 ° C elsewhere). Seawater (Cl^- = 19,000ppm; Na^{+2} = 10,000ppm; δO^{18} = 0 per mil) was allowed to infiltrate the system from the top layer, outside the perimeters of the well field region.

Using a trial and error procedure a match for the data was obtained. The results suggest a reservoir volume of 0.75 - 1.0 km^3 and a porosity between 2 and 3%. It must be emphasized that due to the coarseness of the grid, these are only rough estimates of the field parameters and flow patterns. However, they are in close agreement with the values obtained from the match with the pressure history.

The 316 element grid used in modeling the temperature and pressure was then employed to further study the Seltjarnarnes field by combining the previous results with all available chemical data from the field. The initial chemical concentrations in the wellfield region were the same as those used in the two layer model. Since the results of the pressure and chemistry simulation studies performed on the Seltjarnarnes geothermal field were in close agreement, the chemistry match in this study was not aimed towards verifying field parameters such as the permeabilities, porosities, and reservoir volume. Rather, the purpose of the study was to define the boundaries of the seawater adjacent to the well field.

To achieve the most accurate results for the chemistry match, the calculated and observed data were matched individually for each well. The results for oxygen-18, chloride, sodium and silica are plotted for well SN-03 in Figure 8. For the best match, the seawater boundary follows approximately the land/sea boundary, surrounding the wells on three of four sides, and lying within 350 m of wells SN-02 and SN-05 to the northeast. Figure 9 shows the suggested seawater/meteoric water boundary.

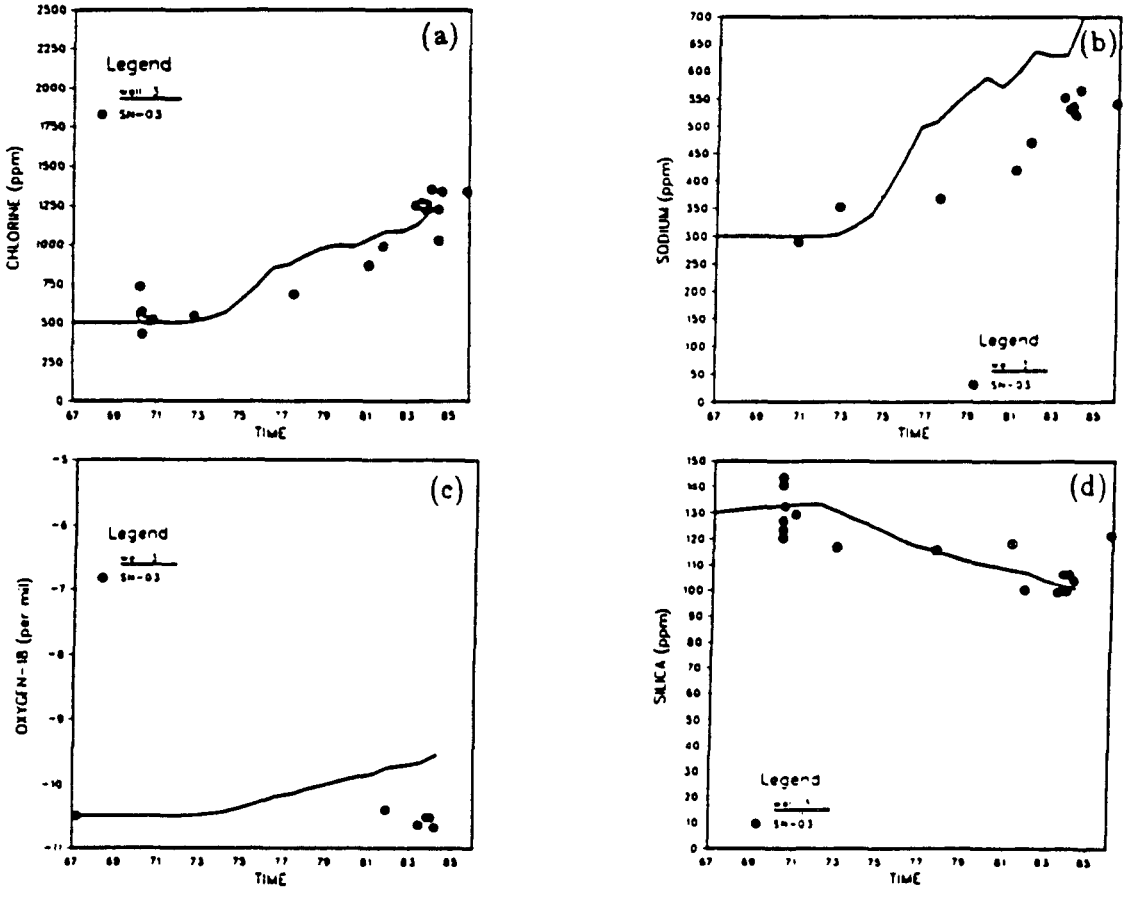


Figure 8. The results of the chemistry matches for well SN-03 for (a) chloride, (b) sodium, (c) oxygen-18 and (d) silica.

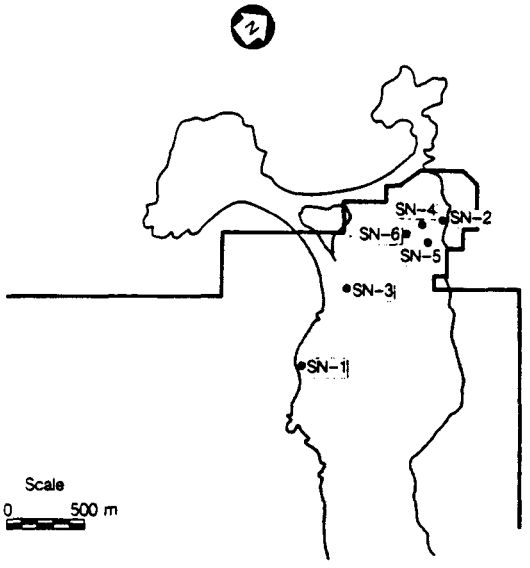


Figure 9. Suggested seawater/meteoric water boundary. The area above the solid line is assumed to contain seawater.

The results also raised several other points. The match with the chloride data was very good (Figure 8a), however, the match with the sodium data was not (Figure 8b). This suggests that the sodium cations in the system sustain significant ionic-exchange reactions, and are not truly conservative as was assumed in the present model. The matches with the oxygen-18 data for the individual wells were not good; the numerical model showed a much more rapid increase in oxygen-18 than the field data (Figure 8c). This could be due to three-dimensional effects, suggesting that fluid having a lower oxygen-18 content than present in the system (<-10.5 per mil) is recharging the system from either above or below. Or, it is possible that the fluid infiltrating the system, considered to be seawater, is actually of meteoric origin, but it is flowing through a salty formation before entering the wellfield region. The salts would readily dissolve into fluid, while the oxygen-18 content would remain low.

The results of the silica match (Figure 8d) suggest that kinetic reactions play a strong role in the transport of silica in the Seltjarnarnes system. To achieve the best match for silica, the A/V (surface area open to reaction per volume) value was set at 25.0, indicating fairly rapid kinetic reactions (Spencer, 1986). The kinetic reactions do not appear significant in modeling the oxygen-18, which is probably due to the fractured nature of the reservoir.

Although the chemistry modeling has identified some shortcomings of the two-dimensional model, the model can be used to roughly predict the future influence of the seawater on the system. Thus, an estimate of the amount of influx of seawater into the field in the future could be obtained. The potential corrosion problems may then be evaluated and the necessary steps taken to minimize or alleviate these problems.

PERFORMANCE PREDICTIONS

The main objective of the reservoir simulation studies was to develop a model of the geothermal reservoir to use in predicting changes in pressure and temperature with future production. The model that gave the best match with the production history was used to predict the changes for the next 20 years. Two cases were studied:

(a) Constant production of 70 l/s;

(b) Constant production of 70 l/s for the first five years then 30 l/s increase in production every five years thereafter from two new wells close to well SN-05.

Figures 10a and b show the calculated and measured drawdown in well SN-02 for the two cases. For the simulation, the production period from August 1966 to October 1984 was used. The maximum pressure drawdown after 20 years with no increase in production (case a) is estimated to be 7.4 bars; the maximum temperature decrease would be 3 °C. The maximum pressure drawdown for case b was calculated to be 15.5 bars, with a 7 °C decline in temperature.

CONCLUSIONS

A two-dimensional model for the Seltjarnarnes geothermal field in Iceland has been developed, incorporating thermal, chemical and pressure transient data. Results of matching the model with the observed drawdown data revealed six regions of different permeabilities and porosities. The wellfield lies within a region of high permeability (80 md) and low porosity (2%). The porosities increase away from the field, up to 15% at a distance of 4 km. The model shows no thermal decline, in agreement with observed data. The fluid chemistry modeling indicates that the seawater is very near the wellfield to northwest. The performance predictions showed a maximum drawdown of 15.5 bars over 20 years and a maximum temperature decline of 9 °C, if the production of the field were to increase by 30 l/s every five years beginning in 1991. From the pattern of the observed chemical data, the salinity could increase greatly under this production scheme.

ACKNOWLEDGEMENTS

The primary author would like to thank the National Energy Authority of Iceland for sponsoring her work at LBL, and the Earth Sciences Division of LBL for their cooperation during this work. The authors thank the Seltjarnarnes District Heating Service for allowing publication of the field data. This work was supported by the National Energy Authority of Iceland and the U.S. Department of Energy through Contract No. DE-AC03-76SF00098 by the Assistant Secretary for Conservation and Renewable Energy, Office of Renewable Technology, Division of Geothermal Technology.

REFERENCES

Arnasson, B., Groundwater Systems in Iceland Traced by Deuterium, Soc. Sci. Isl., v. 42, 236 pp., 1976.

Bodvarsson, G.S., Mathematical Modeling of the Behavior of Geothermal Systems Under Exploitation, PhD dissertation, University of California, Berkeley, 1982.

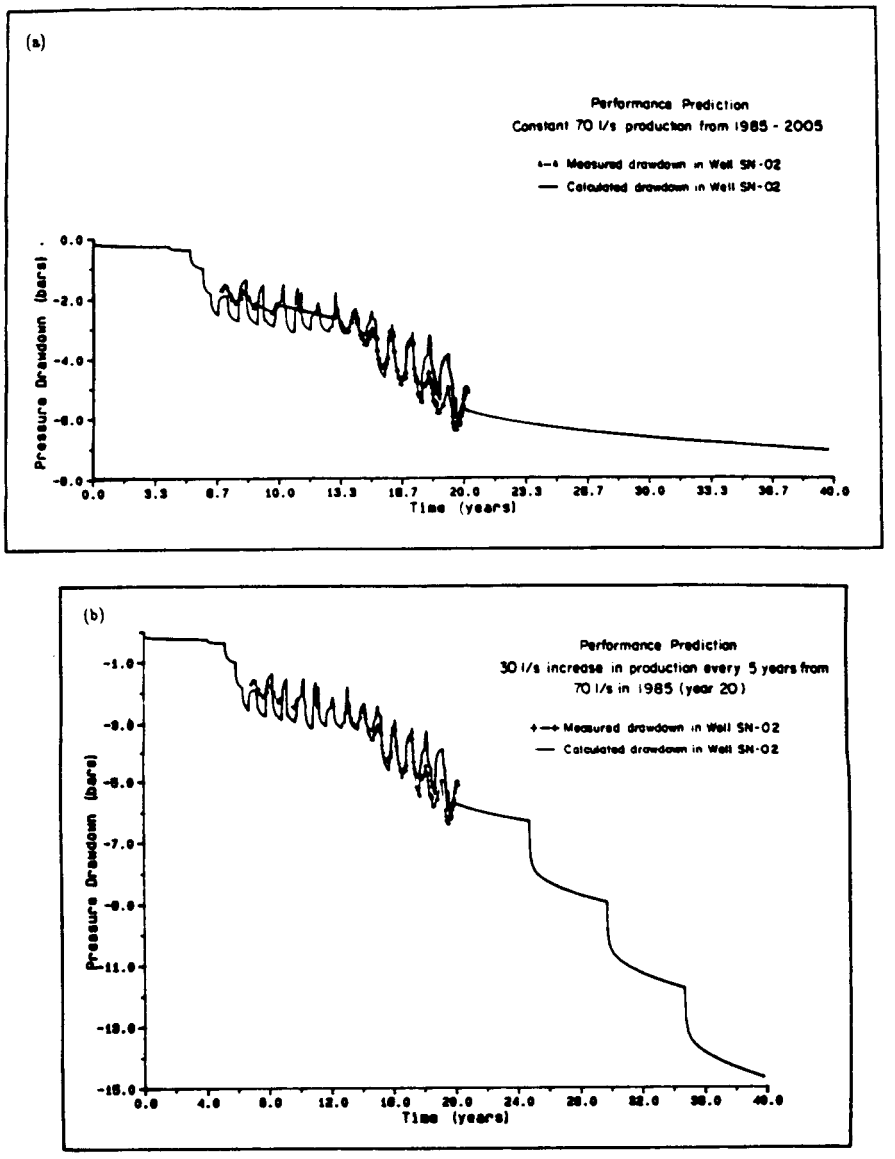


Figure 10. Performance predictions: (a) Constant production of 70 l/s; (b) Base production of 70 l/s, increasing every five years.

Haraldsdottir, S.H., Inhouse Reports (in Icelandic), National Energy Authority, Iceland, OS-84059/JHD-19 B (a); OS-84059/JHD-20 B (b); OS-84059/JHD-21 B (c); July, 1984.

Kristmannsdottir, H., Inhouse Report (in Icelandic), National Energy Authority, Iceland, OS-83106/JHD-19, December, 1983.

Kristmannstottir, H., Inhouse Reports (in Icelandic), National Energy Authority, Iceland, OS-84068/JHD-27 B (a); HK-84/02 (b); HK 22.08.1984 (c); 1984.

Kristmannsdottir, H., Exploitation-Induced Infiltration of Seawater into the Seltjarnarnes Geothermal field, Iceland, Trans., Geothermal Resources Council, v. 10, pp. 389-393, 1986.

Kristmannsdottir, H., H. Tulinius, Inhouse report (in Icelandic), National Energy Authority, Iceland, H.K.,H.Tul/8406, 1984.

Kristmannsdottir, H., T. Thorsteinsson, J. Tomasson, Inhouse report, (in Icelandic), National Energy Authority, Iceland, 84.02.10, 1984.

Palmason, G., V. Stefansson, S. Thorhallson, T. Thorsteinsson, Geothermal Field Developments in Iceland, Ninth Workshop on Geothermal Reservoir Engineering, Stanford, California, 1983.

Sigurdsson, O., S.P. Kjaran, T. Thorsteinsson, V. Stefansson, G. Palmason, Experience of Exploring Icelandic Geothermal Reservoirs, GRC 1985 International Symposium on Geothermal Energy, Kailua-Kona, Hawaii, Aug. 26-30, 1985.

Spencer, A., Modeling of Thermodynamic and Chemical Changes in Low-Temperature Geothermal Systems, Masters Thesis, University of California, Berkeley, 1986.

Sveinbjornsdottir, A.E., J. Tomasson, T. Thorsteinsson, Inhouse Report (in Icelandic), National Energy Authority, Iceland, OS-84091/JHD-41 B, November, 1984a.

Sveinbjornsdottir, A.E., D. Sigursteinsson, H. Tulinius, H. Kristmannsdottir, S. Benediktsson, Inhouse Report (in Icelandic), Icelandic National Energy Authority, Iceland, OS-84081/JHD-34 B, October, 1984b.

Thorsteinsson, T., Inhouse report (in Icelandic), National Energy Authority, Iceland, TTH. 18.08.1970, (a,b); 1970.

Thorsteinsson, T., Inhouse report (in Icelandic), National Energy Authority, Iceland, T.TH.-80104, 1980.

Thorsteinsson, T., Inhouse report (in Icelandic), National Energy Authority, Iceland, TTH-85/06, 1985.

Thorsteinsson, T., J. Eliasson, Geohydrology of the Laugarnes hydrothermal system in Reykjavik, Geothermics, v. 2, Special Issue, p.1191, 1970.

Thorsteinsson, T., J. Tomasson, Inhouse report (in Icelandic), National Energy Authority, Iceland, T.Th./J.T. 30.8.72, 1972.

Thorsteinsson, T., H. Kristmannsdottir, A.E. Sveinbjornsdottir, H. Tulinius, Inhouse report (in Icelandic), National Energy Authority, Iceland, TTh-HK-AES-HTul-85/02, 1985.

Tulinius, H., O.B. Smarason, J. Tomasson, I.B. Fridleifsson, G. Hermannsson, Inhouse Report (in Icelandic), Orkustofnun OS-86060/JHD-22 B, 1986.

Tulinius, H., A.L. Spencer, G.S. Bodvarsson, H. Kristmannsdottir, T. Thorsteinsson, A. Sveinbjornsdottir, Modeling Studies of the Seltjarnarnes Geothermal Field, Iceland, Internal report, Lawrence Berkeley Laboratory, Berkeley, California, 1987.

Tomasson, J., K. Saemundsson, Inhouse report (in Icelandic), National Energy Authority, Iceland, November, 1970.

Tomasson, J., T. Thorsteinsson, H. Kristmannsdottir, I. B. Fridleifsson, Inhouse Report (in Icelandic), OSJHD 7703, Hitaveita Reykjavikur, February, 1977.

PROCEEDINGS, Twelfth Workshop on Geothermal Reservoir Engineering
Stanford University, Stanford, California, January 20-22, 1987
SGP-TR-109

CONCEPTUAL MODEL OF THE KLAMATH FALLS, OREGON GEOTHERMAL AREA

R. H. Prucha, S. M. Benson, and P. A. Witherspoon

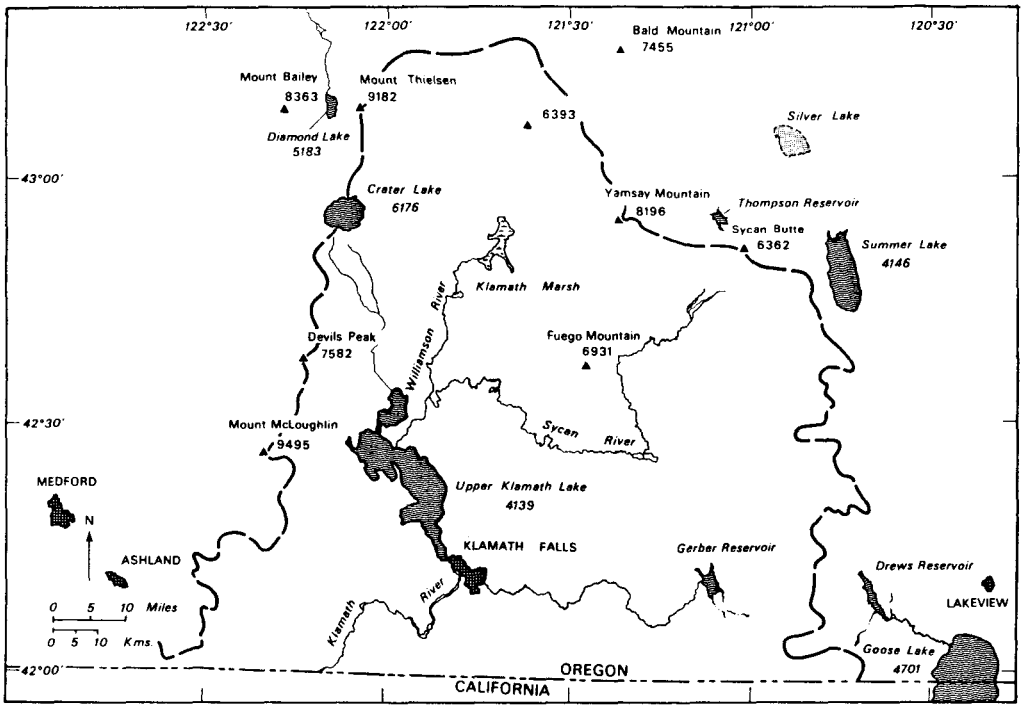
Earth Sciences Division
Lawrence Berkeley Laboratory
University of California
Berkeley California, 94720

ABSTRACT

Over the last 50 years significant amounts of data have been obtained from the Klamath Falls geothermal resource. To date, the complexity of the system has stymied researchers, leading to the development of only very generalized hydrogeologic and geothermal models of the area. Recently, the large quantity of available temperature data have been re-evaluated, revealing new information on subsurface heat flow and locations of faults in the system. These inferences are supported by borehole, geochemical, geophysical, and hydrologic data. Based on re-evaluation of all available data, a detailed conceptual model for the Klamath Falls geothermal resource is proposed.

INTRODUCTION

The Klamath Falls KGRA (Known Geothermal Resource Area), located in south-central Oregon, is a low- to moderate-temperature resource (Figure 1). The approximately 2 square mile shallow thermal anomaly is associated with an adjacent large normal fault, shown in Figure 2 (Sammel, 1984). Over 500 wells have been drilled in the area, ranging in depth from 90 to 1900 ft. Most temperatures encountered in these wells range from 70 to 120 ° C. Temperatures in one well have been measured as high as 140 ° C, but this data is somewhat suspect (Gene Culver, personal communication). The geothermal resource has been used for space heating for some 70 years; special uses



XBL 784-1822

Figure 1. Location map of Klamath Falls, Oregon.

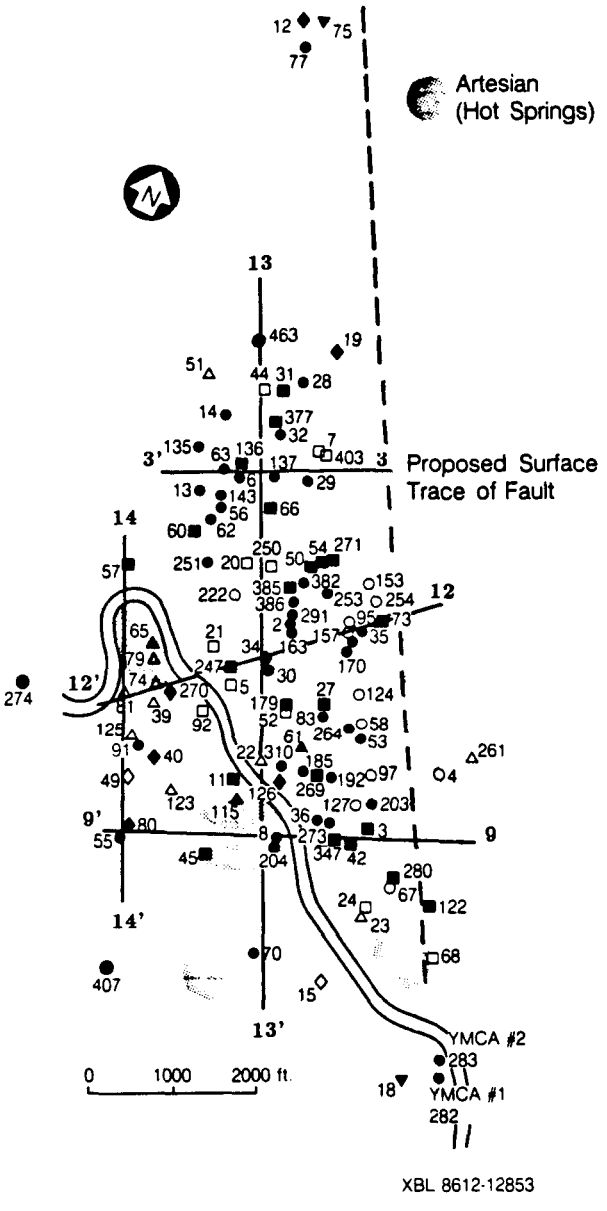


Figure 2. Wells supplying temperature data. Lines drawn across the wells indicate the location of temperature profile cross-sections.

include heating greenhouses and swimming pools, snow melting, and milk pasteurization.

Various investigators have obtained and evaluated data from the Klamath Falls geothermal area. Moore (1937) was the first to describe the rocks of the greater Klamath region. Meyers and Newcomb (1952) and Newcomb (1958) were the first to describe the geology in detail and evaluate the groundwater resources of the region. Peterson and McIntyre (1970) investigated the economic potential of eastern Klamath and western Lake Counties by reconnaissance geology methods, and proposed a conceptual model for the system. These authors postulate that the heat source is a shallow, igneous dike or sill-like body of Pliocene-Peistocene age, intercalated in lacustrine deposits which transform cold flowing groundwater into steam that rises along fault zones and heats the surrounding reservoir rock.

Sammel (1980) presents an alternate conceptual model for the Klamath Falls geothermal system. He proposes that water is circulated to great depths along faults, where it is heated to rock temperatures corresponding to a 30° C/km gradient. The hot water then rises to shallow depths through conduits closely associated with major faults, until it begins to flow laterally towards the southwest through horizontal permable strata. Stark et al. (1980) studied the geophysical characteristics of the Klamath Basin; in particular they studied the Swan Lake, Klamath Hills and Klamath Falls areas. They found no direct evidence to either support or refute the possible existence of an igneous heat source, or the concept of deep circulation along fault zones penetrating a hotter-than-average crust.

In 1983, Lawrence Berkeley Laboratory, Stanford University, Oregon Institute of Technology (OIT), and the U.S. Geological Survey collaborated in pumping and injection tests at Klamath Falls. The hydrologic data confirm the highly-fractured and faulted nature of the system as indicated by the high degree of connectivity between wells and high transmissivity of the aquifer. A recent well test near OIT also indicates a high transmissivity for the reservoir (Nork, Inc., 1986).

This paper reviews conceptual models proposed to date, and considers a new model for the Klamath Falls geothermal system based on recent interpretations. By analyzing the temperature distribution in detail, it is possible to detect the locations of several subsidiary faults to the large northwest-trending normal fault identified in previous reports. The existence of these faults is verified by high-altitude infrared photographs of the area. A detailed model that emphasizes the role of subsidiary faults has been developed.

GEOLOGY

The Klamath Falls geothermal area, east of the Cascade Range and north of the Medicine Lake Highlands, California, is situated in a horst and graben structure typical of the Basin and Range province. The Klamath graben complex extends some 80 km, from Lower Klamath Lake, to as far north as Crater Lake, trending approximately N40W. Faulting in the area is believed to have commenced during the late Pliocene and continued well into the Pleistocene. Large, steeply dipping normal faults with vertical throws up to 1600 ft flank either side of the graben complex and trend

N25-35W. On the western shore of Upper Klamath Lake the large fault blocks dip towards the southwest, while on the eastern shore they dip to the northeast, suggesting that the axis of the graben complex passes through the lake.

The two types of faulting occurring in the immediate region are NW-trending normal faults and NE-trending, strike-slip cross-faults. Donath (1962) describes these two sets of faults as being contemporaneous, originally developing as conjugate strike-slip shears in a stress system with a north-south maximum principal stress and an east-west minimum principal stress. The system forms what Donath refers to as a rhombic fracture pattern. Lawrence (1976) interprets the Basin and Range faulting in Oregon as being separated by four strike-slip zones trending WNW. The fault blocks between these strike slip fault zones exhibit the rhombic fracture pattern suggested by Donath (1962). Lawrence (1976) suggests that the rhombic pattern of normal faulting in the region is a result of the interaction of extensional faulting between the fault zones and right-lateral strike-slip motion at the edges of the blocks.

The geology of the area has been mapped and described by Peterson and McIntyre (1970). Four dominant rock units occur in the immediate Klamath Falls area, identified by outcrops and borehole data Newcomb (1958). These rock units are, from earliest to most recent, a Pliocene basement basalt, the thick Pliocene Yonna Formation, a Pleistocene andesitic-basaltic flow sequence, and Quaternary alluvium.

The Pliocene basaltic rock of undetermined thickness is defined by Newcomb (1958) as the basement rock. Although this basalt does not outcrop in the immediate vicinity of the resource, it has been penetrated by wells at the OIT campus, 2 miles north of Klamath Falls city, and by the two YMCA wells in the southern part of the resource.

The Pliocene Yonna Formation, comprised of a sequence of lacustrine and fluvial tuffaceous siltstone, sandstone, ashy diatomite, basaltic tuff and breccia, and a few thin basalt flows, uncomformably overlies the basement rock (Newcomb, 1958). This formation is primarily subaqueous, as evidenced by the brecciated and altered basalt flows, deposited during a period when swamps and lakes covered the region. Explosive and quiescent volcanisms were nearly contemporaneous with the deposition of the Yonna Formation, as is suggested by the maars, tuff rings, and welded tuffs. The Yonna Formation is estimated by Newcomb (1958) to be approximately 1000 ft thick. Sammel (1980) estimates the thickness to be at least 850 ft. This formation represents the oldest rock unit that outcrops in the immediate Klamath Falls geothermal area.

The Yonna Formation is a large sequence of interbedded strata with high vertical and horizontal variability. Extensive erosion of this unit is indicated by the varying thickness encountered in outcrops and in driller's logs, as well as unconformable rock contacts.

Outcrops of an andesitic-basaltic flow sequence(s) with volcaniclastic interbeds of late Pliocene-early Pleistocene age, lying above the Yonna Formation, range in thickness from 0-180 ft. Just north of the immediate Klamath Falls geothermal area, on the southeast shore of Upper Klamath Lake, Peterson and McIntyre (1970) mapped several basalt eruptive centers. Newcomb (1958) describes several dikes which cut through or into sedimentary Tertiary rocks in the area surrounding the geothermal anomaly. These igneous features are considered to be contemporaneous with the Pliocene-early Pleistocene basalt flow sequence.

Much of the lower valleys in the Klamath Basin are covered by Quaternary alluvium. To the immediate south of the geothermal area, however, Quaternary fluvial terraces and lacustrine deposits are found.

Nearby volcanic activity has been dated by both paleontological data and potassium/argon (K/Ar) methods. K/Ar methods have indicated volcanic activity as recent as 1.9 m.y.b.p. and up to 4 to 5 m.y.b.p., for rocks on the KGRA periphery (M. O'Brian, personal communication). Diatom species obtained from well cuttings were used to correlate and date strata. It was concluded that surface outcrops are late Pliocene while subsurface samples range from mid to late Pliocene. Correlation of lithologic strata was difficult, due to the hydrothermal alteration of diatomaceous sediments (M. O'Brien, personal communication).

WELL TESTING

Numerous interference tests have been conducted within the Klamath Falls KGRA. From these tests, the hydrological parameters of the reservoir (kH/μ and $\phi c_t H$) have been determined and the nature of the thermal aquifer has been investigated. Results of these tests, summarized in Table 1, show the aquifer to be highly permeable. In general, the pressure transients are indicative of a naturally fractured system, with high permeability fractures and relatively low permeability matrix blocks (Sammel et al, 1984). Several localized heterogeneities have also been detected in the reservoir, including a high-permeability region centered in the Old Fort Road area and a semi-permeable fault near OIT (Benson and Lai, 1986; Nork, Inc., 1986).

Unexpectedly, the faults and fractures in the KGRA behaved neither as constant potential boundaries, nor as no-flow boundaries. Several

Table 1. Reservoir Parameters

Well Location	Transmissivity (kH/μ) x $10^{-6}m^3/Pa \cdot s$	Storativity ($\phi c_t H$) x $10^{-6}m/Pa$	Source
south central area	2.192	0.102-1.02	Lund, 1978
south central area	1.096	0.102-1.02	Sammel, 1980
south central area	4.21-4.51	0.106-.345	Benson, 1980
south central area	3.0-9.03	0.039-0.088	Benson, 1982a.
south central area	6.017	-----	Benson, 1982b.
south central area	1.955	0.0301	Benson, 1983
OIT area	.498-7.48	0.0408-1.02	Nork Inc., 1986
south central area	2.11	0.0221	Sammel et al., 1984

hypotheses were suggested to explain this observation, including: (1) the hot water upwells over a broad zone instead of a single fault zone, (2) the permeability of the fault zone is similiar to that of the near surface strata permeability, or (3) a single fault is responsible for the deep fluid upwelling, but the fault's effective width increases towards the surface, creating a diffuse permeable zone (Sammel et al, 1984).

GEOPHYSICS

Peterson and McIntyre (1976) prepared a Bouger gravity map for the Klamath Basin. He estimated the thickness of the valley fill in the graben structure to be on the order of 3000 ft southeast of Klamath Falls, and 6000 ft southwest of Klamath Hills. Stark et al. (1980) employed various geophysical methods to investigate the geothermal system in the Klamath Basin. Based on the results of remote sensing, gravity, geology, aeromagnetic and resistivity survey data, they conclude that the shallow hydrothermal circulation is related to the intersection of northeast-trending cross-faults and northwest-trending normal faults. These surveys did not reveal any new information on the heat source; however, they did suggest that either the conceptual model proposed by Peterson and McIntyre (1970) or Sammel et al (1984) could be correct.

THE GEOTHERMAL AQUIFER

Based on logs from a well drilled at the OIT campus, Sammel (1980) concluded that the rocks comprising the geothermal aquifer are believed to extend to at least 2000 ft. In the aquifer, water flows preferentially through strata consisting of volcanic breccia (cinders, broken lava, porous lava, etc.), jointed and fractured vesicular basalt flows, and fractured, indurated lacustrine sediments. These strata range in thickness from one to a few feet and have high vertical and areal variability. The permeable strata are interspersed with layers of lacustrine and tuffaceous sediments and diatomite, from 30 to 150 ft thick.

Fluid flows from the fault zone toward the southwest, following the general surface topography, as indicated by static water level maps drawn by Lund (1978) and Sammel et al. (1984).

GEOCHEMISTRY

Geochemical data contributes valuable information regarding maximum reservoir temperatures, mixing of thermal waters, fluid residence times and possible sources of recharge. Janik et al. (1985) used tritium data to determine the cold water residence time in the aquifer to be at least 30 years, and that of the thermal waters to be at least 60 years. From tritium and deuterium data they were also able to conclude that the cold water recharge probably does not originate from the modern Klamath Lake (Sammel, 1980). The tritium data also leads Janik et al. (1985) to suspect two cold water sources—a very shallow one containing tritium and a deeper one that is tritium-free. Geothermometry and mixing models indicate a maximum source-water temperature of 190 ° C.

Janik et al. (1985) developed a conceptual model consisting of a shallow 70-100 ° C thermal aquifer, caused by the mixing of 100-120 ° C and 20 ° C waters. The hot water may be derived from a deeper source where mixing of older tritium-free hot and cold water occurs. Although the maximum source-water temperature has not been encountered yet, geothermometry indicates temperatures of 150 to 190 ° C somewhere in the system.

TEMPERATURE DATA

Temperature data are very important to the understanding of a hydrothermal system. The temperature data used in this study were obtained primarily from drillers' logs. Temperatures in most cases were measured using a maximum reading thermometer or a simple thermistor apparatus. A few reports (Lund, 1978; Sammel and Peterson, 1976; and Sammel, 1980; Sass and Sammel, 1976) also recorded independent temperature data for

the Klamath Falls geothermal area. According to Sass and Sammel (1976), temperature profiles in the Basin and Range province are classified into four distinct types:

1. near-isothermal temperature profiles, indicating hydrologic recharge;
2. quasi-conductive temperature profiles;
3. convex-upward profiles with elevated temperatures, indicating areas of discharge;
4. temperature profiles exhibiting varied types of curvature, implying a combination of upward and downward flow.

As shown in Figure 3, profiles from Klamath Falls exhibit all four types of data; however, most temperature profiles show a combination of conductive and convective heat flow.

METHODOLOGY

In this section we discuss the methodology used to infer the location of faults from the large amounts of temperature data available from the Klamath Falls geothermal area. The data are depicted both in cross-sections and as contour plots. Both offer a good deal of information regarding the location and relative size of faults, size of the system and influence of surface phenomena.

Cross-sections were constructed approximately parallel and perpendicular to the proposed surface trace of the main normal fault associated with the geothermal system. Twenty such cross-sections were constructed for the geothermal area; five are shown in Figures 4 and 5 and their locations are shown in Figure 2. Since relatively little temperature data exist east of the normal fault, no cross-sections or horizontal contour maps were constructed for that area.

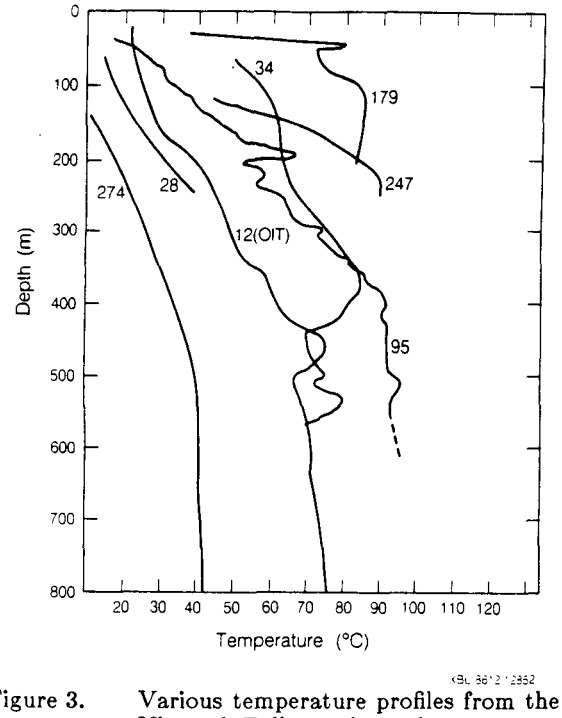


Figure 3. Various temperature profiles from the Klamath Falls geothermal resource.

Figure 4 shows two cross-sections parallel to the main normal fault, while Figure 5 shows three cross-sections perpendicular, or oblique, to the fault. Both sets of cross-sections show thermal features which can only be explained by complex convection heat transfer mechanisms. Cross-section 13, which is parallel to the fault, shows temperatures at both ends of the anomaly decreasing rapidly. We propose that northeast-trending cross-faults limit the northern and southern extension of the resource, and that the region between wells 31 and 9 is the primary zone of hot water recharge.

In cross-sections 3, 12, and 9, perpendicular to the normal fault, a higher thermal gradient zone is seen on the right (NE) side, most likely indicating the location of the main normal fault. This helps to confirm the existence and define the location of this normal fault, as suggested in previous reports. In Figure 2, perpendicular cross-sections not shown in this report, indicate similiar trends in temperature distribution.

Both sets of cross-sections show the locations of very high, near-surface thermal gradients (see wells 31, 386, 179, 137, 74, 247, 45). When the cross-sections are aligned these thermal anomalies fall along lineaments, interpreted in this report as faults (see Figure 6). Several 3-dimensional models were constructed revealing these fault lineaments in more detail. Cross-sections 3, 12 and 9 in Figure 5 suggest the existence of a subsidiary normal fault (Fault 1b) parallel to the main normal fault (Fault 1a) intersecting wells 45, 247, and 137. The northern and southern extent of the subsidiary normal fault cannot be determined from the available data.

The locations of several right lateral strike-slip cross-faults, roughly perpendicular to the main normal fault are also inferred from cross-sections 13 and 14 (Figure 4). These faults intersect wells, 31, 137, 386, and 179, as seen in Figure 6.

Figure 7 shows contour maps of the temperature distribution at three elevations (4100, 3900, and 3600 ft, a.s.l.). The locations of artesian springs, a canal that runs through the city, main roads, and the trace of the main normal fault are also shown. In general, at greater depths and larger distances from the center of the anomaly, fewer data are available. Consequently, only general inferences can be made for these areas. Dashed lines in both cross-sections and horizontal contour plots represent areas where data are limited.

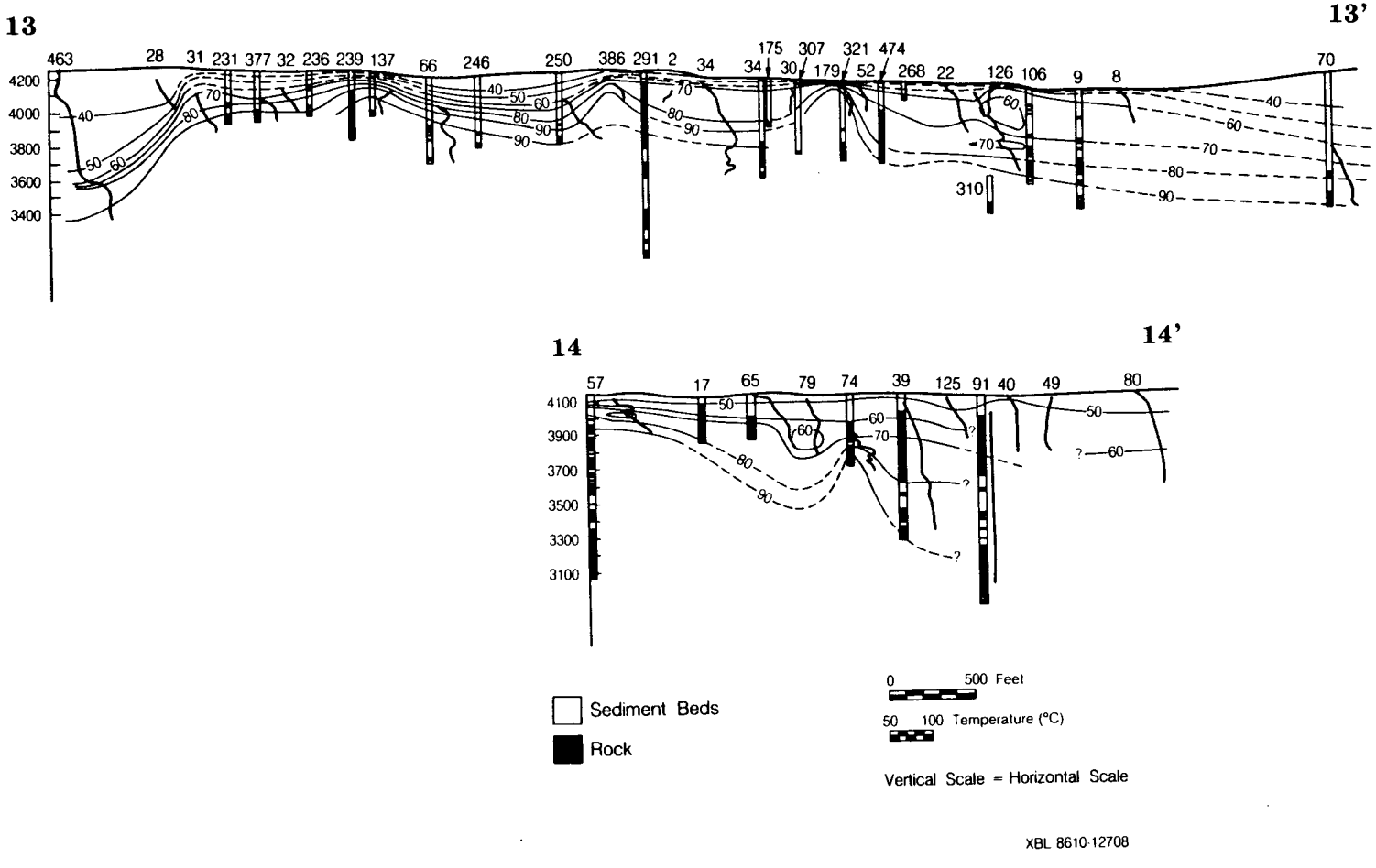


Figure 4. Cross-sectional temperature profiles drawn parallel to the main normal fault. Well numbers appear above the isotherms.

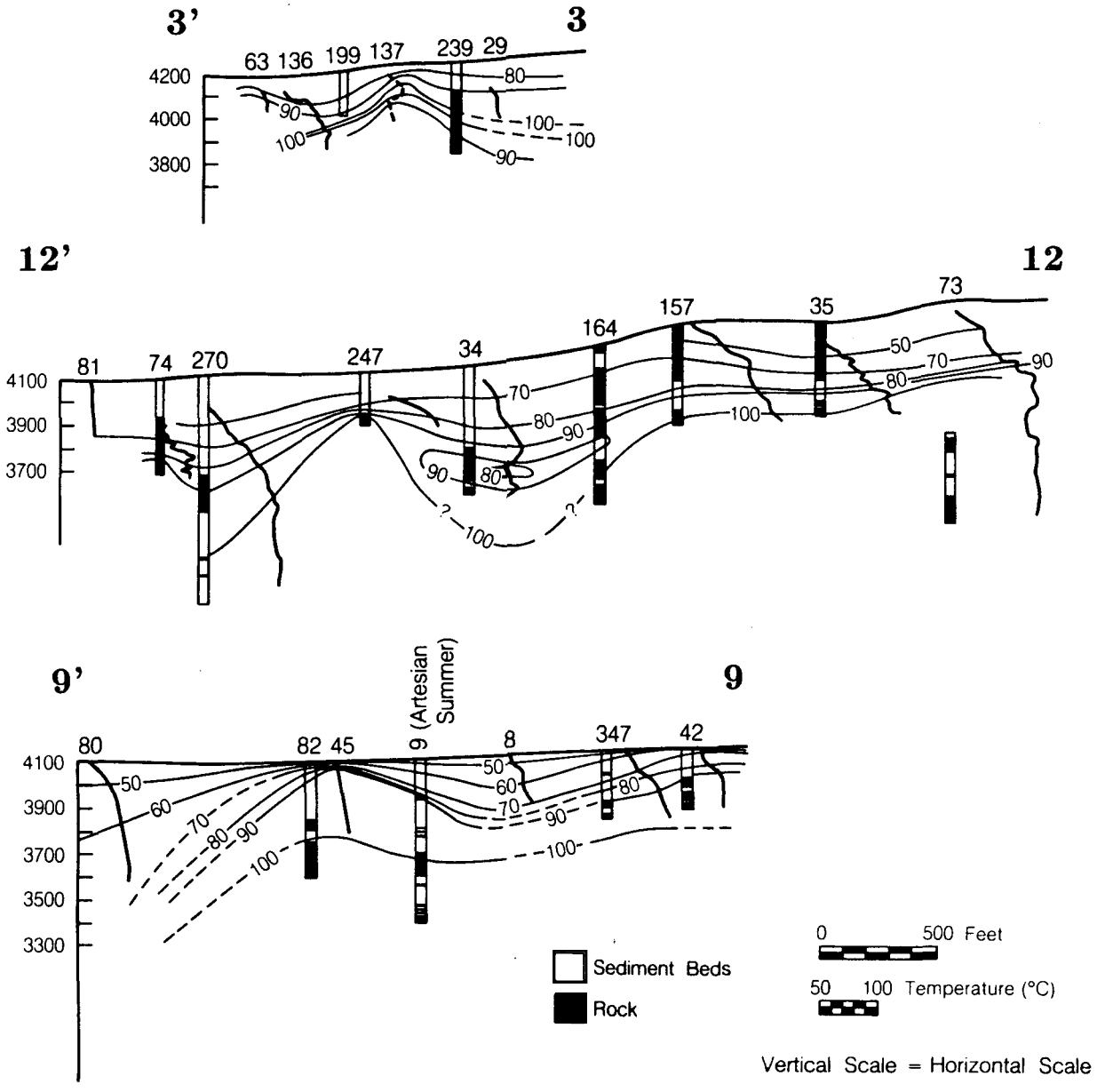


Figure 5. Cross-sectional temperature profiles drawn perpendicular to the main normal fault. Well numbers appear above the isotherms.

Although the temperatures in most wells increase quickly with depth, temperatures to the southwest of the artesian springs seem to increase much more slowly. This might be explained by a third normal fault (Fault 1c) trending northwest (see Figure 7), which impedes the flow of hot water toward the southwest. This same characteristic feature is seen in wells located southeast of Fault 2, and northwest of Fault 8, which seems to imply that the thermal anomaly is bounded on all sides by large faults.

Near surface temperatures are much more variable, as seen in Figure 7. This can be attributed to surficial effects and to a greater amount of data available at shallow depths. The temperature distribution is correlated with faults, artesian springs, regional groundwater flow, and the city canal. At all depths maximum temperatures are associated with the faults shown in Figure 6, while at shallow depths, high temperatures are also related to the artesian springs. On the other hand, cooler temperatures are associated with the canal, which leaks cold water into the surrounding formation. Temperatures decrease towards the southwest in response to the south-southwesterly regional flow of cold groundwater.

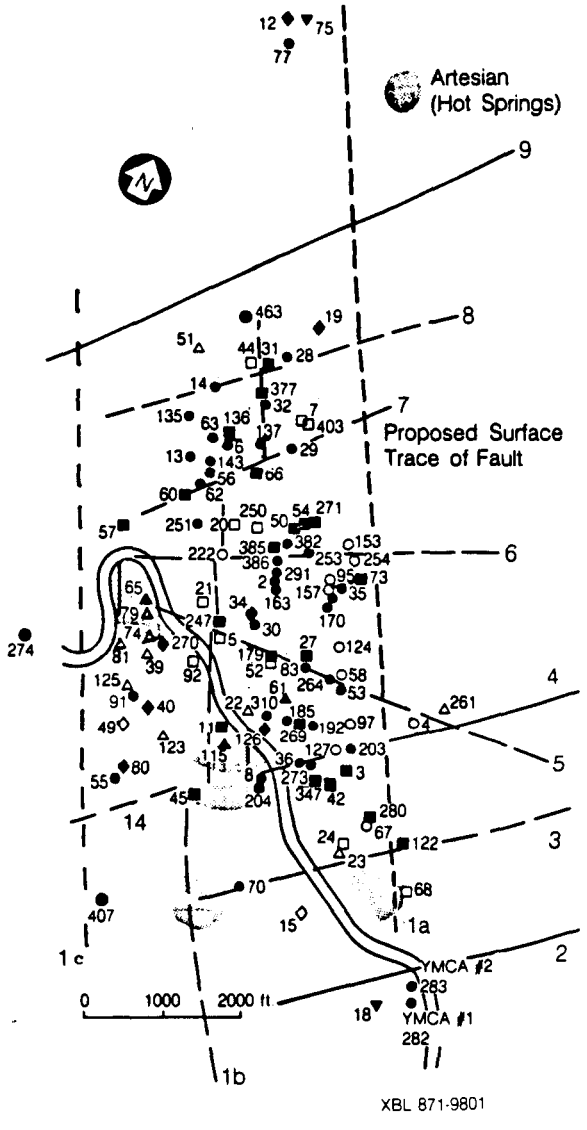


Figure 6. Fault locations inferred from the temperature profile cross-sections and temperature contour maps.

FAULT LOCATIONS

In order to confirm the existence of the faults shown in Figure 6, hydrologic, geophysical, and lithologic data as well as high altitude infrared photographs were analyzed. From high altitude photographs, Faults 1a, 2, 3, 4, 8 and 9 were easily identified because of their clearly visible surface traces. Faults 5, 6 and 7 were less pronounced because their traces tend to be localized, while fault 1b could not be detected. The exact locations of Faults 2, 3, and 9 were more easily recognized using areal photographs, as their traces were found to extend well into the region east of the main normal fault (Fault 1a).

The ease of detecting the various faults is due to differences in their size and displacement. Faults 1b, 5, 6, and 7 appear much smaller than Faults 1a, 2, 3, 4, 8, and 9, in view of the size of their relative temperature disturbance. All of the faults in Figure 6 conform to the regional fault pattern, which trends either northwest or northeast.

Lithologic data were re-examined with the intention of confirming the existence of the newly-proposed faults; however, this proved more difficult than anticipated. Poor lithologic correlations were found between nearby wells, both within the fault blocks and across fault block boundaries. This is partly due to the poor quality of the drillers' logs, and the complexity of the sedimentation and erosion processes. However, the system most likely experienced faulting concurrently with erosion and deposition of sediments, resulting in the highly complex subsurface geologic structure.

Also supportive of the new faults are the results of well testing in Klamath Falls. The geothermal reservoir appears to have a high degree of transmissivity and connectivity between wells, implying a highly fractured and faulted medium. The results of the many well tests conducted in the area can be interpreted within the framework of a fault and fracture dominated hydrologic regime. The normal faults, cross-faults and contacts between lithologic layers act as high-permeability conduits. Low permeability strata within the fault blocks provide a large storage volume for the thermal fluids. The double-porosity behavior reflected by the well test data support this interpretation (Benson and Lai, 1986).

The data interpretation for one of the well tests suggest the existence of and an approximately cylindrical region with a permeability 7.5 times higher than the rest of the reservoir. This region coincides with the proposed intersection of Faults 1a, 4 and 5.

Local regions with higher permeability are expected at each intersection of two or more faults. Although data to support this hypothesis at Klamath Falls are not yet available, the locations of once-active artesian hot springs generally coincide with the intersection of the strike-slip and normal faults (see Figure 6). This suggests that higher permeability regions are associated with the intersections of two or more faults throughout the KGRA.

Geophysical data, although very regional, suggest that the whole Klamath Basin graben has been offset along northeast-trending cross-faults. Although these cross-faults are indicated only on a regional scale, it was suggested that the shallow hydrothermal circulation is related to the intersection of northeast trending cross-faults and the northwest trending normal faults (Stark et al., 1980).



Figure 7. Temperature contour maps drawn at 4100 ft, 3900 ft and 3600 ft.

CONCEPTUAL MODEL

Figure 8 represents a conceptual model of the Klamath Falls geothermal area. The reservoir consists of a shallow and a deep aquifer. For the sake of simplicity, three permeable layers represent the shallow aquifer zone. The deep aquifer is inferred from geochemical data, although it has not been penetrated by wells. The two aquifers are connected through the main normal fault and possibly by the two subsidiary normal faults. Although upflow occurs along fault planes, we propose that the most permeable zones occur at the intersections of the normal and cross-faults as described in the previous section.

The dominant normal fault and two subsidiary normal faults indicate down-throws toward the southwest. This displacement might explain the successively lower temperatures encountered at greater distances from the main normal fault.

Hot water recharge may be derived from two possible sources. It is possible that thermal waters flow into the geothermal system from the upthrown block (mountainous region to the east of the main normal fault). Hot water could also be recharged from the west indicating a possible connection to a deep aquifer within the klamath Falls graben. At depth, it is unclear whether hot water from the deep aquifer is driven up individual faults, or whether the main normal fault recharges the two subsidiary normal faults at a shallower depth.

At shallow depths thermal waters spread laterally through permeable strata, and mixes with colder regional groundwater. Mixing also occurs along the faults. As the thermal water flows toward the southwest, temperatures are cooled to regional groundwater temperatures.

An age of 2 to 4 million years is estimated for the geothermal system. Silicified palagonitic tuff, found at elevations up to several hundred feet above the present geothermal system suggests that the system was associated with early fault displacements (Sammel, 1980). The fresh appearance of the normal fault scarps in the area indicates recent fault displacements. Paleontological dates and the age of recent volcanic activity suggest that faulting in the region began during the late Pliocene and continued well into the Holocene.

Two hypotheses have been made on the possible heat source. Peterson and McIntyre (1970) suggest the heat source is associated with a cooling dike or sill. Sammel and Peterson (1976) consider the Klamath Falls KGRA as a normal geothermal gradient system. This would require a fault zone that extends to nearly 6 km in order to reach temperatures approaching 190 °C at depth. Sammel and Peterson (1976) point out that no noticeable surficial volcanic manifestations or dike intrusions are found within the KGRA. Although this is true for the KGRA, geologic maps indicate a high degree of relatively recent volcanic activity in the surrounding area.

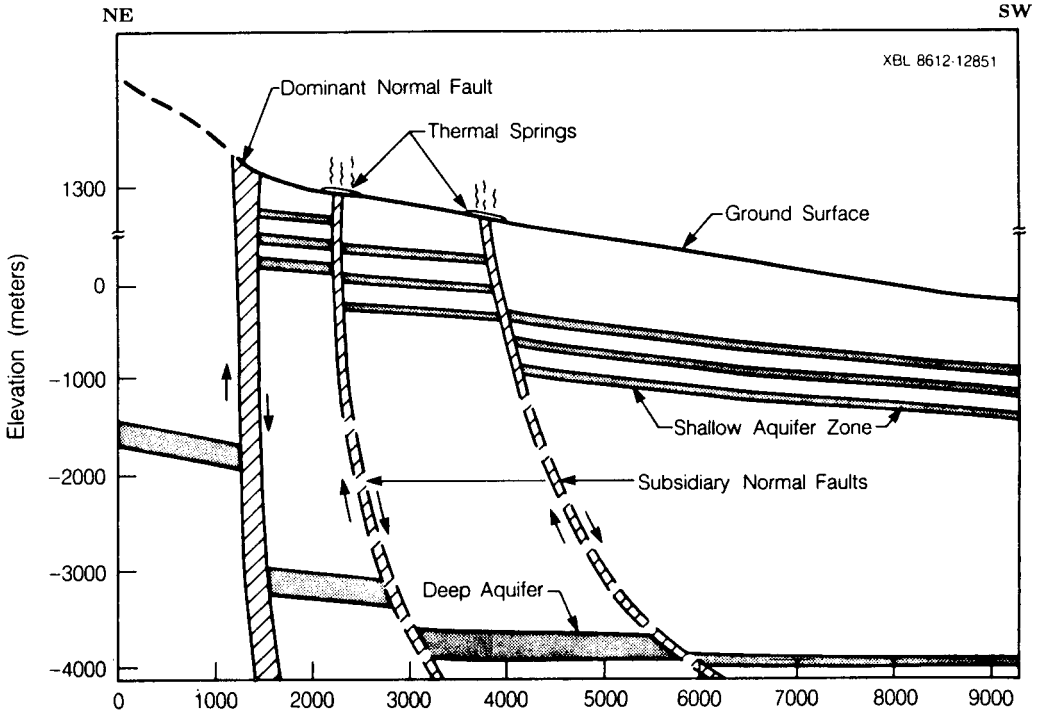


Figure 8. Conceptual model for the Klamath Falls geothermal system.

Additional deep drilling is needed to further characterize the source recharging the Klamath Falls geothermal system. Further work is still needed to identify and describe the actual fault systems in the area and determine the role of the different faults in the development and dynamics of the geothermal reservoir.

ACKNOWLEDGEMENTS

This work was supported through U.S. Department of Energy Contract No. DE-AC03-76SF00098 by the Assistant Secretary for Conservation and Renewable Energy, Office of Renewable Technology, Division of Geothermal Technology. The authors are indebted to Kent Colahan of Klamath Falls, and both Gene Culver and Paul Lineau for supplying crucial data needed for this report. We also thank M. Lippman, N.E. Goldstein, and S. Halfman for critical review of this paper.

REFERENCES

Benson, S.M., 1982a, Klamath Falls (WP-1 and WP-2) system check, Sept. 29 through 30, 1981, unpublished report to the city of Klamath Falls, OR, 13 p.

Benson, S.M., 1982b, Klamath Falls (WP-1, Supply and distribution network, Museum Well) system check, February 8 through 12, 1982, unpublished report to the city of Klamath Falls, OR, 8 p.

Benson, S.M., 1983, Interpretation of interference data from the Klamath Falls, Oregon geothermal resource, Lawrence Berekeley Laboratory Report, LBL-16671, 6 p.

Benson, S.M., Goranson, C.B. and Schroeder, R.C., 1980, Evaluation of City Well 1, Klamath Falls, Oregon, Lawrence Berkeley Laboratory Report, LBL-10848, 9 p.

Benson, S.M. and Lai, C.H., 1986, Analysis of interference data in a highly heterogeneous and naturally fractured geothermal reservoir, Society of Petroleum Engineers Paper SPE-13252, p. 236-248.

Donath, F.A., 1962, Analysis of basin-range structure, south-central Oregon, Geol. Soc. America Bull., v. 73, no. 1, 16 p.

Janik, C.J., Truesdell, A.H. Sammel, E.A. and White, A.F., 1985, Chemistry of low-temperature geothermal waters at Klamath Falls, Oregon, Transactions, Geothermal Resources Council, vol. 9, p. 325-331.

Lawrence, R.D., 1976, Strike-slip faulting terminates the Basin and Range province in Oregon: Geol. Soc. of America Bull., vol. 87, p. 846-850.

Lund, J.W., Principal Investigator, 1978, Geothermal hydrology and geochemistry of Klamath Falls: Oregon, urban area, Klamath Falls, Oregon Institute of Technology, Geo-Heat Utilization Center, Final report to the U.S. Geological Survey (Grant 14-08-0001-G-291), 123 p.

Meyers, J.D. and Newcomb, R.C., 1952, Geology and ground-water resources of the Swan Lake-Yonna valleys area, Klamath county, Oregon., USGS, 151 p.

Moore, B.N., 1937, Nonmetallic mineral resources of eastern Oregon, U.S. Geol. Survey Bull. 875, 180 p.

Newcomb, R.C., 1958, Yonna Formation of the Klamath River Basin, Oregon, Northwest Sci., vol. 32, no. 2, p. 41-48.

Newcomb, R.C. and Hart, D.H., 1958, Preliminary report on the groundwater resources of the Klamath River Basin, Oregon, U.S. Geological Survey Open-File Report, 248 p.

W.E. Nork, Inc., 1985, Hydrologic assessment of the geothermal aquifer, Klamath Falls, Oregon, prepared for City of Klamath Falls, 73 p.

W.E. Nork, Inc., 1986, College Industrial Park Well No. 1 aquifer stress test results, prepared for, Oregon Institute of Technology, 34 p.

Peterson, N.V. and McIntrye, J.R., 1970, The reconnaissance geology and mineral resources of eastern Klamath County and western Lake County, Oregon, Portland, Oregon Department of Geology and Mineral Industries Bulletin 66, 70 p.

Sammel, E.A. and Peterson, D.L., 1976, Hydrologic reconaissance of the geothermal area near Klamath Falls Oregon, USGS Water Resources Investigations 76-127, 129 p.

Sammel, E.A., 1980, Hydrogeologic appraisal of the Klamath Falls geothermal area, Oregon, USGS Professional Paper 1044-G, 45 p.

Sammel, E.A., Truesdell, A.H., Janik, C.J., Gudmundsson, J.S., Benson, S.M., Solbau, R.D. and Lai, C.H., 1984, Analysis and interpretation of data obtained in tests of the geothermal aquifer at Klamath Falls, Oregon, USGS, Water Resources Investigations Report 84-4216.

Sass, J.H. and Sammel, E.A., 1976, Heat flow data and their relation to observed geothermal phenomena near Klamath Falls, Oregon, Journal of Geophysical research, vol. 81, no. 26, p. 4863-4868.

Stark, M., Goldstein, N.E. and Wollenberg, H.A., 1980, Geothermal exploration assessment and interpretation, Upper Klamath Lake area, Klamath Basin, Oregon, Lawrence Berkeley Laboratory Report LBL-10140, 84 p.

PROCEEDINGS, Twelfth Workshop on Geothermal Reservoir Engineering
Stanford University, Stanford, California, January 20-22, 1987
SGP-TR-109

ON FLUID AND HEAT TRANSFER IN DEEP ZONES OF VAPOR-DOMINATED GEOTHERMAL RESERVOIRS

K. Pruess, R. Celati‡, C. Calore‡, and G. Cappetti†*

* Earth Sciences Division, Lawrence Berkeley Laboratory
University of California, Berkeley, California 94720

‡Istituto Internazionale per le Ricerche Geotermiche,
CNR, Piazza Solferino 2, 56100 Pisa, Italy

†ENEL, Unita Nazionale Geotermica,
Via Andrea Pisano, 56100 Pisa, Italy

INTRODUCTION

The vapor-dominated reservoirs of Larderello, Italy, The Geysers, California, and Matsukawa, Japan, have been under exploitation for several decades. Much geological, geophysical, geochemical, and reservoir engineering information on these systems has been published in the technical literature. Conceptual models have been developed which explain important physical and chemical conditions and processes in these systems (Ferrara et al., 1970; Sestini, 1970; White et al. 1971; Truesdell and White, 1973; Weres et al., 1977; D'Amore and Truesdell, 1979; Pruess and Narasimhan, 1982).

Vapor-dominated reservoirs are overlain by a caprock of generally low permeability, in which heat transfer occurs mainly by conduction. In the main vapor-dominated zone vertical gradients of temperature and pressure are small, so that conductive heat flow is negligibly small. Heat transfer in these zones occurs by means of a vapor-liquid counterflow process known as "heat pipe" (White et al., 1971; Martin et al., 1976; Straus and Schubert, 1981; Pruess, 1985). Vapor originates at depth from boiling of liquid. It rises to shallower horizons where it condenses, depositing its large latent heat of vaporization. The condensate then returns to depth driven by gravity force.

Little is known about fluid and heat transfer processes, and thermodynamic conditions of formation fluids beneath the main permeable zones of vapor-dominated systems. Systematic long-term increases in production temperatures with strong superheating have been reported for Larderello (Sestini, 1970). These observations suggested that fluids with very high enthalpy can be delivered from greater depths (2-4 km). In recent years a programme of deep exploration has been carried out at Larderello by the Ente Nazionale per l'Energia Elettrica (ENEL), results of which have been presented by Cappetti et al. (1985). Several wells have been drilled to depths of 3000 m and more, and temperatures in excess of 300 °C have been observed. More recently, similarly high temperatures and high-enthalpy fluids have been reported for a deep well at The Geysers (Drenick, 1986).

In this paper we present temperature data for deep horizons at Larderello, and we attempt to analyze the data with a view on identifying reservoir conditions and processes at depth. Of particular interest are the mechanisms and rates of fluid and heat flow in the natural state and in response to exploitation, and the permeability structure of the reservoir.

DATA ON DEEP TEMPERATURES

Temperature logs are run in Larderello wells during drilling stops mainly to locate permeable zones. In some cases drilling stops are sufficiently long to permit bottom-hole temperatures to stabilize at values indicative of formation conditions. For shorter drilling interruptions (24-48 hours) it is possible to estimate formation temperatures from a record of the temperature recovery at bottomhole (Barelli and Palama, 1981; Grant et al., 1982). Such estimation provides reliable results when formation permeability at bottomhole is low. After completion, temperatures tend to stabilize throughout the depth of the borehole, but the presence of internal flows [with heat loss and boiling and condensation effects] generally make wellbore temperatures different from formation temperatures. In some wells high rates of internal flow between different permeable intervals are present in shut-in conditions, so that in the vicinity of fluid entry points temperatures are relatively unperturbed by heat loss effects in the wellbore. However, due to the predominance of fracture permeability in Larderello it is generally not possible to correlate temperatures measured at a major

feed with formation temperatures at the same depth.

Because of these difficulties, only few reliable measurements of formation temperatures are available from Larderello. In Figure 1 we present temperature-depth data obtained from three productive wells located in the central area of Larderello, which has been under production for some forty years. Note that temperatures at any given depth are generally similar for the three wells. Down to approximately 500 m depth there is a conductive gradient of approximately 0.49 °C/m. From 500 to 2400 m depth there is a very small gradient of 0.015 °C/m, which is typical of the main zone of vapor-dominated systems. Substantially higher temperature gradients, approaching boiling point-for-depth (B.P.D.) conditions, are encountered at greater depth.

The temperatures of the fluids produced at Larderello have increased considerably over decades of exploitation (Sestini, 1970). It is not known how formation temperatures such as shown in Figure 1 differ from the conditions that were present before exploitation.

HEAT FLOW ANALYSIS

As an introduction into analyzing heat transfer conditions at depth we shall briefly discuss the natural state of a vapor-dominated system. The following observations and assumptions can be made:

- in the natural undisturbed state, heat transfer in vapor-dominated systems is essentially vertical; horizontal components of heat flux will only be significant at the reservoir margins, where temperature gradients have large horizontal components;
- in the natural state, a reservoir is close to steady-state conditions of fluid and heat flow; this together with the assumption made above implies that vertical heat flux is very nearly constant down to "great depth";
- total vertical heat flux contains conductive and convective components; convective heat transfer is accomplished by steam-water counterflow (heat pipe);
- in the natural state, steam-water counterflow will be very nearly balanced, so that net vertical fluid flux will be very small;
- the reservoir is in two-phase conditions all the way down to great depth where supercritical conditions may be reached (Cappetti et al., 1985).

On the basis of these assumptions it is possible to write the total vertical heat flux as a sum of conductive and convective contributions (Martin et al., 1976). Assuming the z-axis to point downward, we have for upward heat flux:

$$Q = Q_{conv} + K \frac{dT}{dz} \tag{1}$$

$$Q_{conv} = k \frac{(\rho_l - \rho_v) h_{vl} g}{\frac{\mu_l}{k_{rl}\rho_l} + \frac{\mu_v}{k_{rv}\rho_v}} \tag{2}$$

$$\frac{dT}{dz} = \left(\frac{1}{\rho_v} - \frac{1}{\rho_l}\right) \frac{(T+273.15)g}{h_{vl}} \frac{\frac{k_{rv}\rho_v^2}{\mu_v} + \frac{k_{rl}\rho_l^2}{\mu_l}}{\frac{k_{rv}\rho_v}{\mu_v} + \frac{k_{rl}\rho_l}{\mu_l}} \tag{3}$$

Here K is thermal conductivity, T is temperature in °C, k is absolute permeability, ρ is density, $h_{vl} = h_v - h_l$ is vaporization enthalpy, g is acceleration of gravity, μ is viscosity, k_r is relative permeability, and subscripts l and v denote liquid and vapor phases, respectively.

From Eq. (2) it can be seen that the heat flux associated with balanced liquid-vapor counterflow will tend to zero as temperatures approach the critical point (374.15 °C for pure water). It is well known that for a given convective heat flux a balanced liquid-vapor counterflow is possible in two distinct conditions, corresponding to vapor-dominated and liquid-dominated heat pipes, respectively (Martin et al., 1976; Pruess, 1985). Formally, this can be seen from Eq. (2), which for given Q_{conv} has one solution in which k_{rl} is small and another in which k_{rv} is small. In the vapor-dominated state the vertical pressure gradient is somewhat larger than vapor-static, so that there is a large effective force for downward flow of liquid. A balanced counterflow of vapor and liquid is then possible for conditions of very small liquid relative permeability (large vapor saturation). Conversely, in the liquid-dominated state there is a large force for upward vapor flow, and under conditions of balanced counterflow both vapor saturation and vapor relative permeability are small.

We have evaluated Eqs. (1) - (3) over a wide range of temperatures, assuming that the sum of liquid and vapor relative permeabilities is equal to 1, as is appropriate for a fractured medium (Pruess et al., 1983). Temperature and pressure dependence of water properties was computed from equations given by the International Formulation Committee (1967). The results are plotted in Figures 2 and 3. It is seen that vapor-dominated heat pipes show only modest variations in heat transfer rates over the temperature range from 150 to 300 °C. In contrast, heat flux in liquid-dominated heat pipes has

a fairly sharp maximum near 320 ° C. However, no dramatic reduction in heat flux is observed for temperatures up to 350 ° C in either case.

As an alternative to Eqs. (1) - (3) one can write

$$kk_{rv} = \frac{Q - K\frac{dT}{dz}}{\frac{\rho_v h_{vl}}{\mu_v}\left[\frac{h_{vl}}{(\frac{1}{\rho_v}-\frac{1}{\rho_l})(T+273.15)}\frac{dT}{dz} - \rho_v g\right]} \quad (4)$$

which expresses effective vapor permeability k^*k_{rv} as a function of total heat flux, reservoir temperature, and temperature gradient. (Note that all water properties appearing in Eq. (4) are to be evaluated on the saturation line; i.e., they are functions of temperature only.) An analogous relationship can be written for effective liquid permeability. For a vapor-dominated reservoir total heat flux is known from the conductive gradient in the caprock. With Eq. (4) it should then be possible to obtain estimates of vertical permeability for vapor and liquid from data on temperatures and temperature gradients. If for relative permeabilities in a fractured system one further assumes that $k_{rv} + k_{rl} = 1$ one could obtain absolute vertical permeability k at each depth level, and also liquid and vapor relative permeabilities separately. In practice, estimation of vertical permeability from Eq. (4) is problematic, even if good data on undisturbed formation temperatures are available. We have performed numerical simulations of heat pipes of varying vertical permeability, and have analyzed the simulated temperature data by means of Eq. (4) and an analogous relationship for effective liquid permeability. In a liquid-dominated heat pipe vertical pressure gradient deviates little from hydrostatic, so that small inaccuracies in temperatures translate into large variations for estimated permeabilities. In vapor-dominated heat pipes the deviations from a vapor-static gradient tend to be much larger, so that practically useful permeability estimates may be possible.

It is instructive to apply Eq. (4) to some of the temperature data from Larderello, even though the assumptions on which it is based are not valid in a producing reservoir, where there is a large net upward flow. Figure 4 shows results for vertical permeability obtained from well A temperatures, which are particularly interesting because the transition to a higher temperature gradient is well defined near 2400 m depth (see Fig. 1). The permeability values obtained represent lower limits, because the analysis did not take into account that vertical vapor fluxes are substantially increased in response to exploitation. An alternative estimation of vertical permeability near well A can be obtained by assuming that vertical vapor flux is equal to the stabilized long-term production rate at Larderello. This will provide an upper limit for vertical permeability, because vertical flux will in fact diminish with depth as fluid is being released from storage. Furthermore, at shallower horizons the reservoir has evolved single-phase vapor conditions with smaller pressures and larger pressure gradients than obtained from the assumption that pressures are equal to saturation pressures at given temperatures. Calculating permeability from a given vapor flux and a low estimate for pressure gradient will result in an upper limit for permeability. Assuming a representative value of 100 tonnes/hour/km^2 for stabilized production rate at Larderello results in estimates of vertical permeability approximately 40 times larger than obtained from the assumption of undisturbed natural conditions (see Fig. 4). Actual vertical permeability should be intermediate between the two estimates, being closer to the values inferred from the stabilized production flux at shallower horizons, and trending more towards the values obtained from the natural state flow model at greater depth, where conditions are less severely affected by exploitation.

NUMERICAL SIMULATIONS

A more precise estimation of vertical permeability should be possible from numerical simulations. A numerical model for long-term field depletion must be consistent with the concepts of heat transfer outlined in the previous section, and it must adequately represent observed trends of production rates and flowing enthalpies, as well as reservoir pressures. The main constraints on a model are (1) the total vertical heat flux in the natural state, which is rather well known from the depth to reservoir top and the undisturbed temperature there [from well A data we have $Q = K \cdot dT/dz = 2.3 \times 0.49 = 1.12$ W/m^2]; (2) a rather rapid initial decline in flow rate of most wells by a factor of typically 3-5 in the first few years of production, followed by a stabilization of rates; (3) a long-term rise in produced enthalpy, from initial values near 2800 kJ/kg to values near 2900 kJ/kg and larger; and (4) a trend of increasing temperatures of produced fluids over some 20 years of exploitation, at a rate of 1 - 1.5 ° C/year (Sestini, 1970); presently temperatures at the reservoir top are near 240 ° C.

Using LBL's geothermal reservoir simulator MULKOM (Pruess, 1983), we have performed numerical simulations of one-dimensional vertical sections which were designed to represent the important attributes of the Larderello system in a generic way. Vertical permeability structure was chosen based on the results of the analysis presented above (see Fig. 4). Initial conditions are not known but can be reasonably well constrained from available temperature data and the heat pipe mechanism of vertical heat transfer. In Figure 5 we have plotted a temperature profile corresponding to a

vapor-static pressure gradient, with T = 240 ° C at 500 m depth. Temperatures increase with depth by approximately 4 ° C per km. In realistic vapor-dominated heat pipe conditions temperature and pressure gradients may be 1.5 - 5 times larger (depending on heat flux and vertical permeability), but it is clear that a vapor-dominated heat pipe can not reach temperatures of 300 ° C or more at 3000 m depth as have been measured in the field. Clearly, therefore, at some depth a transition to a liquid-dominated heat pipe must have been present in the natural state. The depth at which this transition occurred is unknown; it was chosen as 2100 m in the simulations. This appears reasonable in view of measured temperatures, and the inferred reduction in vertical permeability near 2100 m depth (see Fig. 4). Ultimately, of course, this as well as other modeling assumptions and parameters need to be verified by comparison of simulated reservoir behavior with field data.

Table 1 lists parameters used in the simulations, which are intended to represent typical conditions at Larderello; the large irreducible liquid saturation (80%) was chosen to approximately account for the large enthalpies of fluids produced from fractured-porous media. Selected results for production rates per km^2, production enthalpies, and temperatures at reservoir top (at 500 m depth) are given in Figures 6 and 7. Before discussing these results we will briefly give a qualitative discussion of simulated reservoir response to exploitation.

In response to fluid withdrawal boiling will be induced in the reservoir, with accompanying increase in vapor saturation and decline of reservoir pressure and temperature. These effects will be initially confined to the vicinity of the production interval (reservoir top), but will over time propagate to greater reservoir depths. Important effects are induced when the disturbance in reservoir conditions reaches the liquid-dominated heat pipe at depth. In this region large vertical pressure gradients are present, and a strong increase in the rate of vapor upflow will occur when vapor saturation and mobility increase. The upflowing vapor will in part condense at shallower levels, as a consequence of which temperature decline may slow down or even reverse in the condensation zone.

In a porous medium model it is possible to adequately represent the long-term trend of production rate, but produced enthalpies and temperatures at the reservoir top are underpredicted (see Fig. 6). We made various modifications to parameters (see Table 1) in order to enhance rate and enthalpy of fluids rising from depth, including: increase in vertical permeability all the way to the upper limit obtained above (see Fig. 4); decrease in reservoir porosity; downward extension of the permeable reservoir to a depth of 4300 m, where temperatures in the liquid-dominated heat pipe reach 355.6 ° C. These modifications were tried one at a time as well as in combination, but they were unable to deliver enthalpies as large as observed in the field. Simulated flowing enthalpies reached maximum levels of 2830 kJ/kg.

In order to obtain higher-enthalpy fluids two possible mechanisms can be considered. One possibility is that supercritical fluids of very high enthalpy may flow up from great depth and make increasing contributions to production as shallower horizons are being depleted. Such fluids have been encountered in the deep drilling at Larderello (Cappetti et al., 1985). An alternative possibility is that fluids of very high enthalpy may be obtained from a process of enthalpy enhancement which is peculiar to two-phase flow in fractured-porous media. When low-permeability rocks containing two-phase fluid are made to discharge into fractures, the flowing enthalpy of the discharge can be substantially enhanced by an interplay between two-phase flow and heat conduction in the rock matrix (Pruess and Narasimhan, 1982).

Contributions of supercritical fluids are very difficult to evaluate. In the present work we have focussed on fracture effects for subcritical two-phase fluids. Several simulation runs were made in which fracture-matrix interactions were represented using a multiple interacting continua approach (MINC; Pruess and Narasimhan, 1982, 1985). Results given in Figure 6 indicate that substantially higher flowing enthalpies (up to 2875 kJ/kg) and higher temperatures at the reservoir top were obtained. Figure 7 shows that there is a complex structure to reservoir depletion at different depths, with important flow effects occurring in the vicinity of the original transition from vapor- to liquid-dominated conditions (2100 m depth). The depletion mechanism is rather different for fractured than for porous systems. The former permit far better access to heat stored in deep reservoir rocks. We expect that a satisfactory agreement between the predictions from a fractured reservoir model and field observations will be obtainable through a more extensive parameter search.

The observed long-term rise in produced fluid temperatures has not yet been modeled. We believe that this effect arises from localized boiling after a well is first opened, which causes a rapid initial temperature drop to near 210 ° C; followed by reheating of the formations by high-enthalpy fluids from depth. Modeling of these processes is in progress; it requires a rather detailed spatial resolution near the well feeds, especially for horizontal flow.

CONCLUSIONS

We have presented a preliminary analysis of permeability structure and fluid and heat flow conditions in the deeper horizons of the Larderello geothermal system. Our main observations and findings are:

(1) Measurements in deep Larderello wells have indicated formation temperatures near 300 ° C at 3000 m depth, and even higher temperatures at greater depth.

(2) From an analysis of heat transfer mechanisms we suggest that a transition from vapor-dominated to liquid-dominated conditions must have been present in the natural state of the Larderello geothermal system. No reliable determination of the depth at which this transition occurred has yet been made, but a depth of approximately 2000 m or more appears most likely.

(3) From temperature-depth data in two-phase reservoirs it is in principle possible to estimate vertical permeability.

(4) For exploited reservoirs such as Larderello, reconstruction of permeability and temperature trends with depth can be made indirectly, using numerical simulation. Our preliminary results indicate that production of high-enthalpy fluids can be explained from two-phase flow effects in a fractured-porous medium.

ACKNOWLEDGEMENT

The U.S. Department of Energy, Geothermal Technology Division, provided financial support to LBL for its participation in this study under Contract No. DE-AC03-76SF00098. A critical review of the paper by M. Lippmann and S. Benson is appreciated. For assistance in the preparation of the manuscript the authors are indebted to L. Fairbanks and D. Swantek.

REFERENCES

Barelli, A. and Palama, A., A New Method for Evaluating Formation Equilibrium Temperature in Holes During Drilling, *Geothermics,* Vol. 10, No. 2, pp. 95-102, 1981.

Cappetti, G., Celati, R., Cigni, V., Squarci, P., Stefani, G., and Taffi, L., Development of Deep Exploration in the Geothermal Areas of Tuscany, Italy, 1985 International Symposium on Geothermal Energy, International Volume, *Geothermal Resources Council,* pp. 303-309, 1985.

D'Amore, F., and Truesdell, A. H., Models for Steam Chemistry at Larderello and The Geysers, Proceedings Fifth Workshop Geothermal Reservoir Engineering, Stanford, California, pp. 283-297, 1979.

Drenick, A., Pressure-Temperature-Spinner Survey in a Well at The Geysers, paper presented at 11th Workshop Geothermal Reservoir Engineering, Stanford University, Stanford, California, January 1986.

Ferrara, G., Panichi, C., Stefani, G., Remarks on the Geothermal Phenomenon in an Extensively Exploited Field, Results of an Experimental Well, *Geothermics, Special Issue 2,* Vol. 2, Part 1, pp. 578-586, 1970.

Grant, M. A., Donaldson, I. G., and Bixley, P. F., *Geothermal Reservoir Engineering,* Academic Press, New York, 1982.

International Formulation Committee, A Formulation of the Thermodynamic Properties of Ordinary Water Substance, IFC Secretariat, Düsseldorf, Germany, 1967.

Martin, J. C., Wegner, R. E., and Kelsey, F. J., One-Dimensional Convective and Conductive Geothermal Heat Flow, Proceedings, Second Workshop on Geothermal Reservoir Engineering, Stanford University, pp. 251-262, 1976.

Pruess, K., Development of the General Purpose Simulator MULKOM, Annual Report 1982, Earth Sciences Division, report LBL-15500, Lawrence Berkeley Laboratory, 1983.

Pruess, K., A Quantitative Model of Vapor-Dominated Geothermal Reservoirs as Heat Pipes in Fractured Porous Rock, Transactions, Geothermal Resources Council, Vol. 9, Part II, pp. 353-361, 1985.

Pruess, K., Bodvarsson, G. S., and Stefansson, V., Analysis or Production Data from the Krafla Geothermal Field, Iceland, paper presented at Ninth Workshop on Geothermal Reservoir Engineering, Stanford University, Stanford, CA., December 1983.

Pruess, K., and Narasimhan, T. N., On Fluid Reserves and the Production of Superheated Steam from Fractured, Vapor-Dominated Geothermal Reservoirs, *Journal of Geophysical Research,* Vol. 87, No. B11, pp. 9329-9339, 1982.

Pruess, K., and Narasimhan, T. N., A Practical Method for Modeling Fluid and Heat Flow

in Fractured Porous Media, *Society of Petroleum Engineers Journal,* Vol. 25, No. 1, pp. 14-26, February 1985.

Sestini, G., Superheating of Geothermal Steam, *Geothermics,* Special Issue 2, pp. 622-648, 1970.

Straus, J. M., and Schubert, G., One-Dimensional Model of Vapor-Dominated Geothermal Systems, *Journal of Geophysical Research* Vol. 86, No. B10, pp. 9433-9438, October 1981.

Truesdell, A. H., and White, D. E., Production of Superheated Steam from Vapor-Dominated Geothermal Reservoirs, *Geothermics,* Vol. 2, No. 3-4, pp. 154-173, September-December, 1973.

Weres, O., Tsao, K., and Wood, B., Resource, Technology and Environment at The Geysers, Lawrence Berkeley Laboratory report LBL-5231, Berkeley, California, July 1977.

White, D. E., Muffler, L. J. P., and Truesdell, A. H., Vapor-Dominated Hydrothermal Systems Compared with Hot-Water Systems, *Economic Geology,* Vol. 66, No. 1, pp. 75-97, 1971.

Table 1. Parameters for Numerical Simulations*

Parameter	Value
Formation Parameters	
rock grain density	2600 kg/m^3
rock specific heat	920 J/kg . °C
formation heat conductivity	2.3 W/m . °C (caprock) 2.7 - 3.5 W/m . °C (reservoir)
formation porosity	3 - 5%
vertical permeability ‡	0.1 - 24 x 10^{-15} m^2
effective fracture porosity †	0.1 - 0.5%
rock matrix permeability †	0.1 - 2.0 x 10^{-18} m^2
fracture spacing †	50 m
depth of permeable reservoir	3200 - 4300 m
liquid relative permeability	$k_{rl} = (S_l - 0.8)/0.2$
vapor relative permeability	$k_{rv} = 1 - k_{rl}$
capillary pressure	0
Initial Conditions	
temperatures**	240 °C at 500 m depth; beneath 500 m heat pipe with a heat flux of 1.12 W/m^2; vapor-dominated down to 2100 m depth, then liquid-dominated
pressures	saturation pressures at prevailing temperatures
liquid saturation	as obtained for steady-state heat pipe with heat flux of 1.12 W/m^2 (slightly larger than 80% in vapor-dominated section; close to 100 % in liquid-dominated section)
Production Specifications ("Wells")	
flowing bottomhole pressure	5 bars
productivity index #	4.88 x 10^{-17} m^3

* parameters for which a range is given were varied in the simulations;

‡ variation with depth shown in Figure 4;

† for fractured medium simulations only;

** see Figure 7;

\# adjusted to obtain an early-time rate approximately four times larger than stabilized rate of 100 tonnes/hour/km^2

Table 2. Specifications of Cases shown in Figures 6 and 7‡.		
	Case A	**Case B**
reservoir description	porous medium	fractured-porous
vertical permeability	low*	high*
matrix porosity	5%	5%
matrix permeability	*	0.2×10^{-18} m^2
fracture porosity	(no fractures)	0.1%
depth to bottom of permeable reservoir	3200 m	3200 m

‡ additional specifications as in Table 1.
*see Figure 4

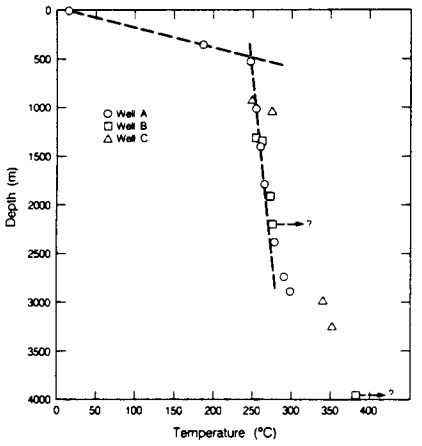


Figure 1. Measured temperatures for three deep wells in the central area of Larderello. The lines are drawn to guide the eye.

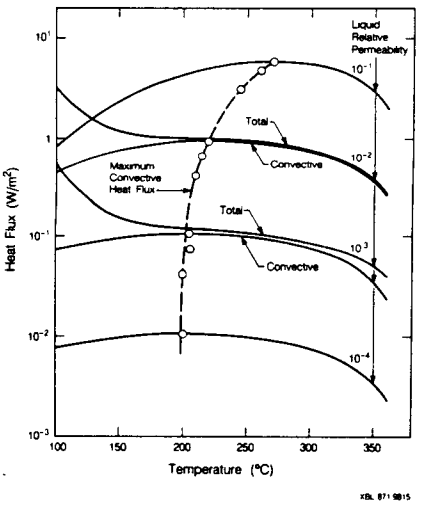


Figure 2. Heat flux for balanced steam-water counterflow in vapor-dominated conditions (permeability 10^{-15}m^2; formation heat conductivity 2.5 W/m·°C).

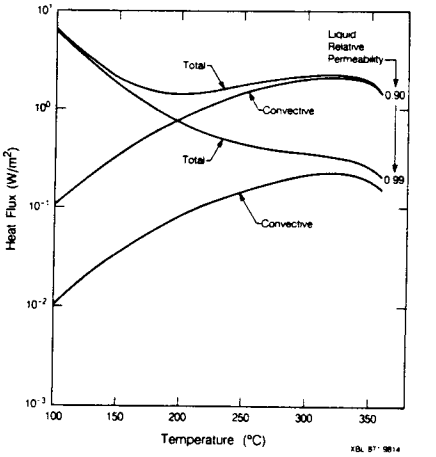


Figure 3. Heat flux for balanced steam-water counterflow in liquid-dominated conditions (permeability 10^{-15}m^2; formation heat conductivity 2.5 W/m·°C).

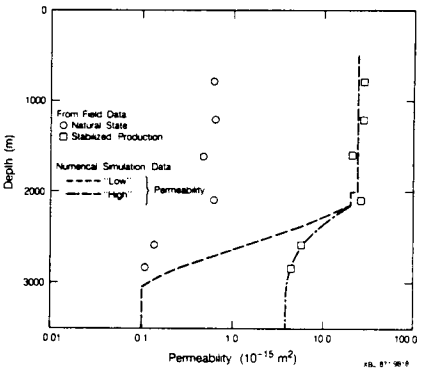


Figure 4. Vertical permeability distributions as derived from temperature data for well A. Permeability values used in numerical simulations are also shown.

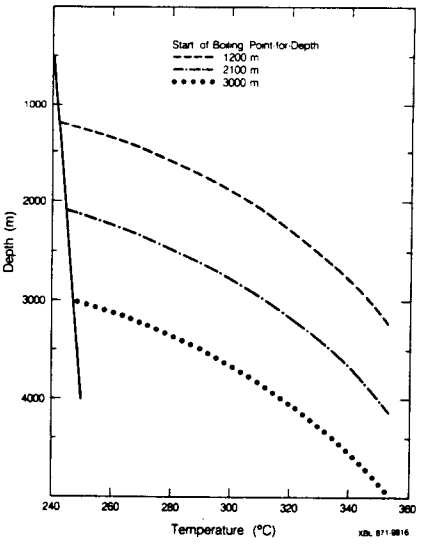
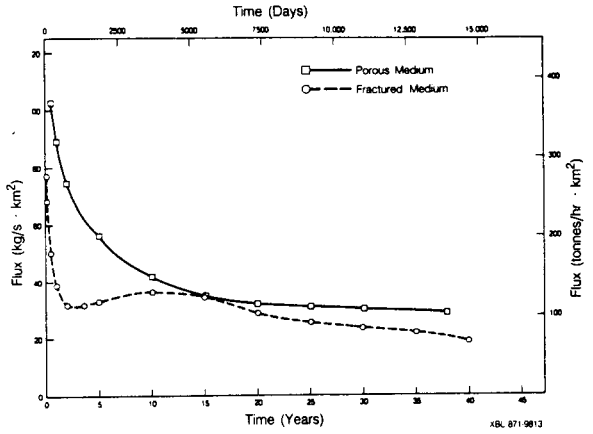
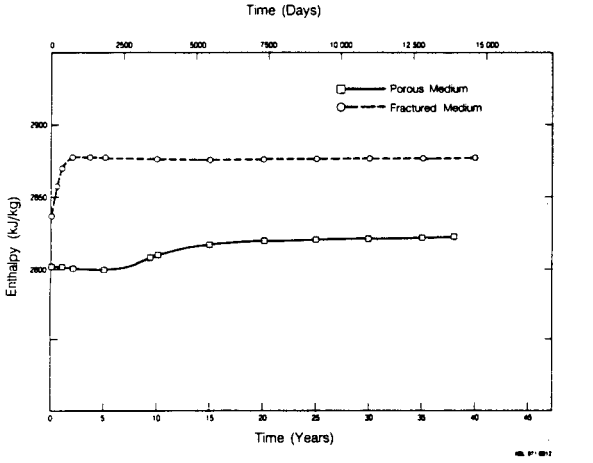


Figure 5. Temperature versus depth for boiling point-for-depth conditions beneath a vapor-static gradient.





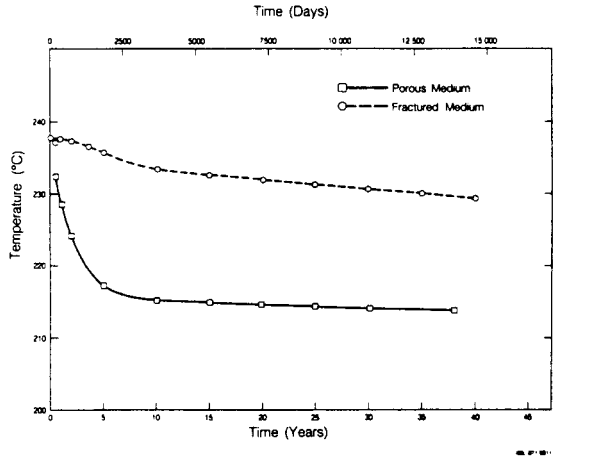
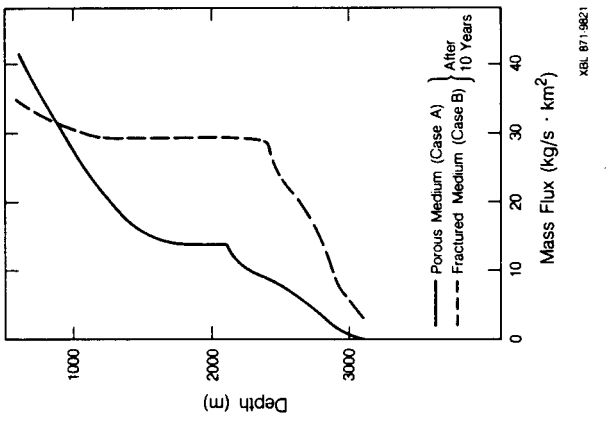
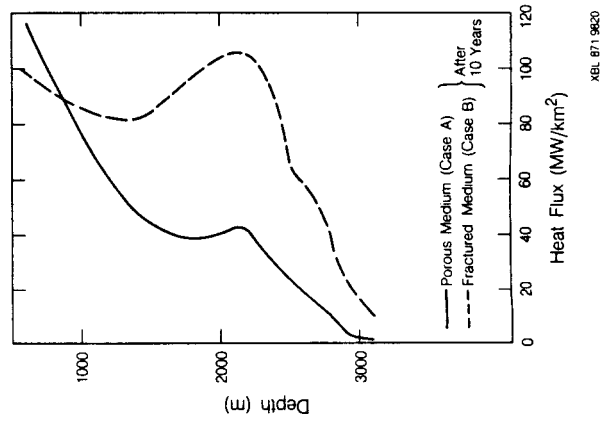


Figure 6. Simulated results for flow rates, enthalpies, and temperatures of produced fluids. Parameters are defined in Tables 1 and 2.





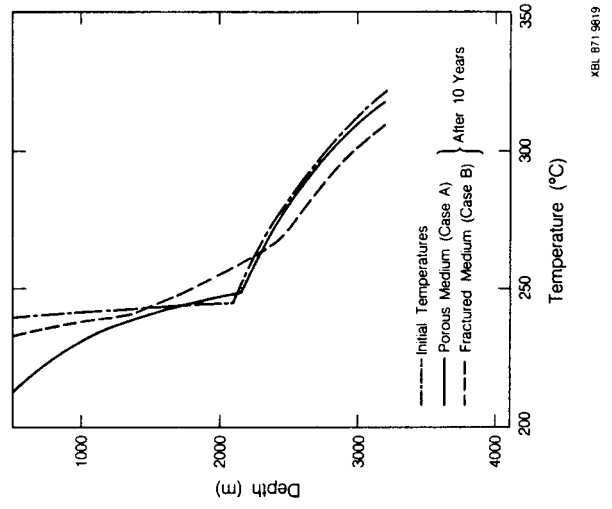


Figure 7. Simulated temperature profiles, and heat and fluid flow rates, after 10 years of production. Parameters are defined in Tables 1 and 2. The initial temperature profile corresponding to a steady state heat pipe with a flux of 1.12 MW/km^2 is also shown.

PROCEEDINGS, Twelfth Workshop on Geothermal Reservoir Engineering
Stanford University, Stanford, California, January 20-22, 1987
SGP-TR-109

HEAT SWEEP ANALYSIS OF THERMAL BREAKTHROUGH AT LOS HUMEROS AND LA PRIMAVERA FIELDS, MEXICO

P. Kruger+, S. Lam+, R. Molinar*, and A. Aragon*

+Stanford Geothermal Program
Stanford University
Stanford, CA

*Geothermal Division
Comision Federal de Electricidad
Morelia, Mich.

ABSTRACT

Early evaluation of the potential for thermal breakthrough of reinjected fluids in newly developed geothermal fields can be obtained with the SGP one-dimensional heat sweep model. The model was used to estimate fluid cooldown from wells selected for the first wellhead generating units to be installed at the Los Humeros and La Primavera geothermal fields in Mexico, based on staff-compiled geometric and geologic data, thermal properties of the reservoir rock, and expected production conditions. Geometric considerations were evaluated with respect to known and postulated fault zones and return flow angle of the reinjected fluid. The results show the range of parameter values that affect the rate of thermal breakthrough to an abandonment temperature of 170 °C corresponding to the minimum inlet pressure to the CFE 5-MW wellhead generator units.

INTRODUCTION

Los Humeros and La Primavera are geothermal fields in Mexico at which the Comision Federal de Electricidad (CFE) has announced installation of first 5-MW wellhead units for 1987-88. In management planning of field operation, one of the early decisions required for these first units is the choice of reinjection wells for the separated brines and condensates. An important aspect of such choices is the thermal behavior of the reinjected fluid from either surface-stored water bodies or directly from the liquid leg of the wellhead separators. The one-dimensional heat sweep model, described by Hunsbedt, Lam, and Kruger (1983), can be used as a tool for early estimate of the potential for thermal breakthrough of recharge fluids to geothermal wells under steady production. An advantage in the use of this simple, one-dimensional model, especially for newly developed geothermal fields, is in the selection of a practical range of values for the parameters of temperature distribution, reservoir flow geometry, formation structure, thermal properties of the formation composition, and planned production conditions. The model allows rapid evaluation of the estimated wellhead fluid temperature decline curve over a wide variety of assumed reservoir and production parameters.

The model is based on the equations for heat transfer from a distribution of fractured rock blocks to the pore fluid in a geothermal reservoir. The basic equations for heat transfer from a distribution of rock blocks described as lumped equivalent radius spheres were given by Kuo et al. (1977) and Hunsbedt et al. (1979). The one-dimensional heat sweep model, improved by Lam (1986), allows for five types of fluid flow geometry and fluid mixing near the production wells; linear and radial flow geometries between single and lines of injection and production wells either by heat sweep alone or by mixing flow with percolation recharge flow from above and/or hot water flow from the reservoir.

The model has been applied to a number of projects in Mexican geothermal fields, for example the Cerro Prieto field in Baja California (Kruger, 1985) and the Los Azufres field in Michoacan (Molinar, et al., 1986). The model has been applied at two new fields, Los Humeros in Puebla and La Primavera in Jalisco. This report describes the initial results of the studies carried out jointly between the Stanford Geothermal Program and the Comision Federal de Electricidad to evaluate the planned reinjection schemes for the first 5-MW wellhead units to be installed at the Los Humeros and La Primavera geothermal fields.

LOS HUMEROS UNIT 1 STUDY

The Los Humeros geothermal field is located in the State of Puebla, 200 km east of Mexico City, along the Mexican volcanic axis described by Alonso (1975). A description of the field and available pre-production data for the wells drilled to date are reported by the Residencia de Perforacion (1986). A map of the geothermal area is given in Figure 1. The structural geometry of the geothermal zone lies along a general NW-SE axis with three principal collapse areas, an outer ring mainfested primarily in the western border, an intermediate ring with characteristic walls noted in the south and east of the field, and a central collapse zone with subsidence walls noted in the north and east. The Los Humeros corridor is aligned primarily NW-SE bounded laterally by the regional tectonic structure.

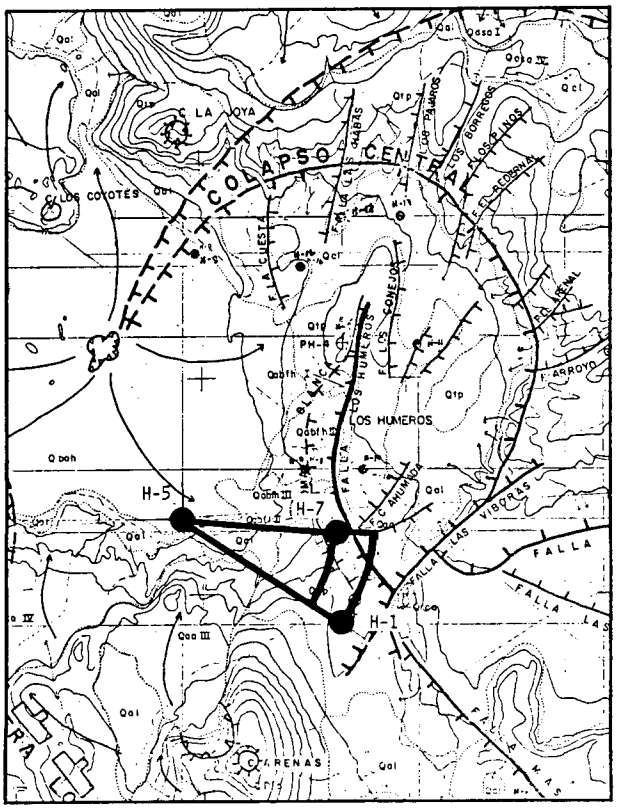


Fig. 1. Radial flow geometry from the proposed reinjection well H-5 to the two production wells H-7 and H-1 for the first 5-MW wellhead unit at Los Humeros.

The thermal manifestations of the field have been evaluated geochemically in five zones by noncondensable gas geothermometry as follows:

1. 290-320 °C
2. 307-324 °C = Zone A
3. 312-330 °C
4. 280-300 °C = Zone B
5. 310-330 °C = Zone C

with zones 2 and 3 being considered the more important areas. Fifteen wells have been drilled in the central collapse zone to delineate the production potential of the field. Data for the wells that have been evaluated are given in Table 1. The last three of these wells are being considered as candidate wells for reinjection recharge.

Planning is underway to initiate exploitation of the field with the installation of three or four 5-MW wellhead flash units of the type presently operating at the Los Azufres geothermal field in Michoacan. The first of these units is being considered for the pair of wells H-1 and H-7 with possible reinjection into well H-5. The heat sweep model was used to evaluate the potential for thermal breakthrough for this system of two production wells each at different flow rates. A

Table 1

PREPRODUCTION DATA FOR 12 LOS HUMEROS WELLS*

Well No	Depth (m)	P_{wh} (MPa)	Q_v** (t/h)	Q_w (t/h)	H (kJ/kg)
H-1	1458	1.5	44	114	1300
H-6	2543	1.5	26	17	1905
H-7	2340	1.5	35	2	2606
H-8	2388	1.5	23	9	2142
H-9	2500	1.5	89	5	2630
H-10	2158	1.14	10+	1	2612
H-11	2388	1.5	31	2.7	2562
H-12	3104	1.5	42	8	2305
H-16	2048	1.5	48	3.6	2606
H-2	2301	—	+	--	--
H-4	1880	—	+	--	--
H-5	1905	—	+	--	--

+ wells contemplated for stimulation or reinjection
** at separator pressure = 0.8 MPa.
* from Residencia de Perforacion (1986).

plan view of these wells is indicated in Figure 1, which shows the geometry for the radial flow heat sweep modeling study.

Figure 2 shows the data accumulated in conjunction with the technical staff at Los Humeros. Two recharge sweep temperatures were selected, 35 °C to reflect the ambient surface water temperature on storage of the separated brine, and 115 °C to reflect the brine temperature on direct reinjection from the wellhead separators. The injection and reservoir fluid flowrates for wells H-7 and H-1 were obtained from Table 1. Well H-7 which is closer to the proposed injection well H-5 would produce only 19 % of the total Unit flow, but 44 % of the steam supply. The fraction of reinjected fluid would be only 2 % of the well flowrate. Well H-1 essentially controls the rate of reinjected fluid return. A value of $-0.005\ y^{-1}$ was selected as the expected cooldown rate, based on experience at two other fields. Since the angle between the two production wells from the injection well is about 21 degrees, heat sweep for the two wells was considered as independent small-angle radial flows ranging from 2.5 degrees (essentially direct return flow) to 20 degrees (dispersed return flow).

The results of the heat sweep runs for recharge sweep flow from well H-5 to well H-7 are shown in Figure 3. The values for the number of heat sweep units parameter were 8.5 for 2.5 degree flow and 17.1 for 5 degree flow, indicating the relatively long residence time of the sweep fluid. The small sweep fluid fraction (5 %) coupled with the small reinjection flowrate results in sufficient heat transfer to sustain the sweep fluid at 280°C while the reservoir fluid temperature declines with the assumed cooldown rate of $-0.005\ y^{-1}$. In this example, reinjection heat sweep prolongs the thermal life of the well.

Figure 4 shows the results of the well pair H-5 to H-1. In this case, the larger sweep

Problem Name: HSP5b Los Humeros Unit 1 (A25)
Date of Analysis (DD-Mmm-YY): 20-Oct-86 (A9)

Reservoir Data for Heat Sweep

T(initial)	280 (°C)	T(recharge)	115 (°C)	2F10.2
Porosity	0.08 (fraction)	Q(injection)	0.6 31.7 (kg/s)	2F10.2
Mean Frac. Spacing	50 (m)	Res. Thickness	665 (m)	2F10.2

Geometry for Linear Sweep

Length	(m)	Width	(m)	2F10.2

Geometry for Radial Sweep

			H7 H1	
Inner Radius	0.0889 (m)	Outer Radius	1250, 1650 (m)	2F10.2
Flow Angle	α (°)			F10.2

Reservoir Data for Fluid Mixing

T(perc)	0 (°C)	Q(perc)	0 (kg/s)	2F10.2
Res. Cooldown Rate	-0.005 (y^{-1})	Q(res)	10.3 12.6 (kg/s)	2F10.2

Thermal Properties

Rock: Density	2700 (kg/m^3)	Spec. Ht. Cap.	1164 (J/kgK)	2F10.2
Fluid: Density	920 (kg/m^3)	Spec. Ht. Cap.	4870 (J/kgK)	2F10.2
Rock Thermal Cond.	1.90 (W/mK)	Heat Xfer Coeff.	1703 (W/m^2K)	2F10.2
Res. Heat Loss	0 (W/m)	BETA	-1.0 d12 (1/sec)	2F10.2

Program Constants

IFLAG	4	ITERM	14	2I5
NTIME	60	KTIME	4	2I5
DELT	1.0			F10.2
NSPACE	100	NUMLOC (1-5)	1	2I5
ISPLOC (I)	100			5I3

Fig. 2. Input data sheet for the two radial flows to wells H-7 and H-1 at Los Humeros.

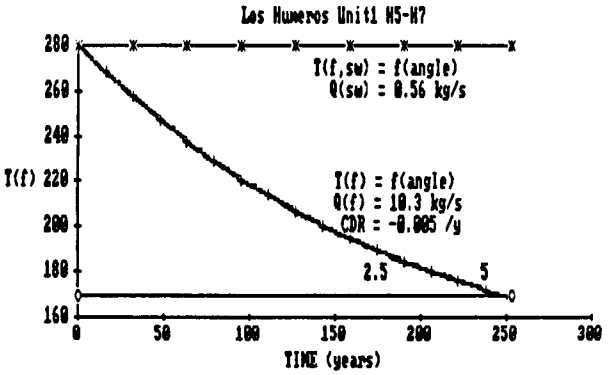


Fig. 3. Heat sweep results for recharge flow from well H-5 to H-7 at Los Humeros. Upper curve is for sweep fluid temperature for all angles; lower curve for mixed fluid temperature with reservoir fluid cooldown rate of -0.005 y^{-1}.

flow fraction and injection flowrate results in a small number of heat sweep units and a more rapid sweep fluid temperature decline, which combined with the 72 % reservoir fluid flow at a cooldown rate of -0.005 y^{-1}, accelerates the production fluid cooldown.

The parameter most useful to assess the results of these model runs is the time to fluid cooldown to the abandonment temperature of 170 °C corresponding to the minimum inlet pressure for the 5-MW wellhead generators.

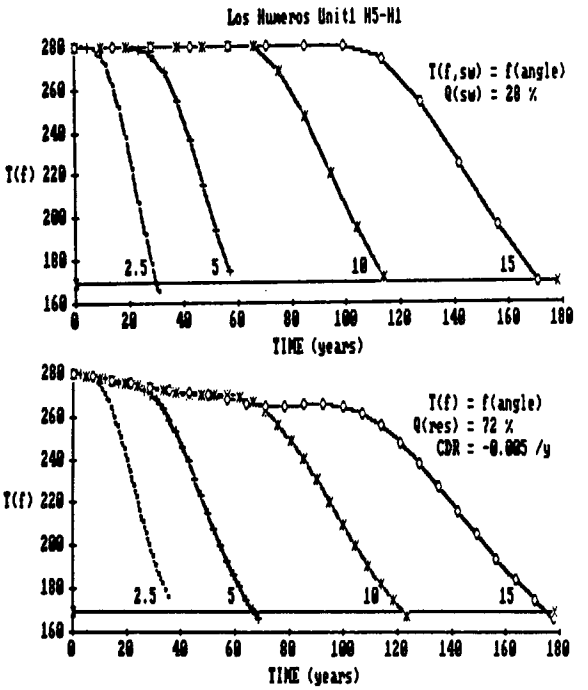


Fig. 4. Heat sweep results for recharge flow from well H-1 to H-7. Upper curves are for sweep fluid temperature as a function of recharge flow angle; lower curves for mixed fluid temperature with reservoir cooldown rate of -0.005 y^{-1}.

The data for the two radial flows are summarized in Table 2, together with an estimate of the combined flow at the Unit based on the respective reinjection flowrates and the individual cooldown curves. The longer sustained temperature at well H-7 seems to add about 7 years to the time to abandonment based on well H-1 alone.

LA PRIMAVERA UNIT 1 STUDY

The La Primavera geothermal field is located in the State of Jalisco, near the city of Guadalajara. A description of the field and its geologic setting is given in the report of the first survey prepared by JICA (1986). A map of the area, showing the boundaries of the collapse zones and the location of existing production wells is given in Figure 5. From prior surveys, the general structure of the field is described as a set of fractures to a depth of about 1000 m along a NE-SW direction, with high-angle fractures below 1000 m in a NW-SE direction. To date, wells of 600 - 3000 m depth have been drilled and from the geologic studies, the zone of thermal upflow has been reasonably well identified. The earliest studied wells include PR-1, PR-5, PR-8, and PR-9. Available data for 5 la Primavera wells are given in Table 3, and a section through them with stabilized bottom-hole temperature contours is shown in Figure 6.

Table 2

LOS HUMEROS UNIT 1 THERMAL COOLDOWN TIMES

Injection Flow Dispersion Angle (degrees)	Time to T(f) = 170 °C Well H-7 (yrs)	Well H-1 (yrs)	Combined (yrs)
2.5	243	37	44
5	243	67	74
10	--	121	--
15	--	174	--

Table 3

PREPRODUCTION DATA FOR 5 LA PRIMAVERA WELLS*

Well No	Depth (m)	T(bh) (C)	T(Na-K-Ca)[a] (C)	T(SiO_2)[b] (C)	[Cl^-] (mg/l)	[NCG] (%)
PR-1	1820	260	297	295	1160	2.2
PR-2	1995	240	223	237	1120	0.21
PR-5	1213	220	250	242	780	--
PR-8	1860	292	295	280	929	3.5
PR-9	2986	250	290	293	870	0.2

[a]from Fournier and Truesdell (1973)
[b]from Fournier and Potter (1982)
*from JICA (1986)

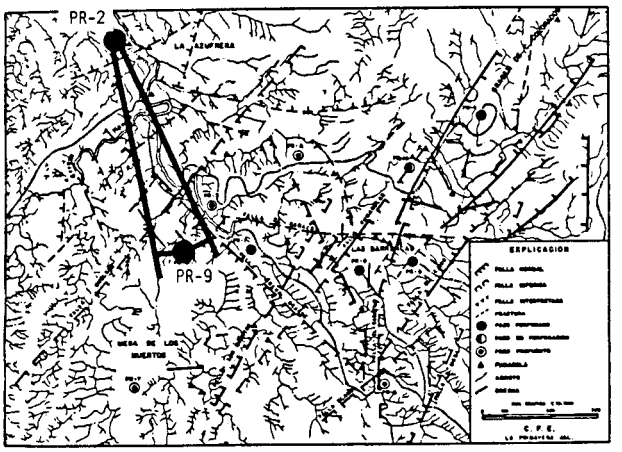


Fig. 5. Radial flow geometry from proposed reinjection well PR-2 to production well PR-9 for the first 5-MW wellhead unit at La Primavera.

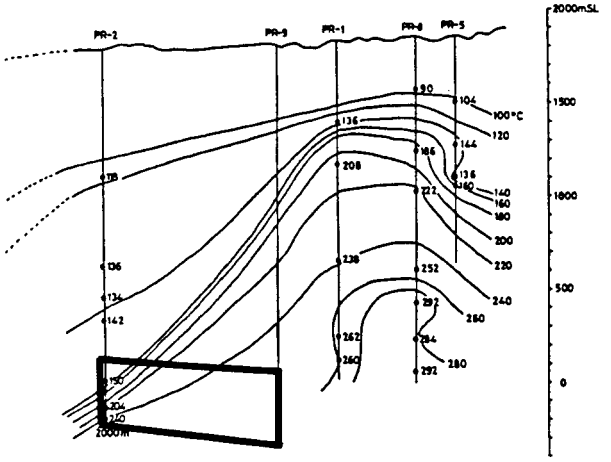


Fig. 6. Reservoir temperature distribution across the expected flow sweep zone from injection well PR-2 to production well PR-9.

The temperature contours suggest that the major thermal upflow zone is between wells PR-1 and PR-8. The development plan for La Primavera visualizes well PR-9 for the first 5-MW wellhead unit with well PR-2 possibly as an injection well for reinjection of the brine from the separator. Compililation of the data for recharge thermal breakthrough estimates were achieved with the technical staff at the field. The data set is shown in Figure 7. The initial reservoir temperature was estimated as the mean temperature from the contours in Figure 6. Recharge temperature was taken as 70 °C for surface-stored brine and 143 °C for direct reinjected brine from the wellhead separators. The flow rates are from production testing, and the reservoir flow, at an assumed cooldown rate of $-0.005\ y^{-1}$, was assumed equal to the steam flow through the turbine.

Problem Name: HSP6b La Primavera PR2-PR9 A25
Date of Analysis (DD-Mmm-YY): 24-Oct-86 A9

Reservoir Data for Heat Sweep
T(initial): 280 (°C) T(recharge): 70, 143 (°C) 2F10.2
Porosity: 0.10 (fraction) Q(injection): 26.1 (kg/s) 2F10.2
Mean Frac. Spacing: 90 (m) Res. Thickness: 428 (m) 2F10.2

Geometry for Linear Sweep
Length: (m) Width: (m) 2F10.2

Geometry for Radial Sweep
Inner Radius: 0.0889 (m) Outer Radius: 965 (m) 2F10.2
Flow Angle: 2.5, 5, 10, 20 (°) F10.2

Reservoir Data for Fluid Mixing
T(perc): 0 (°C) Q(perc): 0 (kg/s) 2F10.2
Res. Cooldown Rate: -0.005 (y^{-1}) Q(res): 20.7 (kg/s) 2F10.2

Thermal Properties
Rock: Density: 2450 (kg/m^3) Spec. Ht. Cap.: 1164 (J/kgK) 2F10.2
Fluid: Density: 920 (kg/m^3) Spec. Ht. Cap.: 4870 (J/kgK) 2F10.2
Rock Thermal Cond.: 1.786 (W/mK) Heat Xfer Coeff.: 1703 (W/m^2K) 2F10.2
Res. Heat Loss: 0 (W/m) BETA: -1.0 d12 (1/sec) 2F10.2

Program Constants
IFLAG: 4 ITERM: 14 2I5
WTIME: 60 KTIME: 4 2I5
DELT: 1.0 F10.2
NSPACE: 100 NUMLOC (1-5): 1 2I5
ISPLOC (I): 100 5I3

Fig. 7. Input data sheet for the radial flow at recharge temperatures of 70 °C for surface stored brines and 140 °C for direct brine reinjection from the separator.

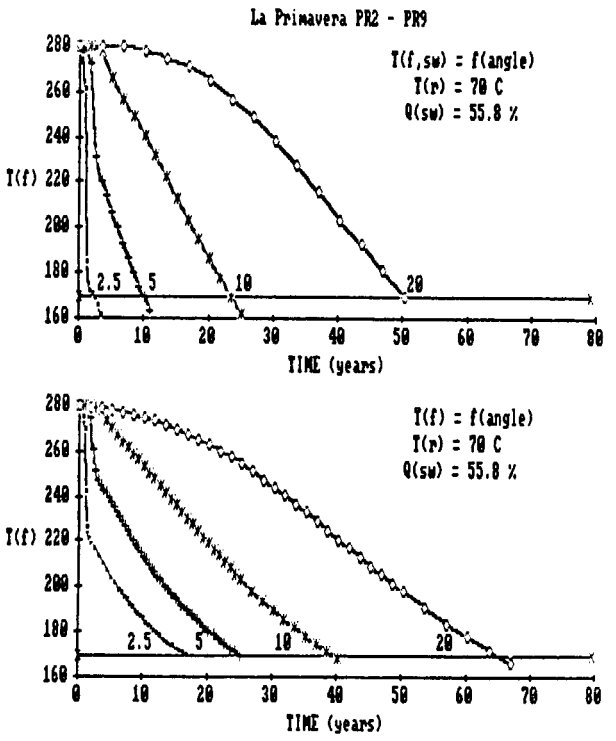


Fig. 8. Heat sweep results for recharge brine temperature of 70 °C. Upper curves are for sweep temperature cooldown as a function of return flow angle; lower curves mixed fluid temperature with reservoir cooldown rate of $-0.005\ y^{-1}$.

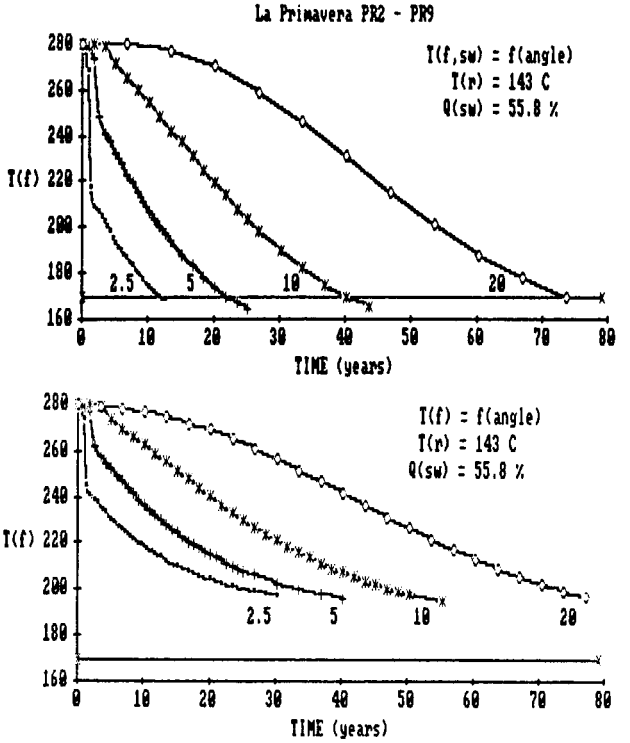


Fig. 9. Heat sweep results for recharge brine temperature of 143 °C. Upper curves are for sweep temperature cooldown as a function of return flow angle; lower curves mixed fluid temperature with reservoir cooldown rate of $-0.005\ y^{-1}$.

With no apparent geologic boundaries for containing the recharge flow, the estimates were obtained for radial flow with angles from 2.5 deg (essentially direct fracture flow) to 20 deg (more dispersed flow). The results for the reinjection temperature of 70 °C are shown in Figure 8 and of 143 °C in Figure 9. The upper part of each figure shows the temperature decline curve as it reaches the production interval and the lower part shows the mixed fluid temperatures in the well. The equilibrium mixed fluid temperature, without cooldown of the resource fluid, would be 163 °C for the 70 °C recharge sweep and 203 °C for the 143 °C recharge sweep. Figures 8 and 9 show the approach to cooldown with the assumed cooldown rate of $-0.005\ y^{-1}$. A summary of the cooldown times under this set of assumptions is given in Table 4.

Table 4

LA PRIMAVERA UNIT 1 THERMAL COOLDOWN TIMES

Injection Flow Dispersion Angle (degrees)	Time to T(f) = 170 °C T(r) = 70 °C Q(sw) (yrs)	Q(f) (yrs)	T(r) = 143 °C Q(sw) (yrs)	Q(f) (yrs)
2.5	2.3	16	12	160
5	10	25	22	160
10	23	40	40	160
20	50	65	73	160

ACKNOWLEDGMENT

The authors acknowledge the cooperation of Luis Templos of the CFE Los Humeros staff and Jose Perezyera of the CFE La Primavera staff for providing the production and chemistry data used in this paper. The Stanford Geothermal Program part was supported by the U.S. Department of Energy under Contract No. DE-AC03-86SF16482.

REFERENCES

Alonso, H. "Potencial Geotérmico de la República Mexicana, Proceedings, Second United Nations Symposium on the Development and Use of Geothermal Resources, 1, 17-20, (USGPO, 75-32682, Vol 1., pp 17-20, 1985).

Fournier, R. O. and R. W. Potter, A Revised and Expanded Silica (Quartz) Geothermometer, Bulletin GRC 11, 3-12 (November, 1982).

Fournier, R. O. and A. H. Truesdell, An Empirical Na-K-Ca Geothermometer for Natural Waters, Geochim. et Cosmochim. Acta 37, 1255-1275 (1973).

Hunsbedt, A., R. Iregui, P. Kruger, A. L. London, "Energy Recovery from Fracture-Simulated Geothermal Reservoirs," Proceedings, ASME/AIChE 18th National Heat Transfer Conference, Paper 79-HT-92, 1979.

Hunsbedt, A., S. Lam, and P. Kruger, User's Manual for the 1-D Linear Heat Sweep Model, Stanford Geothermal Program Technical Report No. 75, 1983.

Japan International Cooperation Agency, "La Primavera Geothermal Development Project in United Mexican States," Draft Report, July, 1986.

Kruger, P. "Application of the SGP 1-D Linear Heat Sweep Model," Proceedings, 7th New Zealand Geothermal Workshop, (1985).

Kuo, M. C. T., P. Kruger, W. E. Brigham, "Shape-Factor Correlations for Transient Heat Conduction from Irregular-Shaped Rock Fragments to Surrounding Fluid," Proceedings, AIChE/ASME Heat Transfer Conference, Paper 77-HT-54, 1977.

Lam, S. T., "Heat Extraction Modeling of Single-Phase Sweep Flow in Fractured Geothermal Reservoirs," Ph.D. Thesis, Stanford University, 1986.

Molinar, R., A. Aragon, P. Kruger, S. Lam, "One-Dimensional Heat Sweep and Fluid Mixing at the Los Azufres Geothermal Field," Proceedings, 8th New Zealand Geothermal Workshop, (1986).

Residencia de Perforacion Los Humeros, Resultados de la Exploracion en El Campo Geotermico de Los Humeros, Puebla, Internal Report, October, 1986.

PROCEEDINGS, Twelfth Workshop on Geothermal Reservoir Engineering
Stanford University, Stanford, California, January 20-22, 1987
SGP-TR-109

Pressure Depletion Calculations for Liquid Geothermal Reservoirs

R.C. Schroeder

Berkeley Group Incorporated
1330 Broadway, Suite 1450
Oakland, CA 94612

ABSTRACT

One of the key problems in geothermal field management is to determine how many wells will be needed, and when in the project lifetime the new wells will come on-line. To make this determination requires an estimate of the field depletion.

Methods used for approximating the field behavior are discussed, and examples are provided using data from some liquid-dominated reservoirs in the U.S. and abroad. The calculated decline curves are compared to a few cases for which field production data is available.

INTRODUCTION

This paper considers the depletion of a single phase, liquid geothermal reservoir producing from wells in two-phase flow. While there are other cases of interest (two-phase reservoir, vapor-dominated reservoir, downhole pumps, etc), we will limit our comments to the case described above.

An estimate of reservoir depletion (decreasing production) is important to geothermal developers, lenders, and field engineers. Depletion estimates provide the necessary data to determine how many wells must be drilled; when the wells will be needed to support production; and (in some cases) where the most desirable well locations are in the field. Drilling schedules and well locations (because of cost and lease-related factors) are the most important field-management decisions to be made for a geothermal project, because the drilling is usually the most costly field item. Occasionally gathering systems are comparable in cost, but for most projects drilling costs are paramount. For that reason, it is of great importance - financially as well as technically - to minimize the initial number of production and injection wells, and to maximize the time until new (makeup) wells must be drilled. This strategy maximizes the return on investment by "pushing" the well costs out into a higher discounted time frame.

Reservoir depletion estimates, and an estimated or updated drilling schedule, are needed both prior to power plant startup and after production is underway. The pre-production estimates are crucial to both developers and lenders in making financial appraisals of a project. Continued estimates are required after the power plant has been in operation to both verify the pre-production estimates and to take into account changes that have occurred. For example, the actual location and production of newly drilled wells can vary substantially from estimates made before drilling.

In the remainder of this paper the methodology, data, and calculational tools are explained; and examples are given of field depletion for a case prior to power plant startup; and for a case of a field that has been in production for about 7 years. In both cases the data is still proprietary, and some of the quantitative information can not be provided at this time. The field locations and well names must also remain anonymous.

METHODOLOGY

We are concerned here only with the case of a liquid reservoir producing from two-phase wellbores. Some of the methods and calculations can be simplified or altered for application to other possible cases.

The general approach is to use a wellfield pressure simulator to estimate reservoir/wellbore conditions, and a two-phase wellbore

simulator to estimate wellhead conditions. The power plant design criteria impose constraints on the wellhead conditions (the required power plant inlet pressure and enthalpy usually have a relatively narrow design range for maximum power plant efficiency), but the reservoir also imposes constraints on the wellhead conditions (well productivity and reservoir enthalpy can vary substantially over the field), and interference and depletion results in reservoir pressures that decrease with time. In the examples given below the calculations are done for reservoir enthalpy that does not vary from well to well; however, the variation in field enthalpy must be taken into account when the data is available. This can be done by using well test data and exploratory temperature profiles if they are available. The variation in enthalpy is most important for the calculation of the wellhead conditions from downhole values, since the wellbore simulator is most sensitive to variations in enthalpy.

The primary emphasis in this report is on the pressure depletion (and associated production decline) when the field feeds a power plant at (approximately) constant pressure. The constant pressure constraint results in well production declines, and for the case of two-phase wellbore flow, the wellhead conditions are not a linear function of the reservoir drawdown (pressure depletion). Therefore, a combination of reservoir and wellbore simulation is needed to accurately estimate the field decline during production and to accurately estimate the corresponding drilling demands to meet the minimum power plant requirements. For reservoirs that remain single phase, and have relatively small amounts of dissolved gases, the downhole wellbore enthalpy is often approximately constant over time periods of a few years. This allows the initial declines to be calculated with a minimum of effort and cost through the use of pressure simulators using linear superposition of analytical solutions. Long term field declines require the use of more detailed hydrothermal simulation using discrete simulators that calculate both pressure and enthalpy changes, and take into account the change in reservoir (wellbore) enthalpy with time. The methodology is summarized in Table 1, below.

Table 1. Summary of Methodology

- Use measured well test data and downhole productivity curve to calibrate a wellfield pressure simulator.
- Use measured downhole and wellhead productivity curves and flowing wellbore profiles to calibrate two-phase wellbore simulator.
- Use measured reservoir enthalpy and calculated reservoir pressure from wellfield simulator to calculate wellhead conditions.
- Through parametric study determine when the wellfield pressure will decline below the required minimum for power plant needs.
- Add a well (or wells), lower the flowrates in the new wellfield and continue the calculation.

THE SIMULATORS

The calculations shown below have been done using commercially available wellfield and wellbore simulators (ref 1). The programs run on an IBM PC microcomputer and provide cost effective tools for reservoir engineers involved in well testing and field simulation.

The pressure simulator - MRMW Version 3.0 - uses linear superposition to calculate the wellfield pressure (ref 2). Several model options are available, and the program also has options to allow type-curve matching of production or injection well test data, can be used for interference test analysis, and can generate dimensionless type curves.

The wellbore simulator - WELF Version 3.0 - is a steady state, two-phase simulator that includes options for variable wellbore diameters, heat losses, and large fluid TDS (ref 3).

Both simulators return the calculated values within seconds, and allow numerous numerical studies to be done quickly and easily.

DATA

Two examples are included and are summarized in Table 2, below.

Table 2. Examples used in calculations

Case 1 - US field not yet in production

A) Injection outside the field
B) Power plant requirement = 2.5×10^6 #/hr
C) Minimum wellhead pressure = 200 psi
D) Maximum flashpoint (bubble point) depth is above production string
E) 8 production wells and 3 injection wells at plant startup

Case 2 - Overseas field with seven years of Production

A) Injection inside the field
B) Power plant requirement = 3200 Tonnes/hr (7×10^6 #/hr)
C) Currently 13 production wells and 16 injection wells

The first case to be considered is a wellfield that was in the planning stage when these calculations were made. The initial wellfield pattern, including eight production wells and three injection wells, is shown in Figure 1. The proposed injection is defined to be outside the producing field, and is constrained by current lease positions. The power plant requires 2.5×10^6 lb/hr of fluid at the minimum reservoir enthalpy. Production and interference well test data were used to estimate the average reservoir parameters using the pressure simulator described above. The wellhead and downhole production curves are shown in Figure 2. As seen in Figure 2, the reservoir pressure is non-linear with respect to flowrate. Ideal Darcy flow produces a sandface productivity curve that is a straight line. However, many geothermal wells - particularly those producing with two-phase wellbore flow - have non-Darcy downhole productivity curves. This type of non-linearity requires care in applying well test analysis results to pressure depletion applications. Typically the reservoir and wellbore parameters are obtained from production tests where the well is flowed at nearly its maximum rate.

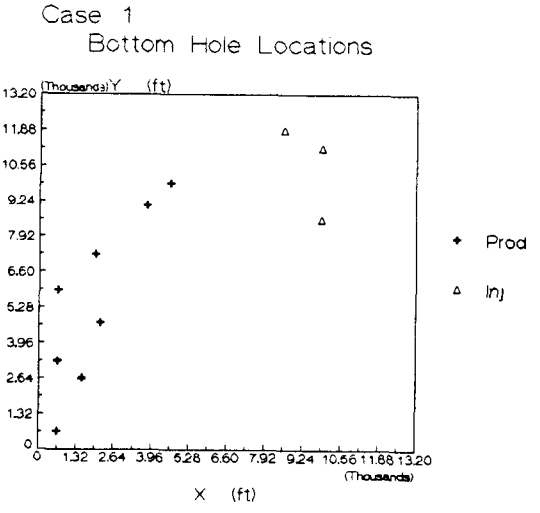


Figure 1. The initial wellfield showing bottomhole locations of the production and injection wells.

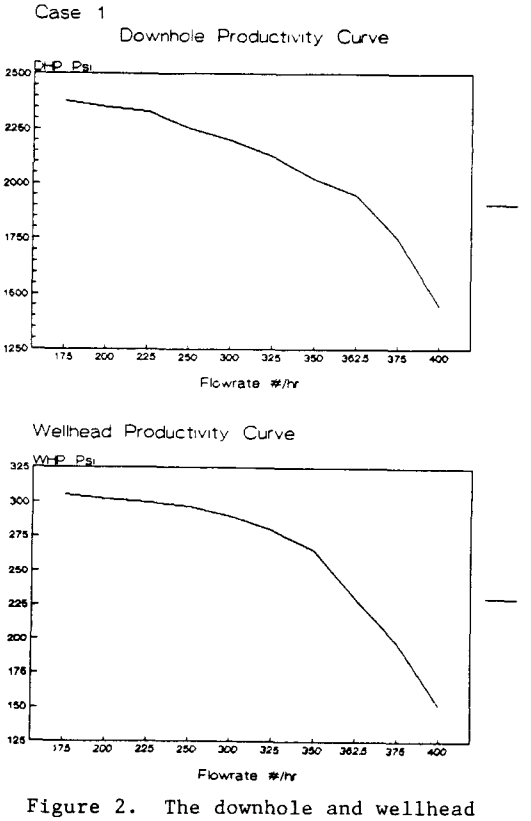


Figure 2. The downhole and wellhead productivity curves for Case 1.

As shown in Figure 3, the non-Darcy effects are a maximum at high flowrates. Typically, if a test is conducted at a single flowrate, the non-Darcy effect is interpreted as a large skin effect. The apparent skin factor can be written as

$$S_a = S_d + S_{pp} + Dq^{n-1} \qquad (1)$$

where

Sa is the apparent skin effect from well test data

Sd is the true skin due to sandface damage

Spp is a pseudoskin due to a partially penetrating well

Dq^{n-1} is the non-Darcy flow effect expressed as an exponential term (D is an empirically determined constant and q is the total mass flowrate).

Usually non-Darcy flow is approximated by an equation based on the modifications to Darcy's law shown in equation (2).

$$q + Dq^2 = K \frac{dp}{dx} \qquad (2)$$

For many geothermal wells the non-Darcy exponent in Equation (1) that is required to match the productivity data from well test measurements is between 1 and 5.

The importance of the non-Darcy effect in pressure depletion calculations is apparent from Figure 3. If a well test is analyzed with data for one flowrate and a large apparent skin factor is obtained, then when that large (constant) skin is used in the pressure depletion calculations, the late time depletion (at lower flowrates) will be vastly over-estimated, since the apparent skin factor should decrease as the flowrates in the field decline. The pressure simulator referred to in Reference 1 includes the effects of non-Darcy flow.

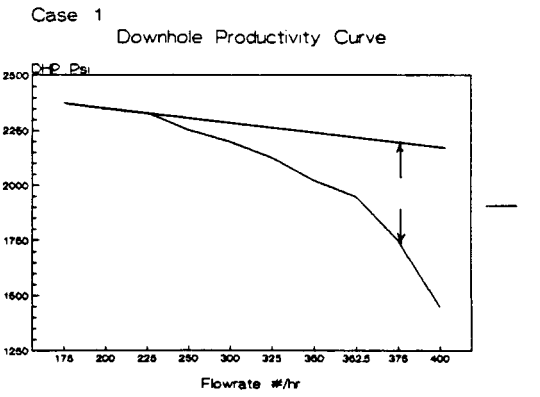


Figure 3. Demonstration of non-Darcy flow component at high flowrate.

For Case 1 the power plant inlet design pressure requires that the wellhead pressures downstream of a wellhead choke remain greater than 200 psia. Figure 4 shows 3 wellbore profiles from flowing, downhole, pressure measurements. Downhole, flowing pressure and temperature measurements are essential for complete and accurate interpretation of two-phase well test data. The casing shoe limits the depth that the flash point can be allowed to reach while maintaining a single-phase liquid reservoir. For the Case 1 wellfield it is critical that the reservoir remains single-phase in order to maintain an approximately constant wellhead enthalpy, and to maintain the single-phase productivity.

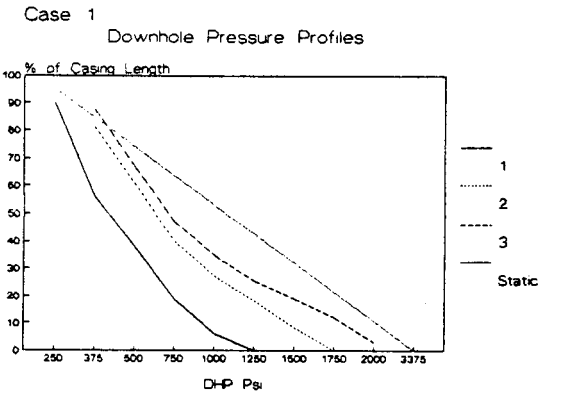


Figure 4. The downhole pressure profiles for the static well and for three different flowrates.

The second case to be considered is a wellfield that has been producing power at a constant rate for about 7 years. The wellfield (reservoir) pressure is shown in Figure 5. There are currently 13 production wells and 16 injection wells in use. The injection wells are inside the wellfield. The power plant requires about 3200 Tonnes/hr (7 x 10^6 lbs/hr).

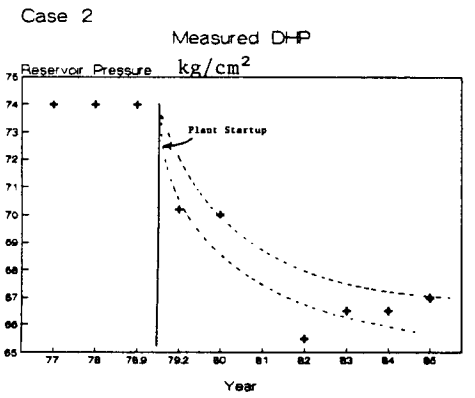


Figure 5. Downhole pressures as a function of time for Case 2.

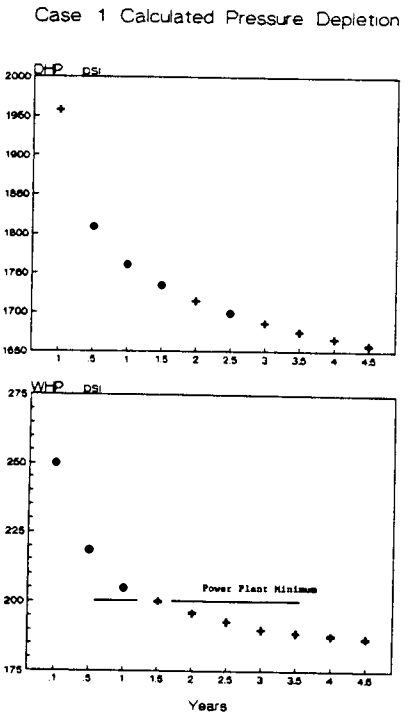


Figure 6. Calculated pressure at an average well when the wellfield delivers to the powerplant.

CALCULATIONS

The productivity curves and wellbore profiles for Case 1 shown above were obtained from well tests during which a single production/injection well-pair was flowing. When the wellfield is brought on-line for power production the interference effects between wells result in substantially larger drawdowns than measured from individual (doublet) tests. For Case 1 where the field had not yet been drilled, a test with all wells flowing was not possible. The only way to estimate the drawdowns and adequacy of the planned wellfield is through simulation.

Figure 6 shows the calculated average wellfield production decline for the Case 1 (the initial wellfield pattern is shown in Figure 1). The depletion (decline) curve in Figure 6 shows the typical steep startup decline that is characteristic of liquid reservoirs. This startup decline was also shown in the data for Case 1. The calculation for Case 1 was stopped at about 5 years, since the data and methodology do not warrant further predictions.

The power plant requirement of 2.5 x 10^6 #/hr sets the average initial well flowrate, and shows that eight wells constitute a 25% excess capacity at plant startup. The calculation also shows that a make up well would be needed within 1/1-2 years from startup for this case. Although additional calculations are not shown in Figure 6, it is clear that when production and injection makeup wells are added at 1-1/2 years, the average well flow is reduced about 11% with a corresponding increase in wellhead pressure. The depletion calculations can then be continued from that point with the new wellfield pattern and flowrates as input to the calculation.

Several wells have been added since startup in our second example, Case 2, over the past 7 years. The field decline and schedule of drilling have been used to obtain the average reservoir parameters for the field, and are currently being used to study certain key reservoir management problems.

SUMMARY

The need and uses for depletion analysis of liquid geothermal reservoirs was outlined. The importance of the drilling schedule on economic appraisals of a project were reviewed. The types of data, and subsequent methodology that can be used to make pressure depletion calculations, was described. Commercially available microcomputer simulators make the parameter studies fast and cheap. Data was shown for a field that has produced for several years to provide a measured example of reservoir pressure decline in a liquid reservoir producing from two-phase wellbores.

REFERENCES

1. User Manuals for MRMW and WELF describe the simulators, BG Software, Oakland CA.

2. R.C. Erlougher Jr. SPE Monograph "Advances in Well Testing", 1977.

3. Basic descriptions of some wellbore models are given in the following list:

M. Natenson, Jour. Research U.S. Geol. Survey, Vol 2 No 6, 1974;

P. Atkinson, H. Ramey Jr, SPE Paper 6792, 1977

C. Miller, LBL report #10910, 1980.

PROCEEDINGS, Twelfth Workshop on Geothermal Reservoir Engineering
Stanford University, Stanford, California, January 20-22, 1987
SGP-TR-109

LINEAR WATER INFLUX OF AN INFINITE AQUIFER THROUGH A PARTIALLY COMMUNICATING FAULT

Anil K. Ambastha and Abraham Sageev

Stanford University

Stanford, CA 94305

ABSTRACT

This paper presents a linear flow water influx analysis method where the aquifer is separated from the reservoir by a partially communicating fault. Transient pressure distributions are considered both in the reservoir and in the aquifer. Cases where the leaky fault is located within the aquifer can be analyzed with this model given a superposition of constant rate flow periods at the oil-water interface. Constant production rate is specified at the inner boundary, without inner boundary storage and skin. The partially communicating fault is modeled as a boundary skin of infinitesimal thickness having no storage. The aquifer considered in this paper is infinite in the lateral extent. The problem is posed and solved using the Laplace transformation, yielding Laplace solutions of the exponential form.

The solutions presented in this paper, along with a set of type curves extend the transient linear flow work presented by *Hurst* (1958) and by *Nabor and Barham* (1964). When the inner region, the reservoir, has an infinite permeability and a finite storage, it acts like a tank, where the boundary pressure is equal to average pressure in the inner region. This case is identical to the linear water influx model presented by *Hurst* (1958). When the inner region has no storage associated with it, the constant inner boundary rate is transmitted to the second infinite region, hence yielding the simple linear flow case presented by *Nabor and Barham* (1964).

This paper extends the current solutions by allowing pressure variations in the reservoir or the inner region as well as in the infinite aquifer. Also, the model presented in this paper considers the effects of skin located at the boundary between the two regions of the system that may be caused by a partially communicating fault separating these two regions.

INTRODUCTION

Techniques for reservoir performance calculations for linear and radial water-drive systems have been developed in a series of papers by *van Everdingen and Hurst* (1949), *Hurst* (1958) and *van Everdingen* et al. (1953). In such reservoir performance calculations, one of the following two conditions may be encountered:

1. Given a reservoir pressure history, we determine cumulative water encroachment for the reservoir-aquifer system.
2. Given reservoir rate history, we determine the pressure decline behavior for the reservoir-aquifer system.

Performing these analyses requires the knowledge of transient pressure or influx behavior of the assumed configuration of reservoir-aquifer system. In addition, the key assumption is that the average reservoir pressure is equal to the pressure at the interface between the two differing regions.

The behavior of linear homogeneous aquifers has been examined in the literature. *Hurst* (1958) considered linear water influx into a hydrocarbon reservoir. In his model, the material balance equations for the reservoir are coupled to the transient linear flow diffusivity equation for the aquifer. Hence, pressure transients in the reservoir are not accounted for, and the main parameter controlling the water influx function is the compressibility ratio between the two parts of the system. *Miller* (1962) studied the behavior of closed outer boundary and infinite aquifers. In his analysis, separate curves were needed for each aquifer size. *Nabor* and *Barham* (1964) extended *Miller's* (1962) equations and presented a single working log-log type curve, that is applicable to any aquifer size. They also included the case of constant pressure outer boundary. Non-homogeneous aquifer responses were generated by *Mueller* (1962) using finite-difference techniques. *Mueller* (1962) considered linear variations of thickness, permeability or porosity-compressibility product with distance. Recently, *Ambastha and Ramey* (1987) obtained a suite of analytical response functions for non-homogeneous aquifers. Their results compared well with Mueller's (1962) results. *Bowman and Crawford* (1962) presented a method for calculating transient pressure distribution in linear semi-infinite water-drive reservoirs having different rock and fluid properties in each zone.

A true composite system has two distinct regions, with different properties in each region, as shown in Figure 1. In such a composite system, pressure transients are allowed to develop in both regions. When the inner region has infinite transmissivity and a finite storativity, it acts like a tank, where the boundary pressure is equal to average pressure in the inner region. This case is identical to the linear water influx model presented by *Hurst* (1958). If the inner region has no storativity associated with it, the constant inner boundary rate is transmitted to the second infinite region, hence, yielding the simple linear flow case presented by *Nabor* and *Barham* (1964). Alternatively, a composite system with the same transmissivity and storativity in both regions is identical to the linear semi-infinite homogeneous aquifer model discussed by *Miller* (1962), and *Nabor* and *Barham* (1964). Thus, we can view regions I and II as reservoir and aquifer portions respectively, as an analogy to *Hurst* (1958) model, or consider both regions as an aquifer system extending across a boundary, as an analogy to *Miller* (1962), and *Nabor* and *Barham* (1964) models.

The above discussion implicitly assumes that the boundary separating the two regions of composite system is

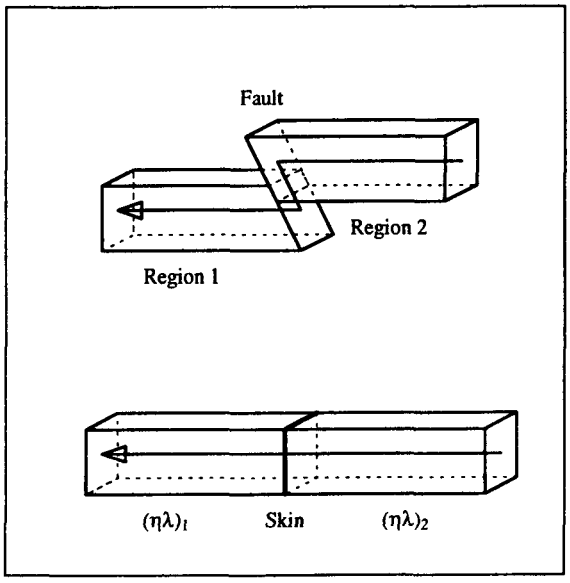


Figure 1: Schematic representation of a composite system.

fully communicating. However, since these boundaries may be created due to geological factors, such as faulting, facies changes or pinchouts, it is possible that these boundaries will resist the flow across them, and be partially communicating. We model this resistance using the "thin skin" concept similar to that proposed by *Hurst* (1953), *van Everdingen* (1953), and *Carslaw* and *Jaeger* (1959). We term it "boundary skin" to distinguish it from "wellbore skin" in the usual sense. In this study we present an analytical solution to the transient flow problem in a linear semi-infinite composite system with property contrasts and boundary skin. Constant rate is specified at the inner boundary. Though the problem is solved with property contrasts in the two regions, we mainly present the results for homogeneous systems with boundary skin. The relationship of the general model to *Hurst* (1958), and *Nabor* and *Barham* (1964) models is presented. Late and early time behavior for special cases are developed. A type curve is presented for homogeneous systems with boundary skin. Finally, a modification of Example No. 2 of *Nabor* and *Barham* (1964) has been solved under different model conditions to demonstrate the effects of boundary skin.

MATHEMATICAL CONSIDERATIONS

The geometrical configuration considered is presented in Figure 2. The dimensionless diffusivity equations describing the pressure response of a semi-infinite composite horizontal linear system are:

$$\frac{\partial^2 p_{D1}}{\partial x_D^2} = \frac{\partial p_{D1}}{\partial t_D} \qquad \text{for} \quad 0 \le x_D \le A \tag{1}$$

$$\frac{\partial^2 p_{D2}}{\partial x_D^2} = \frac{1}{\eta}\frac{\partial p_{D2}}{\partial t_D} \qquad \text{for} \quad A \le x_D \le \infty \tag{2}$$

where the dimensionless variables are defined as:

$$p_{D1} = \frac{k_1 bh\,[p_i - p_1(x,t)]}{q\mu_1\ 1} \tag{3}$$

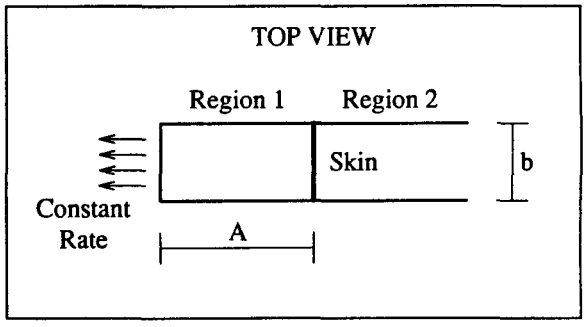


Figure 2: Simplified linear composite system.

$$p_{D2} = \frac{k_1 bh\,[p_i - p_2(x,t)]}{q\mu_1\ 1} \tag{4}$$

$$x_D = \frac{x}{1} \tag{5}$$

$$t_D = \frac{k_1 t}{(\phi\mu c_t)_1\ 1^2} \tag{6}$$

$$\eta = \frac{\eta_2}{\eta_1} = \frac{\left[\dfrac{k}{\phi\mu c_t}\right]_2}{\left[\dfrac{k}{\phi\mu c_t}\right]_1} \tag{7}$$

The characteristic length of unity is used in the definitions of dimensionless distance, pressure and time. The associated initial and outer boundary conditions are:

$$p_{D1}(x_D,0) = 0 \tag{8}$$

$$p_{D2}(x_D,0) = 0 \tag{9}$$

$$p_{D2}(\infty,t_D) = 0 \tag{10}$$

The inner boundary condition is:

$$\left.\frac{\partial p_{D1}}{\partial x_D}\right]_{x_D=0} = -1 \tag{11}$$

The conditions at the skin boundary are:

$$\frac{\partial p_{D1}}{\partial x_D} = \frac{-1}{S}(p_{D1} - p_{D2}) \qquad at\ \ x_D = A \tag{12}$$

$$\frac{\partial p_{D1}}{\partial x_D} = M\frac{\partial p_{D2}}{\partial x_D} \qquad at\ \ x_D = A \tag{13}$$

where S, the boundary skin, is defined by:

$$S = \frac{k_1 bh[p_i - p_1(a,t)]}{q^*\mu_1\ 1} \tag{14}$$

In Equation (14), q^* is the flow rate at the boundary that changes with time. A and M are the dimensionless boundary distance and mobility ratio respectively and are defined by:

$$A = \frac{a}{1} \tag{15}$$

$$M = \frac{\lambda_2}{\lambda_1} = \frac{k_2\mu_1}{k_1\mu_2} \tag{16}$$

The other terms are defined in the nomenclature. Taking the Laplace transformation of Equations (1), (2), and (10) through (13) with respect to the dimensionless time, t_D, using initial conditions of Equations (8) and (9) yields:

$$\frac{d^2\bar{p}_{D1}}{dx_D^2} - s\bar{p}_{D1} = 0 \tag{17}$$

$$\frac{d^2\bar{p}_{D2}}{dx_D^2} - \frac{1}{\eta}\, s\bar{p}_{D2} = 0 \tag{18}$$

$$\bar{p}_{D2}(\infty,s) = 0 \tag{19}$$

$$\left.\frac{d\bar{p}_{D1}}{dx_D}\right]_{x_D=0} = -\frac{1}{s} \tag{20}$$

$$\frac{d\bar{p}_{D1}}{dx_D} = \frac{-1}{S}\,(\bar{p}_{D1}-\bar{p}_{D2}) \qquad at\ \ x_D = A \tag{21}$$

$$\frac{d\bar{p}_{D1}}{dx_D} = M\,\frac{d\bar{p}_{D2}}{dx_D} \qquad at\ \ x_D = A \tag{22}$$

The solutions to the ordinary differential Equations (17) and (18), and the associated boundary conditions, Equations (19) through (22) are:

$$\bar{p}_{D1}(x_D,s) = C_1\, e^{\sqrt{s}\,x_D} + C_2\, e^{-\sqrt{s}\,x_D} \tag{23}$$

$$\bar{p}_{D2}(x_D,s) = C_3\, e^{\sqrt{s/\eta}\,x_D} + C_4\, e^{-\sqrt{s/\eta}\,x_D} \tag{24}$$

The Laplace dimensionless pressure drop at the inner boundary is derived by letting $x_D = 0$:

$$\bar{p}_{wD} = C_1 + C_2 \tag{25}$$

C_1 through C_4 are given by the following expressions:

$$C_1 = \frac{D\left[-1 - \dfrac{M}{\sqrt{\eta}}\,(S\sqrt{s}-1)\right]}{\dfrac{Ms\sqrt{s}}{\sqrt{\eta}}\left[(S\sqrt{s}(D-E) - (D+E)\right] + s\sqrt{s}\,(D-E)} \tag{26}$$

$$C_2 = C_1 + \frac{1}{s\sqrt{s}} \tag{27}$$

$$C_3 = 0 \tag{28}$$

$$C_4 = \frac{(D\,C_2 - E\,C_1)}{\dfrac{M}{\sqrt{\eta}}\; e^{-A\sqrt{s/\eta}}} \tag{29}$$

where D and E are given by:

$$D = e^{-A\sqrt{s}} \tag{30}$$

$$E = e^{A\sqrt{s}} \tag{31}$$

Using Equation (27) in Equation (25) yields:

$$\bar{p}_{wD} = 2C_1 + \frac{1}{s\sqrt{s}} \tag{32}$$

Solutions for some special cases appear next. From Equations (23) and (26), $M/\sqrt{\eta}$ is recognized as a correlating parameter for the dimensionless pressure drop in region I. However, $M/\sqrt{\eta}$ is not a correlating parameter for the dimensionless pressure drop in region II because of the appearance of $\sqrt{s/\eta}$ in the exponential argument in Equation (24).

EARLY AND LATE TIME APPROXIMATIONS

Examination of Equation (26) shows that $C_1 \to 0$ as $s \to \infty$ for arbitrary M, η, S and A. Thus, at early time, $\bar{p}_{wD}$ is:

$$\bar{p}_{wD} = \frac{1}{s\sqrt{s}} \tag{33}$$

that inverts to:

$$p_{wD} = 2\sqrt{\frac{t_D}{\pi}} \tag{34}$$

Equation (34) is the infinite acting homogeneous linear flow solution that was presented by *Nabor* and *Barham* (1964).

At late time, $t \to \infty$ and $s \to 0$. For any set of M, η, S and A, the expression for $2C_1$ at late times is:

$$2C_1 = \frac{1}{\dfrac{M}{\sqrt{\eta}}\, s\,\sqrt{s}} + \frac{S}{s} - \frac{1}{s\sqrt{s}} \tag{35}$$

since $D \to 1$ and $E \to 1$ as $s \to 0$. From Equations (32) and (35), the dimensionless Laplace pressure solution simplifies to:

$$\bar{p}_{wD} = \frac{1}{\dfrac{M}{\sqrt{\eta}}}\,\frac{1}{s\sqrt{s}} + \frac{S}{s} \tag{36}$$

that inverts to:

$$p_{wD} = \frac{2}{\dfrac{M}{\sqrt{\eta}}}\sqrt{\frac{t_D}{\pi}} + S \tag{37}$$

For a homogeneous aquifer ($M = 1$ and $\eta = 1$), Equation (37) reduces to:

$$p_{wD} = 2\sqrt{\frac{t_D}{\pi}} + S \tag{38}$$

RELATIONSHIP WITH *NABOR AND BARHAM* MODEL

We saw that the early time behavior of a composite system with property contrast and boundary skin is given by the *Nabor* and *Barham* (1964) model. Also, Equation (37) shows that in the absence of boundary skin, proper combinations of M and η such that $M/\sqrt{\eta} = 1$ will result in a homogeneous semi-infinite linear aquifer solution as presented by *Nabor* and *Barham* (1964). Actually, in such a case when $M/\sqrt{\eta} = 1$ and $S = 0$, even the intermediate time behavior is the same as *Nabor* and *Barham* (1964) model as shown in Figure 3.

Also, if the inner region has a low storativity associated with it, a specified real time corresponds to a large t_D, and the system behavior will be given by Equation (37). Hence, we would have a half slope on a log-log graph similar to that obtained for *Nabor* and *Barham* (1964) linear semi-infinite aquifer model.

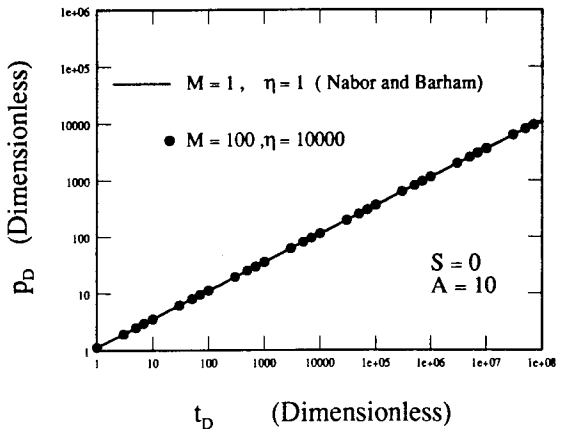


Figure 3: Comparison with the *Nabor* and *Barham* (1964) model.

RELATIONSHIP WITH *HURST* MODEL

Equation (17) of *Hurst's* (1958) paper representing linear water influx model is:

$$\Delta p = \frac{\phi \mu_w c_w q_o}{k N c_o \lambda^2} f(\lambda \sqrt{t_D}) \tag{39}$$

where

$$t_D = \frac{kt}{\phi \mu_w c_w 1^2} \tag{40}$$

$$\lambda = \frac{bh\phi c_w}{NB_{oi}c_o} \tag{41}$$

$$f(\lambda \sqrt{t_D}) = e^{\lambda^2 t_D} erfc(\lambda\sqrt{t_D}) - 1 + 2\lambda\sqrt{t_D/\pi} \tag{42}$$

and other terms are defined in *Hurst's* (1958) paper. In our notation, the *Hurst* (1958) model is represented as:

$$\lambda p_D = f(\lambda \sqrt{t_D}) \tag{43}$$

where

$$\lambda = \frac{(\phi c_t)_2}{A (\phi c_t)_1} \tag{44}$$

$$p_D = \frac{k_2 bh\Delta p}{\mu_2 q} \tag{45}$$

$$t_D = \frac{k_2 t}{(\phi \mu c_t)_2 1^2} \tag{46}$$

The subscripts 1 and 2 refer to region I (oil zone) and region II (aquifer zone) respectively. Equation (43) shows that *Hurst* (1958) model can be represented by just one curve if λp_D is graphed against $\lambda\sqrt{t_D}$. The solid line in Figure 4 is the *Hurst* (1958) model. Circles represent the computation using the general solution developed in this study with M = 0.001, A = 10, S = 0 and η = 1. The agreement between the two models shows that the behavior of the system with a high transmissivity and a finite storativity in the inner region representing the reservoir is identical to the linear water influx model presented by *Hurst* (1958).

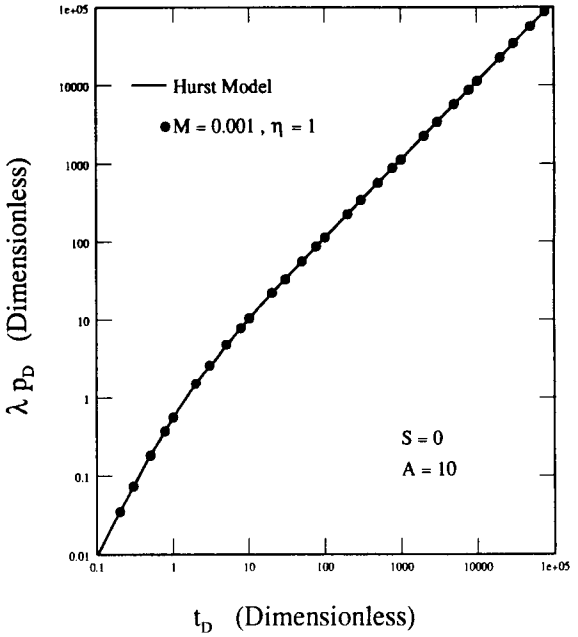


Figure 4: Comparison with the *Hurst* (1958) model.

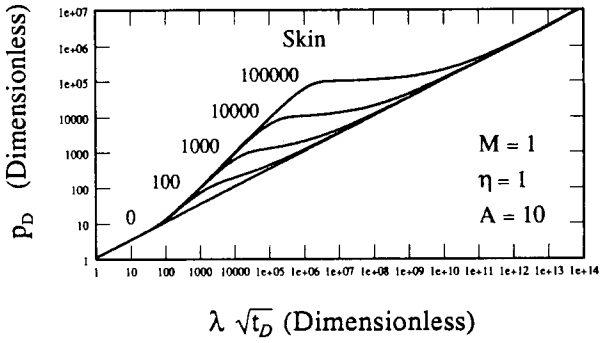


Figure 5: Effects of boundary skin on dimensionless pressure responses.

TYPE CURVE DEVELOPMENT

The Laplace solution of Equation (32) was inverted numerically using an algorithm developed by *Stehfest* (1970). Figure 5 examines the effects of boundary skin with a fixed distance to the boundary. All the curves are identical at early time as predicted by Equation (34), representing the infinite acting linear flow period controlled by the properties of the inner region. The infinite acting linear flow period is characterized by a one half slope on the log-log graph. All the curves depart from the infinite acting behavior at the same time, doubling the slope to unity, representing pseudo steady state (PSS) depletion of the inner region. Then, depending on the value of boundary skin, the pressure response tends to stabilize, joining at late time the infinite acting linear pressure response. The higher the value of boundary skin, the longer is the PSS flow period. Also, the late time curves are separated by the value of boundary skin, as predicted by Equation (38), but due to the log-log presentation, the constant difference

Table 1: Late Time Dimensionless Pressure Drop at the Inner Boundary for Unit Mobility and Diffusivity Ratio

Skin	0	10^3	10^4	10^5	10^6
$t_D\ 10^{-12}$	$p_D\ 10^{-6}$	$p_D\ 10^{-6}$	$p_D\ 10^{-6}$	$p_D\ 10^{-6}$	$p_D\ 10^{-6}$
1	1.128	1.129	1.138	1.228	2.128
5	2.523	2.524	2.533	2.623	3.523
10	3.568	3.569	3.578	3.668	4.568
50	7.979	7.980	7.989	8.079	8.979
100	11.28	11.28	11.29	11.38	12.28
500	25.23	25.23	25.24	25.33	26.3

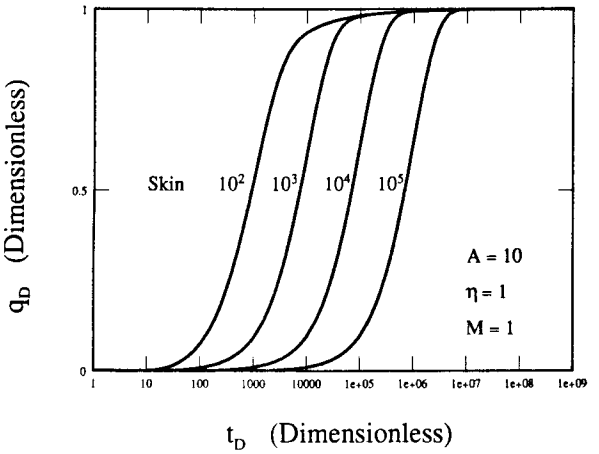


Figure 6: Dimensionless influx rate across the fault for different values of skin.

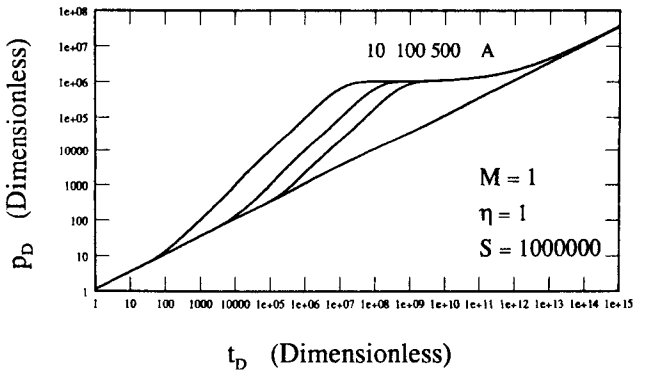


Figure 7: Effects of boundary distance on dimensionless pressure responses.

is not visible. This separation at late time is presented in Table 1.

Figure 6 presents the effect of boundary skin on the dimensionless influx rate for a fixed boundary distance. The dimensionless influx rate is zero at early time, characterizing the infinite acting linear flow period controlled by the properties of the inner region. The duration of the transition from an influx rate of zero to one depends on the value of the boundary skin. As the boundary skin increases, the significant flow across the fault is delayed. Thus, the pseudo steady state depletion lasts longer for larger value of boundary skin, as seen in Figure 5. Once an appreciable influx starts occurring across the fault, the pressure response tends to stabilize (See Figure 5). Finally, the dimensionless influx rate becomes one that corresponds to the late time infinite acting linear flow period. Hence, Figure 6 provides a physical explanation for the pressure behavior observed in Figure 5.

Table 2: Dimensionless Departure Time Data for Linear Semi-infinite Homogeneous Systems with Boundary Skin

A	$t_{D,d}$	$\sqrt{t_{D,d}}$	C
10	40	6.32	1.581
50	1,000	31.62	1.581
100	4,000	63.24	1.581
500	100,000	316.2	1.581

Note: $C = \dfrac{A}{\sqrt{t_{D,d}}}$

Figure 7 presents the effects of boundary distance with a fixed value of boundary skin. The departure of the pressure response from the infinite acting linear flow period is controlled by boundary distance. As A increases, the departure time is delayed. Table 2 lists the dimensionless departure times for different values of A, and a linear correlation between the square root of dimensionless departure time and dimensionless boundary distance is presented in Figure 8. This correlation is independent of boundary skin, and is described by:

$$A = 1.581\ \sqrt{t_{D,d}} \qquad (47)$$

The effects of the boundary distance and skin on the pressure response are presented in Figure 9. Here, the lowermost thick curve represents infinite linear flow behavior. The onset of the unit slope representing PSS flow (or equivalently, the departure of the pressure response from the infinite acting flow period) is controlled by the value of the distance to the boundary. The stabilized portions of the curves are controlled by the value of the boundary skin. The curves in Figure 9 can be correlated by shifting them horizontally and vertically in some manner. Figure 10 shows an example of the curve for A = 100 and S = 1000 shifted and matched to the curve for A = 10 and S = 100. Numerically, the two curves match within less than 0.1%. Thus, the behavior of homogeneous semi-infinite aquifers with boundary skin is summarized as a type curve presented in Figure 11 that applies for all values of A. We arbitrarily chose to correlate all the curves with the curves for A = 10. Any other choice of A would also have sufficed.

Matching reservoir data to the type curve presented in Figure 11 offers a method for detecting the boundary and also determining if there is a skin associated with this boundary. However, the determination of the values of A and S is not unique. If we have the distance to the boundary, we can estimate the magnitude of the skin. Also, this type curve may help examining the possible ranges of A and S for a given set of data, hence helping in setting some realistic limits on the distribution of reservoir heterogeneities.

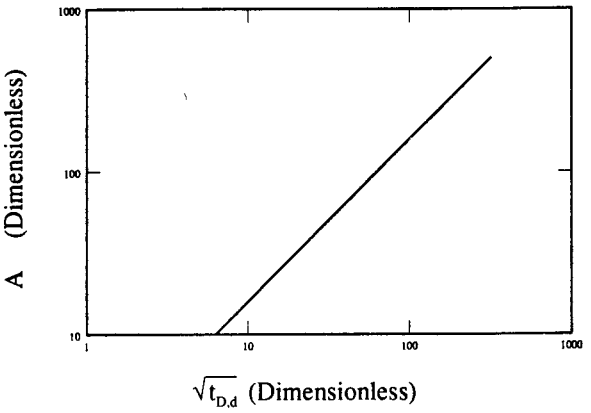


Figure 8: Correlation between dimensionless boundary distance and dimensionless departure time.

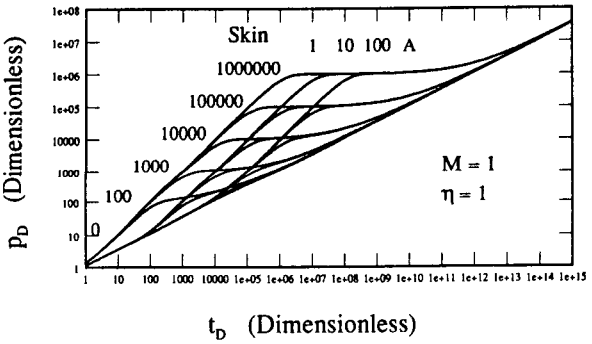


Figure 9: Combined effects of boundary distance and skin on pressure responses.

EXAMPLE CALCULATION

We solve a modification of Example No. 2 of *Nabor* and *Barham* (1964) for different cases to demonstrate how to use the type curve of Figure 10. The example involves estimation of the pressure drop at the aquifer-reservoir boundary for a constant influx rate of 53.1 bbl/Day over a 91 day time period. Aquifer properties are given in Table 3. We assume the boundary distance to be 1000 ft (ie, A = 1000). To apply *Nabor* and *Barham* (1964) model, we assume the aquifer length, L, to be 1000 ft. Thus, for the *Nabor* and *Barham* (1964) model,

$$t_{D,N+B} = \frac{kt}{\phi\mu c_t L^2}$$

$$= \frac{(1.8985)\ (91)}{(0.25)\ (1)\ (6.2 \times 10^{-6})\ (1000^2)} = 111.5 \quad (48)$$

However, for our model,

$$t_D = \frac{kt}{\phi\mu c_t} = 111.5 \times 10^6 \quad (49)$$

and therefore

$$t_D(10/A)^2 = 1.1 \times 10^4 \quad (50)$$

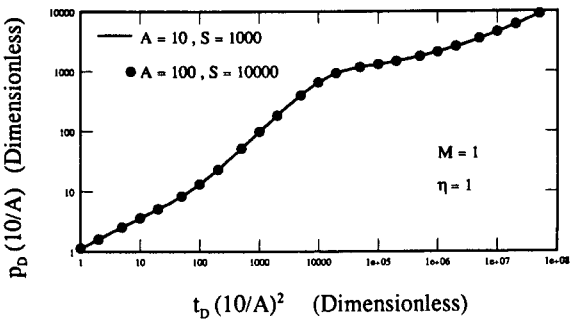


Figure 10: Establishing S/A as a correlating parameter for pressure responses.

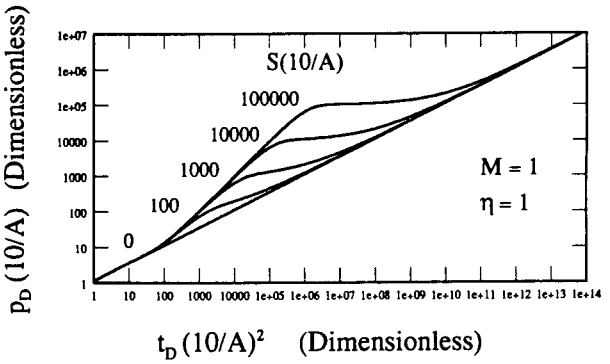


Figure 11: Type curve for linear infinite homogeneous systems with boundary skin.

Table 3: Aquifer Properties (after *Nabor* and *Barham*, 1964)

Property	Value
b	2000 ft
h	41 ft
k	300 md
ϕ	0.25
μ_w	1 cp
c_t	6.2×10^{-6} psi^{-1}

Calculations required to get p_D values at the above t_D for different boundary skin values are shown in Table 4. The values of p_D x 10/A are read from the type curve of Figure 10. An illustration for getting the p_D x 10/A values for the example calculation is shown in Figure 12.

Table 5 shows the results of pressure drop calculations for different cases. Cases 1 and 2 use the *Nabor* and *Barham* (1964) model and pressure drop is calculated by:

$$\Delta p_{N+B} = \frac{q\mu L}{kbh}\, p_D\,(t_D)$$

$$= \frac{(298.1)\ (1)\ (1000)}{(1.8985)\ (2000)\ (41)} p_D\,(t_D)$$

$$= 1.915\, p_D\,(t_D) \quad (51)$$

Table 4: p_D from Type Curve for $t_D\,(10/A)^2 = 1.1x10^4$

S	10 S/A	p_D x (10/A)	p_D
0	0	119.1	1.19 x 10^4
10^4	10^2	207.7	2.08 x 10^4
10^5	10^3	699.7	7.00 x 10^4
10^6	10^4	1059.1	10.59 x 10^4

Table 5: Pressure Drop Estimations

No.	Case	Model	Δp calc. (psi)
1	Semi-infinite	Nabor and	23
2	Closed, 1000 ft long	Barham	214
3	$S = 0$		23
4	$S = 10^4$	New	40
5	$S = 10^5$	Model	134
6	$S = 10^6$	(Semi-infinite)	203

Table 6: Pressure Drop Estimations at Different Locations

Case	Skin	Calculated Pressure Drop, psi			Average Pressure Drop, psi
		x_D=0	x_D=500	x_D=1000	
3	0	23	22	21	22
4	10^4	40	39	38	39
5	10^5	134	133	132	133
6	10^6	203	202	202	202.3

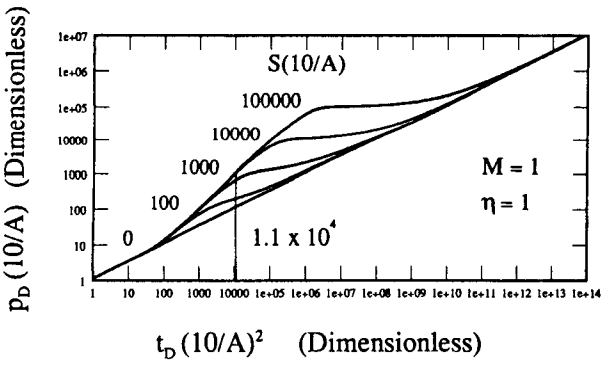


Figure 12: p_D×10/A values from the type curve for t_D×$(10/A)^2$=1.1×10^4.

Cases 3, 4, 5 and 6 use our model and the pressure drop is calculated by:

$$\Delta p = \frac{q\mu}{kbh}\, p_D\,(t_D)$$

$$= 1.915 \times 10^{-3}\, p_D\,(t_D) \qquad (52)$$

Equations (51) and (52) are different because of our definition of p_D. There are two points to be made regarding the pressure drop results in Table 5. The first point is that we need a large boundary skin to create appreciable effect on the influx calculations. Also, the farther the skin boundary, larger the skin needed to create an influx effect. The second point is that ignoring the effect of partially communicating boundaries may result in an incorrect assumption of a closed aquifer that could lead to erroneous results in reserve estimations and history matching.

The calculated pressure drop for our model in Table 5 refers to the production boundary (x_D = 0). However, *Nabor* and *Barham* (1964) model gives the average pressure drop in the inner region. Since our model allows pressure transients to develop in the inner region, pressure drop will be lower as the pressure point moves toward the fault. Figure 13 shows the pressure responses for different locations with a fixed boundary distance and skin. The effect of the location of the pressure point on the pressure response is significant at early time. We re-calculated the pressure drops with our model using different pressure point locations for the example calculation, presented in Table 6. The average pressure drop is calculated as the the average of calculated pressure drops for the three pressure locations The average pressure drop in any case is close to the calculated pressure drop at the production boundary (x_D = 0). Also, since pressure locations only affect the pressure response at early time as in Figure 13, it should be sufficient to calculate pressure drop at the production boundary using our model for most cases. However, we found that x_D x (10/A) and S x (10/A) are the correlating parameters for the pressure responses in the inner region. Figure 14 shows an example of this correlation with x_D x (10/A) = 5 and S x (10/A) = 10^4. Thus, if calculating average pressure drop were necessary, a type curve for the pressure responses in the inner region could be developed using x_D x (10/A) and S x (10/A) as the correlating parameters.

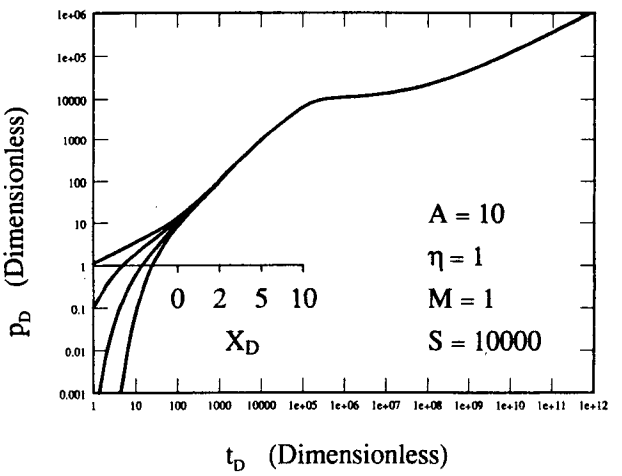


Figure 13: Pressure responses for different locations with a fixed boundary distance and skin.

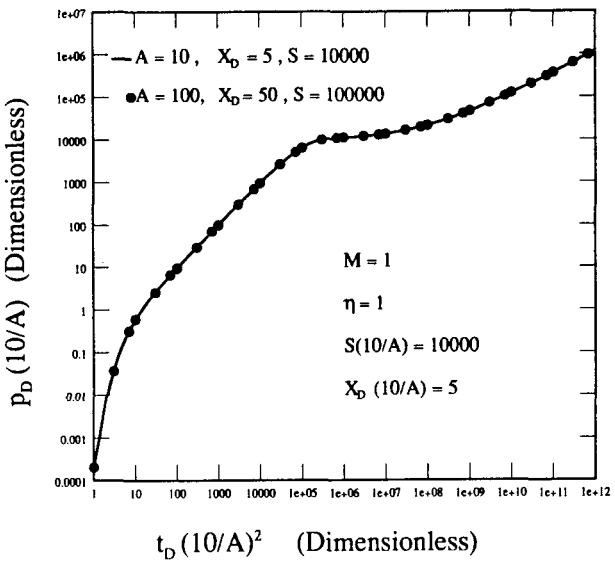


Figure 14: Establishing correlating parameters for pressure responses in the inner region.

CONCLUSIONS

1. The transient pressure behavior of a semi-infinite composite linear system with property contrast and boundary skin has been analytically solved. This paper extends the applicability of the presently known linear influx models. Only constant rate at the inner boundary has been considered.
2. *Hurst* (1958), and *Nabor* and *Barham* (1964) linear influx models are special cases of the new general model described in this paper.
3. The departure of the pressure response at the production boundary from the infinite-acting linear response is only controlled by the distance to the boundary. A linear correlation between the dimensionless boundary distance and the square root of dimensionless departure time is presented.
4. The transition between early and late time infinite acting behavior is explained in terms of the dimensionless influx rate behavior across the fault. The dimensionless influx rate is zero at early time and approaches unity at late time.
5. The pseudo steady state depletion lasts longer for larger value of boundary skin. When appreciable influx starts occurring across the fault, the pressure response tends to stabilize before reaching late time infinite acting linear flow behavior.
6. Boundary skin and the distance to the boundary determine the pressure response for linear homogeneous systems. A type curve is presented in Figure 10 in terms of the correlating parameter 10 *S/A*. Though the results are not presented for composite systems with property contrasts, $M/\sqrt{\eta}$ is the other correlating parameter for pressure responses in region I, as suggested by Equations (23) and (26).
7. A large skin is needed to create an appreciable effect on the influx calculations. However, ignoring the effect of partial communication at the boundary may result in the selection of an improper aquifer model leading to possible errors in reserve estimations and history matching.
8. Different pressure locations in the inner region significantly affect the pressure responses at early time. For most cases, calculating pressure drop at the production boundary should be sufficient.
9. The pressure responses in the inner region can be correlated in terms of the parameters x_D x (10/*A*) and *S* x (10/*A*).

ACKNOWLEDGEMENTS

Financial support was provided by the Stanford Geothermal Program, DOE Contract No. DE-AT02-80SF11459, and by Stanford University.

NOMENCLATURE

A	Dimensionless boundary distance
a	Boundary distance
b	System width
C_1–C_4	Constants in the solutions
c_t	Total system compressibility
D,E	Parameters given by Equations (30) and (31)
h	Thickness
k	Permeability
M	Mobility Ratio
p	Pressure
p_D	Dimensionless pressure
$\bar{p}_D$	Dimensionless pressure drop in Laplace space
p_i	Initial pressure
p_{wD}	Dimensionless pressure drop
q	Influx rate
S	Boundary skin
s	Laplace variable
t	Time
t_D	Dimensionless time
$t_{D,d}$	Dimensionless departure time
x	Distance
x_D	Dimensionless distance

Greek symbols

∂	Partial derivative
η	Diffusivity ratio
λ	Mobility (Also Hurst model parameter as given by Equation (41) or (44))
ϕ	Porosity
μ	Viscosity

Subscripts

1	Zone 1
2	Zone 2
D	Dimensionless
i	Initial
t	Total

REFERENCES

Ambastha, A.K. and Ramey, H.J.,Jr.: "An Analytical Study of Transient Flow in Linear Nonhomogeneous Aquifers," *SUPRI* Tech. Report (to be published).

Bowman, C.H., and Crawford, P.B.: "A Practical Method for Calculating the Transient Pressure Distribution in Linear Semi-infinite Water Driven Reservoirs Having Different Fluid and Rock Properties in Each Zone," SPE Paper 272 (1962).

Carslaw, H.S. and Jaeger, J.S.: *Conduction of Heat in Solids*, second edition, Clarendon Press, Oxford (1959) 18-23.

Hurst, W.: "Establishment of the Skin Effect and Its Impediment to Fluid Flow Into a Well Bore," *The Petroleum Engineer* (Oct. 1953) B6-B16.

Hurst, W.: "The Simplification of the Material Balance Formulas by the Laplace Transformation," *Trans.* AIME (1958) 213, 292.

Miller, F.G.: "Theory of Unsteady-State Influx of Water in Linear Reservoirs," *Journal Institute of Petroleum* (Nov. 1962) 48, 365.

Mueller, T.D.: "Transient Response of Nonhomogeneous Aquifers," *Soc. Pet. Eng. J.* (March 1962) 33-43.

Nabor, G.W., and Barham, R.H.: "Linear Aquifer Behavior," *J. Pet. Tech.* (May 1964) 561-563.

Stehfest, H.: "Algorithm 368, Numerical Inversion of Laplace Transforms," D-5, *Comm. of ACM* ,13, No.1 (Jan. 1970), 49.

Van Everdingen, A.F.: "The Skin Effect and Its Influence on the Productive Capacity of a Well," *Trans.*, AIME (1953) Vol. 198, 171-176.

Van Everdingen, A.F., and Hurst, W.: "The Application of the Laplace Transformation to Flow Problems in Reservoirs," *Trans.*, AIME (1949) Vol. 186, 305.

Van Everdingen, A.F., Timmerman, E.H., and McMahon, J.J.: "Application of the Material Balance Equation to a Partial Water-Drive Reservoir," *Trans.*, AIME (1953) Vol. 198, 51.

PROCEEDINGS, Twelfth Workshop on Geothermal Reservoir Engineering
Stanford University, Stanford, California, January 20-22, 1987
SGP-TR-109

MULTIPHASE, MULTICOMPONENT COMPRESSIBILITY IN GEOTHERMAL RESERVOIR ENGINEERING

L. Macias-Chapa and H. J. Ramey, Jr.

The University of Tulsa, Tulsa, OK
Stanford University, Stanford, CA

ABSTRACT

Coefficients of compressibilities below the bubble point were computed with a thermodynamic model for single and multicomponent systems. Results showed coefficients of compressibility below the bubble point larger than the gas coefficient of compressibility at the same conditions. Two-phase compressibilities computed in the conventional way are underestimated and may lead to errors in reserve estimation and well test analysis.

INTRODUCTION

The expansion properties of a two-phase liquid-vapor system are different from the corresponding properties of the individual phases. It is a common error to assume that the expansion properties of a two-phase system are a volumetric average of the liquid and gas properties.[1] Martin[2] derived an expression relating three phase flow (oil, gas, and water) to an equivalent single phase flow. This expression defined a Total System Compressibility that was a volumetric average of individual phase compressibilities and considered solution of gas in liquids. This expression is widely used in well test analysis and reservoir simulation. Although this approach appears reasonable for the segregated flow of the three phases, the true thermodynamic path for many expansion processes requires different averaging conditions.

Work by Grant and Sorey[3] indicated that apparent system compressibility for two-phase systems in a porous medium could be much larger than gas compressibility for geothermal systems.

Thus the objective of this paper was to study two-phase compressibilities for single and multicomponent systems. In order to perform the study, the change in volume for the total mixture with respect to pressure was computed with a thermodynamic model for a flash system. The thermodynamic model included of a mass and energy balance, with appropriate thermodynamic relationships for enthalpy and equilibrium ratios utilizing the virial equation of state.

The total system effective compressibility for multiphase systems for different production modes was also computed in this study. The production modes included either gas production, or production according to relative permeability-saturation relationships.

Results from these calculations provide information on the multiphase coefficient of compressibility and the total system effective compressibility useful for the interpretation of well test analysis and other reservoir calculations. Theory and pertinent literature concerning the coefficient of compressibility and total system compressibility will be considered in the next section.

THEORY AND DEFINITIONS

The common kinds of compressibilities considered are: coefficient of isothermal compressiiblity, coefficient of adiabatic compressibility, total system compressibility, and two-phase apparent compressibility. A brief description of each follows.

Coefficient of Isothermal Compressibility

The isothermal compressibility is a point function, and can be calculated from the slope of an isotherm of a pressure versus specific volume curve, or from differentiation of an equation of state, and is defined as:

$$c = -(1/V)(dV/dp)_T \qquad \text{.....(1)}$$

For the coexisting two-phase compressibility (gas and liquid), it can be shown from a p-V diagram[4], Fig. 1, that the inverse of the slope of an isotherm for the two-phase region will be larger than the corresponding reciprocal slope of either the gas or the liquid regions. We now turn to consideration of adiabatic compressibility.

Adiabatic Compressibility

Measuring the change in temperature and volume for a given small pressure change in a reversible adiabatic process provides enough information to calculate the adiabatic

compressibility, which is given by:

$$c_s = -(1/V)(dV/dp)_H \quad \text{.....(2)}$$

Keiffer[5] in a study of the velocity of sound in liquid-gas mixtures, calculated sonic velocities for water-air and water-steam mixtures that were smaller than the sonic velocity of the gas phase. Sonic velocity can be related to adiabatic compressibility by the expression:

$$u_s = (c_s \cdot V)^{-0.5} \quad \text{.....(3)}$$

From Eq. 3, it is apparent that a small sonic velocity u_s corresponds to a large compressibility. The existence of gas or vapor bubbles in a liquid reduces the speed of sound in the liquid. This phenomenon was explained[1] by suggesting that a two-phase system has the effective density of the liquid but the compressibility of a gas. This phenomenon is considered to be of importance in systems with the presence of bubbles from a process like gas leaving solution. It was suggested that sonic velocity measurements can be used to measure compressibility of a gas-liquid mixture.[1]

Total System Compressibility

Perrine[6] presented an empirical extension of single-phase pressure build-up methods to multiphase flow situations. He suggested that improper use of single-phase buildup analysis for multiphase flow could lead to errors in the estimation of static formation pressure, permeability and well condition. A theoretical foundation for Perrine's suggestion was established by Martin.[2] It was found that under certain conditions of small saturation and pressure gradients, the equations for multiphase fluid flow may be combined into an equation for effective single-phase flow. After some mathematical manipulations, Martin[2] developed to the following definition of total system isothermal compressibility:

$$c_t = S_o[-(1/B_o)(\partial B_o/\partial p) + (B_g/B_o)(\partial R_s/\partial p)] + S_w[-(1/B_w)(\partial B_w/\partial p) + (B_g/B_w)(\partial R_{sw}/\partial p)] + S_g[-(1/B_g)(\partial Bg/\partial p)] \quad \text{.....(4)}$$

Perrine[6], Martin[2], and later Ramey[7], showed that for multiphase buildup analysis, the parameter corresponding to isothermal compressibility in the dimensionless time group should refer to the total system compressibility of oil, gas, water, and reservoir rock, including changes of solubility of gas in liquid phases.

Two-Phase Apparent Compressibility

Grant and Sorey[3] considered the fluid volume change and heat evolved from rock in a phase change process with gas production to give an approximation of the adiabatic two-phase apparent compressibility.[3] An example presented by Grant and Sorey[3] showed a two-phase apparent compressibility that was 30 times larger than the gas compressibility at the same conditions.

From the proceding, it appears that many fluid thermodynamic factors affect multiphase system compressibility. In view of the importance of this factor in petroleum reservoir engineering, the main objective of this study was to consider methods for an investigation of multiphase compressibility. We now consider the method used in this study.

METHOD OF SOLUTION

The method of solution to determine the coefficient of compressibility and the total system compressibility for a two-phase, single or multicomponent system will be discussed in the following section.

Coefficient of Compressibility

Compressibility computations were considered for either a single-component or multicomponent system with specified conditions of temperature, pressure, composition, and fractional vaporization for a flashing process allowing an increase in volume with a fixed decrease in pressure. To obtain the change in total volume with respect to pressure for single and multicomponent systems, the following procedure was used:

$$c = (1/V_{mix})(\Delta V_{mix}/\Delta p)_{T \text{ or } H} \quad \text{.....(5)}$$

where:

$$V_{mix} = V_l + x(V_g - V_l) \quad \text{.....(6)}$$

Vapor-Liquid Equilibrium calculations for a given system of m components at a specified pressure, composition and temperature were performed with a thermodynamic flash model[8] utilizing the virial equation of state, which is appropriate for polar compounds at pressures below 1440 psi (9927.36 kPa). Further details are given by Macias-Chapa.[9]

Total System Apparent Compressibility

In order to calculate the total system apparent compressibility in a similar fashion to that calculated by Grant and Sorey[3], the thermodynamic model[8] was modified[9] to perform a constant volume flash, after a small pressure drop within a given rock-fluid system. Below, or at the bubble point, there is a phase change in the system, allowing production from a fixed volume reservoir. The thermodynamic model was modified to include a porous medium contribution to the enthalpy balance. Two modes of production were allowed: gas production only and pro-

duction of both liquid and gas according to relative permeability-saturation relationship. The total system apparent compressibility is:

$$c_a = (1/V_{pore})(\Delta V_{prod.}/\Delta p) \quad \ldots\ldots\ldots(7)$$

where $\Delta V_{prod.}$ corresponds to the initial fluid volume after the flash minus the fluid volume remaining after production. The V_{pore} term represents the fixed pore volume. Figures 2 and 3 given a schematic representation of the two production modes considered in ths study.

RESULTS

Results are presented for each system studied. First, the coefficient of compressibility is considered, then the production controlled systems.

Coefficients of compressibility below the bubble point were calculated for fluid systems ranging from geothermal fluids to hydrocarbon systems. The systems include pure water, water-carbon dioxide, several multicomponent hydrocarbon systems, and hydrocarbon-water systems. The systems containing pure water and water-carbon dioxide were treated as adiabatic. The hydrocarbon and the hydrocarbon-water systems were considered to be isothermal. Discussion of isothermal systems are given in Refs. 9 and 10.

H_2O and H_2O-CO_2 systems-Fig. 4 shows the adiabatic coefficient of compressibility of water-steam at an initial pressure of 1440 psi (9927.36 kPa) together with the coefficient of compressibility of steam at the same conditions computed with the virial equation of state. The adiabatic coefficient of compressibility for the two-phases is larger than the coefficient of compressibility for the steam at the same conditions, een for small steam qualities. Similar behavior was observed for runs made at initial saturation pressures of 576 psi (3970.94 kPa) and 133.92 psi (923.24 kPa), Fig. 5 and 6. These results are in agreement with thermodynamic theory (p-V diagram) and with studies [1,5] of sonic velocities in liquid-gas mixtures. An explanation of this phenomenon[1] is that a liquid-gas system has nearly the density of the liquid but the compressibility of the gas, specially when the gas quantity is small. The effect of quality is more noticeable at low pressures.[9]

In order to study a simple two-component system, carbon dioxide was added to water in the liquid phase.[9] Contamination of a single component system causes a reduction in the coefficient of two-phase compressibility. Results for the adiabatic coefficients of compressibility for the H_2O-CO_2 systems showed the same general behavior as the H_2O system: The two-phase adiabatic coefficient of compressibility was larger than the gas (H_2O-CO_2) coefficient of compressibility. A comparison of one-component, two-phase compressibility and two-component, two-phase compressibility with gas compressibility, Fig. 7, shows that the two-phase compressibility of a single-component system is larger than the two-phase compressibility of a two-component system, and also larger than the gas compressibility for the same conditions.

Total System Apparent Compressibility was computed for a pure water system at different saturation pressures and rock porosities in an adiabatic process for two modes of production: gas production (steam), and production from a geothermal system wherein both water and steam are producted as multiphase flow relative permeability relationships would dictate. Both modes of production are discussed in the following.

Gas Production

After a pressure drop, some of the initial liquid vaporizes. The amount of gas remaining in the system fills the volume that was occupied by the vaporized liquid. The rest of the gas is produced. Single-component water systems at different initial pressures were studied. These systems include a rock component evident through the enthalpy balance. Figure 8 presents results for a system of saturated water at an initial pressure of 576 psi (3970.94 kPa) in a 10% porosity rock.

The computed apparent compressibility is shown versus pressure. As the system depleted, the apparent compressibility increased. The values of apparent compressibility obtained in this process agreed with the values obtained by Grant and Sorey.[3] The two-phase apparent compressibility was magnitudes larger than the gas (steam) compressibility at the same conditions.

Multiphase Production

For this production mode, liquid and gas were produced in proportion to relative permeabilities as determined from an average saturation. Figure 9 represents a system of saturated water at an initial pressure of 576 psi (3970.94 kPa) in a 25% porosity rock. Apparent compressibility is initially large because of a change in mass due to liquid production and liquid changing to gas. Apparent compressibility then decreases because gas saturation increases sufficiently to allow gas to be produced. Apparent compressibility was much larager than the gas (steam) compressibility at the same conditions throughout the two-phase reservoir condition. From the results shown in Figs. 8 and 9 for different modes of production, it can be seen that the apparent compressibility depends strongly on the manner in which a reservoir is produced.[9]

CONCLUSIONS

A thermodynamic model has been used to compute coefficients of compressibility and apparent compressibility for both isothermal and adiabatic conditions. For the cases studied, it was observed that the compressibility of a two-phase system was always larger than the compressibilty of the corresponding gaseous phase at the same conditions. The model used can yield information about coefficients of compressibility and apparent compressibility for well test analysis and simulation of reservoirs below the bubble point. Other equations of state appropriate for different fluids can be used in the model. In addition apparent compressibility could be larger than the coefficient of adiabatic two-phase compressibility, or the compressibility of the gaseous phase at the same conditions, and is also affected by the way fluids are removed from a given reservoir.

ACKNOWLEDGEMENTS

Financial support was provided by Stanford University, INTEVEP, and the Department of Energy.

REFERENCES

1. McWilliam, D. and Duggins, R. K.: "Speed of Sound in Bubbly Liquids," Proc. Instn. Mech. Engrs., 184(3C), 102, 1969.

2. Martin, J. C.: "Simplified Equations of Flow in Gas Drive Reservoirs and the Theoretical Foundations of Multiphase Pressure Buildup Analysis," Trans. AIME, 216, 309-311, 1959.

3. Grant, M. A. and Sorey, M. L.: "The Compressibility and Hydraulic Diffusivity of Water-Steam Flow," Water Resources Research, 153, 684-686, 1979.

4. Sage, B. H. and Lacey, W. N.: Volumetric and Phase Behavior of Hydrocarbons, Gulf Publishing Co., 1949.

5. Keiffer, S. W.: "Sound Speed in Liquid-Gas Mixtures: Water-Air and Water-Steam," Journal of Geophysical Research, 82, 20, 1977.

6. Perrine, R. L.: "Analysis of Pressure Buildup Curves," Drilling and Production Practice, 482, 1956.

7. Ramey, H. J., Jr.: "Rapid Methods of Estimating Reservoir Compressibilities," JPT (Apr. 1964), 447-454.

8. Prausnitz, J. M., Anderson, T. F., Grens, E. A., Eckert, C. A., Hsieh, R., O'Connel, J. P.: Computer Calculations for Multicomponent Vapor-Liquid and Liquid-Liquid Equilibria, Prentice-Hall, 1980.

9. Macias-Chapa, L.: "Multiphase Multicomponent Compressibility in Petroleum Reservoir Engineering," Ph.D. Dissertation, Petroleum Engineering Dept., Stanford University, 1985.

10. Macias, L., H. J., Ramey, Jr.: "Multiphase Multicomponent Compressibility in Petroleum Reservoir Engineering," SPE 15538, paper presented at the 61st Annual SPE Fall Meeting, New Orleans, Oct. 5-8, 1986.

NOMENCLATURE

B	= formation volume factor res B/std B; res m^3/st m^3
c	= coefficient of compressibility psi^{-1}; kPa^{-1}
H	= enthalpy BTU/lb; J/Kg
p	= pressure psi; kPa
S	= saturation, fraction of pore volume
T	= temperature °F; °C
u_s	= sonic velocity ft/s; m/s
V	= specific volume or total volume ft^3/lb; m^3/Kg
V_{mix}	= mixture volume ft^3/lb; m^3/Kg
V_{pore}	= pore volume ft^3; m^3
ΔV_{prod}	= change in volume due to production ft^3; m^3
x	= quality, mass of gas/mass total lb/lb; Kg/Kg

Subscripts

a	= apparent
g	= gas
l	= liquid
o	= oil
s	= adiabtic
w	= water

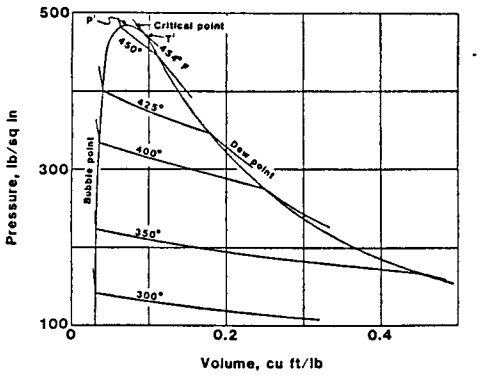


Fig. 1 Pressure vs specific volume, two component system n-heptane - n-pentane, from Sage B. H., and Lacey W.N[4]

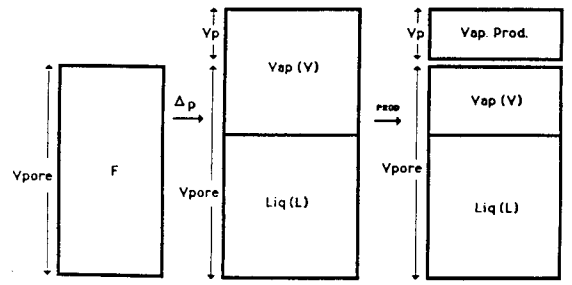


Fig. 2 Gas production mode

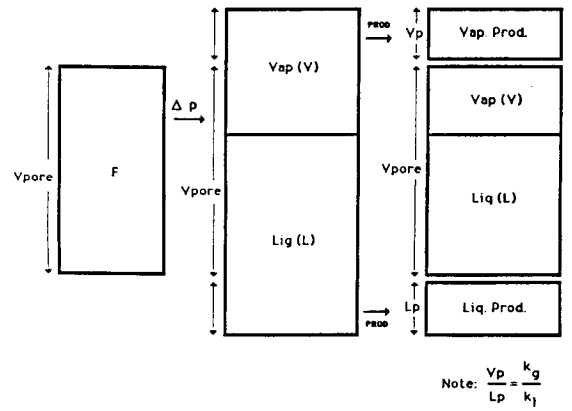


Fig. 3 Multiphase production mode (according to relative permeability-saturation relationship)

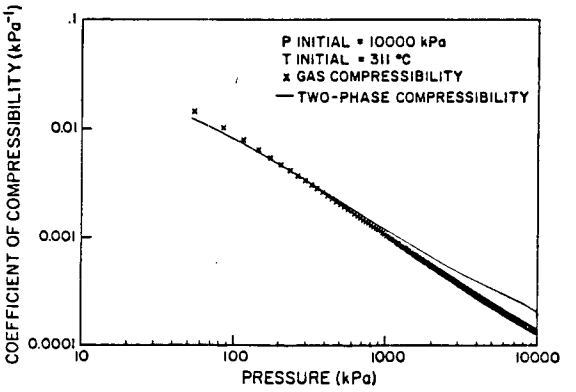


Fig. 4 Log-log graph of coefficient of adiabatic compressibility vs. pressure, pure water system.

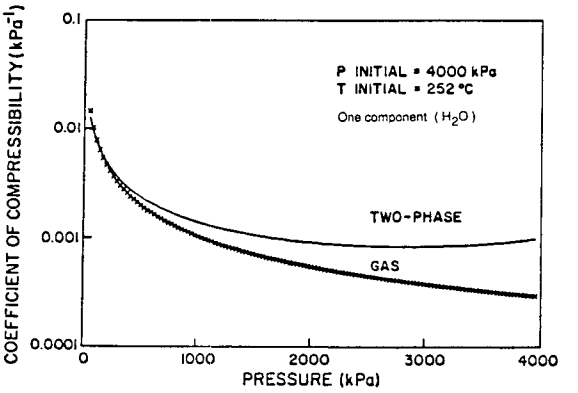


Fig. 5 Semilog graph of coefficient of adiabatic compressibility vs. pressure, pure water system.

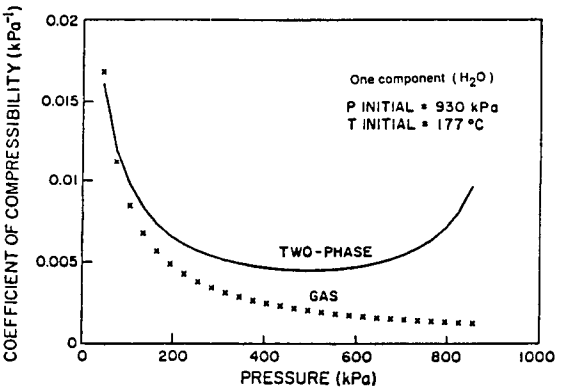


Fig. 6 Coefficient of adiabatic compressibility vs. pressure, pure water system.

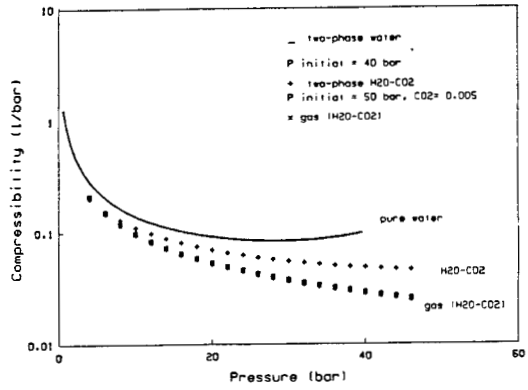


Fig. 7 Coefficient of adiabatic compressibility vs. pressure, pure water and H_2O-CO_2 systems.

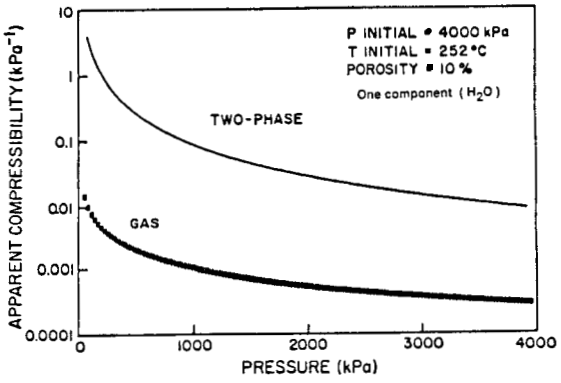


Fig. 8 Apparent compressibility vs. pressure for steam production from a 10 % porosity rock initially containing hot water.

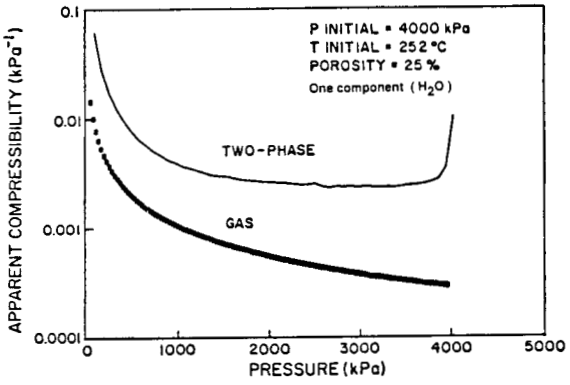


Fig. 9 Apparent compressibility vs. pressure for multiphase production from a 25% porosity rock initially containing hot water.

PROCEEDINGS, Twelfth Workshop on Geothermal Reservoir Engineering
Stanford University, Stanford, California, January 20-22, 1987
SGP-TR-109

RADIAL DISPERSION IN A DOUBLE-POROSITY SYSTEM WITH FRACTURE SKIN

Allen F. Moench

U.S. Geological Survey
Menlo Park, CA

ABSTRACT

The problem of dispersion, advection and adsorption of a tracer in a double-porosity reservoir due to tracer injection in a well with a steady, radially divergent flow field was solved for the case of constant tracer concentration in the injection well. Longitudinal dispersion and advection was assumed to dominate transport in the fracture system and tracer diffusion and adsorption was assumed to dominate movement of the tracer in the matrix blocks. The blocks were assumed to be sphere shaped and covered with a thin skin of material that provides resistance to the diffusion of tracer into the blocks. Values of dimensionless concentration in the fracture system versus dimensionless time were computed by numerical inversion of the Laplace transform solution to the Airy equation. Type curves demonstrate effects of changing reservior characteristics and show the usefulness of the concept of fracture skin in understanding dispersive processes in fractured porous media.

INTRODUCTION

There has been a recent surge of interest in analytical solutions to problems of radial dispersion in porous media. Such analytical solutions can be used in tracer injection tests to evaluate dispersive and adsorptive properties of groundwater and geothermal aquifers, and can be used to verify the accuracy of numerical, solute-transport codes. Hsieh (1986) pointed out that the radial dispersion problem is of particular interest because it is perhaps the simplest case involving a spatially varying velocity field.

Unfortunately, because the coefficient of longitudinal hydrodynamic dispersion is linearly related to velocity, solutions to the one-dimensional, advection dispersion problem in radial coordinates are difficult to obtain. Ogata (1958) appears to have been the first to obtain a closed-form analytical solution to the radial dispersion problem. His solution is based upon the assumption that a steady, radially divergent flow field has been established around the injection well prior to the establishment of a step change in tracer concentration in the well bore.

Because of the form of the Ogata solution, it is difficult to evaluate and alternative forms have appeared in the literature (Tang and Babu, 1979; Hsieh, 1986).

In a fractured porous medium it is believed that a tracer may become dispersed not only by hydrodynamic dispersion but also by diffusion into the porous matrix. Feenstra et al. (1984) proposed a radial flow model for a single, horizontal fracture that accounts for matrix diffusion. Their model is simplified considerably by neglecting effects of longitudinal dispersion in the fracture. Chen (1985, 1986) proposed radial flow models that account for both matrix diffusion and longitudinal dispersion. Both Chen and Feenstra et al. assume that the aquifer or fracture is bounded by porous blocks of infinite thickness.

In this paper a new dimension of complexity, and therefore versatility, is added to the radial dispersion problems. The aquifer or geothermal reservoir is assumed to be composed of highly fractured, porous rock that might be characterized as a double-porosity system (Barenblatt, 1960). Longitudinal dispersion and advection is assumed to dominate tracer transport in the fractures and diffusion and adsorption is assumed to dominate tracer movement in the matrix blocks. Blocks are assumed to be sphere shaped for mathematical simplicity and coated with a thin skin of material that may provide resistance to the diffusion of tracer into the blocks. This skin may be the result of the deposition of minerals or the alteration of minerals due to the natural circulation of geothermal fluids. For a literature review of flow to a well in a double-porosity system and for a description of fracture skin as it relates to the flow problem see Moench (1983, 1984). As regards to diffusion in sphere-shaped blocks with skin, the proposed model is similar to the model of Rasmusen and Neretnieks (1980). It differs in that the more complicated case of radial flow in the fracture system is considered instead of one-dimensional, planar flow. Also, Rasmusen and Neretnieks did not

present any computational results showing the effects of the diffusion barrier or skin.

MATHEMATICAL MODEL

The model is developed under the following general assumptions: (1) As depicted in Figure (1) a vertically oriented injection well of finite diameter fully penetrates a horizontal, confined, double-porosity aquifer of constant thickness and of infinite radial extent. (2) A steady state flow field, which is radially divergent and axially symmetric with respect to the injection well, is present in the fracture system as a result of the constant-rate injection of tracer-free fluid. (3) Advection in the blocks is negligible. (4) At the start of a test a step change in concentration occurs in the injection well. (5) Tracer is transported in the fracture system by radial advection and longitudinal mechanical dispersion: transverse mechanical dispersion and molecular diffusion in the fractures are negligible. Mechanical dispersion is assumed to be linearly related to velocity and is therefore a function of radial position. (6) Tracer diffuses in the sphere-shaped blocks (see Figure 2) in accordance with Fick's law. (7) As depicted in Figure 2, the blocks are coated with a thin layer (skin) of material that impedes the diffusion of tracer at the block-fracture interface and does not allow for the storage of tracer. (8) Tracer is attenuated in the porous blocks by adsorption, which is described by an equilibrium, adsorption isotherm. (9) Adsorption on the fracture surfaces is negligible.

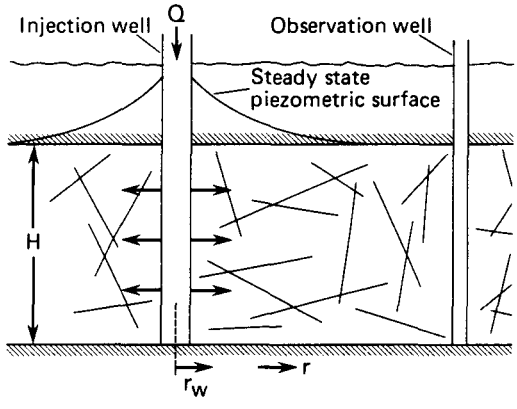


Figure 1. Schematic diagram of a double-porosity aquifer of thickness H with a steady state flow field established around an injection well.

The advection-dispersion equation for plane radial flow in a porous medium is given by Bear (1979, p. 247). For a double-porosity system it may be written as,

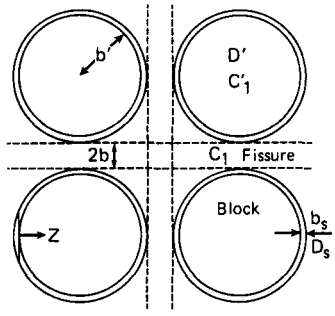


Figure 2. Geometrical configuration for sphere-shaped blocks with fracture skin.

$$\frac{\partial}{r\,\partial r}\left[rD_L \frac{\partial C_1}{\partial r} \right] - \frac{\partial}{r\,\partial r}[rVC_1] - q = \frac{\partial C_1}{\partial t} \qquad r > r_w \qquad (1)$$

where $$q = -\frac{3D'}{b'}\left[\frac{\partial C_1'}{\partial z}\right]_{z=0}$$

for sphere-shaped blocks (see Moench, 1984, equations 29-31). The symbols are defined in the Nomenclature.

The first two terms on the left hand side of equation (1) represent, in order, the transport of solute by dispersion and advection. The third term represents the exchange of solute at the block-fracture interface by matrix diffusion. The term on the right hand side of equation (1) represents the accumulation of tracer in the fracture system.

The coefficient of longitudinal hydrodynamic dispersion is assumed to take the form

$$D_L = \alpha_L V \qquad (2)$$

where molecular diffusion has been neglected. The longitudinal dispersivity, α_L, is assumed to be a characteristic property of the fracture system. The velocity, V, is described mathematically as

$$V = A/r \qquad (3)$$

where $A = 3Q/2\pi\phi_f H$.

In order to solve equation (1) the following boundary conditions and initial conditions are used:

$$C_1(r_w,t) = C_0 \qquad (4)$$

$$C_1(r\to\infty,t) \to 0 \qquad (5)$$

$$C_1(r,0) = 0 \qquad (6)$$

The diffusion equation for the sphere-shaped blocks, allowing for linear equilibrium sorption, is

$$D'\frac{\partial^2(zC'_1)}{\partial z^2} = \phi'R'\frac{\partial(zC'_1)}{\partial t} \qquad 0 \le z \le b' \qquad (7)$$

The boundary conditions used to solve equation (7) are,

$$\frac{\partial C'_1(b',t)}{\partial z} = 0 \qquad (8)$$

$$D_s\frac{[(C'_1)_{z=0} - C_1]}{b_s} = D'\left(\frac{\partial C'_1}{\partial z}\right)_{z=0} \qquad (9)$$

Equation (9) represents continuity of diffusive flux across the skin and derives from heat flow theory (see Carslaw and Jaeger, 1959, p. 20). It is assumed that the skin is negligibly thin and does not accomodate the accumulation of mass.

Using the dimensionless parameters defined in the Nomenclature, the controlling equations and boundary conditions are rewritten in dimensionless form. The coupled, dimensionless boundary-value problems become, for the fracture system,

$$\frac{\partial C^2}{\rho\,\partial\rho^2} - \frac{\partial C}{\rho\,\partial\rho} - q_D = \frac{\partial C}{\partial t_D} \qquad \rho > \rho_0 \qquad (10)$$

where $q_D = -3\gamma\left(\frac{\partial C'}{\partial z_D}\right)_{z_D=0}$

$$C(\rho_0,t_D) = 1 \qquad (11)$$

$$C(\rho\to\infty,t_D) \to 0 \qquad (12)$$

$$C(\rho,0) = 0 \qquad (13)$$

and, for the block system,

$$\frac{\partial^2(z_DC')}{\partial z_D^2} = \frac{\sigma}{\gamma}\frac{\partial(z_DC')}{\partial t_D} \qquad 0 \le z_D \le 1 \qquad (14)$$

$$C'(0,t_D) - C = S_F\left(\frac{\partial C'}{\partial z_D}\right)_{z_D=0} \qquad (15)$$

$$\frac{\partial C'(1,t_D)}{\partial z_D} = 0 \qquad (16)$$

$$C'(z_D,0) = 0 \qquad (17)$$

Equations (10)-(17) are solved by the method of Laplace transformation.

LAPLACE TRANSFORM SOLUTIONS

The Laplace transform solutions are, for the fracture system,

$$\bar{C} = \frac{1}{p}\exp\left(\frac{\rho - \rho_0}{2}\right)\frac{Ai(\beta^{1/3}y)}{Ai(\beta^{1/3}y_0)} \qquad (18)$$

where $y = \rho + (4\beta)^{-1}$

$y_0 = \rho_0 + (4\beta)^{-1}$

$\beta = p + \bar{q}_D$

$$\bar{q}_D = \frac{3\gamma[m\coth(m) - 1]}{1 + S_F[m\coth(m) - 1]}$$

$m = (\sigma p/\gamma)^{1/2}$

and, for the block system,

$$\bar{C}' = \bar{C}\,\frac{\sinh[m(1-z_D)]\,\mathrm{csch}(m)}{(1-z_D)\{1 + S_F[m\coth(m) - 1]\}} \qquad (19)$$

The Laplace transform variable, p, is inversely related to the dimensionless time, t_D. The bar over C, C' and q_D designates their Laplace transforms.

BREAKTHROUGH CURVES

The Laplace transform solutions given by equations (18) and (19) are easily inverted with the Stehfest (1970) algorithm to produce dimensionless breakthrough curves. Figure 3 shows dimensionless breakthrough curves, due to tracer injection, for the indicated values of the parameters, comparing the case of zero matrix diffusion with finite matrix

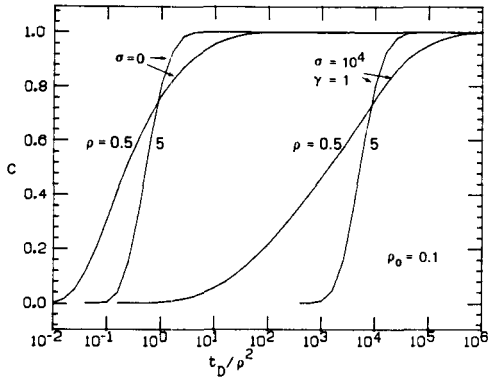


Figure 3. Dimensionless concentration breakthrough curves for the case of zero matrix diffusion (σ=0) compared with a case of finite matrix diffusion ($\sigma=10^4,\gamma=1$).

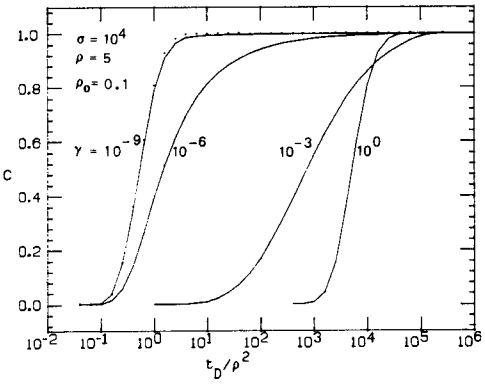


Figure 4. Dimensionless concentration breakthrough curves for the case of zero matrix diffusion (plotted points) compared with finite matrix diffusion for various values of γ and fixed σ (solid lines).

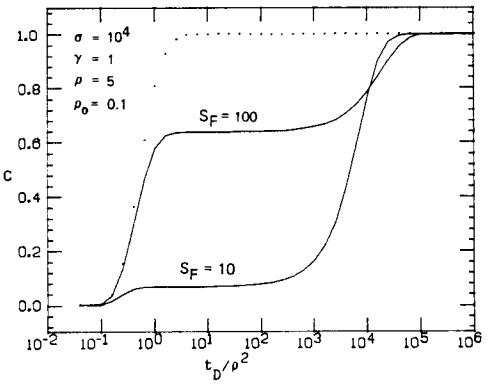


Figure 5. Dimensionless concentration breakthrough curves for the case of zero matrix diffusion (plotted points) compared with finite matrix diffusion with fracture skin for ρ=5.0 and ρ_0=0.1 (solid lines).

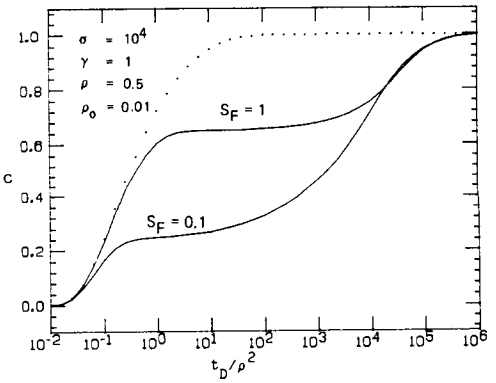


Figure 6. Dimensionless concentration breakthrough curves for the case of zero matrix diffusion (plotted points) compared with finite matrix diffusion with fracture skin for ρ=0.5 and ρ_0=0.01 (solid lines).

diffusion. As expected the effect of matrix diffusion is such as to delay the arrival of the breakthrough curve at a given radial distance from the injection well. The amount of delay is directly related to the magnitude of the parameter σ, which is dependent upon the retardation factor and the porosity of the block system and the porosity of the fracture system (see Nomenclature). Also the greater the dispersivity of the aquifer system, α_L, the greater is the spreading of the tracer.

Figure 4 shows tracer breakthrough curves for various values of γ given fixed values of ρ, ρ_0 and σ. The parameter γ is proportional to the diffusion coefficient for the block system (see Nomenclature). This shows that as γ decreases, due to reduced diffusion coefficient, effects of matrix diffusion diminish and the response approaches that expected for no matrix diffusion. It is of interest to note the steepening of the curve for $\gamma=10^0$ in Figure 4. This curve corresponds to the case where, because of a large diffusion coefficient, the tracer is taken up by the blocks almost instantaneously causing a long delay in the appearance of the breakthrough curve. It is as though there is enhanced storage of tracer in the fracture system. The response for $\gamma=10^0$ is about the same as that for $\gamma=10^{-9}$ except that it is shifted to the right by a factor of $1+\sigma$.

Figure 5 shows effects of fracture skin upon tracer breakthrough curves. A concentration plateau separates the breakthrough curve for zero matrix diffusion from the breakthrough curve for finite matrix diffusion. For S_F=100 the concentration buildup faithfully follows the case of zero matrix diffusion at early time. For S_F=10 the concentration buildup follows the case of finite matrix diffusion at late time. Similar responses are shown in Figure 6 using a larger value of α_L.

CONCLUSIONS

The figures showing hypothetical dimensionless breakthrough curves in observation wells illustrate tracer spreading due to dispersion in the fracture system and matrix diffusion in sphere-shaped blocks. The barrier to diffusion (or fracture skin) located on block surfaces causes a concentration "plateau" to occur in the breakthrough curves separating the response for zero matrix diffusion from that for finite matrix diffusion. The magnitude of the separation depends upon the retardation factor for the blocks and the block and fracture porosity. Because this model includes the effects of a radially varying velocity field in the fractures, the diffusion of tracer in the matrix blocks, and the barrier to diffusion at the fracture block interfaces, it should be useful in helping to validate large numerical models for chemical transport problems.

NOMENCLATURE

A	$[= 3Q/2\pi\phi_f H]$ advection parameter, L^2/T.
$Ai(x)$	Airy function.
b	half thickness of a representative fracture, L.
b'	radius of a representative, sphere-shaped block, L.
b_s	average thickness of fracture skin, L.
C_0	input concentration of the tracer, M/L^3.
C_1	concentration of tracer in the fracture system, M/L^3.
C'_1	concentration of tracer in block system, M/L^3.
C	$[= C_1/C_0]$ dimensionless concentration in fracture system.
C'	$[= C'_1/C_0]$ dimensionless concentration in block system.
D_L	longitudinal hydrodynamic dispersion at a point in the fracture system, L^2/T.
D'	diffusion coefficient for block system, L^2/T.
D_s	diffusion coefficient for fracture skin, L^2/T.
H	aquifer thickness, L
K_d	distribution coefficient for porous blocks, L^3/M.
p	Laplace transform variable.
Q	rate of fluid injection in the well, L^3/T.
q	source term for tracer diffusion at block-fracture interface, M/L^3T.
q_D	dimensionless form of q.
r	radial distance from center line of injection well, L.
r_w	radius of injection well, L.
R'	$[= 1 + \rho_b K_d/\phi']$ retardation factor for blocks.
S_F	$[= D'b_s/D_s b']$ dimensionless skin factor for diffusion.
t	time, T.
t_D	$[= At/\alpha_L{}^2]$ dimensionless time.
V	average radial velocity at a point in the fracture system, L/T.
z	radial distance in sphere-shaped blocks, directed inward from skin-block interface, L.
z_D	$[= z/b']$ dimensionless radial distance in sphere-shaped blocks.
α_L	longitudinal dispersivity for the fracture system, L.
ρ	$[= r/\alpha_L]$ dimensionless radial distance in fracture system.
ρ_0	$[= r_w/\alpha_L]$ dimensionless dispersivity.
ρ_b	bulk density of porous blocks, M/L^3.
ϕ'	porosity of blocks.
ϕ_f	$[= 3b/b']$ fracture porosity.
σ	$[= 3\phi'R'/\phi_f]$ dimensionless grouping for porosity and tracer sorption.
γ	$[= \alpha_L{}^2 D'/Abb']$ dimensionless grouping for dispersion and diffusion.

REFERENCES

Barenblatt, G.I., Iu. P. Zheltov, and I.N. Kocina (1960), "Basic Concepts in the Theory of Seepage of Homogeneous Liquids in Fissured Rocks (strata)", J. Appl. Math. Mech. Engl. Transl., v. 24, 1286-1303.

Bear, J. (1979), Hydraulics of Groundwater, McGraw-Hill, Inc., New York, 569 pp.

Carslaw, H.S., and J.C. Jaeger (1959), Conduction of Heat in Solids, 2nd ed., Oxford University Press, London, 510 pp.

Chen, C.S. (1985), "Analytical and Approximate Solutions to Radial Dispersion from an Injection Well into a Hydrogeologic Unit with Simultaneous Diffusion into Adjacent Strata", Water Resour. Res., v. 21, no. 8, 1069-1076.

Chen, C.S. (1986), "Solutions for Radionuclide Transport from an Injection Well into a Single Fracture in a Porous Formation", Water Resour. Res., v. 22, no. 4, 508-518.

Feenstra, S., J.A. Cherry, E.A. Sudicky, and Z. Haq (1984), "Matrix Diffusion Effects on Contaminant Migration from an Injection Well in Fractured Sandstone", Groundwater, v. 22, no. 3, 307-316.

Hsieh, P.A. (1986), "A New Formula for the Analytical Solution of the Radial Dispersion Problem", Water Resour. Res., v. 22, no. 11, 1597-1605.

Moench, A.F. (1983), "Well Test Analysis in Naturally Fissured, Geothermal Reservoirs with Fracture Skin", Proc. 9th Workshop on Geothermal Reservoir Engineering, Stanford University, Stanford, CA, 175-180.

Moench, A.F. (1984), "Double-Porosity Models for a Fractured Groundwater Reservoir with Fracture Skin", Water Resour. Res., v. 20, no. 7, 831-846.

Ogata, A. (1958), "Dispersion in Porous Media", Ph.D. dissertation, Northwestern University, Evanston, Ill. 121 pp.

Rasmuson, A., and I. Neretnieks (1980), "Exact Solution of a Model for Diffusion in Particles and Longitudinal Dispersion in Packed Beds", A.I.Ch.E. Journal, v. 26, no. 4, 686-690.

Stehfest, H. (1970), "Numerical Inversion of Laplace Transforms", Commun. ACM, v. 13, no. 1, 47-49.

Tang, D.H., and D.K. Babu (1979), "Analytical Solution of a Velocity Dependent Dispersion Problem", Water Resour. Res., v. 15, no. 6, 1471-1478.

PROCEEDINGS, Twelfth Workshop on Geothermal Reservoir Engineering
Stanford University, Stanford, California, January 20-22, 1987
SGP-TR-109

ACTIVE SEISMICS TO DETERMINE RESERVOIR CHARACTERISTICS OF A HOT DRY ROCK GEOTHERMAL SYSTEM.

A S P Green and R Baria

Camborne School of Mines Geothermal Energy Project
Rosemanowes Quarry, Penryn, Cornwall, England

ABSTRACT

Since 1981 three wells have been drilled to depths of between 2.0 and 2.6 km in the Carnmenellis granite, Cornwall, England in order to create a HDR geothermal system. These wells are separated by between 150 and 300 m and have been hydraulically connected by massive injections of both water and viscous gel (50 cpoise). Passive microseismic monitoring of the hydraulic stimulation and circulation experiments has been used since 1982 to determine the size and structure of the reservoir, and monitor its growth.

The active seismic survey techniques of cross-hole seismics and vertical seismic profiling (VSP) have been introduced to complement the passive microseismic monitoring in characterising the reservoir.

The cross-hole seismic surveys indicate that the microseismicity defines the area of joint dilation. The attenuation of high frequencies in the region of microseismicity suggests that the reservoir is composed of a complex zone of cracks rather than a single large fracture.

VSP surveys also show a good agreement between the the microseismically defined reservoir and seismic signal attenuation.

Recent improvements in hardware, computer processing and interpretation indicate that active seismics will play an increasingly important part in mapping and understanding geothermal reservoirs.

INTRODUCTION

The Camborne School of Mines (CSM) has been researching into hot dry rock (HDR) geothermal energy since the mid 1970's. The development of an HDR reservoir at 2 km depth has been underway since 1980. This has been designated Phase 2, Phase 1 being a 300 m system developed in the late 1970's. Phase 2 is split into Phase 2A and Phase 2B. Phase 2A comprised the drilling of two wells (RH11 and RH12) and the subsequent circulation of water between these two wells. Phase 2B commenced with the drilling of a third well (RH15) followed by the fracturing of this and the circulation of water between RH12 and RH15. Several aspects of the project have been presented at previous Stanford Workshops (Batchelor 1986, Pine 1984). These details will not be repeated here.

Phase 2A work started in 1981 with the drilling of wells RH11 and RH12 in a Hercynian granite to true vertical depths (TVD) of 2038 m and 2058 m. The wells have a maximum deviation of 30° at the base and a closest approach of 150 m in the uncased sections. During 18 months of fracturing and circulation, 300 000 m^3 of water was injected into the system and only 100 000 m^3 recovered. In the period in which 200 000 m^3 of water was lost 30 000 microseismic events were detected of which over 5000 were located. (Baria et al, 1985). The microseismic locations showed a systematic downward growth and suggest that this was where the lost water went (Pine and Batchelor 1984). This phase of the project was completed in 1983.

Phase 2B started in 1983 and involved the drilling of a third well.

Based on the analysis of the microseismic data a highly deviated third well (RH15) was drilled to a depth of 2653 m TVD, beneath RH11 and RH12 to intersect the region of seismicity. RH15 was drilled in 1984 with a gas (nitrogen) lift test run immediately. Flow logs run during the test showed that the only flowing zones were in regions where the well intersected microseismicity (Baria and Green 1986).

The hydraulic connection between RH15 and RH12 was still not adequate for a prolonged circulation to take place. A massive viscous injection of RH15 was designed to improve the hydraulic connection. The bottom 365 m of RH15 was sanded off so the hydraulic energy could be concentrated on a 146 m section of open well between the casing shoe and the top of sand. The injection took place on 4 July 1985 when 5500 m^3 of viscous gel (50 cpoise) was pumped into RH15 over an 8 hour period at an average flow rate of 198.2 l/s. This was followed by 200 m^3 of water. The peak wellhead pressure was 15 MPa during the viscous injection and 16.3 MPa during the water injection.

A total of 270 microseismic events were detected during the test of which 202 were located (Baria and Green 1986). The majority of the seismicity was detected during the first 2 hours, after which the event rate declined. The seismicity was located in a vertical tubular structure approximately 70 m by 70 m by 200 m encompassing a volume of 800 000 m^3.

The hydraulic connection between RH15 and RH12 (Phase 2B) was much better than that of the old RH11/RH12 system (Phase 2A). The hydraulic impedance reduced from about 1.9 MPa/l/s (RH11/RH12) to about 1.0 MPa/l/s (RH12/RH15) and the water losses in circulation reduced from 70% to 20%. The impedance has subsequently reduced to 0.6 Mpa/l/s.

It has been generally assumed that regions of seismicity define the areas of enhanced permeability. There has been some support for this from the comparison of the flow zones in RH15 and the Phase 2A microseismicity described above. However it is not clear whether there are aseismic areas were fluid flow and increased permeability also occur.

Active seismic surveys provide a means of determining the relationship between the hydraulic reservoir and the microseismic reservoir. The two techniques employed were cross-hole seismic surveys and large offset vertical seismic profiling (VSP).

Both types of surveys were performed in all three wells before and after the Phase 2B viscous injections. The collected data set is large and it is only proposed to examine a small part in this paper.

The VSP data collected after Phase 2A but before the Phase 2B viscous injection wil' be examined to determine the effect of the Phase 2A circulation.

The cross-hole data collected immediately before (pre-stimulation) and after (post-stimulation) the Phase 2B viscous injection will be compared to assess the affect of the injection.

VERTICAL SEISMIC PROFILES

Vertical seismic profiles were performed on all three wells (RH11, RH12 and RH15) after the fracturing and circulation between RH11 and RH12 (Phase 2A). These surveys were designed to image the Phase 2A reservoir and provide a base for surveys carried out later, after the Phase 2B viscous injection.

The surveys were large offset (2.4 km) surveys using 250 gm of explosive in a water filled quarry as a source. The receiver was a hydrophone with recordings taken every 2.5 m interval in the open hole sections (Figure 1).

The amplitude, velocity and frequency of a seismic wavelet are all sensitive to changing

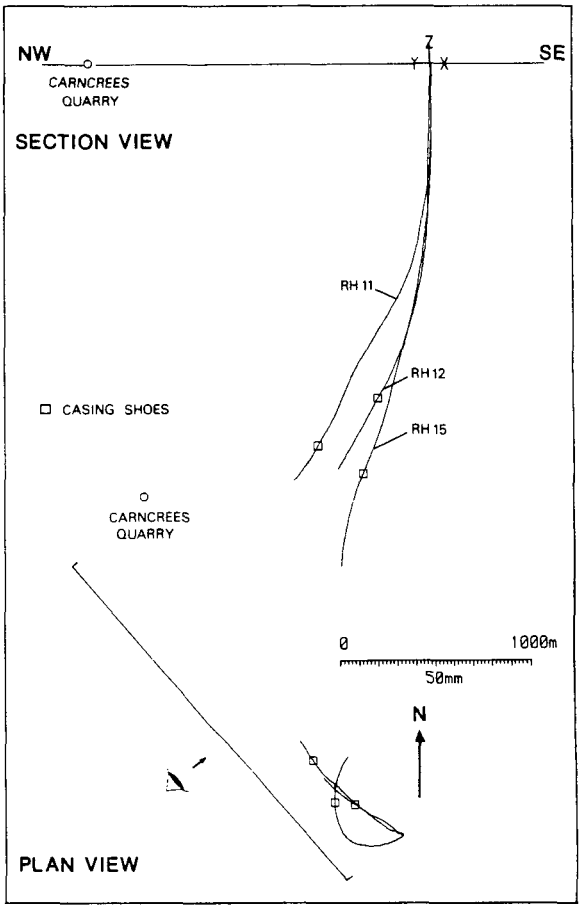


Figure 1. The locations of the three wells and the VSP source.

rock properties. The amplitude is a particular sensitive parameter, however a source with a consistent signature is necessary and borehole effects need to be taken into account.

The explosive source proved to have a very consistent source signature and the large distance from source to receiver meant that the ray angle to the borehole was similar for all hydrophone positions.

In order to compare the VSP results with the microseismic data a stimulation index was determined from the event locations. This is based on the number of events within 50 m of a straight line raypath between each shot and receiver position (CSM 1986, Hearn 1986). The distance of 50 m was based on the accuracy of the locations.

Seismograms with the stimulation index and first arrival amplitude curves for RH12 and RH15 are shown in Figures 2 and 3. The amplitude of the first arrival was determined from the signal envelope (Farnbach 1975).

The data for RH12 (Figure 2) can be divided into two groups; (i) above and (ii) below a measured depth (MD) of 2000 m. The data above

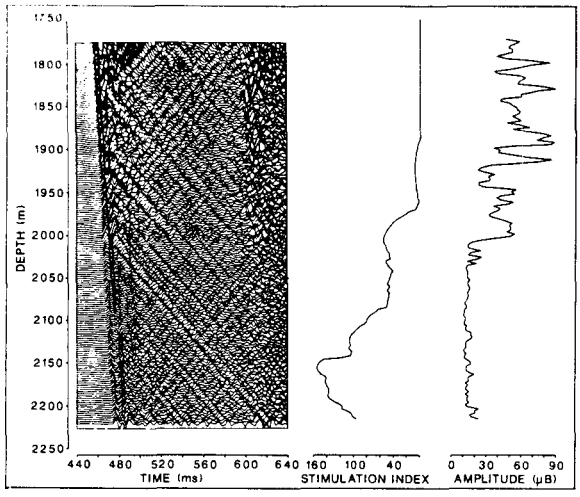


Figure 2. VSP results for well RH12.

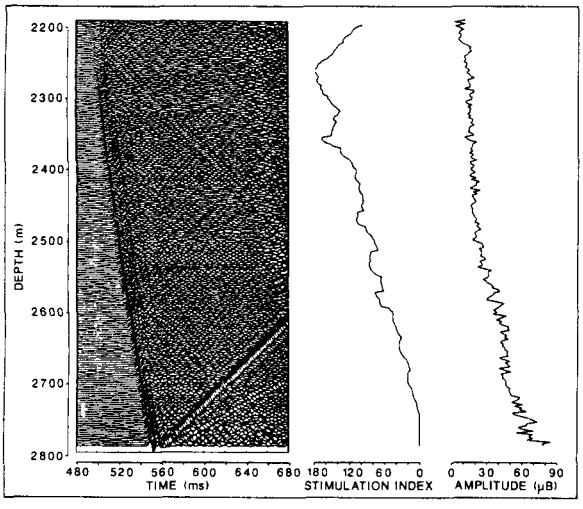


Figure 3. VSP results for well RH15.

2000 m MD show high amplitudes but with large variations, while the data below 2000 m MD shows only low amplitudes. The stimulation index shows that above 2000 m MD the rays passed through zones of low microseismicity but below 2000 m MD the rays pass through zones of high microseismicity. There is a good correlation between the attenuation and stimulation index. The variation in amplitude above 2000 m MD is probably caused by fractures close to the borehole wall.

Figure 3 contains the data for the VSP survey in RH15. The results show a smooth increase in the first arrival amplitude with depth consistent with gradual decrease in in the stimulation index.

The good correlation between the amplitude and stimulation index support the view that the microseismicity represents regions of stimulated rock and that aseismic ares have remained largely unaffected by the Phase 2A fracturing and circulation.

CROSS-HOLE SEISMIC SURVEY

The cross-hole seismic method, whereby seismic signals are transmitted between wells, has been in use for a number of years (Fehler 1982, McCann et al, 1986). The advantage over surface methods is that it avoids the weathered surface rocks which attenuate the high frequencies and reduce resolution.

The difficulties that have prevented its widespread application are the design of reliable and easy to use downhole sources and receivers. The CSM HDR project has designed and manufactured its own source and receiver. The source is a detonator tool holding up to 12 detonators. The receiver a high pressure marine hydrophone used both as a single unit and as part of a three hydrophone string.

The pre-stimulation survey was performed in May 1985, four months after the completion of RH15 and 2 months before the Phase 2B viscous injection. A total of 71 shots were fired with the detonator tool in RH15, the single hydrophone in RH12 and the three hydrophone string in RH11 (Figure 4).

The shooting in RH15 was started at the bottom. As the shot positions progressed up RH15 the hydrophones were kept stationary until the source and hydrophone in RH12 were at the same vertical depth. The hydrophone and source were then pulled up together to perform a horizontal scan. The three hydrophone string in RH11 was kept stationary throughout the survey.

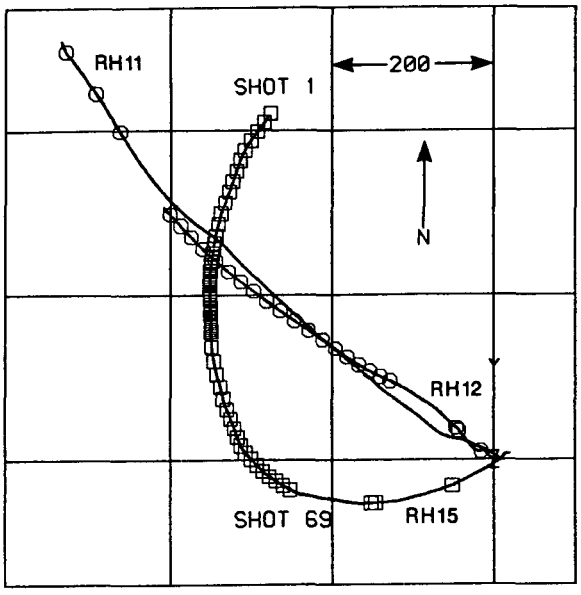
During the survey there was no wellhead pressure at RH15 or RH11 and only a small pressure on RH12 (0.2 MPa).

The post-stimulation survey was performed in November 1985, 6 months after the Phase 2B viscous injection. The deeper 59 shots of the pre-stimulation survey were repeated, a shortage of detonators preventing all the shots being repeated.

The wellhead pressure and injection flow rate at RH12 were maintained at over 6 MPa and 9 l/s for most of the period of the survey, so that the reservoir would be inflated. RH15 was shut in and maintained a wellhead pressure of between 6 and 7 MPa. RH11 was vented between 0.5 and 2 l/s.

As we have seen the amplitude was observed to be a sensitive measure of the rock properties in the VSP surveys. However the effect of the borehole wall on both the source and receiver in the cross-hole survey make it difficult to extract the part of the attenuation that is caused by joint dilation. The velocity and frequency variations have proved to be less ambiguous to interpret.

Figures 5 and 6 show the pre- and post-stimulation seismograms from the bottom hydrophone in RH11. The first arrivals have been



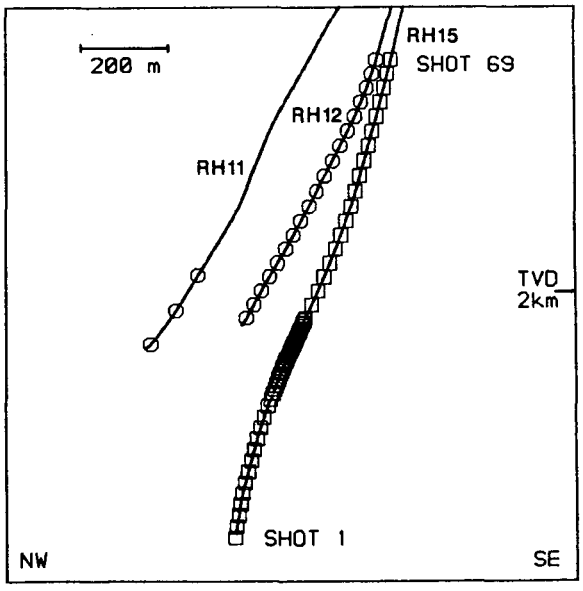


Figure 4. Source and receiver locations for the cross-hole seismic survey.

aligned and the amplitudes normalised for ease of display. Figures 7 and 8 show the frequency spectra for the same seismograms. It is clear that the energy in the 3 to 4 kHz band has been severely attenuated in the post-stimulation survey for shots shallower than 2480 m (shot 12) in RH15.

The same pattern is apparent for recordings on the other hydrophones in RH11. The recordings on the hydrophone in RH12 show attenuation of the high frequency energy for all shots.

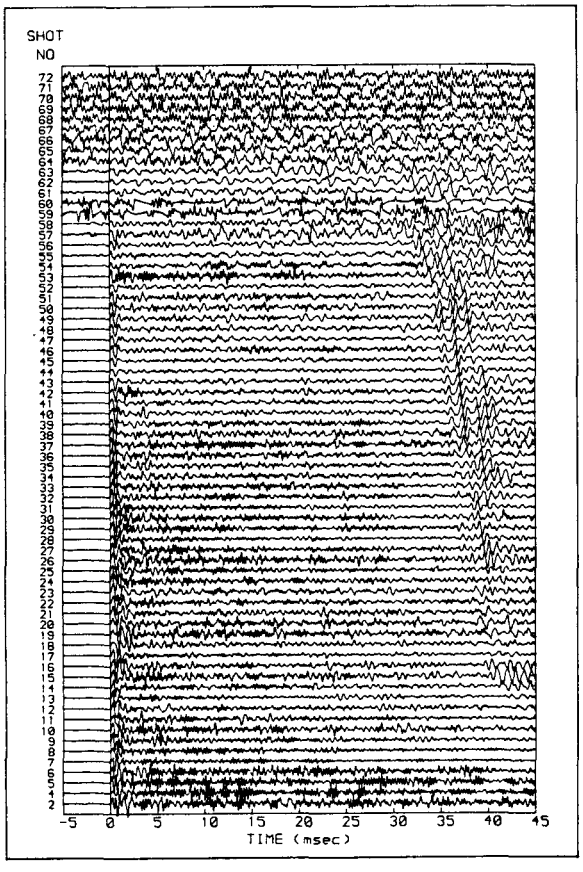


Figure 5. Pre-stimulation cross-hole seismiogram for the bottom hydrophone in RH11.

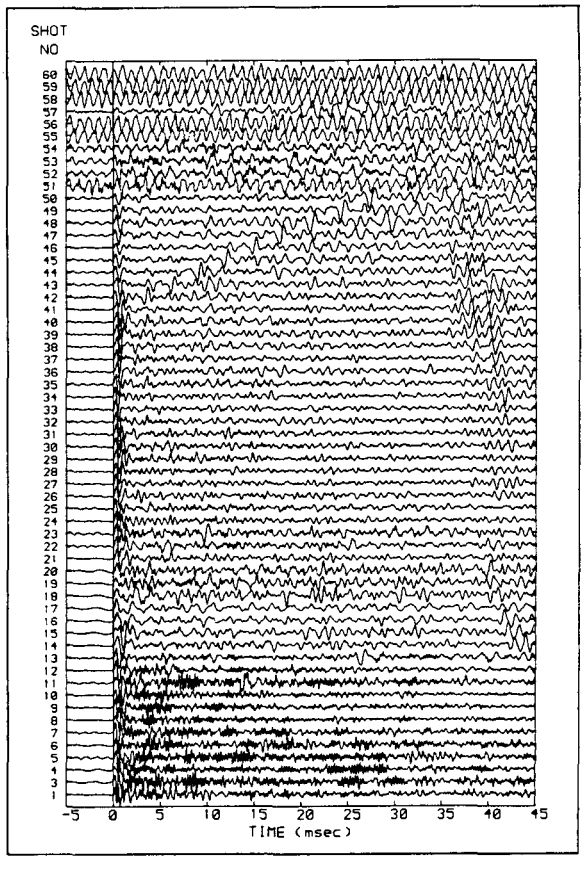


Figure 6. Post-stimulation cross-hole seimmogram for the bottom hydrophone in RH11.

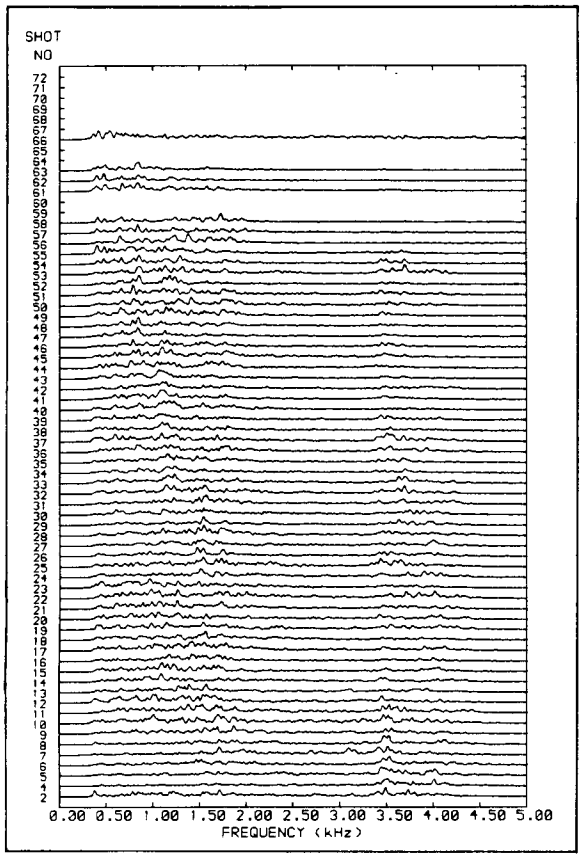


Figure 7. Frequency spectra of pre-stimulation cross-hole seismogram in Figure 5.

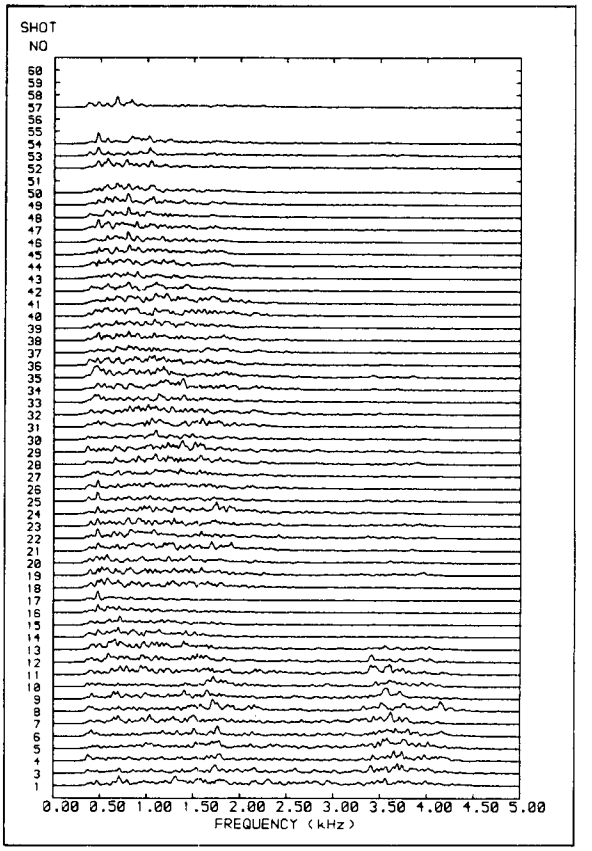


Figure 8. Frequency spectra of post-stimulation cross-hole seismogram - Figure 6.

Figure 9 shows the difference in compressional wave velocity between the pre and post-stimulation survey for the middle (hydrophone 2) and bottom (hydrophone 3)in RH11 and the hydrophone in RH12 (hydrophone 4). The top hydrophone in RH11 did not occupy the same position for both surveys, so a direct comparison cannot be made.

Figure 9 shows that for shot depths in RH15 shallower than 2500 m (shot 10) the compressional wave velocity recorded by the hydrophones in RH11 has been reduced by up to 0.05 km/s. The velocity recorded by the hydrophone in RH12 is reduced by as much as 0.07 km/s for all shots.

The attenuation of the high frequencies and the reduction of the compressional wave velocity can be understood if the ray paths for the surveys are superimposed upon the Phase 2B microseismicity generated during the viscous injection (Figures 10 and 11).

Figure 10 shows the ray paths for explosive shots in RH15 to the bottom hydrophone in RH11. The 10 rays from the deepest shots do not cross the microseismicity. It is these rays that show no attenuation of high frequency energy or velocity reduction. It can be shown that this is not due to a change in the shot characteristic by inspection of the ray paths to the hydrophone in RH12 (Figure 11). All the ray paths cross the microseismic cloud and all shots in the cross-hole survey show frequency attenuation and velocity reduction.

The microseismic events detected during Phase-2B were caused by shearing of natural joints within the granite (Baria and Green 1986). Shearing causes dilation of the joints and during pressurization of the system more fluid is stored in these joints. It is this joint dilation which is responsible for the high frequency attenuation and reduction in velocity.

The close correspondence between the microseismicity and the cross-hole data indicates that the regions of microseismicity have enhanced permeability and that furthermore the aseismic regions do not.

CONCLUSION

Cross-hole seismic and VSP surveys have shown that variations in the amplitude, frequency and velocity of a seismic signal can be used to define regions of enhanced permeability. These surveys indicate that reservoir growth during the hydraulic stimulation as monitored

by the generated microseismicity does represent regions of increased permeability. There is little evidence of aseismic reservoir growth.

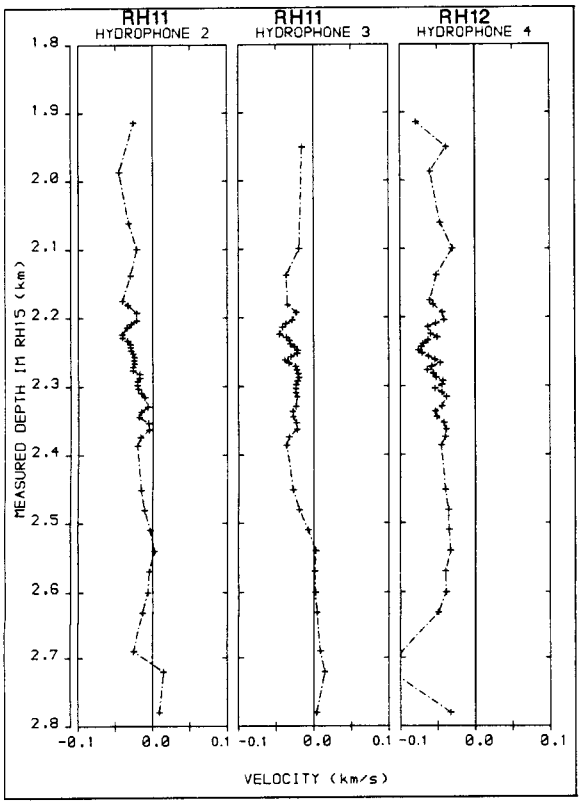


Figure 9. Difference in velocity for pre- and post-stimulation cross-hole surveys.

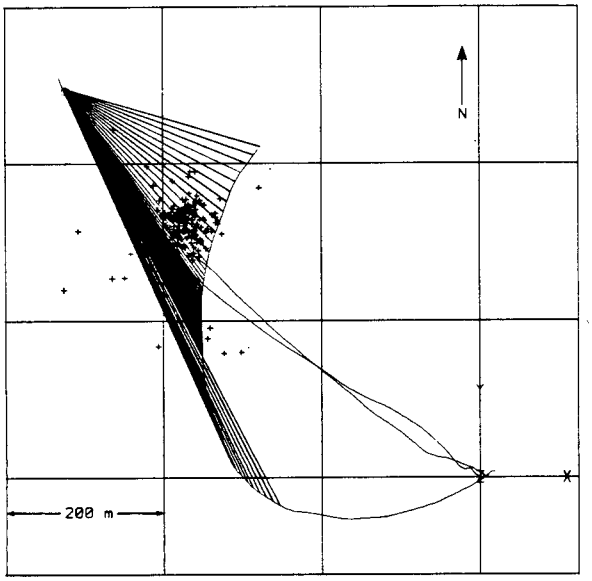


Figure 10. Raypaths from the shot in RH15 to the bottom hydrophone in RH11 (H3) with the seismicity generated during the Phase 2B viscous injection of well RH15.

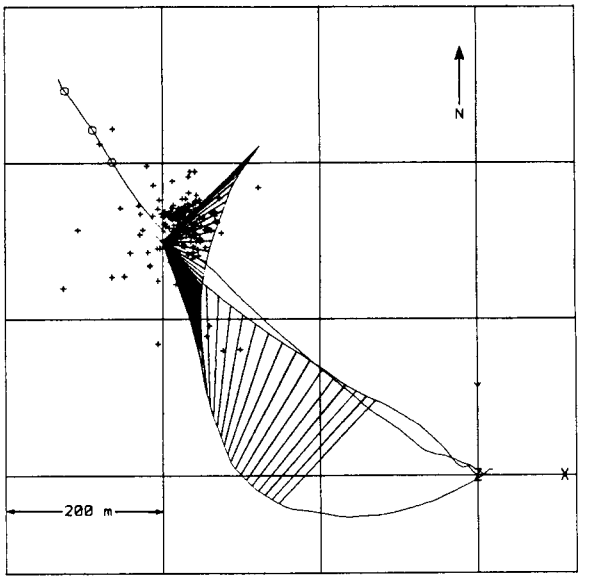


Figure 11. Raypath from the shot is RH15 to the hydrophone is RH12 (H4) with the seismicity generated during the Phase 2D viscous injection of well RH15.

Relatively simple analysis has shown that the active seismic surveys can play an important part in defining the shape of the reservoir and improving the interpretation of the microseismicity. The interpretation of active seismic data can be improved by the use of tomographic inversion algorithms. However the highly deviated nature of the wells makes the usual two dimensional approximation difficult to implement. To collect the large amounts of data that a full three-dimensional inversion would demand requires the development of new tools. Particularly important is a fast recycling downhole source with a consistent source signature. The CSM HDR project is developing such a source for use not only at 2 km but also in any future 6 km system.

ACKNOWLEDGEMENTS

This work was carried out under the contract to the European Economic Comminity and the United Kingdom Department of Energy contract numbers EG-D-2-003-UK(N), E/5A/CON/125/960 and E 5A/CON/137/1593. The support and encouragement of the staff of these organisations and the project is gratefully acknowledged.

REFERENCES

Baria R, Hearn K and Batchelor, (1985). The monitoring of induced seismicity during the hydraulic stimulation of the potential hot dry rock geothermal reservoir. In 4th conf on acoustic emission/microseismic activity in geological structures and materials, Penn State Univ, Oct 1985.

Baria R and Green A S P. (1986) Seismicity induced during a viscous stimulation at the

Camborne School of mines hot dry rock geothermal energy project in Cornwall, England. In Progress in acoustic emission III, proc 8 int acoustic emission symp., Tokyo, Japan, Oct 21-24, 1986.

Batchelor A S. (1986) Reservoir behaviour in a stimulated hot dry rock system. In 11th workshop on geothermal reservoir engineering, Stanford University, California, Jan 1986.

Camborne School of Mines Geothermal Energy Project. Vertical seismic profiling results. Phase 2 report, 1986, (in prep).

Farnbach J S. (1975) The complex envelope in seismic signal analysis. Bull seismol Soc of Am, Vol 65, No 4, pp 951-962.

Fehler M. (1982) Using dual-well seismic measurements to infer the mechanical properties of a hot dry rock geothermal system. J geophys Res, Vol 87, pp 5485-5494.

Hearn K. (1986) Application of surface to borehole seismic surveys to delineate a hot dry rock geothermal reservoir. In Society of professional well log analysts 10th European formation evaluation symposium, Aberdeen, 22-25 April, 1986.

McCann D M, Baria R, Jackson P and Green A S P. (1986) Applications of cross-hole seismic methods in site investigation surveys. Geophysics, Vol 51, No 4, pp 914-929.

Pine R J. (1984) Pressure transient analysis for large scale hydraulic injections in the Carnmenellis granite, England. In 9th workshop on geothermal reservoir engineering, Stanford University, California, Dec 1983.

Pine R J and Batchelor A S (1984), Downward migration of shearing in jointed rock during hydraulic injections. International Journal of Rock Mechanics Mining Sciences and Geomechanical Abstracts. Vol 21, No 5, pp 249-263.

PROCEEDINGS, Twelfth Workshop on Geothermal Reservoir Engineering
Stanford University, Stanford, California, January 20-22, 1987
SGP-TR-109

SENSITIVITY ANALYSIS OF DUAL-PERMEABILITY SYSTEMS

Laurence C. Hull and Tom M. Clemo

Hydrology Unit
Idaho National Engineering Laboratory

ABSTRACT

The substitution of matrix permeability for fracture permeability to simplify the simulation of complex fracture systems requires a radically different treatment of transport in the matrix. The spatial distribution of pressure is reasonably well described by inclusion of only the major fractures. Transport of tracer and heat, however, depends on a detailed knowledge of fluid velocities. These velocities are dependent on the active porosity of the system. Because fractures channel flow, the active porosity may be much smaller than the total porosity of the system. Characterization of this active porosity is necessary to quantify tracer and heat movement.

INTRODUCTION

Simulation of complex geothermal reservoirs is frequently accomplished by substituting matrix permeability for fracture permeability. This results in a saving of computer resources and permits the simulation of larger and more complex fracture systems. The substitution of a continuum to represent fracture permeability involves a number of assumptions which must be evaluated. Development of continuum properties for representation of discrete fracture systems is an area of active research. Studies have been conducted by Clemo (1986), Dershowitz (1984), Endo et al., (1984), Long and Witherspoon (1985), and Schwartz and Smith (1983).

The more intersections between fractures in a fracture network, the more the system is likely to behave as a porous medium. On a large scale (reservoir scale) an equivalent hydraulic response can be obtained by using an appropriate hydraulic conductivity. Transport depends on a detailed knowledge of fluid velocities, not just fluxes. As a result, the pore volume of the system involved in the movement of water must be well characterized. One method of treating transport is through the development of an active porosity. The active porosity may be much less than the total porosity of the system due to fracture orientation and preferred flow paths.

A dual-permeability model was used to study the effects of replacing fracture permeability with matrix permeability. The dual-permeability approach is uniquely qualified for this type of study because the replacement can be performed gradually so that the cumulative effects can be evaluated. This paper illustrates the effects of replacing discrete fracture permeability with matrix permeability on spatial pressure distribution and tracer transport. The effects on heat transfer are also considered.

CODE DESCRIPTION

The study was conducted using the FRACSL code developed at the Idaho National Engineering Laboratory (Miller, 1983; Clemo and Hull, 1986). The code simulates flow in porous matrix blocks and discrete, parallel sided fractures. Transport processes included are advection, diffusion, dispersion, and diffusion from the fracture into the surounding matrix. For this study, simplified heat transport capabilities were added to the code. Heat transport by advection and conduction are computed. All boundaries are considered perfect insulators and there is no coupling of flow with thermal effects.

SYSTEM DESCRIPTIONS

The system studied consists of an injection and a production well in a geothermal reservoir 1200 m long and 90 m high. The simulation is two-dimensional and a slice of unit thickness through the reservoir assumed. Fluid properties used were those for 175°C. Six variations were simulated. The base system is a fracture network consisting of 22 fractures (Figure 1). Three

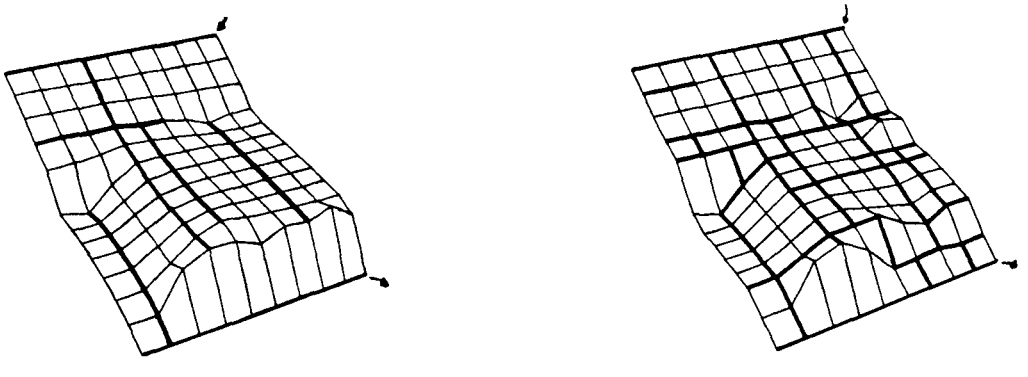
Table 1. Summary of characteristics of the six dual-permeability systems simulated.

System	Description	Number of Fractures	Connecting Paths	Hydraulic Conductivity (m/day)	Active Pore Volume (%)
1	Matrix only	0	0	7.9	108
2	No fracture connection between wells	5	0	0.78	78
3	One cross connection between wells	10	4	0.42	36
4	Several connections between wells	14	12	0.18	44
5	Full network	22	21	0.009	40
6	Single fracture	1	1	0.009	16

additional fracture networks were derived from the base system by removing fractures from the system, starting with the smallest fractures. This created four fracture systems of differing complexity. A fifth system was created which consists entirely of porous matrix. The sixth and final system is a single fracture connecting the injection and production wells.

System 5 was defined as the base case and the other systems were derived from System 5. Table 1. shows the characteristics of the six systems. All the systems have the same effective hydraulic conductivity. For the same steady-state injection and production rates, the pressure difference between injection and production wells is identical. This is accomplished by increasing matrix permeability as fractures are removed from the system. For System 6, the matrix permeability was set equal to that for System 5 and the aperture of the single fracture adjusted until the pressure difference matched that of System 5.

The porosity of the fracture system, calculated by dividing the volume of fractures by the total volume of the reservoir, is 10^{-4}. Therefore, the matrix porosity of the systems was set to 10^{-4} to mimic that of the fracture system. This small matrix porosity was used so that the matrix flow rates would be similar to flow rates in the fracture system. One consequence of this very small matrix porosity is that diffusion of tracer into the matrix is essentially prevented. Tracer can, however, advect into the matrix for the systems with significant matrix permeability.



System 2, No fracture connections

System 5, Full fracture network

Figure 1. Steady-state pressure distributions for dual-permeability fracture networks. The networks are shown as darker lines on the grid representing the pressure distribution.

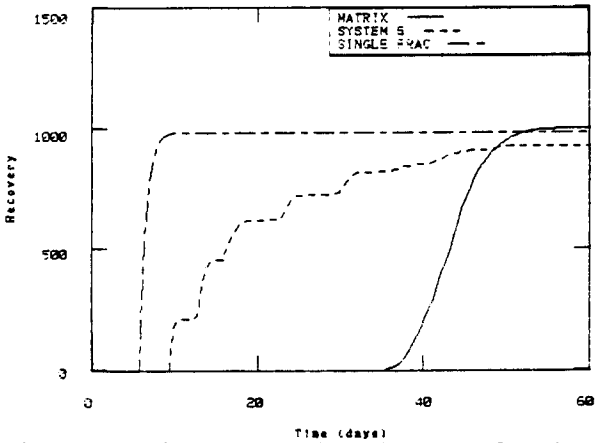


Figure 2. Tracer breakthrough curves for the single fracture, full fracture network, and the porous matrix representation of the geothermal reservoir. One-thousand particles were injected.

The active pore volume shown in Table 1 is the ratio of pore volume calculated from tracer breakthrough to total system pore volume. Tracer breakthrough pore volume is calculated from the volume of fluid which had been pumped at the time 50% of the injected tracer had been recovered. For the single fracture representation of the reservoir, only a very small volume of the system is actively involved in solute transport. For the porous matrix representation, the entire system participates in solute transport. The various fracture systems have an intermediate value for active porosity.

SIMULATION RESULTS

Simulations for each of the six systems provided steady-state pressure distribution, tracer breakthrough, and distribution of the thermal front.

Pressure Distribution

The steady-state pressure distribution for Systems 1 and 6 showed a uniform, featureless pressure decline from the injection well to the production well. The fracture networks, however, showed spatial variations in pressure due to the distribution of fractures. The spatial variations in pressure are very similar for all of the fracture networks (Figure 1). This indicates that only the largest, most significant fractures need be included in a simulation to obtain a reasonable estimate of spatial pressure distribution. As a result, the general distribution of flow in the systems should be fairly similar. This similarity requires replacing the smallest fractures with matrix and explicitly simulating the larger fractures. The more dominant effects of the major fractures must be retained.

Tracer Transport

The method of representing permeability has a tremendous effect on tracer transport. Figure 2 shows tracer breakthrough for Systems 1, 5, and 6. The concept of active porosity is most easily demonstrated with this figure. For the single fracture, all fluid moves along a single path which encompasses a very small volume of the reservoir. As a result, tracer breakthrough occurs rapidly and is distributed over a very short time interval. On the other hand, the entire volume of the reservoir is swept by the tracer when a porous matrix representation is used. Thus the active porosity is a maximum, and the arrival of the tracer takes the longest time. Because flow is uniformly distributed over the reservoir, the distribution of arrival times is very clustered, and the breakthrough curve is fairly steep.

For the fracture network, an intermediate breakthrough curve is obtained. Some tracer arrives fairly rapidly, moving along the most direct discrete fracture pathway. Other tracer moves along less direct pathways and takes a longer time to arrive at the production well. Because of the wide distribution of flow rates in the many fracture flow paths, the distribution of tracer arrival times is very broad.

Breakthrough curves are more similar for the three systems where a fracture connection between the injection and production wells was retained (Figure 3). Small differences exist due to the number of connecting paths and the replacement of discrete fracture pathways with porous matrix. The general shape of the breakthrough curves is similar because most of the tracer still travels through the fracture system. The tail on the breakthrough curves for Systems 3 and 4,

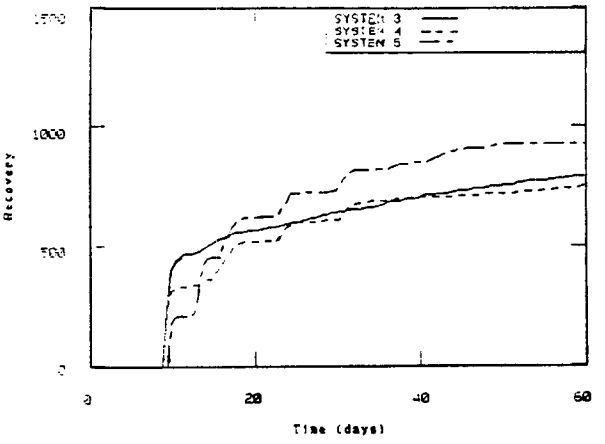


Figure 3. Tracer breakthrough curves for three fracture networks which retain a discrete connection between the injection and production wells but which have different matrix conductivity.

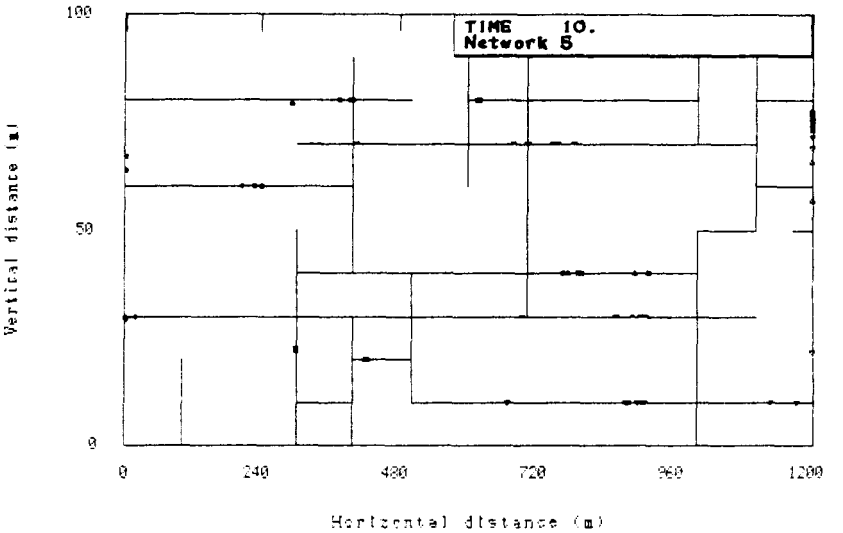


Figure 4. Spatial distribution of tracer remaining in System 5 at 10 days.

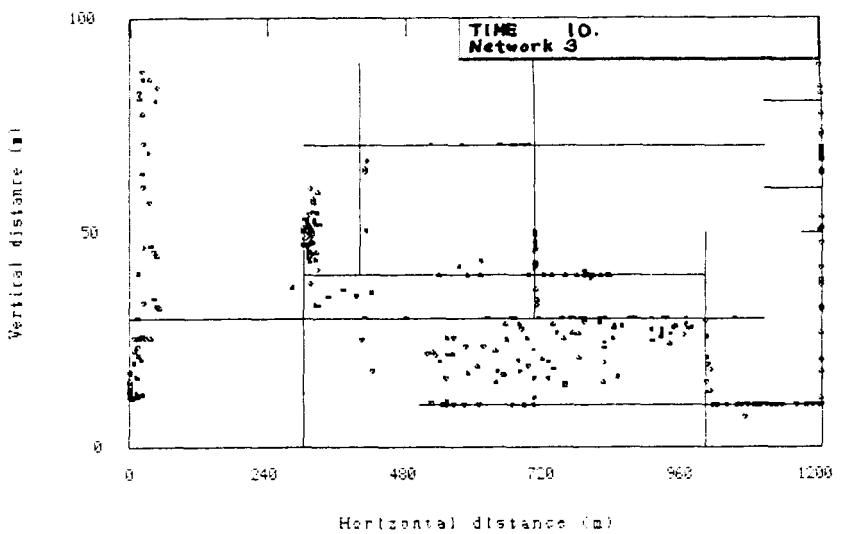


Figure 5. Spatial distribution of tracer remaining in System 3 at 10 days.

however, is much longer than the tail for System 5. This is because significant matrix permeability in Systems 3 and 4 results in tracer entering the matrix. Even though the matrix porosity is 10^{-4}, there is a significant increase in the residence time of tracer in the reservoir. Thus, simply using a matrix with a small porosity to represent fractures may not be sufficient.

The increase in active porosity is shown by comparison of Figures 4 and 5. These figures show the spatial distribution of tracer 10 days into the injection test. For System 5 (Figure 4), the tracer has remained in the fractures and the matrix does not participate in the movement of tracer. Figure 5 shows the distribution of tracer for System 3, which has significant matrix permeability relative to System 5. In this case, tracer moves from the fractures through the matrix. This matrix increases the residence time of the tracer that travels by these paths.

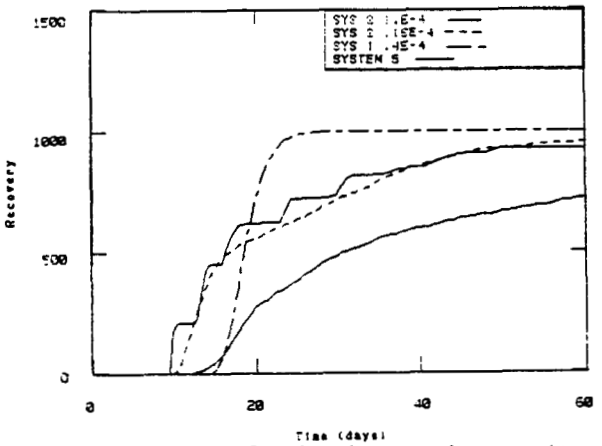


Figure 6. Effect of adjusting matrix porosity to match active porosity estimates on tracer breakthrough.

The effect of fractures on channeling flow through the system can be seen in Figure 5. Tracer is not uniformly distributed throughout the matrix, but is confined to matrix in a few areas between fractures. The rate of tracer movement is not dependent on the pore volume of the entire reservoir, but on the porosity of a fraction of the reservoir. This fraction of the reservoir which is actively involved in the transport of tracer is the active porosity. The active porosity for this reservoir is on the order of 40% for tracer transport (Table 1).

When fracture permeability was replaced with matrix permeability, the active porosity of that part of the system was increased. Based on the results from System 6, a single fracture has an active porosity 0.16 times the total porosity. As most matrix blocks

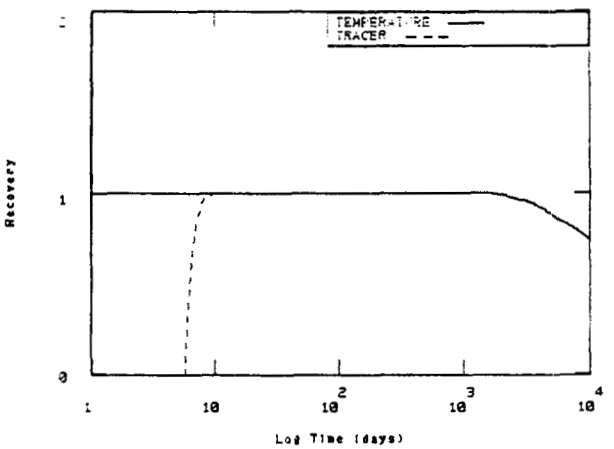


Figure 7. Comparison of tracer and thermal breakthrough for a single fracture connecting an injection and production well.

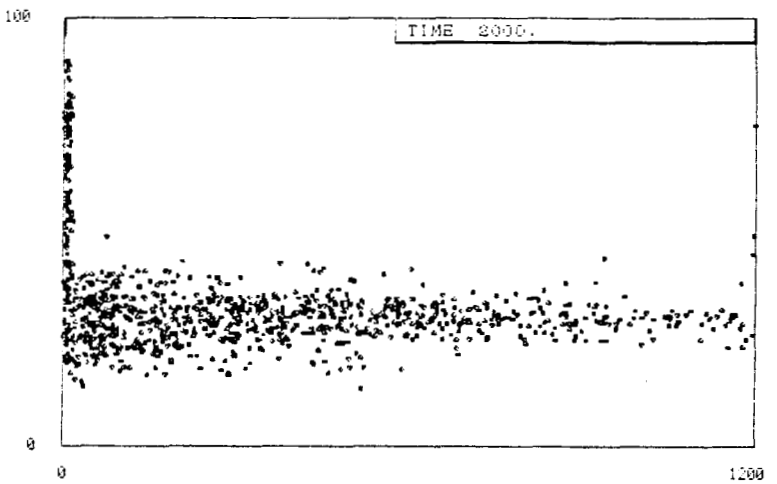


Figure 8. Spatial distribution of cooling in the geothermal reservoir at 2000 days due to injection for flow through a single fracture. Vertical spreading of the thermal front is exagerated by a factor of 7.4.

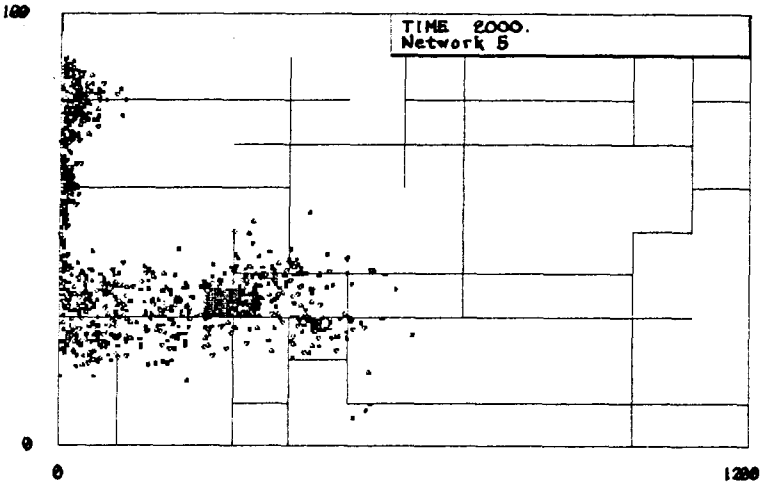


Figure 9. Spatial distribution of cooling in the geothermal reservoir at 2000 days due to injection in the fracture network.

represent the replacement of a single fracture, using a matrix porosity of $1.0X10^{-4}$ may overestimate the active porosity by a factor of 6.25. System 2 was resimulated using a value of $0.16X10^{-4}$ for the matrix porosity to determine if the active porosity did a better job of emulating the full network. The active porosity for the entire reservoir, based on Systems 3, 4, and 5, is on the order of 40%. System 1 was resimulated using a porosity of $0.4X10^{-4}$ to match the active porosity of the fracture networks.

Figure 6 shows the effects of using the active porosity to simulate transport in the matrix rather than the total porosity. Using an active porosity of $0.16X10^{-4}$ in System 2 resulted in a tremendous improvement in matching the response of the full fracture network. Using an active porosity for the full matrix representation improved the match to the mean arrival time, but the breakthrough curve has the wrong shape. Too much information on the flow system was lost when all the fracture permeablitity was replaced with matrix permeability. When the major fractures were explicitly considered, sufficient information on the flow system remained to achieve a good match between the full fracture system and a system where most of the fracture permeability had been replaced with matrix permeability.

Thermal Response

As used for these simulations, the code does not take into account the effects of density differences between fluids. Simple calculations indicate that density differences can induce pressure differences as large or larger than those developed from the flow alone. Therefore, the results presented here are more applicable to the phenomenon of heat conduction from the fracture to the matrix than for reservoir scale transport.

The time required for the system to respond thermally is much greater than the time required for the system to respond to tracer injection. This difference is attributable to two differences between tracer and heat. Diffusion of tracer into the matrix is dependent on the open porosity of the matrix and on the diffusion coefficient of the tracer. Both these numbers are very small. The diffusion of heat into the matrix (conduction) is dependent on the heat capacity of the matrix and on the thermal diffusivity of the rock. These number combine to give a factor about three orders of magnitude greater for thermal conduction than for tracer diffusion.

Figure 7 shows the difference in time for tracer breakthrough and thermal breakthrough to occur for the single fracture. The time scale is logarithmic to accommodate the large difference in breakthrough times. Figure 8 shows the portion of the reservoir that has cooled at a time 2000 days after injection began. Only a small fraction of the reservoir is participating in the reheating of the injected fluid. Figure 9 shows the portion of the reservoir that has cooled after 2000 days for the full fracture system. The cooling front has moved only about one-third of the distance across the reservoir. This shows that the front will progress at a rate roughly proportional to the active porosity of the reservoir. The active porosity of System 5 is about 2.5 times the active porosity of System 6. If this is indeed the case, then the information on active porosity obtained from tracer testing will be very applicable to prediction of thermal breakthrough.

For the porous matrix representation of the reservoir, System 1, the thermal front progresses very slowly away from the injection well. This slow rate of movement is due to the complete extraction of heat from the reservoir rock. Use of the porous matrix representation of the reservoir would greatly overestimate the time for thermal breakthrough to occur.

CONCLUSIONS

Simulations were conducted of six representations of a geothermal reservoir. The systems differed with respect to the number of fractures, the connectivity of the fracture system, and the permeability of the matrix material. Steady-state pressure response and tracer breakthrough were calculated for each of the systems. Very good agreement was obtained between dual-permeability representations of fracture networks and the fracture network when active porosity was used in the matrix elements.

Thermal response of the single fracture, the complete fracture network, and of the porous medium system were calculated. Thermal breakthrough in the single fracture case occurred after some 2000 days of injection while tracer breakthrough occurred within a few days. The rate of advance of the thermal front seems to be related to the active porosity of the system. If this is the case, then active porosity determined from tracer tests will be a useful tool in calculating thermal breakthrough.

ACKNOWLEDGEMENTS

Funding for this study was provided by the U. S. Department of Energy, Geothermal Injection Technology Program, under contract DE-AC07--76ID01570.

REFERENCES

Clemo, T. M., Representative Element Modeling of Fracture Systems Based on Stochastic Analysis, Eleventh Workshop on Geothermal Reservoir Engineering, Stanford University, January, 1986.

Clemo, T. M., and L. C. Hull, FRACSL Code Status and Verification Studies, in: Geothermal Injection Technology Program Annual Progress Report, FY-85, EGG-2445, pp. 18-34, 1986.

Dershowitz, W. S., Rock Joint Systems, Unpublished Ph.D. Thesis, Massachusetts, Institute of Technology, Cambridge, MA, 1984.

Endo, H. K., J. C. S. Long, C. R. Wilson, and P. A. Witherspoon, A Model for Investigating Mechanical Transport in Fracture Networks, Water Resources Research, 20, 10, pp. 1390-1400, 1984.

Long, J. C. S., and P. A. Witherspoon, The Relationship of the Degree of Interconnection to Permeability in Fracture Networks, Jour. of Geophysical Research, 90, B4, pp. 3087-3098, 1985.

Miller, J. D., A Fundamental Approach to the Simulation of Flow and Dispersion in Fractured Media, Ninth Workshop on Geothermal Reservoir Engineering, Stanford University, December 1983.

Schwartz, F. W. and L. Smith, Stochastic Analysis of Macroscopic Dispersion in Fractured Media, Water Resources Research, 19, 5, pp. 1253-1265, 1983.

PROCEEDINGS, Twelfth Workshop on Geothermal Reservoir Engineering
Stanford University, Stanford, California, January 20-22, 1987
SGP-TR-109

Two Phase Streaming Potentials

S. S. Marsden
Pet. Eng. Dept., Stanford University

M. W. Wheatall
ARCO International

ABSTRACT

The streaming potentials generated by the flow of both liquid and gas through either a Pyrex capillary tube or else an unconsolidated Pyrex porous medium were investigated. This mixture of distilled water plus nitrogen gas simulated wet steam but allowed experiments to be run at room temperature.

Single-phase flow of distilled water alone resulted in a constant voltage-to-pressure drop ratio, $E/\Delta p$, of +0.15 v/psi for the capillary tube and -0.52 v/psi for the porous medium. For both single- and two-phase flow through the capillary tube, the upstream potential was always positive relative to the downstream electrode while the opposite was true for the porous medium. The maximum two-phase potentials generated in the porous medium were about four times as great as those generated in the capillary tube for similar gas fractions, Γ.

For the capillary tube experiments the potentials generated when $\Gamma < \approx 0.5$ were equal to or slightly less than those for single-phase flow, while for the porous medium the potentials were always greater than those for single-phase flow. When $\Gamma > \approx 0.5$ for both kinds of flow systems Γ had a profound effect on streaming potential and reached a pronounced maximum when $0.94 < \Gamma < 0.99$. The implications of these streaming potentials for geothermal exploration and delineation of geothermal reservoirs is also discussed in the paper.

INTRODUCTION

The streaming potenial (or electrokinetic potential as it is more commonly known these days) is a voltage difference generated when a fluid flows through an electrically non-conducting conduit such as a tube or a porous medium. It has been recognized and studied in the field of colloid science for almost a century and to a limited extent in petroleum engineering research because of the contribution it is believed to make to the SP log. It is of considerable interest elsewhere in the petroleum industry because of its being the source of ignition for many loading terminal and tanker explosions and fires (Klinkenberg and van der Minne (1958)) Attempts have also been made to use it to monitor the progress of steam and fire fronts in enhanced oil recovery projects (Dorfman et al. (1977) and in the prediction of earthquakes (Corwin and Morrison (1977)). The relationship between self-potenial anomalies and buried geothermal resources have been well documented in a number of papers by Ishido et al. (1983).

Many years ago we studied the streaming potentials generated by the flow of aqueous foams in Pyrex capillary tubes (Raza and Marsden (1967)) and of O/W emulsions in the same kinds of conduits (Dowdle and Marsden (1974)). More recently we have described the streaming potentials produced by the flow of wet steam in Pyrex capillary tubes (Tyran and Marsden (1985) and Marsden and Tyran (1986)). In this latter work we showed that while dry steam produced no measurable potential (as was expected), wet steam generated potentials up to and greater than 100v. These potentials increased with time and probably would have eventually reached greater values if the electrodes had not been intentionally shorted out in order to keep the recorder on scale. They also increased with pressure drop and flow rate but in an unknown and non-linear manner.

While the studies of Tyran and Marsden established that on a laboratory scale wet steam flow generated streaming potentials, the parameters describing the phenomenon were not well defined. It was expected that the volumetric vapor fraction of the steam, Γ, would be important but the difficulties of both maintaining it constant, measuring it accurately and operating at elevated temperatures had already become apparent. Hence, we decided to go to a simulated wet steam which consisted of a reasonably uniform dispersion of nitrogen gas, N_2, in distilled water and with all experiments being done at room temperature. With this arrangement, we were able both to control and to measure Γ to an accuracy of two decimal places. Pressure drop and hence flow rate were both variable and also reasonably well controlled.

In addition, a porous medium consisting of crushed, sieved Pyrex glass contained in a Pyrex tube could be easily substituted in the equipment in place of the capillary tube.

It should be noted that in all of this work we follow the convention that has become established for foam in the petroleum industry of using the volumetric fraction, Γ, and referring to it as steam quality rather than the terminology of using mass fraction of vapor which is widely used in industry.

Experimental

Both the flow conduit and pressure transducer as well as the electrical system were the same as those described earlier by Tyran and Marsden (1985) but the steam generator was replaced by a N_2 tank plus a distilled water reservoir to which N_2 pressure could be applied as a driving force. Also the previous steam flow rate measuring components were replaced with a graduated cylinder for the water followed by a soap-film flowmeter for the gas. A schematic diagram of the equipment is shown in Fig. 1.

Flow Conduits and Fluids

The ends of the capillary tube in the earlier runs or the glass tube containing crushed Pyrex in the later runs were sealed in especially made teflon manifolds, which also had pressure taps, and for the upstream end a N_2 inlet as

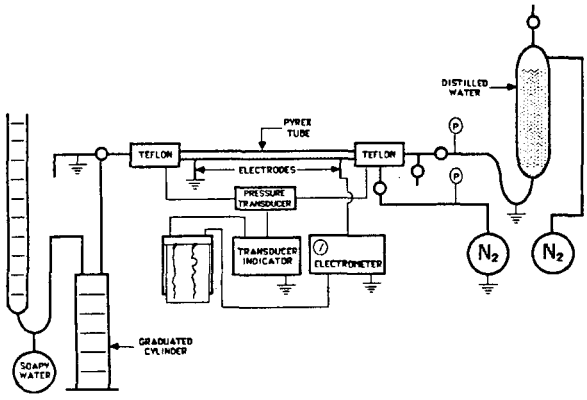


Figure 1: Schematic diagram of the streaming potential apparatus

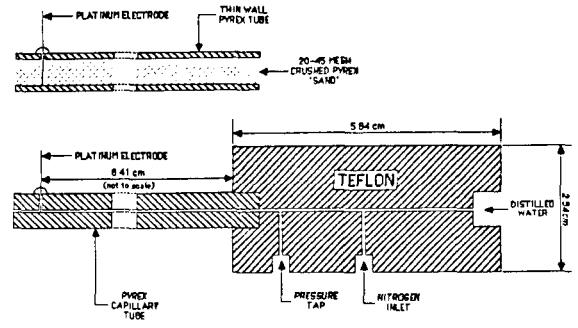


Figure 2: Teflon manifold and Pyrex tubes

well. The OD of both capillary tube and glass tube were almost the same so one manifold was used in both cases. A diagram is shown in Fig. 2. Holes for the Pt electrodes were drilled in both kinds of Pyrex tubing by using a fine diamond tipped jewelers drill. The Pt wires, which had been salvaged from a damaged ring of a duNuoy surface tensiometer, were carefully sealed in place with epoxy resin cement.

The water was distilled and run through the deionizing resins of a Corning Model LD-5A purifier before being stored in a large sealed Pyrex bottle for the short time before use. Its conductivity was measured with a calibrated dip cell and a L & N Model 4866 conductivity bridge.

The capillary tube had a length of 91.3 cm, an OD of 0.803 cm and an ID of 0.775 mm. These dimensions were determined with a meter stick and a micrometer and by weighing a measured column of mercury contained in the tube. The glass tube containing the crushed Pyrex had the same length, an OD of 0.808 cm and an ID of 0.597 cm, both measured with a micrometer. The porous medium was obtained by crushing and sieving another identical, thin-well Pyrex tube to produce a "sand" of 20-45 mesh. In both cases the Pt electrodes were 72.5 cm apart.

Electrical System

The streaming potential was measured with the same Keithley Model 610A high impedence electrometer used earlier by Raza and Marsden (1967) and by Tyran and Marsden (1985). The electrometer output was connected to the second channel of a two-channel Kipp and Zonen Model BD9 chart recorder. Both electrometer and recorder were calibrated with a H-P Model 6215A power supply and a Model 3465A multimeter. The upstream electrode was connected to the electrometer via a Keithley Model 6101A shielded test lead while the downstream electrode was grounded.

Pressure Measuring System

Pressure taps in the two teflon manifolds were 92.5 cm apart and were connected via 1/16 in. OD polyethylene tubing to a Celesco Model KP-15 differential pressure transducer. This was fitted with the 25 psi stainless steel diaphragm and connected to a Celesco Model CD 25A transducer indicator whose output was connected to channel one of the Kipp and Zonen chart recorder. The combination was calibrated with a 30 psi Heise bourdon tube pressure gage.

Flow Rate System

The N_2-water mixture exiting from the outlet manifold went via surgical tubing through a two-holed neoprene stopper into a 50 cc graduated cylinder. The N_2 coming out of the latter went to a 100 cc burette serving as a soap film flowmeter. The former, of course, measured the aqueous flow rate and the latter the total flow rate (water plus gas) so the ratio gave the complement of the gas volumetric fraction, Γ.

Cleansing of the System

The upstream end of the flow system up to the inlet manifold consisted of a 1-l.#316 stainless steel water reservoir and associated tubing which was cleansed by filing successively with 70 wt. % HNO_3, 37 wt. % HCl, acetone and soapy water, with distilled water flushes in between. The exterior surfaces of the glass components and the electrodes were also carefully rinsed with acetone, soapy water and distilled water and then carefully dried.

Making the Runs

Water deliberately left in the system at the end of the previous runs was flushed out and the reservoir refilled with newly distilled water whose resistivity and temperature was measured at first and again at the end of the run. With the flow conduit empty of liquids, the electrodes were shorted briefly and both chart zeros adjusted here and also when flow ceased during and at the end of the runs. After emptying the graduated cylinder and wetting the burette walls with soapy water, the flow was ready to begin.

After water flow was started, N_2 was admitted to produce a steady two-phase flow. A fine dispersion of bubbles in water rather than slug flow was determined visually. While the electrical potential and pressure drop were being recorded automatically, both liquid and total fluid rates were being measured by noting volumes and using stop watches. Only when all four quantities remained reasonably constant and when the pens returned to zero after flow stopped, were the results accepted as being valid.

RESULTS AND DISCUSSION

While the experiments of importance involved the flow of N_2 plus distilled water in either the capillary tube or else the porous medium, it was also essential to carry out preliminary experiments with water alone both to check the performances of the equipment and to see if the results are in agreement with what was expected. In all cases no attempt was made to control temperature and so the measurements were made at "room temperature" and downstream

pressure was atmospheric. Nominal variations of both were expected to have no significant effect on the results obtained.

Capillary Tube, Single Phase Flow

As was expected, a linear relationship between pressure drop, Δp, and flow rate, q, was found for a dozen or so measurements. All flow rates were calculated to fall well within the viscous flow regime. In all cases the upstream electrode was found to be positive with respect to the downstream one. A graph of pressure drop, Δp, vs streaming potential, E, is shown in Fig. 3 and while there is a linear relationship, it does not go through the origin as would be predicted by the Helmholtz-Smoluchowski Equation. Most other studies similar to this one have verified the linearity and have shown similar finite intercepts for liquids having little or no electrolyte dissolved in them. This is believed by Overbeek and others to be due to the contribution made by the surface conductivity of the glass when the liquid conductivity is extremely low as it is here. Everything considered, the results were believed to be acceptable and warranted our going on to the two-phase flow measurements.

Capillary Tube, Two-Phase Flow

By careful adjustment of the N_2 regulator, stable flow of both fluids was achievable over most of the Γ range. A two-phase, Reynolds number calculation using an apparent viscosity showed that all flow should have been well within the laminar regime. Again the upstream electrode was positive.

While the pressure remained steady over the course of a run, the fluctuations in the streaming potential increased as Γ did. It was observed that these fluctuations were associated with slugs of bubbles going through the tube and that this led to a momentary increase to a higher potential. This was probably due to increased electrical resistivity of the system as a result of the non-conducting gas bubbles and therefore a momentary decrease in the conduction current. The maximum electrical potential usually had about the same value and we designate it as as E_{max} while E is simply the time averaged potential. The difference between the two values of potential was generally less than 10% and graphs of both vs Γ were very similar in their various features. Throughout this report we shall simply deal with E.

A graph of E vs Γ is presented as Fig. 4. The octagon symbols used for the data points represent the calculated uncertainty in the points based on an error analysis. Although most points were taken at 10 psi, pressures ranged from 6 to 10 psi. The four data points for $0 < \Gamma \leq 0.05$ had the greatest scatter because they are for almost single-phase flow and here the flow is a strong function of pressure. For higher values of Γ up to about 0.4 the streaming potential is essentially constant. Here the N_2 flow rate was more easily controlled because there was more of it than at the lower values of Γ.

The first two-phase effects were noticed at $\Gamma \approx 0.5$, where the E rose slightly and then declined linearly (slope ≈-1) until $\Gamma \approx 0.75$. This may have been due to a decrease in flow rate at essentially constant pressure because of gradually increasing effective viscosity of the two-phase mixture. No data could be obtained for $0.79 <= \Gamma \leq 94$ because the flow was very unstable in this region.

The flow restabilized at $\Gamma \approx 0.94$ and E increased rapidly to a peak at $\Gamma \approx 0.98$. Here there is still enough water flowing to produce the convection current but the increasing concentration of N_2 increased electrical resistivity

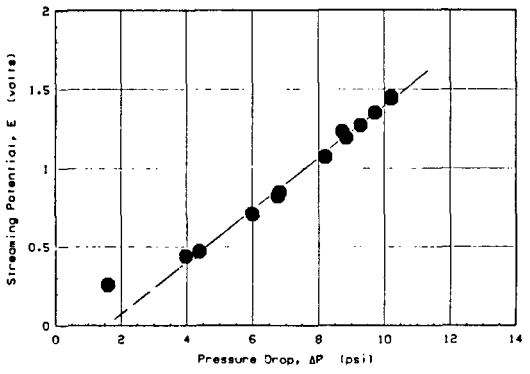


Figure 3: Streaming potential vs pressure drop

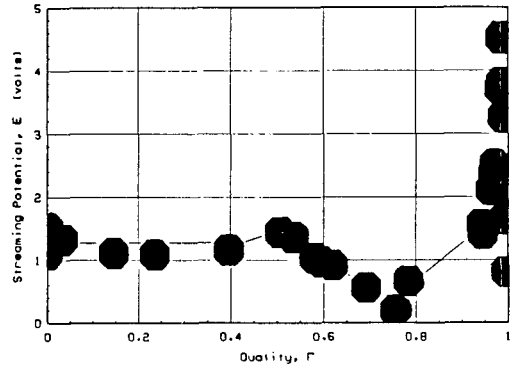


Figure 4: Streaming potential vs quality

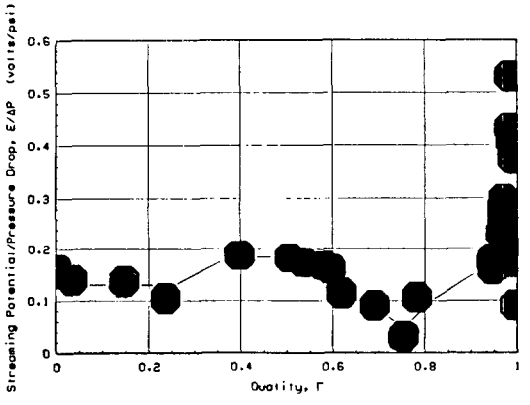


Figure 5: Streaming potential/pressure drop vs quality

and hence decreased the conduction current. Beyond this maximum, E decreased rapidly to almost zero at $\Gamma = 1.00$; this was probably due to a thin film of water left on the tube and being dragged along by the N_2 flow.

While the streaming potential is sensitive to changes in pressure for single-phase and low Γ two-phase flow, it is generally more sensitive to changes in Γ than in pressure for most two-phase flow. This is shown in Fig. 5 which is a plot of E/Δp vs Γ. The features of this plot are somewhat similar to those of the previous one and hence further discussion is not needed at this point.

Porous Medium, Single Phase Flow

Calculations showed that under all of the flow conditions for the ten measurements made with only water flowing, we were still in the viscous flow regime. Once the valve adjustments were made, both the potential and the pressure drop pens on the recorder remained both steady and constant. However, here it was found that the downstream electrode was always positive relative to the upstream one which was just the opposite of what we had found for the capillary tube runs. This is what we would expect for cations being transported downstream by the flowing liquid.

A graph of Δp vs flow rate (not shown) gave the expected straight line with a not unexpected intercept of about 1.0v. Because the flow resistance of the porous medium was significantly greater than that for the capillary tube, we could not use the same Δp's and flow rates for both flow conduits without changing some other parameter such as the cross-sectional area or length. Because it was experimentally simpler, we decided to keep the pressure drops similar. Therefore, the flow rates for this set of runs was about 20% of the capillary tube runs for similar pressure drops.

A graph of E vs Δp is shown in Fig. 6. Again we have a linear relationship but of negative slope and having a slightly positive E value of $\approx$ 0.5v at Δp=0. In comparing the slope of this to that of Fig. 3, we see that the streaming potential generated by the porous medium is about four times as great as that generated by the capillary tube. This may have been due to the surface area of the former being almost 100 times that of the latter.

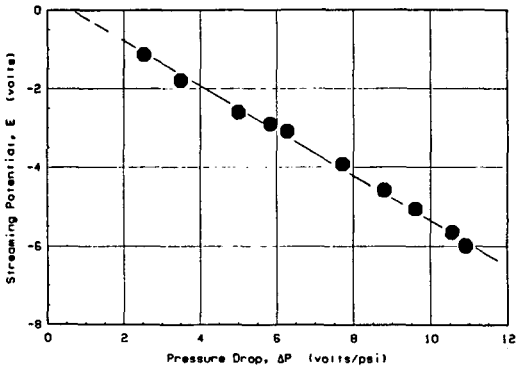


Figure 6: Streaming potential vs pressure drop

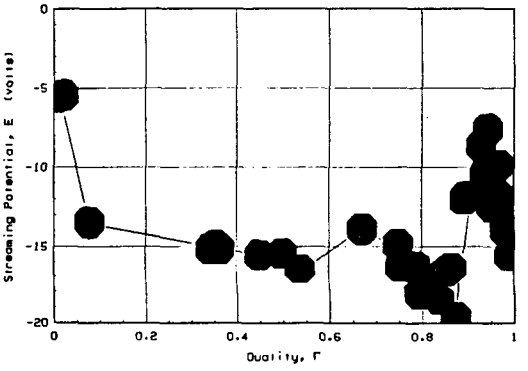


Figure 7: Streaming potential vs quality

Porous Medium, Two-Phase Flow

Two phase flow in the porous medium appeared to be quite homogeneous and without any gravity override. The upstream electrode was again negative and although the streaming potential did fluctuate somewhat, the spikes were toward lower potentials on the strip chart. This means that the spikes were toward the maximum, i.e. less negative, potentials as was qualitatively the same for the two-phase capillary flow.

In the graph of E vs Γ (Fig. 7) the size of the octagons again represents the maximum calculated uncertainty for each data point. It was almost impossible to obtain any data in the range of essentially $0<\Gamma<0.35$ because of the difficulties with controlling small N_2 flows, but the one point obtained indicates that E falls off quickly, i.e. becomes more negative, as gas enters the system. This differs considerably from the two-phase capillary tube case (Fig. 4) where E was almost constant for $\Gamma<=0.5$.

The right-hand half of Fig. 7, however, bears a remarkable resemblance to Fig. 4 (after a proper adjustment for the difference in sign) with a slight decrease in E for $\Gamma \approx 0.55$ to ≈ 0.65 followed by an increase (slope again $\approx$-1) ending at $\Gamma \approx 0.85$. Next there is a sudden decrease in Γ to about $\Gamma \approx 0.95$ and finally an increase in E as Γ goes to unity.

An important point to consider in analyzing this data is the probable relationship that exists between the measured Γ value and the actual gas saturation that exists within the capillary tube or porous medium. (In petroleum engineering terms the former would be fractional flow of gas and the latter would be the resident gas saturation.) We have defined Γ as being the flowing gas volume fraction and for the capillary tube, it would be essentially the same as the resident gas saturation with possibly a small and negligible correction for an immobile water film on the glass. It is well-known that (in the absence of foam) gas and liquid generally flow at different volumetric rates in porous media and at rates which differ from their resident saturations in the porous medium. Even when gas is still being injected and water is not, there is still a finite water saturation which in the case of an unconsolidated porous medium like ours might occupy about 5% of the pore space. This water is essentially immobile and is held at the grain contacts as pendular rings. This residual water plus the water films remaining on the pyrex grains serves as an electrically conducting film for the conduction current which counter-balances the convection current generating the streaming potential. It is remarkable that even after no more water is being injected and none being produced, there is still a relatively high streaming potential being generated. We did not run the porous medium experiments to the point where all of this residual water was vaporized by the flowing N_2 but this should be tried in the future.

The question remains as to why the polarity of the streaming potentials generated in the capillary tube was the opposite of that generated in the porous medium. Each had the same Pt electrodes in the same teflon holder and both were constructed of Pyrex glass. Although different types of Pyrex are available, their chemical compositions are nearly the same and so an error in selecting the materials for the two kinds of flow conduits is unlikely the source of the polarity differences. We understood that precision bore capillary tubing of the sort used here is annealed in manufacture while the crushed Pyrex for the porous medium may well have strains in it and certainly had a cleaved

rather than annealed surface, but again this would be expected to be insufficient.

Glass surfaces in contact with water lose cations to the diffuse layer near the solid surface, which then assumes a negative charge. When the water is forced to flow parallel to the surface, the cations are removed downstream and the static glass surface upstream then has a negative charge. Hence, we would expect the upstream electrode to be negative relative to the downstream, which is what we have found for the experimental results with the porous medium. Why the capillary tube results were different, we don't know for sure but it may have been due to adsorption of detergent or other ions used in the preliminary cleaning operation. More work is obviously needed to clarify this important matter.

The potential applications of these results are widespread as is the additional work needed. If there is indeed a difference in polarity for the two kinds of flow conduits, we may have a means of distinguishing between fracture and matrix flow in subsurface formations. The relationships between streaming potential and gas or vapor content of the flowing fluid mixture may give us information on the relative amounts of each fluid in the subsurface formations. Finally, as Ishido et al. (1987) have just reported at this Geothermal Workshop, the change of measured potentials during geothermal fluid production will add considerably to our knowledge of geothermal reservoir engineering.

Acknowledgements

We would like to express our appreciation to the Department of Petroleum Engineering, the Getty Oil Company and the Institute for Energy Studies of Stanford University for their generous support for this study.

CONCLUSIONS

The following conclusions are based up on the results of experiments involving the flow of both distilled water and nitrogen gas through either a Pyrex capillary tube or a Pyrex unconsolidated porous medium. We believe, however, that they may be applied to other physical systems, in particular, to the rock-water system thought to be the main contributor to the self-potential anomalies measured near geothermal resources.

1. The flow of either distilled water alone or else distilled water and nitrogen mixtures through a Pyrex capillary caused the upstream electrode to be positive with respect to the downstream electrode. When these same fluids flowed through an unconsolidated, crushed-Pyrex porous medium, the upstream electrode was negative with respect to the downstream one. The reason for these differences is not clear.
2. For the two-phase flow of water plus N_2 through the capillary tube, the measured streaming potential, E, did not change with the flowing volume fraction of gas, Γ, until the latter reached about 0.5. In this range of compositions, E was principally dependent on pressure drop, Δp. Here the gas flow did not materially disturb the ionic distribution in the double layer and also did not significantly affect the total fluid resistivity unless there were counterbalancing effects.
3. For $\Gamma > 0.5$ there was first a slight increase of E with Γ, then a consistent decrease to a minimum at about $\Gamma \approx 0.75$, next a pronounced maximum at about $0.95 < \Gamma < 0.99$ and finally a decrease to zero at $\Gamma = 1.00$, i.e. with only gas flowing. The pronounced second maximum was probably due to the large concentration of non-conducting N_2 bubbles, which decreased the conduction current significantly while not affecting the convection current materially. The reasons for the slight increase in E with Γ followed by the decrease before the second maximum are not now known.
4. For two-phase flow through the porous medium, the E was also found to be Γ dependent, and in a very pronounced way the relationship between the two variables was similar to that for the capillary tube. Because E was of the opposite sign as for the results with the tube, the two curves were something like mirror image with the rotation being about the horizontal axis. The strong maximum in E at very high values of Γ was again quite apparent and it was probably due to the same reasons here.
5. There were two significant differences in the results for the porous medium and the capillary tube. The values of E for the former were about four times those for the latter for comparable values of Δp. This may have been related to the surface area of the porous medium being an estimated 100 times that of the capillary tube. Also E did not return to zero when the flowing Γ reached 1.00 which may have been related to the finite value of the irreducible water saturation, S_{wi}. While the flowing and resident values of Γ were the same for the capillary tube, they were not always the same for the porous medium.

REFERENCES

Corwin, R.F. and Morrison, H.F. (1977): "Self-Potential Variations Preceding Earthquakes in Central California," Geop. Res. Letters, 4, No. 4, 171-174.

Dorfman, M.H. et al. (1977): "Self-Potential Profiling--A New Technique for Determination of Heat Movement in a Thermal Oil Recovery Flood," SPE 6790, Annual Fall Tech. Conf., Denver, CO, Oct.

Dowdle, W.L. and Marsden, S.S. (1974): "Some Aspects of the Streaming Potential of Concentrated Emulsions," J. Col. and Interface Sci. 48, No. 3, 523-524.

Ishido, T. et al. (1987): "The Electrokinetic Mechanism of Hydrothermal-Circulation-Related and Production-Induced Self-Potentials," Presented at the Twelfth Stanford Workshop on Geothermal Reservoir Engineering, Stanford, CA (Jan.)

Ishido, T. et al. (1983): "Streaming Potential Observations Using Geothermal Wells and In Situ Electrokinetic Coupling Coefficients Under High Temperature," Tectonophysics, 91, 89-104.

Klinkenberg, A. and van der Minne, J.L. (1958) Electrostatics in the Petroleum Industry, Elsevier Pub. Co., London.

Marsden, S.S. and Tyran, C.K. (1986): "Streaming Potentials Generated by Flow of Wet Steam in Capillary Tubes," Presented at Eleventh Workshop on Geothermal Reservoir Engineering, Stanford, CA (Jan.)

Raza, S.H. and Marsden, S.S. (1967): "The Streaming Potential and Rheology of Foam," Soc. Pet. Eng. J. (Dec.) 359-368.

Tyran, C.K. and Marsden, S.S. (1985): "The Streaming Potential of Steam," Presented at the GRC Annual Meeting, Kailua-Kona, Hawaii, (Aug.).

Wheatall, M.W. and Marsden, S.S. (1986): "The Streaming Potential Generated by Wet Simulated Steam," Presented at Fifth International Symposium on Water-Rock Interaction, Reykjavik, Iceland, (Aug.), 623-5.

PROCEEDINGS, Twelfth Workshop on Geothermal Reservoir Engineering
Stanford University, Stanford, California, January 20-22, 1987
SGP-TR-109

CERRO PRIETO
CONTENTS OF THE TECHNICAL INFORMATION FILES GENERATED AT THE FIELD

Miguel Angel Ayuso Olmos

COMISION FEDERAL DE ELECTRICIDAD
Gerencia de Proyectos Geotermoeléctricos
Apartado Postal 31-C
Morelia, Michoacan 58270

ABSTRACT

The creation of a computer data bank for the Cerro Prieto Geothermal Field, resulted from the need for fast and flexible management of the increasing and voluminous information generated from the large number of wells drilled in recent years. The data are needed for updating the thermodynamic evolution of the field in order to define field history and validate mathematical analyses applications. This data bank compiles 20 files with all technical information issued from the time of initial field exploration to the end of 1986. To use the data bank, a series of programs and subroutines were created simultaneously for data base management to allow access and add new data as well as data analysis and data graphics.

Tables of global statistics of the informations contained in the 20 files are shown in the paper, as an example of one application of the general use of the data base. For particular and specific applications, depending on users' needs for the data.

INTRODUCTION

The Cerro Prieto Field has evolved greatly since its creation, having nowadays an installed electrical generation of 620 MW divided into: 1 unit of 30 MW and 4 of 37.5 in CP-I, 2 units of 110 in CP-II and 2 more units of 110 in CP-III.

This continuous evolvement is due to the favorable results obtained in the constant explorations that have been carried out in search of new explotation and expansion areas of the field, in such a way that from May of 1960, date of the first well drilled (M-1A), up to date there are more than 150 wells drilled between those that are exploratory and those in production. Their location is the following: 95% are located within the explotation area and its surroundings (including CP-IV) and the remaining 5% in the adjoining areas such as Riito, Tulecheck, Aeropuerto, Laguna Salada, etc.

Consequently, year after year, the volume of administrative and technical information has increased up to limits that handling it manually has become a very difficult and heavy task, this encouraged to search for more flexible and dynamical procedures to handle the information based on that advantages that a computer offers and on the fact that Cerro Prieto as well as CFE in general, have the neccesary and sufficient elements for the use of a computer.

OUTLINING OF THE PROJECT AND ITS OBJECTIVES

The outline to form the data bank, that is to say, the type, quantity and content of the files is based in: 3 premises in which the structure and the capacity of the data bank is indicated, plus 4 general objectives for application which convert it into an useful system and not into a duplicate of the information.

PREMISES

- To create computarized files which will contain all of the necessary and indispensable technical information for the understanding and development of the Field.
- The information in the files should contain all the data accumulated since the beginning of the exploration up to 1986 and it should continuously be updated.
- Elements of particular interest: reservoir, wells and superficial installations.

OBJETIVES

- To define the thermodynamic evolution, the detail and with a methodological rigor in time and space; analyzing the information by its dates, productive layers, not only pressure and temperature data but the combination of all parameters.
- To support modeling, establishing the initial conditions and matching the history and the simulation results, beginning from the previous objective, with a higher decgree of reliance for the prediction phase.

- To create systems of classification and arrangement of data, to form preliminary statistics, for the different group of wells, dates, flowing conditions, depths, recurrance of interventions, correlation of periods, indexes of growth and economical investment, etc.

- To facilitate the planning and fulfillment of the activities, specially those of monitoring, sampling and measurements of the wells through the periodical revision of the files, taking out the last data or group of data, related to a certain action and the date in which it was carried out, to be compared with the present information as well as measuring the time ellapsed; that is to say, this objective implies the presentation of the actual state of the wells and the Field.

The previous objectives generalize and cover most of the analyzing and calculating activities which are completed in the technical departments of the Field and Gerencia de Proyectos Geotermoeléctricos, however, we can mention some other specific objectives which would depend on the users of the data bank.

COMMENTS

The revision of the information before and after storage has permitted us to observe its evolution and the different stages through which it has gone during its 13 year history of production, arising that:

- The original formats of feeding data were to be corrected and up-dated in their presentation and in the units that report the information.

- More specific objectives were defined for monitoring, sampling and measuring, adjusting to the general objectives and being more careful with the quality of the results rather than the quantity.

Programs for calculations and handling of the files have been implemented, similar to those programs that handle the data base which correlates a group of files with the others as well as individually, with graphs and printed outputs.

The internal configuration (in the computer) of the data and files, is independent and different from the structure that it has in the original forms and in the printouts; being subjected to: no entry of any data that can be calculated from the others and using the least possible storage space with a built-in system of auto-protection to avoid the accidental erasing or loss of the information.

In the future, the number of files will be increased and diversified at once the information from other departments, such as the design and construction of plants, will be incorporated and addapted to this system.

LIST OF TABLES AND FIGURES

- Table 1.- List of files and content of the parameters.
- Table 2.- Nomenclature of the files. Parameters and units.
- Table 3.- List of files and quantity of parameters.
- Figure 1.- Cerro Prieto Geothermal Field. Wells location map.

ACKNOWLEDGEMENTS

I would like to thank the technical personnel of the Field for their cooperation in selecting and providing with the previous information and also the great effort of the persons dedicated to review and entry data in the computer.

TABLE 1.- LIST OF FILES AND CONTENT OF THE PARAMETERS

FILE	PARAMETERS
1.- GENERAL INFORMATION ON THE WELLS.	Name of the well, coordinates, date of construction, company that built it, field, type of wells, observations.
2.- PRESSURE LOGS.	Well, log number, date, condition of the well, depth and maximum pressure, depths vs. pressures, observ.
3.- TEMPERTURE LOGS.	Well, log number, date, condition of well, depth and maximum temperature, depths vs. temperatures, observ.
4.- CALIBRATION LOGS.	Well, log number, date, condition of well, calibrating diameter vs. depth, observ.
5.- STATIC WATER LEVELS.	Well, quantification number, date, depth of level, observ.
6.- EVALUATIONS (DEVELOPMENT).	Well, evaluation number, method, date, diameter of the orifice, wellhead pressure, enthalpy, flowrate of steam, water and mixture, temperature observ.
7.- PRODUCTION DATA (MONTHLY REPORT).	Well, branch, date, diameter of the orifice, well head and separator pressure and flowrate of steam, water and mixture, enthalpy, temperature, vapor quality, water-vapor relation, observ.
8.- CHEMICAL ANALYSIS OF SEPARATED WATER.	Well, sample number, date, condition of the well, data: Na, K, Ca, Li, Cl, Sio_2, HCO_3, Mg, B, CO_3, SO_4, Ph, STD, observ.
9.- CHEMICAL ANALYSIS OF GASES IN THE WELLS, BRANCHES AND PLANTS.	Well, sample number, date, operating condition, data: CO_2, H_2S, NH_3, CH_4, N_2, Ar, H_2, He, totals, observ.
10.- CHEMICAL ANALYSIS OF THE INCRUSTATIONS IN THE WELL.	Well, sample number, date, depth from which the sample was taken, data: Na, K, Ca, Mg, Fe, S=, Sio_2, others, % of magnetic particles, observ.
11.- WELL COMPLETION OUTLINES.	Well, date, data on: casing head, holes, casing, accesories, slot liner, shot casing, plug casing, deviations, total depth, observ.
12.- LITHOLOGICAL COLUMN.	Well, lithology every 10 m., % of: mudstone, coffee-colored shale and/or siltsone, gray shale and/or siltsone, sandstone, other rocks. Mineralogy: sandstone cement, other minerals, fault traces and the temperature of the circulating drilling mud, observ.
13.- GEOPHYSICAL LOGS.	In process, information is being compiled.
14.- PERIODS OF THE WELL.	Well, name of period (stage), initial and final date, brief description, observ.(*)
15.- INTERVENTIONS (REPAIRINGS)	Well, type of intervention, initial and final dates, brief description, observ.(*)
16.- ELECTRICAL GENERATION.	Unit number, date, MW/hr, accumulated MW/day, vapor tons, plant factor, number of integrated wells, observ.

TABLA 1.- CONTINUATION

FILE	PARAMETERS
17.- PRESSURE TESTS.	Not defined.
18.- INJECTION.	Not defined.
19.- SUPERFICIAL INSTALLATIONS, SEPARATOR, SILENCER, VAPOR AND WATER LINES, ETC.	Not defined.
20.- AUXILIARY ELEMENTS FOR GRAPHS.	Coordinates, names of plants, highways, channels, evaporation lagoons, etc. (+), observ.

*.- The formation of a sub-file is in process to broaden the description of the period of intervention mentioned.

+.- The information from this file is for graphing at different scales and colors, schematic map of the field.

TABLE 2.- NOMENCLATURE OF THE FILES. PARAMETERS AND UNITS.

PARAMETERS	UNITS
COORDINATES.	DETENAL.
DATE.	YEAR/MONTH/DAY.
DIAMETER OF THE ORIFICE.	INCHES.
PRESSURE.	Kg/cm^2.
TEMPERATURE.	°C
ENTHALPY.	Kj/Kg.
FLOWRATE.	T/H.
CHEMICAL ANALYSIS OF WATER.	ppm.
CHEMICAL ANALYSIS OF GASES.	mg/Kg.
CHEMICAL ANALYSIS OF INCRUSTATIONS	% IN WEIGHT.
LITHOLOGY AND MINERALOGY.	% IN CONTENT.

TABLE 3.- LIST OF FILES AND QUANTITY OF PARAMETERS

FILE	WELLS (-)	INFORMATION OF (*)
1.- GENERAL INFORMATION ON THE WELLS.	160	160 WELLS.
2.- PRESSURE LOGS.	132	2530 LOGS.
3.- TEMPERATURE LOGS.	140	4525 LOGS.
4.- CALIBRATION LOGS.	120	927 LOGS.
5.- STATIC WATER LEVELS.	109	2019 MEASUREMENTS.
6.- EVALUATIONS (DEVELOPMENT).	120	256 DEVELOPMENTS.
7.- PRODUCTION DATA (MONTHLY REPORT).	109	180 MONTHS, 3456 MEASUREMENTS.
8.- CHEMICAL ANALYSIS OF SEPARATED WATER.	87	5627 SAMPLES.
9.- CHEMICAL ANALYSIS OF GASES IN THE WELLS, BRANCHES AND PLANTS.	90	3024 SAMPLES.
10.- CHEMICAL ANALYSIS OF THE INCRUSTATIONS IN THE WELL.	90(+)	1562 SAMPLES.
11.- WELL COMPLETION OUTLINES.	160	234 WELL COMPLETION OF OUTLINES.
12.- LITHOLOGICAL COLUMN.	160	160 LITHOLOGICAL COLUMNS.
13.- PERIODS OF THE WELL.	145	145 WELLS.
14.- INTERVENTIONS (REPAIRINGS).	68	141 INTERVENTIONS.
15.- ELECTRICAL GENERATION.		DATA ON 180 MONTHS OF EVERY UNIT, OF EACH PLANT.

(-).- Quantity of wells in which the information is compiled.

(*).- Quantities reported in the third column, refer to groups of classified data and not to the number of entry records; example: In the temperature record files, if an average of 25 pairs of data per group is considered, then a quantity of 113125 computer records is obtained. This situation is the same for other files.

(+).- In the file of chemical analysis incrustations, we consider not only the 90 wells reported but superficial instalation analysis of: plants, branches, separators and silencers.

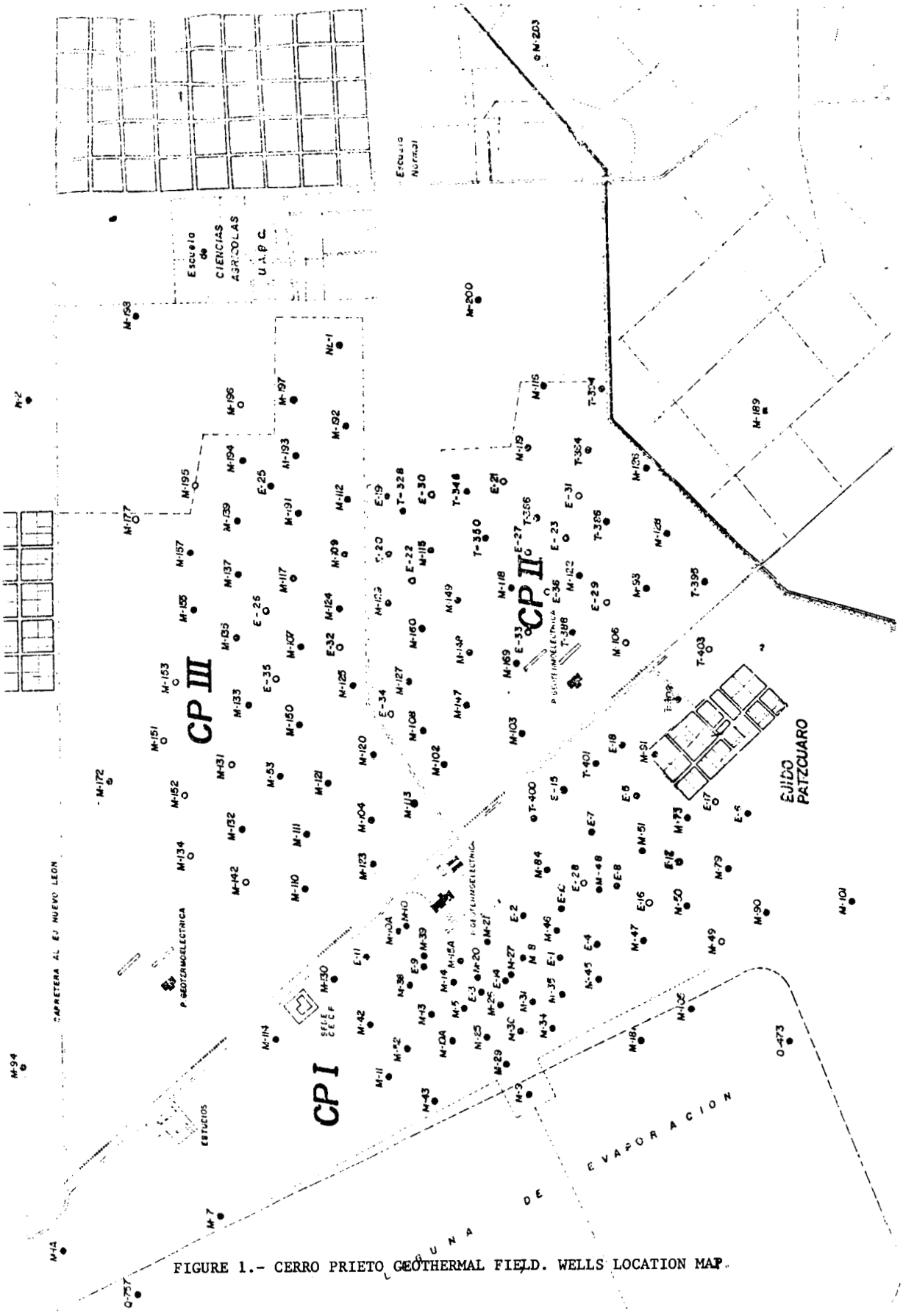


FIGURE 1.- CERRO PRIETO GEOTHERMAL FIELD. WELLS LOCATION MAP.

PROCEEDINGS, Twelfth Workshop on Geothermal Reservoir Engineering
Stanford University, Stanford, California, January 20-22, 1987
SGP-TR-109

DEVELOPMENT DRILLING, TESTING AND INITIAL PRODUCTION OF THE BEOWAWE GEOTHERMAL FIELD

V. T. Hoang, E. D. James, I. J. Epperson

Chevron Resources Company
San Francisco, California

ABSTRACT

The Beowawe geothermal field in north central Nevada is generating 16MW using two production wells (Ginn 1-13 and 2-13) and one injection well (Batz). Drilling the second production well (Chevron Ginn 2-13) in 1985 led to the discovery of a second productive strand of the Malpais fault zone. The wells are completed in the Malpais fault zone and are capable of producing 420+°F geothermal fluid at rates exceeding 1,000,000 lbs/hr. Initial testing suggests that the completion zones of the two production wells have no pressure communication, therefore providing what is essentially a second production zone for future development. Injection of produced fluids into a fault parallel with the Malpais shows no pressure communication with other wells. One year of production in the system shows no pressure depletion or enthalpy decline in the producing area.

INTRODUCTION

This paper presents an overview of the Beowawe development drilling, testing and initial production of the 16 MW power plant. The 16 MW plant utilizes two production wells: the Ginn 1-13, drilled by Chevron in 1974 (Layman, 1984; Epperson, 1982 & 1983); and the Chevron Ginn 2-13, drilled during the summer of 1985. The Ginn wells are completed in separate strands of the Malpais fault zone (MFZ).

The Beowawe geothermal field is located in north-central Nevada, about 50 miles southwest of the town of Elko. The field is in the Basin and Range province at the boundary between a plateau of volcanics to the south and the downfaulted Whirlwind Valley to the north. Active surface manifestations in "The Geysers" area cover one-half square mile, and include a large sinter terrace, geysers, fumaroles, and hot springs (Figure 1). The reservoir is thought to be in lower Paleozoic carbonates at depths of perhaps 20,000 to 30,000 feet. No wells have penetrated the carbonates, but the low salinity, sodium-bicarbonate nature of the Beowawe thermal water suggests that these rocks are the ultimate deep reservoir. Geothermal fluid flows upward from the deep reservoir through the Malpais fault (MFZ) system, charges permeable horizons along the way and finally discharges at the surface.

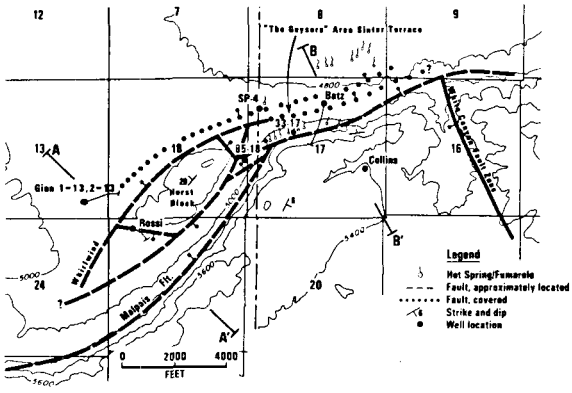


Figure 1. Well locations and surface features.

BEOWAWE GEOTHERMAL FIELD EVALUATION

The Beowawe area has been well known for many years due to the geysers, fumaroles, and boiling springs that exist there. These numerous geothermal surface manifestations led Magma Power Company and Sierra Pacific Power Company to drill 11 shallow wells in the sinter terrace area from 1959 through 1965. Chevron acquired the leases in 1973-1975 and began an extensive geologic study of the area. Chevron drilled five more wells, starting with Ginn 1-13 in 1974 to a depth of 9563 feet, and numerous shallow temperature holes in the evaluation and development process.

Magma conducted the first Beowawe well tests on four of their wells on the sinter terrace. During a year long flow, visual checks of the discharge indicated an apparent decrease in flow rate and temperature. Based on these data, it was concluded that the Beowawe reservoir was depleting and being invaded by cold water. Recent Chevron data indicates that the reduction in flow rate and temperature is due to the cooler fluid contribution from a high permeability fault below the main fault feeding these wells (Epperson, 1983).

Chevron began an extensive testing program to evaluate the reservoir with the completion of Beowawe 33-17 on the sinter terrace in 1979. During 1981, after drilling Beowawe 85-18, Chevron conducted numerous flow tests and monitored pressure interference effects in several surrounding shut-in wells to evaluate the degree of continuity between wells. A summary of Chevron flow test results prior to 1985 is presented in Table 1. Note that all wells except Rossi 21-19 flowed at rates of about 300,000 lbs/hr total mass. The relative low flow rates are due to mechanical completion restrictions. The permeability-thickness (kh) for most Beowawe wells is in the range of 200,000 to 800,000 md-ft., thus indicating the extremely prolific nature of the reservoir.

Interference tests conducted at Beowawe before completion of Ginn 2-13 show pressure communication between all the wells, excepting the Batz well (drilled by Magma.) Response times are less than one hour, irrespective of the distance between wells. Analyses of the interference data verifies the calculated kh from the individual drawdown and build-up analyses. These results are illustrated in Figure 2.

TABLE 1

BEOWAWE FLOW TEST SUMMARY

	Ginn 1-13	33-17	85-18	Vulcan 2	Rossi 21-19	Batz
Number of flow tests	1	6	4	1	3	3
Max. static temp., °F	420	365	360+	360+	386	240
Flow rate, Mlb/hr	285	305	320	240	280*	200**
Kh, md-ft	232,000	800,000	550,000	780,000	8,953	850,000x
PI, lb/hr/psi	8,900	200,000	7,800	24,000	300	27,070

*Flow with nitrogen gas lift. **Injection rate. x Upper injection zone.

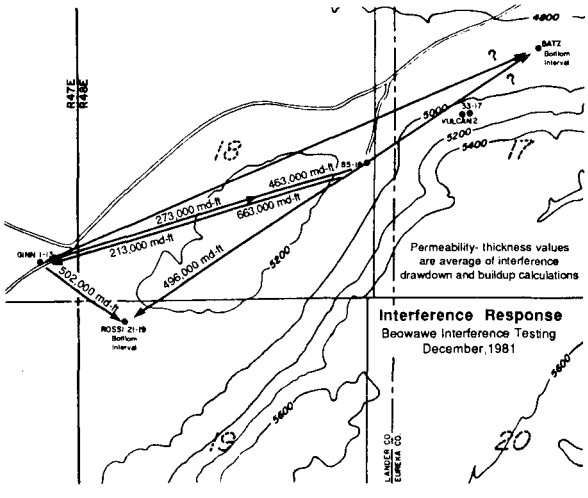


Figure 2. Interference response, December 1981.

SIMPLE FAULT MODEL FOR BEOWAWE GEOTHERMAL SYSTEM

Models proposed for thermal water flow in Beowawe system are varied, but all involved in the Malpais fault zone. The current model (Layman, 1984) incorporated temperature profiles, drilling history, cutting description, and kh distribution to show the importance of the MFZ as a primary conduit at Beowawe and provided a simple model to locate producing zones in the Beowawe field. Geologic mapping indicated that a simple planar fault can be constructed through MFZ intercepts in wells and the surface trace. The fault dip appears constant at 65-70° to the depth of the deepest well at 9563'.

Mapping of temperature in the MFZ shows that 420°F waters at depths greater than 9000' in Ginn 1-13 rise obliquely up the MFZ towards the northeast where there is an abrupt, up-dip diversion of flow at the prominent bend in the MFZ. This upwelling feeds the surface discharge at the Geysers.

Variations in permeability within the MFZ and siliceous vein - filling in the cuttings from low kh wells suggest that part of the fault zone is sealed-off. The region of the MFZ penetrated by Ginn 1-13, 85-18 and wells on the sinter terrace is open and very permeable. However, the MFZ at the Rossi and Batz wells is less permeable than other areas. Rossi was apparently drilled into the low permeability cap of the fault. At Batz, the MFZ does not seem to be in pressure communication with any other wells. The MFZ is tight at Batz probably due to silica sealing. The temperature and permeability data indicate good potential for expansion of the producing area down-dip of the MFZ from the 85-18 and Ginn 1-13 wells, and along strike south west of Ginn 1-13 (Figure 3).

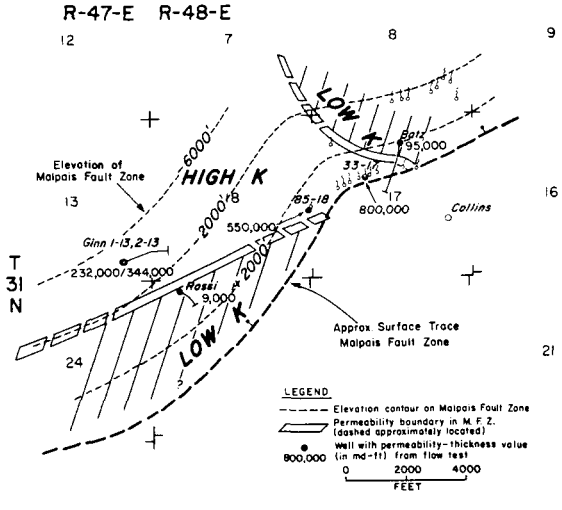


Figure 3. Permeability and elevation of the Malpais F.Z.

DEVELOPMENT OF THE 16 MW POWER PLANT

In 1985, Chevron drilled a second production well, Ginn 2-13, to supply steam for a 16 MW power plant which was built by Crescent Valley Energy Company. The well was programmed to penetrate the MFZ northeast of the Ginn 1-13. The well tested the concept that the MFZ was open over the large interval between the Ginn 1-13, Rossi wells to the west and the sinter terrace area to the east. The well, however, encountered a major lost circulation zone 500 feet above the target MFZ which was interpreted as a second fault. This fault trace is parallel with the main Malpais fault trace which was intersected in both the Ginn 1-13 and Rossi wells (Figure 4). Minor lost circulation and siliceous alteration mark the second fault in these wells.

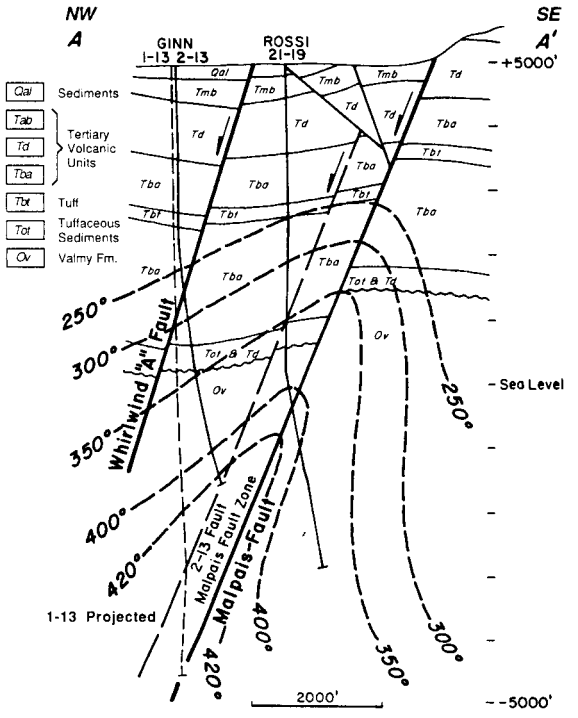


Figure 4. Geologic cross-section A-A'.

A short flow test soon after completion evaluated Ginn 2-13 productivity and reservoir properties. The Ginn 1-13 was monitored during the test to evaluate interference effects between the two fault strands. A James tube instrument was installed to gather data for flow rate and enthalpy estimation. Bottomhole flowing pressures were measured using helium filled capillary tubing and expansion chamber with a surface quartz transducer. The test results indicated that Ginn 2-13 encountered a very permeable zone, kh= 340,000 md-ft , containing 420$^{\pm}$ ^{o}F geothermal fluid. Ginn 1-13 produces the same temperature fluid from the main Malpais fault trace. A wellhead performance test showed that Ginn 2-13, after clean up of drilling damages, would provide over one million lbs/hr of fluid for the power plant. Pressure monitored during the test and during the plant start-up period indicated no interference between Ginn 2-13 and the other wells completed in the main Malpais fault trace.

The discovery of the second fault has greatly extended the development potential of the Beowawe field.

At present, the two production wells, Ginn 2-13 and 1-13, supply 1.3 million lbs/hr of 420°F fluid to a 16 MW dual flash power plant. The produced fluid contains a relatively low TDS ($^{\pm}$ 1,200 PPM) and noncondensible gases ($^{\pm}$ 550 PPM CO_2). The unflashed geothermal fluid returned from the plant is pressurized for injection at the plant and is transported via a 10" diameter two-mile insulated pipeline to the existing Batz well (Figure 5). At the Batz well, the fluid is injected into a shallow, cool zone of high permeability above the MFZ intercept. This zone is interpreted as a range-front fault parallel with and hydrologically unconnected to the MFZ (Figure 6), but is believed to be connected to the carbonate reservoir. During one year of operation, no injection effects were observed in the monitoring wells, indicating this range-front fault is an attractive target for future injection wells.

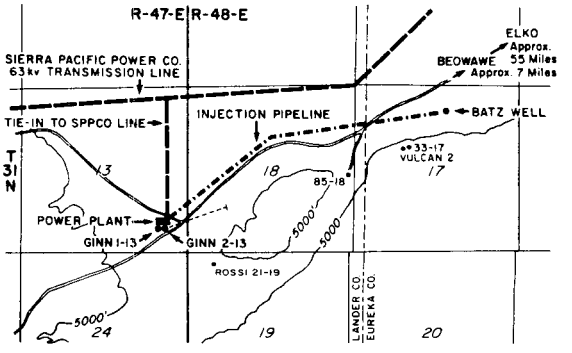


Figure 5. Plant and surface facilities.

During the October 1986 Beowawe power plant shutdown for maintenance and inspection, a small amount of calcite scale was recovered in the upper portion of the producing wells. However, the scale deposit did not affect the wells' performance significantly. Well performance tests, after the scale was milled out, indicated that Ginn 2-13 and Ginn 1-13 were capable of producing 1.2 million lbs/hr and 800,000 lbs/hr of fluid respectively at $^{+}$ 102 psia wellhead pressure. Ginn 1-13 bottomhole pressure built up rapidly to the reservoir initial pressure after shut-in indicating no pressure depletion in the producing area. Enthalpy of the produced

fluid, measured during the plant shutdown, showed no change from the value obtained before the plant start-up. The production data gathered during the first year of operation reconfirms the prolific nature of the Beowawe reservoir.

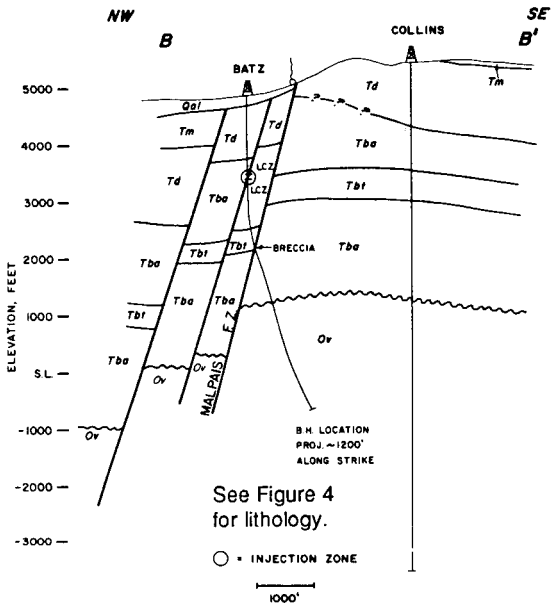


Figure 6. Geologic cross-section B-B'.

An important question to be answered is the estimated size of the reservoir and the ultimate development potential of the field. Due to the geologic complexity of Beowawe, this question can only be partially answered now. A semi-steady state analysis of the long term flow test data by Chevron indicates an extremely large fluid volume (in excess of 10^{10} bbls). The steady-state performance of Beowawe 33-17 after about 200 hours of flow in a 1980 test is indicative of a infinite reservoir or perhaps a constant pressure "boundary" (IJE 1983). Flow data from other Beowawe wells indicate fluid volume in excess of 10^{12} bbls. None of the tests have ever indicated a flow barrier or reservoir boundary, so these fluid volume estimates are only minimum values. The proven productive area of the two faults indicate a development of at least 200 MW.

CONCLUSIONS

1. Wells completed in the two strands of the Malpais fault zone are highly productive with potential to produce 420°F fluid at rates exceeding 1,000,000 lbs./hr. Testing indicates that the two faults are essentially separate production zones, thus providing a large area for future development.

2. Injection of produced fluid into a range-front fault parallel with the Malpais shows no pressure communication with other wells. This fault is an attractive target for additional future injection.

3. After one year of production no pressure depletion or enthalpy reduction has been observed within the producing area.

4. The minimum potential of the proven reservoir at Beowawe is 200 MW, based on 10 MW/well and 40 acre spacing between wells in the two fault zones.

ACKNOWLEDGEMENT

The authors would like to thank Chevron Resources Company for permission to publish this paper.

REFERENCES

1. Epperson, I. J. (1982), "Beowawe, Nevada, Well Testing: History and Results," GRC Trans., Vol. 6, p. 257-260.

2. Epperson, I. J. (1983), "1981 Interference Well Testing: Beowawe, Nevada," GRC Trans., Vol. 7, p. 413-416.

3. Epperson, I. J. (1983), "Beowawe Acid Stimulation," GRC Trans., Vol. 7, p. 409-411.

4. Layman, E. B. (1984), "A Simple Basin and Range Fault Model for the Beowawe Geothermal System, Nevada," GRC Trans., Vol. 8, p. 451-457.

5. Swift, C. M. (1979), "Geophysical Data, Beowawe Geothermal Area, Nevada," GRC Trans., Vol. 3, p. 701-703.

PROCEEDINGS, Twelfth Workshop on Geothermal Reservoir Engineering
Stanford University, Stanford, California, January 20-22, 1987
SGP-TR-109

GEOCHEMISTRY AND TRACER BEHAVIOR DURING A THIRTY DAY FLOW TEST OF THE FENTON HILL HDR RESERVOIR

Bruce A. Robinson, Ronald G. Aguilar, Yuji Kanaori,
Pat Trujillo, Dale Counce, Stephen A. Birdsell and Isao Matsunaga

Los Alamos National Laboratory
Los Alamos, New Mexico 87545

ABSTRACT

During the most recent circulating flow test of the Fenton Hill Hot Dry Rock (HDR) geothermal reservoir, the geochemical behavior of the produced fluid was monitored continuously to determine the concentrations of dissolved anions and cations and dissolved gases. Chemistry results have aided in the development of reservoir models and in the determination of potential chemistry-related operation problems such as corrosion and gas handling in future energy extraction tests. Results of two radioactive tracer experiments suggest flow through a large, highly-fractured region of rock. This rock volume is equivalent to a sphere of diameter approximately equal to the separation distance between the injection and production points in the two wells.

INTRODUCTION

A 30-day closed-loop circulation test of the current HDR reservoir at Fenton Hill, NM has been performed to determine the hydraulic, seismic, and chemical characteristics of the reservoir, in anticipation of a long-term energy extraction test scheduled to start in January 1988. Hendron (1987) summarized this flow test, focusing on the overall reservoir performance. The present study examines the geochemistry and tracer results obtained from continuous sampling of the production fluid and the injection of radioactive tracers to measure fracture volumes and dispersive characteristics.

GEOCHEMISTRY OF THE FLOW TEST

GEOCHEMISTRY DATA

Sampling Apparatus and Procedures: The apparatus used to collect produced fluid gas and liquid samples is shown in Figure 1. Hot, pressurized fluid from a sidestream off the production wellhead flowed to a small chemistry laboratory containing this equipment. The fluid was cooled under pressure in a heat exchanger and directed to the various apparatus in the figure either manually or automatically, depending on the sample being collected. Filtered and unfiltered liquid samples were collected manually through

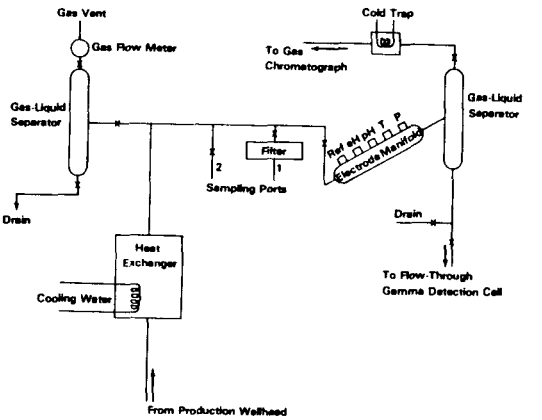


Figure 1. Schematic of the sampling apparatus for production fluid liquids and gases.

the ports labeled 1 and 2. Alternatively, fluid passed through an instrumented manifold kept at a pressure sufficient to prevent degassing. The eH, pH, and electrical conductivity of the fluid were recorded automatically in this manifold. The gas separation equipment on the right side of the figure supplied gas samples for the gas chromatographic and radon analyses. This separator was operated continuously, with gas samples directed periodically to the gas chromatograph after passing through a cold trap to remove any remaining moisture. In addition, the liquid effluent from this separator was directed to the gamma counter during the radioactive tracer experiments.

The other gas separation unit was used to simultaneously measure gas and liquid flow rates to obtain the gas mass fraction in the produced fluid. The separator was manually adjusted to achieve a constant liquid level and gas flow rate, and the gas and liquid flow

rates were measured simultaneously. Since the gas was predominantly CO_2, the concentration of CO_2 (in weight percent) in the produced fluid was determined directly.

The procedures employed at Fenton Hill for analyzing gas and liquid samples for dissolved anions, cations, gas concentrations, suspended solids, and other species is described in detail elsewhere (Trujillo et al., 1986).

Major Dissolved Species: Figure 2 shows the concentration-time behavior of the major dissolved anions and cations in the produced fluid. Table 1 shows the concentrations in a sample collected six days into the flow test, after the geochemical behavior had reached a quasi-steady state. The concentrations of most species are 2-3 times higher than in previous shallower reservoirs, probably because of higher reservoir temperatures and a larger contribution from the in situ pore fluid. The total dissolved solids value of 4300 ppm, equivalent to ionic strength I = 0.05 m, is low enough that major brine handling problems are not expected.

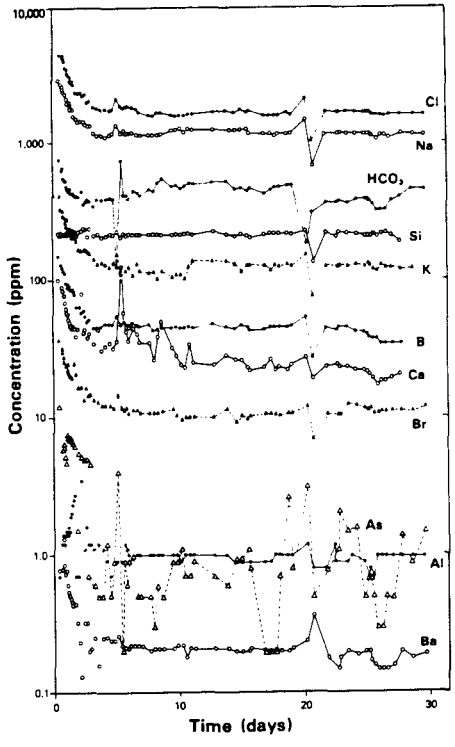


Figure 2. Concentration-time behavior of the major dissolved species in the production fluid.

Non-Condensable Gas Analyses: Gas analysis consisted of total gas flow rate (Figure 3) and gas chromatograph analysis of the dry gas composition. After the initial transient in the first few days of the flow test, the average gas flow rate was about 0.2% CO_2 by weight. Dismissing the high gas flow rates during a nitrogen injection experiment on day 20, the highest values were observed during the experiment start-up. The high value of 0.9% is the best estimate of the CO_2 concentration in the pore fluid. Higher gas concentrations may have been present during periods of two-phase flow, but our sampling apparatus did not enable us to obtain a representative sample of the fluid during two-phase flow.

Gas chromatograph analyses determined the dry gas to be predominantly CO_2 (typically 90-95%), with lesser quantities of N_2, and minute amounts of H_2S, O_2, and occasionally CH_4 and C_2H_6.

Table 1.

Typical Ion Concentrations (Sample Collected on Day 6)

Component	Concentration (ppm)
As	0.6
B	48
Br	11.5
Ca	42
Cl	1814
F	10.4
Fe	2.1
HCO_3	408
K	114
Li	23.4
Na	1180
pH	5.79
SiO_2	452
SO_4	183
TDS	4300 (I = 0.05m)

INTERPRETATION OF GEOCHEMISTRY

Time-Dependent Behavior: When fluid of different concentration than the underground pore fluid is injected into a circulating HDR reservoir, the resulting produced fluid geochemistry behavior will be governed by three mechanisms: 1) displacement of the downhole fluid by the injected water, 2) rock-water dissolution, precipitation, or alteration reactions, and 3) adsorption of chemical species on the reservoir rock. Throughout most of the flow test, the downhole, injection, and makeup fluids were all at similar concentrations (approximately those listed in

Table 1). However, early in the test the inlet and outlet concentrations were different, and can be interpreted most effectively by defining a non-dimensional concentration C* (Grigsby, 1983):

$$C^* = \frac{C - C_{in}}{C_o - C_{in}} \quad (1)$$

where C_{in} is the injection concentration and C_o is the initial produced fluid concentration, which is the true downhole concentration of the component if the sample is collected immediately after the wellbore fluid is displaced. The most common behavior is that of

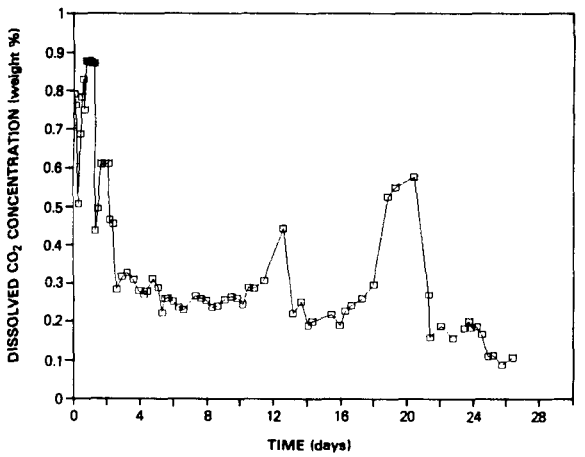


Figure 3. Dissolved CO_2 concentration in the production fluid.

an inert, nonadsorbing species, which behaves like a tracer for a negative step change in injection concentration. Injected fluid gradually sweeps the concentrated underground pore fluid from the reservoir until the produced fluid concentrations approach the injection values (Figure 4). Chloride ion, Cl, as well as B, Br, K, Li, Na, electrical conductivity, and total dissolved solids all fall in this category.

Two other characteristic concentration-time responses are exhibited in Figure 5. The dissolved silica concentration remained constant during the initial sweep of pore fluid from the reservoir and throughout the entire 30 day test. Quartz dissolution supplies a constant source of silica to the undersaturated injection fluid, allowing the solution to reach equilibrium in one pass through the reservoir. The third type of time-dependent behavior is for species whose concentration decreases to a value below the injection value. This result implies consumption of the component, either by adsorption on the rock surface or precipi-

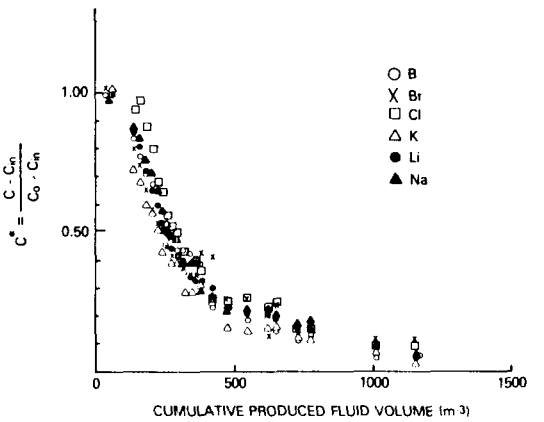


Figure 4. Dimensionless concentration versus produced fluid volume for inert species during initial reservoir operation. Concentrations start at high downhole values and decline to injection fluid concentration.

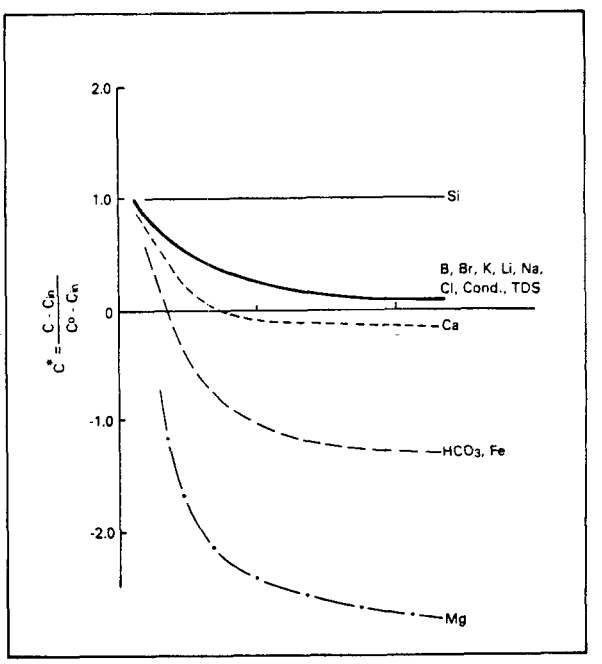


Figure 5. Different types of concentration-volume behavior observed during initial reservoir operation.

tation reactions. Divalent cations such as Mg clearly show a propensity to adsorb on granite, and, as shown in the figure, fall into this third category. Calcium, bicarbon

ate, and iron also exhibit this behavior, though the mechanisms for these three components are as yet unclear. Finally, a few species such as Ba, Mn, and SO_4 exhibit anomalous time dependences which have not been explained.

Sources of Dissolved Species: The origin of dissolved species in hot dry rock geothermal fluids has been treated by Grigsby et al. (1983). The two primary sources of dissolved species are displacement of downhole pore fluid and dissolution of minerals. Current models postulate a continuous extraction of the original pore fluid from the fractured rock mass over long periods of time. The most compelling argument supporting this theory is the presence and continued supply of chemically inert species such as boron and chloride, which are not found in the reservoir granite and hence are not supplied by a dissolution reaction.

Since most reservoir fluid samples are composed of the original downhole fluid after dilution with injected fluid, true values of the pore fluid concentrations are difficult to obtain. Grigsby (1983) has demonstrated that even when the pore fluid is diluted, the ratios of ions in solution should remain constant for conservative species supplied only by pore fluid, rather than by mineral

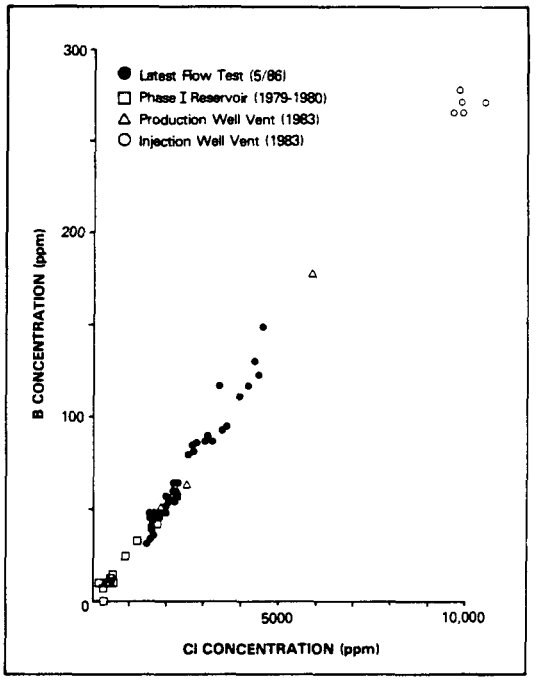


Figure 6. B versus Cl for fluid samples collected in the Fenton Hill HDR reservoir over the past eight years.

dissolution or alteration. When the concentration of one component is plotted directly against another, the data should fall on a single straight line if the source of the pore fluid is the same. Figure 6 is a plot of B versus Cl for the latest flow test and previous Fenton Hill circulation experiments and events of the past eight years. The new data all fall on the same straight lines as those for other fluid samples collected at Fenton Hill. The evidence now even more strongly supports the pore fluid hypothesis and suggests that a single underground fluid supplies the conservative species found in fluid samples at the Fenton Hill site.

Rock-water reactions are also important in the production or consumption of some species. For example, quartz dissolution controls the concentration of dissolved silica in the production fluid. The constant concentration measured during the flow test implies that the kinetics of quartz dissolution were rapid enough for the fluid to reach saturation in one pass through the system. Robinson (1982) measured the rate of quartz dissolution as a function of temperature and rock surface area and determined the following relation:

$$\ln \Phi = \ln \left[\frac{C^{\infty} - C}{C^{\infty} - C_{in}}\right] = -ka^{*}t \qquad (2)$$

where a* is the quartz surface area to fluid volume ratio ($2f_q/b$ for a flat fracture, where b is the fracture aperture and f_q is the fraction of quartz present in the granite), C^{∞} is the saturation concentration, and k is the rate constant for dissolution. To obtain a minimum value for a*, or a maximum value for the average fracture aperture, the following values will be used:

- Φ = 0.1 (equivalent to the dissolution reaction reaching 90% of its equilibrium value)
- t = 10 hr (the residence time at the peak tracer response)
- k = 4.13×10^{-8} m/s at 250°C (Robinson, 1982)
- f_q = 0.3

These assumptions yield a* = 1550 m^{-1}, or b = 0.4 mm. In other words, the average aperture encountered by fluid should be no greater than about 0.4 mm, and quite possibly less in order for the system to reach saturation with respect to quartz in one pass through the reservoir. Future models for the permeability and tracer behavior of the reservoir must be consistent with this information.

Another set of reactions affecting the produced fluid chemistry is the dissolved carbon dioxide-bicarbonate equilibrium reactions, which are coupled to the calcite dissolution reaction. Carbon dioxide is present in the underground pore fluid and is produced along with other pore fluid elements. If calcite (calcium carbonate, $CaCO_3$) is present, its solubility is also affected by the presence of

dissolved CO_2. For a CO_2-rich fluid in equilibrium with calcite, the following chemical reaction applies:

$$CaCO_3 + H_2O + CO_{2(g)} \rightleftharpoons Ca^{2+} + 2HCO_3^- \quad (3)$$

with equilibrium constant K_{eq} equal to

$$K_{eq} \frac{\gamma_{Ca}\,\gamma^2_{HCO_3}\,[Ca][HCO_3]^2}{P_{CO_2}} \quad (4)$$

The concentrations are in mol/l, the γ's, the activity coefficients, are related to ionic strength and temperature using the Debye-Huckel equation (Henley et al., 1984) and P_{CO_2}, the partial pressure of CO_2 is given by

$$P_{CO_2} = K_H\, x_{CO_2} \quad (5)$$

where K_H, the Henry's law constant for CO_2, is a function of temperature, and x_{CO_2} is the fraction of CO_2 in the liquid. Using the measured values of all concentrations, and expressions supplied by Henley et al. (1984) for K_H and the γ's, we may iteratively calculate the equilibrium temperature at which these dissolved species were produced. For the 75 samples analyzed, the average calculated temperature was 211°C, with a standard deviation of 16°C. These temperatures are in reasonable agreement with the measured downhole production temperature of about 232°C, suggesting that for a given downhole P_{CO_2}, calcite dissolution is governing the equilibrium between dissolved CO_2, bicarbonate ion, and Ca. As significant changes in downhole temperatures occur due to thermal drawdown or exposure of hotter fluid flow paths, corresponding changes in these concentrations should also occur. However, to use these equilibrium reactions to evaluate reservoir temperature patterns, further refinements of the calculations will be required to explain the 20°C discrepancy between the actual and average calculated temperatures.

Geothermometer Readings: Since rock-mineral dissolution or alteration reactions are temperature dependent, the concentrations of certain dissolved species will depend on temperature. The calculations just presented are one example. Two more commonly used chemical geothermometers which exploit this temperature sensitivity are the quartz and Na-K-Ca geothermometers. These two measurements are shown for samples collected throughout the flow test in Figure 7. The recorded geothermometer temperature for quartz dissolution of about 250°C agrees fairly closely with the actual downhole temperature. The reactions governing the Na-K-Ca geothermometer do not reach equilibrium in short times, however. Thus, since the produced fluid is a mixture of the injection fluid and underground pore fluid, these geothermometer readings are not as precise. The Na-K-Ca temperatures decrease from essentially the known rock temperature to a somewhat lower value. In future work we will model this behavior, as well as the carbon dioxide-bicarbonate equilibrium reactions, as the mixing of fluids of different concentrations and temperatures to attempt to determine what concentrations and flow fractions are required to match the results.

CHEMICAL EFFECTS ON OPERATIONS

Corrosion Studies: Due to the large number of metal hardware failures attributed to metallic corrosion during the drilling of the injection and production wellbores, corrosion monitoring was performed during this flow test. Of greatest concern are the high temperatures, gas concentrations, and concentrations of corrosive ions such as Cl^-. This one month flow test provided data for future surface loop design.

Corrosion coupons were placed on side streams off the mainstream flow on both the hot and cold sides of the heat exchanger. Each station contained two coupons attached to a coupon holder of sufficient length that the coupons were exposed to a representative sample of the fluid. The coupons were oriented parallel to the fluid flow to avoid possible corrosion due to erosion. Shutoff valves placed at both stations allowed the coupons to be removed periodically. Pressure taps were placed at the entrance and exit

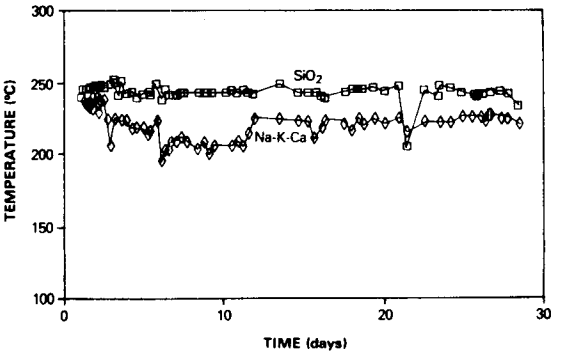


Figure 7. Silica and Na-K-Ca geothermometer temperatures.

points of the side stream piping to direct the fluid flow to the coupons. The coupons were analyzed periodically for corrosion rate (by measuring coupon weight loss over a specified time, typically 150 hr), type of corrosion, and scale formation.

The corrosion rates at various times during the flow test are presented in Figure 8. The more rapid corrosion rates occurring on the hot side of the heat exchanger are due to the

increased temperature, which increases the attack of metal hardware by elemental species present in the production fluid. The highest corrosion rate of 15 mils per year (mpy), occurring with the second set of coupons, will be used as the design criterion for the surface equipment for future tests. In the final set of coupons, the hot-side corrosion rate decreased dramatically. We attribute this result to equipment malfunctions which prevented liquid flow from reaching the coupons.

The type of corrosion observed on both sample stations was generalized and uniform. This behavior is typical of metal exposed to acidic fluid under flowing conditions. The only deviation from this pattern was in the final set of coupons on the cold side, where the corrosion rate increased and extensive pitting was observed. This anomalous behavior is probably due to the increase in dissolved oxygen observed at this time.

When assessing the potential for corrosion damage in geothermal systems, the type of corrosion is more important than the rate of metal dissolution. A high concentration of Cl^- or dissolved O_2 induces pitting, which increases potential equipment failures dramatically. The lack of heavy pitting on our corrosion coupons suggests that materials will not be subjected to severe corrosive attack. Nonetheless, surface hardware durability and performance in future flow tests can be enhanced with appropriate corrosion treatment. Alternatively, corrosion-resistant materials or heavy-walled pipe could be used, but in our

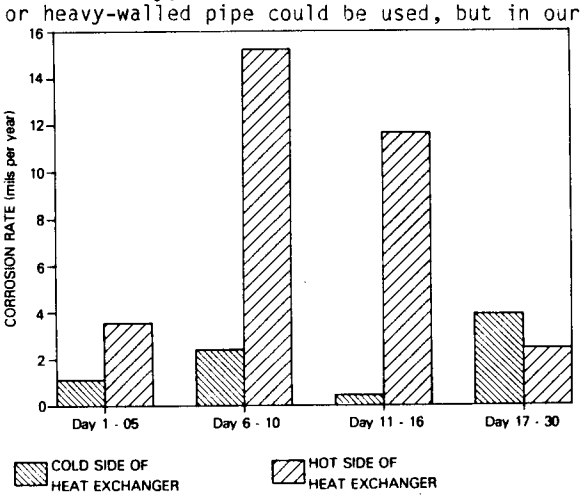


Figure 8. Corrosion rates measured on the hot and cold sides of the heat exchanger. Each value is obtained from a weight loss determination for a coupon exposed to fluid during the times labelled.

case the cost advantages of light carbon steel equipment outweigh the possible benefits of these approaches, particularly if dissolved gases are handled properly. To minimize corrosion during longer periods of operation, dissolved oxygen in the injection fluid will be kept low (in the parts per billion range) by injecting an oxygen scavenger such as ammonium bisulfite or hydrazine.

Gas Handling: To keep a geothermal fluid containing dissolved CO_2 single-phase, the total system pressure must be greater than the sum of the partial pressures of CO_2 and water:

$$P > P_{CO_2} + P_W \qquad (6)$$

This expression is valid for a closed system not open to the atmosphere. The partial pressure of water, P_W, is approximately equal to its vapor pressure. The term P_{CO_2} is a function of the concentration of CO_2 in the liquid phase and its Henry's law constant K_H, as given by Eqn. (5). The constant K_H and P_W are both functions of temperature. Figure 9 shows the minimum pressure required to keep the solution a single phase liquid for different temperatures and concentrations of dissolved CO_2.

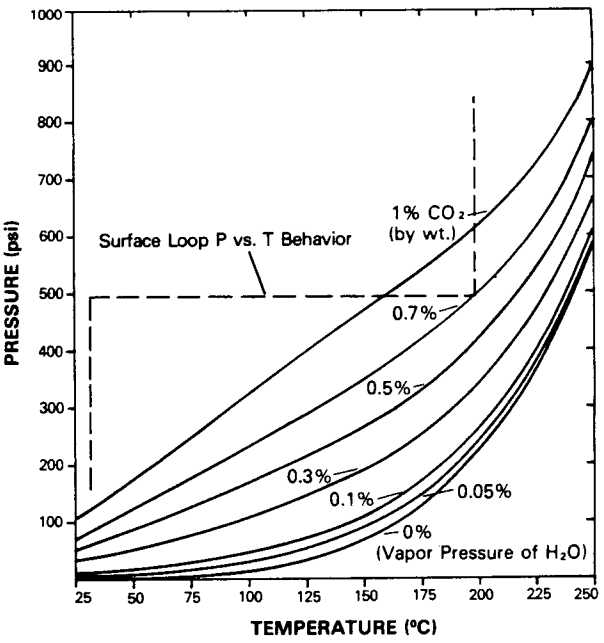


Figure 9. Pressure required to keep a CO_2 - H_2O solution single-phase for different CO_2 concentrations and temperatures. Dotted line is a typical (P,T) curve for an element of fluid passing through the surface loop equipment.

During most of the flow test, dissolved CO_2 remained in the liquid phase and was reinjected after energy extraction. A simple calculation or use of Figure 9 shows why this was possible.

The dotted line in Figure 9, representing the pressure-temperature behavior of fluid in the surface loop, shows that only fluids with dissolved CO_2 concentrations greater than 0.7% will cause flashing. For the typical value of 0.2 - 0.3%, mixture will remain a single phase. Occasionally, new regions of the reservoir were accessed and a transient period of high CO_2 concentration occurred. Phase separation in the production wellbore prevented us from collecting a representative sample, but Figure 9 shows that the CO_2 concentration must have been about 1% or greater. For future operations we will install a high pressure, high temperature gas separator to handle these occasional gas surges.

Scale Deposition: The two types of scale deposition which were of greatest concern before the flow test were silica and calcite precipitation. When water saturated with respect to quartz at reservoir temperatures is cooled, it becomes supersaturated with respect to all forms of silica. Hence a driving force for silica scaling is present. Calcite precipitation occurs for a different reason. Flashing of CO_2 from solution creates disequilibrium which, according to elementary chemical thermodynamics, will cause the reaction of Eqn. (3) to proceed to the left to reachieve equilibrium. Thus, calcite ($CaCO_3$) is deposited.

Despite these potential mechanisms, very little scale deposition was uncovered in a post-experiment examination of the surface loop, and this scale did not adversely affect the performance of the equipment. Only a small amount of calcium carbonate scale was found on a pipe leading to the heat exchanger, while no silica deposits were found. However, some magnetite scale was detected in the inlet manifolds of the heat exchangers, although we cannot determine whether it was deposited during this or a previous flow test. In addition, a yellowish precipitate containing about 4% arsenic was detected on the corrosion coupons on the cold station of the heat exchanger and in the heat exchanger itself.

RADIOACTIVE TRACER EXPERIMENTS

PROCEDURES

Two radioactive tracer experiments, the first on day 10 and the second on day 25, were carried out using an irradiated form of the water soluble salt, ammonium bromide, NH_4Br. The tracer, ^{82}Br, a gamma-emitting radionuclide with a half-life of 35.3 hr, has been used as a conservative (nonreacting, nonadsorbing) tracer at Fenton Hill for several years (Robinson and Tester, 1984). In each tracer experiment a sample was irradiated in Los Alamos's Omega West nuclear reactor, assayed, and transported to the Fenton Hill site. Accounting for radioactive decay during the transportation, the injected pulse strengths were 61.9 mCi and 70.2 mCi. Measurements of gamma activity as a function of time were obtained in the mobile chemistry laboratory by flowing a liquid sidestream through a continuous flow cell equipped with a NaI scintillation counter.

RESULTS

To obtain a residence time distribution (RTD) curve from a pulse injection tracer experiment, the background radioactivity must be subtracted and the resulting value corrected for radioactive decay. Then, the RTD f(V) is given by

$$f(V)= \frac{C(V)}{m_p} \qquad (7)$$

where C(V) is the corrected concentration at produced fluid volume V, and m_p is the mass of the tracer pulse.

When the produced fluid is recirculated, as in the first test, the concentration-time response must also be corrected for the reinjection of radioactive fluid using a mathematical deconvolution technique (Robinson and Tester, 1984). This calculation was performed for the first experiment, while the second test was conducted in the open loop injection mode with production fluid returns temporarily vented to a holding pond. Thus in the second test the true RTD was obtained directly from Eqn. (7).

The RTD curves for the two experiments are shown in Figure 10. The most striking difference from tracer tests in past Fenton Hill reservoirs is the low recovery of tracer. The ^{82}Br tracer experiment is limited to 2-3 days due to its half-life, so the low tracer recoveries actually imply that a larger percentage of the fluid has residence times longer than 3 days. According to current models of tracer flow through fractured reservoirs, the present system must contain flow paths of large volume which conduct at least half the fluid. In addition, the modal volume (produced fluid volume at the peak of the response curve), a standard correlating parameter for estimating the heat transfer capacity of a fractured HDR reservoir, (Robinson and Tester, 1984) is larger by roughly a factor of two than previous Fenton Hill reservoirs at a similar stage of operation. Hence we expect a longer-lasting reservoir with more gradual production fluid temperature drawdown than in the past.

Comparing the two tracer curves, the response is shifted to larger volumes, and less tracer was recovered in the second test. This result is due to the transient state of the reservoir during the flow test - throughout the test, the difference of the inlet and outlet flow rates, commonly thought of as water loss, was in large part going into charging the reservoir. Thus a dramatic increase in the integral mean volume (the volume of all fractures connecting the two wellbores, re-

gardless of residence time) from 2180 to 8440 m^3 was observed. The post-experiment vent of the reservoir supports the idea that the observed water loss was caused by the need to fill the fracture system. Of the total of 12000 m^3 net water lost to the fracture system, 6400 m^3 has returned during the vent. Both of these values are rough agreement with the fracture volume of 8440 m^3 measured in the second tracer test.

The fracture volume estimates aid in the development of conceptual models of the flow system. Assuming a homogeneous fracture network of known porosity, fracture volumes may be used to calculate the swept rock volume. The value of fracture porosity may be bounded between 0.0002 - 0.001, based measurements of seismicity and reservoir compressibility calculations. For a fracture porosity of 0.001, the rock volumes calculated from the two tracer experiments correspond to a sphere of diameter 160 m for the first and 250 m for the second. Although the value of porosity is inexact, the resulting sphere diameters are of the same order of magnitude as the wellbore separation distance of 110 m. Thus the conceptual model of flow through a large network of fractures with a point source and sink is a reasonable first approximation.

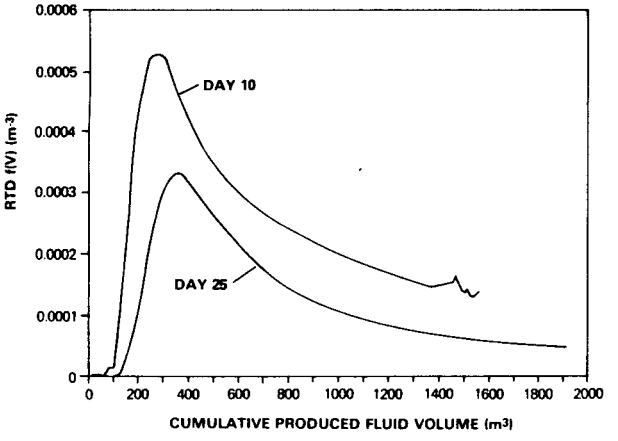


Figure 10. Residence time distribution curves obtained from the two radioactive tracer experiments.

CONCLUSIONS

1. The geochemistry of the production fluid over the first 5 days of the experiment followed three characteristic trends: 1) the decline of inert species from their initial concentrations to the injection fluid concentration; 2) no change in concentration, indicating a supply of the dissolved species via dissolution reactions (SiO_2); 3) and decline of concentration to below the injection concentration, caused by absorption, precipitation, or ion exchange reactions.
2. The Na-K-Ca and SiO_2 geothermometers yielded temperatures which agree well with the known downhole temperature. Also in agreement with these temperatures are the equilibrium reactions of calcite dissolution and bicarbonate-dissolved CO_2.
3. Corrosion coupon studies found generalized and uniform corrosion at rates of 10-15 mpy. One case of pitting was observed, which we attribute to increased dissolved O_2. An oxygen scavenger will be injected in future operations to minimize pitting corrosion. Scale deposition was minimal and did not affect operations.
4. Several periods of high dissolved CO_2 concentration, estimated at 1% by weight, created a temporary two-phase flow condition at a shallow depth in the production wellbore and in the surface loop. Future operations will require a gas separator to handle these transients.
5. Two radioactive tracer experiments resulted in modal volumes about twice as large as previous reservoirs at Fenton Hill. Furthermore, tracer recoveries are lower, indicating flow through a large number of fractures. The total swept fracture volume increased during this flow test as injected fluid continued to fill the reservoir. The total swept rock volume, calculated from tracer-determined fracture volumes and reasonable estimates of fracture porosity, is equivalent to a sphere of diameter equal to approximately the wellbore separation distance. This agreement lends credence to a point-source, point-sink model of flow through a network of fractures.

ACKNOWLEDGEMENTS

The authors thank George Cocks, Charles Grigsby, Motoyuki Inoue, Yoshihisa Shida, and Hideaki Kitamura for their assistance in collecting fluid and gas samples, and Joe Skalski, Lynn Brewer, and Bill Spurgeon for their help in setting up the sample collection equipment. Thanks also go to Hugh Murphy for reviewing this paper and to Cheryl Straub for typing the manuscript. This work was funded by the U.S. Department of Energy and the Government of Japan.

NOMENCLATURE

a^*	quartz surface area to fluid volume ratio (m^2/m^3)
b	fracture aperture (m)
C	concentration (kg/m^3)
C^*	dimensionless concentration in Eqn. (1)
C_{in}	injection fluid concentration (kg/m^3)
C_o	initial production fluid concentration (kg/m^3)
C^∞	silica saturation concentration (kg/m^3)
f_q	fraction of quartz present in granite
$f(V)$	residence time distribution curve (m^{-3})

k quartz dissolution rate constant (m/s)
K_{eq} equilibrium constant
K_H Henry's law constant (bar/mole fr.)
m_p mass of tracer injected (kg)
P pressure (bar)
P_{CO_2} partial pressure of CO_2 (bar)
P_w vapor pressure of water (bar)
t time (s)
V cumulative produced fluid volume (m^3)
x_{CO_2} mole fraction of CO_2
γ_i activity coefficient for component i
Φ dimensionless concentration in Eqn. (2)

REFERENCES

Hendron, R.H., "Fenton Hill Hot Dry Rock Overview", presented at the Twelfth Workshop on Geothermal Reservoir Engineering, Stanford University, Stanford, CA, Jan. 20-22 (1987).

Henley, R.W., Truesdell, A.H., and P.B. Barton, "Fluid-Mineral Equilibria in Hydrothermal Systems," Reviews in Economic Geology, V. 1 (1984).

Grigsby, C.O., "Rock-Water Interactions in Hot Dry Rock Geothermal Systems: Reservoir Simulation and Modeling," MS Thesis, Massachusetts Institute of Technology Dept. of Chemical Engineering (1983).

Grigsby, C.O., Tester, J.W., Trujillo, P.E., Counce, D.A., Abbott, J., Holley, C.E., and L.A. Blatz, "Rock-Water Interactions in Hot Dry Rock Geothermal Systems: Field Investigations of In Situ Geochemical Behavior," J. Volcan. and Geothermal Res., 15, 101-136 (1983).

Robinson, B.A., "Quartz Dissolution and Silica Deposition in Hot Dry Rock Geothermal Systems," MS Thesis, Massachusetts Institute of Technology Dept. of Chemical Engineering (1982).

Robinson, B.A., and J.W. Tester, "Dispersed Fluid Flow in Fractured Reservoirs: An Analysis of Tracer-Determined Residence Time Distributions," J. Geophys. Res., 89, B12, 10374-10384 (1984).

Trujillo, P.E., Counce, D., Grigsby, C.O., Goff, F., and L. Shevenell, "Chemical Analysis and Sampling Techniques for Geothermal Fluids and Gases at Fenton Hill Laboratory," Los Alamos National Laboratory internal report (1986).

PROCEEDINGS, Twelfth Workshop on Geothermal Reservoir Engineering
Stanford University, Stanford, California, January 20-22, 1987
SGP-TR-109

Interference Tests at Kawerau, New Zealand*

John G. Burnell and Mark J. McGuinness

Applied Mathematics Division, DSIR
Wellington, NewZealand

Abstract

Analysis of interference tests at the Kawerau geothermal field in New Zealand has indicated that the reservoir may be viewed on a coarse scale as a two-layer structure. While these layers have high permeabilities, they are in poor hydrological communication with each other. The shallower layer is modelled as a finite cylindrical reservoir. The deeper layer is modelled as a larger cylindrical reservoir with recharge from the sides. The fitted permeabilities and storativities suggest the importance of flow in fractures at Kawerau.

1 Introduction

The Kawerau geothermal field has been in production since 1956, and supplies steam at up to 270 t/hr to the Tasman Pulp and Paper mill. The early shallow wells ceased production within four years, due to cooling of the production zone, and the steam supply was maintained by drilling deeper. The deeper wells have lasted longer, and cooling has led to progressively deeper wells and more exploratory wells.

During August, September and October 1985, interference testing was carried out at Kawerau by the Ministry of Works and Development, Wairakei. Seven wells were monitored (Figure 1), KaM1, KaM2, KaM4, Ka11, Ka14, Ka17 and Ka31. KaM3 was used as an injection well. The two major producing wells at the time, Ka21 and Ka35, were throttled back (see Figures 2, 3 and 4). Responses fell into two groups, with the shallower feeding wells responding to injection into the shallow feeding KaM3, and the deeper feeding wells responding to the changes in production of the deep feeding Ka21 and Ka35. Ka14, which feeds at intermediate depth, responds only to Ka21, suggestive of more complicated structure.

	KaM1	KaM2	KaM4	Ka11
kh (d-m)	575	392	511	1600
ϕch (m/Pa $\times 10^{-7}$)	2.6	6.9	1.6	3.5
ϕcV (m^3/Pa)	16	18	26	10

Table 1: Parameter values obtained from fitting a finite reservoir model to the shallow responses to KaM3. A dynamic viscosity for 150°C water of $\mu = 1.8 \times 10^{-4}$ Pa.s was assumed.

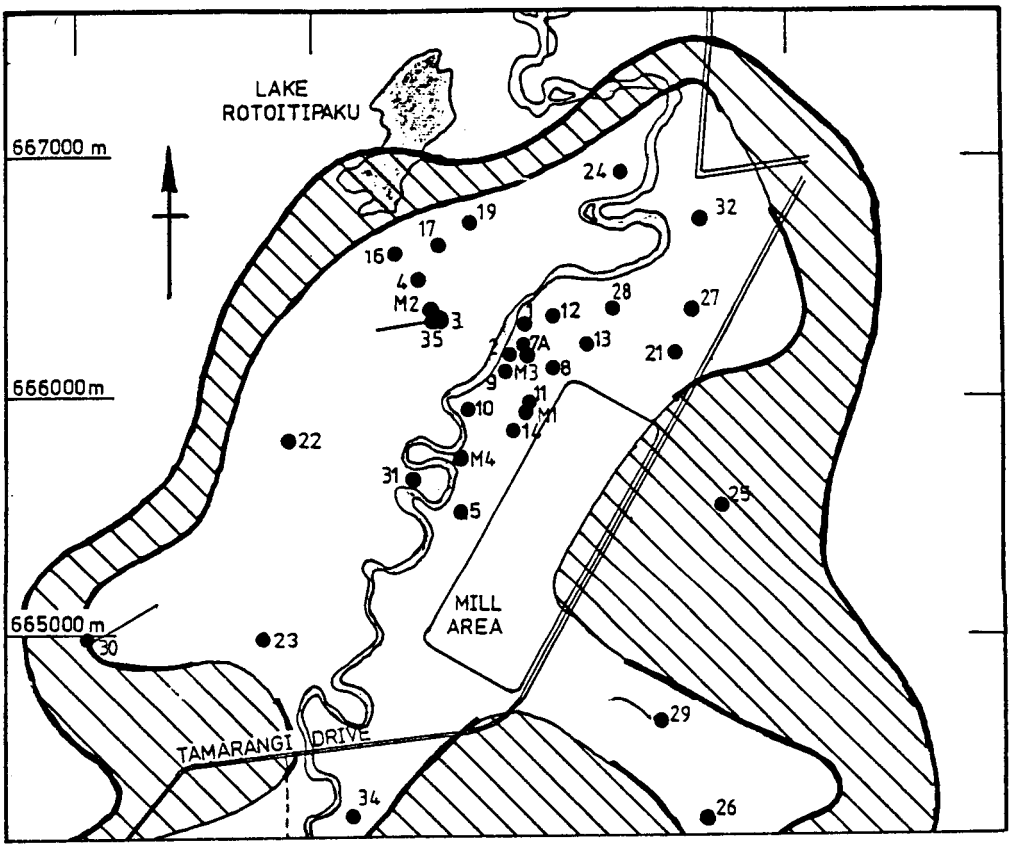
2 Shallow Responses

The wells with responses to injection into KaM3 had varying transient pressure changes, and also featured net pressure increases of 2 to 4 KPa. These pressure increases would be consistent with a finite reservoir effect. Hence the shallow reservoir was modelled as a cylinder with no-flow boundaries. The solution in Matthews and Russell (p.11) was simplified into three parts, an early time transient line-source exponential integral solution, a late time steady drawdown solution, and a linear intermediate time segment joining the other two parts (Burnell and McGuinness, 1986). This finite cylindrical reservoir solution, together with atmospheric pressure variations, was fitted to each responding well numerically, using standard nonlinear least-squares routines from the NAG library on the Applied Mathematics Division VAX. The fits obtained are plotted in Figures 5, 6, 7 and 8. The fitted parameter values obtained are in Table 1.

2.1 Results

If the storativity ϕch in Table 1 is interpreted for a model of the shallow reservoir as a closed box of fluid, with a compressibility $c = 4 \times 10^{-10}$ Pa^{-1} for 150°C water, and using the depth $h = 500$ m, unrealistically large values of porosity ϕ of 0.78–3.5 result. If the reservoir is modelled as open-topped, with an effective compressibility $c = 1/\rho gh = 2 \times 10^{-7}$ Pa^{-1}, the porosity ϕ takes values ranging from about 0.001 to

*this analysis was made under contract to the Gas and Geothermal Trading Group, Ministry of Energy, Wellington, New Zealand



Feed Depths of the Bores (metres), with the major feed listed first.

KAM1	145
KAM2	130, 95, 112
KAM3	100
KAM4	85
KA11	400
KA14	800, 500
KA17	930, 1360
KA21	1080, 710, 800, 1160
KA31	1500, 700, 1100
KA35	1010

Figure 1: Wellsites at the Kawerau Geothermal Field and Feed Depths.

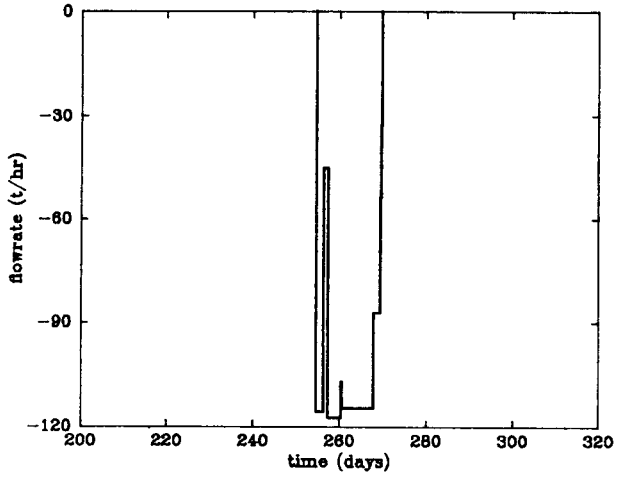


Figure 2: Measured Flowrate Changes in KaM3

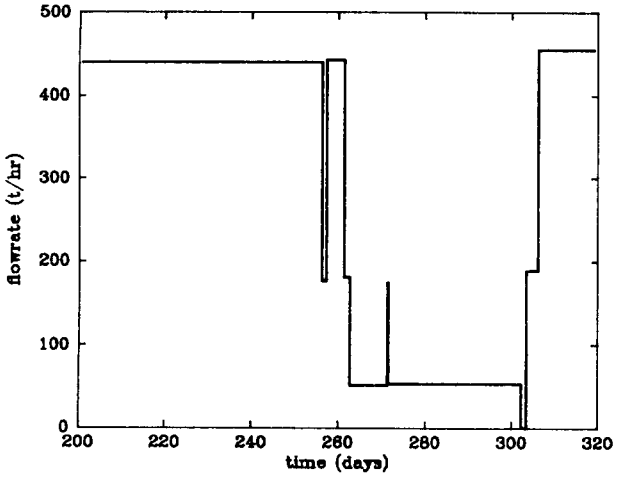


Figure 3: Measured Flowrate Changes in Ka21.

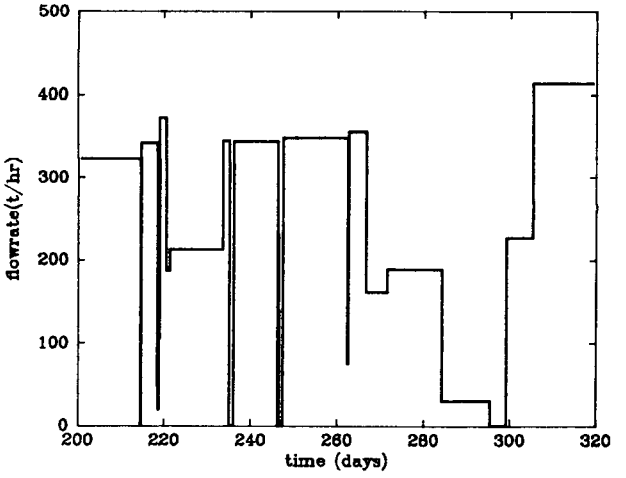


Figure 4: Measured Flowrate Changes in Ka35.

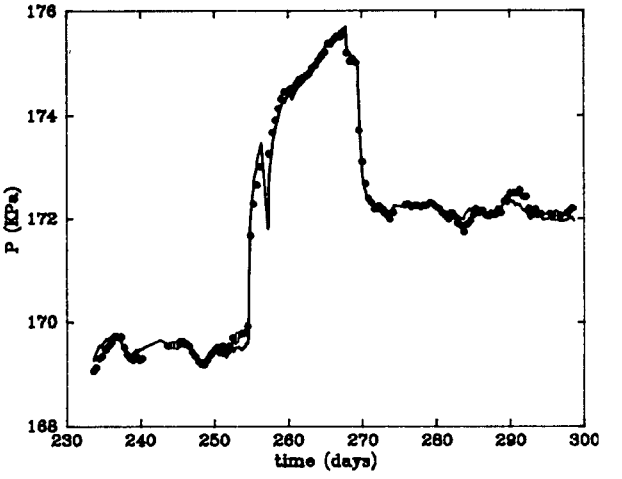


Figure 5: KaM1 pressure data and fitted finite reservoir response to KaM3.

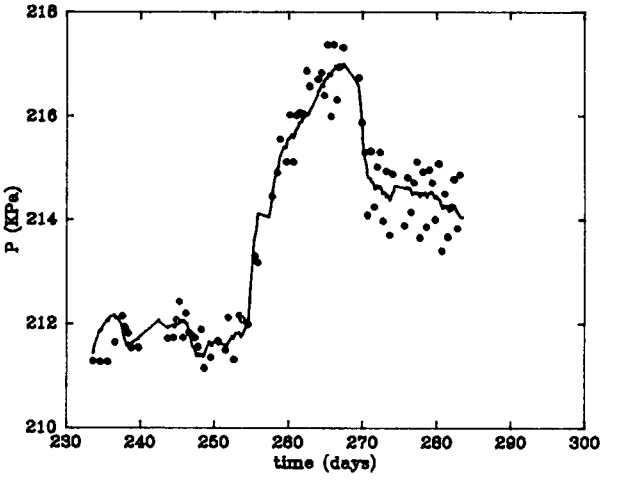


Figure 6: KaM2 pressure data and fitted finite reservoir response to KaM3.

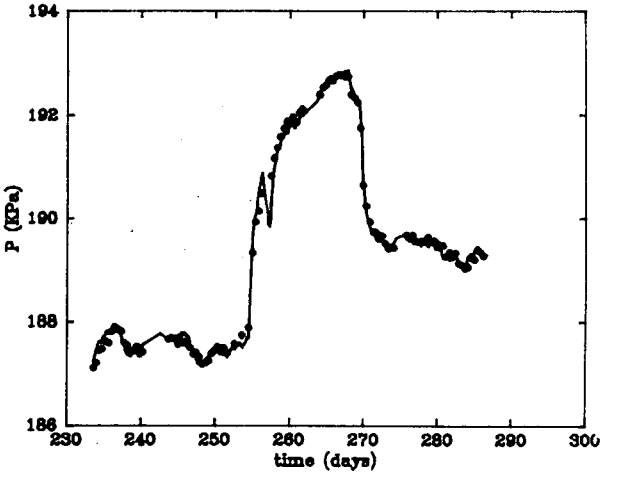


Figure 7: KaM4 pressure data and fitted finite reservoir response to KaM3.

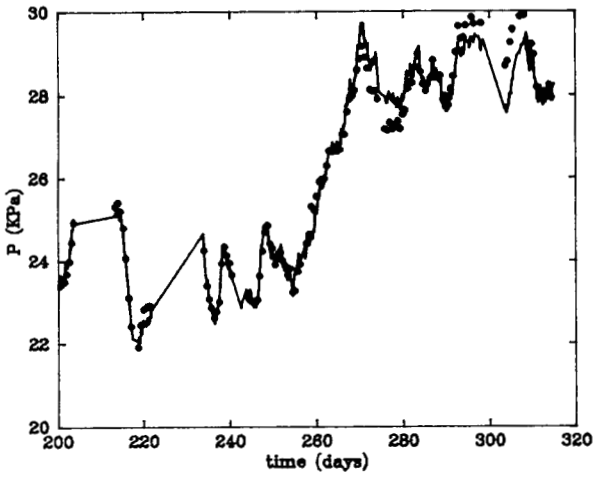


Figure 8: Ka11 pressure data and fitted finite reservoir response to KaM3.

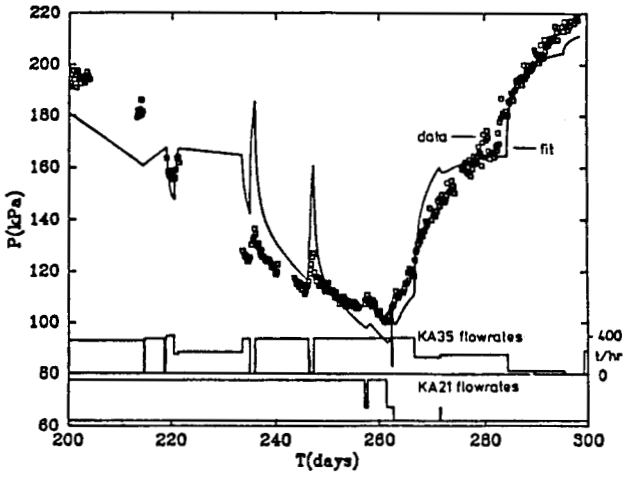


Figure 9: Ka17 pressure data and fitted Theis solution response to Ka21 and Ka35.

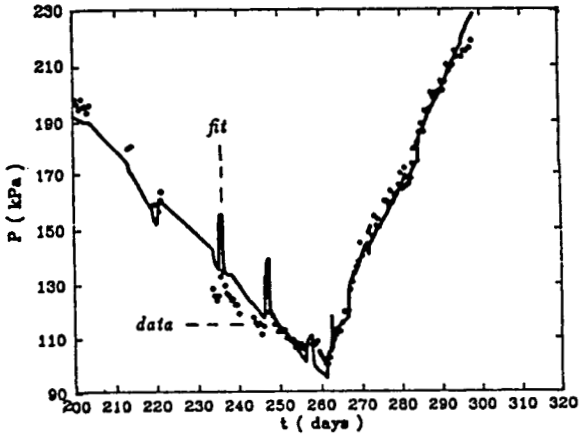


Figure 10: Ka17 pressure data and fitted finite reservoir with recharge response to Ka21 and Ka35. Uniform permeabilities were used.

0.007. This porosity is very small, suggesting a fracture network, at least at the fluid surface.

The values fitted to kh and ϕch are obtained from the early-time transient part of the model solution. The value of the storage coefficient ϕcV is obtained from fitting the late-time part of the model solution. If the early-time values of ϕch are used together with $h = 500$ m, a shallow reservoir volume in the range 14–87 Km^3 is obtained, or an area in the range 28–164 Km^2. This is much larger than expected at Kawerau — the area inside the resistivity boundary is 6–10 Km^2. This implies that the shallow reservoir may be in good hydrological communication with surrounding cooler groundwaters. An alternative possibility is that the early-time values of ϕch might not be appropriate at later times, due to double-porosity behaviour. Under this option, the early-time storativity is dominated by high permeability, low porosity fractures or contacts between layers of different reservoir materials, while at later times a higher storativity is obtained as the effect of blocks or layers of lower permeability material becomes important (see, for example, Gringarten, 1984, Moench, 1984 and McGuinness, 1986). Assuming the late-time storativity corresponds to a porosity $\phi = 0.2$, a compressibility $c = 2 \times 10^{-7}$ Pa^{-1} and a depth $h = 500$ m gives a reservoir surface area in the range 0.5–1.3 Km^2.

3 Deep Responses

The deeper-feeding wells Ka17 and Ka31 responded to changes in production of Ka21 and Ka35. Ka14, which has a major feed at intermediate depth, responds only to Ka21 within measurement accuracy.

Recharge is expected to be important in modelling the deeper responses, since the deeper reservoir has been under production for many years, and reservoir pressures have not dropped more than 2 bars (Grant, 1985). Hence a cylindrical reservoir with pressure-dependent recharge from the sides was chosen as a model. This model is developed and solved for in Burnell and McGuinness, 1986. The solution is simplified in a similar approach to that used for the shallow model, with an early-time transient solution merging into a late-time steady-state solution.

For comparison purposes, the response at Ka17 was initially fitted with the infinite-acting exponential integral solution. The effects of flowrate changes in Ka21 and Ka35 were superposed. The numerical pro-

	Ka17	Ka31	Ka14
$k_{35}h$ (d-m)	585	679	
$k_{21}h$ (d-m)	48	95	390
ϕch (m/pa$\times 10^{-7}$)	1.1	0.9	12.0
ϕcV (m^3/pa)	35	41	34
γ (m^3/Pa.s$\times 10^{-6}$)	.25	1.5	7.0

Table 2: Parameter values from fitting the cylindrical reservoir with recharge to deep responses. A dynamic viscosity for 270°C water of $\mu = 1.0 \times 10^{-4}$ Pa.s was assumed.

cedure converged to the fit shown in Figure 9. The response to long-term production was simply modelled as a linear trend. This fit is used as a reference with which improvements may be compared.

An improved fit is obtained when the model developed in Burnell and McGuinness (1986) is used. Figure 10 shows the resulting fit. The short-time pulse-like responses to changes in Ka35 flowrates are not very accurately modelled. With the possibility of vertical structure in mind, the permeability used in responses to Ka21 was allowed to be different to the permeability used in responses to Ka35. This further improved the fit, as seen in Figure 11. This model, of a cylinder with lateral recharge and different permeabilities for Ka21 and Ka35, was also successfully fitted to the responses of Ka31 and Ka14 (see Figures 12 and 13). The response of Ka14 to Ka35 flowrate changes was not significantly different from zero. The parameter values obtained from these fits are presented in Table 2.

Other wells in production at the time of the test constituted about 20% of the maximum total mass flowrate. While these wells, Ka16, Ka19, Ka27 and Ka28 were not continuously monitored, records of when they were shut and what their average flowrate was, were incorporated into the model. Ka16, which went on bleed near the beginning of the test, has been found to be in poor communication with Ka17 (McGuinness, 1985), and was ignored. The small changes (up to 50 t/hr) in the flowrate of Ka28 were incorporated into the Ka21 flowrate changes. Ka21 and Ka27 discharge into the same separator and are treated as one well since their flowrates are measured as a combined one. The flowrate changes in Ka19 were added into those for Ka35, since Ka35 took over from Ka19 on day 213. Startup time for Ka19 (Ka35) was taken from a workover which improved production at about day 0. Startup time for Ka21 was also taken to be day 0. This was an arbitrary choice, and subsequent information indicates that a better choice would be about five years earlier. These factors reduce the reliability of the results, especially the estimates of recharge and field size. In general, changing to an earlier startup time for Ka21 would be expected to increase the estimated field size and the estimated recharge to the field, making these results conservative.

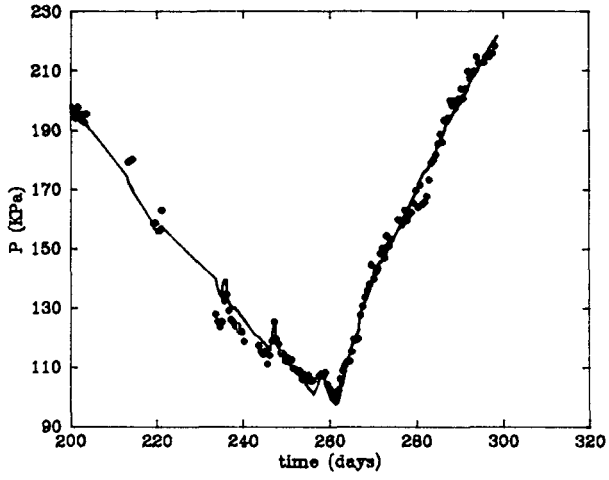


Figure 11: Ka17 pressure data and fitted finite reservoir with recharge response to Ka21 and Ka35. Permeabilities were allowed to differ for the two source wells.

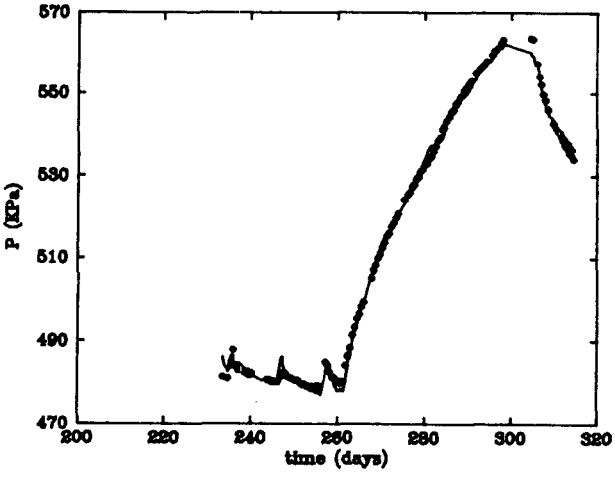


Figure 12: Ka31 pressure data and fitted finite reservoir with recharge response to Ka21 and Ka35. Permeabilities were allowed to differ for the two source wells.

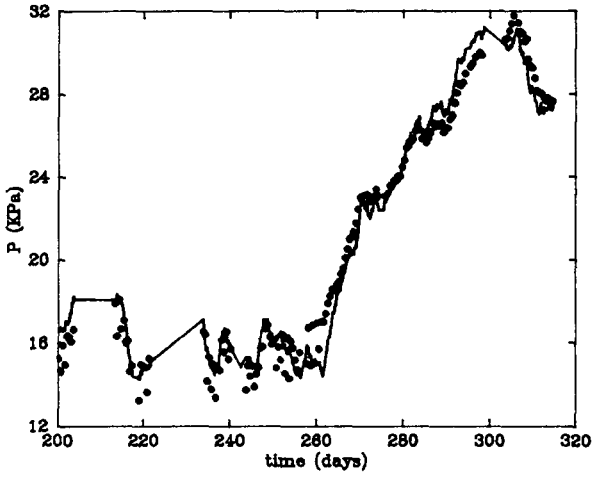


Figure 13: Ka14 pressure data and fitted finite reservoir with recharge response to Ka21 and Ka35. Permeabilities were allowed to differ for the two source wells. Response to Ka35 was insignificant.

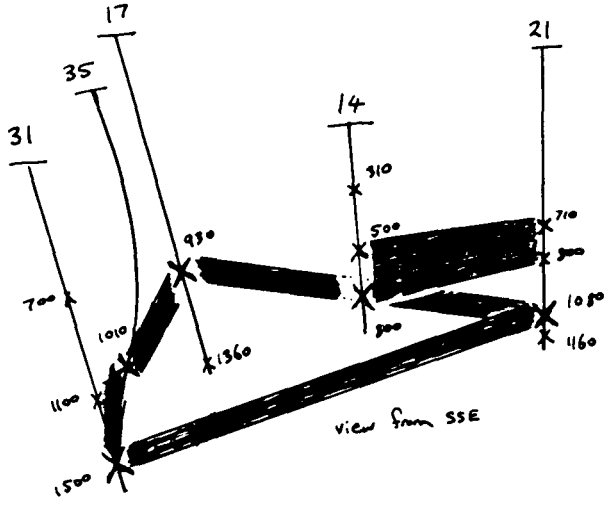


Figure 14: Possible communication paths of deep responding wells

3.1 Results

There is a consistent pattern in the fitted permeabilities in Table 2. The responses to Ka35 are smaller than those to Ka21, which gives larger permeabilities for Ka35 when using the infinite reservoir solution. This could be due to the existence of two deeper aquifers, one overlying the other. Ka21 with its multiple feedpoints may produce from both aquifers, affecting Ka14 pressures through its intermediate depth feedpoints and affecting Ka17 and Ka31 through its deepest feedpoints. See Figure 14 for a sketch of the possible communication paths.

The fitted permeabilities are high, consistent with a fractured reservoir.

The storativities ϕch are of comparable size to the values in Table 1, but with the compressibility of 260°C fluid, $c = 1.4 \times 10^{-9}\text{Pa}^{-1}$, reasonable values of ϕ result for Ka17 and Ka31. Ka14 has an anomalously high value, possibly reflecting communication with atmospheric pressure or two-phase fluid. Christenson (1986) associates degassing of fluid in the central part with a two-phase zone, surrounded by a region where the hot source fluid has mixed with cooler groundwaters.

The storage coefficients ϕcV obtained for these deep-feeding wells are larger than obtained for the shallow feeding wells, suggesting that there is more fluid available at deeper levels, about two or three times that available at shallow levels. If the values fitted to the early-time part of the solution are used, a reservoir volume of 120–140 Km^3 is obtained. With an assumed depth of 500 m, this implies an area of 240–280 Km^2, which is larger than expected at Kawerau.

The values obtained for the recharge coefficient mean that a 2 bar pressure drop would lead to 50–1400 Kg/s recharge flow. This compares with a total fluid mass production rate of up to about 400 Kg/s.

4 Conclusions

These interference tests conducted at Kawerau have led to new and vital insights into the reservoir's hydrological structure, which will point the way for improved numerical models.

Shallow feeding wells respond to injection into KaM3 in a manner consistent with a finite cylindrical reservoir model. These responses range over feed depths of about 85–400 m. There is no observable pressure communication between these wells and the deeper-feeding set of wells. The deeper-feeding wells communicate in a depth range of about 800–1010 m, in a manner consistent with a cylindrical reservoir model with lateral recharge.

A picture emerges of a smaller shallow reservoir overlying a larger deep reservoir. The shallow reservoir may be as large as 28–164 Km^2 in area. The deep reservoir may be up to 240–280 Km^2 in area. The shallow reservoir appears to be in communication with the atmosphere, and has small porosities, suggestive of the importance of fractures or contact planes. The deep reservoir has larger values of porosity, and some indication of possible communication with a two-phase zone. There is evidence of some structure in the deeper

reservoir, with larger pressure changes resulting from flow changes in Ka21 than Ka35.

This two-reservoir structure is confirmation of the good sense of the policy of drilling deeper wells at Kawerau. Shallow wells were short-lived presumably because of good communication with cooler overlying and surrounding groundwaters. Deeper wells are more shielded, by an umbrella possibly associated with sedimentary formations found at about 500 m depth in many petrological logs.

Acknowledgements

This work was made possible by the financial support of the Gas and Geothermal Trading Group, Ministry of Energy, Wellington, New Zealand. The tests were conducted and the data collected by the Ministry of Works and Development, Wairakei.

References

Burnell, J. G. and McGuinness, M. J. (1986) Kawerau Interference Tests (August–October 1985), an *Applied Mathematics Division Report* prepared for the Gas and Geothermal Trading Group, Ministry of Energy, Wellington, November 1986.

Christenson, B. W. (1986) Hydrology and Fluid Chemistry of the Kawerau Geothermal System, *in* The Kawerau Geothermal Field: Contributions from the 1982 Kawerau Seminar and Other Scientific Investigations, *DSIR Geothermal Report Number 10,* Chapter 5. This report was compiled for the Gas and Geothermal Trading Group, Ministry of Energy, New Zealand, and is confidential to them as a whole.

Gringarten, A. C. (1984) Interpretation of Tests in Fissured and Multilayered Reservoirs With Double-Porosity Behaviour: Theory and Practice, *J. Pet. Tech.* (April 1984) pp. 549–564.

Moench, A. F. (1984) Double Porosity Models for a Fissured Groundwater Reservoir With a Fracture Skin, *Water Resour. Res.* 20 #7 pp. 831–846.

McGuinness, M. J. (1985) Interference Between Ka17 and Ka27, *Report KA-1985-MJM-1* prepared for the Gas and Geothermal Trading Group, Ministry of Energy, Wellington.

McGuinness, M. J. (1986) Pressure Transmission in a Bounded Randomly Fractured Reservoir of Single-Phase Fluid, to appear in *Transport in Porous Media,* Volume 2.

Matthews, C. S. and Russell, D. G. (1967) *Pressure Buildup and Flow Tests in Wells,* Monogr. No. 1, SPE, Dallas, Texas.

Grant, M. A. (1985) Pressure Changes in the 500m Zone of Kawerau, *Report KA-1985-MAG-2,* prepared for the Ministry of Energy, Wellington.

PROCEEDINGS, Twelfth Workshop on Geothermal Reservoir Engineering
Stanford University, Stanford, California, January 20-22, 1987
SGP-TR-109

RESPONSE OF THE LOS AZUFRES GEOTHERMAL FIELD TO FOUR YEARS OF 25 MW WELLHEAD GENERATION

P. Kruger*, J. Ortiz+, C. Miranda+, and M. Gallardo+

*Stanford Geothermal Program
Stanford University
Stanford, CA

+Los Azufres Geothermal Field
Comision Federal de Electricidad
Ciudad Hidalgo, Michoacan

ABSTRACT

Production and chemical data have been compiled and analyzed on a six-month averaged basis for the first four years of electric energy generation with five 5-MW wellhead generators at the Los Azufres geothermal field. The data were evaluated with respect to the extent of observable thermal drawdown of the reservoir from 25 MW of generation in relation to the estimated capacity of the field of several hundred megawatts of power. The analysis updates the previous one compiled after the first two years of continuous production, at which time the results indicated that differences in reservoir temperature estimated from geochemical thermometers and wellhead production data were not statistically significant based on the number of data and the standard deviations. Analysis of the data after four years of operation were made for the larger number of data and smaller standard deviations. The results review the adequacy of the sampling frequency and the reliability of the measurements from statistical t-Test of the means of the first and second two-year periods.

INTRODUCTION

An important aspect of the development of geothermal resources is the observation of the effects on the reservoir from early sustained production with small generating units used to initiate potentially large fields. Such observations have been a continuous objective of the electric power production program started at the Los Azufres geothermal field in the summer of 1982 with five 5-MW wellhead units. Since production startup, a large database of production and chemical data has been compiled to characterize the well and reservoir conditions during the startup period and to establish the initial conditions of the reservoir near the production wells. The latter objective is of importance for observing changes in reservoir characteristics with production prior to installation of additional generating capacity planned for the near future.

The Los Azufres geothermal field is located in the State of Michoacan, about 200 km northwest of Mexico City. It is part of the Transmexico Neovolcanic Axis across central Mexico (Mooser, 1972). The geothermal reservoir is a complex structural and thermodynamic system, containing several major parallel faults. Sustained production in the field started with three 5-MW wellhead generator units in the northern (Maritaro) zone producing two-phase fluid and two 5-MW units in the southern (Tejamaniles) zone producing essentially all-steam or large steam fraction fluid. A review of the operating characteristics of the 5-MW turbine-generator units was given by Hiriart (1983).

A significant body of information on the Los Azufres field has been compiled since the early reports by de Anda (1951) on the geologic, geophysical, and geochemical characteristics. Geologic maps, first prepared by Camacho (1976), are continuously updated. The structural and volcanic features were described by de la Cruz (1982) and more recently by Dobson and Mahood (1985). Data for brine chemistry and noncondensable gases were reported by Templos and Lopez (1980) and Templos and Laredo (1980). An overview of the distribution of chemical and isotopic composition of Los Azufres geothermal fluids prior to startup was reported by Nieva et al (1983). Their data showed much heterogeneity of the liquid phase in the reservoir. The chemical data showed phase separation around the wells without evidence of recharge by infiltrating groundwater. From several chemical geothermometers, the temperature range in the northern (Maritaro) zone was estimated in the range of 248 to 315 °C, and in the southern (Tejamaniles) zone in the range of 248 to 328 C. Iglesias et al. (1983) investigated reservoir pressure as a function of depth in the Tejamaniles zone wells. They concluded that a continuous steam phase did not exist in the reservoir, but that isolated pockets of steam were developing by boiling of nearby immobile liquid water.

Two earlier evaluations of the startup effects of the 5-MW wellhead units have been reported. The first of these (Kruger, et al, 1985a) examined the initial chemical and reservoir conditions during the first two-year startup period with data compiled as six-month average values for each of the

Table 1

Six-Monthly Averaged Production Data

Well No.	Period	P(wh) (MPa)	P(sep) (MPa)	Q(wh) (kg/s)	X(v)	H(wh) (kJ/kg)
I. Tejamaniles Zone						
Az-6	2-82	0.84	—	12.4	1.00	2771
	1-83	0.80	—	11.7	1.00	2769
	2-83	0.82	—	11.7	1.00	2770
	1-84	0.81	—	11.7	1.00	2770
	2-84	0.85	—	10.4	1.00	2772
	1-85	0.85	—	10.8	1.00	2772
	2-85	0.91	—	10.5	1.00	2774
	1-86	0.95	—	10.7	1.00	2776
Az-16AD	2-83	0.94	0.93	8.4	0.89	2549
	1-84	0.92	0.92	9.0	0.77	2304
	2-84	0.93	0.92	9.1	0.74	2246
	1-85	0.91	0.90	8.9	0.73	2234
	2-85	0.96	0.94	9.0	0.72	2213
	1-86	0.95	0.92	9.6	0.65	2064
Az-17	2-82	2.16	0.88	17.4	1.00	2769
	1-83	2.02	0.90	17.2	1.00	2770
	2-83	1.98	0.93	17.2	1.00	2771
	1-84	1.88	0.96	16.7	1.00	2773
	2-84	1.88	0.86	15.4	1.00	2770
	1-85	1.82	0.83	15.8	1.00	2771
	2-85	2.00	0.84	15.8	1.00	2771
	1-86	1.89	0.91	15.2	1.00	2778
II. Maritaro Zone						
Az-5	2-82	3.10	0.90	26.5	0.63	2023
	1-83	2.77	0.92	26.5	0.62	2001
	2-83	2.68	0.94	26.8	0.60	1963
	1-84	2.72	0.96	26.4	0.62	2011
	2-84	2.55	1.01	28.6	0.60	1977
	1-85	2.46	0.93	30.0	0.61	1991
	2-85	2.29	0.94	29.3	0.61	2044
	1-86	2.13	0.86	29.1	0.60	1971
Az-13	2-82	1.07	0.85	27.8	0.60	1954
	1-83	0.88	0.86	28.2	0.60	1960
	2-83	1.01	0.85	27.9	0.59	1936
	1-84	0.84	0.83	29.7	0.57	1889
	2-84	0.84	0.81	32.6	0.52	1795
	1-85	0.76	0.74	31.9	0.55	1847
	2-85	0.77	0.75	31.9	0.54	1830
	1-86	0.79	0.78	30.6	0.55	1855
Az-19	2-82	0.83	0.83	17.0	0.44	1626
	1-83	0.89	0.87	15.6	0.32	1387
	2-83	0.76	0.74	15.9	0.28	1282
	1-84	1.19	*	*	*	*
	2-84	1.83	0.78	15.5	0.26	1245
	1-85	1.66	0.80*	10.4*	0.41*	1560
	2-85	1.44	0.71	11.3	0.36	1447
	1-86	1.34	0.63	11.3	0.30	1300
Az-28	1-84	1.10	—	27.8	0.48	1451
	2-84	1.26	0.78	25.4	0.37	1474
	1-85	1.14	0.80*	22.8*	0.34*	1425
	2-85	1.04	0.71	20.6	0.38	1488
	1-86	0.90	0.63	20.0	0.39	1491

*well shut-in part or all of semester.

Table 2

Aqueous Chemistry Data

Well No.	Period	pH	[Cl] (g/kg)	[Na] (mg/kg)	[K] (mg/kg)	[Ca] (mg/kg)	[SiO_2] (mg/kg)
Az-5	2-82	7.2	2.85	1654	399	7.4	1064
	1-83	7.0	3.07	1691	425	10.1	1168
	2-83	7.1	3.15	1741	429	3.6	1108
	1-84	7.1	3.03	1680	451	10.0	1081
	2-84	-	2.92	1607	446	7.2	907
	1-85	7.0	3.22	1680	472	7.5	1025
	2-85	7.2	2.98	1678	461	6.8	1069
	1-86	7.0	3.09	1723	468	7.5	1114
Az-13	2-82	7.6	3.00	1765	406	13.4	747
	1-83	7.7	2.77	1507	355	12.0	865
	2-83	7.8	2.94	1661	366	9.3	645
	1-84	7.7	2.84	1572	394	12.8	918
	2-84	7.6	2.73	1517	399	9.9	805
	1-85	7.6	2.88	1498	392	10.9	805
	2-85	7.8	2.87	1645	412	9.8	799
	1-86	7.6	2.84	1634	411	10.0	892
Az-16AD	1-84	7.6	3.11	1816	370	32.8	419
	2-84	7.5	3.25	1870	386	26.4	576
	1-85	7.6	3.37	1751	390	36.7	660
	2-85	7.6	3.38	1937	402	32.9	683
	1-86	7.4	3.40	1977	425	38.9	695
Az-19	2-82	7.4	2.88	1633	387	7.4	1034
	1-83	7.4	2.61	1445	343	8.1	910
	2-83	7.5	2.80	1580	357	5.3	961
	1-84	7.2	2.71	1537	412	8.1	1058
	2-84	6.9	2.82	1571	422	15.6	1015
	1-85	7.9	2.81	1462	372	7.3	900
	2-85	7.5	2.42	1355	365	6.9	889
	1-86	6.5	2.40	1305	343	5.9	856
Az-28	1-84	6.8	3.41	1972	508	12.1	1170
	2-84	6.3	2.66	1532	412	10.9	797
	1-85	6.9	3.44	1625	463	6.6	938
	2-85	7.1	2.70	1510	412	5.3	904
	1-86	6.7	2.68	1457	415	5.7	808

unit wells. From these data, initial reservoir and bottom-hole temperatures were estimated. It was noted that the data were obtained under a variety of objectives and analytical techniques with consequent uncertainties in the mean values larger than desirable for use as indicators of change with production. The second report (Kruger et al., 1985b) was based on a quality analysis of the sampling and chemistry data to reduce the uncertainty in the averaged values, and with the addition of an additional half-year of data, the initial thermodynamic and chemical characteristics of the reservoir were re-evaluated. The components of the chemical data included aqueous chemistry of the brines for the two-phase wells, noncondensable gases including radon for all of the wells, and geothermometer reservoir temperatures from the aqueous chemistry data.

The results of these two evaluations showed the clear delineation of the two major zones of the field, the vapor-dominated Tejamaniles (southern) zone with an initial temperature of about 260 ± 5 °C consistent with the observations of Iglesias et al. (1983) for the depth of these wells and an initial temperature of about 300 ± 10 °C for the two-phase Maritaro (northern) zone. Based on the two-year averaged reservoir temperature data, an isoenthalpic progression of steam fractions and temperatures from the reservoir to the wellhead were noted from the Fournier and Truesdell (1973) Na-K-Ca geothermometer and the Fournier and Potter (1982) silica geothermometer. The lower silica temperatures were in accord with the views of Truesdell et al. (1984) and Grant et al. (1984) that the silica based geothermometer indicates reservoir conditions closer to the wellbore as boiling increases the steam fraction and silica precipitates before fluid production. Over the first two years of production, no discernable changes were noted by statistical t-Test analysis of the first vs second year's data due primarily to the small number of samples and the relatively large standard deviations of the means. These data have now been updated with production and chemical data for the first four years of operation of the 5-MW generator units. At this time, a larger number of samples and reduced uncertainty in the means have allowed more reliable t-Tests of the data grouped into two 2-year periods.

ACCUMULATED DATA

Production data have been compiled for the original wells used for the five 5-MW wellhead units: Az-6 and Az-17 in the Tejamaniles zone and Az-5, Az-13, and Az-19 in the Maritaro zone. Two of the units have since required additional steam supply; in 1983 flow from well Az-16AD was added to the flow from Az-6 in the Tejamaniles zone and in 1984, flow from Az-28 was added to the flow from Az-19 in the Maritaro zone. Due to a heavy influx of cold water, well Az-19 has been shutin on occasion since then.

Table 1 summarizes the mean six-monthly production data for the five generator units over the four year period. Table 2 summarizes the mean six-monthly chemical data for the five wells in the Maritaro two-phase zone. Table 3 shows the mean six-monthly reservoir temperatures calculated by the Na-K-Ca geothermometer of Fournier and Truesdell (1973) and the SiO_2 geothermometer of Fournier and Potter (1982). Also given in Table 3 are the mean wellhead enthalpies obtained from production data and the reservoir enthalpies corresponding to the silica geothermometer relationships from Fournier and Potter (1982).

The production data in Table 1 reflect the continuous steam production in wells Az-6 and Az-17 in the Tejamaniles zone. The small and declining production rate in well Az-6 has been augmented with flow from well Az-16AD. For the northern Maritaro zone, the data show the steady operation of wells Az-5 and Az-13 with slowly increasing flowrates as steam fraction declines. The data for well Az-19 reflect the continued cold-water influx with production augmented by the somewhat better quality flow from well Az-28. The separator pressure has been maintained at the minimum inlet pressure required for the 5-MW wellhead unit turbines.

The aqueous chemistry data are monitored by the chloride concentration, which shows no discernable change for wells Az-5 and Az-13. The chloride concentration seems to increase in well Az-16AD and decrease in the fourth year at well Az-19 and more rapidly in well Az-28. The sodium, potassium, and silica concentrations appear to follow these trends. The geothermometer temperature data in Table 3 indicate an increase in the Na-K-Ca temperature in several of the wells and a decrease in SiO_2 temperature in others. Figure 1 shows the data and trend line of the 33 individual Na-K-Ca temperatures for well Az-5 in comparison to the observed wellhead fluid enthalpy. The slope of the Na-K-Ca temperature trend line is +3.5 °C/yr and the slope of the wellhead enthalpy trend line is +2.6 kJ/kg-yr. Figure 2 shows these data for well Az-13. For this well the rate of increase of the Na-K-Ca temperature is +3.9 °C/yr and the rate of change of the wellhead enthalpy is essentially zero. Figure 3 shows the data and trend lines for the two reservoir temperature geothermometers for well Az-19, where cold-water intrusion from a casing break above is known to be occuring. The slopes of the trend lines are +0.25 °C/yr for the Na-K-Ca and -0.38 °C/yr for the SiO_2 geothermometers.

Table 3

Mean Semi-Annual Temperature - Enthalpy Data for the Maritaro Wells

Well No.	Period	Num Obs	T(Na-K-Ca) (°C)	T(SiO_2) (°C)	H(wh) (kJ/kg)	H(SiO_2) (kJ/kg)
Az-5	2-82	3	308 ± 2	293 ± 15	2023	1303 ± 74
	1-83	5	309 ± 12	302 ± 17	2001	1355 ± 99
	2-83	1	320	298	1963	1325
	1-84	6	311 ± 5	295 ± 13	2011	1311 ± 63
	2-84	5	318 ± 5	277 ± 13	1977	1223 ± 63
	1-85	5	320 ± 6	289 ± 5	1991	1284 ± 26
	2-85	4	319 ± 2	294 ± 8	2044	1305 ± 40
	1-86	4	317 ± 3	298 ± 5	1971	1328 ± 26
Az-13	2-82	6	292 ± 8	268 ± 21	1954	1180 ± 06
	1-83	6	295 ± 12	272 ± 17	1960	1200 ± 87
	2-83	1	294	248	1936	1080
	1-84	5	300 ± 4	283 ± 5	1889	1252 ± 26
	2-84	6	306 ± 4	267 ± 10	1795	1174 ± 50
	1-85	6	304 ± 4	266 ± 5	1847	1170 ± 26
	2-85	5	305 ± 2	266 ± 8	1830	1178 ± 42
	1-86	5	304 ± 2	276 ± 11	1855	1215 ± 53
Az-16AD	1-84	6	274 ± 7	216 ± 18	2304	923 ± 83
	2-84	3	280 ± 3	239 ± 10	2246	1036 ± 48
	1-85	6	278 ± 2	249 ± 3	2234	1085 ± 15
	2-85	4	276 ± 2	252 ± 10	2213	1101 ± 48
	1-86	6	278 ± 3	254 ± 7	2064	1109 ± 33
Az-19	2-82	4	304 ± 3	292 ± 7	1626	1298 ± 37
	1-83	3	299 ± 9	278 ± 8	1387	1225 ± 38
	2-83	1	303	283	1282	1251
	1-84	2	312 ± 7	293 ± 1	—	1300 ± 10
	2-84	4	315 ± 15	288 ± 7	1245	1279 ± 36
	1-85	2	297 ± 13	277 ± 2	1560	1221 ± 11
	2-85	4	310 ± 2	275 ± 9	1447	1214 ± 43
	1-86	6	310 ± 2	272 ± 10	1300	1197 ± 49
Az-28	1-84	4	311 ± 2	305 ± 3	1451	1365 ± 15
	2-84	4	310 ± 11	263 ± 32	1474	1156 ± 158
	1-85	6	322 ± 3	280 ± 12	1425	1239 ± 60
	2-85	5	319 ± 2	277 ± 9	1488	1222 ± 46
	1-86	6	321 ± 9	266 ± 15	1491	1170 ± 76

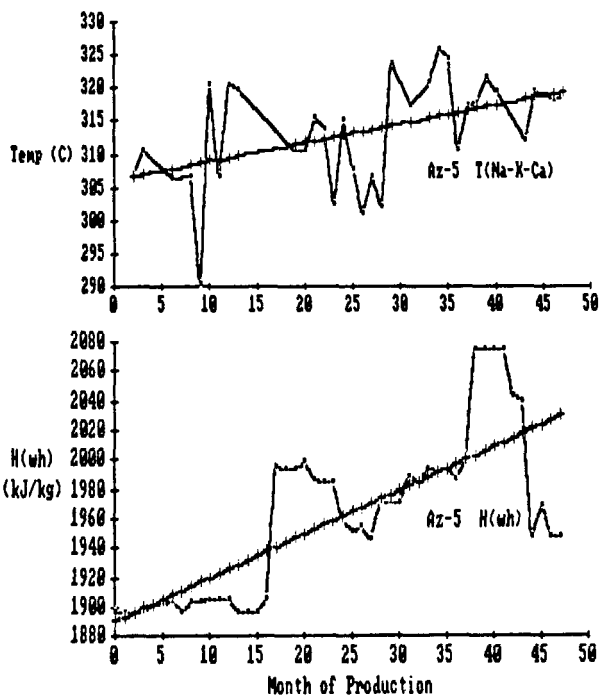


Fig. 1. Reservoir temperatures calculated by the Na-K-Ca geothermometer and wellhead enthalpies observed for well Az-5.

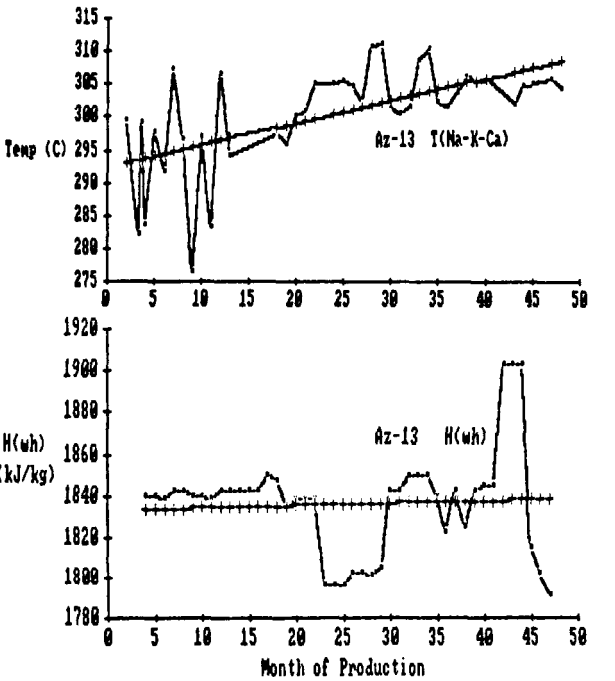


Fig. 2. Reservoir temperatures calculated by the Na-K-Ca geothermometer and wellhead enthalpies observed for well Az-13.

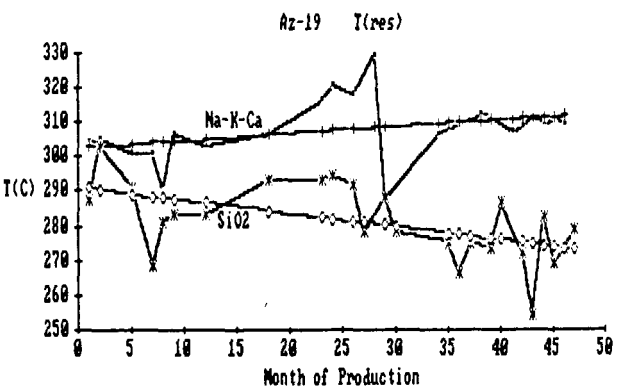


Fig. 3. Reservoir temperatures calculated by the Na-K-Ca and SiO_2 geothermometers for well Az-19.

t-TEST ANALYSIS OF THE GEOCHEMICAL DATA

To obtain a more systematic estimate of the changes that have occured in the Maritaro zone wells with four years of sustained production, the Student t-Test was applied to the data combined as two sets of two-year data samples. The standard t-Test, (see e.g., Volk, 1958) is used to determine the confidence level with which two sets of data belong to the same distribution, based on their means, standard deviations, and number of observations. It is especially useful for small data sets of a few to about 30 total observations. The t statistic is defined as

$$t = \frac{\left|\bar{x}_1 - \bar{x}_2\right|}{\bar{s}(\bar{x})\left[1/n_1 - 1/n_2\right]^{1/2}}$$

where $\bar{x}$ = means of the two data sets
n = number of obseravations in each data set
$\bar{s}(\bar{x})$ = pooled estimate of standard deviations from both data sets.

The t statistic for a given pair of data sets with the corresponding number of degrees of freedom, defined as $\nu = n_1+n_2-2$, determines in a standard table of t distributions, the value of α, the probability of a larger absolute value of t. Where a change in means can be either + or -, the two-sided t-Test is used, for which the $\alpha/2$ significance level allows for exceedence on either side of the distribution.

Table 4 shows the results of the t-Test applied to the data for the Maritaro zone wells calculated from a microcomputer program which incorporates the standard t-Test table values for confidence levels of α = 0.8, 0.9, 0.95, 0.98, and 0.99. Two means are generally accepted as belonging to the same distribution for $\alpha/2 < 0.975$. Table 4 shows the large confidence levels for the increase in mean Na-K-Ca geothermometer temperature and wellhead enthalpy for well Az-5. The decrease in SiO_2 geothermometer temperature and corresponding reservoir enthalpy is marginally signifcant due to the larger standard deviations of the silica measurements. The results for well Az-13 show only a significant increase in Na-K-Ca geothermometer temperature without a corresponding significant increase in wellhead enthalpy. The change would have been significant at the 95 % confidence level if the standard deviation of the mean for years 1+2 had been the same as that for years 3+4. For well Az-19, the 5 % increase in mean Na-K-Ca temperature does not exceed the 95 % confidence level, but the 4 % decrease in mean SiO_2 temperature does.

Table 4

t-Test Results of Maritaro Zone Well Data

Well No.	Parameter	Year (1+2) No.	Year (1+2) Mean ± SD	Years (3+4) No.	Years (3+4) Mean ± SD	t-stat Value	Confid Level(%)
Az-5							
	[Cl] (g/kg)	16	3.02 ± 0.17	17	3.06 ± 0.22	-0.59	< 80
	T(Na-K) (C)	15	310 ± 8	18	318 ± 4	-3.70	> 99
	T(SiO_2) (C)	15	297 ± 14	18	289 ± 11	1.95	~ 95
	H(Si)(kJ/kg)	15	1325 ± 75	18	1281 ± 56	1.92	~ 95
	H(wh)(kJ/kg)	23	1928 ± 43	24	1994 ± 45	-5.14	> 99
Az-13							
	[Cl] (g/kg)	18	2.84 ± 0.17	22	2.83 ± 0.19	0.30	< 80
	T(Na-K) (C)	18	295 ± 9	22	305 ± 3	-4.84	> 99
	T(SiO_2) (C)	18	273 ± 17	22	269 ± 9	0.99	< 80
	H(Si)(kJ/kg)	18	1201 ± 86	22	1180 ± 44	0.99	< 80
	H(wh)(kJ/kg)	20	1806 ± 147	24	1834 ± 33	-0.91	< 80
Az-19							
	[Cl] (g/kg)	10	2.76 ± 0.14	15	2.65 ± 0.39	0.85	< 80
	T(Na-K) (C)	10	304 ± 7	16	310 ± 10	-1.60	~ 85
	T(SiO_2) (C)	10	287 ± 9	16	277 ± 10	2.42	> 95
	H(Si)(kJ/kg)	10	1272 ± 45	16	1225 ± 50	2.42	> 95
	H(wh)(kJ/kg)		n/a	14	1400 ± 127	—	—

DISCUSSION

Four years of data accumulated for the wells providing steam to the five 5-Mw wellhead unit turbines show an interesting array of results with respect to near-well reservoir characteristics. The two units in the southern Tejamaniles zone do not provide sufficient aqueous chemistry data and the possibly most useful in-situ gas component, radon, has not been measured sufficiently often to afford a means to evaluate the extent of changes in reservoir thermal properties. The mean six-monthly production data do show a steady flow of fluid for well Az-6, with steadily declining steam fraction and enthalpy since the two-phase well Az-16AD was added to elevate the steam supply. Flowrates in well Az-17 have declined slowly as the system is operated at constant separator pressure, possibly indicating an increase in boiling in the formation around the well. Kruger et al. (1985b) have noted from the wellbore simulator developed by Ortiz (1983) based on the Orkiszewski (1967) method of estimating pressure drop in vertical pipes that the bottom-hole steam fraction in wells Az-6 and Az-17 was 100 percent. The data for these wells imply the need for careful reservoir management when the next step in field development occurs in 1987/88 with sustained production from 15 wells for the first 55-MW central power plant in the Tejamaniles zone.

The three units in the northern Maritaro zone, with the growing database of 30 or more chemical samples at each well, can be evaluated in terms of both production and chemical data. The decline in wellhead pressure at these units are noted as the separator steam quality changes, slowly at well Az-5 and more rapidly at wells Az-13 and Az-19+Az-28. The chemical data in Table 2 do not reflect these thermal declines, where except for wells Az-19+Az-28 in which cold water is known to be inflowing, the major component concentrations have remained essentially the same within the large standard deviations. The implication is that the replacement water from further out in the formation

has essentially the same gross chemical composition. However, the thermal properties of the fluid seem to be changing over the four years of production. The trends, supported by t-Test statistics, show for well Az-5 a 3.5 °C/yr increase in the Na-K-Ca temperature, a mean annual increase of 2.6 kJ/kg in fluid enthalpy, but no significant change in SiO_2 temperature. On the other hand, with a larger rate of increase of 4 °C/yr in the Na-K-Ca temperature, the change in both fluid enthalpy and SiO_2 temperature for the 40 total number of samples is not significant. Even for well Az-19, where cold water is entering, the chemical composition of the produced fluid does not appear to have changed, but there is an almost significant increase in the Na-K-Ca temperature and a significant decrease in the SiO_2 temperature and associated reservoir fluid enthalpy.

These observations may be considered to be in accord with the views of Truesdell et al. (1984) and Grant et al. (1984) about the silica based temperatures noted earlier. It may be possible to examine the thermodynamic changes in the reservoir in a simple way by considering the reservoir around each well as a hydrologic system with a just-penetrating well. Under this assumption the annual integrated flow for each well can be considered as a series of concentric hemispheric shells. Muskat (1937) noted that for a well which just taps the production zone in a porous medium, the flow regime can be expressed as a hemispherical flow system in which the Laplace equation for the potential function, $\Phi = -k/\mu(p-\rho gz)$, has as its solution

$$Q = 2\pi\ (\Phi_e - \Phi_w)/(1/r_w - 1/r_e)$$

where k = permeability, μ = viscosity, p = pressure, ρ = density, g = gravitational constant, and the subscripts w and e refer to the well location and the effective external boundary where pressure is unchanged by drawdown. For just-penetrating wells, the annual production volumes can be calculated by

$$V_i = 3.16x10^7 * Q_i/\rho\phi$$

and the outer effective radius by

$$R_o = (3V_i/2\pi + R_i^3)^{1/3}$$

To obtain an idea of the dimensions of the reservoir size supporting the two 5-MW units at wells Az-5 and Az-13, the successive radii were calculated based on a fluid density of 920 kg/m^3 at formation temperature and a mean porosity estimated by the Los Azufres staff as 8 percent. The calculations are given in Table 5.

The results show that for the essentially equal mean annual flowrates for both wells, the dimensions of the reservoir extraction

Table 5

Annual Reservoir Depletions from Az-5 and Az-13 as Just-Penetrating Wells

Well No.	Year	Mean Annual Flow Rate (kg/s)	Depletion Volume (10^7 m)	Outer Shell Radius (m)	Shell Thickness (m)
Az-5	1	26.5	1.13	175	175
	2	26.6	1.14	221	46
	3	29.3	1.25	256	35
	4	29.2	1.25	283	27
Az-13	1	28.0	1.20	179	179
	2	28.0	1.23	226	47
	3	32.3	1.39	263	37
	4	31.2	1.33	291	28

over the four years are of the order of 300 m, without accounting for either fluid recharge or boiling. The implication of these values is that small generator units on potentially large geothermal fields indicate effects on the field only within the zone of drawdown influence.

In using a model of just-penetrating wells, it is noted that r_e is almost always very large with respect to r_w, and thus the flow from a hemispherical system varies linearly with r_w compared to the much slower logarithmic dependence of r_w on flow from a radial system. With the further assumptions that gravity is not important in the reservoir and that the well just penetrates into a sufficiently fractured system to resemble porous media, the flowrate should be linearly related to the pressure drawdown and the wellbore radius. Studies on the ability to examine these relationships are underway.

ACKNOWLEDGMENTS

The authors express their appreciation to the Comision Federal de Electricidad (CFE) for providing the Los Azufres production and chemical data for this study. The Stanford Geothermal Program (SGP) is supported by the U.S. Department of Energy under Contract No. DE-AC03-86SF16482.

REFERENCES

Camacho, P., Mapa Preliminar del Area Geotermica de Los Azufres, Mich., CFE Technical Report, 1976.

de Anda, L. F., Primer Estudio para el Aprovechamiento de la Energia Geothermica para la Generacion de Energia Electrica en Mexico, International Geological Congress, (1951).

de la Cruz, V., Estudio Geologico Estructural a Detaile del Campo Geothermico de Los Azufres, Mich., CFE Technical Report, 1982.

Dobson, P. F. and G. A. Mahood, Volcanic Stratigraphy of the Los Azufres Geothermal Area, Mexico, J. Volc. and Geoth. Res. 25, 273-287 (1985).

Fournier, R. O. and R. W. Potter, A Revised and Expanded Silica (Quartz) Geothermometer, Bulletin GRC 11, 3-12 (November, 1982).

Fournier, R. O. and A. H. Truesdell, An Empirical Na-Ka-CA Geothermometer for Natural Waters, Geochim. et Cosmochim. Acta 37, 1255-1275 (1973).

Grant, M., A. Truesdell, and A. Mañon, Production Induced Boiling and Cold Water Entry in the Cerro Prieto Geothermal Reservoir Indicated by Chemical and Physical Measurements, Geothermics 13, 117-140, 1984.

Hiriart, G., One Year Experience with Portable Back-Pressure Turbines in Los Azufres, Proceedings, Ninth Workshop on Geothermal Reservoir Engineering, Stanford University Report SGP-TR-74, December, 1983.

Iglesias, E., V. Arellano, A. Garfias, C. Miranda, J. Hernández, and J. Gonzalez, A Method to Recover Useful Geothermal Reservoir Parameters from Production Characteristic Curves (1) Steam Reservoir, Proceedings, Ninth Workshop on Geothermal Reservoir Engineering, Stanford University Report SGP-TR-74, December, 1983.

Kruger, P., L. Semprini, S. Verma, R. Barragán. R. Moliuar,A. Aragón, J. Ortiz, C. Miranda, A. Garfias, and M. Gallardo, Initial Chemical and Reservoir Conditions at Los Azufres Wellhead Power Plant Startup, Proceedings, Tenth Workshop on Geothermal Reservoir Engineering, Stanford University Report SGP-TR-84, January, 1985a.

Kruger, P., Proceedings, 1985 International Symposium on Geothermal Energy, Geothermal Resources Council, August, 1985b.

Mooser, F., El Eje Neovolcanico Mexican, Debilidad Cortical Prepaleozoica Reactivada, Part 3, Proceedings, Second National Convention Sociedad Geologica Mexicana, 1972.

Muskat,, M., The Flow of Homogeneous Fluids Through Porous Media, (McGraw-Hill, NY, 1937).

Nieva, D., L., Quijano, A. Garfias, R. Barragán, and F. Laredo, Heterogeneity of the Liquid Phase, and Vapor Separation in Los Azufres (Mexico) Geothermal Reservoir, Proceedings, Ninth Workshop on Geothermal Reservoir Engineering, Stanford University Report SGP-TR-74, December, 1983.

Orkiszewski, J., Predicting Two-Phase Pressure Drops in Vertical Pipes, J. Petrol. Engr., June, 1967.

Ortiz, J., Two-Phase Flow in Geothermal Wells: Development and Uses of A Computer Code, Stanford University Report SGP-TR-66, June, 1983.

Templos, L. A. and F. Laredo, Geoquimica de los Gases Incondensables del Campo Geotermico de los Azufres, Michoacan, Mexico, Third National Symposium on Geothermy and Geology, Mexico, DF, September, 1980.

Templos, L. A. and J. M. Lopez, Estudios Quimicos del Agua Separeda de los Pozos Productores del Campo Geotermico de los Azufres, Michoacan, Mexico, Third National Symposium on Geothermy and Geology, Mexico DF, September 1980.

Truesdell, A., N. Nehring, J. Thompson, C. Janik, and T. Coplen, A Review of Progress in Understanding the Fluid Geochemistry of the Cerro Prieto Geothermal System, Geothermics 13, 65-74, 1984.

Volk, Applied Statistics for Engineers (McGraw-Hill, NY, 1958).

PROCEEDINGS, Twelfth Workshop on Geothermal Reservoir Engineering
Stanford University, Stanford, California, January 20-22, 1987
SGP-TR-109

PRESSURE BUILDUP TESTING OF WELL 18 IN LOS AZUFRES FIELD, MÉXICO

Pedro Sánchez Upton+ and Jón-Steinar Gudmundsson*

+ Comisión Federal de Electricidad, Morelia, México
* Orkustofnun, Reykjavík, Iceland

INTRODUCTION

Well 18 is a production well in the southern zone of Los Azufres geothermal field in México (see Figure 1). The well is located on the eastern flank of the drilled area, and produces a steam/water mixture from a depth of 1200-1250 m. A 19 hour pressure buildup test that was carried out in March 1986, is the subject of this paper. It is a part of work reported by Sánchez-U. (1986) at the Geothermal Training Programme in Iceland.

WELLS AND FIELD

Since 1972, 47 wells have been drilled in Los Azufres field: 27 producers, 8 injectors, and 12 exploration (Reyes-S., 1985). The wells in the southern Tejamaniles zone produce higher enthalpy fluids than wells in the northern Maritaro zone: 2485 kJ/kg and 1915 kJ/kg, respectively. The total flowrates of the production wells are reported 1500 tonne/hour in the southern zone and 1419 tonne/-hour in the northern zone.

The explored surface area of the Los Azufes geothermal field is 32 km² (Molinar-C., 1985). The reservoir can be described as saddle-shaped, with a dome-like structures extending to the surface in the southern Tejamaniles zone and the northern Maritaro zone. The thermodynamic state of the reservoir fluid has been investigated by Iglesias et al. (1985). In the main, the subsurface temperature follows the boiling-point-for-depth curve, except in the upper part of the southern zone, where the pressure profile indicates vapor-dominated conditions. Such reservoir conditions are discussed by Gudmundsson (1986a), for example.

The Los Azufres reservoir has been exploited since 1972 (Hiriart-L., 1983; Ortega-P. 1985) using 5 non-condensing 5 MW units, in total 25 MW. The inlet steam pressure of these units is about 8 bar-a and the steam flowrate 60 tonne/hour. A 50 MW central power plant is under construction in the Tejamaniles zone - there are plans to add 7 more non-condensing units (Alonso-E., 1985). Well 18 is scheduled to supply steam to one of these non-condensing units. The well is 1328 m deep and completed 13-3/8" to 300 m, 9-5/8" to 1000 m, and 7" from 959 m to bottom, the slotted section starting at 1013 m depth. This completion is typical in Los Azufres.

MEASUREMENTS

A temperature log from June 1983, shows the subsurface temperature profile to be rather flat, increasing from 251°C at 100 m depth to 266°C at 1000 m, reaching a maximum temperature of 268°C at 1200 m depth. The well was output tested in March, 1986, where the mass flowrate and mixture enthalpy were measured at four settings. These measurements are shown in Figure 2. A maximum flowrate of 43 kg/s was measured at a wellhead pressure of 9 bar-a and mixture enthalpy of 1763 kJ/kg. The well was then shut in and kept that way for several days.

On March 17, 1986, well 18 was opened and discharged for two days (52 hours), which is typically the time required for Los Azufres wells to reach stable flowing conditions. The mass flowrate and mixture enthalpy were measured 16.2 kg/s and 1314 kJ/kg, respectively, using the lip pressure and weir method, at a wellhead pressure of 32 bar-a. At this setting, the well discharged at a relatively low flowrate and enthalpy.

An enthalpy of 1314 kJ/kg corresponds to liquid water just below 295°C. This temperature is considerably above the maximum of 268°C measured

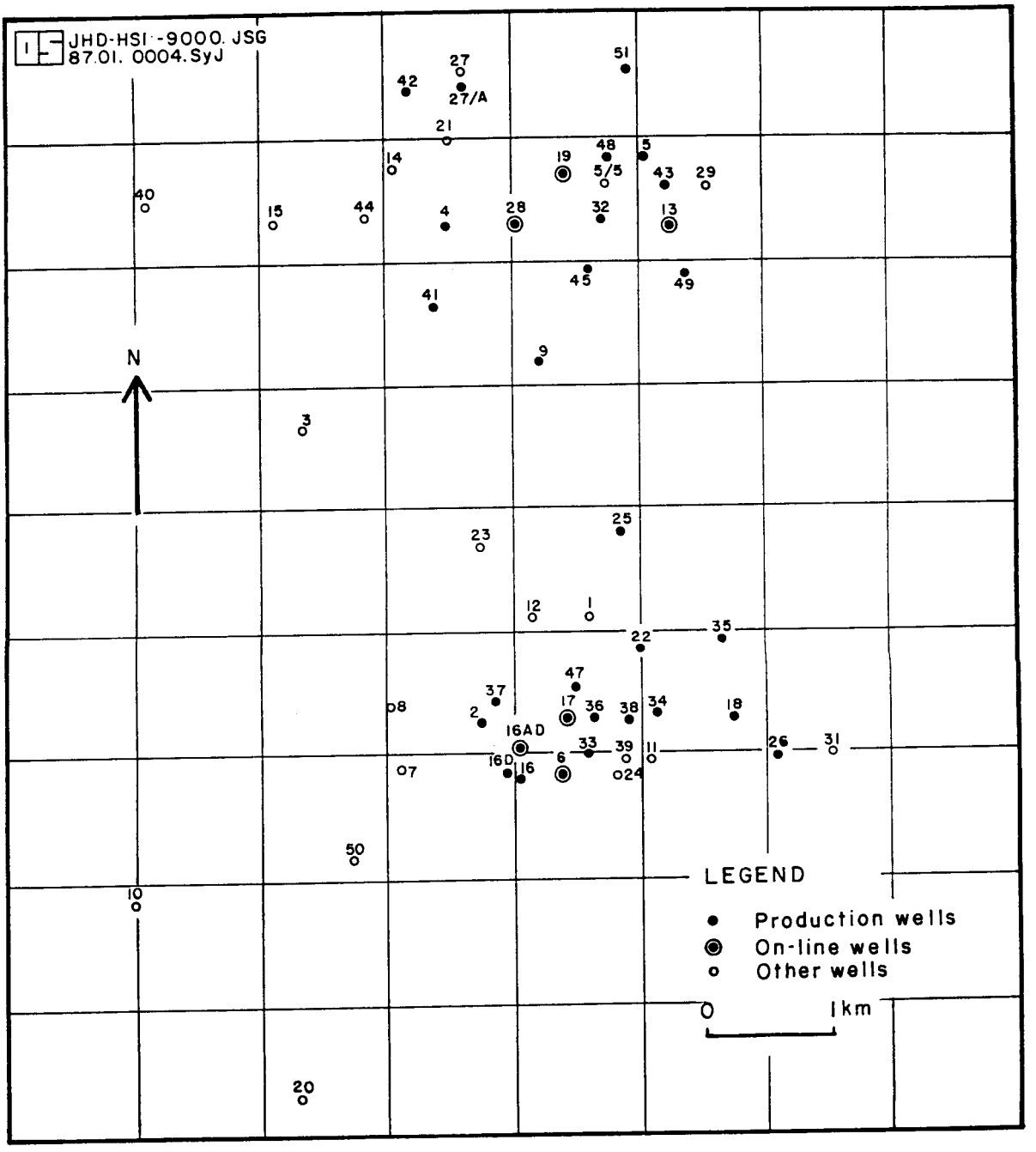


Figure 1 - Los Azufres field map.

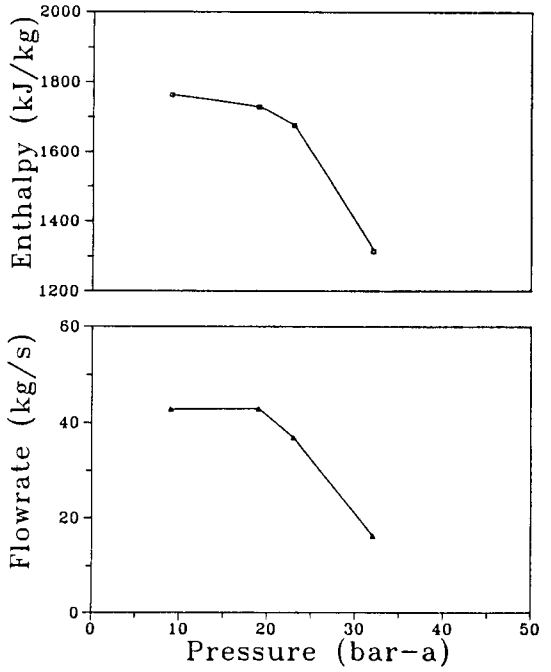


Figure 2 - Output curve well 18.

in the well three years earlier, in June 1983. It means that a two-phase steam/water mixture enters the well at typical flowing conditions - the well has excess enthalpy. This general behavior is discussed by Gudmundsson (1986b), for example. It is of interest that Iglesias et al. (1985) report that the liquid-dominated part of Los Azufres has an average enthalpy of 1317 kJ/kg - this is the liquid below the steam cap in the southern zone. Of interest also is that measured downhole temperatures in Los Azufres wells are consistently below the values determined by geothermometers (Nieva et al., 1983). For example, the downhole temperature in well 18 was measured 250°C in 1982, while silica indicated 266°C and sodium-potassium-calcium 290°C.

BUILDUP DATA

Before the well was shut in, temperature and pressure elements (Kuster) were lowered to 1200 m depth. The main feed zone of the well is located in the interval 1200-1250 m. Pressure buildup and temperature were recorded for 19 hours after shut-in. These data are shown in Table 1. The temperature increased quickly from 263°C to 265°C. The Cartesian plot of the pressure data are shown in Figure 3, showing that the wellbore was liquid-filled during the buildup

TABLE 1. Pressure and temperature buildup.

dt (h)	Press. (MPa)	Temp. (C)	t+dt / dt	dp (MPa)
0.000	5.135	263		0.000
0.100	5.271	264	531.000	0.136
0.133	5.282	264	398.000	0.147
0.167	5.295	264	319.000	0.160
0.200	5.299	-	266.000	0.164
0.233	5.303	-	228.143	0.168
0.267	5.307	-	199.750	0.172
0.300	5.312	-	177.667	0.177
0.333	5.316	-	160.000	0.181
0.417	5.320	-	128.200	0.185
0.500	5.323	-	107.000	0.188
0.667	5.327	-	80.500	0.192
0.833	5.332	-	64.600	0.197
1.000	5.327	264	54.000	0.192
1.333	5.323	-	40.750	0.188
1.667	5.323	-	32.800	0.188
2.000	5.320	264	27.500	0.185
2.333	5.316	-	23.714	0.181
2.667	5.316	-	20.875	0.181
3.000	5.316	264	18.667	0.181
3.667	5.320	-	15.455	0.185
4.333	5.323	264	13.231	0.188
5.000	5.327	264	11.600	0.192
6.000	5.332	264	9.833	0.187
7.000	5.336	-	8.571	0.201
8.000	5.340	-	7.625	0.205
9.000	5.344	264	6.889	0.209
10.000	5.352	-	6.300	0.217
11.000	5.361	264	5.818	0.226
12.000	5.369	-	5.417	0.234
13.000	5.381	264	5.077	0.246
14.000	5.393	-	4.786	0.258
15.000	5.406	264	4.533	0.271
17.000	5.422	264	4.118	0.287
19.000	5.438	264	3.789	0.303

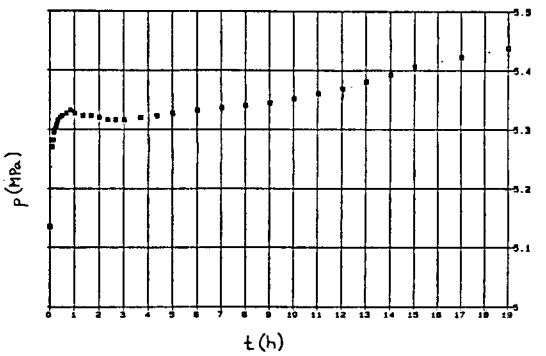


Figure 3 - Cartesian plot.

test. The pressure increased about 2 bar the first hours, and then decreased about 0.2 bar the next two hours, and then increased gradually 1.2 bar by the end of the 19 hour test. The 0.2 bar pressure decrease cannot be explained readily. It may be an artifact of the two-phase nature of the reservoir-wellbore system; it may result from wellbore storage or perhaps interzonal flow.

Flashing in the formation, as indicated by the above data, makes it difficult to apply traditional pressure transient analysis techniques,

as discussed by Gulati (1975) and Gringarten (1978), for example. However, this is reported less of a problem in buildup than drawdown tests (Gringarten, 1978). In the present buildup test, it was assumed that the two-phase zone around the wellbore had not developed much during the 52 hour flowing period. That the well was liquid-filled during the buildup test, as shown by the simultaneous temperature and pressure logs at 1200 m depth, supports this assumption.

INTERPRETATION

The methodology of pressure transient data interpretation, as presented by Gringarten (1985), guided most of the present work. Furthermore, the interpretation was carried out in the spirit that "many different conditions can cause the same or similar well-test response," as pointed out by Earlougher (1977, p.123). Therefore, the interpretation presented here is one possible interpretation of the data.

Several diagnostic (log-log) and specialized (log-linear) plots were made of delta-pressure and its derivative with respect to time, some of which will now be presented. The diagnostic plot in Figure 4 shows an inner boundary with a slope between one-half and one-quarter, which indicates a single medium conductivity fracture. Also in Figure 4, there are two straight lines of the same slope evident in the infinite acting period. This behavior is typical of double-porosity reservoirs.

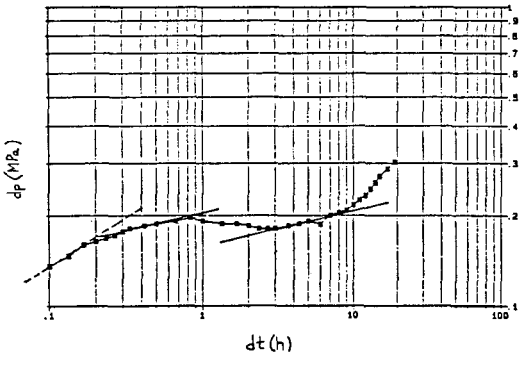


Figure 4 - Diagnostic plot.

At late time, the pressure begins to increase faster, which is characteristic of an outer boundary. A specialized plot was constructed to investigate this further, see Figure 5.

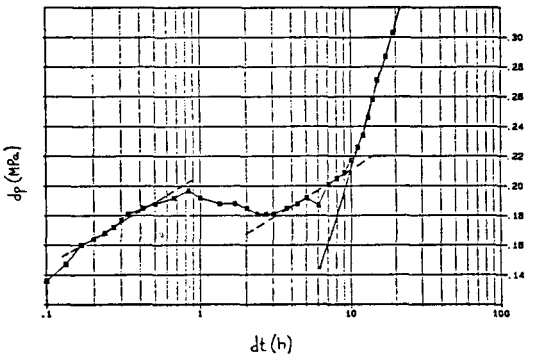


Figure 5 - Specialized plot.

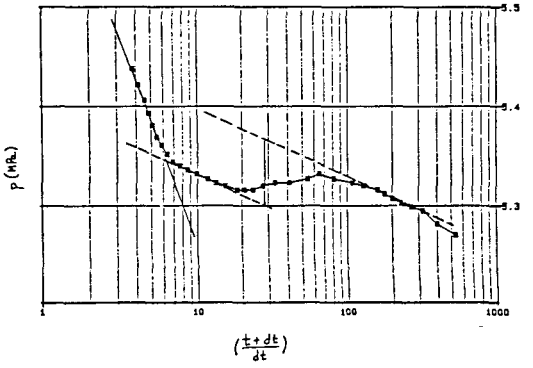


Figure 6 - Horner plot.

The slope of the late time straight line is about four times that of the total system reservoir slope. This sharp increase in pressure, indicates the existence of some boundary other than a single fault - perhaps that the drainage volume of the well is between two (intersecting) faults.

A Horner plot of the buildup data is shown in Figure 6. An extrapolation of the late time data to when dt >> t, indicates an average reservoir pressure at 1200 m depth as 5.7 MPa (57 bar-a). The slope, m, of the two parallel stratight lines was found from

$$m = 0.1832\ (wv\mu/kh) = 0.0713$$

where w is the mass flowrate and v the specific volume in S.I. units. This slope gives the following permeability-thickness product

$$kh = 5.4 \times 10^{-12}\ m^3 = 18{,}000\ md\text{-}ft$$

These values were calculated for liquid water at 265°C with specific volume $v = 1.287 \times 10^{-3}$ (m^3/kg) and viscosity $\mu = 1.0 \times 10^{-4}$ (Pa.s). For

an assumed porosity of $\phi = 0.1$, a total compressibility of $c = 1.9 \times 10^{-9}$ Pa^{-1} and a reservoir thickness $h = 50$ m, the skin value was estimated

$$s = -5.3$$

The pressure increment, δp, between the two parallel straight lines on the Horner plot in Figure 6, can be used to evaluate ω, the ratio of the storativity of the fissure system to the storativity of the total fissure-matrix system (Gringarten, 1985). The pressure increment read from Figure 6 was 0.07156 MPa, giving

$$\omega = 10^{-\delta p/m} = 0.10$$

DISCUSSION

Results from six pressure transient tests on four wells in Los Azufres field have been reported by Nieva et al. (1985). The analyses were carried out using double-porosity type curves. It was found that the "fracture permeability" varied from 1-25 md, while the "matrix permeability" varied from 0.003-5 μd. It was further stated that these latter values were consistent with measurements on cores. The "storage ratio" of the double-porosity system was reported 0.01 by the same authors.

The permeability-thickness product determined in the present buildup test, 5.4 dm, corresponds to about 100 md if the reservoir thickness, h, is assumed 50 m. Clearly, this value is much greater than the values reported by Nieva et al. (1985): 4-100 greater than the "fracture permeability." Similarly, the storativity ratio determined in the present test was an order of magnitute larger than that reported by Nieva et al. (1985).

The great difference between the results of the present work and that reported by Nieva et al. (1985), needs to be clarified. The permeability-thickness product reported in this paper for Los Azufres well 18, appears to fall within what is reasonable for typical geothermal wells, while the storativity ratio from both studies appear satisfactory. The fact that Nieva et al. (1985) found their field test values to be consistent with core data, suggests that the permeability-thickness product reported in the present work, may be more representative - permeability values derived from geothermal well tests are generally higher than laboratory values on cores from the same wells.

Well 18 was discharged for about two days at a high wellhead pressure and a low flowrate - the mixture enthalpy of the well was at its lowest value. However, this enthalpy was higher than that of liquid water at the highest temperature measured downhole, but similar to the water in the liquid part of the overall reservoir. During the subsequent 19 hour buildup period, the wellbore was liquid-filled at depth of 1200 m, where the pressure and temperature were measured with time - the main feed zone of the well is in the range 1200-1250 m depth . The pressure buildup data, therefore, were analysed assuming all-liquid conditions. The first few hours of pressure buildup may have been complicated by condensation phenomena.

CONCLUSIONS

The permeability-thickness product of well 18 in Los Azufres field was determined 5.4 dm from a Horner plot. The well was found to be intersected by a fracture, as evident from the slope on a log-log plot at early time, and a skin value of -5.3. The overall pressure buildup of the well was found to be typical for double-porosity reservoir behavior, having a storativity ratio of 0.1. An outer boundary behavior was observed in the pressure buildup data.

ACKNOWLEDGEMENTS

The first author would like to thank the Comisión Federal de Electricidad for the permission to attend the Geothermal Training Programme in Iceland, and the United Nations University for providing the fellowship that made it possible.

REFERENCES

Alonso-E., H. (1985): "Current perspectives on the development of geothermics in México," EPRI Geothermal Conference and Workshop, San Diego, California.

Earlougher, R.C., Jr., (1977): Advances in well test analysis, Society of Petroleum Engineers, Dallas, Texas.

Gudmundsson, J.S. (1986a): "Composite model of geothermal reservoirs," GRC Bulletin, January, pp. 3-10.

Gudmundsson, J.S. (1986b): "Two-phase wells," GRC Bulletin, March, pp. 10-16.

Gulati, M.S. (1975): "Pressure and temperature buildup in geothermal wells," Proc., Workshop Geothermal Reservoir Engineering, Stanford, California.

Gringarten, A.C. (1978): "Well testing in two-phase geothermal wells," SPE paper 7480, 53rd Annual Fall Technical Conference Exhibition, Houston, Texas.

Gringarten, A.C. (1985): "Interpretation of transient well test data," Chapter 5 in Developments in Petroleum Engineering, (R.A. Dawe and D.C. Wilson, eds.), Elsevier, New York.

Hiriart-L., G. (1983): "One year experience with portable back-pressure turbines in Los Azufres," Proc., 9th Workshop Geothermal Reservoir Engineering, SGP-TR-74, Stanford, California, pp. 275-278.

Iglesias, E.R., Arellano, V.M., Garfias, A., Miranda, C. and Aragon, A. (1985): "A one-dimensional vertical model of the Los Azufres, México, geothermal reservoir in its natural state," Trans., Geothermal Resources Council, Vol. 9, Part II, 331-336.

Molinar-C., R. (1985): "Recent activities in reservoir engineering at México's geothermal fields," EPRI Geothermal Workshop and Conference, San Diego, California.

Nieva, D., Iglesias, E., Arellano, V., Contreras, E., Gonzalez, A. and Reyes, E. (1985): "Multidisciplinary studies on the Los Azufres geothermal field, México," EPRI Geothermal Workshop and Conference, San Diego, California.

Ortega-P., L. (1985): "Operation of the mobile units of Los Azufres," EPRI Geothermal Workshop and Conference, San Diego, Californaia.

Reyes-S., R. (1985): "Development of the Los Azufres geothermal field," EPRI Geothermal Workshop and Conference, San Diego, California.

Sánchez-U., P. (1986): Reservoir and production engineering of well A-18 in the Los Azufres geothermal field in México, UNU Geothermal Training Programme, Reykjavík.

PROCEEDINGS, Twelfth Workshop on Geothermal Reservoir Engineering
Stanford University, Stanford, California, January 20-22, 1987
SGP-TR-109

PETROPHYSICAL PROPERTIES OF TWENTY DRILL CORES FROM THE LOS AZUFRES, MEXICO, GEOTHERMAL FIELD

E. R. Iglesias, E. Contreras L., A. García G.
Instituto de Investigaciones Eléctricas
Apartado Postal 475
Cuernavaca, Morelos 62000, México

Bernardo Domínguez A.
Comisión Federal de Electricidad
Av. Las Camelinas 3527, 10° P.
Morelia, Michoacán, México

ABSTRACT

For this study we selected 20 drill cores covering a wide range of depths (400-3000 m), from 15 wells, that provide a reasonable coverage of the field. Only andesite, the largely predominant rock type in the field, was included in this sample. We measured bulk density, grain (solids) density, effective porosity and (matrix) permeability on a considerable number of specimens taken from the cores; and inferred the corresponding total porosity and fraction of interconnected total porosity. We characterized the statistical distributions of the measured and inferred variables. The distributions of bulk density and grain density resulted approximately normal; the distributions of effective porosity, total porosity and fraction of total porosity turned out to be bimodal; the permeability distribution resulted highly skewed towards very small (1 mdarcy) values, though values as high as 400 mdarcies were measured. We also characterized the internal inhomogeneity of the cores by means of the ratio (standard deviation/mean) corresponding to the bulk density in each core (in average there are 9 specimens per core). The cores were found to present clearly discernible inhomogeneity; this quantitative characterization will help design new experimental work and interpret currently available and forthcoming results. We also found statistically significant linear correlations between total density and density of solids, effective porosity and total density, total porosity and total density, fraction of interconnected total porosity and the inverse of the effective porosity, total porosity and effective porosity; bulk density and total porosity also correlate with elevation. These results provide the first sizable and statistically detailed database available on petrophysical properties of the Los Azufres andesites.

INTRODUCTION

Prior to this work, little information existed about petrophysical properties of rocks from the Los Azufres geothermal field. This paucity of information adversely affected several important geothermal engineering activities related to the field, such as reserve and producibility assesment, design of drilling bottomhole assemblies, and design and interpretation of stimulation and reinjection operations. In this paper we present a relatively extensive original set of petrophysical data and correlations pertaining to andesite rock from the field. The scope of this work has been outlined in the Abstract and will not be repeated. It is worth noting however, that the results presented here are only the first part of a significantly greater effort that will also include mechanical, thermal and petrological properties of these cores.

Previous work on the subject reduces to that of Iglesias et al. (1985), and Contreras et al. (1986). In the 1985 paper we presented results on bulk and grain density, effective porosity, permeability, mechanical properties and thermal properties of Los Azufres andesites from 5 different outcrops. In the other paper we also dealt with a limited amount of material (samples from 8 outcrops, and a total of 4 drill cores, from wells Az-1, Az-5, Az-9 and Az-19). In this case we measured 10 different properties, though most of them on a very limited amount of samples: bulk density and effective porosity (all outcrops and cores), permeability (cores Az-5, Az-9 and Az-19), bulk compresibility (one outcrop and cores Az-9 and Az-19), compressional and shear wave velocities (one outcrop), electrical resistivity (one outcrop), thermal conductivity (core Az-19), thermal diffusivity (core Az-19), and thermal expansion (one outcrop). The present work is

significantly more extensive and in-depth, presenting statistically characterized results of 7 properties (see Abstract) corresponding to 20 new cores from 15 wells.

MATERIALS AND METHODS

The cores for this study were selected according to availability, type of rock (only andesite, the largely predominat type in the field was included), and degree of hidrothermal alteration (efforts were made to try and include samples covering the whole range of alteration).

Fig. 1 presents the areal distribution of the cores in the field, which shows a reasonable coverage. Table 1 summarizes other characteristics of the cores. The percentage of hydrothermal alteration quoted is actually the average hydrothermal alteration in a 40 m interval straddling the depth of the core, and was obtained by thin section

Table 1. Characteristics of drill cores used in this study

Well	Core	Hydrothermal alteration (%)	Number of specimens (#)
Az-3	1	90	16
Az-3	4	85	14
Az-3	5	90	9
Az-4	3	95	14
Az-5	1	30	8
Az-8	2	80	9
Az-10	1	75	10
Az-20	1	50	10
Az-20	3	70	8
Az-22	2	85	9
Az-25	1	84	11
Az-26	2	80	6
Az-26	3	85	8
Az-29	1	71	10
Az-29	3	45	6
Az-41	2	77	8
Az-46	3	90	6
Az-47	4	95	8
Az-48	4	N.A.	5
Az-50	3	27	5

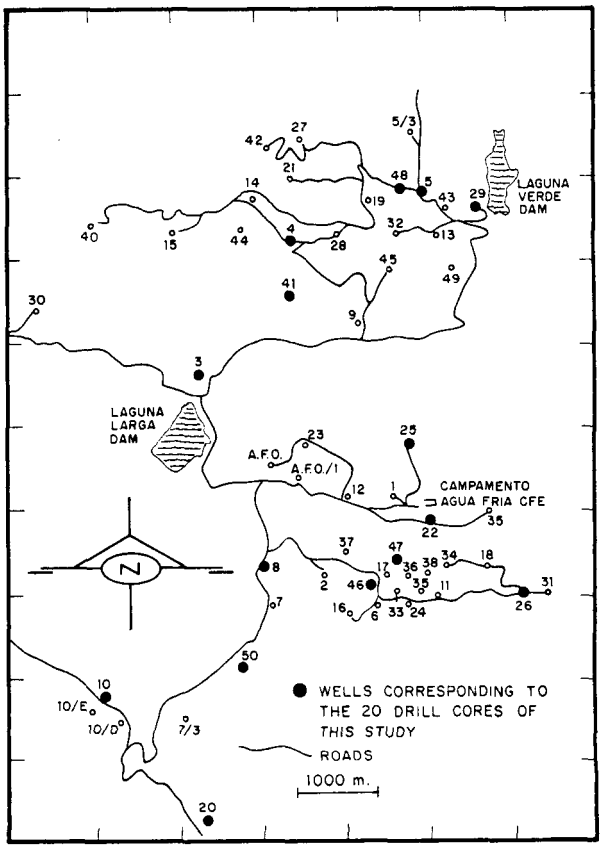


Fig. 1 Areal distribution of the cores in the field.

petrographic studies of drill cuttings (Martiñón-García, 1986); thus, this parameter must be taken only as possibly indicative of the alteration of the cores. Detailed petrographic studies of the cores are currently underway.

The altitude distribution (Fig. 2) is skewed towards shallow cores, and there are no samples in the 1100-1500 m a.s.l. interval. It is hoped that more cores will be available in the future to improve the representativity of the sample.

Bulk and grain density, and effective porosity were measured by methods recommended by the International Society for Rock Mechanics (ISRM, 1972). Permeability was measured with a Core Lab gas permeameter; dry air and nitrogen were used as fluids; results were corrected for slippage (Klinkenberg effect). Bulk density was measured in 180 specimens, and effective porosity was measured in 179 specimens from the 20 cores (e.g., Table 1); permeability was measured in 50 specimens from 17 cores, due to availability. Grain density,

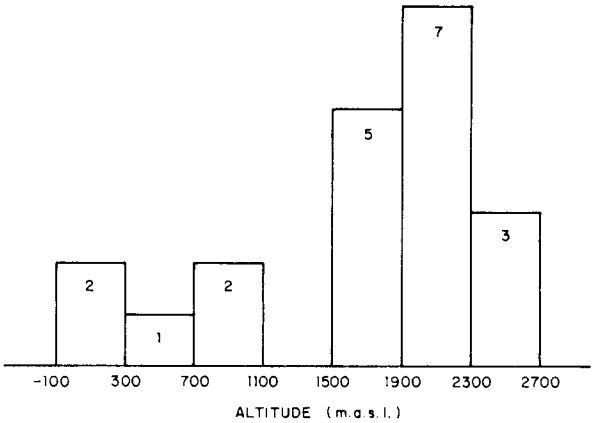


Fig. 2 Altitude distribution of the cores.

approximately averaged over each core, was measured on rock powder obtained by grinding several leftover pieces of core (typically 300 g). Mean total porosity for each core was inferred from the corresponding average bulk and grain density. The mean fraction of interconnected porosity for each core was inferred from the corresponding average effective and total porosity.

The raw data suggested a significant degree of internal inhomogeneity in some of the cores. Thus, we set off to quantitatively characterize the inhomogeneity. We considered the bulk density and effective porosity results obtained for each core. The existence of about 9 specimes, in average, per core, provided mean values and standard deviations of these properties for each core. To characterize the inhomogeneity we examined the ratios of the standard deviation to the corresponding mean, for both properties. To avoid any possible dependence of the accuracy of the measurements on the magnitude of the measured property, we tested the data for the existence of correlations between standard deviations and the corresponding means. We found that, unlike effective porosity, bulk density did not reveal such correlation, and therefore can confidently be used to characterize the inhomogeneity of the cores.

RESULTS AND DISCUSION

Fig. 3 displays the distribution of the grain density, averaged over each core, for the 20 cores. The corresponding mean and standard deviation are 2.799 and 0.092 g cm^{-3} respectively. Very nearly 50% of the population lies at each side of the mean, suggesting a normal distribution.

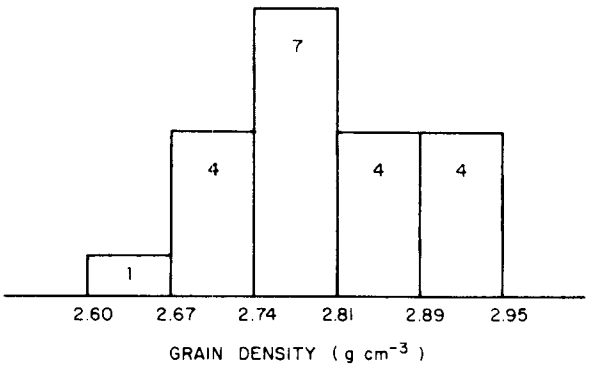


Fig. 3 Distribution of grain density.

Fig. 4 presents the distribution of bulk density, as inferred from 180 specimens from the 20 cores. The corresponding mean and standard deviation are 2.468 and 0.225 g cm^{-3} respectively. In this case too, nearly 50% of the population lies at each side of the mean, suggesting a normal distribution.

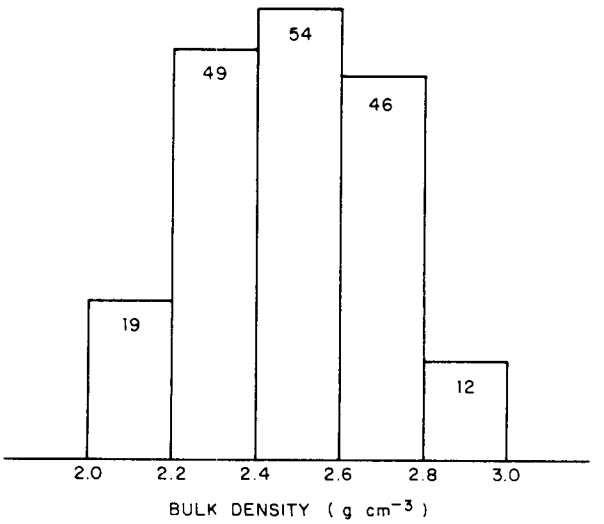


Fig. 4 Distribution of bulk density.

The histogram of Fig. 5 (179 specimens, 20 cores) suggests a bimodal distribution for effective porosity, with a lower mode of approximately 2%, and an upper mode of approximately 14%. Note that more than 32% of the sample presents effective porosity values greater than or equal to 14%, which could be regarded as atypically high for andesites. We suspect that the high-porosity peak is associated with hydrothermal alteration while the low-porosity peak reflects unaltered rock; confirmation of this speculation is contingent upon completion of the ongoing petrographic studies.

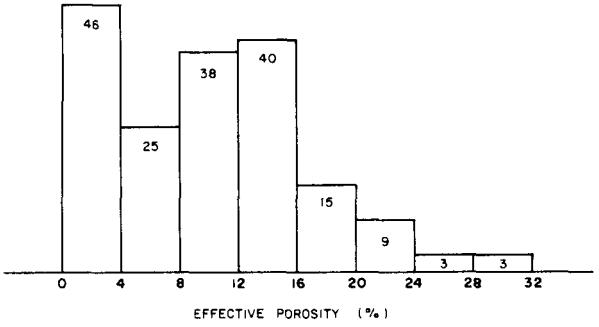


Fig. 5 Distribution of effective porosity.

Fig. 6 ilustrates the permeability distribution [50 specimens, 17 cores, no measurements were possible for cores Az-29(3), Az-46(3) and Az-48(4)]. Note that the vertical scale is logarithmic. About 80% of the sample has permeability values of less than 2.3 mdarcy, which may be regarded as consistent for these tight igneous rocks; the rest lies in the range 2.3-400 mdarcy. None of the specimens showed microfractures perceptible to the naked eye; thus, we speculate that the high permeability tail might be related to hidrothermal alteration. Again, confirmation of this possibility is contingent upon completion of ongoing petrographic studies. The present results, which reflect matrix (as opposed to fracture) permeability, are consistent with previous findings (Iglesias et al., 1985; Contreras et al. 1986).

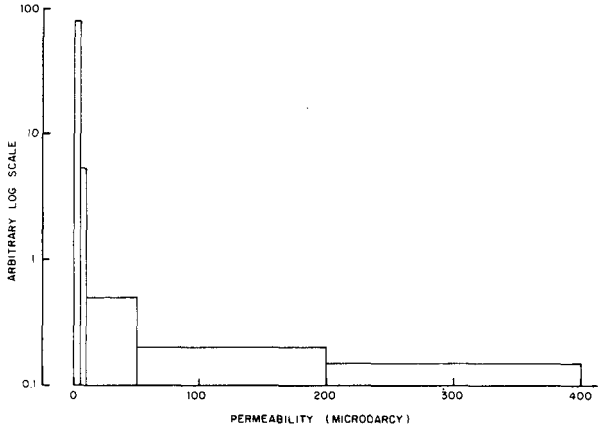


Fig. 6 Distribution of (matrix) permeability.

The inferred distribution for total porosity (average per core) looks bimodal (Fig. 7), with a lower mode of approximately 6%, and an upper mode of approximately 14%. Not surprisingly, the bimodality of this distribution corresponds to that of the effective porosity. The discrepancy between the values of the lower modes of both porosity distributions is an artifact of the differing sizes (n=179 for effective porosity, n=20 for total porosity) of the samples involved. In fact, the discrepancy disappears if average effective porosity per core is used instead of the 179 measured values.

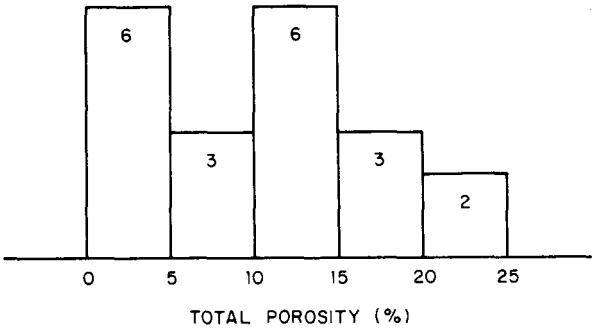


Fig. 7 Distribution of total porosity.

The histogram of Fig. 8 suggests a bimodal distribution for the inferred fraction of interconnected total porosity, with a lower mode of about 0.3, and an upper mode of about 0.9. Interestingly, roughly 70% of the sample displays high (>0.8) connectivity.

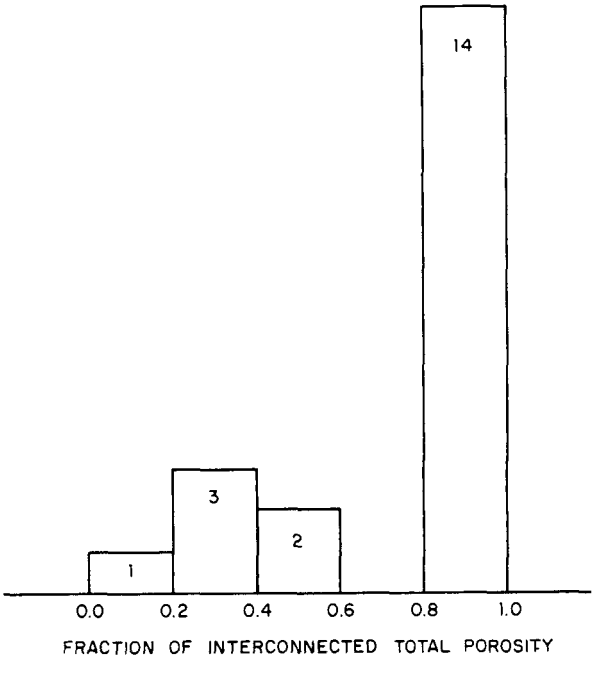


Fig. 8 Distribution of fraction of interconnected total porosity.

The distribution of the heterogeneity ratio (from bulk density) ilustrated in Fig. 9., is skewed to the left, with a mode approximately equal to 0.0090, and mean and standard deviation equal to 0.0149 and 0.0085 respectively. Thus, the cores examined present a relatively moderate, but clearly discernible inhomogeneity. An inmediate application of these results was to provide a quantitative criterium for deciding how many thin sections should be studied for each core, for petrographic characterization. These results also help to understand the variability found in the correlations that follow.

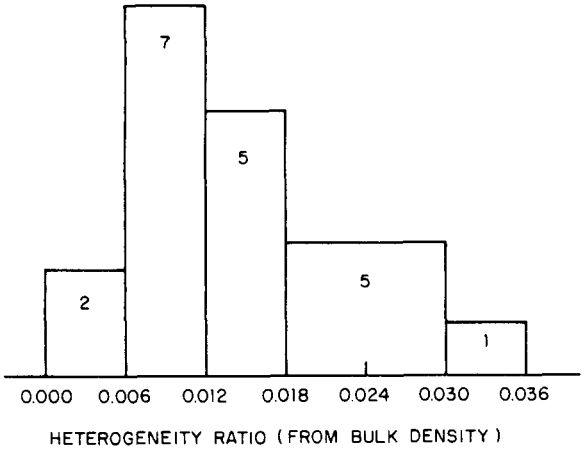


Fig. 9 Distribution of heterogeneity ratio.

Several interesting linear correlations, all of them statistically significant at the 99.5% confidence level, were found among these physical properties. A relatively loose correlation is present between bulk density and grain density (Fig. 10). Thus, the data indicates that approximately $100r^2=45\%$ of the variability of r_B is due to r_G.

A tight correlation exists between effective porosity and bulk density (Fig. 11).

The fraction of interconnected total porosity also correlates with bulk density (Fig. 12), though the correlation is weaker than that of effective porosity.

Total porosity correlates very tightly with effective porosity (Fig. 13).

The fraction of interconnected total porosity correlates with the inverse of

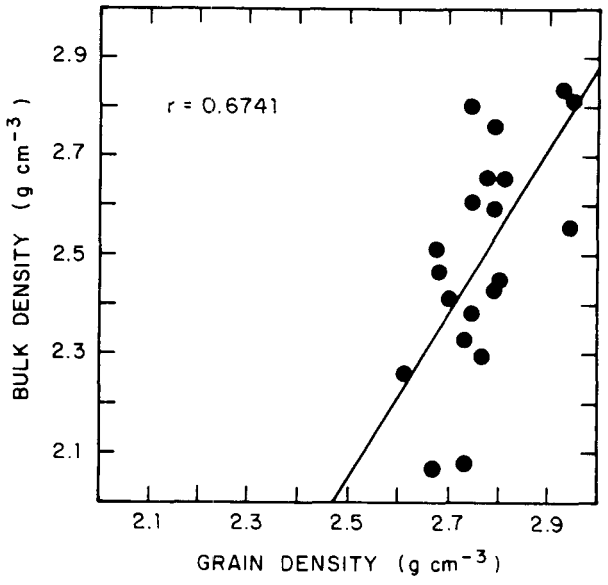


Fig. 10 Correlation between bulk and grain density.

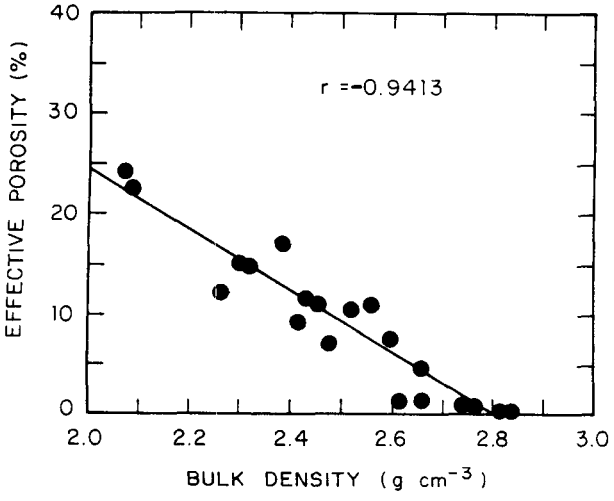


Fig. 11 Correlation between effective porosity and bulk density.

the effective porosity (Fig. 14). The bimodal character of the fraction of interconnected total porosity is evident in the graph.

Finally, both bulk density and total porosity correlate with altitude (Figs. 15 and 16 respectively), reflecting lithostatic load.

The present results are extremely useful for several important geothermal engineering activities related to the field, such as reserve and producibility assesment, design of drilling bottomhole assemblies, and design and interpretation of stimulation and reinjection operations.

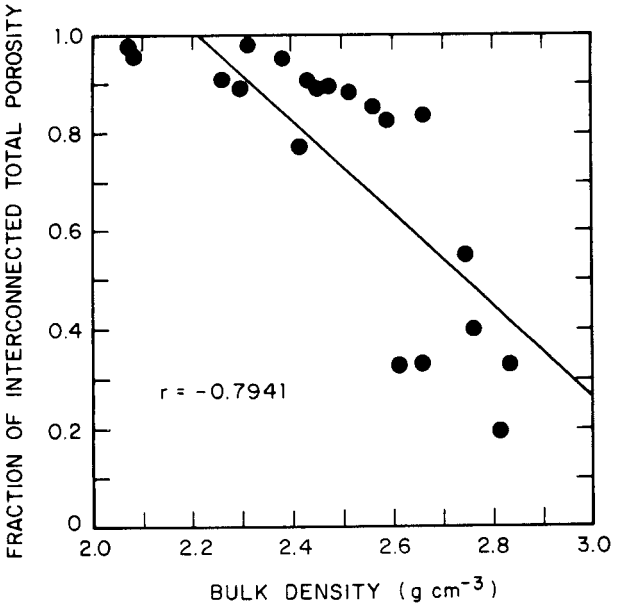


Fig. 12 Correlation between fraction of interconnected total porosity and bulk density.

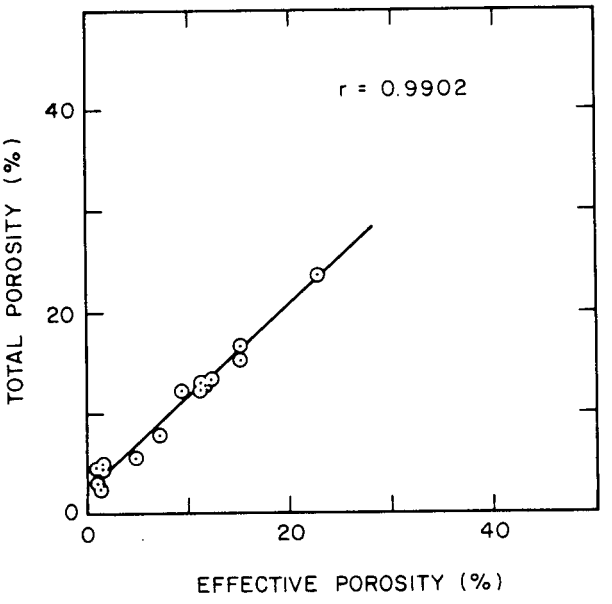


Fig. 13 Correlation between total and effective porosity.

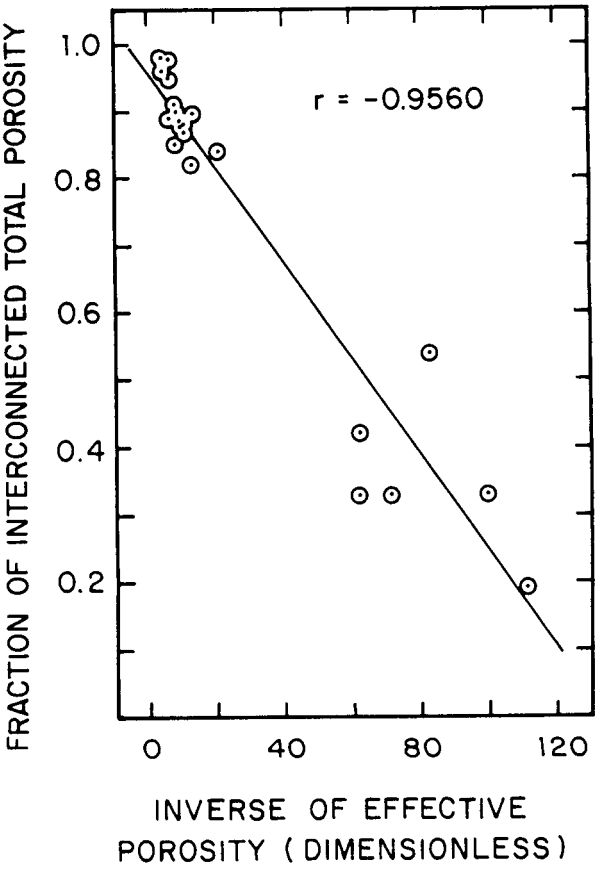


Fig. 14 Correlation between fraction of interconnected total porosity and inverse of effective porosity.

REFERENCES

Contreras E., Iglesias E.R. and Razo A., 1986 "Initial measurements of petrophysical properties on rocks from the Los Azufres, Mexico, geothermal field", Proc. 11th. Workshop Geothermal Reservoir Engineering, pp. 51-57, Stanford University, SGP-TR-93.

Iglesias E.R., Contreras E. and García A., 1985 "Propiedades petrofísicas de andesitas superficiales del campo geotérmico Los Azufres", Report IIE/11/2014/I 01/P, 102 pp., Instituto de Investigaciones Eléctricas.

ISRM, 1972 "Suggested methods for determining water content, porosity, density, absorption and other related properties", International Society for Rock Mechanics, Commission on Standarization of Laboratory and Field Tests, Document No. 2, Lisbon, Portugal.

Martiñón-García H., 1986 "Porcentajes de alteración en núcleos de pozos de Los Azufres, Michoacán", Comunicación de Geología 11/86, 4 pp., Gerencia de Proyectos Geotermoeléctricos, Comisión Federal de Electricidad.

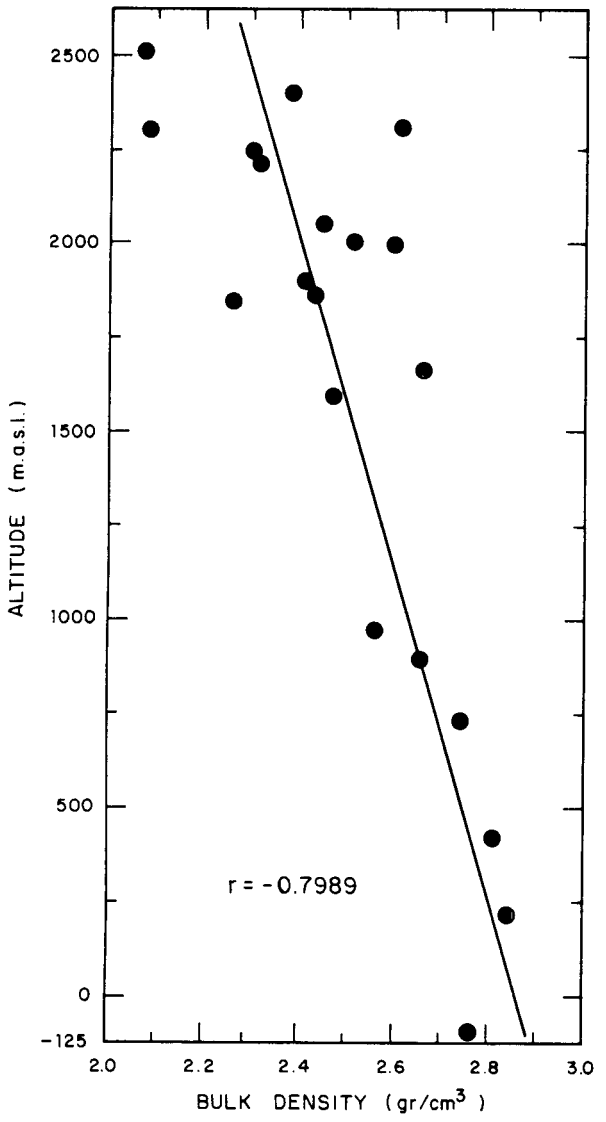


Fig. 15 Correlation between bulk density and altitude.

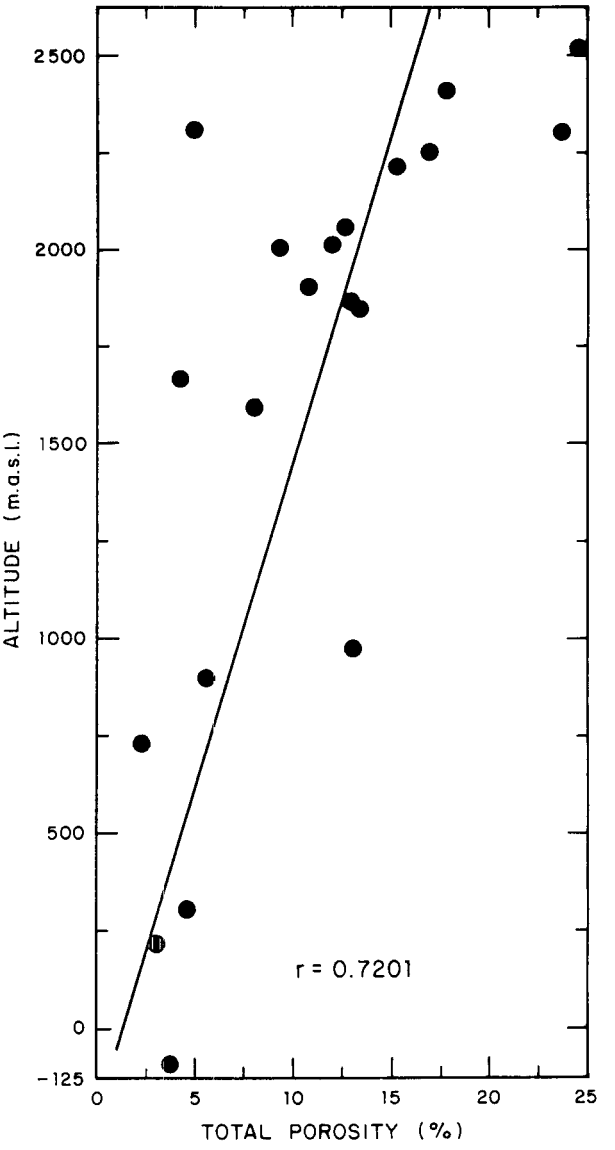


Fig. 16 Correlation between total porosity and altitude.

PROCEEDINGS, Twelfth Workshop on Geothermal Reservoir Engineering
Stanford University, Stanford, California, January 20-22, 1987
SGP-TR-109

DEVELOPMENT AND EXPLOITATION OF LOW ENTHALPY GEOTHERMAL SYSTEMS: EXAMPLE OF "THE DOGGER" IN THE PARIS BASIN, FRANCE

J. Rojas, A. Menjoz, J.C. Martin, A. Criaud and C. Fouillac

Institut Mixte de Recherches Géothermiques
BRGM, BP 6009, 45060 ORLEANS CEDEX, FRANCE

ABSTRACT

A feature of French geothermal engineering is the development of industrial projects in normal gradient, non-convective areas. The economic feasibility of exploiting wells producing between 150 and 350 m^3/h at temperatures from 55° to 85° from depths of 1,500 to 2,000 meters, in sedimentary basins with normal gradient, for direct heat production has been proved by 50 plants providing heating for over 500,000 people during the last few years. This opens new possibilities for geothermal energy development the world over, in particular for areas where heat consumption is higher than 2,500 Tons oil equivalent (Toe)/year over several square kilometers.

The recent and rapid development of geothermal projects in France, in particular in the Paris Basin has provided much more information on the characteristics of the Jurassic Dogger, which is the unit tapped by geothermal doublets (one production and one injection well).

Detailed study of the Dogger reservoir in the Paris Basin is one of the main objectives of the IMRG research and development program drawn up in 1983. The preliminary results presented here are oriented towards (1) improved knowledge of the potential geothermal resources, and (2) analysis of optimum development conditions.

INTRODUCTION

The sedimentary beds of the Paris Basin host numerous aquifers. The main ones are shown in figure 1. Several of these deep aquifers offer good geothermal energy possibilities, but the main interest was concentrated on the Dogger limestone. This limestone is better known because it was the subject of intensive drilling for petroleum exploration. Thanks to this drilling and also geothermal energy research this formation was found to be a very large aquifer. At present it constitutes the no. 1 geothermal energy objective in France and alone provides 90% of the geothermal energy resources in the country. The reserves in place are estimated at 6×10^8 calories, i.e. the equivalent of 600 millions Toe.

1 - CHARACTERISTICS OF THE RESERVOIR

1.1 - Methodology

The sedimentological analysis aimed to:

(1) Characterize the sedimentary environments and their distinguishing criteria and study the relations between the various facies and the different productive layers.
(2) Draw up vertical well sections including all these components in order to establish correlations between wells as a base on which to reconstitute the paleogeography of the reservoir.

The work was carried out in successive stages comprising:

(1) Detailed sedimentological analysis of a cored drill hole so as to define the facies, (depositional) environments, petrology and diagenetic phenomena affecting the reservoir.
(2) Well logging characterization of facies cut by this drillhole enabling facies in other boreholes to be identified by morphological study of curves (electrofacies).

At the same time as the logs were gone through, cuttings from some boreholes were examined section by section so as to:

Check a logging hypothesis.
Try to characterize the porosity from cuttings impregnated with coloured resin and mounted on thin sections.

1.2 - Lithostratigraphy

The Dogger of the Paris Basin corresponds to a predominantly limestone litho stratigraphic assemblage located between the marl at the top of the Lias and the lower Callovian marl.

During the Bathonian, a large carbonate platform was built up and its formation accelerated with subsidence of the basin.

Oolitic reef bars formed on the basin borders and progressed towards the centre leaving behind them a protected internal shelf zone. This zone, in which lagoon-type facies (Comblanchian) were deposited came progressively to occupy the center of the basin at the end of the Bathonian (Fig. 2). This northwest-striking carbonate body is bounded on the west by a marly belt which in its turn limits the oolitic reef flat installed on the Armorican margin.

All the geothermal wells are located east of the marl belt. The rocks encountered in the wells comprise the lower part of the Callovian and a great thickness belonging to the Bathonian. These Bathonian facies come within the regressive changes known to occur at this time in the Paris Basin.

This change is characterized by the successive deposition, from the base to the top, of external shelf sediments (Alternances) of reef deposits (White oolite) and internal shelf sediments (Comblanchian).

As an example, the description of the type stratigraphic succession encountered in one of the geothermal wells is given below and in figure 3. From the bottom to the top:

At the base, the first unit, belonging to the "Alternances", comprises more-or-less clayey, gravelly-bioclastic limestone of external facies, or more granular facies (grainstone to packstone) of the fore reef. In some wells the first productive layers are found in these fore reef facies.

The second unit belonging to the "White oolite" comprises granular reef facies of grainstone type. The main productive horizons are located in these facies.

The third unit corresponds to Comblanchian lagoon facies with beige micrite and grainstone-type oolitic passages. The productive layers occurring in this unit generally correspond to the oolitic facies.

1.3 - Facies - physical characteristics relations

Study of the porosity in the limestones showed that their physical characteristics depend on:

The depositional environments and their hydrodynamic energy.
Diagenetic changes which can affect them.

The porosity is clearly of two types:

(1) Macroporosity, intergranular (pore radius > 7.5 microns) typical of oolitic grainstone of reef facies (Fig. 4).
(2) Microporosity, inter or intragranular (pore radius < 7.5 microns) typical of gravelly-bioclastic facies of the external shelf (Fig. 5).

The permeability = f (total porosity) relation is not clear but a good correlation is obtained when applied to the macroporosity.

(1) Thus high permeability values are shown by samples with high macroporosity. These values are obtained in reef facies and more particularly in the "White oolite".
(2) Normal decrease in the permeability is shown by facies further away from the oolitic reef domain. In the external facies microporosity is prevalent.

The values obtained by interpretation of porosity logs do not convey the degree of productivity of the rock. In fact, at equal porosity values, the limestone from the series of "Alternances" does not have the same productivity as the "White oolite" (Fig. 3). The origin of this difference is probably due to different diagenetic evolution in these ancient reservoirs: thus rocks belonging to the "Alternances" sequence are blocked with a deposit of cement reducing the intergranular space, while at the same time, the micropore network is increased by reduction of the macropores and by microsolution of the matrix. On the other hand, the limestone belonging to the "White oolite" facies and the Comblanchian, have kept their original porosity and in places it is even increased by fracturing-solution.

2 - GEOCHEMISTRY OF DOGGER AQUIFER FLUIDS

We present here the preliminary results concerning isotopic and chemical studies. The gas chemistry is described in another paper (Criaud, et al., this volume).

2.1 - Analytical procedures

The major element chemistry for 55 drillholes is available (Criaud, et al., 1986). Most of them were sampled (by the BRGM) under steady state flow conditions (during production) but a few analyses were taken from drill reports. Nonetheless these analytical data do not induce significant error and prove useful for understanding the general chemistry of the aquifer.

The general methods for field and laboratory operations are described.

The geothermal fluids are sampled as close as possible to the well head. Temperature and pH are measured on site. Total alkalinity was determined on site because of abundant dissolved hydrogen sulfide. Total H_2S is measured by potentiometry in the same conditions.

The waters were filtered on line through

0.45 micron membranes and immediately acidified with concentrated HCl for cations determination. Cadmium acetate is added in excess to precipitate sulfide, and the surnageant is analyzed for sulfate and corrected for dilution.

Cations were determined by ICP and flame atomic absorption spectrophotometry. Boron was determined with spectrophotometric method for the earlier results and by ICP since 1983.

Standard ion chromatography (Dionex) with conductivity detector was used to measure Cl, SO_4 and F. Non-suppressed ion chromatography with a UV detector was used for bromide determination.

2.2 - Discussion

The chemical analyses are widely disparate in composition and total salinity (from 6.4 to 35 g/l) and a number of phenomena may account for these differences. Assuming an initial fluid close to sea water, evaporation, diagenesis, mixing with dilute or saline water, and dissolution of evaporites, may occur separately or have a general effect in the sedimentary environment.

First, attempts were made to explain these variations by a simple mixing model involving two components - this was sustained by the correlation between Cl and Br (Bastide, 1985). The Cl/Br molal ratios comparable to the composition of present-day seawater, and is explained by the diagenetic evolution of initial seawater concentrated by evaporation. Then this ratio would remain constant through simple mixing with a low TDS component.

The oxygen 18 and deuterium isotope studies indicate present-day recharge of the aquifer, as shown by isotope composition of the most southern samples. The regression line δD-$\delta^{18}O$ does not intersect the SMOW $\delta^{18}O$ value and the highest mineralized fluids do not correspond to the highest isotope enrichment. Complex processes including membrane filtration effect, exchange with host rocks and mixings have been proposed (Fouillac, et al., 1986) but obviously the aforementioned mixing model must be discarded.

The variations in boron or sulfate contents in relation to chloride enable several groups to be distinguished among the fluids according to the different Cl/B and Cl/SO_4 ratios. A general enrichment in boron relative to seawater is observed, and both elements are considered as conservative due to mixing processes.

(1) The water from the Seine-St-Denis area is recognized as the oldest component, B is quite constant, but not Cl; the high sulfide content and the sulfate isotope study (Fouillac, et al., 1986) show that bacterial reduction has proceeded in a uniform way. Cl/SO_4 ratio is best explained by diagenetic changes in seawater.
(2) The samples from south of Paris are characterized by a unique molal ratio Cl/B = 265 (seawater = 1330) and a fair correlation between Cl and SO_4. The sulfide concentrations are low. A mixing model involving a high salinity and temperature fluid distinct from the water which lead to the group (1) above, and a low mineralized water satisfactorily explains the homogeneity of this area (Criaud, et al., 1986).
(3) The southernmost samples of low TDS are marked by low Cl/SO_4 and Cl/B ratios. In this group a young and dilute component is detected (Criaud, et al., 1986).
(4) The fluids from the borders (east and west) of the study area are distinct and do not belong to any of these groups.

Local linear trends in the correlations between chloride and, calcium or magnesium again show that the water/rock interactions occurred in different ways depending on the area and the processes involved (Criaud, et al., 1986). Bastide (1985) demonstrated that the concentration of Ca and Mg remained under the control of the solubility of calcite and dolomite during evolution.

All the fluids are close to equilibrium with chalcedony, albite, microcline, kaolinite and fluorite. Na/K and silica geothermometers provide good estimations of the downhole temperatures of the fluids.

3 - CHARACTERISTICS OF PRODUCTIVE LAYERS

Detailed analysis of the parameters of the productive layers is particularly important for several practical reasons:

(1) Characterization of the reservoir (temperature of the resource, productivity, mapping, etc.).
(2) Location of the two boreholes of a geothermal doublet (distance between wells, thermal breakthrough, lifetime, production pressures, etc.).
(3) The management of the resource (distance between doublets, respective orientation, hydraulic and thermal interference, invasion of the reservoir by reinjected cold water, etc.).

3.1 - Methodology

The principal hydraulic and thermal parameters are determined by three types of measurements in the reservoir (open hole):

(1) The diameter-flowmeter profile in production.
(2) The temperature (absolute and differential) profile in production.

(3) Recording of the pressure and temperature at the casing shoe during a production test followed by a build up (about 24 h).

The various geometrical, physical and chemical data from each geothermal well (111 boreholes at present) are archived in two forms:

(1) A data bank containing raw information, for consultation.
(2) A data base where data from different interpretations are filed. This information is subsequently exploited so as to estimate the regional distribution of parameters and modelling of the reservoir.

The detailed information on the producing units are, in principal, not essential in the case of normal exploitation, function basically concerned with the general transmissivity of the reservoir. However this information is of great interest for knowledge of the reservoir, optimization of future projects and particularly if possible operational anomalies arise during production: deposits, dissolution or clogging of productive layers, drift of injection pressures and drawdown over a period of time.

3.2 - Vertical structure of the reservoir

The systematic use of flowmeter profiles and thermometry showed that there are six to eighteen units, with an effective thickness only up to as much as a meter, participating in productivity or injection (Fig. 6). The various productive layers show a high average permeability range that is very variable: from 200 mD per measure on the cores, up to 20 Darcy locally, from the production tests. Secondary permeability related to local fracturing and to dissolution is generally added to the matrix permeability of these layers.

These secondary characteristics, often very local and unpredictable, make standard correlation between individual layers difficult and uncertain, however spatial correlation by groups of layers from the same assemblage is possible, i.e. according to facies classification. Generally, for the wells under consideration, the main productive layers (i.e; between 50% and 80% of the total flow rate of a well) are located in the middle oolite facies. The rest of the production is assured by small layers, distributed in part in the Comblanchian facies. Only some of the layers from the "Alternances" facies, at the base of the reservoir, participate somewhat uncertainly in the total production.

The first study area, about 26 km by 17 km (domain 1, Fig. 7) northeast of Paris was selected to be analyzed in detail according to the facies classification under consideration. Vertical limits of the facies enabling classification of layers are deduced from examination of logs, cuttings, estimation of permeability, and a reference borehole cored on the whole reservoir. Figure 8 shows the respective contributions of three facies: Comblanchian, Oolite, and Alternances, with the total production for the 26 wells located in this domain. Note that for approximately all the wells (88%) more than 50% of the production is assured by the oolite facies, i.e. an average flow rate of 100 m^3/h for a cumulated productive thickness of about 10 m.

A similar facies analysis is in progress in a second domain about 26 km by 28 km, with a high well density, south of Paris (domain 2, Fig. 7). Taking into account the nearness of the southwest impermeability limit (marl belt) examination of the detailed characteristics of the productive layers enabled the lateral limits of each of the facies to be fixed locally by noting their presence or absence in each well.

The main conclusion from the analysis of the characteristics of the various productive layers for each well is the identification of the vertical heterogeneity of the reservoir:

Multiple productive layers.
Stratified structure.
High variability in permeability and productivity for each layer.
Low (about 16 to 30 m) total productive thickness in comparison to the thickness of the Dogger formation (100-300 m).

This particular fine structure was identified by the systematic establishment of flowmeter profiles in production associated with thermometry measurements.

3.3 - Regional distribution of parameters

After identifying the structure and vertical heterogeneity of the reservoir in a limited number of places (wells) the second stage was to estimate the lateral continuity of the productive layers and the regional distribution of their parameters from this spot information.

Verification of the hydraulic continuity of the reservoir and the possible limits is especially important in the case of development of the resource by well doublets with reinjection. Firstly, it's because of reinjection and the continuity of the reservoir that their productivity can be maintained; thanks to hydraulic interference between the two doublet wells the exploitation pressure can be maintained fairly constant over a period of time. However, in the case of scarce and thin productive layers there is a risk of quick recyclage of reinjected cold water towards the production well.

Exact knowledge of the geometrical characteristics enables the distance between the wells and the production flow rate to be planned in correspondance with the desired life time of the system.

3.4 - Methodology

An interference test (or loop) is realized on site after carrying out production tests on the two doublet wells. For practical and economic reasons, this short period test (about 12 h) only checks whether interference does or does not occur. It is generally not long enough to reliably identify the average transmissivity of the reservoir between the two wells which are about 1000 m apart.

The regional distribution of the parameters and the continuity of the reservoir are estimated by geostatistical methods, by digital processing of spot information filed in the data base.

Geostatistics is a method of estimating based on the theory of regionalized variables (Chiles, 1977). Its implementation comprises two main stages:

(1) Determination of a variogram which defines the structure of the experimental values: continuity, uncertainty factor, notion of overall regional drift, notion of range, i.e. the distance from the interior of which a correlation exists between the values of the variable under consideration.
(2) Estimation of the value of the variable at every one of the intersections of a regular grid by exploiting the aforementioned variogram model.

This method, well adapted to the problem under consideration enables an efficient and reliable relation to be established between, the analysis of spot data on the wells, and the simulation of reservoir behaviour by heterogeneous models requiring a large quantity of data. The method offers three main advantages:

Automatic mapping of the estimated parameters.
Mapping the precision of the estimations (standard deviation).
Automatic generation of data files at the geometric grid intersections identical to that required by the simulation models.

3.5 - Parameters studied

The main parameters studied are those required by the modelling and the estimation of the geothermal energy resource:

(1) Geometric, barycentric depth of levels ZB and depth of top of reservoir ZT in meters in comparison to sea level.
(2) Hydraulics, transmissivity Kh (Dm), permeability K (D), cumulated production thickness h (m), reservoir pressure PG (bars).
(3) Thermal, temperature measured at the top of the reservoir in production, TP.
(4) Chemistry, total salinity of the fluid TDS (g/l).

The analysis is first realized for all the productive layers, then selectively for each of the 3 facies under consideration. Table 1 summarizes the principal statistical results of samples analyzed subsequently (all the layers).

Table 1
Statistical results on boreholes analyzed in domain 3

Variables	KH(Dm)	TP(°C)	TDS(g/l)
Number of points	66	66	31
Mean	38.9	69.9	20.5
Standard deviation	25.3	6.4	5.3
Minimum	6.7	56.6	10.2
Maximum	113.8	79.7	30.5

3.6 - Study domain

The area studied is represented by a square of side 50 km, approximately centered on the Parisian agglomeration (domain 3, Fig. 7). This domain comprises 79 boreholes of which 66 only were used in this study taking into account data collection in progress or being processed. The 32 boreholes located outside domain 3, and too far away, are not included in this analysis because they provide little information concerning geostatistical estimation.

The domain is bounded to the southwest by an impermeable zone (marl belt) which constitutes the limit of lateral extension of the various productive facies.

3.7 - Production temperature at bottom hole, TP

The production temperature measured at the casing shoe, i.e. the mean temperature of the reservoir, is a continuous physical variable (Fig. 9) characterized by a low variance of estimation. The regional east-west drift is very marked, this drift is in good correlation with the depth of the top of the aquifer, and the maximum temperatures measured to the east and outside the domain (85 °C at a depth of 1,950 m).

This distribution of temperatures characterizes the geothermal energy resource in the central part of the Dogger reservoir where a fairly constant normal geothermal gradient is between 3 and 3.5 °C/100 m.

3.8 - Mean transmissivity of reservoir Kh

The mean transmissivity of the reservoir is a more heterogeneous parameter which also shows a fair northeast regional drift. On a larger scale, the characteristic southeast strike and the regional drift identified are consistent with the occurrence of the impermeable marl belt to the west and the various regression stages of the paleogeographic model (Fig. 10).

3.9 - Mean salinity of reservoir TDS

This reservoir fluid mean variable is similar to the temperature variable, and is very continuous with an overall regional drift in a northeast-southeast direction (Fig. 11). Interpretation of the distribution of this parameter is complex and calls for specific studies. The different causes, still poorly known concern: the origin of the salinity (see 2), the regional flow path responsible for mass transfer, the age of the water in relation with the fluid velocity and supply to the reservoir.

4 - CONCLUSIONS

At present the main subject of geothermal energy research in France, the Dogger reservoir limestone of the Paris Basin, is one of the most developped low-enthalpy fields in the world. At the end of 1986, 55 geothermal doublets, i.e. 110 wells were realized. These various wells, realized and analyzed first with petroleum technology methods, then more specifically with geothermal methods have progressively provided a large quantity of information for analysis and the detailed knowledge of the reservoir.

Firstly, the development of the resource is distinguished from that of wells for water and petroleum on two main points: (1) an average temperature of 70 °C and (2) a high production of about 150 to 250 m^3/h per well.

The characteristics of the initial oversimplified concept of an homogeneous reservoir progressively changed towards a more complex representation of a stratified structure, with a large number of thin producing levels, more-or-less continuous, with high permeability.

Study of the fluid geochemistry shows a wide geographic variability of chemical parameters over the whole basin. Depending on the area considered, phenomena such as evaporation of seawater, chemical interaction with the surrounding rocks, confinement and complex mixings are recognized, so salinities cannot be explained by a single process.

The geometrical characteristics and the understanding of numerous heterogeneities, both vertical and horizontal, still comprise a certain number of unknowns related notably to the paleogeography and the fluid history of the reservoir.

ACKNOWLEDGEMENTS

This work benefited from financial aid from the BRGM, the AFME and the Commission of European Communities. Contract EN 36 0046-F (CD).

The authors thank these organizations for authorization to publish the preliminary results of this work.

REFERENCES

Bastide, J.P. (1985), "Etude géochimique de la nappe du Dogger du Bassin Parisien," Thèse 3 ème cycle, Université Paris VII, 152 pp.

Chiles, J.P. (1977), "Géostatistique des phénoménes non-stationnaires," Doc. Ing. Thèse, Université de Nancy, 152 pp.

Criaud, A., Fouillac, C., Marty, B. and Wei, M.F. "Gas geochemistry of the Dogger geothermal reservoir," (this volume).

Criaud, A., Fouillac, C. and Brach, M., "Chemical evolution of the fluids from the Dogger Aquifer," Workshop on geochemistry, CEC contractors, Anvers, 5 November 1986.

Fouillac, C., Fouillac, A.M., Criaud, A., Iundt, F. and Rojas, J., "5th symposium on Water/Rock Interaction,"Reykjavik, 8-17 August 1986, 201 pp.

Menjoz, A. and Sauty, J.P. (1982), "Characteristics and effects of geothermal resources exploitation," J. of Hydrology, no. 56, p. 49-59.

Rojas, J. et al. (1984), "Le réservoir géothermique du Dogger en région parisienne: Exploitation, gestion," Hydrogéologie, vol. 2, p. 57-86.

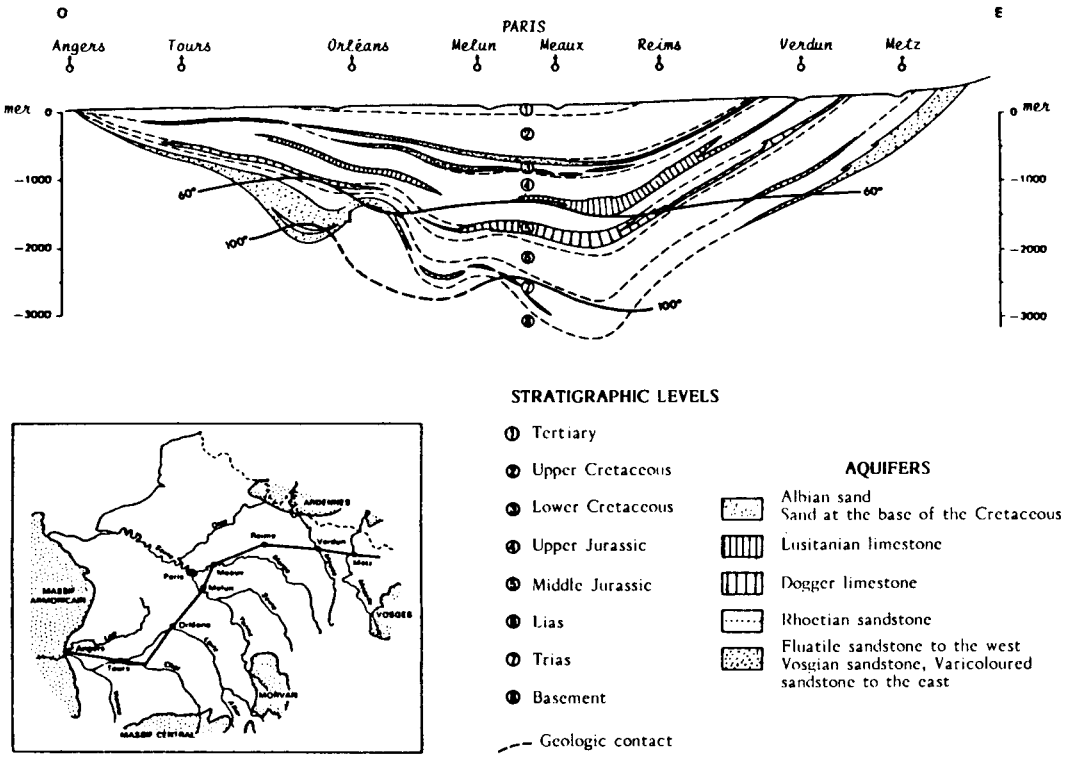


Figure 1 - Generalized cross-section of deep aquifers in the Paris Basin

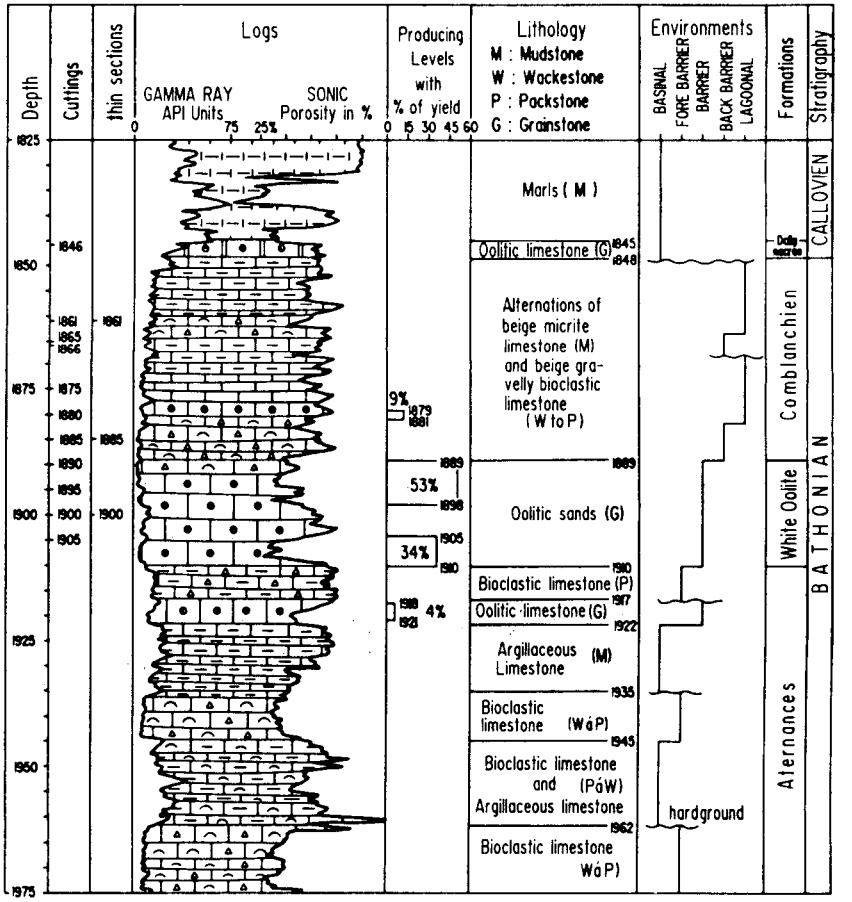


Figure 3

Typical sequence of Dogger in the Paris Basin

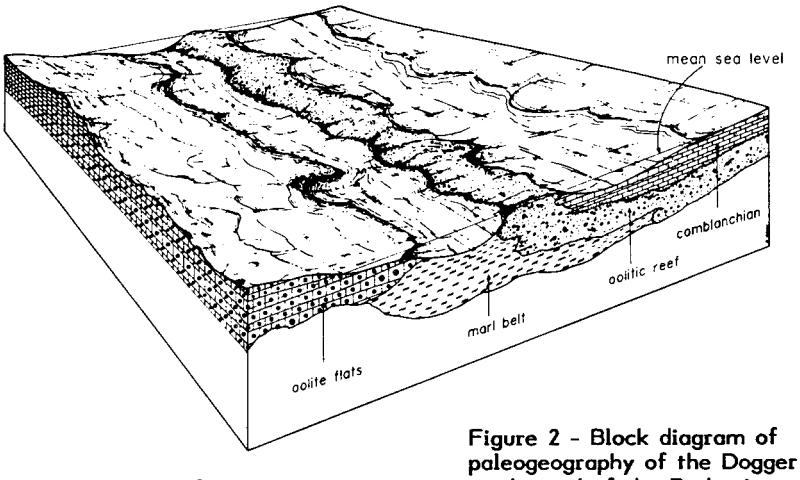


Figure 2 - Block diagram of paleogeography of the Dogger at the end of the Bathonian.

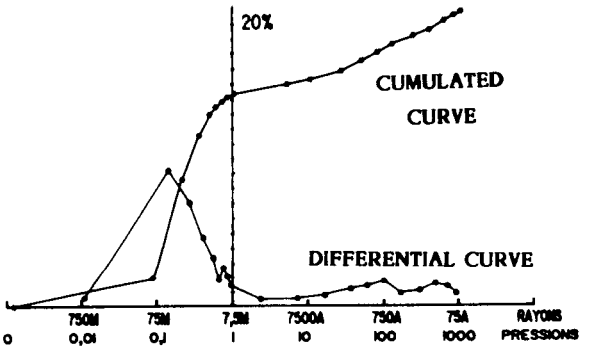


Figure 4

Oolitic limestone from the reef 1 730,5 m

Permeability : 200 mdy

Macroporosity : 14.16 %

Microporosity : 5.51 %

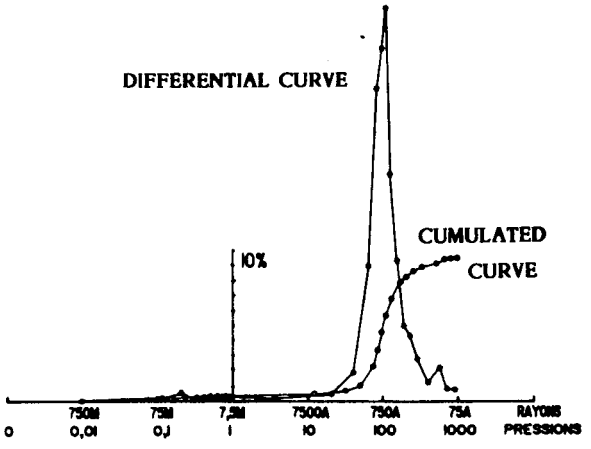


Figure 5

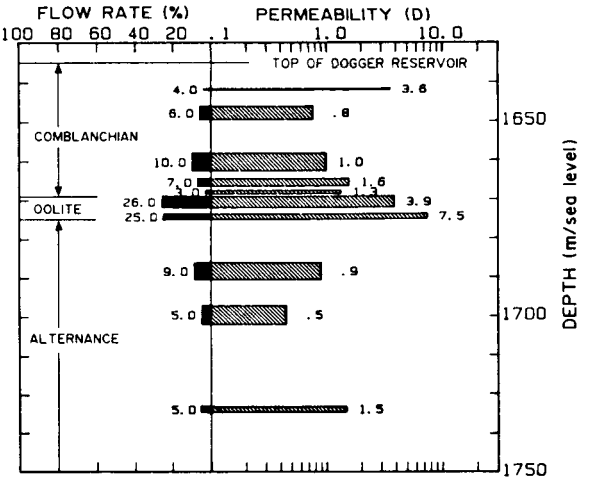
Compact micrite

External shelf 1 782,50 m

Permeability : 0,007 mdy

Macroporosity : 0.32 %

Microporosity : 9.42 %



WELL:AULNAY-SOUS-BOIS-1

MEAN PARAM.	FACIES COMBL.	FACIES OOLITE	FACIES ALTER.	ALL FACIES
H m	11.5	4.5	11.0	27.0
KH Dm	13.5	22.9	8.5	44.8
K D	1.2	5.1	.8	1.7
Q %	30.0	51.0	19.0	100.0
ZB NGF	1657.3	1672.3	1700.6	1673.2

Figure 6 - Detailed vertical structure of productive layers calculated from flowmeter and temperature logs.

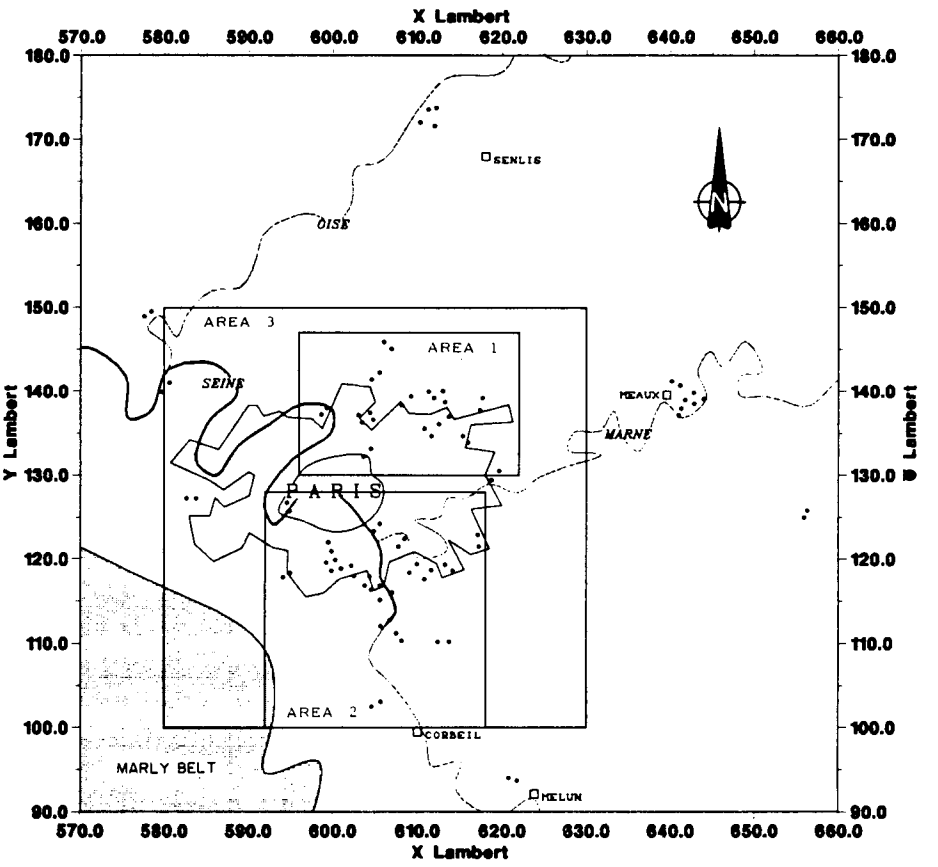


Figure 7 - Location of the geothermal wells in the Dogger reservoir (all wells not represented)

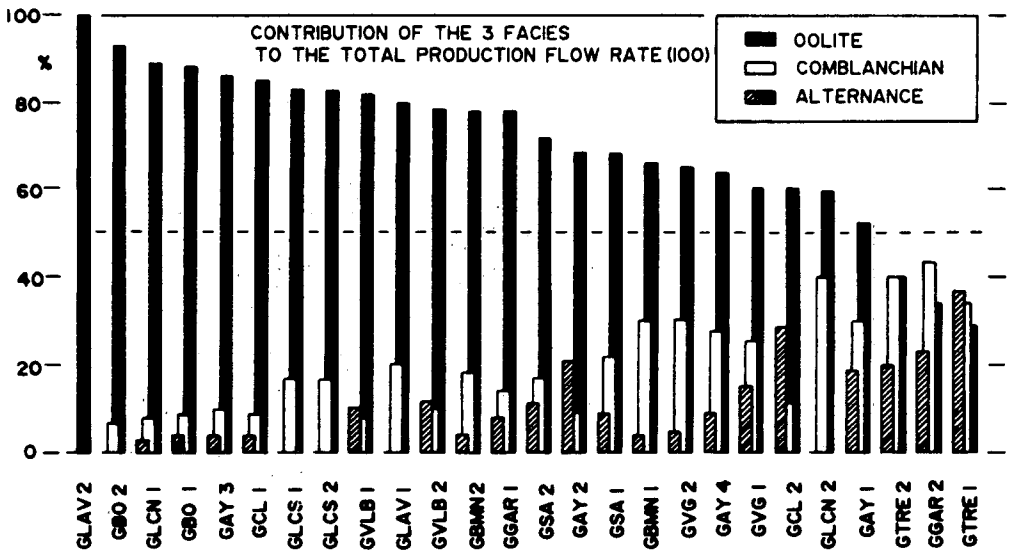


Figure 8 - Relative production of the 3 facies from 26 geothermal wells drilled in domain 1, classed according to the contribution of oolite facies.

FIGURE 9 - RESERVOIR TRANSMISSIVITY IN D.M (FROM PRODUCTION TESTS)

LEGEND :

ABOVE	*80.0*
60.0 – 80.0	
40.0 – 60.0	
20.0 – 40.0	
BELOW	*20.0*

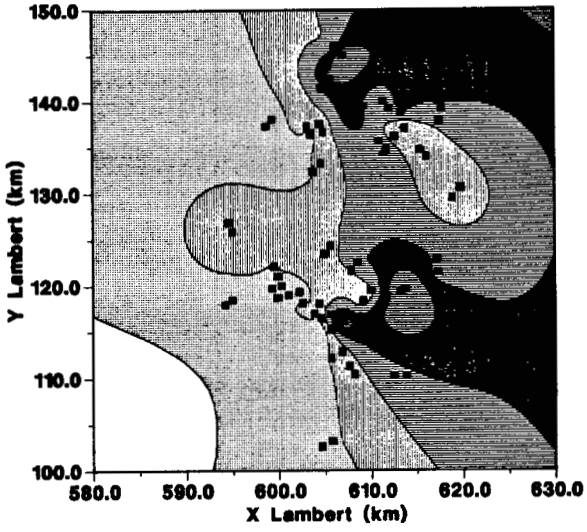


FIGURE 10 - TEMPERATURE OF RESERVOIR FLUID (MEASURED DOWN HOLE IN CELSIUS DEGRES)

LEGEND :

ABOVE	*80.0*
75.0 – 80.0	
70.0 – 75.0	
65.0 – 70.0	
60.0 – 65.0	
BELOW	*60.0*

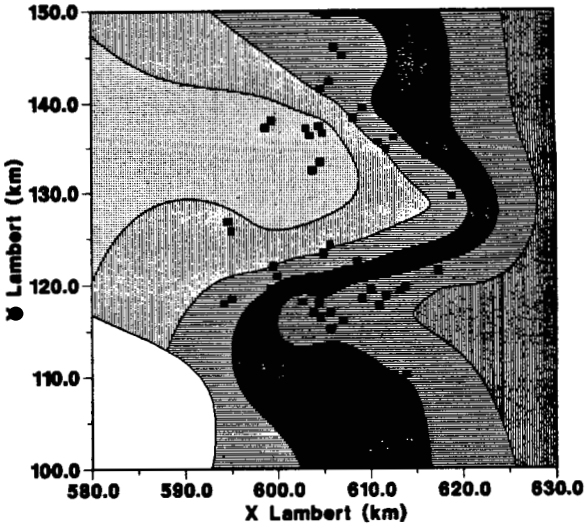
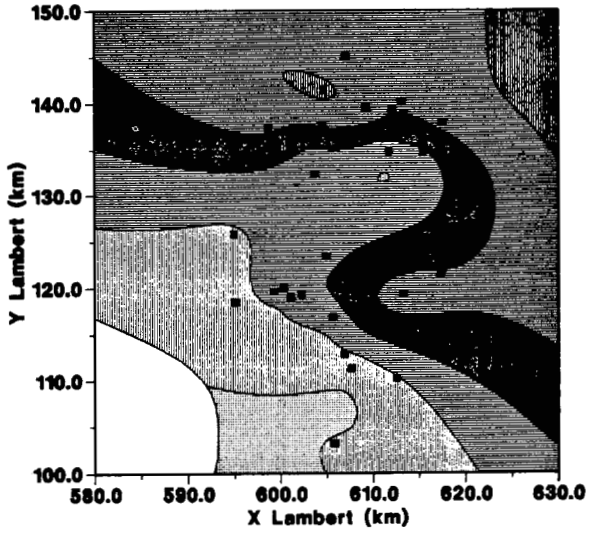


FIGURE 11 - FLUID TOTAL SALINITY (WELL HEAD MEASUREMENTS IN G/L)

LEGEND :

ABOVE	*30.0*
25.0 – 30.0	
20.0 – 25.0	
15.0 – 20.0	
10.0 – 15.0	
BELOW	*10.0*



PROCEEDINGS, Twelfth Workshop on Geothermal Reservoir Engineering
Stanford University, Stanford, California, January 20-22, 1987
SGP-TR-109

TRACER FLOW IN A FRACTURED GEOTHERMAL RESERVOIR MODEL

M.Bayar, E.Okandan

Middle East Technical University
Petroleum Engineering Dept.,
Ankara/Turkey

ABSTRACT

Tracer injection for identifying reservoir and transport parameters in geothermal sources has become an important procedure for designing an optimum reinjection program. Field tests have been analyzed using convection-diffusion equation to predict fracture size, width and probable thermal breakthrough times. The present study was conducted in a laboratory fractured reservoir model whose physical properties were known. The tracer, KI, breakthrough profiles were analyzed for different injection-production depth schemes. For different patterns different preferential flow paths existed which were then affected by flow through auxiliary paths.

A correlation between heat and mass transport was used to define an apparent heat transfer coefficient for the flow.

INTRODUCTION

In many geothermal development programs, waste geothermal fluids are reinjected for the purposes of disposal and pressure maintenance. The known effects are improved or degraded thermal recovery depending on flow paths and velocities and pressure maintenance. Since these beneficial and harmful results have been observed, reservoir tests to detect and predict the behavior of injected water are desired. In this respect interwell tracer tests have made significant contributions to understand the behavior of reinjected cold water within the reservoir and to develop an optimum injection program to maximize energy production.

Mathematical models for tracer flow through a porous matrix[6], through a double porosity reservoir[4] and through fractures[1,2] have been discussed in literature. The properties of the medium, porosity, permeability and degree of heterogeneity affect the tracer breakthrough profile in a producing well, where tracer is injected from a nearby injection well. The properties of the tracer like its diffusion, dispersion and adsorption also characterize the concentration profile.

In this work a laboratory fractured reservoir model was used for tracer injection tests. In this model matrix blocks do not have any permeability so the flow is through fractures only, which were created between uniform matrix block surfaces.

TEST PROCEDURE

The test procedure and experimental set up were explained in Hosca and Okandan[3]. The same procedure was followed with constant injection and production rates of 40 gr/min. Different flow paths were created by changing the injection production depth combinations designated as H_i/H_p with depths measured from the bottom of the model. KI at 4000 ppm concentration was injected as a slug and then displaced by water. The concentration of effluent was measured by an on line conductivitymeter. Cooling of the medium by the injected cold water was measured by 44 thermocouples present at different points in the model.

Tracer breakthrough profile was also obtained from a single fracture where the marble blocks (10x10 cm) were kept at 80°C (Fig.1) while KI solution was injected.

ANALYSIS OF DATA

The breakthrough concentration profile was analyzed using Sauty's hydrodispersive transport model[6]. In this study the system of fractures were treated with porous medium concept. The diffusion and adsorption in matrix and in fractures were assumed to be zero. Then one-dimensional tracer mass transport equation given as equation 1 is used

$$\frac{\partial c}{\partial t} + V \frac{\partial c}{\partial x} = \mathcal{D}_L \frac{\partial^2 c}{\partial x^2} \qquad (1)$$

for slug injection at the inner boundary

$$c(x,o) = M/\phi_f \cdot \delta_x \qquad (2)$$

where Dirac Impulse of mass M per unit of model pore volume was applied. With the semi-

infinite boundary assumption

$$c(\pm \infty, t) = 0 \tag{3}$$

the solution of equation 1 is[6],

$$C_R = \frac{K}{t_r^{1/2}} \exp\left(-\frac{Pe}{4t_R}(1-t_R)^2\right) \tag{4}$$

where

$$K = (t_{R_{max}})^{1/2} \exp\left(\frac{Pe}{4t_{R_{max}}}(1-t_{R_{max}})^2\right) \tag{5}$$

with

$$t_{R_{max}} = (1+Pe^{-2})^{1/2} - Pe^{-1} \tag{6}$$

and

$$C_R = C/C_{max} \tag{7}$$

For tracer reaching the outflow end apparent Peclet number is

$$Pe = \frac{v_B L}{\mathcal{D}_L} \tag{8}$$

and

$$t_R = \frac{v_B \cdot t}{L}$$

where v_B is the darcy velocity, $\mathcal{D}_L$ apparent dispersion coefficient of the medium and L is the distance between injection and production points.

The concentration profiles for different injection production depth combinations were compared with the analytical curves obtained using equations 4-7 for different Peclet numbers and the time when maximum concentration is obtained. The Peclet number and residence time t_R which gave the best fit were then used to calculate, fracture permeability, block size and fracture width and dispersivity in the medium.

The first arrival time of tracer at the producing end indicated the shortest path of flow which will also be the preferential route for cold water. So these first arrival times were used to calculate thermal breakthrough time using

$$t_{BT} = \left[\frac{\phi_f}{3}\right]\left[\frac{\pi h L^2}{b.a.v}\right]\left[\frac{(1-\phi_f)\rho_r C_r + \phi_f \rho_w C_w}{\phi_f \rho_w C_w}\right] \tag{10}$$

where h is the thickness of the bed, b fracture opening, a block size (fracture spacing), v velocity in the preferential path.

A mass transport-heat transport correlation proposed by Sieder and Tate[7] as

$$Nu_m = 1.86\,(Re.Pr.\frac{b}{L})^{0.33} \tag{11}$$

was used with the assumption that there is no variaton in physical properties of water within the fracture. An average effective heat transfer coefficient, h_m for the flow medium was obtained using equation 11 and Pe=Re Pr

$$h_m = 1.86\,(Pe \cdot \frac{D}{L})^{0.33}\,\frac{K_f}{L} \tag{12}$$

where K_f is the thermal conductivity of fluid and D hydraulic diameter of the rectangular conduit.

ANALYSIS OF DATA AND DISCUSSION

Tracer breakthrough profiles obtained for different injection-production depth combinations indicated flow paths differed in each case. (Fig.2-5) Experimental data from conductivity measurements were also checked by colorimetric analysis .

The fluctuations indicated secondary fracture flow paths which fed the main flow route. The match between the analytical model and the experimental data was acceptable. The model was not sufficient to model the tailing end of the breakthrough profile because of heterogeneities in flow.

Table 1 gives the parameters calculated using the Peclet numbers and residence times obtained from the analytical model and laboratory model.

Although the residence time of tracer slug for injection from bottom and production from top (H_i/H_p = 0.25/0.75) was similar to that of injection from top and production from bottom configuration, the difference in Peclet number and first arrival times indicated the flow pattern to be different.

Table 1. Peclet Numbers and Residence Time for Different Injection-Production Depths

H_i/H_p	Pe	Dispersion Coeff. $\mathcal{D}_L$ (cm^2/min)	Dispersivity $\mathcal{D}_L/V_B$ (cm)	First Arr. Time (min)	Res. Time (min)	Darcy Velocity in preferen.path, ν (cm/min)	Darcy velocity of the bulk; v_B (cm/min)
0.75/0.25	10.5	11.5	8.1	10	60	8.5	1.42
0.25/0.75	19.5	6.0	4.4	20	62	4.3	1.37
0.75/0.75	3.75	22.2	22.7	6	87	14.2	0.98
0.25/0.25	15.0	6.2	5.7	9	77.5	9.4	1.10

The permeabilities of these flow paths were calculated using darcy equation. A simple two dimensional flow model around cubical blocks, [4] was used to estimate effective fracture size and fracture spacing in the preferential path (Table 2).

Table 2. Calculated Values of Fracture Size and Fracture Spacing in the preferential path

H_i/H_p	kf (darcy)	Frac.Size,b, (mm)	Frac.Spacing,a (cm)
0.75/0.25	30.5	1.16	8.7
0.25/0.75	15.3	0.82	6.2
0.75/0.75	50.8	1.50	11.3
0.25/0.25	33.9	1.22	9.2

The values calculated for fracture spacing were comparable with 10x10 cm of the marble block dimensions.

The thermal breakthrough times were estimated from calculated values of fracture size b, fracture spacing a and darcian velocity along the preferential path. Early breakthrough will be observed in H_i/H_p of 0.75/0.75 which indicated the shortest path for cold water (Table 3).

Effective heat transfer coefficients for each flow pattern was calculated from the correlation given in equation 12. Injection of cold water at deeper points was more preferable in terms of heat efficiency of reinjection.

Table 3. Effective Heat Transfer Coefficient During Cold Water Injection

H_i/H_p	b,cm	h_m (W/m^2 °C)	Thermal BT time (min)
0.75/0.75	0.116	0.43	13.5×10^4
0.25/0.75	0.082	0.47	27.8×10^4
0.75/0.75	0.150	0.33	12.3×10^4
0.25/0.25	0.122	0.49	15.7×10^4

CONCLUSION

A laboratory model study was conducted for interpretation of tracer breakthrough profile in a fractured geothermal system whose properties were known.

The analytical model used to fit the experimental data had made it possible to predict apparent Peclet numbers and residence times of flow.

Changes in the depths of injection and production points resulted in different flow paths, which was also reflected in the dispersivities calculated from apparent Peclet numbers.

The fracture size and spacing calculated from experimental results were similar to the block dimensions in the model.

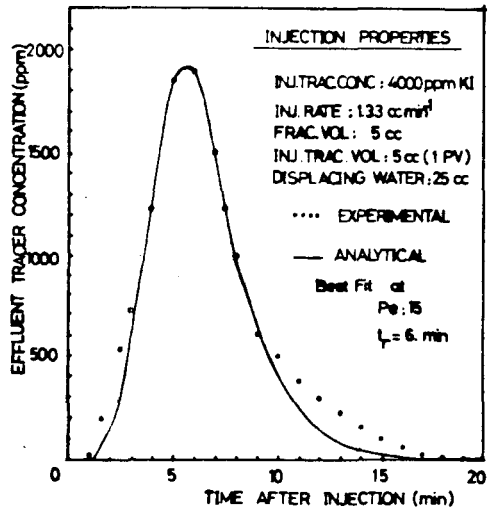


Figure 1. Tracer Breakthrough Profile in a Single Horizantal Fracture

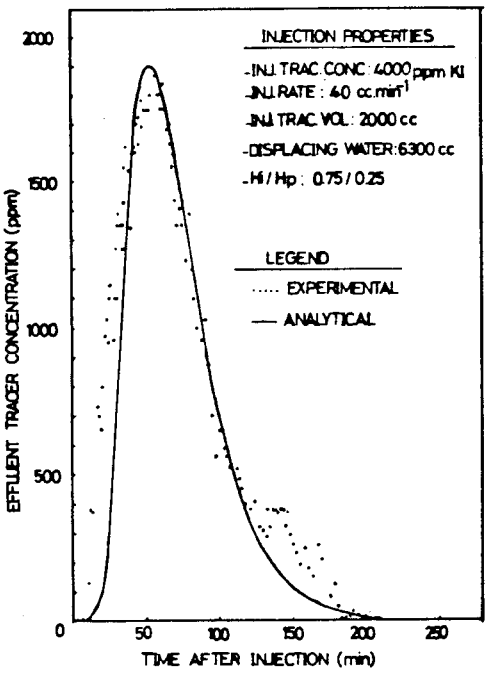


Figure 2. Tracer Concentration Profile at the Producing end for H_i/H_p of 0.75/0.25

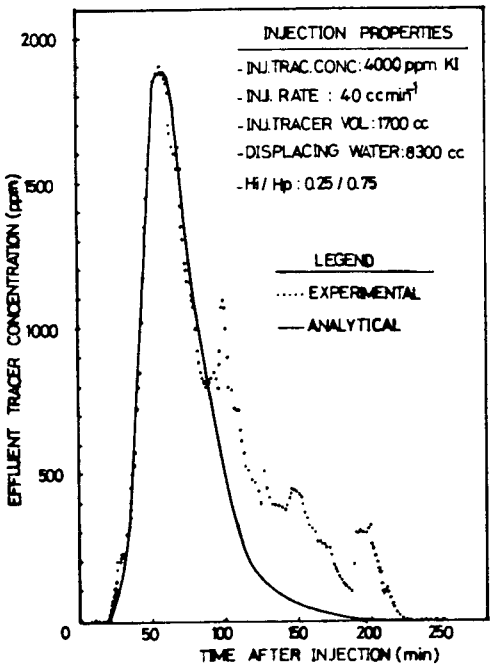


Figure 3. Tracer Concentration Profile at the Producing end for H_i/H_p of 0.25/0.75

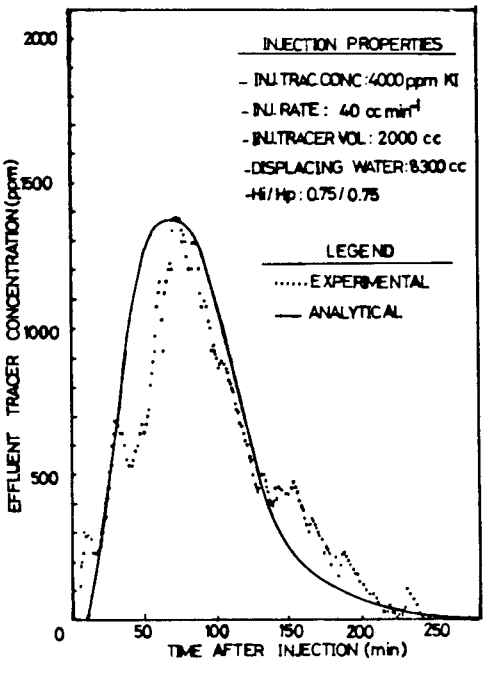


Figure 4. Tracer Concertration Profile at the Producing end for H_i/H_p of 0.75/0.75

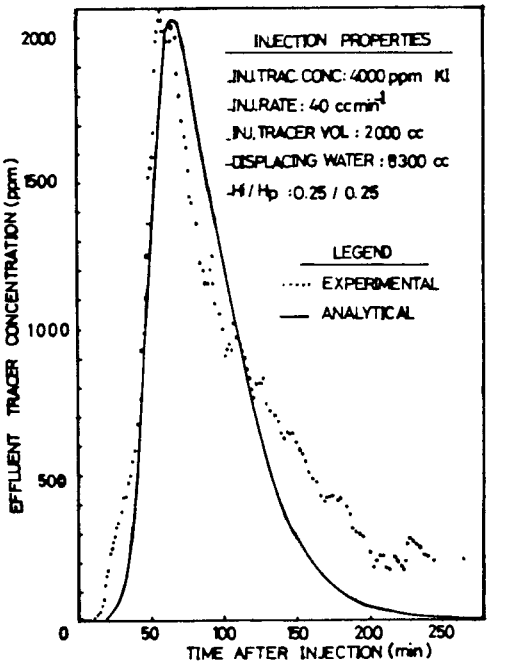


Figure 5. Tracer Concentration Profile at the Producing end for H_i/H_p of 0.25/0.25

REFERENCES

1. Fossum, M.P. and Horne, R.N. (1982), "Interpretation of Tracer Return Profiles at Wairakei Geothermal Field Using Fracture Analysis", Geothermal Resources Council, Transactions, Vol.6, October 1982.

2. Horne, R.N. and Rodriguez, F. (1983), "Dispersion in Tracer Flow in Fractured Geothermal Systems", Geophysical Research Letters, Vol.10, No.4, pp 289-292, 1983.

3. Hosca, H., Okandan, E., (1986), "Reinjection Model Studies in Fractured and Homogeneous Geothermal Systems", Proceeding presented at 11th Workshop on Geothermal Reservoir Engineering, held in Univ. of Stanford, CA, in Jan.21-23,1986.

4. Jensen, C.L. and Horne, R.N. (1983), "Matrix Diffusion and Its Effect on the Modelling of Tracer Returns from the Fractured Geothermal Reservoir at Wairakei, New Zealand", SGP-TR-71, Univ.of Stanford, CA, December 1983.

5. Okandan, E. (1986), "Tracer Injection in Fractured Reservoir Models", TUBITAK, Research Project, MAG.688.

6. Sauty, J.P. (1980), "An Analysis of Hydrodispersive Transfer in Aquifers", Water Resources Research, Vol.16, No.1, pp 145-158, February 1980.

7. Sieder, E.N. and Tate, C.E., "Heat Transfer and Pressure Drop of Liquids in Tubes", Ind. Eng. Chem., Vol.28, p.1429, 1936.

PROCEEDINGS, Twelfth Workshop on Geothermal Reservoir Engineering
Stanford University, Stanford, California, January 20-22, 1987
SGP-TR-109

THE THEORY AND SELECTION OF CHEMICALLY REACTIVE TRACERS FOR RESERVOIR THERMAL CAPACITY PRODUCTION

Jefferson W. Tester, Bruce A. Robinson*, and
James Ferguson

Chemical Engineering Department
Massachusetts Institute of Technology
Cambridge, Massachusetts 02139

ABSTRACT

The theory behind how chemically reactive tracers are used to characterize the velocity and temperature distribution in steady flowing systems is reviewed. Ranges of kinetic parameters are established as a function of reservoir temperatures and fluid residence times for selecting appropriate reacting systems. Reactive tracer techniques are applied to characterize the temperature distribution in a laminar-flow heat exchanger. Models are developed to predict reactive tracer behavior in fractured geothermal reservoirs of fixed and increasing size.

INTRODUCTION AND SCOPE

Inlet-outlet tracer measurements are an accepted experimental method for determining internal characteristics of continous flow sytems. Typically, a known amount of material is injected into the inlet with concentrations monitored at the outlet. Chemical reactors, process equipment, biologic systems, and underground reservoirs are examples of flow sytems in which tracers have been utilized successfully.

Unfortunately, in most flow systems of practical interest, inlet-outlet tracer techniques cannot uniquely determine the details of internal convective flow and fluid mixing. This non-uniqueness problem becomes even more severe when other characteristics of the system must be determined, such as internal temperatures, or local porosities and permeabilities. Frequently, a deterministic flow model with adjustable parameters is used to fit experimental tracer data. Thus, some non-uniqueness results in the absence of complete hydrodynamic and geometric information.

The primary focus of the present study is to develop new reactive tracer techniques and methods of data analysis which provide model-independent information about the internal flow and temperature fields of nonisothermal, continuous flow systems. A transient response experiment in which the tracer disperses and partially reacts contains information about both the internal flow and temperature fields of a flow system. Residence time distribution (RTD) theory (Danckwerts, 1953) and its extensions (Nauman and Buffham, 1983) are employed in the analysis of this chemically reactive tracer technique. In this paper, we outline the mathematical development necessary to rigorously describe the behavior of a reacting tracer in a nonisothermal flow system. Simplifications to yield practical models are discussed next, followed by a review of the quantitative criteria used in selecting tracers for geothermal reservoir diagnostics. Results of experiments in a laminar flow heat exchanger are presented to verify the validity of the reactive tracer technique, and to identify practical uncertainties and limitations of the theoretical concepts. Finally, applications to geothermal reservoir analysis are introduced through the use of simplified models of fractured systems undergoing heat extraction.

As this paper only overviews our current work on chemically reactive tracers, interested readers should consult Robinson and Tester (1986) and Robinson, Tester, and Brown (1987) for complete detailed coverage of the subject.

THEORETICAL DEVELOPMENT

When a non-reacting tracer of mass m_p is injected as a pulse into an isothermal steady flow system, the concentration-time response C(t) is measured in the outlet, and the residence time distribution (RTD) f(t) is obtained:

$$f(t) = QC(t)/m_p \qquad (1)$$

For steady state, incompressible fluid flow, f(t)dt = the fraction of fluid in the exit stream with residence times between t and t + dt. If another tracer that undergoes an irreversible, first-order reaction

*currently with the Los Alamos National Laboratory, Los Alamos, NM 87545

is introduced into the same isothermal system, the dimensionless, steady state, outlet conversion C_o/C_{in} is given exactly by:

$$C_o/C_{in} = \int_0^\infty f(t)\exp(-kt)dt \quad (2)$$

Equation (2) demonstrates that when an estimate of chemical reactor conversion or performance is desired for a first order reaction, the RTD is quite useful even without a detailed description of the flow field once f(t) is known. However, for reservoir engineering studies utilizing tracers, the internal flow and temperature patterns or other characteristics are often needed, and thus flow modeling is employed. For fractured reservoirs with relatively small deviations from plug flow caused by turbulent or mechanical mixing, a two-or one-dimensional axial dispersion model can be used to describe tracer dispersion. In this case the mathematical expression describing dispersive mixing of a reactive tracer in a convective flow field is:

$$\nabla\cdot(\underset{\sim}{D}\nabla C) - \underset{\sim}{U}\cdot\nabla C - kC = dC/dt \quad (3)$$

where $\underset{\sim}{D}$ is the dispersion coefficient tensor and $\underset{\sim}{U}$ the flow velocity vector. The term -kC has been introduced to account for the disappearance of tracer by way of a first order chemical reaction whose instantaneous rate is linearly proportional to the local concentration of tracer (C).
For systems with substantial internal flow maldistribution (that is large-scale internal velocity gradients) which cannot be modeled adequately assuming either perfect backmixing (the CSTR) or plug flow with axial dispersion, the situation becomes more difficult. Internal slow-moving (sluggish) or channeling zones must be described using models which treat the overall flow system as a composite of superimposed internal regions of different flow velocity.

Equation (3) is directly coupled to the in situ temperature field within the system because k, the first order rate constant, is a strong function of temperature. Its dependence is commonly expressed in Arrhenius form as:

$$k = A_r\exp\,[-E/RT] \quad (4)$$

For typical reactions in aqueous geothermal environments ranging from say 50 to 250°C from the injection to the production region, k will vary by several orders of magnitude.

One very important potential application of reactive tracers is to provide a measure of reservoir thermal capacity before actual thermal breakthrough occurs. The concept is actually quite simple incorporating the strong temperature dependence of k given in equation (4). Suppose a slug of tracer is injected into an initially hot reservoir and the overall conversion given by equation (2) is about 50% (C_o/C_{in} = 0.5). After some period of heat extraction a second slug of tracer is introduced. The conversion this time should be less than 50% given that a portion of the reservoir has been cooled reducing the value of k and the reaction rate in that region. Consequently, a series of reactive tracer tests will, in theory, map the rate of growth of the cooled region of the reservoir as heat extraction proceeds, and hopefully provide early warning of thermal drawdown.

The theory of generalized reaction times was proposed by Nauman (1977) and Nauman and Buffham (1983) to extend the existing mathematics of RTD theory to handle a greater number of reacting flow systems. By appropriately defining an equivalent reaction time for the more complex case, conventional RTD analysis may be used simply by replacing the residence time with a generalized reaction time, and the RTD with a generalized time distribution. The first such extension of RTD theory was proposed by Orcutt et al. (1962), who demonstrated the usefulness of the contact time in the analysis of a fluid-solid catalytic reactor.

For nonisothermal systems, the relevant generalized time is the thermal time θ proposed by Nauman (1977):

$$\theta = \int_0^t \exp(-E/RT)dt \quad (5)$$

for which an Arrhenius expression is assumed. The integral is performed over the time-temperature history of a molecule in a nonisothermal system. For a group of reactant molecules traveling through the same nonisothermal path, the integrated first order rate law is

$$C/C_{in} = \exp(-A_r\theta) \quad (6)$$

Note that the rate law of Eqn. (6) reduces to exp[-kt] in an isothermal system.

Nauman (1977) then defined a thermal time distribution (TTD) $h(\theta)$ as follows: $h(\theta)d\theta$ = the fraction of molecules in the exit stream with thermal times between θ and $\theta + d\theta$. For nonisothermal system, Eqn. (2) may be converted by replacing t with θ and f(t) by h (θ) to give:

$$C_o/C_{in} = \int_0^\infty h(\theta)\, \exp(-A_r\theta)d\theta \quad (7)$$

which is rigorous for a single-phase, irreversible, first-order reaction in a steady state, nonisothermal system.

A system of this type can be described with a bivariate thermal/residence time distribution function $P(t,\theta)$: $P(t,\theta)dtd\theta$ = the fraction of molecules in the exit stream with residence time between t and t + dt and thermal time between θ and $\theta + d\theta$. This normalized function represents an inventory of thermal and residence time properties of molecules in the exit stream. It is at the intersection of f(t) and $h(\theta)$, where the normalization is carried out so that,

$$\int_0^\infty \int_0^\infty P(t,\theta)dtd\theta = 1 \quad (8)$$

The function $P(t,\theta)$ is defined so that it is related to f(t) and to the thermal time distribution $h(\theta)$. Integrating over all thermal times at a given residence time:

$$f(t) = \int_0^\infty P(t,\theta')d\theta' \quad (9)$$

Likewise, integrating over all residence times for a given thermal time:

$$h(\theta) = \int_0^\infty P(t',\theta)dt' \quad (10)$$

If the distribution function approach is to be used, the bivariate distribution function $P(t,\theta)$ must enter into any rigorous description of a nonisothermal flow system. This is true because fluid or reactant molecules exiting with the same residence time need not have experienced the same time-temperature histories. Thus, the outlet chemical concentration of molecules at a given residence time is, in general, a result of superimposed reactant concentrations from different flow and temperature paths which have reacted to different extents.

The physical significance of the RTD f(t), TTD $h(\theta)$, and bivariate distribution $P(t,\theta)$ can each be demonstrated using a simple thought experiment. Picture the injection of a tracer pulse containing a very large number of small droplets of identical size which contain a reactant undergoing a first order reaction. The droplets are immiscible in the reactor fluid, yet follow the same flow paths with the same RTD as the injected fluid. Assume also that the droplets are collected at the outlet and analyzed separately so that the residence time and extent of reaction within each drop are known. This idealized experiment could, in theory, be used to measure the RTD, the TTD, and the bivariate distribution $P(t,\theta)$.

f(t): If the outlet fluid is collected between t and t + dt, the number of droplets in this sample, divided by the total number injected, equals f(t)dt.

$h(\theta)$: The dimensionless concentration in a droplet equals $\exp[-A_r\theta]$. Thus, a thermal time may be obtained for each droplet from a measurement of the extent of reaction. The number of droplets for which the thermal time falls between θ and $\theta + d\theta$, regardless of residence time, divided by the total number of droplets, equals $h(\theta)d\theta$.

$P(t,\theta)$: The number of droplets which exit between t and t + dt and possess thermal times between θ and $\theta + d\theta$, divided by the total number of droplets, equals $P(t,\theta)dtd\theta$.

INTERPRETATION OF EXPERIMENTAL TRACER DATA

Although the theoretical experiment just described facilitates an explanation of the various distribution functions in a nonisothermal reacting flow system, it is obviously too cumbersome an experiment to carry out practically. Thus, we propose a simpler form of the experiment, called the transient reactive tracer experiment, in which a pulse of a miscible tracer is injected into a nonisothermal flow system, and the concentration-time behavior of the reactant or product is monitored at the outlet. The term "transient" refers to the time-dependent nature of the tracer measurement, and not to time-varying operating conditions of the flow system. Only steady state (or quasi-steady state) flow and temperature fields are considered. In addition to the convective, molecular diffusive, and mechanical dispersive mechanisms that influence inert tracer behavior, the reactive tracer also undergoes an irreversible, first order reaction.

The amount of tracer remaining at different residence times will be measured at the outlet. The dispersion of both the reactants and products is governed by the f(t) curve, while the percent reaction at each residence time is controlled by the internal time-temperature histories of the tracer. It can be shown that the outlet conversion (C_o/C_{in}) given rigorously by equation (7) can alternatively be expressed in terms of $P(t,\theta)$ as,

$$C_o/C_{in} = \int_0^\infty \int_0^\infty P(t,\theta)\exp(-A_r\theta)d\theta dt \quad (11)$$

The key to understanding the transient reactive tracer analysis is that the C(t) and f(t) data provide conversion or thermal time information for molecules of different residence time. Since the thermal time, which is the fundamental variable for reaction in nonisothermal systems, is calculated from an integral along the flow path, conversion data is a lumped, macroscopic result which does not provide a microscopic description of the actual time-temperature history. Nonetheless, the experiment will directly detect nonisothermalities which are specifically linked to residence time. For example, if the temperature field encountered by fluid of small residence time t is different than that of the long-residence-time fluid, the transient reactive tracer response will indicate this phenomenon. However, temperature patterns along a flow path cannot be determined from the single transient tracer analysis unless other information about the temperature pattern is available.

In many systems large-scale heterogeneities cause the observed RTD. These would include multifracture reservoirs with channeling or multidimensional flow in specific fractures, where different residence times are associated with specific physical locations within the reservoir. If these internal flow regions possess different temperature fields, then the C(t) response may be interpreted to obtain the extent of nonisothermality. For maldistributed flow fields, a useful simplification of the internal flow and temperature field is to assume that each residence time corresponds to one and only one value of the thermal time. This assumption will hereafter be called the residence time-thermal time correspondence criterion. Under these conditions in our hypothetical droplet experiment, all droplets exiting at a given time t would have the same chemical reaction conversion. This implies that the bivariate distribution function $P(t,\theta)$ is nonzero for only one value of thermal time, expressed using a Dirac delta function $\delta()$ as,

$$P(t,\theta) = \delta[\theta - \theta(t)]f(t) \qquad (12)$$

where $\theta(t)$ is the thermal time corresponding to the flow path of residence time t. The steady state outlet conversion given by equation (7) is used in equation (2) to calculate an "isothermal equivalent" $\bar{k}$, which is the rate constant required for the same steady state conversion in an isothermal reservoir having an identical RTD or f(t) curve. The isothermal equivalent response curve $C_p(t)$ to a pulse injection is then determined from:

$$C_p^I(t)/f(t) = \exp(-\bar{k}t) \qquad (13)$$

Correspondence between residence time and thermal time, if it exists, will be observed by comparing $C_p^I(t)$ with the actual $C_p(t)$ data.

The calculated $C_p^I(t)$ curve will exhibit differences in reactant conversion with residence time which are due only to the residence time, while the measured $C_p(t)$ curve may take a different shape depending on the temperature field. There are at least three types of internal flow/temperature fields which could give rise to different reactive tracer behavior, as shown conceptually in Figure 1. The first, labelled uniform reaction environment, results in identical $C_p(t)$ curves for the actual and isothermal equivalent cases. In such a system, all flow paths encounter similar temperature fields, regardless of residence time. Obviously, all isothermal systems are examples of uniform reaction environments, with $\theta(t) = t\exp(-E/RT)$. Nonisothermal systems may also exhibit this behavior if all fluid elements experience the same temperature field, regardless of residence time.

In the temperature-enhanced reaction environment, the extent of reaction at longer residence times is greater than that which can be explained by residence time alone. A temperature effect compounds the normal increase in reactant conversion with residence time. For a system exhibiting this type of reactive tracer behavior, the longer residence time flow paths are, on average, at higher temperatures.

By the same reasoning, the temperature-compensated reaction environment is one in which longer residence times correlate with cooler average temperatures. A single transient reactive tracer experiment, when analyzed using the isothermal equivalent method, provides model-independent information for complex, nonisothermal systems. The analysis just outlined could be used as the starting point in the construction of a descriptive flow and thermal model. Internal flow zones of different volume, flow velocity, and temperature could be established on the basis of an analysis of the inert f(t) and reactive $C_p(t)$ responses.

REACTIVE TRACER SELECTION AND CHARACTERIZATION

In addition to having all the desirable characteristics of inert tracers, reactive tracers kinetic parameters (A_r and E) should be such that the characteristic reaction time $\tau_r = 1/k$ for a 1st order reaction is of the same order of magnitude as the mean residence time τ.

Kinetic experiments were performed in a constant-temperature reactor to identify candidate reactive tracers for different geothermal applications. The rates of hydrolysis of six organic esters and three unsubstituted amides were determined in a buffer system consisting of mixtures of sodium bicarbonate and acetic acid in deionized water. The kinetic rate law for the alkaline hydrolysis of ethyl acetate is given by

$$d[EA]/dt = -k_2[OH^-][EA] \qquad (14)$$

In these buffered solutions of pH between 5.6 and 7.3, $[OH^-]$ is constant during an experiment, but its value at elevated temperature is much higher than at 25°C due to the temperature-dependence of the equilibrium constants of the water, bicarbonate, and acetic acid dissociation reactions. A chemical equilibrium model was developed to predict $[OH^-]$ at high temperature for a closed system of known chemical conditions at 25°C.

This model is used to evaluate the autoclave hydrolysis data obtained for ethyl acetate in buffered solutions as summarized in Figure 2. The autoclave data agree with alkaline hydrolysis kinetic parameters obtained at high pH and low temperature (typically 0.01 M NaOH and 30-60°C) by previous investigators and in the present study. However, if we merely assume $[OH^-]=10^{(pH-14)}$, without accounting for temperature, the observed reaction rates are 2-3 orders of magnitude higher than expected. Also, experiments performed at higher pH exhibited the rate behavior predicted by the $[OH^-]$ model.

Similar agreement with published alkaline hydrolysis data was obtained for all but one of the esters (t-butyl acetate). The amides also appear to follow the proper rate versus $[OH^-]$ behavior, but the absolute rates were higher than expected from the extrapolated literature results. Figure 3 shows the results of the autoclave hydrolysis experiments in the form of reaction time $(1/k_2[OH^-]$ versus $1/T$ for geofluid of pH 6. Finally, preliminary rock compatibility studies using crushed granite showed no evidence of catalytic effects, but the esters of higher molecular weight had a slight tendency to adsorb on the rock surface.

VERIFICATION OF REACTIVE TRACER ANALYSIS TECHNIQUES

The reactive tracer techniques introduced earlier were verified experimentally for the case of a vertical, countercurrent, shell and tube heat exchanger with laminar flow. Assuming a parabolic velocity profile, temperature independent thermal physical properties, and negligible axial conduction of heat, the well known Graetz solution is applicable (see Eckert and Drake (1972) for details). Under these conditions the axial and radial temperature profile is given by:

$$T^+ = T^+(x^+,r^+) = \sum_{n=0} C_n R_n(r^+)\exp(-\lambda_n^2 x^+) \qquad (15)$$

when C_n is a numerical constant corresponding to each Eigenvalue λ_n. $R_n(r^+)$ are the radial function for each Eigenvalue λ_n. Equation (15) can be asymptotically approximated by

$$T^+ = T^+(x^+,r^+) = 0.7764\int_0^{\eta} \exp(-\eta^3/3)d\eta \qquad (16)$$

where dimensionless variables are defined as:

$$x^+ = x/(r_o RePr) \; : \; r^+ = r/r_o$$

$$T^+ = (T-T_w)/)T_o-T_w)$$

Fluid flows up through the inside tube and is heated or cooled from the outside. First, the constant-wall temperature Graetz solution was coupled to the theoretical tracer response assuming the parabolic velocity profile and no molecular diffusion of tracer. Calculated reactive tracer response curves are shown in Figure 4 for cold injection fluid heated from the outside and hot fluid cooled from the outside. The dramatic difference detected by the transient reactive tracer curves demonstrates that the $C_p(t)$ response can be used to evaluate the internal temperature field of this system.

Heat transfer and inert and reactive tracer experiments were performed in a laminar flow heat exchanger (Re = 100) to evaluate the Graetz model and the reactive tracer techniques. The chemical reaction used was the alkaline hydrolysis of ethyl acetate (EA) to ethanol and acetic acid. When $[EA] >> [OH^-]$, the pseudo-first order rate law is

$$d[OH^-]/dt = -k[OH^-], \qquad (17)$$

where $k = \exp(-E/RT)A_{r,2}[EA]$ is the psuedo-first order rate constant. The term $\exp(-E/RT)A_{r,2}$ is the second order rate constant for the reaction, and the apparent A_r under these conditions is $A_{r,2}[EA]$. In this case the reactive tracer is OH^-

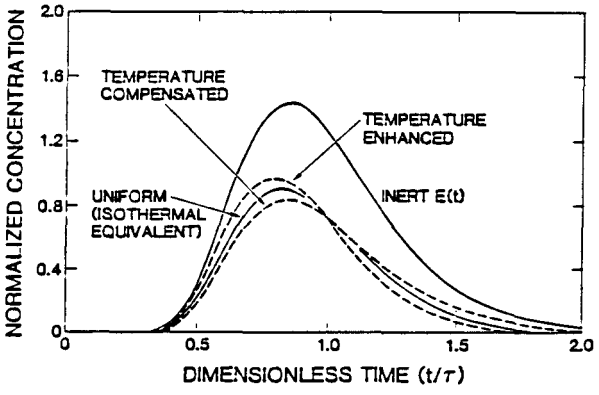


Figure 1. Typical reactive tracer pulse response curves for the three reaction environments.

measured on-line in the outlet stream using a pH electrode. Varying [EA], while always keeping it large compared to [OH^-], is a convenient way to vary A_r or k over a large range. The inverse step or washout tracer technique was employed in these tests. Stock solution (EA dissolved in deionized water) and OH^- in the form of a concentrated solution of NaOH, were injected continuously until a steady state outlet value of C_o/C_{in} was obtained. At t = 0, the OH^- stream was shut off, and the transient response to the negative step of [OH^-] was measured at the exit. Non-reactive tracer tests were performed similarly by injecting a stock solution of pure deionized water without EA. Equations governing this mode of tracer injection and resulting "washout" curves were derived from the pulse response equations.

The experimental heat transfer and non-reactive tracer results suggest that a combined forced-free convection flow field existed in the heat exchanger. Calculated heat transfer coefficients for both heating and cooling from the outside were much larger than predicted from the Graetz solution, which considers only forced convection. Also, the non-reactive tracer response for the three nonisothermal flow fields were similar to each other, but dramatically different than an experiment performed in the isothermal tube as shown in Figure 5. The shapes of the nonisothermal response curves indicated more uniform flow and less long-residence-time tailing which is consistent with the model of natural circulation and mixing of fluid near the wall. The possible effects of temperature-induced viscosity variations across the tube radius were also considered and found to be a much less likely explanation for the data.

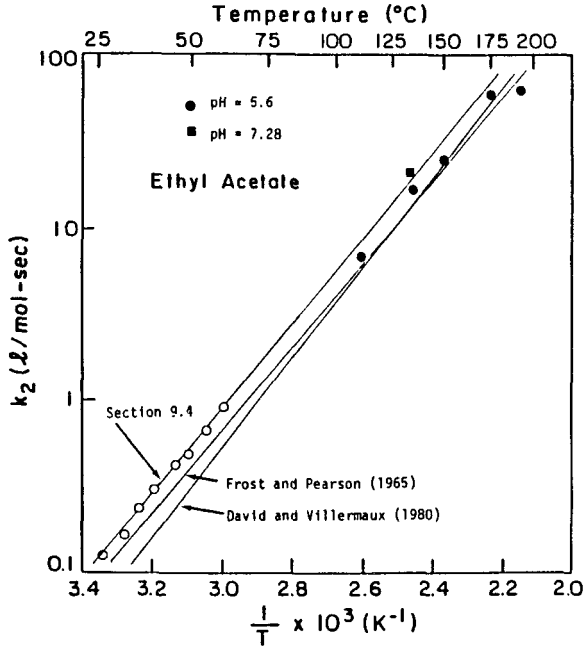


Figure 2. Comparison of ethyl acetate hydrolysis parameters obtained in basic solutions

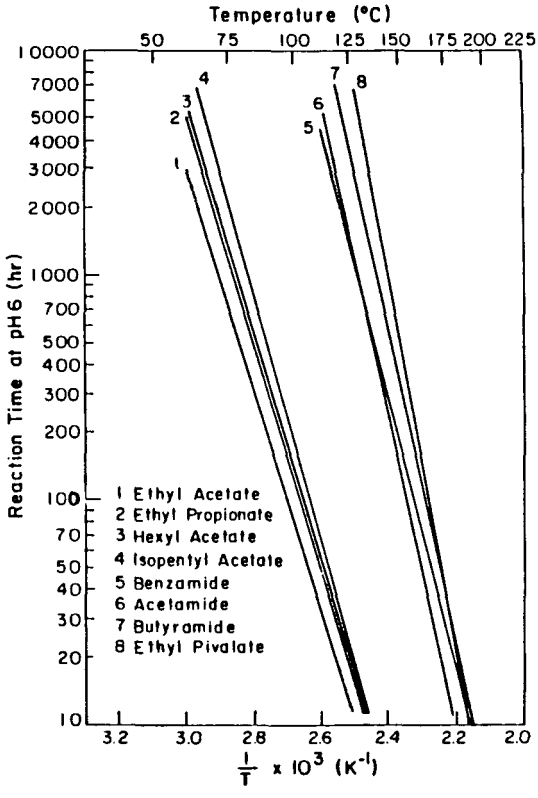


Figure 3. Summary of alkaline hydrolysis kinetic experiments: reaction time versus temperature in a geothermal fluid of pH = 6

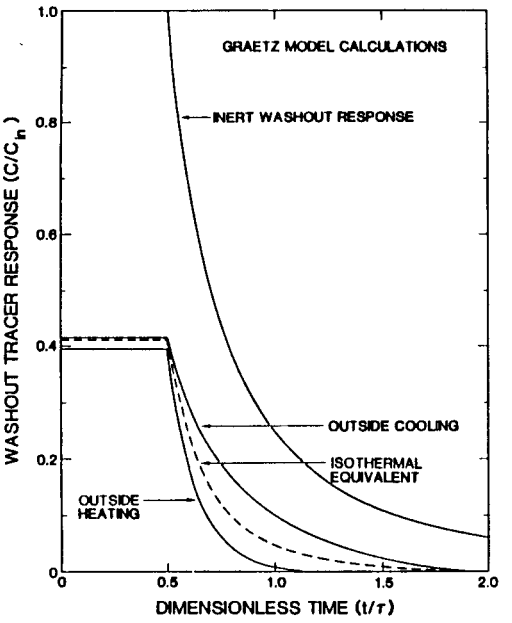


Figure 4. Transient reactive tracer response curves calculated assuming the Graetz solution applies for heating or cooling to a fluid flowing in laminar flow inside a tube

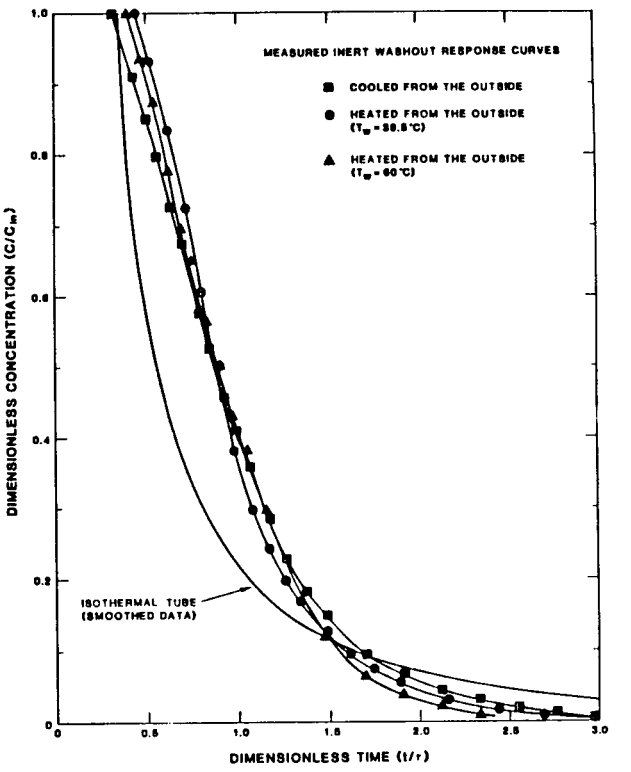


Figure 5. Comparison of measured inert tracer response in a washout experiment for the three thermal situations: isothermal, outside heating, and outside cooling.

APPLICATIONS TO FRACTURED RESERVOIR SIZING

A major challenge facing the development of artificially stimulated hot dry rock (HDR) reservoirs is the prediction of lifetime and thermal capacity early in the production history of the reservoir. (Armstead and Tester, 1987). This is a very difficult task in view of the complex flow systems that seem to typify the prototype HDR systems developed in the US at the Fenton Hill site and in the U.K. at the Rosemanowes site. The RTD's of both systems appear to be composites of superimposed flow from a number of separate/fracture joint systems (Batchelor, et al., 1986 and Robinson et al., 1987). An additional complication appears as the reservoir undergoes dynamic changes during the heat extraction period. Observations at Fenton Hill and Rosemanowes both indicate a large increase in reservoir volume over relatively short periods of heat removal (30 days to 400 days). It is quite likely that this increase in size will also lead to an increase in thermal lifetime at the same heat extraction rate. (Tester, et al., 1986).

To summarize, HDR reservoir systems created by hydraulic stimulation in low permeability crystalline rock are generally characterized by highly dispersed flow as a result of superimposed, multidimensional flow in interconnected joint sets. Furthermore, this composite fracture system undergoes dynamic changes induced by thermal and/or hydraulic stress effects as a result of pressurized circulation of fluid to extract heat. Our initial modeling approach for reactive tracer analysis has been to simplify the system enough to make it tractable but to retain sufficient complexity to capture the basic physical and chemical phenomena that are occurring.

Rather than try to deal with the composite fracture system in its entirety, we have decided to subdivide the reservoir into separate flow systems as a starting point for analysis. Initially, a multiple set of individual joints with 1-dimensional areal flows and specified geometries was assumed to contribute to the early portion of the RTD near the modal volume while the longer tail of the RTD with extremely large residence times was due to more volumetric-like flow in highly fractured secondary flow paths. A numerical heat transfer model was developed to account for transient effects in the fracture system and to

provide estimates for spatial temperature distributions along each fracture. Individual fractures were assumed to be non-interacting thermally but relative flow rates could be altered to simulate reservoir growth and other dynamic changes. The thermal field was simulated for each individual fracture over a given heat extraction period with fracture geometry, thermal physical properties, and a flow rate schedule specified. Then the inert and reactive tracer response was estimated using a numerical finite difference solution to equation (3) written for 1-dimensional flow with a fixed Peclet number (Pe = UL/D). For initial trials a value of 50 was used for Pe to represent an appropriate level of dispersion within a single fracture. The thermal simulation was used to specify values of k spatially along the fracture face. Finally the predicted outlet tracer conversions for individual fracture were superimposed to provide a composite result for comparison with field values.

CONCLUSIONS

A rigorous theoretical treatment of the behavior of chemically reacting tracers has been presented to show its potential application to fractured geothermal reservoir analysis. Simplifications were proposed to allow for modeling estimates in the absence of complete fracture geometry, flow field and temperature field specification. The most significant of these was the residence time-thermal time correspondence criterion. Verification of the theoretical techniques developed was established for a laminar flow heat exchanger. A tractable approach for employing reactive tracers in modeling the thermal performance of fractured HDR geothermal systems was presented.

ACKNOWLEDGEMENT

The authors would like to thank the entire staffs at both the Los Alamos National Laboratory and the Camborne School of Mines for their help and stimulating discussions. In particular, we are grateful to H. Murphy, C. O. Grigsby, R. Potter and L. Brown of Los Alamos and K. Kwakwa and A. S. Batchelor (now of GeoScience, Ltd) for their input and review of our work. The partial financial support provided collectively by the U.S. and U.K. Departments of Energy is gratefully acknowledged.

NOMENCLATURE

A_r- reaction pre-exponential factor (s^{-1})

C- concentration of product or reactant (mol/liter or kg/liter)

C(t)-concentration versus time response of a tracer (kg/liter)

D- dispersion coefficient (m/s)

E- reaction activation energy (kJ/mol)

f(t)-residence time distribution function (s^{-1})

F(t)-cumulative residence time distribution function

$h(\theta)$-thermal time distribution function (s^{-1})

k- 1st order reaction rate constant (s^{-1})

$\bar{k}$- isothermal equivalent reaction rate constant (s^{-1})

k_2- 2nd order reaction rate constant (liter/mol s)

L- fracture length (m)

m_p- mass of tracer injected in a pulse experiment (kg)

r_o- tube radius (m)

R- Universal gas constant = 8.314 J/mol K

Re- Reynolds number

$P(t,\theta)$-bivariate residence time/thermal time distribution function (s^{-2})

Pe- dispersional Peclet number

Pr- Prandtl number

T- Temperature (°C or K)

t - time (s)

u- fluid velocity

GREEK

τ- mean residence time (s)

τ_r- characteristic reaction time = 1/k (s)

η- dummy variable in equation (15)

λ_η- Eigenvalues in Graetz series solution

θ- thermal time (s^{-1})

REFERENCES

Armstead, H.C.H. and J. W. Tester, Heat Mining, E. F. Spon, London (1987).

Batchelor, A.S. et al, "Reservoir Behavior in a Simulated HDR System", 11th Annual Workshop On Geothermal Reservoir Engineering, Stanford University, Stanford, CA (Jan. 21-23, 1986).

David, R. and J. Villermaux, "Comments on: A Mixing Model for a Continuous Flow Stirred Tank Reactor", Ind. Eng. Chem. Fundamentals 19, 326-327 (1980).

Eckert, E.R.G. and R. M. Drake, Analysis of Heat and Mass Transfer, 2nd ed., McGraw Hill, NY (1972).

Frost, A.A. and R. G. Pearson, Kinetics and Mechanism, 2nd ed., J. Wiley and Sons, NY (1965).

Orcutt, J.C., J. F. Davidson, and R. L. Pigford, "Reaction Time Distributions in Fluidized Catalytic Reactors", Chem. Eng. Prog. Symp. Ser., No. 32, 58, 1-15 (1962).

Nauman, E. B., "Non-isothermal reactors: Theory and Application of Residence Time Distributions" Ind. Eng. Chem. Fundamentals 32, 359-367 (1977).

Nauman, E.B. and B. A. Buffham, Mixing in Continuous Flow Systems, J. Wiley and Sons, NY (1983).

Robinson, B. A. and J. W. Tester, "Temperature Field Determination Using Chemically Reactive Tracers: Part 1. Theory and Part 2. Experimental Determination in a Laminar-flow Heat Exchanger". (submitted to Ind. Eng. Chem. Res.) (1986).

Robinson, B. A. and J. W. Tester, "Reservoir Sizing Using Inert and Chemically Reacting Tracers", Soc. Pet. Eng. Journal (Reservoir Engineering) (accepted for publication)(1987).

Tester, J. W., H. D. Murphy, C. O. Grigsy, R. M. Potter, and B. A. Robinson, "Fractured Geothermal Reservoir Growth Induced by Heat Extraction", SPE 15124, presented at the 56th California Regional Meeting of the Society of Petroleum Engineers, Oakland, CA (April 2-4, 1986).

PROCEEDINGS, Twelfth Workshop on Geothermal Reservoir Engineering
Stanford University, Stanford, California, January 20-22, 1987
SGP-TR-109

Parallel Fractures Model for Tracer Flow Through Geothermal Reservoirs - Preliminary Results

J. R. Rivera
Pet. Eng. Dept., Stanford University

J. S. Ramirez and F. G. Rodriguez
Universidad Nacional Autonoma de Mexico

ABSTRACT

A parallel fractures model, having equal width and spacing, has been developed to study the flow of tracers through naturally fractured geothermal reservoirs. The model is capable of handling either a single fracture or a system of two or more parallel fractures, interacting with associated porous bodies. The reservoir is treated as being composed of two regions; a mobile region where diffusion and convection are allowed and a stagnant or immobile region where only diffusion and adsorption are allowed. Both regions are interconnected by means of a very thin fluid film contained within the immobile region which controls the fluid and mass transfer between both regions. The mobile region represents the system of fractures, where tracer is free to flow reaching high velocities, whereas non-homogeneities of the reservoir rock, such as microfractures and dead-end fractures are represented by means of an equivalent porous body where fluid remains immobile. The boundary-value problem for the system is stated and its solution into Laplace's space is presented. Numerical inversion of this solution was performed by means of the Stehfest algorithm. Preliminary results showing results obtained from the proposed model are included. Further work is underway to apply the model for interpretation of actual tracer flow field data.

INTRODUCTION

In the past few years, reinjection of separated brine back into the producing formation for pressure maintenance purposes has been a major issue for an adequate development of liquid-dominated geothermal resources. To date, some practical experience on reinjection of geothermal brine into the reservoir has been gained. This experience seems to indicate that rapid inter-well movement of injected fluid has occurred, causing an undesirable early thermal breakthrough (Horne, 1982). Therefore, careful selection of injection-production wells schemes are required in order to reduce the risks of having this early temperature drop in the production wells (Rivera et al., 1982). Tracer flow testing is an appropriate technique for obtaining a good idea on how injected fluids travel in the reservoir and a correct interpretation of the tracer return curves at production wells provides with parameters that can be used to study the heat and mass transfer processes taking place in the reservoir.

Since geothermal reservoirs are known to be highly-naturally fractured reservoirs, standard tracer interpretation techniques developed for flow through porous media in the hydrogeology and petroleum technical literature are not applicable. Most of the models published to date for interpretation of tracer return curves in geothermal reservoirs allow mostly qualitative estimation of reservoir parameters (Fossum, 1983, Tester et al., 1982, Jensen, 1983) and only few of them allow quantitative determination of basic reservoir parameters (Walkup and Horne, 1985).

In this study a parallel fractures model was developed to quantitatively determine basic geothermal reservoir parameters from tracer return curves. This model seems to be simpler than that proposed by Walkup and Horne since it only requires one Laplace's inversion and four fitting parameters; meanwhile the former requires two numerical inversions and has five parameters to adjust.

PARALLEL FRACTURES MODEL

The proposed model is shown in Figure 1. The fractured heterogeneous medium is represented by means of a system of equally spaced parallel fractures alternated with porous blocks. As shown in Fig. 1, this system is made up of two connected regions; a mobile region constituted by the fracture itself, where diffusion and convection processes are taking place and an immobile region where only diffusion and adsorption are allowed. These later processes go first through the very thin stagnant fluid layer of δ thickness, spreading then into the porous body. The idea of dividing the flow system into two interconnected regions has already been used by several authors (Deans, 1963; Walkup and Horne, 1985, Maloszewski and Zuber, 1985 among others).

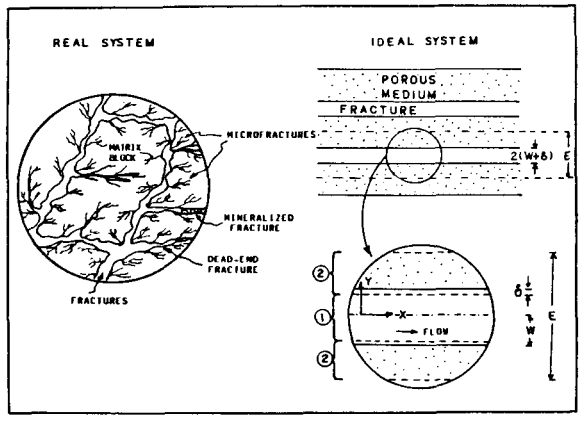


Figure 1: Proposed parallel fractures model.

Taking a mass balance on the mobile region and assuming the following: a) no production or reaction of the chemical species within the control volume; b) continuous injection of tracer into the fracture system; c) flow in the fractures is fast enough so that only steady convective flow in the x direction takes place; d) tracer distribution across the fracture width can be assumed constant due to efficient transverse diffusion and dispersion; e) constant density, the governing equation for the mobile region is as follows:

$$D_m \frac{\partial^2 C_m}{\partial x^2} - V_m \frac{\partial C_m}{\partial x} - \lambda (C_m - C_i) + \frac{\phi_e}{W-\delta} D_e \frac{\partial C_e}{\partial y}\bigg|_{W-\delta} - \frac{\partial C_m}{\partial t} = 0 \quad (1)$$

Taking a mass balance on the immobile region and assuming that only diffusion in the y– direction is important and that reversible adsorption with a linear adsorption isotherm is taking place, the governing equation for this region is given by

$$\frac{D_e}{1 + \frac{\rho k(1-\phi_e)}{\phi_e}} \frac{\partial^2 C_e}{\partial y^2} - \lambda (C_e - C_i) - \frac{\partial C_e}{\partial t} = 0 \quad (2)$$

In order to complete the problem, the following initial and boundary conditions are defined:

Initial conditions:

$$C_m (x,y,o) = C_i \quad (3)$$

$$C_e (x,y,o) = C_i \quad (4)$$

Boundary conditions:

$$C_m (o,t) = C_o \quad (5)$$

$$C_e (x,W-\delta,t) = C_m (x,t) \quad (6)$$

$$C_m (\infty,t) = C_i \quad (7)$$

$$\frac{\partial C_e}{\partial t}\bigg|_{(x,\frac{E}{2},t)} = 0 \quad (8)$$

Equations (1) through (8) can be simplified by means of the following dimensionless variables:

$$C_{D1} = \frac{C_m - C_i}{C_o - C_i} \quad (9)$$

$$C_{D2} = \frac{C_e - C_i}{C_o - C_i} \quad (10)$$

$$x_D = \frac{x}{W} \quad (11)$$

$$y_D = \frac{y}{W} \quad (12)$$

$$t_D = \frac{V_m}{W} t \quad (13)$$

Equations (1) and (2) can then be written as follows:

$$\frac{1}{P_{e1}} \frac{\partial^2 C_{D1}}{\partial x_D^2} - \frac{\partial C_{D1}}{\partial x_D} - \frac{W}{V_m} \lambda C_{D1} + \frac{\varepsilon}{P_{e2}} \frac{\partial C_{D2}}{\partial y_D}\bigg|_{\frac{W-\delta}{W}} - \frac{\partial C_{D1}}{\partial t_D} = 0 \quad (14)$$

$$\frac{\gamma}{P_{e2}} \frac{\partial^2 C_{D2}}{\partial y_D^2} - \frac{W}{V_m} \lambda C_{D2} - \frac{\partial C_{D2}}{\partial t_D} = 0 \quad (15)$$

where:

$$P_{e1} = \frac{V_m W}{D_m} \quad (16)$$

$$P_{e2} = \frac{V_m W}{D_e} \quad (17)$$

$$\varepsilon = \frac{W \phi_e}{W - \delta} \quad (18)$$

$$\gamma = \frac{1}{1 + \frac{\rho k(1-\phi_e)}{\phi_e}} \quad (19)$$

Equations (14) and (15) can be solved by means of the Laplace's transform. Solution for concentration distribution in the mobile and immobile regions in Laplace's space are as follows:

$$\overline{C}_{D1} = \frac{1}{s} \exp\left\{\left[\frac{P_{e1}}{2} - \left[\frac{P_{e1}^2}{4} + \left\{s + \frac{W\lambda}{V_m} + \frac{\varepsilon\sqrt{\beta}}{P_{e2}} \tanh\left[-\frac{\sqrt{\beta}}{2W}(E-2(W-\delta))\right]\right\} P_{e1}\right]^{1/2}\right] x_D\right\} \quad (20)$$

$$\overline{C}_{D2} = \left\{\frac{\exp\left[-\sqrt{\beta}\left(\frac{E}{W} - y_D\right)\right] + \exp(-\sqrt{\beta}\, y_D)}{\exp\left[-\frac{\sqrt{\beta}}{W}(E-W+\delta)\right] + \exp\left[-\frac{\sqrt{\beta}}{W}(W-\delta)\right]}\right\} \overline{C}_{D1} \quad (21)$$

where:

$$\beta = \frac{P_{e2}\left(s + \frac{\lambda W}{V_m}\right)}{\gamma} \quad (22)$$

Numerical inversion by means of the Stehfest algorithm is used in order to compute concentration distribution in real space from equations (20) and (21).

As it was pointed out by Walkup and Horne, the solution of an spike-input is the time derivative of a step input. Therefore, to obtain the solution for a spike-input all that is needed is to multiply the expression for the step

input in (x,y,s) space (eq. (20)) by s before it is inverted to (x,y,t) space. Thus:

$$(C_{D1})_{spike} = \frac{\partial C_{D1}}{\partial t} = L^{-1}\left\{ s\,\bar{C}_{D1} \right\} \qquad (23)$$

For a detailed derivation of equations (20) and (21) the reader should refer to the report by Ramirez (1987).

Preliminary Results

Further work to extend the model's applicability to include field data is still in progress. Thus far only preliminary results had been obtained from the model. Table 1 includes data used to obtain results shown on Figures 2 through 4. Figure 2 illustrates concentration profiles for the mobile region with dimensionless time going from 0.1 to 1000 for a velocity of 0.01 (m/day). Figures 3 and 4 show the effect of velocity on concentration profiles in the mobile region for two different times, 0.12 and 1.2 hours.

Table 1

Data used to test the model. (Some data were taken from Example 1, Hugakorn et al., 1983).

V_m = 0.01 (m/day)
λ = 0.000154 $(day)^{-1}$
W = 5×10^{-5} (m)
δ = 10^{-7} (m)
γ = 1
ε = 1.18775
D_e = 1.382×10^{-7} (m^2/day)
D_m = 1.975×10^{-4} (m^2/day)

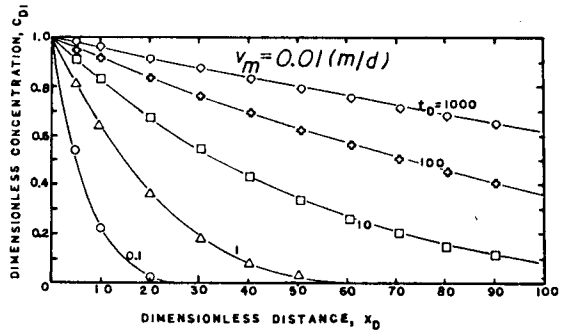


Figure 2: Dimensionless concentration profiles at t_D = 0.1, 10, 100, 1000. V_m = 0.01 (m/day).

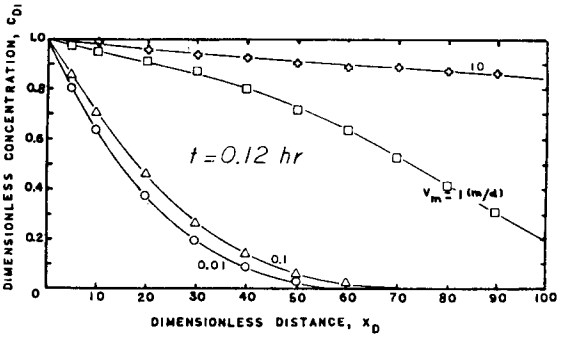


Figure 3: Effect on velocity on dimensionless concentration profile. V_m = 0.01, 0.1, 1, 10 (m/day). t = 0.12 hr.

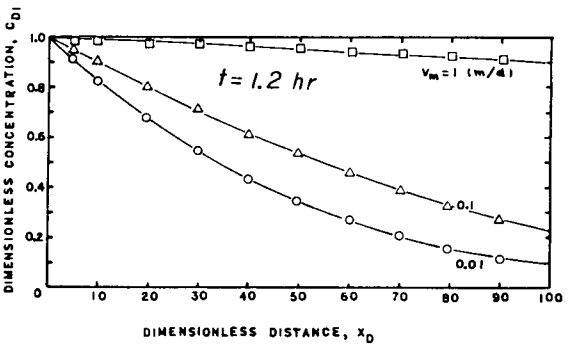


Figure 4: Effect on velocity on dimensionless concentration profile. V_m = 0.01, 0.1, 1, (m/day). t = 0.12 hr.

NOMENCLATURE

C = Concentration, (M/L^3)
D = Diffusion coefficient, (L^2/t)
E = Fracture spacing, (L)
k = Adsorption constant, (L^3/M)
L^{-1} = Inverse Laplace's operator
P_e = Peclet number, (dimensionless)
s = Laplace operator
t = Time, (t)
V = Velocity, (L/t)
W = Fracture half-width, (L)
x = Distance in x-direction, (L)
y = Distance in y-direction, (L)

Greek Symbols

β = Dimensionless group defined by eq. (22)
γ = Dimensionless group defined by eq. (19)
δ = Stagnant fluid film thickness, (L)
ε = Dimensionless group defined by eq. (18)

ϕ = Porosity, referred to total-bulk volume, (dimensionless)

λ = Radioactive decay constant, (t^{-1})

ρ = Density, (M/L^3)

Subscripts

D = Dimensionless variable (distance, time or concentration)

e = Refers to the immobile (stagnant) region

i = Refers to initial conditions

m = Refers to the mobile (fractured) region

o = Refers to inlet conditions

1 = Refers to mobile region

2 = Refers to immobile region

REFERENCES

1. Deans, H. A.: "A Mathematical Model for Dispersion in the Direction of Flow in Porous Media", Soc. Pet. Eng. Jour. (March, 1963) 49-52.
2. Fossum, M. P.: *Tracer Analysis in a Fractured Geothermal Reservoir: Field Results from Wairakei, New Zealand*, Stanford Geothermal Program, SGP-TR-56, (June, 1982), Stanford, CA.
3. Horne, R. N.: "Geothermal Reinjection Experience in Japan", Jour. Pet. Tech., (March, 1982) 495-503.
4. Hugakorn, P. S., Lester, B. H., and Mercer, J. W.: "An Efficient Finite Element Technique for Modeling Transport in Fractured Porous Media - 1. Single Species Transport", Water Resources Research, Vol. 19, No. 3 (June, 1983) 841-854.
5. Jensen, C. L.: *Matrix Diffusion and Its Effect on the Modeling of Tracer Returns from the Fractured Geothermal Reservoir at Wairakei, New Zealand*, SGP-TR-71 (Dec. 19830, Stanford, CA.
6. Maloszewski, P. and Zuber, A.: "On the Theory of Tracer Experiments in Fissured Rocks with a Porous Matrix", Journal of Hydrology, 79 (1985) 333-358.
7. Ramirez, J. S.: *Modelo de Fracturas Paralelas Para el Estudio del Flujo de Trazadores en Yacimientos Geotermicos*, MSc. Report, Division de Estudios de Posgrado, Facultad de Ingenieria, Universidad Nacional Autonoma de Mexico, (1987).
8. Rivera, J. R., Vides, A. R., Cuellar, G., Samaniego, F. V., and Neri, G. I.: "A Status Report on the Exploitation Conditions of the Ahuachapan Geothermal Field", Proceedings, Ninth Workshop on Geothermal Reservoir Engineering, Stanford, CA (Dec. 1983).
9. Stehfest, H.: "Algorithm 368 Numerical Inversion of Laplace Transforms", Communications of the ACM, January (1970).
10. Tester, J. N., Bivens, R. L., and Potter, R. M.: "Interwell Tracer Analysis of Hydraulically Fractured Granitic Geothermal Reservoirs", Soc. Pet. Eng. Jour., (1982), Vol. 22, 537-545.
11. Walkup, G. W., Jr., and Horne, R. N.: "Characterization of Tracer Retention Processes and Their Effect on Tracer Transport in Fractured Geothermal Reservoirs", paper SPE 13610 presented at the 1985 SPE California Regional Meeting, Bakersfield, CA (March, 1985) 229-240.

PROCEEDINGS, Twelfth Workshop on Geothermal Reservoir Engineering
Stanford University, Stanford, California, January 20-22, 1987
SGP-TR-109

Analysis of Injection-Backflow Tracer Tests in Fractured Geothermal Reservoirs

I. Kocabas and R.N. Horne

Stanford University, Stanford, CA

ABSTRACT

Tracer tests have been an important technique for determining the flow and reservoir characteristics in various rock matrix systems. While the interwell tracer tests are aimed at the characterization of the regions between the wells, single-well injection-backflow tracer tests may be useful tools of preliminary evaluation, before implementing long term interwell tracer tests.

This work is concerned with the quantitative evaluation of the tracer return profiles obtained from single well injection-backflow tracer tests. First, two mathematical models of tracer transport through fractures, have been reviewed. These two model are based on two different principles: Taylor Dispersion along the fracture and simultaneous diffusion in and out of the adjacent matrix. Then the governing equations for the transport during the injection-backflow tests have been solved. Finally the results were applied to field data obtained from Raft River and East Mesa geothermal fields. In order to determine the values of the parameters of the models that define the transport mechanisms through fractures a non-linear optimization technique was employed.

INTRODUCTION

Reinjection of waste hot water has been commonly practiced in many geothermal reservoirs either as a means of disposal or as a way to maintain the reservoir pressure and liquid volume. In some cases, however, it has been observed that the process had detrimental effects such as early breakthrough of the injected fluids and reduction in the enthalpy *(Horne 1982)*.

Since both beneficial and detrimental effects are possible, for the design of a successful reinjection program, the mechanisms of the fluid flow in the reservoir have to be understood. Tracer tests have been one of the important tools of studying the flow characteristics of various rock matrix systems. The quantitative interpretation of the test results can be accomplished through studying the mixing curves by using mathematical models describing the transport mechanism in the reservoir.

As far as the flow of tracer through porous media is concerned, a fairly large number of research results have been published *(Ogata and Banks, 1961; Deans, 1963; Perkins and Johnston, 1963; Coats and Smith, 1964; Lenda and Zuber, 1970; Brigham, 1974; van Genuchten and Wieranga, 1976; Ivanovich and Smith, 1978; Antunez and Brigham, 1984)*. The models developed for the porous media flow, however, are not necessarily applicable to geothermal reservoirs which are usually highly fractured in nature. Recent studies on flow through fractured media led to the development of new models describing the physics of the tracer transport through fractures.

Grisak and Pickens (1980) formulated a double porosity model combining a convective-dispersive transport in the fractures and a diffusive transport in the unfractured matrix. A finite element method was developed for simulating non-reactive and reactive solute transport by convection, mechanical dispersion and diffusion in a unidirectional flow field.

In 1981, *Rodriguez and Horne* presented a theoretical study of the one-dimensional convective-dispersive flow through fractures. In that work, they derived an expression for for the dispersivity in flow through a fracture. *Fossum and Horne* (1982) applied this model to interwell tracer test data obtained from Wairakei, New Zealand with some success. They used a non-linear optimization technique to match the model to field data.

In 1982, from the studies of migration of radionuclides in bedrock surrounding nuclear waste repositories, *Neretnieks, Eriksen and Tahtinen* developed a matrix diffusion model describing the tracer movement in a single fissure in granitic rock. Using this matrix diffusion model *Jensen and Horne* (1983) were able to obtain a better match to the data obtained from Wairakei, New Zealand as compared to the dispersion model used by *Fossum and Horne* (1982).

So far, interwell tracer tests have been a useful technique in determination of the interconnections between the injectors and the producers. The single well (injection-backflow) tests, on the other hand, have been proposed as tools for characterizing the flow field within the radius of influence around the injectors. Even though the injection-backflow tests are proposed as preliminary evaluation tools before the employment of long term interwell tests, the amount of information that can be recovered from these tests is potentially as much as that can be obtained from interwell tracer tests.

In 1982, *Downs* and his coworkers presented a preliminary study of the injection-backflow tests conducted at Raft River Geothermal Field. Later in 1983, *Capuano et al.* presented the qualitative analysis of the tests conducted at both Raft River and East Mesa fields. It was concluded that the injection-backflow tracer tests can be successfully used to characterize the flow in the near well-bore environment.

In this work, a theoretical study of the return profiles from injection-backflow tracer tests is presented. Both convection-dispersion and matrix diffusion models are employed in the analysis of the return profiles of both continuous injection and spike injection cases. In addition, the theoretical results of the continuous injection case are applied to the field data from Raft River and East Mesa geothermal fields by using a non-linear least squares optimization technique, in order to determine the effective parameters of the tracer transport.

MATHEMATICAL DEVELOPMENTS

The injection-backflow tests can be divided into three stages *(Antunez and Brigham, 1984)* : a) Injection period , b) Shut-in period, c) Backflow period. However, if the test is not aimed at the determination of regional flow beyond the test well's radius of influence, it may be completed in only two stages, injection and immediate backflowing.

Since the transport of tracers through geothermal reservoirs is primarily through fractures, the success of interpretive analysis of the return curves depends on the understanding the physics of the mixing process during the flow. In this work, two mathematical models based on two principal mechanisms, dispersion in fracture and the diffusion into the matrix, were employed to analyze the tracer return profiles from injection and immediate backflowing tests.

The injection-backflow tests can be conducted by either injecting a tracer fluid of concentration C_o continuously during the injection period (continuous injection case) or injecting a tracer slug followed by the untraced fluid (slug or spike injection case). Here, both continuous injection and spike injection cases for both convection-dispersion and matrix diffusion models will be considered.

A- CONVECTION DISPERSION MODEL

In a fracture, under either laminar or turbulent flow the fluid will be transported faster in the center of the fracture than near the walls. The result of this non-uniform "convective" transport is the dispersion of the tracer over the region of the transport. Although this convective smearing of the tracer gives rise to large concentration gradients across the narrow width of the fracture, molecular diffusion tends to rapidly equalize the tracer concentration across the fracture, thus counteracting the effect of convective dispersion *(Horne and Rodriguez, 1983)*.

The combination of the transverse diffusion and convective dispersion in the flow channel is known as "Taylor Dispersion" and was derived by *Taylor* (1953) for pipe flow. **The net result of the Taylor Dispersion is that the tracer front propagates with the mean speed of the flow.** The expression for the net longitudinal dispersivity for the flow in a fracture is given by *Horne and Rodriguez* (1983).

A.1- Continuous Injection Case

Taylor (1953) presents the equation governing the effective longitudinal dispersion in an infinite medium.

$$\eta \frac{\partial^2 C}{\partial z^2} = \frac{\partial C}{\partial t} \qquad (1)$$

The boundary and initial conditions are:

$$C = 0 \qquad at \qquad t = 0$$
$$C \to C_o \qquad as \qquad z \to -\infty$$
$$C \to 0 \qquad as \qquad z \to \infty$$

The solution to Eq.1 with the above boundary and initial conditions is given by *Taylor* (1953):

$$C_D = \frac{C}{C_o} = \frac{1}{2} erfc\left[\frac{x - ut}{2\sqrt{\eta t}}\right] \qquad (2)$$

Eq.2 represents the concentration profile during the injection period and it is symmetric about $x = ut$ which is the average distance traveled by the front. Also the point $x = ut$ corresponds to position of the 50 percent concentration contour. If L_t is the zone of transition in which C_D changes from 0.9 C_D to 0.1 C_D , the expression for L_t , is given by *Taylor* (1953):

$$L_t = 3.62\sqrt{\eta t} \qquad (3)$$

Taylor also mentioned that as t increases L_t increase proportionally to $\sqrt{t}$ whereas the distance traveled by the particles of fluid are proportional to t. Eventually as t increases L_t become small compared with $L = ut$ which is the distance traveled by the moving plane traveling with the mean speed of flow, u. Therefore there is a minimum injection time requirement for the theory to be applicable. To obtain the concentration profile at the end of the injection period, the variable t in Eq. 2 is replaced by t_j

The analysis of the injection-backflow tests is not a simple one-dimensional problem, because of the change in flow direction during the backflow period. There is also a possibility of change in the average flow velocity during the backflow period. For these reasons, to obtain the backflow period profile the governing equations have to be solved with appropriate initial and boundary conditions. However, for this specific problem, we will apply a simple technique developed by *Antunez and Brigham* (1983), to obtain the solutions.

In this case, first with the assumption of equal average flow velocities during the injection and backflow periods, the problem is simplified. The concentration profile at the and of the injection period is given by the middle curve in Fig. 1.

The 50 percent concentration point is at a distance of $x = L$ to the injection point $x = 0$, and the profile is symmetric about this point. At this point, first of all, we have to remember that the front propagates with the mean speed of the flow. To obtain the backflow period solution we utilize both the equal injection and backflow average velocities and the symmetry of the profile. During the backflow period we imagine a pseudo-front going away from the injection point as if the injection period is continuing, while the real front approaches the well. Since the injection and backflow velocities are imagined to be equal for both real and pseudo fronts, the distance traveled by them will also be equal as it is seen in Fig. 1.

Then the concentration of the pseudo-profile at any distance x is given by:

$$\frac{C_p}{C_o} = \frac{1}{2} erfc\left[\frac{x - u(t_j + t_p)}{2\sqrt{\eta(t_j + t_p)}}\right] \qquad (4)$$

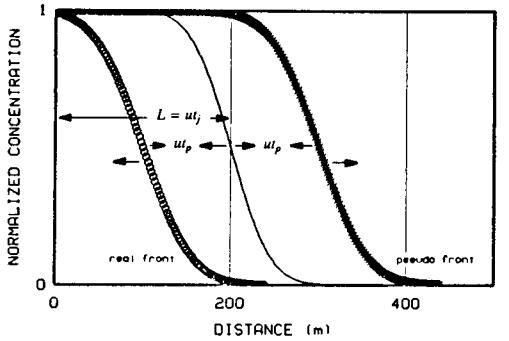


Figure 1: Dispersion of a sharp interface caused by Taylor dispersion.

If the concentrations of the pseudo-profile are to be calculated at $x = 2L = 2ut_j$, then when the 50 percent concentration of the pseudo-front reaches to $x = 2L$, the same concentration of the real front will reach to the well which is taken as the measurement point. Therefore, the concentrations measured at the well can be calculated by using the pseudo-front concentrations evaluated at $x = 2L$. The pseudo concentration C_p is related to the actual concentration C_r, by:

$$C_D = \frac{C_r}{C_o} = 1 - \frac{C_p}{C_o} = \frac{1}{2} + \frac{1}{2}\, erf\left[\frac{\alpha(t_j - t_p)}{2\sqrt{t_j + t_p}}\right] \qquad (5)$$

where

$$\alpha = \frac{u}{\sqrt{\eta}}$$

A.2- Spike Injection Case

Using the assumption of equal injection and backflow velocities and the symmetry of the injection period profile, we can find the spike injection case solution as:

$$C_D = \frac{C}{C_o} = \frac{\alpha t_i}{2\sqrt{\pi(t_j + t_p)}}\; e^{\frac{-\alpha^2 (t_j - t_p)^2}{4(t_j + t_p)}} \qquad (6)$$

B- MATRIX DIFFUSION MODEL

When a tracer fluid flows in a fracture, the tracer will diffuse into the porous matrix adjacent to the fracture. Assuming the porosity ϕ, and the apparent diffusion coefficient D_a are constant throughout the matrix contacted by the fluid the one-dimensional form of the equation of the diffusion into the porous matrix is given by:

$$D_a \frac{\partial^2 C_p}{\partial y^2} = \frac{\partial C_p}{\partial t} \qquad (7)$$

When the source of the tracer fluid is discontinued the effect will be to flush the fracture and reverse the concentration gradient causing tracer to migrate from the matrix into the fracture.

Assuming the concentration profile across the fracture is evened out due to molecular diffusion, the flow and sorption from the water in fracture is represented by:

$$\frac{\partial C_f}{\partial t} + u\,\frac{\partial C_f}{\partial x} = 2\frac{D_e}{\delta}\,\frac{\partial C_p}{\partial y}\bigg]_{y=0} \qquad (8)$$

The two diffusion coefficients D_a and D_e in Eq. 7 and Eq. 8 are related by:

$$D_e = \phi\, D_a \qquad (9)$$

Equations 7 and 8 are the system of equations describing the physical situation of one-dimensional convective flow through a fracture with simultaneous tracer diffusion into the surrounding porous matrix *(Neretnieks, 1980; Neretnieks et. al. 1982; Jensen, 1983).*

B.1- Continuous Injection Case

For a constant solute source of C_o at $x = 0$, initially the media are saturated with fluids free from the tracer, the boundary and initial conditions are given as:

$$\begin{aligned} C_f = C_p &= 0 \quad at \quad t = 0 \\ C_f &= C_0 \quad at \quad x = 0 \\ C_p &= C_f \quad at \quad y = 0 \\ C_p &\to 0 \quad as \quad y \to \infty \end{aligned}$$

If we assume $C_o = 1$ then the solutions obtained will be the concentrations normalized by C_o. At the end of the injection period of time t_j , the solutions representing the profiles in the fracture and in the porous matrix respectively are:

$$C_f = erfc\left\{\frac{\sqrt{D_e\phi}}{\delta}\,\frac{x}{u}\,\frac{1}{\sqrt{t_j - \frac{x}{u}}}\right\} \qquad \text{for} \quad t_j \geq \frac{x}{u} \qquad (10)$$

$$C_f = 0 \qquad \text{for} \quad t_j < \frac{x}{u}$$

$$C_p = erfc\left\{\left[2\frac{\sqrt{D_e\phi}}{\delta}\,\frac{x}{u} + \sqrt{\frac{\phi}{D_e}}\,y\right]\frac{1}{2\sqrt{t_j - \frac{x}{u}}}\right\} \quad \text{for } t_j \geq \frac{x}{u} \qquad (11)$$

$$C_p = 0 \qquad \text{for} \quad t_j < \frac{x}{u}$$

The injection period profile in the fracture will be as in Fig. 2.

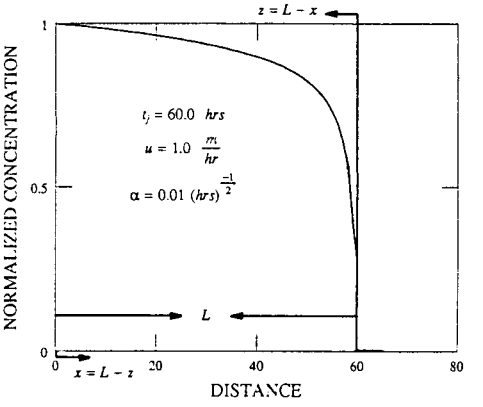


Figure 2: Dispersion of a sharp interface caused by matrix diffusion.

To account for the change in the direction of the velocity vector in the backflow period, the governing differential equations have to be modified. The modification will be done by utilizing the nature of the injection period solution and making a simple coordinate change.

Looking at the profile at the end of the injection period we see that the concentration in the fracture is zero after a distance of $x = ut_j = L$, (see Fig. 2). When the origin of the new coordinate system is chosen at $x = L$ and the new space variable is defined as z, the injection period profile can be expressed in terms of z, by simply replacing x by $L - z$.

Now with the new coordinate system, the governing differential equation of flow in the fracture becomes:

$$\frac{\partial C_f}{\partial \tau} + u\frac{\partial C_f}{\partial z} = \frac{2D_a}{\delta}\frac{\partial C_p}{\partial y}\bigg|_{y=0} \tag{12}$$

where τ is the time coordinate, starting from the beginning of the backflow period.

As far as the diffusion of tracer into or out of the matrix is concerned, there is no change in the conditions for constructing the governing equation. Hence, the equation remains the same, except for the time variable.

$$D_a\frac{\partial^2 C_p}{\partial y^2} = \frac{\partial C_p}{\partial \tau} \tag{13}$$

The boundary conditions are:

$$\begin{array}{llll} C_f = 0 & at & z = 0 & \tau \geq 0 \\ C_p = C_f & at & y = 0 & \tau \geq 0 \\ C_p \rightarrow \infty & as & y \rightarrow \infty & \tau \geq 0 \end{array}$$

and the initial conditions are given by Eq. 10 and Eq. 11

However, attempts to obtain the real space solutions to Equations 12 and 13 failed because of the complexity introduced by the initial conditions. Hence, the Laplace transformed forms of the initial conditions will be preserved, and a solution in the Laplace space will be obtained.

The initial conditions in Laplace space are:

$$\bar{C}_f = \frac{1}{s}e^{-\frac{x}{u}s}\, e^{\frac{-2\sqrt{D_a\phi}x}{\delta u}\sqrt{s}} \tag{14}$$

$$\bar{C}_p = \frac{1}{s}e^{-\frac{x}{u}s}\, e^{-\left[\frac{2\sqrt{D_a\phi}}{\delta}\frac{x}{u} + \sqrt{\frac{\phi}{D_a}}y\right]\sqrt{s}} \tag{15}$$

where

$x = L - z$

Now the initial conditions are given by Equations 14 and 15. Taking the Laplace transform of Eq. 13 with respect to the time variable, τ, we obtain :

$$\frac{\partial^2 \tilde{C}_p}{\partial y^2} - \frac{p}{D_a}\tilde{C}_p = -\frac{1}{s\,D_a}e^{-\beta\sqrt{s}}\, e^{-\frac{x}{u}s}\, e^{-\sqrt{\frac{s}{D_a}}y} \tag{16}$$

where

$$\beta = \frac{2\sqrt{D_a\phi}\,x}{\delta u}$$

Eq. 16 is a linear nonhomogeneous differential equation and the solution of Eq. 16 is given by:

$$\tilde{C}_p = \tilde{C}_f\, e^{-\sqrt{\frac{p}{D_a}}y} - e^{-\frac{x}{u}s}\,\frac{e^{-\beta\sqrt{s}}}{(p-s)}\left[e^{-\sqrt{\frac{p}{D_a}}y} - e^{-\sqrt{\frac{s}{D_a}}y}\right] \tag{17}$$

Laplace transform of Eq. 12 yields a term containing the derivative of Eq. 17 with respect to y. Therefore differentiating Eq. 17 with respect to y at $y = 0$, and substituting its derivative into the Laplace transform of Eq. 12, we obtain :

$$p\,\tilde{C}_f - \bar{C}_f + u\frac{\partial \tilde{C}_f}{\partial z} =$$

$$\frac{2D_a}{\delta}\left\{-\tilde{C}_f\sqrt{\frac{p}{D_a}} - \frac{\sqrt{s}-\sqrt{p}}{\sqrt{D_a}(p-s)}e^{-\frac{x}{u}s}\, e^{-\beta\sqrt{s}}\right\} \tag{18}$$

Eq. 18 is also a linear nonhomogeneous differential differential equation representing the flow in the fracture, and the solution of Eq. 18 is given by:

$$\tilde{C}_f = \frac{1}{s}\left[1 + \frac{2\alpha}{\sqrt{p}+\sqrt{s}}\right]\left[\frac{1}{s+p+2\alpha(\sqrt{p}+\sqrt{s})}\right] \tag{19}$$

where

$$\alpha = \frac{\sqrt{D_a\phi}}{\delta}$$

B.2- Spike Injection Case

Applying the same technique that was used for the continuous injection case, we can find the spike injection case solution as:

$$\tilde{C}_f = \frac{M}{Q}\left[1 + \frac{2\alpha}{\sqrt{p}+\sqrt{s}}\right]\left[\frac{1}{s+p+2\alpha(\sqrt{p}+\sqrt{s})}\right] \tag{20}$$

APPLICATIONS

In the previous section, tracer transport models through fractures have been discussed and extended for the analysis of the return profiles from the single well injection-backflow tracer tests.

Now, the results from the application of the models to field data will be presented. Both models were curve fitted to four sets of data obtained from two wells in two different geothermal fields. The curve fitting was done by using a non-linear optimization program based on the work of *Golub and Pereya* (1973). Each model has only one non-linear parameter to be determined through curve fitting. Equations 18 and 20 are analytic only in *(z,s,p)*-space

which is two Laplace transformations away from the real space. Therefore, three function subprograms were utilized to perform a double numerical inversion process by using *(Stehfest, 1970)* algorithm.

The first two sets of data were from a well in Raft River geothermal field. One of the sets of data was a 4-hour injection test and the other was a 48.5-hour injection test. The other two sets of data were from a well in East Mesa geothermal field. The first one of these sets was a 7.22-hour injection test and the injection period for the second one was 14.22 hours. From the analysis of these sets we were able to compare the ability of the models to represent the flow in the reservoir, as well as analyze the effect of the injection period on the return profiles.

The results of the curve fittings are shown in figures from Fig. 3 to Fig. 10 at the end of this paper.

Observe that the matrix diffusion model gives better fits than the convection-dispersion model does. Also note that the convection-dispersion model gives far better results on the small injection period tests than it does on the long injection period tests. The matrix diffusion model, on the other hand, fits all sets of the data equally well and the fits are excellent.

One important point to note is that the values of the non-linear parameters differed even though they were recovered from data on the same well. The non-linear parameter of the matrix diffusion model is given by:

$$\alpha = \frac{\sqrt{D_e \phi}}{\delta} \tag{21}$$

The effective diffusivity D_e is a function of temperature, porosity, molecular diffusivity and the geometry of the rock. We assumed that the temperature, the porosity and the fracture aperture are constant along the path traveled by the tracer fluid. Therefore, the values of the non-linear parameters obtained from the analysis of the data sets of the same well have to be the same. The reason for the differing numerical values can be found in the effects of the injection periods. Since the assumption of constant fracture aperture and uniform porosity is not absolutely true, the non-linear parameter, α, recovered from the fits represents an average value over the distance traveled by the fluid. Therefore, the longer the injection period the longer the distance traveled by the tracer fluid and, of course, the closer the results to the average values of the whole domain.

The poor fits obtained from the application of the convection-dispersion model may be explained as follow. If the injection time is short, then the amount of the tracer diffusing into the fracture will not be high, so the length of diffusion. Hence, the main contribution to the dispersion within the fracture will come from Taylor Dispersion. As the injection period increases, the effect of the interaction between the adjacent matrix and the fluid in the fracture becomes the dominant mechanism of dispersion. Hence, the convection-dispersion model fails to give a good fit to the data obtained from the long injection period tests.

The last point to be considered is the non-unit normalized concentration value even at the beginning of the backflow period, $t_p = 0$, for the fit of convection-dispersion model to the data of well 2C which is shown in Fig. 6. In order to explain this we need to check the injection time constraint explained in section A.1 of the mathematical developments. Now let's look at the condition for the injection time to be satisfied so that the infinite medium solution is applicable. From the point of view of numerical calculations the argument of the error function must be greater than or equal to 2, for the value of the error function to be 1. Therefore, to be able to get a unit C_D at the injection point, the following has to be satisfied.

$$\alpha\sqrt{t_j} \geq 4 \tag{22}$$

If we look at the values given in Fig. 6 we see that:

$$\alpha\sqrt{t_j} = 1.33 < 4 \tag{23}$$

Now there is two possible explanations can be given for this result:

1) The injection time is not enough for the theory to be applicable
2) The model itself is not applicable.

Of course, the second explanation is the logical one because of the inability of the model to represent the long injection period tests as explained above.

CONCLUSIONS

This study showed that the injection-backflow tracer tests can be used in determining the dispersion characteristics of the area within the radius of influence of the test well. In this study, two mathematical models describing the tracer transport in fractured medium were extended to suit for the quantitative analysis of the return profiles of injection-backflow tracer tests. Then the models were used to match six sets of field data. From these fits it was seen that most of the profiles can be successfully matched by the matrix diffusion model, whereas only short term injection tests could be fitted by the convection-dispersion model. In a short injection-backflow test, the time might not be sufficient for the tracer to diffuse far enough into the porous matrix to produce an asymmetric and long tailed profile. Hence, return profiles of the short injection period tests can be matched by the convection-dispersion model as well as by the matrix diffusion model. In the case of relatively high porosity or long injection periods, however, the return profiles are expected to be asymmetric and long tailed, therefore, can be matched well only by the matrix diffusion model.

It was observed that the non-linear parameters of models determined from fits to different data sets obtained from the same well gave different results. The differences between the two values of the same parameter were small if the differences between the injection periods were not large. In the long injection period tests, the information is obtained from a larger domain than in the short injection period tests. Therefore, the fits to the long injection period test data are expected to give better estimations of the governing parameters of the transport models.

NOMENCLATURE

Convection-Dispersion Model

δ : average velocity
D : molecular diffusivity
η : dispersivity coefficient
C : concentration (mass per unit volume)
C_D : normalized concentration
x : distance along the flow direction
t_j : total injection time
t_p : time variable of production period
t_i : slug injection time
$z = x - ut$: moving space coordinate
α : nonlinear parameter of the solution equation

Matrix Diffusion Model

C_p : concentration in matrix adjacent to fracture
C_f : concentration in fracture
C_o : initial concentration of the traced fluid
D_a : apparent diffusion coefficient
D_e : effective diffusion coefficient
ϕ : porosity of adjacent matrix
x : distance in the flow direction in injection period
y : distance normal to the flow direction
z : distance in the flow direction in backflow period
$L = ut_j$: distance of the front from injection point at the end of the injection period
M : mass of tracer material
A : area open to flow
Q : volumetric injection rate of traced fluid
t_j : total injection time
τ : time variable of production period
p : Laplace parameter corresponding to τ
s : Laplace parameter corresponding to t_j
α : nonlinear parameter of the solution equation

REFERENCES

1. Antunez, U. A. and Brigham, E. W.: "Semi-Analytic Approach to Analyze Single Well Tracer Tests," Stanford University Petroleum Research Institute, SUPRI TR-40, Stanford CA, (1984)
2. Brigham, W. E.: "Mixing Equations in Short Laboratory Cores," SPE of AIME Trans., 91-99, February 1974
3. Capuano, M. R., Adams, C. M. and Wright, M. P.: "Tracer Recovery and Mixing From Two Geothermal Injection-Backflow Studies," Proceedings of Eight Workshop on Geothermal Reservoir Engineering, Stanford university, (1983), 299-304
4. Coats, K. H. and Smith, B. D.: "Dead End Pore Volume and Dispersion in Porous Media," SPE of AIME Trans., 73-84, March 1964
5. Deans, H. A.: "A Mathematical Model for Dispersion in the Direction of Flow in Porous Media," Trans. AIME Vol.228,49-52, 1963
6. Downs, F. W., McAtee, E. R., Capuano, M. R. and Still, W.: "Hydrothermal Injection Experiments at The Raft River KGRA, Idaho," Proceedings of Seventh Workshop on Geothermal Reservoir Engineering, Stanford University (1982), 275-278
7. Fossum, M. P., Tracer Analysis in a Fractured Reservoir: Field Results From Wairakei, New Zealand, Stanford Geothermal Program, SGP-TR-56 Stanford CA, June 1982.
8. Fossum, M. P. and Horne, R. N.: "Interpretation of the Tracer Return Profiles at Wairakei Geothermal Field Using Fracture Analysis," Goethermal Resources Council, Transactions, Vol. 6, October 1982.
9. Golub, G. H. and Pereya, V.: "The Differentiation of Pseudo-Inverses and Non-linear Least squares Problems Whose Variables Separate," SIAM J. Numerical Analysis, Vol. 10, No. 2, 413-431,1973
10. Grisak, G. E. and Pickens, J. F.: "Solute Transport Through Fractured Media," Water Resources Research, Vol. 16, no. 4, 719-739, 1980
11. Horne, R. N.: "Geothermal Reinjection Experience in Japan," Journal of Petroleum Technology, March 1982
12. Horne R. N. and Rodriguez, F.: "Dispersion in Tracer Flow in Fractured Geothermal Systems," Geophysical Research Letters, Vol. 10, No. 4, 289-292, 1983
13. Hydrothermal Injection Research Program Annual Progress Report, University of Utah Research Institute Earth Sciences Laboratory and EG&G, Idaho Inc. Earth and Life Sciences and Energy Programs, 1983
14. Ivanovich, M. and Smith, B. D.: "Determination of Aquifer Parameters by a Two Well Pulsed Method Using Radioactive Tracers," Journal of Hydrology, Vol. 36, 35-45, 1978
15. Jensen, C. L.: "Matrix Diffusion and Its Effect On the Modeling of Tracer Returns from the Fractured Geothermal Reservoir at Wairakei, New Zealand," Stanford Geothermal Program, SGP-TR, Stanford CA, December 1983
16. Kocabas, I., Analyis of Injection-Backflow Tracer Tests, Stanford Geothermal Program, SGP-TR-93 Stanford CA, (1986)
17. Lenda, A and Zuber, A.: "Tracer Dispersion in Ground Water Experiments," in Isotope Hydrology 1970, International Atomic Energy Agency, 619-637, Vienna 1970
18. Neretnieks, I.: "Diffusion in the Rock Matrix: An Important factor in Radionuclide Retardation ?, " J. Geophysical Research, Vol. 85, no.B8, 4379,4397, 1980
19. Neretnieks, I., Eriksen,J. and Tahtinen, P.: "Tracer Movement in a Single Fissure Granitic Rock: Some Experimental Results and Their Interpretation," Water Resources Research, Vol. 18,No. 4, 849-858, 1982
20. Ogata, A and Banks, R. B.: "A Solution of the Differential Equation of Longitudinal Dispersion in Porous Media," U.S Geological Survey Professional Paper 411-A, A1-A47, 1961
21. Perkins, R. K. and Johnston, O. C.: "A Review of Diffusion and Dispersion in Porous Media," Trans. AIME Vol.228,70-84, 1963
22. Stehfest, H.: "Algorithm 368 Numerical Inversion of Laplace Transforms," Communications of the ACM, January 1970
23. Taylor, G.I.: "Dispersion of Soluble Matter in Solvent Flowing Slowly Through a Tube," Proc. Royal Society London, Vol. 219,186-203, 1953
24. van Genuchten, M. TH. and Wieranga, P. D.: "Mass Transfer Studies in Sorbing Porous Media; I, Analytical Solutions," Soil Science of America Journal, Vol. 40, No.4, 473-480, August 1976
25. VARPRO, Computer Science Department, Stanford CA
26. Walkup, W. G. Jr., Characterization of Retention Processes and Their Effects on the Analysis of Tracer Tests in Fractured Reservoirs, Stanford Geothermal Program, SGP-TR-77 Stanford CA, (1984)

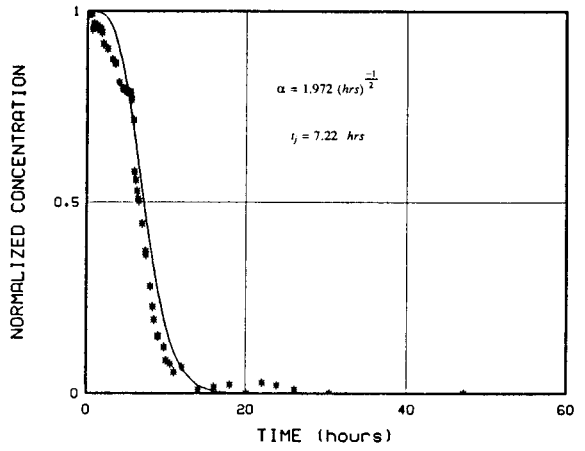


Figure 3: The result of curve fitting the convection-dispersion model to the data from Well #19 - Test 4.

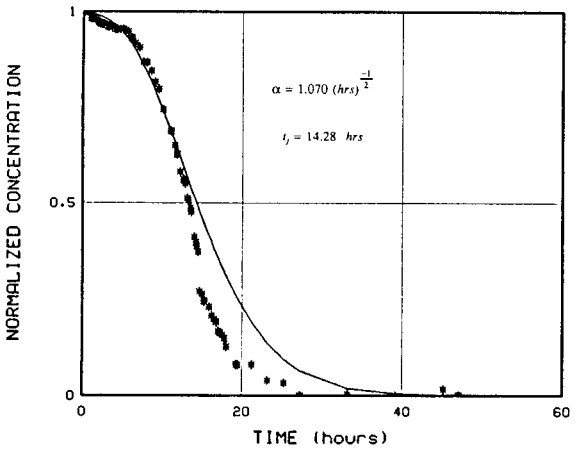


Figure 4: The result of curve fitting the convection-dispersion model to the data from Well #19 - Test 6.

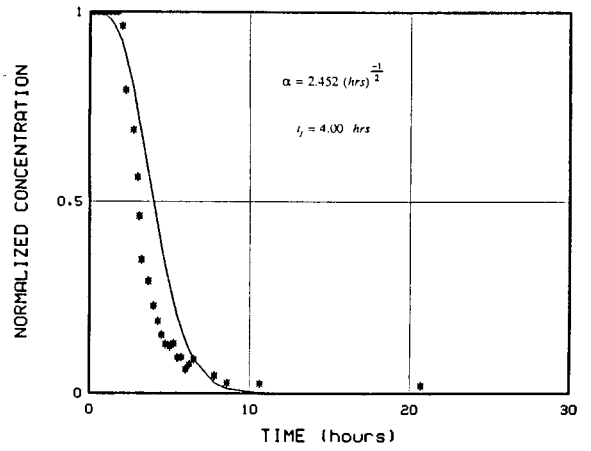


Figure 5: The result of curve fitting the convection-dispersion model to the data from Well #2 - Test a.

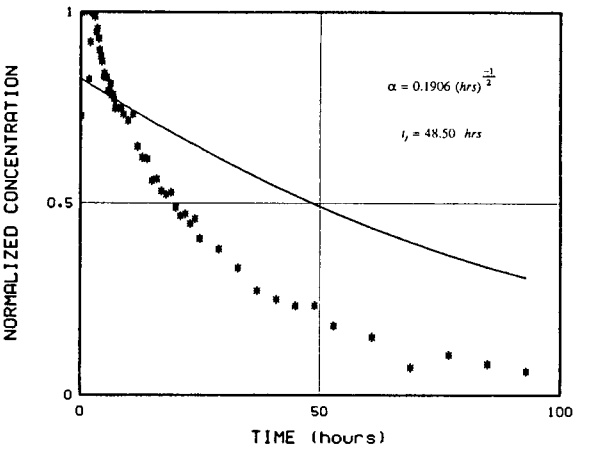


Figure 6: The result of curve fitting the convection-dispersion model to the data from Well #2 - Test c.

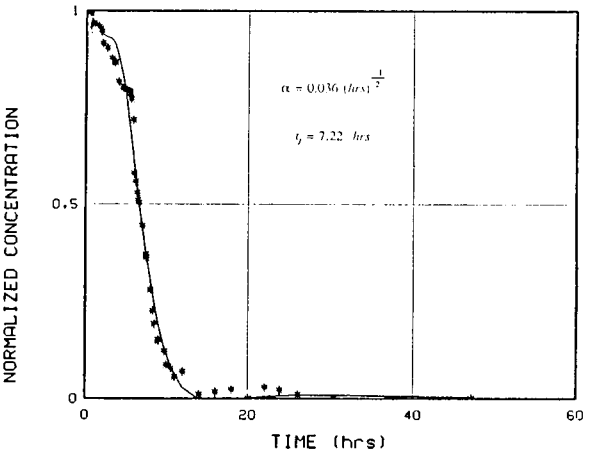


Figure 7: The result of curve fitting the matrix diffusion model to the data from Well #19 - Test 4.

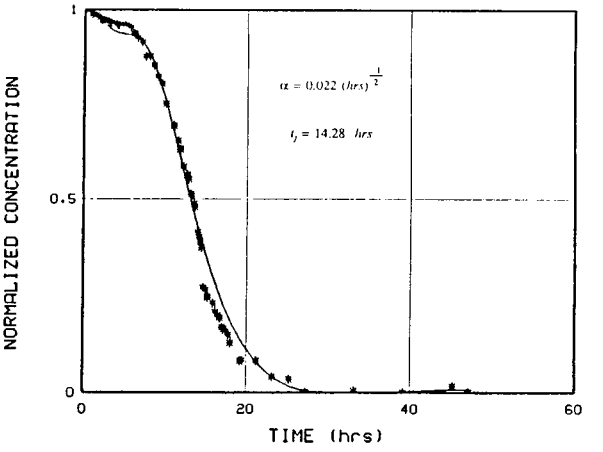


Figure 8: The result of curve fitting the matrix diffusion model to the data from Well #19 - Test 6. Correlation between dimensionless boundary distance and dimensionless departure time.

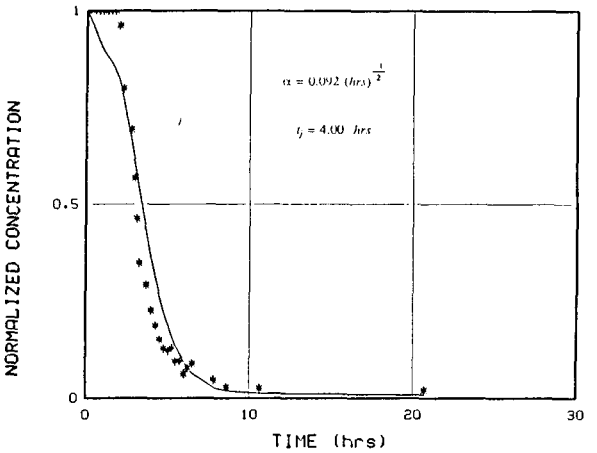


Figure 9: The result of curve fitting the matrix diffusion model to the data from Well #2 - Test a.

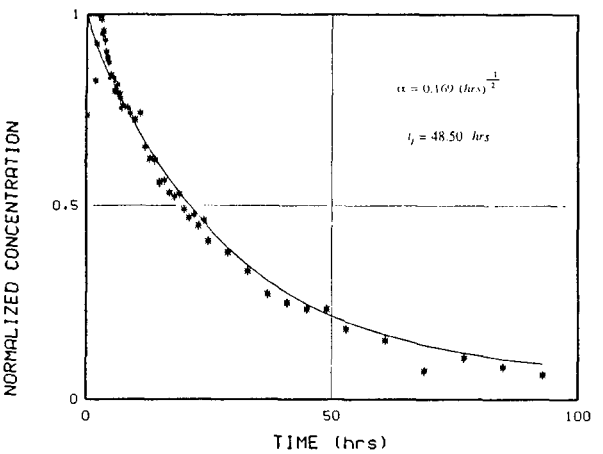


Figure 10: The result of curve fitting the matrix diffusion model to the data from Well #2 - Test c.

PROCEEDINGS, Twelfth Workshop on Geothermal Reservoir Engineering
Stanford University, Stanford, California, January 20-22, 1987
SGP-TR-109

FIELDWIDE CHEMICAL AND ISOTOPIC GRADIENTS IN STEAM FROM THE GEYSERS

By A.H. Truesdell[1], J.R. Haizlip[2], W.T. Box, Jr.[3], and F. D'Amore[4]

[1]U.S. Geol. Survey, Menlo Park, CA
[2]GEO Operator Corp., Santa Rosa, CA
[3]Geysers Geothermal Co., Santa Rosa, CA
[4]Inst. Inter. Ricerche Geotermiche, Pisa, Italy

ABSTRACT

Strong fieldwide gradients from southeast to northwest in gas/steam and $\delta^{18}O$ have been found in steam produced from wells at The Geysers. These gradients result from recharge from the southeast that has increased liquid saturation in the southern part of the reservoir and flushed gases and high $\delta^{18}O$ connate waters to the north and out of the system through surface vents. Variations in the steepness of the gradients are probably related to major venting in the Big Geysers area. Although lateral steam flow and condensation subsequent to flushing explain some local gradients in the southern area, these processes cannot explain the fieldwide variations.

INTRODUCTION

Except for a small number of wells at the southern edge of the field, all wells at The Geysers yield saturated or slightly superheated steam. Geochemical study of well discharges is, therefore, essentially limited to gases, volatile salts, and isotopes. A small number of gas analyses have been reported for steam from The Geysers. Allen and Day (1927) reported that steam from six of the shallow steam wells drilled from 1921 to 1925 contained notably less CO_2 (~63%) and more H_2 (~15%) and CH_4 (~15%) than steam samples from Lassen Park. The difference was probably due to the presence of far more organic matter in The Geysers sedimentary reservoir rock than in the dominantly volcanic Lassen system. Other than providing this observation, the gas analyses were not very useful to Allen and Day. This paucity of data and interpretation continued until the mid-1980's. Small numbers of analyses were reported by Barnes et al. (1973), Weres et al. (1977), Nehring (1981), and Truesdell et al. (1981) without well locations and without significant interpretation.

Gas chemistry has been successfully applied to geothermometry of hot-water systems (Hulston and McCabe, 1962; and others), but direct application of these methods to vapor-dominated systems suggested that gases were not in equilibrium. Some progress (more at Larderello than at The Geysers) was made by D'Amore and Truesdell (1980) in applying semi-empirical gas geothermometers, but understanding of Geysers gas chemistry awaited recognition that wellhead steam was a mixture of reservoir vapor and vaporized reservoir liquid.

Applying concepts that Giggenbach (1980) developed for hot-water systems, D'Amore et al. (1982) and D'Amore and Celati (1983) showed that by combining two gas equilibria with gas solubilities both the reservoir temperature and the vapor fraction or effective reservoir steam saturation (called "y") could be calculated. D'Amore and Truesdell (1985) used this method to show that different parts of The Geysers differed greatly in y but relatively little in temperature (figure 1). Southeast Geysers samples showed y values from 0.005 to 0.1, indicating that produced steam originated almost entirely from vaporized liquid, but samples from the central and west Geysers showed y values of 0.1 to 1.0, indicating a much larger contribution of reservoir vapor to produced steam.

The variation in y is directly related to the variation in gas/steam ratio. Representative gas analyses are given in table 1 for low, medium, and high total gas/steam ratios from three areas of The Geysers.

FIELDWIDE PATTERNS IN STEAM COMPOSITIONS

Studies of the fieldwide gas and isotope chemistry of Larderello steam (Celati et al., 1973; D'Amore et al., 1977) show that, in general, gas concentrations (gas/steam, NH_3) increase from the center of the field toward the edge while concentrations of substances more soluble in liquid (^{18}O, H_3BO_3, Cl) decrease in this direction. These patterns were interpreted by D'Amore and Truesdell (1979) to result from lateral steam movement and condensation that could be modeled as a Rayleigh condensation process. In this process the concentration of each constituent C is related to its original concentration Co and the fraction of remaining steam M/Mo by the equation $(C/Co) = (M/Mo)^{(1/B - 1)}$, in which B is the distribution coefficient of the constituent between vapor and liquid (C_v/C_l). Limited supporting data from The Geysers was presented. This model of convective circula-

tion of steam and condensate was used by Calore et al. (1982) to explain observed variations in the depth to the liquid saturated zone at the margins of the Larderello field and to indicate an extension of the field to the east (R. Celati, oral commun., 1981).

From the isotope data of Haizlip (1985), fragmentary published gas data, and many unpublished analyses, it is known that large concentration gradients of gas and isotope constituents exist at The Geysers. Understanding the natural processes which caused these gradients will advance our knowledge of the field and possibly assist exploitation as it did at Larderello.

With the cooperation of some of the major steam producers (GEO Operator Corp., Geysers Geothermal Co., Unocal, and Sante Fe Geothermal), maps have been drawn of gas/steam ratios (in ppm gas by weight) and $\delta^{18}O$ in steam from the entire drilled Geysers field (figures 2, 3). These maps are highly generalized and represent different densities of data in various parts of the field. Early production data representative of original conditions were sought. Steam compositions indicating influence of injected water have been rejected as have analyses from unusually shallow (gas rich) and low flow rate, subcommercial wells. The maps show variations in only gas/steam ratios and $\delta^{18}O$; other variations in isotopes are shown in figure 4 and in gases in table 1.

NON-RAYLEIGH GRADIENTS

Geysers steam shows wide ranges in gas and isotope compositions much larger than those observed at Larderello. The range in gas/steam is from about 150 ppmw (parts per million by weight) to more than 65,000 ppmw (table 1); the published range at Larderello is from 10 to 120 liters STP/kg (approximately 17,000 to 200,000 ppmw). The range in $\delta^{18}O$ is also larger at The Geysers, -7 to +3 permil compared with -6 to 0 permil at Larderello. The magnitude and direction of these composition gradients at The Geysers are different from those at Larderello and require a different interpretation.

At Larderello composition gradients in the central and Serrazzano zones (about two-thirds of the entire field) are consistent with the Rayleigh condensation model. At The Geysers this model appears to work only in limited areas. One of these areas is at the southern end of the field where steam flow appears to be from west to east, as indicated by gradients in gases and isotopes with increases to the east in total gas and NH_3 and decreases in $\delta^{18}O$ and B (figure 5). Data supplied by Union Oil Co. (now Unocal) for an unspecified section of the central Geysers show the predicted change in CO_2, although this could not be compared with changes in other constituents (D'Amore and Truesdell, 1979). These gradients, similar to those in the southeast

Table 1. Gas Analyses from Typical Wells in Three Regions of The Geysers

	Northwest Geysers					
	High		Medium		Low	
	ppm (wt.)	mole % w/o H_2O	ppm (wt.)	mole % w/o H_2O	ppm (wt.)	mole % w/o H_2O
Total gas	65,200		29,400		8,410	
CO_2	55,500	74.3	26,600	71.8	7,450	69.8
H_2S	1,710	2.96	958	3.34	356	4.31
NH_3	576	1.99	414	2.89	251	6.08
Ar	--	--	.86	.0026	.11	.0012
N_2	560	1.18	270	1.15	48.8	.717
CH_4	2,580	9.49	1,020	7.56	161	4.13
H_2	347	10.1	225	13.3	73.1	14.9
S/G (mole)	30.7		66.1		227	
	Central and West Geysers					
	High		Medium		Low	
Total gas	13,500		5,420		2,620	
CO_2	11,500	62.5	4,460	58.5	2,080	53.6
H_2	662	4.65	310	5.26	184	6.12
NH_3	223	3.13	101	3.41	151	10.0
Ar	<2	<0.01	2.0	0.03	.7	.02
N_2	153	1.3	78.3	1.61	35.5	1.44
CH_4	851	12.7	412	14.8	131	9.24
H_2	133	15.8	57.3	16.4	34.8	19.5
S/G (mole)	133		185		608	
	Southeast Geysers					
	High		Medium		Low	
Total gas	982		443		143	
CO_2	734	51.9	322	51.1	94.7	43.2
H_2S	116	10.6	75	15.3	36.4	21.4
NH_3	30	5.46	34	13.9	.3	.37
Ar	1.0	.08	.03	.006	.01	.0062
N_2	46	5.17	3.3	.82	2.5	1.79
CH_4	43	8.33	3.4	1.54	6.4	8.06
H_2	12	18.4	5.3	18.3	2.4	23.8
S/G (mole)	1,724		3,870		11,100	

Geysers (Mohinder Gulati, pers. commun., 1977), may also be due to Rayleigh condensation. This model does not work, however, for northern Geysers as a whole, as shown by the strong increase of both gas and oxygen-18 in steam from the central Geysers to the northwest. The condensation model requires changes in oxygen-18 and gas concentrations to be opposite. In addition, the magnitude of the observed changes in gas/steam, if caused by condensation, would require more than 99.8% condensation in the northern part of the reservoir which seems highly unlikely. The isotope and gas gradients are less definite for the south central Geysers, and data toward the field boundaries are missing or fragmentary.

The reason for the large fieldwide gradients in steam composition must be highly speculative without more data, but some suggestions may be more plausible than others. Faced with explaining the oxygen-18 data, Haizlip (1985) rejected processes involving the fluid alone (boiling, condensation, etc.) and concluded that only a south-to-north increase in the amount of remnant connate water or in the rock/water ratio could explain the isotope gradient.

CONNATE WATER

The isotopic similarity of steam from the northwest Geysers with connate or metamorphic waters from the Sulphur Bank mine and Wilbur Spring, 25 and 40 km northwest of The Geysers, was noted by Haizlip (1985). These mineralized thermal waters were described by White et al. (1973) as originating from the metamorphism of connate sea water (original $\delta^{18}O$ and $\delta D=0$) contained in Jurassic marine sediments, with $\delta^{18}O$ values increased to +4 to +5 by exchange with silicates and carbonates and δD reduced to -20 to -30 by exchange with low deuterium marine clays. The Sulphur Bank and Wilbur Spring waters are similar in $\delta^{18}O$ to the connate(?) fluids described by Lambert (1976) and Sternfeld (1981) as once present in the central Geysers, and fall approximately along the $\delta^{18}O$-δD trend of northwest Geysers steam (figure 4). Gas compositions are less distinctive. No analyses of Wilbur Spring gases are available, but Sulphur Bank mine gas is mainly CO_2, CH_4, N_2, and trace H_2S (Nehring, 1981). This gas, collected at the surface, may have lost H_2S and H_2, but the high CH_4 contents and light $\delta^{13}C$ in CO_2 are similar to Geysers samples (-14 for Sulphur Bank; about -13 to -20 for The Geysers; Huebner, 1981, and unpublished data).

FLUSHING BY METEORIC RECHARGE

The major gradients in gas and isotope composition of steam are almost certainly due to meteoric recharge entering the reservoir from the southeast. Steam in the southeast Geysers has low gas and $\delta^{18}O$ similar to local meteoric water. Similar steam compositions are observed along the southern and southeastern boundaries of Larderello where recent recharge has been induced by exploitation. The effects of this recharge decrease away from the point of liquid entry.

Wells drilled at the southeast and east edges of The Geysers field are known to produce steam-water mixtures or water alone from the same depth as the steam reservoir a few hundred meters away. The similarity between isotopic compositions of local meteoric water and steam from the southeast Geysers adjacent to these water boundaries (figure 4) and the low gas contents of steam in this area suggest that this part of the field was the site of massive recharge to the system. Recharge adjacent to outcrops of the reservoir rock has been observed at Larderello, with increases in tritium and decreases in gas and $\delta^{18}O$ in steam observed over periods of a few years (Calore et al., 1982; D'Amore et al., 1983). The lack of tritium in the steam at the southeast Geysers suggests that recharge is not a rapid process related to present exploitation (as at Larderello) but has occurred over a longer period or from older waters (>60 yr.).

The low gas content, low $\delta^{18}O$ composition, and high flows of steam from the southern Geysers all suggest that a large proportion of the reservoir fluid consists of liquid water. This liquid water must be held in small fractures and pores of the reservoir rock coexisting with vapor in larger openings because neither drilling nor seismic observations favor the existence of a large well-defined water-saturated zone within the productive volume of the reservoir. In the northern Geysers there is also no evidence of a well-defined water-saturated zone even to the 5-6 km maximum depths of induced seismicity in the oldest producing zone. In this part of The Geysers high gas and $\delta^{18}O$ and lower productivity suggest much lower liquid water contents in the productive reservoir.

BOILOFF THEN FLUSHING

The apparent lack of a deep water-saturated zone in any part of The Geysers suggests that the system has undergone a near-complete boiloff of its original liquid. This is in agreement with geologic, petrologic, and simulation studies which all suggest that The Geysers started as a hot-water saturated reservoir and became vapor-dominated through a deficit of fluid recharge to discharge (see for example, White et al., 1971; Lambert, 1976; Preuss, 1985). This process does not necessarily tend to a stable steady state and the vapor-dominated zone can extend downward as long as there is liquid to displace. It is possible that a seismic event or other disturbance could allow liquid to enter the underpressured vapor-dominated reservoir from the side where adequate permeability exists. If cooler liquid water entered a nearly dry vapor-dominated reservoir, its effect would depend on its quantity and the depth of entry. Shallow entry and moderate quantity would favor recharge of liquid suspended in the reservoir while large quantities and deep entry would produce a liquid saturated zone that might be large enough to reverse the process of vapor domination. In either case, with time the liquid would move throughout the reservoir. The movement of suspended liquid would depend on vaporization and condensation and would be relatively slow unless hastened by removal (production) of steam as observed with recent recharge at Larderello. Venting of steam and resulting lateral pressure gradients must be important in causing lateral movement of liquid away from areas of recharge. The relative locations of recharge areas and vents have

apparently influenced the flow of recharge at The Geysers.

GRADIENTS RELATED TO VENTS

Although surface alteration is found throughout The Geysers, the greatest concentration is in the area of the Big Geysers (units 1-8) along with the largest natural vents. The distribution of vent areas may explain the smaller gradients in ^{18}O and gas between the southeast and central Geysers and the steepening gradients to the northwest. Driven by meteoric recharge from the southeast, gases and high $\delta^{18}O$ steam would have gradually migrated to these vents and left the system. Strong venting in the central Geysers (the Big and Little Geysers areas) would have allowed extensive flushing and homogenization of fluid compositions between this area and the southeast Geysers, while less venting to the northwest would have allowed less flushing and homogenization.

ROCK ALTERATION

If recharge waters enter the system from the southeast, reservoir rocks in this area would undergo the greatest alteration of their oxygen isotopes to reach equilibrium with fresh (unaltered) meteoric water. Reservoir rocks further to the northwest would have been progressively less altered as oxygen-18 in recharge waters increased through exchange with rock or mixture with connate formation waters. The influx of meteoric recharge would also be expected to leach minerals with which it was not in equilibrium. Sulfide minerals and organic matter would be oxidized by air-saturated meteoric recharge; calcite would be dissolved through the refluxing action of steam condensation and downward flow of steam condensate.

STEAM MIGRATION

The observed steam composition gradients throw into question some of our assumptions about vapor-dominated systems. If steam circulates freely within these systems, then convection should either homogenize fluid compositions (as it does in most hot-water geothermal systems) or create patterns around upflow zones. The presence of separate zones of active boiling and condensation in the Rayleigh condensation model of D'Amore and Truesdell (1979) can maintain concentration gradients, but as we have seen, gradients at The northern Geysers are generally opposite to that predicted by this model. Seismic evidence suggests that vertical permeability is much greater than horizontal, since microearthquakes induced by steam production can extend 3 km deeper than the wells but only a few hundred meters laterally (Oppenheimer, 1986).

The existence of Rayleigh condensation gradients at the southern margin of The Geysers (figures 2, 3, 5) that are counter to gradients resulting from flushing suggests that flushing occurred and was complete before the Rayleigh gradients were established. Exploration of this chronology may be possible through petrologic studies.

Present gradients in steam composition suggest that either steam is not very mobile on a fieldwide scale or that rock and liquid compositions control steam compositions on a time scale that is rapid relative to the rate of steam circulation. Both conditions may be true. The original pre-exploitation pressure gradients in the field probably were small, as indicated by shut-in pressures of new wells close to 35 bars in all parts of the field. The pressure drops and steam drainage caused by exploitation may change steam composition patterns but would not be evident in figures 2 and 3 since these represent mostly early data. Of course some areas may have been drained before they were drilled, especially on the margins of the early produced Big Geysers area.

With continued exploitation of The Geysers, reservoir pressure differentials between the reservoir and surrounding ground water will increase and, as at Larderello, increased cold-water recharge may occur and tritium may appear. For this reason the use of tritium as an artificial tracer should be avoided.

CONCLUSION

The Geysers geothermal field is large and geologically and geochemically complex with a history that is only starting to be understood. Natural circulation in vapor-dominated systems like The Geysers is locally and on a short time scale dominated by the "heat pipe" mechanism in which upward flowing steam condenses and produces downward flowing condensate driven by volcanic heat supplied to yet undiscovered boiling zones. Larger scale circulation patterns based on lateral steam flow away from boiling zones (and condensate back flow) indicated by "Rayleigh" composition patterns appear to dominate at Larderello and in parts of The Geysers. Large-scale circulation at The Geysers appears to have been dominated by flushing with meteoric water probably initiated by catastrophic breakthrough of liquid at the margin of the system. In this process recharge introduced in the southeast has progressively removed oxygen-18 and gases (including gas-forming minerals) from the reservoir, with effects diminishing from the southeast, where steam is almost gas free and similar in $\delta^{18}O$ to local meteoric water, to the northwest, where steam is gas and oxygen-18 rich. The exact roles of residual connate waters and high rock/water ratios in the original fluid compositions flushed by meteoric recharge are not yet known. The association of high permeability with highly flushed fluids suggests that the flushing has had physical as well as chemical effects on the reservoir or that flushing was facilitated by existing high permeability.

REFERENCES

Allen, E.T. and Day, A.L. (1927), "Steam wells and other thermal activity at The Geysers, Calif.," Carnegie Inst. Wash. Pub. 378, 106.

Barnes, I., Hinkle, M.E., Rapp, J.B., Heropoulos, C., and Vaughn, W.W. (1973), "Chemical composition of naturally occurring fluids in relation to mercury deposits in part of north-central California," U.S. Geol. Survey Bull. 1382-A, 19 p.

Calore, C., Celati, R., D'Amore, F., and Noto, P. (1982), "Geochemical evidence of natural recharge in the Larderello and Castelnuovo areas," Proc. 8th Workshop Geoth. Res. Eng., Stanford, Dec. 1982, 323-328.

Celati, R., Noto, P., Panichi, C., Squarci, P., and Taffi, L. (1973), "Interactions between the steam reservoir and surrounding aquifers in the Larderello geothermal field," Geothermics, 2, 174-185.

D'Amore, F. and Celati, C.(1983), "Methodology for calculating steam quality in geothermal reservoirs," Geothermics, 12, 129-140.

D'Amore, F., Celati, R., Calore, C. (1982), "Fluid geochemistry applications in reservoir engineering," 8th Workshop Geoth. Res. Eng., Stanford, 295-308.

D'Amore, F., Celati, R., Calore, C., and Bertrami, R. (1983), "Effects of natural recharge on gas composition in the Larderello-Castelnuovo area," 9th Workshop Geoth. Res. Eng., Stanford, Dec. 1983, 221-227.

D'Amore, F., Celati, R., Ferrara, and Panichi, C. (1977), "Secondary changes in the chemical and isotopic composition of the geothermal fluids in Larderello area," Geothermics 5, 153-163.

D'Amore, F. and Truesdell, A.H. (1979), Models for steam chemistry at Larderello and The Geysers, 5th Workshop Geoth. Res. Eng., 283-297.

D'Amore, F., and Truesdell, A.H. (1980), "Gas thermometry for drillhole fluids from vapor-dominated and hot-water geothermal fields," Proc., 6th Workshop Geoth. Res. Eng., Stanford, Dec. 1980, 351-360.

D'Amore, F. and Truesdell, A.H. (1985), Calculation of geothermal reservoir temperatures and steam fraction from gas compositions, Geoth. Res. Coun. Trans., 9-1, 305-310.

Giggenbach, W.F. (1980), "Geothermal gas equilibria," Geochim. Cosmochim. Acta, 44, 2021-2032.

Haizlip, J.R. (1985), "Stable isotope composition of steam from wells in the northwest Geysers, The Geysers, California," Geoth. Resources Council Trans., 9-1, 311-317.

Huebner, Mark (1981), "Carbon-13 isotope values for carbon dioxide gas and dissolved carbon species in springs and wells in The Geysers-Clear Lake region," in U.S. Geol. Survey Prof. Paper 1141, 211-213.

Hulston, J.R., and McCabe, W.J. (1962), Mass spectrometer measurements in the thermal areas of New Zealand. Part 1. Carbon dioxide and residual gas analyses," Geochimica et Cosmochimica Acta, 26, 383-397.

Lambert, S.J. (1976), "Stable isotope studies of some active geothermal systems," California Institute of Technology, Ph.D. thesis, 387.

Nehring, N.L. (1981), Gases from springs and wells in The Geysers-Clear Lake area," in U.S. Geol. Survey Prof. Paper 1141, 205-209.

Oppenheimer, D.H. (1986), "Extensional tectonics at The Geysers geothermal area, Calif.," Jour. Geophys. Res., 91, 11463-11476.

Preuss, Karsten (1985), "A quantitative model of vapor dominated geothermal reservoirs as heat pipes in fractured porous rock," Geoth. Resources Council Trans., 9-2, 353-361.

Sternfeld, J.N. (1981), "The hydrothermal petrology and stable isotope geochemistry of two wells in The Geysers geothermal field, California," Univ. California, Riverside Rept. UCR/IGPP 81/7, M.S. thesis, 202 p.

Truesdell, A.H., Nathenson, M., and Frye, G.A. (1981), "Downhole measurements and fluid chemistry of a Castle Rock steam well, The Geysers, Calif.," Geothermics, 10, 103-114.

Weres, O., Tsao, K., and Wood, B. (1977), "Resource technology and environment at The Geysers: Lawrence Berkeley Lab. LBL-5231.

White, D.E., Barnes, Ivan, and O'Neil, J.R. (1973), "Thermal and mineral waters of nonmeteoric origin, California Coast Ranges: Geol. Society America Bull., 84, 547-560.

White, D.E., Muffler, L.J.P., and Truesdell, A.H. (1971), "Vapor-dominated hydrothermal systems compared with hot-water systems," Economic Geology, 66-1, 75-97.

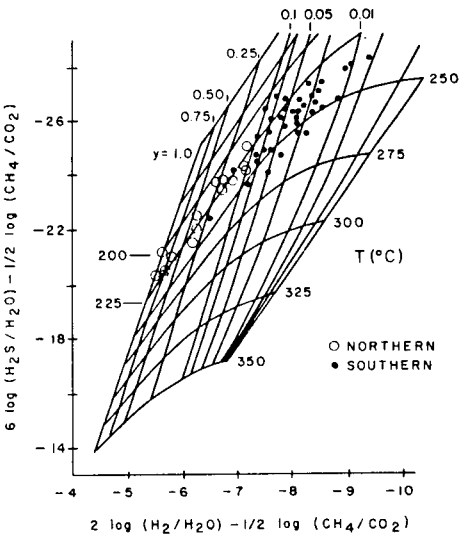


Figure 1. Reservoir temperatures and steam saturation for two areas of The Geysers (from D'Amore and Truesdell, 1985).

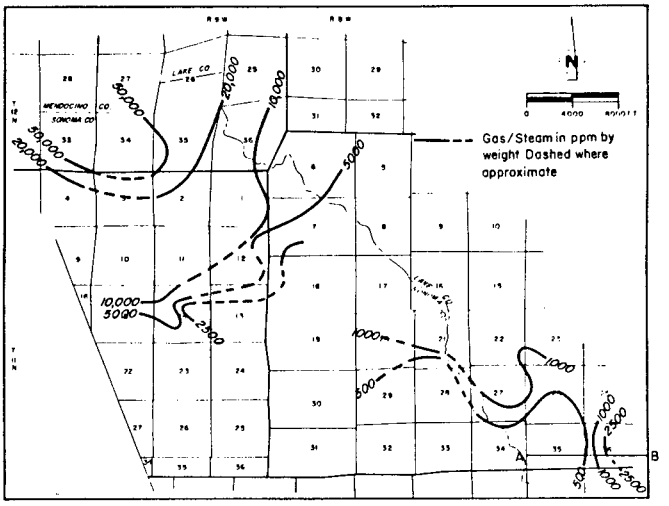


Figure 2. Gas/steam ratios for early production from wells at The Geysers expressed as parts per million by weight. Data from the U.S. Geological Survey and steam-producing companies including GEO Operator, Geysers Geothermal, Unocal Geothermal, and Sante Fe Geothermal.

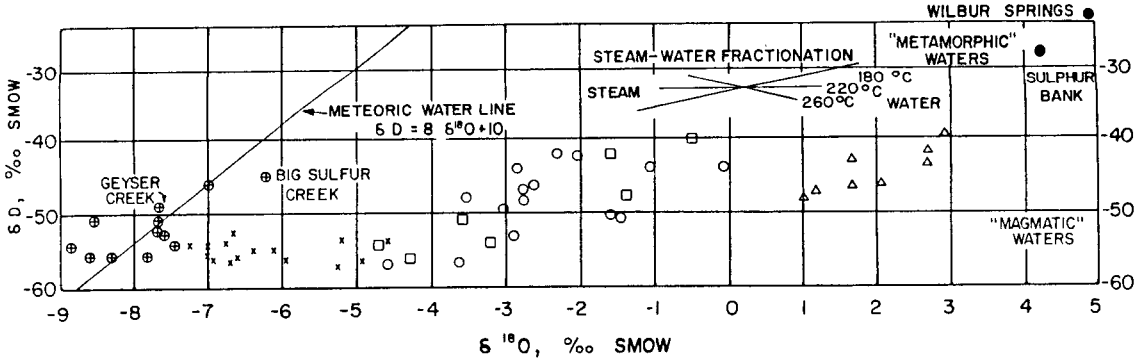


Figure 4. Oxygen-18 and deuterium compositions of early production steam from The Geysers (Data sources as in figure 2). Symbols: × southeast; ○ central; □ west; △ northwest; ⊕ meteoric waters; ● connate or metamorphic waters.

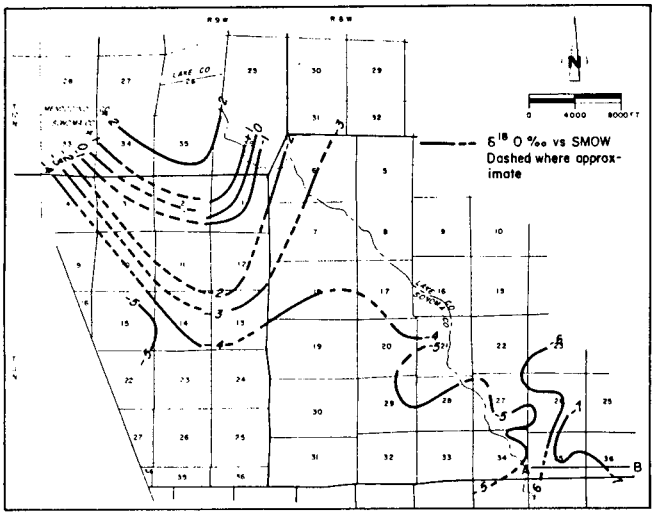


Figure 3. Oxygen-18 compositions of early production steam from The Geysers. Data sources as in figure 2.

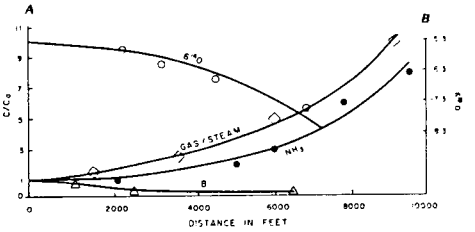


Figure 5. Gradients in steam composition across part of the southern Geysers. Location of cross-section line A-B shown in figures 2 and 3.

PROCEEDINGS, Twelfth Workshop on Geothermal Reservoir Engineering
Stanford University, Stanford, California, January 20-22, 1987
SGP-TR-109

GAS GEOTHERMOMETRY BASED ON CO CONTENT--APPLICATION IN ITALIAN GEOTHERMAL FIELDS

D'Amore, F.[1], Fancelli, R.[1], Saracco, L.[1], and Truesdell, A.H.[2]

[1]International Institute for Geothermal Research, CNR, P.za Solferino 2,
56100 Pisa, Italy
[2]U.S. Geological Survey, 345 Middlefield Rd., MS 910, Menlo Park, CA 94025 USA

ABSTRACT

This paper discusses gas chemical equilibria in geothermal reservoirs involving the species CO_2, CH_4, CO, H_2S, H_2, and H_2O. A set of equations is developed correlating ratios of gas to CO_2 with temperature, steam fraction, and CO_2 partial pressure in the reservoir. A method for solving the set of nonlinear equations is proposed. These equations do not involve discharge gas/total H_2O ratios and may therefore be used for fumaroles and hot-spring fluids. Applications to fumarole and well-discharge fluid compositions in Italian geothermal fields show good correlations between temperatures calculated with this method and the temperatures measured in the reservoir (between 140° to 330°C).

INTRODUCTION

Several studies in recent years have demonstrated chemical equilibria among gas species in geothermal reservoirs. Gas composition has been correlated successfully with reservoir temperature, steam fraction, and redox conditions in both liquid- and vapor-dominated systems.[1/]

Except for empirical geothermometers, the application of gas composition has been limited to fluid discharges for which the gas/(total water) ratio was known. In Giggenbach (1980) and D'Amore and Truesdell (1985) several gaseous species were considered (CO_2, H_2S, H_2, CH_4, NH_3, N_2), but all the geothermometers were based on measured gas/H_2O ratios. In this paper an attempt has been made to utilize the relative concentrations of a limited number of gaseous species, including carbon monoxide, to exclude the gas/H_2O ratio. This method could be used to evaluate reservoir temperature and gas partial pressures when, for various reasons, the original gas/steam ratio is unknown, such as fumaroles, or any natural manifestations in which part of the H_2O cannot be sampled or emerges separately. The method could thus be applied in geothermal exploration. The main conditions are that (1) a precise measurement of CO concentration in the dry gas is available (sensitivity of 0.1 ppm in moles), (2) chemical equilibrium is attained at depth in the system CO_2-H_2-CH_4-H_2S-CO-Fe_3O_4-FeS_2, and (3) the deep gas composition (but not necessarily the gas/steam ratio) is maintained until its emergence. Sometimes the latter condition cannot be fulfilled because of some physical phenomena affecting the fluid during transport to the sampling point, such as selective degassing of liquid, or multistep condensation of vapor, or chemical reaction such as local oxidation of some species or sulfide precipitation.

The limited amount of data on CO content that is available limits for the moment the application of the method to the gas analyses of some Italian geothermal fields: Larderello, Bagnore, and Piancastagnaio on the Monte Amiata volcano, Travale (all in Tuscany), and a fumarole in the Phlegraean Fields. The computed temperatures have been compared with the known temperature conditions existing in the reservoirs.

MODEL DEVELOPMENT

For any gas species, its partial pressure in the reservoir can be expressed as a function of the molar concentration (n_i) with respect to the water at its discharge point (d), the molar steam fraction, y, and the molar distribution coefficient between steam and liquid, B_i (D'Amore and Truesdell, 1985):

$$\log P_i = \log (n_i/n_{H2O})d - \log A_i + \log P(H_2O). \quad (1)$$

In most cases (with $y>0$), $A = y + (1-y) / B_i$, but in gas depleted waters (with $y<0$), $A_i = 1/(B_i(1+y-yB_i))$. In this case y is the fraction of steam lost from the original system (Giggenbach, 1980; D'Amore and Truesdell, 1987). The vapor-liquid distribution coefficients, B_i from 100° to 374°C, are described by the equation, $\log B_i = a + bt°C$, with constants a and b for each gas species given in Table 2 (Giggenbach, 1980; D'Amore and Truesdell, 1987).

For each species, it is possible to express its partial pressure as a function of the concentration of CO_2, dividing equation (1) by the equation for $\log P(CO_2)$ to eliminate H_2O:

$$\log P_i = \log (n_i/n_{CO2})d - \log A_i + \log A_{CO2} + \log P(CO_2). \quad (2)$$

1/ A selection of general references to geothermal gas studies is given in the bibliography.

Table 1. Chemical reactions considered in the present work.

Symbol	Reaction	Equilibrium Expression
H	$H_2O = H_2 + 1/2\ O_2$	$\log K_H = \log P(H_2) + 1/2 \log P(O_2) - \log P(H_2O)$
S	$H_2S = H_2 + 1/2\ S_2$	$\log K_S = \log P(H_2) + 1/2 \log P(S_2) - \log P(H_2S)$
C	$CH_4 + 2\ H_2O =$ $4\ H_2 + CO_2$	$\log K_C = 4 \log P(H_2) + \log P(CO_2) - \log P(CH_4)$ $- 2 \log P(H_2O)$
CO	$CO_2 + H_2 = CO + H_2O$	$\log K_{CO} = \log P(CO) + \log P(H_2O) - \log P(CO_2)$ $- \log P(H_2)$
MP	$1/3\ Fe_3O_4 + S_2 =$ $FeS_2 + 2/3\ O_2$	$\log K_{MP} = 2/3 \log P(O_2) - \log P(S_2)$

For each chemical reaction involving gaseous species, an equilibrium expression can be written in terms of the partial pressure, P_i, of each reactant and product.

The reactions considered and symbols are reported in Table 1. Rearranging the five equations of Table 1 in order to eliminate S_2 and O_2, we obtain the following 3 equations:

$$4 \log P(H_2) + \log P(CO_2) - \log P(CH_4) = \log K_C + 2 \log P(H_2O) \quad (3)$$

$$3 \log P(H_2S) - \log P(H_2) = 2 \log K_H - 3 \log K_S - 3/2 \log K_{MP} + 2 \log P(H_2O) \quad (4)$$

$$4 \log P(CO) - 3 \log P(CO_2) - \log P(CH_4) = 4 \log K_{CO} + \log K_C - 2 \log P(H_2O) \quad (5)$$

Inserting equation (2) for each P_i and using suitable expressions as a function of the absolute temperature (T) for the equilibrium constants (D'Amore and Truesdell, 1987), we obtain the following equations (each gaseous species is expressed in mole % of dry gas samples):

$$4 \log (H_2/CO_2) - \log (CH_4/CO_2) = HC = 6.69 - 12144.08/T + 4.635 \log T + 4 \log A_{H2} - 3 \log A_{CO2} - \log A_{CH4} - 4 \log P(CO_2) \quad (6)$$

$$3 \log (H_2S/CO_2) - \log (H_2/CO_2) = SHC = 17.25 - 10318.15/T - 0.412 \log T + 3 \log A_{H2S} - 2 \log A_{CO2} - \log A_{H2} - 2 \log P(CO_2) \quad (7)$$

$$4 \log (CO/CO_2) - \log (CH_4/CO_2) = COC = 4.73 - 12913.84/T + 0.719 \log T + 4 \log A_{CO} - 3 \log A_{CO2} - \log A_{CH4} \quad (8)$$

The A_i term in equations (3) through (8) is a function of temperature (t) and steam fraction (y) so the following nonlinear set of equations must be solved:

$$HC = F_1(t) + F_1(t,y) - 4 \log P(CO_2) \quad (9)$$

$$SHC = F_2(t) + F_2(t,y) - 2 \log P(CO_2) \quad (10)$$

$$COC = F_3(t) + F_3(t,y) \quad (11)$$

The set of equations (6), (7) and (8) is strongly dependent on temperature but nearly independent of steam fraction when $y \geq 0.1$. It was not possible to write an equation that is strongly y dependent for any possible combination of chemical reactions when considering ratios with CO_2.

Table 2. Distribution coefficients, B_i, as a function of temperature.

Species	a	b	R^2	Validity range t°C
CO_2	5.0358	-0.013292	0.9995	20 - 99
	4.8951	-0.011754	0.9998	100 - 149
	4.7695	-0.010961	0.99996	150 - 320
	5.3934	-0.012947	0.997	321 - 350
	13.1739	-0.035211	1.0	351 - 374
H_2S	4.6005	-0.014363	0.9990	20 - 99
	4.3774	-0.012025	0.9996	100 - 149
	4.0442	-0.009798	0.99992	150 - 330
	7.9880	-0.02133	0.997	331 - 374
H_2	6.8689	-0.021121	0.9986	20 - 99
	6.4325	-0.016323	0.9994	100 - 149
	5.9681	-0.013301	0.9994	150 - 320
	8.4225	-0.02105	0.996	321 - 350
	16.3152	-0.043542	0.991	351 - 374
CH_4	6.5971	-0.017338	0.9998	20 - 99
	6.4000	-0.015902	0.9996	100 - 149
	6.0809	-0.0138746	0.9998	150 - 340
	12.6492	-0.033150	0.993	341 - 359
	16.8590	-0.045012	0.995	360 - 374
CO	6.6890	-0.017588	0.998	20 - 99
	6.4490	-0.014850	0.99998	100 - 140
	6.2865	-0.013729	0.99995	141 - 320
	6.8316	-0.015464	0.9995	321 - 350
	21.9307	-0.058616	1.0	351 - 374

Between 100° and 350°C the terms $F_1(t)$, $F_2(t)$ and $F_3(t)$ vary by about 14, 11, and 14 orders of magnitude, respectively. Each of equations 9, 10 and 11 can then be considered as a potentially effective geothermometer. The term $F_3(t)$ alone was used by Bertrami et al. (1985) to calculate reservoir temperatures for several wells of the Larderello geothermal field. The three terms F(t,y) have small values and change little with temperature for $y \geq 0.1$, but their contribution cannot be neglected when solving the set of equations, especially in the case of high temperatures or small y values (see Table 3). It can be shown that the solution of the set of equations may not give reliable values of the computed y.

PROPOSED SOLUTION OF THE SYSTEM

After determining equilibrium temperature and $P(CO_2)$, we can use the following method to calculate both the order of magnitude of the steam fraction y and the gas/H_2O ratio. A computer program has been developed for these calculations.

Table 3. Values of $F_1(t,y)$, $F_2(t,y)$ and $F_3(t,y)$ at selected temperatures in °C and y values.

t°C	y: -0.1	-0.01	-0.001	0	0.001	0.01	0.1	0.5
				$F_1(t,y)$				
100	-6.47	-6.45	-6.27	-3.24	-0.21	-0.02	0.00	0.00
150	-5.02	-4.95	-4.44	-2.59	-0.60	-0.08	-0.01	0.00
200	-4.36	-4.14	-3.22	-2.13	-1.15	-0.24	-0.02	0.00
250	-3.66	-3.14	-2.22	-1.85	-1.50	-0.58	-0.08	-0.01
300	-2.89	-2.12	-1.64	-1.52	-1.43	-0.97	-0.22	-0.03
350	-0.80	-0.58	-0.54	-0.53	-0.53	-0.49	-0.27	-0.05
				$F_2(t,y)$				
100	5.43	5.37	4.92	2.72	0.51	0.07	0.01	0.00
150	4.98	4.77	3.84	2.50	1.16	0.24	0.02	0.00
200	4.36	3.87	2.83	2.21	1.60	0.56	0.07	0.01
250	3.66	2.87	2.12	1.93	1.73	0.99	0.19	0.01
300	2.76	1.95	1.64	1.59	1.54	1.23	0.42	0.06
350	1.67	1.28	1.22	1.21	1.21	1.15	0.76	0.20
				$F_3(t,y)$				
100	-7.79	-7.77	-7.57	-3.89	-0.22	-0.02	0.00	0.00
150	-7.02	-6.94	-6.37	-3.53	-0.67	-0.09	-0.01	0.00
200	-6.22	-5.97	-4.83	-3.12	-1.42	-0.28	-0.03	0.00
250	-5.34	-4.71	-3.37	-2.72	-2.06	-0.72	-0.09	-0.01
300	-4.35	-3.29	-2.48	-2.32	-2.15	-1.35	-0.28	-0.04
350	-3.27	-2.30	-2.06	-2.03	-2.00	-1.76	-0.79	-0.14

The approach used to solve the nonlinear equation system is based on the fact that equation 11 is independent of $P(CO_2)$ and that the temperature and y value will be such that $P(CO_2)$ computed by equation 9, $P(CO_2)HC$, will be equal to $P(CO_2)$ computed by equation 10, $P(CO_2)SHC$. Starting from an assigned low temperature (t_o), the value of $F_3(t,y)$ is computed by:

$$F_3(t,y) = COC - F_3(t) \quad (12)$$

If this computed value is positive, the t value must be increased. At a certain temperature the difference ($COC - F_3(t)$) will be negative. This will be the first temperature value, t_1, for calculating the two values of $P(CO_2)$. A value of y is obtained from $F_3(t,y)$. From t_1 and y it is possible to calculate $F_1(t)$, $F_2(t)$, $F_1(t,y)$ and $F_2(t,y)$. Inserting these values in equations (9) and (10) it is then possible to compute two independent values of $P(CO_2)$.

$$\log P(CO_2)HC = 1/4\ (F_1(t) + F_1(t,y) - HC) \quad (13)$$

$$\log P(CO_2)SHC = 1/2\ (F_2(t) + F_2(t,y) - SHC) \quad (14)$$

If the temperature used is too low, then $P(CO_2)HC > P(CO_2)SHC$, and the t_1 must be increased and new values of y and $P(CO_2)$ computed from the new value of $F_3(t,y)$ (equation 12).

The following equations can be written from reactions C, CO, and a combination of H, S and MP:

$$\log K_C - \log P(H_2O) - \log P(CO_2) - \log (H_2/CH_4) = 3 \log (H_2/H_2O) - 4 \log A_{H2} + \log A_{CH4} \quad (15)$$

$$\log K_H - 3/2 \log K_S - 3/4 \log K_{MP} + 3/2 \log P(H_2O) - 3/2 \log P(CO_2) - 3/2 \log (H_2S/CO_2) = - 1/2 \log (H_2/H_2O) + 1/2 \log A_{H2} - 3/2 \log A_{H2S} + 3/2 \log A_{CO2} \quad (16)$$

$$\log K_{CO} - \log (CO/CO_2) = - \log (H_2/H_2O) - \log A_{CO} + \log A_{CO2} + \log A_{H2} \quad (17)$$

The left side of the equations contains known factors: temperature-dependent components, $P(CO_2)$, and the ratios (H_2/CH_4), (H_2S/CO_2) and (CO/CO_2). Using suitable thermodynamic data for the equilibrium constants (D'Amore and Truesdell, 1987), the following temperature-dependent components can be used:

$$\log K_C - \log P(H_2O) = - 9.84 - 6000.08/T + 4.635 \log T \quad (18)$$

$$\log K_H - 3/2 \log K_S - 3/4 \log K_{MP} + 3/2 \log P(H_2O) = 11.382 - 6183.08/T - 0.206 \log T \quad (19)$$

$$\log K_{CO} = 5.019 - 2240.44/T - 0.979 \log T \quad (20)$$

Only two unknowns are present, y and the (H_2/H_2O) ratio. Using two at a time of the three possible sets of these equations it is possible to calculate y and the (H_2/H_2O) ratio, and then the (gas/H_2O) ratio from the equation:

$$gas/H_2O = (H_2/H_2O)\ 100/(\%H_2). \quad (21)$$

Average values of the results are considered. Starting from the percentage in the dry gas of five species (CO_2, H_2S, H_2, CH_4, CO), with some restrictions, it is then theoretically possible to evaluate the following parameters for the reservoir: temperature, $P(CO_2)$, y, and gas/H_2O. The P_i of all other gases can be calculated from equation (2).

Generally this method results in convergent values of the two $P(CO_2)$ at some temperature below 370°C, because with increasing t, the computed value of $P(CO_2)SHC$ increases much faster than $P(CO_2)HC$. A special case is when the absolute value of HC is much larger than SHC. This is generally due to H_2 contents much lower than H_2S contents (i.e., by two orders of magnitude). In this case, convergence is never obtained below 370°C, and computed values of $P(CO_2)HC$ are extremely high. This occurs when the gas comes from a boiled water depleted in the less soluble species as H_2. In this case, negative values of y must be used. Starting from t_o (low temperature), $P(CO_2)HC$ and $P(CO_2)SHC$ are computed with different values of negative y (from -0.001 to -0.1). If there is no convergence for t_o, temperature is increased and for any new t we scan with negative values of y. Of course this method will give the minimum temperature of the system (at the value of y closest to 0). Note that when $F_3(t) > -13.330$, $t > 370°C$. In this case all the B_i values are set equal to 1, so that $F_3(t,y)$, $F_2(t,y)$ and $F_1(t,y)$ will be equal to 0.

Sometimes at t_1, $P(CO_2)SHC > P(CO_2)HC$. This means that for some reason the content of carbon monoxide (11) produces an overestimate of temperature. In this case, y is set arbitrarily equal to 1, and to obtain convergence the temperature must be decreased until $P(CO_2)$ values computed from equations (20) and (21) are equal (of course $F_1(t,y)$ and $F_2(t,y)$ are equal to 0). This will produce a minimum calculated temperature.

APPLICATION

In order to calibrate the method, it was applied to 32 well fluids collected in different zones of the Larderello field having very different reservoir temperatures, to 3 well fluids of the Travale field, to 5 well fluids of the Monte Amiata geothermal area (Bagnore and Piancastagnaio fields) showing wide differences in temperature and depth, and to a well-known fumarole of the Phlegraean Fields area (Bocca Grande at Pozzuoli).

Table 4 reports the chemical compositions of the gases and measured gas/H_2O molar ratios (g), together with the sources of data.

Table 5 reports the following parameters for all the wells: wellhead temperature (t_{WH}), temperature (t_r) in the upper part of the reservoir tapped by the well; estimated by in-hole physical measurements (R. Celati, pers. commun., 1978) or computed bottom-hole temperatures (Calore, 1979), and the temperature, $P(CO_2)$, y, and gas/H_2O ratio computed

Table 4. Gas compositions used in this work (mole % in dry gas). [g = molar gas/H_2O ratio. The first 32 wells are located in the Larderello field; (T) = Travale; (A) = Monte Amiata field]

No.	Well	g • 10^3 (a)	H_2	H_2S	CH_4	CO_2	CO • 10^4 (b)	N_2
1	Alloro (c)	21.9	0.74	1.99	1.84	92.95	6.8	2.37
2	Camorsi 1 (c)	16.5	1.96	2.22	1.72	91.80	3.8	2.00
3	Capannoli (c)	6.24	6.03	4.14	1.74	87.29	23.6	0.53
4	Gabbro 1	32.4	1.54	1.49	0.80	95.70	9.5	0.47
5	Gabbro 6 (c)	56.2	1.21	1.09	1.18	94.50	12.2	0.74
6	Gabbro 7	138	0.67	0.33	1.26	96.75	14.4	0.99
7	Guiducci	2.96	1.14	0.53	0.14	97.71	1.7	0.37
8	Lago 7 (c)	7.46	6.03	3.70	0.71	89.90	4.8	1.16
9	Lago 8 (c)	1.5	4.31	8.06	2.35	84.00	10.6	0.11
10	LRA (c)	16.6	2.88	1.68	1.17	93.11	4.9	0.92
11	Lustignano 5	25.5	3.29	2.93	2.24	90.98	23.1	0.65
12	Monterotondo 11 (c)	4.32	6.06	2.85	4.03	85.70	2.7	1.20
13	Monterotondo 21 (c)	4.02	4.14	1.94	5.13	87.58	13.3	1.27
14	Puntone 1 (c)	12.3	5.55	3.18	1.84	88.55	17.5	0.54
15	S. Martino 3 (c)	3.92	4.96	4.39	3.13	85.59	13.5	1.69
16	S. Silvestro (c)	13.5	1.85	2.10	1.62	93.28	2.2	0.48
17	Sasso 9 (c)	9.59	3.12	2.60	1.59	92.07	3.3	0.58
18	S. Vincenzo 1	44.9	0.46	0.35	0.27	98.72	2.9	0.21
19	S. Vincenzo 2	41.4	1.16	1.45	1.23	95.47	6.6	0.64
20	S. Vincenzo 5	42.9	0.95	0.99	0.79	96.92	4.7	0.32
21	S. Vincenzo 9 (c)	108.5	0.37	0.21	1.11	97.05	9.6	0.73
22	Scarzai 1 (c)	10.1	1.81	1.12	0.55	96.58	1.1	0.16
23	VC 10	12.2	3.70	2.73	1.31	90.97	17	1.25
24	Zuccantine	5.94	2.48	2.29	0.74	93.72	2.6	1.00
25	77	21.5	2.08	1.92	1.63	93.62	16	0.75
26	89	9.37	2.32	2.34	1.43	92.91	8.8	1.00
27	113	12.2	1.39	0.90	0.05	97.61	6.0	0.05
28	128 (c)	13.4	0.51	1.08	0.23	95.95	2.9	1.99
29	141 (c)	8.67	1.01	2.48	0.64	94.93	7.2	0.88
30	145 (c)	12.5	1.08	3.02	0.87	94.07	7.4	0.94
31	152	26.1	1.77	1.83	1.17	94.40	14	0.83
32	157 (c)	91.4	0.72	0.91	0.47	96.87	7.9	0.35
33	(A) Bagnore 18 (d)	86.6	0.44	0.031	9.71	85.97	1.1	2.60
34	(A) PC 7 (c)	80.3	0.37	0.52	3.05	95.69	4.2	0.40
35	(A) PC 8 (c)	--	0.52	0.60	3.86	94.30	3.3	0.61
36	(A) PC 26 (c)	--	0.92	2.46	1.05	95.10	12.9	0.45
37	(A) PC 30 (c)	--	0.70	2.19	1.62	95.60	26.2	0.29
38	(T) R 6 (c)	39.1	0.70	1.24	0.54	96.80	2.8	0.72
39	(T) R 9 (c)	29.3	0.54	1.07	1.91	95.52	12.2	0.79
40	(T) R 15 (c)	35.6	0.19	0.69	3.07	95.07	3.6	1.28
41	Fumarole (e)	189	0.124	1.924	0.0104	97.79	1.6	0.142

(a) g data for wells are from ENEL (1984); (b) and (c) data from Istituto di Geocronologia e Geochimica Isotopica, CNR, Pisa, Italy (1984).
(d) 1978 chemical analyses from ENEL (except for CO).
(e) Data for the Bocca Grande Fumarole, February 2, 1984, are from Sabroux et al. (written commun., 1985).

Table 5. With the same order of Table 4, average wellhead temperature during 1984 for each well (t_{WH}); estimated temperature (±5°C) in the upper part of the reservoir (t_r); results obtained from the calculations made in this paper: temperature t_c, $P(CO_2)$ in bars, steam fraction y, gas/H_2O molar ratio g.

No.	t_{WH}	t_r	t_c	$P(CO_2)$	y	g • 10^3
1	229	260	261	3.62	0.004	1.34
2	192	235	227	0.68	0.007	0.33
3	250	270	273	1.05	0.95	19.9
4	242	260	256	2.08	0.051	3.06
5	241	260	261	3.39	0.070	6.16
6	189	230	233	3.14	0.617	68.63
7	185	200	197	0.34	0.570	13.97
8	217	240	232	0.265	0.083	0.916
9	191	260	268	0.90	0.011	0.51
10	184	230	228	0.57	0.050	1.25
11	229	270	280	2.37	0.136	6.26
12	172	220	204	0.15	0.011	0.148
13	235	270	249	1.06	0.327	10.37
14	249	280	255	0.73	0.732	14.00
15	265	270	261	0.93	0.041	1.21
16	180	240	212	0.42	0.04	0.167
17	184	220	219	0.36	0.009	0.234
18	198	220	222	2.11	0.032	3.28
19	226	240	246	1.98	0.014	1.27
20	198	230	234	1.68	0.015	1.21
21	230	240	244	7.63	0.531	116.9
22	157	200	190	0.20	0.007	0.15
23	259	280	270	1.53	0.315	9.86
24	186	220	217	0.36	0.009	0.22
25	250	260	269	2.61	0.079	4.81
26	255	270	251	1.29	0.026	1.24
27	190	240	209	0.32	0.226	4.08
28	227	230	237	2.04	0.006	0.83
29	234	270	264	2.66	0.008	1.20
30	236	260	267	2.65	0.006	1.09
31	229	270	268	2.69	0.067	4.07
32	204	240	256	3.75	0.030	3.62
33	127	140	122	0.11	0.048	2.97
34	189	225	230	4.11	0.004	1.52
35	204	225	219	2.26	0.004	0.83
36	188	320	284	5.39	0.013	2.85
37	---	330	311	14.78	0.019	9.46
38	183	230	229	1.43	0.004	0.54
39	235	270	272	8.39	0.012	4.42
40	186	255	250	8.85	0.001	2.36
41	158	290	287	7.6	-0.002	2.79

in this work. In the case of the fumarole, a temperature of 290°C was measured in an exploration well drilled in the area of the Solfatara at a depth of 1800 m (data reported in Carapezza et al., 1984). It must be noted that in the Mofete field about 5 km west of the Solfatara, recently drilled wells show large gradients of temperature as function of depth. The maximum value recorded in the deep part of the reservoir (2700 m) is 347°C (Carella and Guglielminetti, 1983).

In Figure 1 the temperatures computed with the geothermometer are compared with those reported in Table 4. The agreement is fair ($r^2 = 0.88$), considering that the temperatures of the reservoir have been estimated by physical data measured before 1978 and that any possible fluid evolution has not been considered.

The computed values of the gas/H_2O ratio are absolutely not consistent with the measured gas/steam ratio. With few exceptions the computed values are much lower.

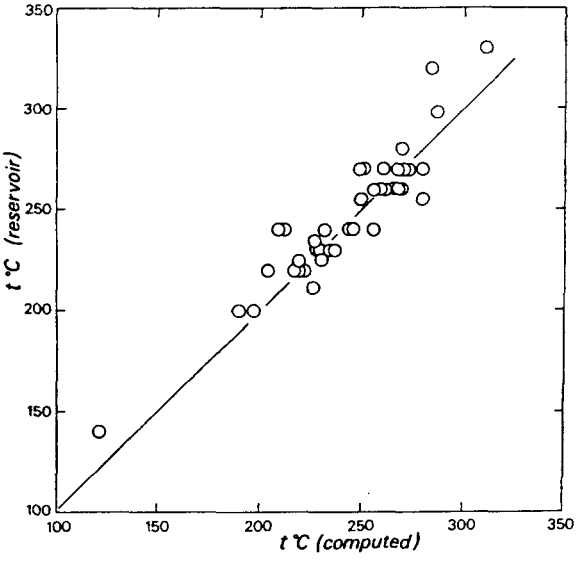


Figure 1. Estimated temperatures in the upper part of the reservoir reported versus the values of temperatures obtained from the calculations made in this paper (see Table 5).

CONCLUSIONS

If the methodology reported in D'Amore and Truesdell (1985) is used, considering molar ratios of chemical species with respect to water, high values of steam fraction y and temperatures are obtained for Larderello data. A typical example is shown in this paper using the grid FT vs. HSH where FT = 4 log (H_2/H_2O) - log (CH_4/CO_2) and HSH = 3 log (H_2S/H_2O) - log (H_2/H_2O). Taking well Gabbro 1 as an example, using data in Table 4, values of t = 287°C and y = 0.40 are obtained with the method of D'Amore and Truesdell (1985). This computed temperature is quite in excess of the local 260°C reservoir temperature and, as observed in D'Amore and Pruess (1986), a value of y = 0.40 corresponds to a volume steam saturation Sv of about 0.95, which is substantially larger than the range of values compatible with total fluid extraction to date in this area of the field. Well Gabbro 1 has a flow rate exceeding 60 tons/h. With this new method that does not utilize the measured gas/steam ratio at wellhead, values of t = 256°C and y = 0.051 are found, which are more consistent with the reservoir characteristics of this well. The computed value of gas/H_2O molar ratio in the reservoir is 3.06×10^{-3} compared to the measured value at wellhead of 32×10^{-3}. This discrepancy may be due to transport phenomena affecting H_2O species between the reservoir and well bottom. As defined in D'Amore and Truesdell (1985), one of the main limitations of the validity of equation 1 (which utilizes molar ratios of each species with respect to H_2O) is that the sample collected at wellhead should be transferred from the reservoir without any mass gain or loss. Those ratios must then be representative of the relative concentrations in the reservoir. This condition cannot be fulfilled if in the decompression volume, between the bulk of the reservoir and well bottom, the steam produced from partial evaporation of the liquid moves faster than liquid phase. Most of the gas present locally in the liquid fraction is transferred in the new formed steam and this steam and gas phase contains a gas/H_2O ratio in excess of that representative of the reservoir. In the method presented in this paper ratios with respect to CO_2 instead of H_2O are used, so that this method may be considered almost independent of H_2O transport phenomena.

Let us see if gas ratio are altered by transport phenomena. Consider, in a given volume of reservoir, there are 1000 moles of water, 50 as steam and 950 as liquid corresponding to y = 0.05, as for well Gabbro 1. For this well at a computed temperature of 256°C, P_{H2O} = 43.9 bar, P_{CO2} = 2.08 bar, and P_{H2S} = 0.031 bar. From these data it is possible to calculate the number of moles of CO_2 and H_2S associated with 50 moles of steam and 950 moles of liquid:

$n_l(CO_2) = 0.38$ $\quad$ $n_l(H_2S) = 0.016$

$n_v(CO_2) = 2.60$ $\quad$ $n_v(H_2S) = 0.039$

Then the ratio H_2S/CO_2 is 0.015 if only the vapor arrives at wellhead and 0.018 if the 950 moles of liquid are also vaporized. The difference is very small, so that ratios with respect to CO_2 used in the model are almost independent of the amount of vaporized water. Of course the final gas/H_2O ratio will depend on the fraction fv of vaporized liquid water which arrives at wellhead. If the total number of gas moles is 3, the final gas/H_2O ratio at WH will be 3/(50+fv).

The proposed methodology requires testing in other active geothermal systems where CO data are available.

REFERENCES

Bertrami, R., Cioni, R., Corazza, E., D'Amore, F., and Marini, D. (1985), "Carbon monoxide in geothermal gases. Reservoir temperature calculation at Larderello (Italy)," Geothermal Resources Council Int. Symposium on Geothermal Energy, August 1985, Kona, Hawaii, Trans., 9, part 1, 299-302.

Calore, C. (1979), "Distribuzione della temperatura al tetto del serbatoio geotermico di Larderello," Unpublished Italian CNR report.

Carapezza, M., Nuccio, P.M., and Valenza, M. (1984), "Geochemical surveillance of the Solfatara of Pozzuoli (Phlegraean Fields) during 1983," Bull. Volcanol., 47, part 2, 301-311.

Carella, R., and Guglielminetti, M. (1983), "Multiple reservoirs in the Mofete Field, Naples, Italy," Proc. Ninth Workshop Geothermal Reservoir Eng., December 1983, Stanford University, Stanford, Calif., 53-64.

D'Amore, F., and Pruess, K. (1986), "Correlations between vapor saturation, fluid composition, and well decline in Larderello," Geothermics, 15, no. 2 (in press).

D'Amore, F., and Truesdell, A.H. (1985), "Calculation of geothermal reservoir temperatures and steam fractions from gas composition," Geothermal Resources Council Int. Symposium on Geothermal Energy, August 1985, Kona, Hawaii, Transactions, 9, part 1, 305-310.

D'Amore, F., and Truesdell, A.H. (1987), "A review of solubilities and equilibrium constants of chemical reactions for gaseous species of geothermal interest," CNR report (in press).

ENEL (1984), Italian Electricity Authority unpublished report of chemical and physical data of Italian exploited geothermal fields.

Giggenbach, W.F. (1980), "Geothermal gas equilibria," Geochim. Cosmochim. Acta, 44, 2021-2032.

GENERAL REFERENCES

Arnórsson, S., and Gunnlaugsson, E. (1985), "New gas geothermometers for geothermal exploration - Calibration and exploration. Geochim. Cosmochim. Acta," 49, 1307-1325.

D'Amore, F., Celati, R., and Calore, C. (1982), "Fluid geochemistry applications in reservoir engineering (vapor-dominated systems)," Proc. Eighth Workshop Geothermal Reservoir Eng., December 1982, Stanford University, Stanford, California, 295-307.

D'Amore, F. and Celati, R. (1983) "Methodology for calculating steam quality in geothermal reservoirs," Geothermics, 12, 129-140.

D'Amore, F., and Gianelli, G. (1984), "Mineral assemblages and oxygen and sulfur fugacities in natural water-rock interaction processes," Geochim. Cosmochim. Acta, 48, 847-857.

D'Amore, F., and Panichi, C. (1980), "Evaluation of deep temperatures of hydrothermal systems by a new gas-geothermometer," Geochim. Cosmochim. Acta, 44, 549-556.

D'Amore, F., and Truesdell, A.H. (1980), "Gas thermometry for drillhole fluids from vapor-dominated and hot-water geothermal fields," Proc. Sixth Workshop Geothermal Reservoir Eng., December 1980, Stanford University, Stanford, California, 351-360.

Nehring, N.L., and D'Amore, F. (1984), "Gas chemistry and thermometry of the Cerro Prieto, Mexico, geothermal field," Geothermics, 13, 75-89.

Truesdell, A.H., and Henley, R.W. (1982), "Chemical equilibria in the Cerro Prieto hydrothermal fluid," Proc. Fourth Symposium on the Cerro Prieto Geothermal Field, August 1982, Guadalajara, Mexico.

Truesdell, A.H., and Janik, C.J. (1986), "Reservoir processes and fluid origins in the Baca geothermal system, Valles caldera, New Mexico," Jour. Geophys. Res., 91, 1817-1833.

Truesdell, A.H., and Nehring, N.L. (1978), "Gases and water isotopes in a geochemical section across the Larderello, Italy, geothermal field," PAGEOPH., 117, 276-289.

PROCEEDINGS, Twelfth Workshop on Geothermal Reservoir Engineering
Stanford University, Stanford, California, January 20-22, 1987
SGP-TR-109

CHEMICAL AND ISOTOPIC EVIDENCE OF STEAM UPFLOW AND PARTIAL CONDENSATION IN LOS AZUFRES RESERVOIR

NIEVA*, D., VERMA*, M., SANTOYO*, E., BARRAGAN*, R.M., PORTUGAL*, E., ORTIZ†, J. AND QUIJANO†, J.L.

*Instituto de Investigaciones Eléctricas
Apartado Postal 475
Cuernavaca, Mor., México 62000

†Comisión Federal de Electricidad
Ave. de las Camelinas 3527, 7° piso
Morelia, Mich., México

ABSTRACT

Data of chemical and isotopic composition of fluids from Los Azufres wells, collected over a two year period, provide evidence of a process of upward flow and partial condensation of steam in the reservoir, which explains part of the previously reported heterogeneity in isotopic composition of the liquid phase (Nieva et al, 1983).

For the southern part of the field, a direct correlation is found between chloride and oxygen-18 concentrations, and an inverse correlation between these parameters and deuterium and carbon dioxide concentrations in the liquid phase of the reservoir. Chloride ion concentrations increase gradually from ca 600 ppm in the production zones of shallow wells to ca 1900 ppm in the case of deep wells. This observations agree with predictions based on the well-known model for vapor dominated systems of White et al (1971).

For the northern part of the field the same correlations are observed, except for the deuterium concentration which in this case correlates directly with oxygen-18. It is concluded that the same process of steam upflow occurs in the northern section but that some other process - perhaps a mixture with other hydrothermal fluid - is also occuring.

INTRODUCTION

The primary geology (Camacho, 1976; Gutiérrez-Negrín and Aumento, 1982; Cathelineau et al, 1987), alteration mineralogy (Cathelineau et al, 1985; Cathelineau and Nieva, 1985) and some features of the hydrological structure of the Los Azufres field (Iglesias et al, 1985; Nieva et al, 1986) have been discussed elsewhere.

A previous analysis of chemical and isotopic composition data from Los Azufres fluids, led to the detection of a significant heterogeneity in the composition of the reservoir fluids produced by various wells (Nieva et al, 1983). This was interpreted as resulting from the mixture of more than one hydrothermal fluid, but no solid conclusions as to their origins could be drawn, except for supporting the assertion that there exists no substantial mixture with local meteoric water (Giggenbach and Quijano, 1981). A more detailed interpretation was impeded by uncertainties concerning well flow conditions (hence about specific enthalpies of the total discharges) at the time of sampling, and also because of the occurrence of phase separation in the formation, leading to uncertainties in the relation between the compositions of the well discharge and the reservoir fluid.

Giggenbach (1980) and D'Amore and Celati (1983) have devised methods to calculate the fractional molar contribution of reservoir steam in the total discharge from a well. This parameter has come to be known as the "y value" (Giggenbach, 1980), steam fraction (D'Amore and Celati, 1983), or steam excess (Nieva et al, 1982; Truesdell et al, 1984). Heretofore this parameter shall be referred to as steam excess, and shall be expressed in units of mole percentage. The original procedure of Giggenbach (1980) has been modified, so as to make it applicable to the case of well fluids with high contents of non-condensable gases (Nieva et al, 1985). Knowledge of the total discharge composition and of the steam excess, allows for the calculation of both the reservoir liquid and steam phases.

This contribution presents an analysis of chemical and isotopic composition data from Los Azufres well fluids, collected over a period of about two years. The sampling program was designed so as to include as many wells as possible, some of them sampled repeatedly; extreme care was taken to select wells in appropriate and characterized flow conditions, and to enhace the reproducibility of the sampling operation and the precision of the isotopic and chemical analysis.

RESULTS

Table 1 presents steam composition data for samples collected between June, 1984 and February, 1986. Some of the wells could be sampled only once, but those which provide steam for the 5 wellhead generators were sampled several times. Included in Table 1 is the best estimate for the reservoir temperature in the production zone of each well.

The calculation of steam excess also allows

TABLE 1. COMPOSITION OF SEPARATED STEAM FROM LOS AZUFRES WELLS

WELL	T_s °C	f_s	X_g	MOLAR FRACTION X 1000 H_2O-FREE BASIS CO_2	H_2S	H_2	CH_4	N_2	NH_3	T_{res} °C	DATE OF SAMPLE
A- 5	182	0.71	8.6	971.	20.0	4.7	0.67	3.5	0.6	300	24 485
A- 5	180	0.71	10.8	976.	16.8	3.0	1.1	2.8	0.4	300	25 685
A- 5	180	0.70	19.8	988.	7.1	1.8	0.35	1.8	0.9	300	12 985
A- 5	179	0.72	9.3	975.	17.6	2.9	0.49	2.4	1.9	300	25 286
A- 5	165	0.73	8.2	970.	19.5	3.5	0.90	3.9	2.2	300	13 586
A- 5	179	0.72	8.3	984.	9.3	2.7	0.59	2.5	0.9	300	24 986
A- 6	192	1.	31.7	989.	5.9	0.9	0.49	3.7	0.3	259	24 485
A- 6	191	1.	28.1	979.	9.3	1.6	1.3	4.5	4.3	259	26 685
A- 6	177	1.	41.5	984.	4.5	0.8	0.49	6.8	3.0	259	11 985
A- 6	179	1.	36.3	983.	5.9	0.9	0.66	7.0	2.2	259	91085
A- 6	180	1.	29.2	977.	6.8	1.1	0.82	7.9	6.6	259	27 286
A- 6	180	1.	35.2	981.	5.9	1.1	1.00	7.5	3.3	259	14 586
A- 6	179	1.	38.7	981.	5.4	1.1	0.76	10.2	1.6	259	24 986
A- 9	148	0.49	2.1	920.	62.3	7.4	0.38	1.1	8.7	330	9 884
A-13	172	0.56	5.1	961.	30.0	5.1	0.36	2.0	1.2	300	24 485
A-13	172	0.58	6.4	969.	22.0	4.1	1.1	1.9	2.2	300	25 685
A-13	172	0.58	13.9	986.	9.3	2.3	0.29	1.3	1.4	300	12 985
A-13	174	0.58	5.9	971.	22.8	3.5	0.48	1.9	0.5	300	101085
A-13	163	0.59	6.3	965.	26.8	5.5	0.32	1.3	1.2	300	26 286
A-13	177	0.58	5.1	959.	26.3	7.4	1.1	2.7	3.4	300	13 586
A-16AD	176	0.75	12.0	981.	9.8	3.8	0.14	4.2	1.5	280	7 684
A-16AD	177	0.75	8.9	877.	9.4	2.4	0.19	109.8	0.9	280	8 585
A-16AD	180	0.75	39.7	917.	3.1	0.6	0.10	75.8	3.7	280	10 985
A-16AD	180	0.75	9.8	886.	9.4	1.0	0.19	98.9	4.2	280	91085
A-16AD	182	0.75	8.1	877.	9.9	8.6	0.08	101.5	3.4	280	26 286
A-16AD	183	0.75	14.9	811.	7.1	17.7	0.74	160.9	2.7	280	14 586
A-17	172	1.	21.5	983.	11.6	3.2	0.28	1.8	0.6	264	6 684
A-17	176	1.	14.2	993.	1.3	1.6	0.11	1.0	2.6	264	10 884
A-17	179	1.	20.9	979.	10.9	2.6	0.30	6.3	0.5	264	23 485
A-17	175	1.	20.0	982.	10.0	1.9	0.60	3.2	2.6	264	26 685
A-17	102	1.	66.6	977.	9.0	2.7	0.26	7.5	3.2	264	11 985
A-17	180	1.	27.2	983.	6.8	1.8	0.28	5.5	2.4	264	91085
A-17	180	1.	15.9	977.	11.0	1.0	0.08	2.1	8.5	264	27 286
A-17	207	1.	15.0	973.	12.8	2.6	0.48	6.9	4.1	264	14 586
A-17	213	1.	16.9	977.	10.1	2.3	0.35	7.5	2.8	264	24 986
A-18	156	0.66	32.3	990.	5.9	1.0	0.09	2.0	0.8	280	8 684
A-18	127	0.69	35.0	986.	5.3	0.8	0.47	3.7	3.4	280	11 985
A-18	158	0.66	28.2	986.	6.7	0.9	0.42	3.1	3.1	280	26 286
A-19	138	0.40	1.1	866.	95.8	18.3	0,24	4.1	16.1	310	9 884
A-19	145	0.39	1.9	926.	63.8	2.9	0.95	1.7	4.4	310	25 685
A-19	165	0.35	5.5	980.	15.1	2.4	0.04	1.5	1.5	310	25 286
A-19	165	0.36	2.6	961.	26.4	6.2	0.80	3.7	2.3	310	13 586
A-22	190	0.43	4.7	963.	24.5	8.5	0.14	2.0	1.5	310	11 684
A-22	197	0.42	8.2	979.	15.3	3.7	0.03	0.6	2.0	310	9 884
A-22	169	0.46	4.7	963.	19.5	6.8	0.44	3.2	6.9	310	91085
A-26	177	0.34	18.3	982.	8.6	1.4	0.99	3.2	3.8	292	26 685
A-28	169	0.36	0.9	873.	83.4	25.0	0.40	2.7	15.6	310	9 884
A-28	165	0.37	2.2	928.	48.4	11.1	3.0	4.0	6.0	310	27 685
A-28	182	0.34	10.8	986.	9.3	2.2	0.09	0.4	2.7	310	12 985
A-28	177	0.35	1.8	941.	38.2	13.1	0.09	1.5	6.4	310	25 286
A-28	177	0.35	1.7	937.	27.1	23.9	1.2	6.1	5.2	310	13 586
A-32	161	0.85	8.8	967.	26.7	4.2	0.33	1.3	0.9	300	8 585
A-33	206	0.84	27.6	987.	7.6	2.0	0.61	2.4	0.8	260	11 684
A-34	197	0.83	45.3	989.	5.6	2.4	0.88	2.2	0.4	265	8 684
A-35	192	0.82	14.9	975.	12.5	6.7	0.58	4.1	0.9	280	11 684
A-36	150	0.67	14.4	981.	11.3	4.2	0.10	2.9	0.9	270	7 684
A-36	148	0.65	17.3	984.	9.7	2.2	0.23	2.3	1.4	270	8 884
A-37	201	1.	3.2	949.	15.5	23.5	1.1	7.7	3.8	263	14 586
A-38	205	0.82	23.1	984.	7.3	3.8	0.44	3.7	0.5	262	7 684
A-38	205	0.82	24.4	985.	7.5	3.1	0.46	3.7	0.4	262	7 684
A-38	182	0.88	18.4	988.	8.2	0.9	0.26	2.5	0.5	262	8 585
A-38	142	0.87	17.5	976.	8.5	1.5	0.34	3.2	10.8	262	27 286
A-46	184	0.31	11.3	969.	24.9	3.7	1.0	0.9	1.0	270	1 785
A-46	185	0.31	9.3	977.	10.8	2.9	0.15	5.8	3.0	270	101085

T_s = steam separation temperature; fs = steam weight fraction in total discharge;

X_g = milimoles of non-condensable gas per mol of H_2O in steam; Tres = reservoir temperature

for the calculation of carbon dioxide (and other volatile species) concentration in the reservoir liquid phase (Nieva et al, 1985). Table 2 shows the calculated values for well A-17. This well is chosen for detailed analysis because of the very high value of steam excess calculated for the sample of September, 1985, which is one of a set of anomalies believed to be precursors of the September, 19 and September 21, 1985 earthquakes (Santoyo et al, 1986). Table 2 includes the isotopic composition of the total discharge, and the calculated composition of the reservoir liquid phase. This data allows for several checks on the internal consistency of the steam excess concept and calculation procedure. One of this checks is the observed (and expected) linear correlation between steam excess and carbon dioxide concentration in the total discharge (plot not shown). The concentration of oxygen-18 would be expected to correlate inversely with the steam excess, since this species partitions preferentially into the liquid phase. This correlation, which provide for a second check, is shown in Figurel. The solid line drawn in the Figure was calculated using the expected relationship given by the formula:

$$[\delta^{18}O]_{td} = [\delta^{18}O]_{res,1} + F_{se} \times (\frac{1-\alpha}{\alpha}) \left[[\delta^{18}O]_{res,1} + 1000\right] \quad (1)$$

where F_{se} is the mass fraction of the steam excess in the total discharge, $[\delta^{18}O]_{res,1}$ and $[\delta^{18}O]_{td}$ are the concentrations of oxygen-18 in the reservoir liquid phase and the total discharge, respectively. α is the partition coefficient of oxygen-18 between steam and liquid, evaluated at the downhole temperature. The value of the last parameter was calculated using data assembled by Truesdell et al (1977). Contrary to oxygen-18, deuterium is expected to increase in concentration with an increase in steam excess, because at the reservoir temperature this species partitions preferentially into the steam phase. This is indeed what is observed, with the inverse correlation being close to the calculated trend (plot not shown for lack of space).

The above correspondence between expected and observed trends, provide confidence on the use of the steam excess concept to calculate the composition of the reservoir liquid phase, from the composition of the total discharge. The procedure consists of a mass-balance calculation, which takes into account the steam/liquid partition coefficient of each species. The procedure was applied to data collected from April, 1985 to February, 1986, and the results are shown in Table 3. The parameters calculated are the concentrations in the liquid phase of the chloride ion, oxygen-18 and deuterium, as well as the molar fraction of carbon dioxide. For each parameter the Table presents the average value and average deviation. Some of the wells were sampled only once, and the single result is provided. The Table includes carbon dioxide concentration data for samples collected before the isotopic study had begun. Also presented is the elevation of the production zone of each well, which was taken as that of the midpoint in the open liner segment.

It is evident from the results in Table 3 that the parameters which could be measured with better precision are the concentrations of chloride ion and oxygen-18. Figure 2 shows the direct correlation that exists between these two parameters. The Figure includes data from wells from both the northern and the southern sections of the field (for a map of the Los Azufres field refer to Nieva et al, 1985, or 1983). Figures 3 and 4 show the distribution of chloride ion concentration with respect to elevation for the southern and northern sections, respectively. In these Figures the vertical bars represent the lenght of the open liner segment in the wellbore. In spite of the large uncertainties in the elevation of the production zones, it is clear that the chloride ion concentration increases with depth.

In the northern part of the field there is a clear inverse correlation between the concentrations of chloride ion and carbon dioxide (Figure 5). For the southern section, there is a trend of increasing carbon dioxide concentration with increasing elevation of the production zone (Figure 6). This last correlation excludes the cases of wells A-18 and A-26, both of which are located in the southeast extreme of the field, and which show several chemical deviations from the general pattern; among these anomalies is the high gas content of the produced fluids, high concentration of calcium ion in the brine, etc.

DISCUSSION

The observations presented above could be summarized by the statement that, in Los Azufres, the concentration of a volatile species (such as carbon dioxide) is higher in the upper levels of the two phase zone of the reservoir, while the concentrations of the less volatile species (such as chloride ion and oxygen-18) increase with depth. The simplest and most reasonable explanation for this set of observations is the occurrence of a process of upflow of steam; the condensation of a fraction of this steam continually dilutes the concentration of the non-volatile species, while the volatile species are continually transported to the upper levels.

The deuterium results corroborate the above model for the southern section of the field. The inverse correlation between the concentrations of deuterium and oxygen-18, which is shown in Figure 7, indicate that the concentration of deuterium (a "volatile" species at the reservoir temperature) decreases with depth. The slope of the fitted line is consis-

TABLE 2. TOTAL DISCHARGE COMPOSITION AND CALCULATED EXCESS STEAM AND COMPOSITION OF RESERVOIR LIQUID PHASE FOR WELL A-17.

		COMPOSITION					
		TOTAL DISCHARGE			RESERVOIR LIQUID PHASE		
DATE OF SAMPLE	STEAM ESCESS (%)	X_{CO_2} x1000	$\delta^{18}O$	δD	X_{CO_2} x1000	$\delta^{18}O$	δD
6 684	17.8	20.7	-	-	1.6	-	-
10 884	7.8	13.9	-	-	2.4	-	-
23 485	13.8	20.1	-4.94	-60.7	2.0	-4.75	-61.2
26 685	8.8	19.3	-4.76	-62.5	3.1	-4.64	-62.8
11 985	47.8	61.0	-5.30	-58.2	1.9	-4.63	-59.9
91085	13.5	26.1	-4.89	-63.9	2.8	-4.70	-64.4
27 286	6.0	15.3	-4.52	-64.8	3.4	-4.44	-65.0

tent with an average temperature of the ascending steam of 230°C to 245°C. The occurrence of this process of steam upflow and partial condensation is in agreement with predictions based on the model for vapor dominated systems proposed by White et al (1971).

In the northern part of the field the distribution with depth of the studied species is the same as in the southern section, except for the case of deuterium. Figure 8 shows the direct correlation between the concentrations of deuterium and oxygen-18. If the steam upflow were the only process responsible for the observed chemical and isotopic heterogeneity of the reservoir fluid, it would be necessary to postulate that the average temperature of the ascending steam is less than 220°C or higher than 375°C, which is inconsistent with measured temperatures. Thus, it is concluded that some other process is also intervening, perhaps the mixture of two hydrothermal fluids.

ACKNOWLEDGEMENTS

The study described in this contribution was partially supported by Consejo Nacional de Ciencia y Tecnología de México, under contract PIT/EN/NSF/1810. The authors wish to express their indebtedness to Ing. Ramón Reyes, and much of the personnel of the Gerencia de Proyectos Geotermoeléctricos, Comisión Federal de Electricidad, for their support and assistance during the conduction of these studies. To Mrs. Ma. Eugenia Calderón for expertly typing the manuscript, to Mr. Adrián Patiño for drafting the figures, and to Departamento de Difusión for photographic assistance.

REFERENCES

Camacho, P. (1976) "Mapa preliminar del área geotérmica de Los Azufres, Mich. Comisión Federal de Electricidad, México, internal report.

TABLE 3. AVERAGE VALUES AND DEVIATIONS FOR CONCENTRATIONS OF ^{18}O, DEUTERIUM, CHLORIDE ION AND CARBON DIOXIDE IN THE LIQUID PHASE OF THE RESERVOIR. ELEVATIONS OF PRODUCTION ZONES.

	$\delta^{18}O$		δD		CHLORIDE (ppm)		MOLAR FRACTION OF CO_2 x 1000		ELEVATION (masl)
WELL	AVE. VALUE	AVE. DEV.	AVE. VALUE	AVE. DEV.	AVE. VALUE	AVE. DEV.	AVE. VALUE	AVE. DEV.	
A- 5	-3.66	0.02	-64.3	1.0	641	23	4.31	0.56	1432
A- 6	-5.54	0.40	-61.0	1.2	-	-	4.95	0.55	2065
A-13	-2.45	0.08	-61.6	0.7	941	7	2.48	0.41	1710
A-16AD	-3.52	0.27	-61.4	1.0	579	19	2.03	1.20	1968
A-17	-4.67	0.09	-62.7	1.5	-	-	2.48	0.51	2210
A-18	-3.32	0.22	-64.8	1.2	1002	29	7.31	1.04	1756
A-19	-3.32	0.24	-61.7	1.3	1241	44	1.56	0.67	1160
A-22	-2.64	-	-66.7	-	1877	-	1.96	0.33	1300
A-26	-2.00	-	-62.9	-	1770	-	5.68	0.50	1665
A-28	-2.51	0.21	-61.0	1.4	1587	4	0.65	0.22	1180
A-32	-2.64	-	-57.9	-	-	-	3.38	0.50	1380
A-33	-	-	-	-	-	-	2.71	-	2150
A-34	-	-	-	-	-	-	2.92	-	2085
A-35	-	-	-	-	-	-	1.57	-	1625
A-36	-	-	-	-	-	-	1.84	0.70	1840
A-37	-	-	-	-	-	-	0.29	0.25	1875
A-38	-4.21	-	-64.1	-	-	-	2.70	1.11	2120
A-46	-	-	-	-	-	-	1.55	0.17	1827

Cathelineau, M., Oliver, R. and Nieva, D. (1987) "Quaternary volcanic series of the Los Azufres geothermal field (México)". Geofísica Internacional, in press.

Cathelineau, M. and Nieva, D. (1985) "A chlorite solid solution geothermometer for the Los Azufres (México) geothermal system". Contrib. Mineral. Petrol. 91, 235-244.

Cathelineau, M., Oliver, R., Nieva, D. and Garfias, A. (1985) "Mineralogy and distribution of hydrothermal mineral zones in Los Azufres (México) geothermal field". Geothermics 14, 49-57.

D'Amore, F. and Celati, R. (1983) "Methodology for calculating steam quality in geothermal reservoirs". Geothermics 12, 129-140.

Giggenbach, W.F. (1980) "Geothermal gas equilibria". Geochim. Cosmochim. Acta 44, 2021-2032.

Giggenbach, W.F. and Quijano, L. (1981) "Estudio isotópico de las aguas del Campo Geotérmico de Los Azufres". Manuscript.

Iglesias, E., Arellano, V., Garfias, A., Miranda, C. and Aragón, A. (1985) "A one-dimensional vertical model of the Los Azufres, México, geothermal reservoir". Proc. Tenth Workshop on Geothermal Reservoir Engineering, Stanford University, pp 241-246.

Nieva, D., Iglesias, E., Arellano, V., Contreras, E., Cathelineau, M. and Quijano, L. (1986) "Developments in geothermal energy in Mexico - Part four: evaluation of geothermal resources. Multidisciplinary studies of the Los Azufres field, México". J. Heat Recovery Systems 6, 201-207.

Nieva, D., González, J. and Garfias, A. (1985) "Evidence of two extreme flow regimes operating in the production zone of different wells from Los Azufres". Proc. Tenth Workshop on Geothermal Reservoir Engineering, Stanford University, pp 233-240.

Nieva, D., Quijano, L., Garfias, A., Barragán, R.M. and Laredo, F. (1983) "Heterogeneity of the liquid phase, and vapor separation in Los Azufres (México) geothermal reservoir". Proc. Ninth Workshop on Geothermal Reservoir Engineering, Stanford University, pp 253-260.

Nieva, D., Fausto, J., González, J. and Garibaldi, F. (1982) "Flow of vapor into the production zone of Cerro Prieto I wells". Proc. Fourth Symp. on the Cerro Prieto geothermal field, Baja California, México. Vol. 2, pp 455-461.

Santoyo, E., Verma, S.P., Nieva, D. and Portugal-Marín, E. (1986) "Anomalous changes in the chemistry of gases discharged from the Los Azufres geothermal field - possible precursors of the 19 September 1985 earthquake (Ms = 8.1) in southern Mexico". Manuscript under revision.

Truesdell, A.H., D'Amore, F. and Nieva, D. (1984) "The effects of localized aquifer boiling on fluid production at Cerro Prieto". Trans. G.R.C. 8, 223-229.

Truesdell, A.H., Nathenson, M. and Rye, R.O. (1977) "The effects of subsurface boiling and dilution on the isotopic compositions of Yellowstone thermal waters". J. Geophys. Res. 82, 3694.

White, D.E., Muffler, L.J.P. and Truesdell, A.H. (1971) "Vapor-dominated hydrothermal systems compared with hot water systems". Econ. Geology 66, 75-97.

FIGURES

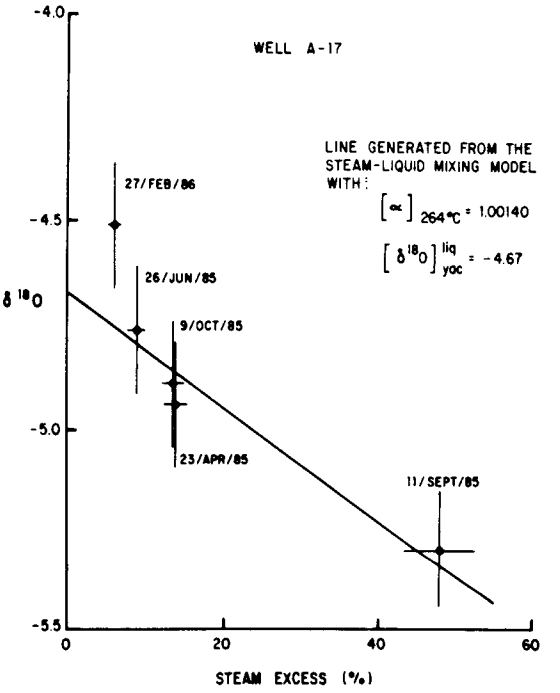


FIGURE 1. Concentration of oxygen-18 vs steam excess in total discharge. The straight line was drawn with equation 1, and the parameter values specified in the Figure.

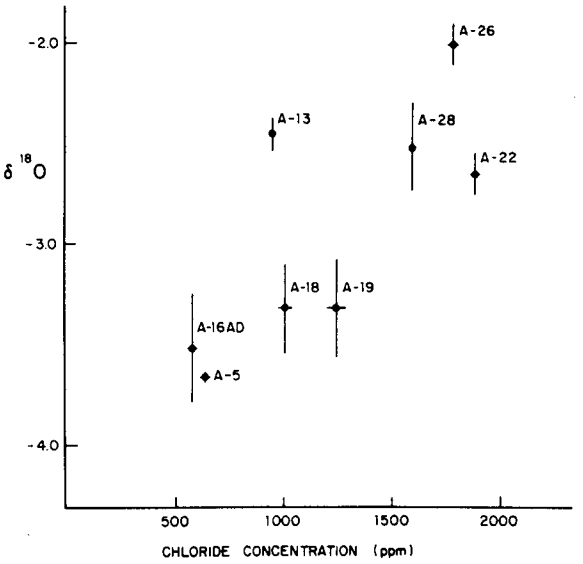


FIGURE 2. Concentration of oxigen-18 vs concentration of chloride ion. Lenght of error bars represents twice the average deviation from the mean for the corresponding parameter.

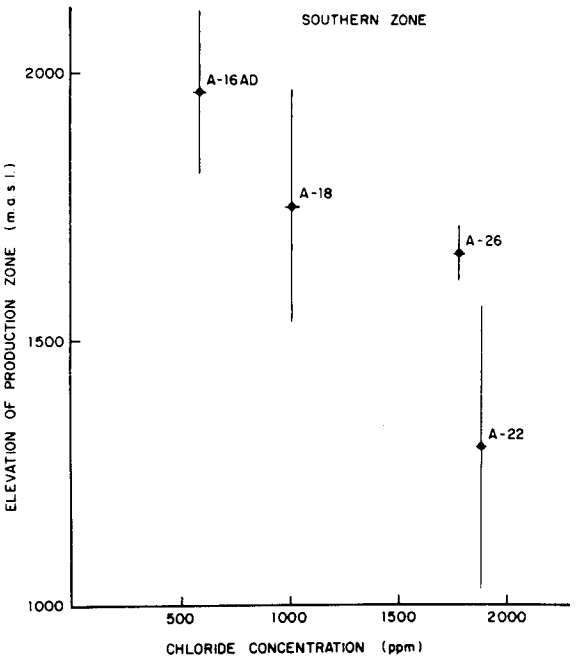


FIGURE 3. Elevation of production zone vs concentration of chloride ion in the liquid phase of the reservoir. Horizontal lines are error bars and vertical lines represent the lenght of the open liner segment in the wellbore.

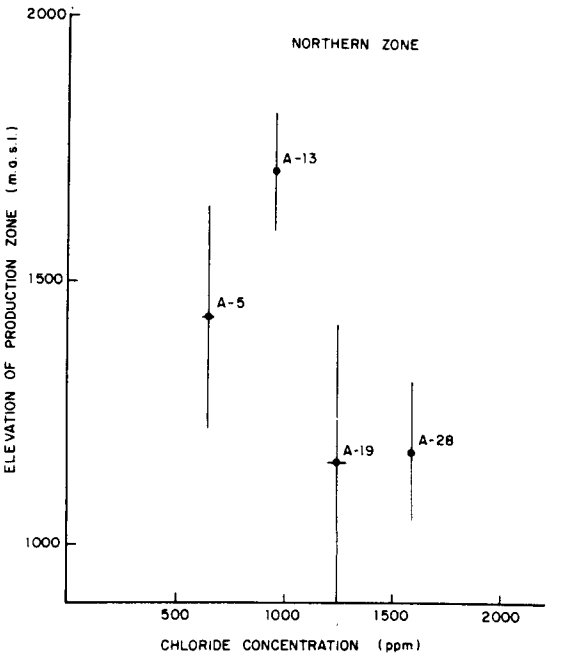


FIGURE 4. Elevation of production zone vs concentration of chloride ion in the liquid phase of the reservoir. Horizontal and vertical lines have the same meaning as in Figure 2.

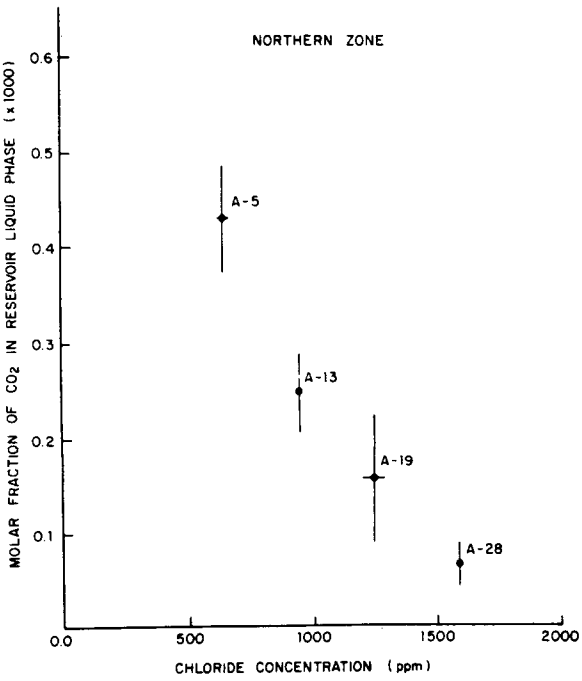


FIGURE 5. Molar fraction of carbon dioxide vs chloride ion concentration in liquid phase.

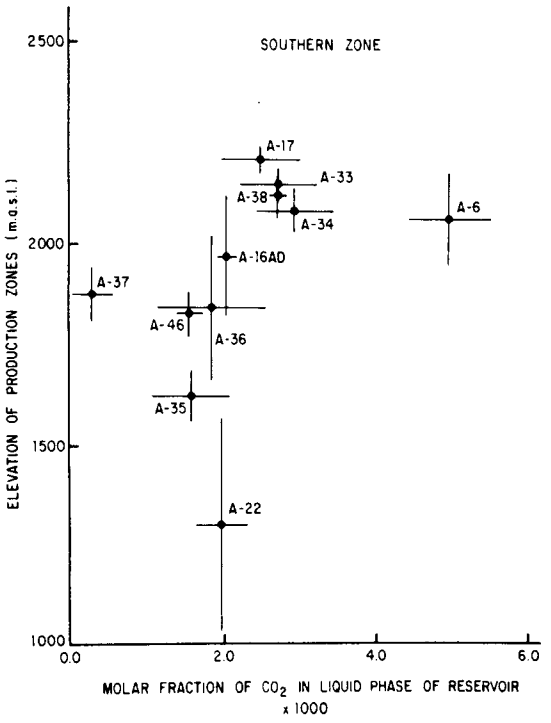


FIGURE 6. Elevation of production zone vs molar fraction of carbon dioxide in liquid phase.

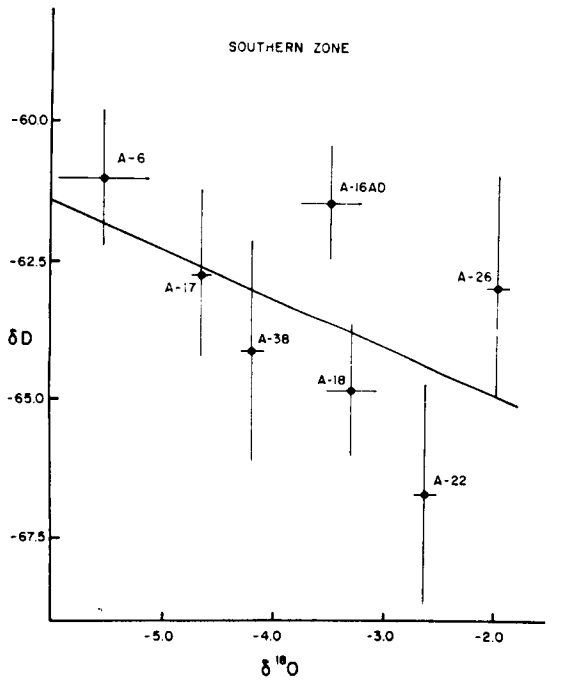


FIGURE 7. Concentration of deuterium vs concentration of oxygen-18 in reservoir liquid phase.

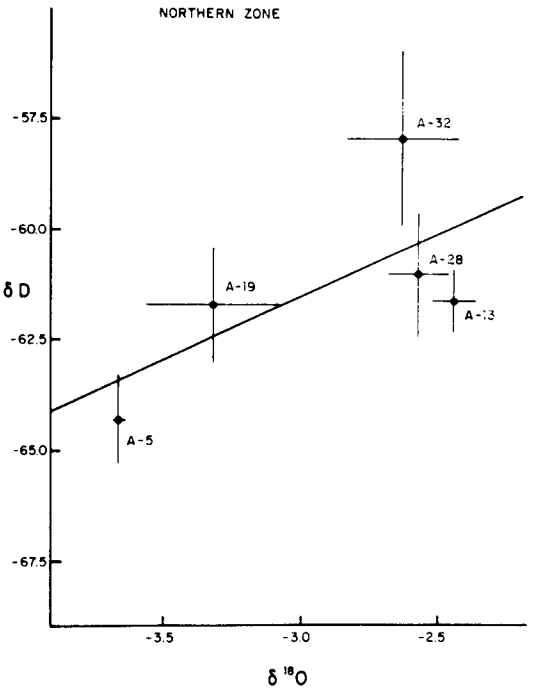


FIGURE 8. Concentration of deuterium vs concentration of oxygen-18 in reservoir liquid phase.

PROCEEDINGS, Twelfth Workshop on Geothermal Reservoir Engineering
Stanford University, Stanford, California, January 20-22, 1987
SGP-TR-109

GEOCHEMISTRY AND THE EXPLORATION OF THE NGAWHA GEOTHERMAL SYSTEM, NEW ZEALAND

D.S. Sheppard

Chemistry Division
DSIR, Petone, NEW ZEALAND

ABSTRACT

The Ngawha geothermal system is atypical of New Zealand geothermal systems, being located outside the Taupo Volcanic Zone, and contained in tight sedimentary structures. Early geochemical surveys of surface discharges indicated a high gas, high borate fluid, discharging in small quantities, to the surface. An initial well (drilled in the early 1960's, to 500m) produced a very gassy fluid before calciting. Deeper wells drilled and discharged in the early 1980's produced large flows of high gas fluid (up to 3wt%), at enthalpies around 1000 kj/kg. These low energy contents coupled with a low water to rock ratio, a very fractured structure, and consequent expected changes in the production fluid following exploitation, led to large scale exploitation plans being scrapped in 1982.

The close attention to geochemical studies before and during the drilling operations enabled predictions of fluid type, physical conditions at depth, fluid disposal problems, and hydrologic reservoir models that have proved to be correct. The project served to indicate the value of comprehensive exploration strategies which preceed the drilling phase, and the further value of, in particular, geochemical studies as an integral part of well testing procedures, for the updating of reservoir models. The close and open cooperation amongst the scientists and engineers involved was also of great value.

Location and Setting

The Ngawha (pronounced nah-fah, and meaning hot pool) Geothermal system is the only known high temperature geothermal system in New Zealand that is not within the Taupo Volcanic Zone, it being some 400km further to the north on the narrow Northland Peninsula (Fig. 1). The system is contained in a lithologic environment quite different from that in the TVZ, since it is hosted in greywackes and capped by marine sediments, rather than silicic volcanics.

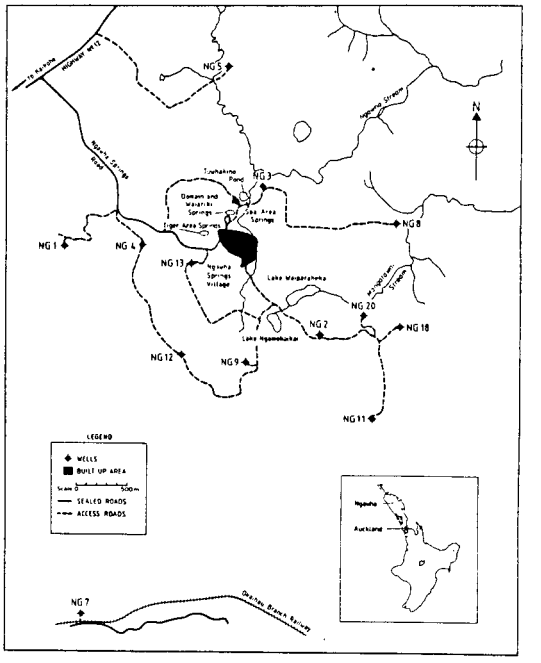


FIGURE 1: Location of the Ngawha system in the North Island, New Zealand.

The Ngawha geothermal system has its surface expression in a shallow basin eroded into claystones which have been locally overlain by lake sediments and Pleistocene olivine basalt flows (Fleming, 1945). Underlying the superficial deposits the claystones continue to depths of 500m, forming part of a Cretaceous-Tertiary allocthonous 'chaos breccia', containing also mudstones,

argillaceous limestones and coal measures, and of low bulk permeability. The breccia uncomformably overlies Waipapa Group greywackes and argillites which outcrop over much of the peninsula to the east; the contact zone itself tends to a coarse conglomerate which has a high permeability (Skinner, 1981).

The geothermal system occurs within a Quaternary-Holocene basaltic province which also contains at least four rhyolite centres, and an andesite dome, all probably emplaced in the Holocene.

The structural environment of the Ngawha area has been extensively discussed by Grindley (1981) and Skinner (1981), and most recently reviewed by Cox (1985). The geological and geophysical evidence suggests that the principle faults in the basement greywacke strike NNW, while the lineations of springs and other surface features have a NE alignment.

Thermal Features

The surface expression of the Ngawha system covers a wide area, but is of low intensity with few hot features. The Ngawha springs village is sited adjacent to a score or so of warm and hot pools which have a very limited liquid outflow (<2 1/s deep fluid). The dominant flow through the surface is of gas, and the outflow of this gas is very much more extensive.

The springs at Ngawha were well known to the Maori people; the earliest recorded European encounters were largely concerned with the mercury mineralisation associated with the thermal features. Small scale mining has been persued on several occasions, but the deposits proved to be superficial, and of limited extent. Interest in the thermal features themselves gave rise to some analyses (Park, 1906) and a comprehensive descriptive narrative by Bell and Clarke (1909). Water temperatures up to 66°C have been commonly recorded, although higher temperatures under the pools are easily located. The smell of hydrogen sulphide in the area of the baths is frequently quite strong, but it was only after a detailed survey in 1944 (Fleming, 1945), that the high boron content of the waters was discovered. Since then there have been several thorough chemical and isotopic surveys, reported by Ellis and Mahon 1966), Giggenbach and Lyon, (1977), and also a monitoring of the discharges during exploration, summarized in Sheppard and Johnston, (1984), and Sheppard, Giggenbach and Johnston (1985).

These surveys showed that the fluids arising in the Ngawha system differ in a number of significant ways from all other New Zealand systems, and have only a few similar analogues throughout the world. While the salinities of Ngawha waters are similar to the TVZ systems, they are higher in ammonia, bicarbonate and borate, relative to chloride (Table 1). The gases are composed primarily of CO_2, and also have comparatively high concentrations of CH_4 (2-3 mol %) and about 1 mol % H_2S (Table 2). The isotopic compositions of the waters shows a very large $\delta^{18}O$ shift (+11‰) with respect to the local metoric water, and a smaller but possibly significant δD shift of -5‰.

The deep well drilling programme began in the early 1960's with the drilling of the 591m deep NG1; in the period 1978 to 1983 a further 14 wells were drilled, mostly to depths about 1200m, but finishing with in the well NG13 to 2333m. Most of these wells have been discharged, but for short periods only, due to the limited ability to dispose of large quantities of discharge fluid. Sampling tended to be intensive, to compensate. In addition, the early wells (NG1, NG2, NG5, NG7) either would not discharge, or sealed due to calciting. The next well discharged, NG4, discharged at more than 500 tonne/hour, which surprised all associated with the field. Usual production fluid temperatures were between 220 and 230°C (i.e. enthalpies about 1000 kj/kg. The bottom temperature in NG13 exceeded 300°C.

Geochemical Models of the field

Most of the data and results of investigations into the Ngawha system are freely avalable, and this allows an assessment of the predications made by the various disciplines at the various stages of the exploration programme. Most such studies were undertaken by the New Zealand Department of Scientific and Industrial Research, and are published in two of their Geothermal Report Series, Numbers 7 (1981) and (1985).

Until the report of Ellis and Mahon (1966) the local basalt flows were assumed to be the heat source and mineralisation source for the fluids

Source	T °C	pH*	Li	Na	K	Rb	Cs	Mg	Ca	NH_3 mg/kg	SiO_2	B	F	Cl	SO_4	HCO_3	$\delta^{18}O$ ‰	δD ‰	CO_2 Wt%
NG 4	224	5.7	11.7	891	77	0.27	0.65	0.09	2.5	111	399	929	1.8	1260	40	271	5.8	-35	0.85
NG 8	209	5.6	9.5	762	69	0.29	0.66	0.40	6.8	222	363	762	1.4	1054	28	394	4.7	-35	1.39
NG 11	225	5.8	10.4	876	78	0.31	0.73	0.13	2.5	100	394	877	1.5	1211	25	458	5.6	-36.5	1.23
NG 18	220	5.3	9.7	818	69	0.26	0.64	0.16	5.4	293	357	844	1.1	1155	29	258	4.8	-36.1	2.37
Jubilee Bath	46	7.4	7.4	621	49	0.20	0.51	1.5	13.7	90	154	603	1.3	831	145	260	-	-	-
Tiger Bath	45	2.4	0.5	125	10	0.05	0.07	4.3	13.5	62	107	40	0.32	162	745	-	-	-	-
Omapere Soda Spring	30	6.6	0.16	58	9	0.03	0.015	13.0	36	2.9	140	6	0.15	15	<10	325	-	-	-
Latera 2	-	-	9.4	2223	318	2.4	4.3	1.6	19	22	368	274	-	2853	390	-			2-4
Latera 30	-	-	13	2796	495	4.2	7.0	0.3	3.2	5	359	571	-	2942	1394	-			2-4
Geysers																			
Clear Lake	42	6.6	0.51	125	22	-	-	144	155	-	163	19	37	78	1	1310			
Calistoga Geyser	100	8.4	1.9	193	8.7	-	-	-	25		150	12	.01	206	13	184			

TABLE 1: Compositions of reservoir and spring fluids from the Ngawha field and other fields. Data from Sheppard, 1984; Sheppard et al., 1985; Carella et al., 1986; Thompson, Sims, Yadav and Rymer, 1981; Thompson, Goff and Donnelly-Nolan, 1981. Well fluids corrected to preflash compositions.

(Bell and Clarke, 1909; Fleming, 1945). By 1966 the experiences gained in the exploitation and exploration of geothermal systems in general had led to the realisation that such was unlikely to be a significant source of heat. Ellis and Mahon, on the basis of the fluid compositions, notably the constant value of Cl/B over the field, argued for a larger heat source, and they postulated a magma injected at a deep level into the sediments underlying the field, releasing water by dehydration, also the other volatiles boron, ammonia, bicarbonate (as CO_2), and chloride, by leaching. The well fluids showed a quartz equilibration temperature of 228°C (close to measured temperatures), and a high gas content in the deep water, this gas having a high (7%) hydrocarbon content.

On the basis of more chemical data from the spring waters and gases, and also water and gas isotope measurements, Giggenbach and Lyon (1977) were able to model the system in more detail (Fig. 2). The essential inferences made from this set of data were:

- that there is an extensive layer of warm, shallow water at about 145°C.
- that the rising thermal waters are subject to processes preventing chemical geothermometers set at depth being preserved, implying a very slow upflow of liquid.
- rather higher temperatures at depth (>360°C) are indicated by the sulphate isotope geothermometer, while gas phase isotope geothermometers indicate temperatures between 200 and 260°C over the centre of the field, and possibly much higher temperatures at greater depth.
- that Ngawha is a gas-rich system.
- there is a low liquid water content, and vapour transport of volatiles at greater depth e.g. B.

Subsequent investigations have resulted in but minor amendments to this model of the upper, central part of the system, apart from the realisation that structural features

Source	CO_2	H_2S	NH_3	He	H_2	Ar	O_2	N_2	CH_4
	millimoles/mole total gas								
NG 4	948	10.5	9.0	0.004	2.81	0.002	<0.002	2.5	27.6
NG 8	949	7.5	12.0	0.005	3.65	-	<0.002	2.9	25.3
NG 11	961	13.4	3.3	0.004	2.02	0.0052	<0.002	1.9	18.0
NG 18	935	6.9	7.4	0.009	7.09	-	<0.028	4.7	38.8
Jubilee Bath	907	2.2	0.03	0.007	8.28	0.043	0.024	11.9	70.8
Tiger Bath	913	1.8	0.03	0.008	2.03	0.010	0.010	10.9	71.9
Omapere Soda Spring	969	0.39	0.067	0.003	0.001	0.032	0.56	18.2	11.4

TABLE 2: Compositions of selected steam samples from wells and pools. Data from Sheppard et al., 1985.

provided vertical and horizontal permeability barriers, resulting in vertical stratification of vapour-rich, two phase fluid from more dense fluids, with mainly gas percolating upwards through structural features of higher permeability (Giggenbach and Sheppard, 1980). This predication has been confirmed by subsequent interference testing on wells (Grant and McGuiness, 1985).

A number of other observations made over this period required explanation. These observations include:

- the observation of Ar^{40}/Ar^{36} in NG2 at 310 to 315 (ie above the atmospheric ratio), which can be taken to indicate long residence time and a very limited access of meteoric water to the system. High He contents, and high gas contents in general support this observation.
- the large $\delta^{18}O$ shift indicates low water/rock and limited water throughput.
- the high nitrogen content of ther gases, usually interpreted as being an indicator of magmatically derived fluids.
- the observed small but significant variations in chemical and isotopic parameters across the field (as determined in the 230°C production fluid) showing

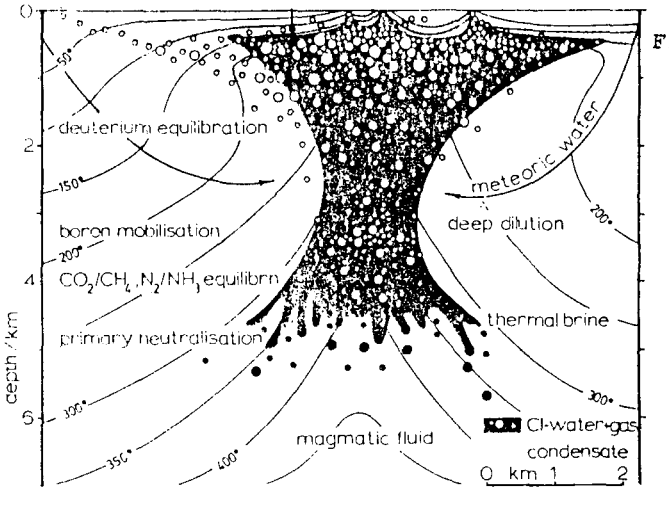


FIGURE 2: Hydrologic model of the subsurface system at Ngawha. Figure from Giggenbach and Lyon, 1977.

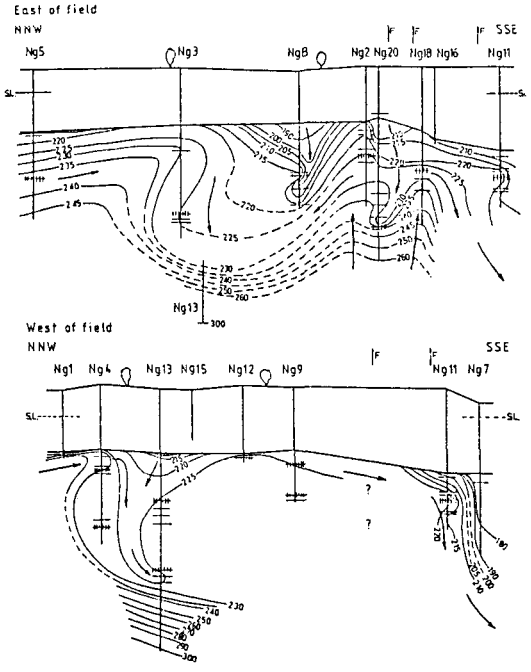


FIGURE 3: NNW-SSE profiles of downhole temperatures, representing the characteristics of the east and west sides of the field. Main feeds are indicated by ++++, inferred fluid flow directions are shown by arrows. Figures from Cox, 1985.

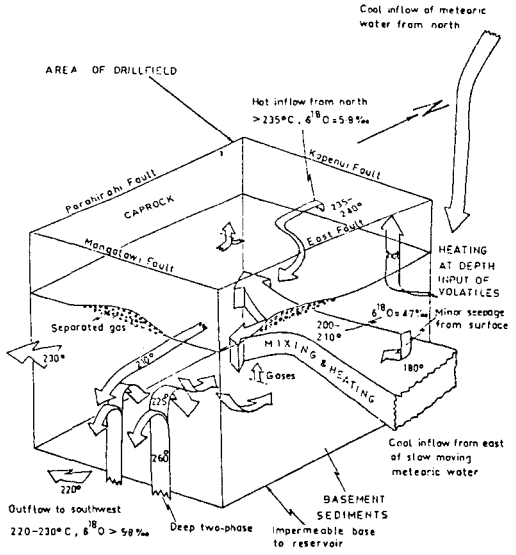


FIGURE 4: Three dimensional block diagram of the Ngawha drillfield, displaying the inferred main hydrological features. From Cox, 1985.

increasing dilution by meteoric water toward the eastern field margin.

- the large interval of near constant temperature with depth between 220 and 240°C, 500 to 1500m depth.

Grant (1981) postulated an upflow over a recirculating, gas depleted reservoir. While this concept is at odds with chemical indicators showing that the reservoir water has had gas added rather than extracted, the large constant temperature reservoir may well be the result of a recirculation process, but with gas being added from below. Cox (1985) has more recently assessed available data from a number of disciplines and has presented the flow models of the system shown in Figures 3 and 4. If this model of the present state is valid, it must explain the observations listed above, particularly those requiring low meteoric water throughput. An explanation for this could be that the fluid presently in the system largely predated the thermal event, which has mobilised the fluid, and that the thermal event was quite recent.

It is clear that there exist higher temperatures at easily accessable depths beneath the explored field. Other fields do exist in the world with the shallow structures and similar chemistry to the Ngawha fluid. These are the Geysers field, in California; Larderello and Latera in Italy (Table 1). All of these fields have large, extensive steam fields at depth. Does Ngawha?

REFERENCES:

Bell, J.M. and Clarke, E. de C. 1909 The geology of the Whangaroa subdivision, Hokianga division. Bull. N.Z. Geol. Survey, No. 8.

Carella, R., Guglielminetti, M., Luccioli, F. and Manetti, G. Development of the Latera field (Italy). Paper presented at 8th N.Z. Geothermal Workshop, University of Auckland.

Cox, M.E. 1985. Geochemical examination of the active hydrothermal system at Ngawha, Northland, New Zealand: Hydrochemical model, element distribution and geological setting. PhD Thesis, University of Auckland.

Fleming, C.A. 1945. Hydrothermal activity at Ngawha, North Auckland. N.Z.J. Sci. Technol. v pp255-276.

Giggenbach, W.F. and Lyon, G.L. 1977. The chemical and isotopic composition of water and gas discharges from the Ngawha geothermal field, Northland. Unpub. DSIR Geothermal Circular, CD 30/555/7 WFG.

Giggenbach, W.F. and Sheppard, D.S. 1980. The chemical composition of water and gas discharges from wells 2, 4 and 9 at Ngawha, Northland, New Zealand. DSIR Unpub. CD Report 30/555/7.

Grant, M.A. 1981 Ngawha geothermal hydrology. in The Ngawha Geothermal Area. DSIR Geothermal Report 7, pp60-86.

Grant, M.A. and McGuiness, M.J. 1985 Hydrology in The Ngawha Geothermal Field: new and updated scientific investigations. DSIR Geothermal Report 8 pp 179-216.

Grindley, G.W. 1981. Geological history and structure of the Ngawha area. in The Ngawha Geothermal Area, DSIR Geothermal Report 7, pp7-13.

Park, J. 1906. Thermal activity in its relation to the genesis of certain metalliferous veins. Trans. N.Z. Inst., v38, pp20-39.

Sheppard, D.S. and Johnston, J.R. 1984. Ngawha hot springs; results of a chemical monitoring programme.

Sheppard, D.S., Giggenbach, W.F. and Johnston, J.R. 1985. A listing of chemical and isotopic analyses on waters and gases from the Ngawha geothermal system and environs. DSIR CD Report 2359.

Skinner, D.N.B. 1981. Geological setting and subsurface geology of Ngawha. in The Ngawha Geothermal Area, DSIR Geothermal Report 7, pp14-35.

Thompson, J.M., Sims, J.D., Yadav, S. and Rymer, M.J. 1981. Chemical compositions of water and gas from five nearshore subaqueous springs in Clear Lake. in Research in the Geysers-Clear Lake geothermal area. USGS prof. Paper 1141 pp 215-218.

Thompson, J.M., Goff, F.E. and Donnelly-Nolan, J.M. 1981. Chemical analyses of waters from springs and wells in the Clear Lake volcanic area. in Research in the Geysers-Clear Lake geothermal area. USGS Prof. Paper 1141 pp 183-192.

PROCEEDINGS, Twelfth Workshop on Geothermal Reservoir Engineering
Stanford University, Stanford, California, January 20-22, 1987
SGP-TR-109

STRUCTURE, PERMEABILITY AND PRODUCTION CHARACTERISTICS OF THE HEBER, CALIFORNIA GEOTHERMAL FIELD

E. D. James, V. T. Hoang, I. J. Epperson

Chevron Resources Company
San Francisco, California

ABSTRACT

The three key permeability elements of the Heber reservoir are; "capping" clays above 1800', a sedimentary "matrix permeability" reservoir from 1800'-5500', and fracture permeability in indurated sediments below 5500'. The fractures are related to NW trending strike-slip faults and NE trending normal faults. Maps and cross sections with dipmeter, lost circulation, temperature and Kh data illustrate the structures and their control on the movement of thermal waters. Production creates a strong initial pressure decline in the field that rapidly stabilizes. The long-term pressure decline is predicted to be low (less than 5%). Temperature data show that current development is north of the source of the thermal plume. Reservoir modeling indicates that reservoir pressures will support further development.

INTRODUCTION

This paper presents data gathered by Chevron in the Heber geothermal reservoir between June, 1984 and December, 1986 during development drilling, initial well testing and the first year of production of the Dravo 52 MW dual flash plant and the SDGE 67 MW binary plant. Fifteen wells had been drilled during the exploration and evaluation phases of work at Heber (Figure 1). Beginning in 1984, nine production wells and seven injection wells were drilled for the Dravo plant and seven production wells and five injection wells for the SDGE plant. In addition, two temperature gradient wells (GTW 4 & 6, Figure 1) were drilled in 1986 to assess the development potential of the southern portion of the field.

Prior to the development drilling, the Heber reservoir was thought to be a fairly homogeneous pile of deltaic sediments, with porosity and permeability decreasing with depth according to the normal induration effects. Production was expected to come from primary matrix permeability of the sediments (Cooper and Salveson, 1982 and Lippman and Bodvarsson, 1983). The development wells were designed to produce fluid from four 2000' thick zones to balance withdrawals over the entire depth range of the sedimentary reservoir. However, the results of the development work show that the reservoir has three major permeability units (Figure 2); "capping" clays from 500-1800', high matrix permeability sandstone "outflow" reservoir from 1800'-5500', and high permeability "feeder" faults and fractures in indurated sediments below 5500'.

This revised reservoir model is being used in planning future development well locations.

RESERVOIR CHARACTERISTICS

The key permeability elements of the Heber reservoir can be seen on the seismic line in Figure 3. The capping clays stand out as strong reflectors from above approximately 1800'. The shallow sedimentary reservoir is represented by the reflectors seen down to approximately 5500'. The poorly reflective zone below 5500' represents the heavily indurated sediments. These sediments are cut by two fault trends; a NW trending right lateral strike-slip zone and a NE trending normal fault on the west. This structural and permeability setting is repeated to the north through the heart of the field as shown by the dipmeter data from the wells on cross section A-A' (Figure 4).

The structural control on permeability is also evident on a map of lost circulation (Figure 5). Here we see that the NW striking right lateral strike slip fault and NE trending normal fault are clearly outlined by the lost circulation contours. These trends of faulting are to be expected in the Salton Trough, repeating the patterns of regional faulting shown on Figure 6.

The temperature distribution of the field illustrates the control that the permeability structure and regional groundwater flow have on the movement of thermal fluids. Temperature isotherms at 6000' (Figure 1) show that the center of the rising thermal water movement is in the southern portion of the field. The maximum temperature measured in the field to date is 390F. Temperature cross section A-A' (Figure 7)

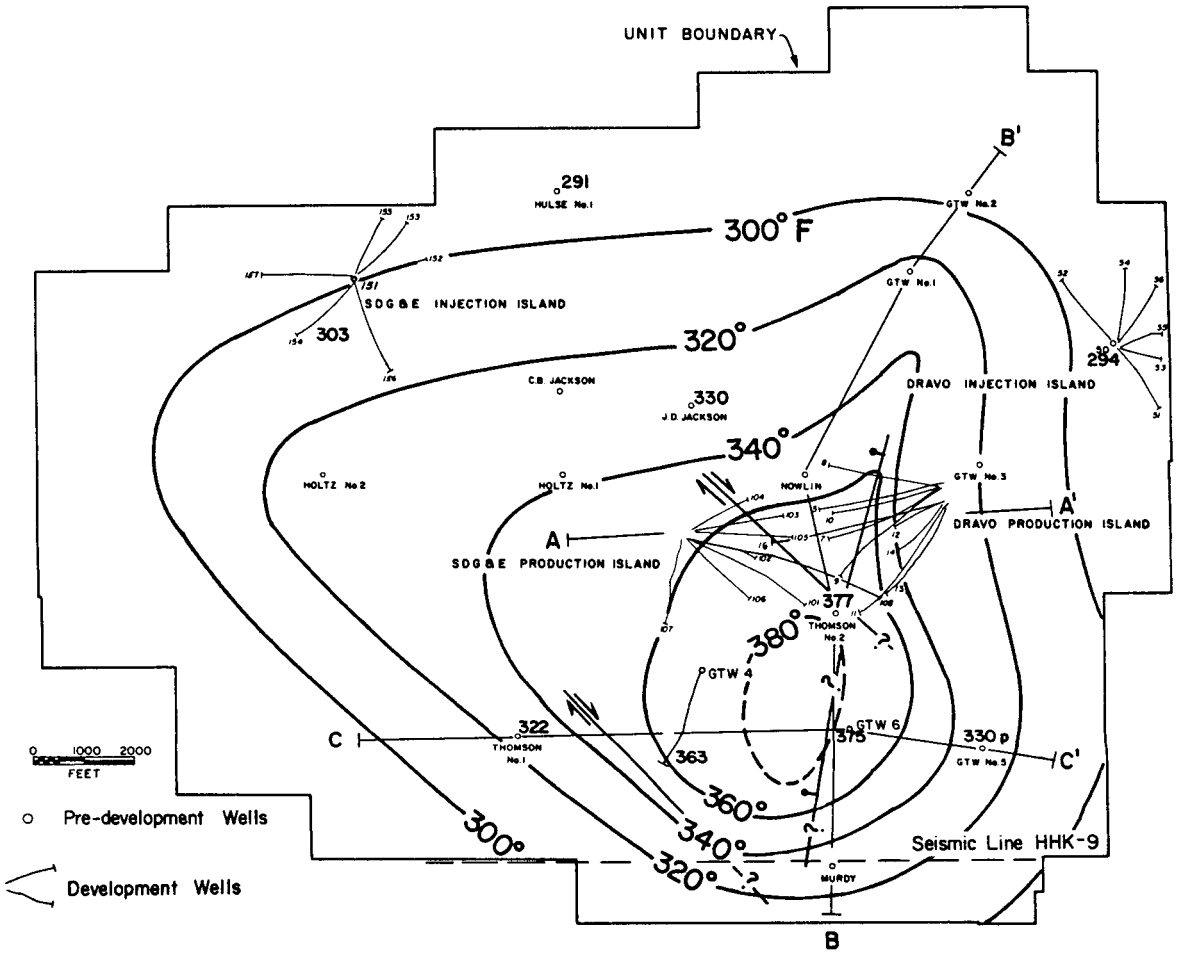


Figure 1. Well locations, structure, and temperature contours at 6000 feet.

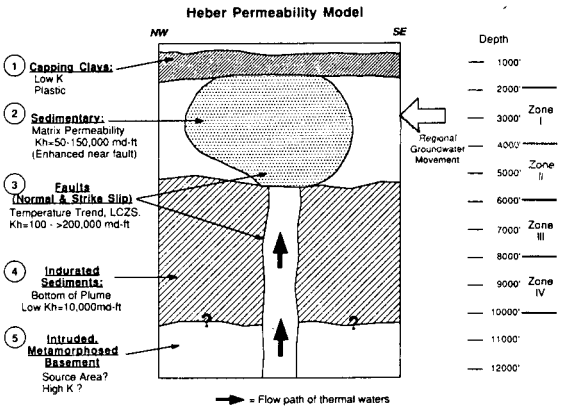


Figure 2. Heber permeability model.

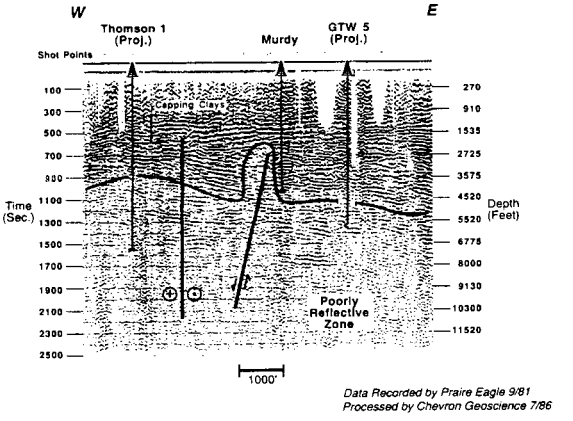


Figure 3. Seismic line HHK-9.

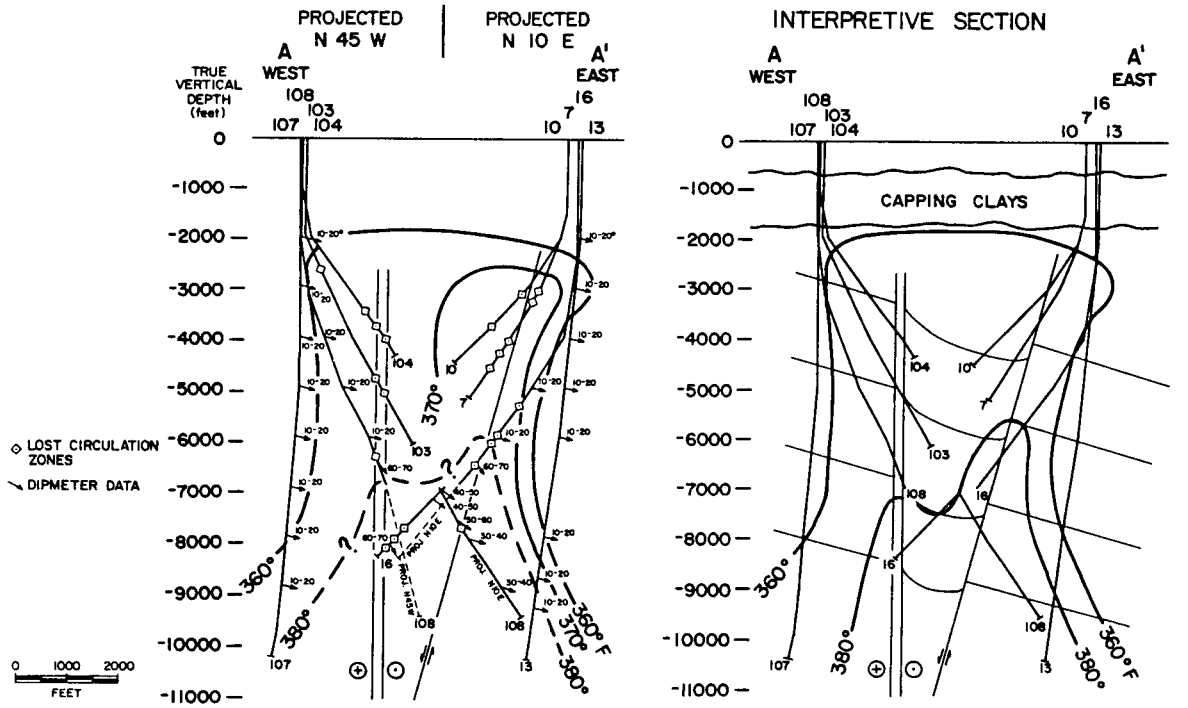


Figure 4. Cross section A-A'. Production wells, temperatures, structure, and lost circulation zones.

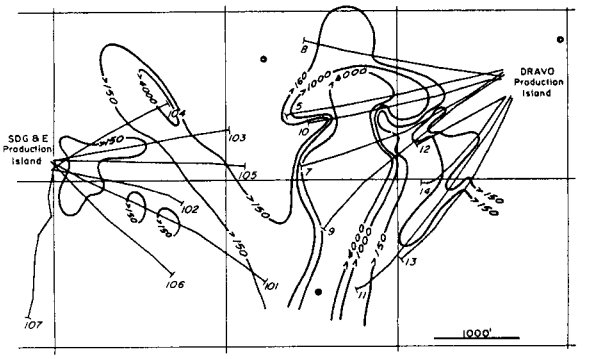


Figure 5. Mud losses (barrels/day) during drilling in Zones I and II.

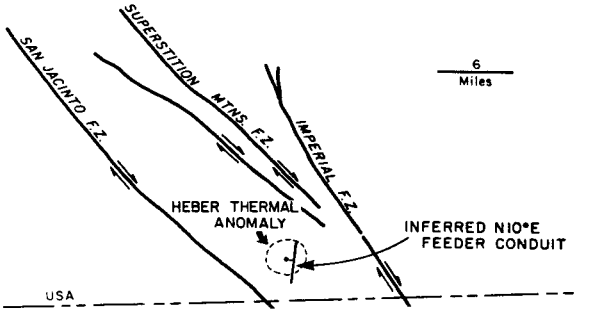


Figure 6. Fault trends in the Heber region showing N10°E feeder conduit in relation to srike-slip structures.

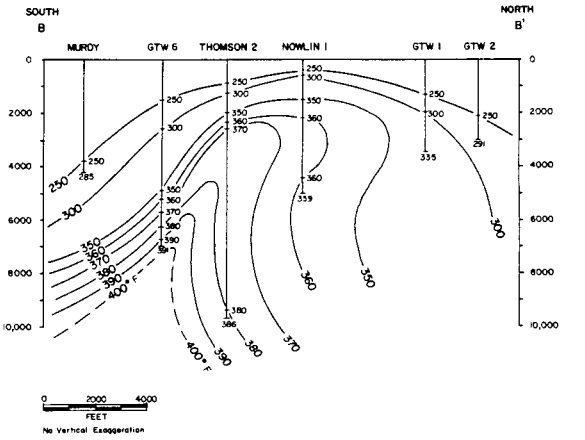


Figure 7. Temperature cross section B-B'.

illustrates the deflection of the rising plume from south to north by groundwater movement. It is also clear from this section that the source of the thermal waters is south of current development near the GTW 6. The shallow matrix reservoir currently under production is at the northern end of the plume. The collapse of the isotherms at the top of the plume is the result of the capping clays sealing in the thermal waters. The strong control of the fracture permeability in the indurated sediments below 5500' is seen in temperature cross section B-B' (Figure 8). The plume is quite narrow east to west and most likely

controlled by a narrow structure of high permeability.

The range of Kh (permeability-thickness) values calculated from well test data is indicative of the different sources of permeability in the Heber reservoir. Values in Zone I (2000'-4000', Figure 9) range from 40-80,000 md-ft in the sedimentary reservoir to 120-140,000 md-ft in the strike slip fault to over 200,000 md-ft in the normal fault. The values in Zone II (4000'-6000', Figure 10) are generally lower, reflecting the increasing induration of the sedimentary section.

The sources of permeability are also clearly seen in spinner surveys taken while the wells are producing. The production from the matrix permeability of the sedimentary section is evenly distributed over the entire open interval (Figure 11). Production from fractures comes in very short intervals (Figure 12). The interplay between matrix and fracture permeability explains the wide range of Kh's seen in the well testing.

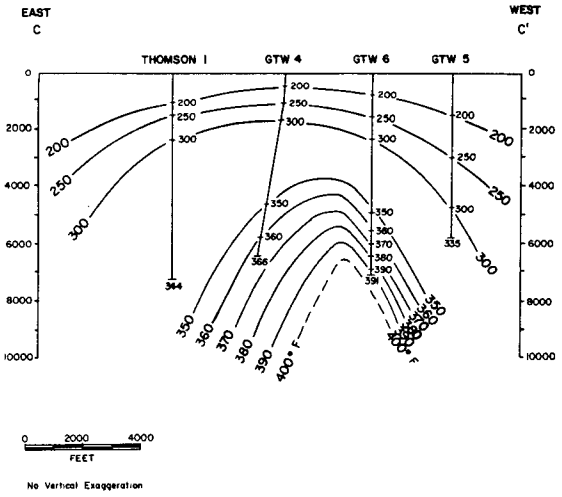


Figure 8. Temperature cross section C-C'.

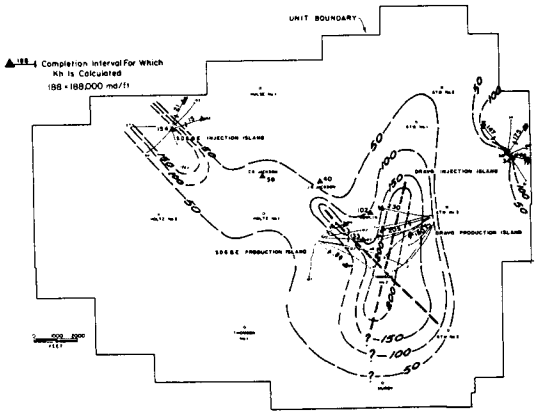


Figure 9. Zone I Kh (1000's millidarci-feet).

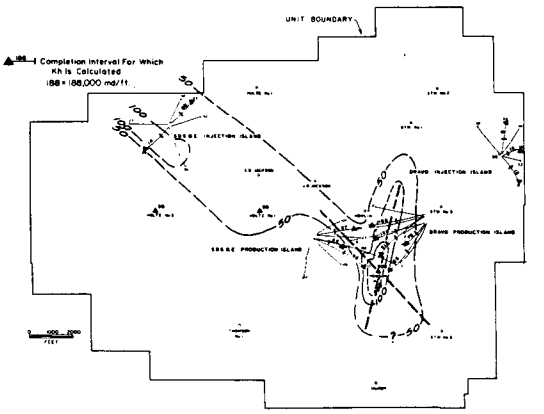


Figure 10. Zone II Kh (1000's millidarci-feet).

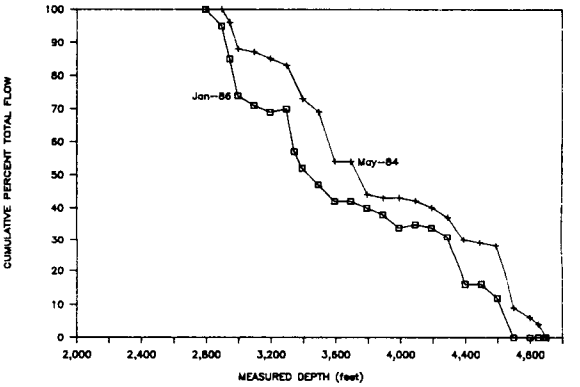


Figure 11. Production spinner surveys from well with sedimentary matrix permeability.

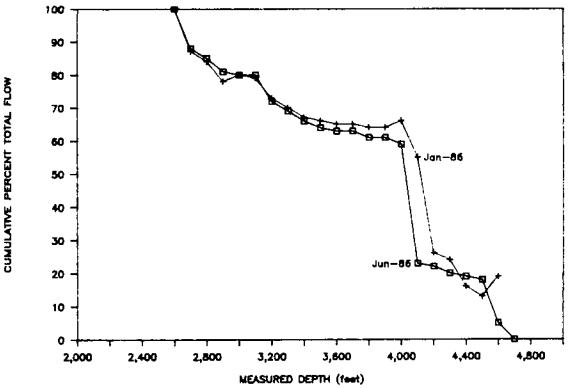


Figure 12. Production spinner surveys from well with fracture permeability.

PRODUCTION CHARACTERISTICS

The productivity index of the wells is closely related to the Kh as calculated from well testing (Figure 13). The most productive wells are completed in the shallow matrix reservoir but are also connected to the fracture system.

The reservoir pressure and production from the wells show a very sharp decline that rapidly stabilizes when the field is brought under full production (Figure 14). The pressure drop created by 50 MW of production is on the order of 80 psi at the observation wells near the center of production. The initial startups of the Dravo and SDGE plants at Heber were staggered and the effect of each plant on the reservoir pressure is clearly seen. The rapid stabilization of pressures indicates the reservoir is very permeable and is strongly supported by the regional aquifer.

A reservoir model was constructed to help predict the pressure behavior of the field and to assess the impact of further development on current production capacity. The permeability model presented in the first section of this paper served as the base of the model. The effect of the regional aquifer support was simulated by using constant pressure boundaries at the edge of the model.

The match to historical data is shown on Figure 14. There is excellent agreement with the data collected. The model predicts very little pressure decline (0-less than 5%) overtime. Additional production will cause an initial pressure drop of similar magnitude to that seen with the present production and pressures will quickly stabilize to the slow decline rate according to model results.

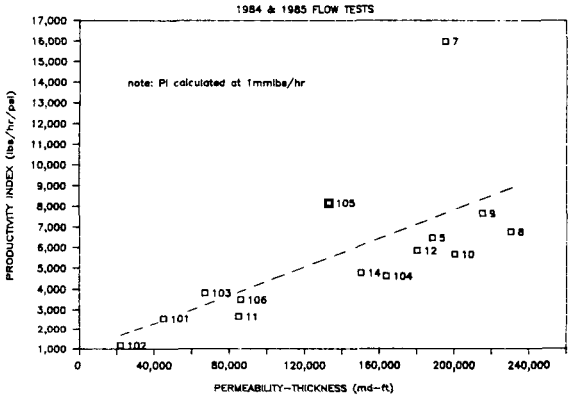


Figure 13. Kh vs productivity.

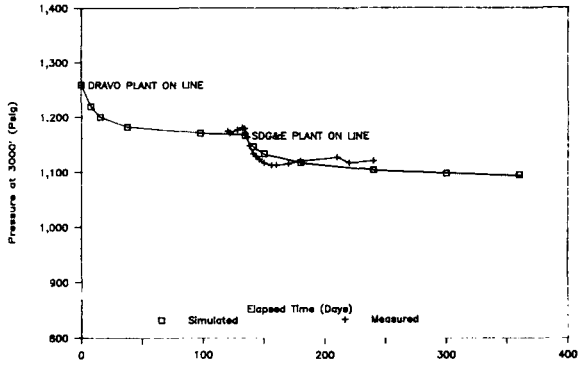


Figure 14. Reservoir pressure at 3000 feet.

CONCLUSIONS

The movement of thermal fluids in the Heber reservoir is controlled by matrix permeability in the shallow sedimentary zone from 1800'-5500' and fracture permeability along NW striking strike-slip faults and NE striking normal faults in indurated sediments below 5500'. Wells produce from both zones giving a range of Kh values from 40,000-200,000 md-ft. Pressures decline steeply under initial production but stabilize rapidly due to regional aquifer support. Decline rates are very low (0-less than 5%).

There is significant opportunity for additional development in the Heber reservoir. Temperature gradient wells drilled in 1986 show that the deep source of the thermal anomaly is south of current production. Modeling suggests that pressure support is adequate for further production.

ACKNOWLEDGEMENTS

This paper is dedicated to the late Mr. A. M. Cooper. His unflagging belief in the future of geothermal energy created the opportunity for the Heber field to be developed. Many ideas presented in this paper were first developed by Mr. E. B. Layman. The authors also would like to thank Chevron Resources Company and Union Geothermal for permission to publish.

REFERENCES

1. Salveson, J. O, and Cooper, A.M., 1979. Exploration and Development of the Heber Geothermal Field, Imperial Valley, California. Geothermal Resources Council Trans., Vol. 3, p. 605-608.

2. Lippman, M.J., and Bodvarsson, G.S., 1983. A modeling study of the Heber Geothermal Field, California. Geothermal Resources Council Trans., Vol. 7, p. 441-448.

PROCEEDINGS, Twelfth Workshop on Geothermal Reservoir Engineering
Stanford University, Stanford, California, January 20-22, 1987
SGP-TR-109

RESULTS OF DEEP DRILLING IN THE WESTERN MOAT OF LONG VALLEY CALIFORNIA

Gene Suemnicht

Unocal Geothermal Division
P.O. Box 6854
Santa Rosa, CA 95406

ABSTRACT

Long Valley caldera has been explored for its potential geothermal resources for at least two decades. Unocal Geothermal drilled two deep test wells on the resurgent dome of the caldera during 1979. Neither of these wells encountered a deep, high temperature geothermal reservoir. The results from these wells and other geologic data focused exploration on the western caldera moat. Encouraging temperature gradient data in 1982 led to the drilling of a deep test well in 1985. That well, IDFU 44-16, encountered deep temperature reversals and a sequence of rocks unlike the previous penetrations on the resurgent dome. Evidently the well is still within the ring fracture system of the caldera and not within a central, upwelling, hydrothermal system which supplies the caldera's discharge.

INTRODUCTION

Long Valley caldera, located in eastern California (figure 1), has been an important geothermal prospect since the 1960's. Numerous public and private exploration efforts have been directed toward assessing the caldera's geothermal potential. After an extensive geothermal research program in the early 1970's, Muffler and others (1978) estimated the initial resource potential of Long Valley at 2100 mw (e). The caution to this assessment was that a "full understanding of the Long Valley geothermal system and an accurate determination of its geothermal resource potential must await a series of deep wells" (Muffler and Williams, 1976). Of the four deep wells drilled within the caldera since 1976, Unocal has drilled three of these. Much of the data from two earlier wells had been released in 1981. The emphasis in this paper is on the results of Unocal's most recent deep test well drilled in 1985 in the western caldera moat.

GEOLOGY

Long Valley caldera resulted from the eruption of an estimated 600 km^3 of Bishop Tuff (Bailey and others, 1976). The majority of the erupted material is thought to have filled the 17 x 32 km depression left by the foundering of the caldera's floor. Smaller but significant volumes of post caldera eruptions have continued to fill the caldera over the last 600,000 yrs. The 500 year old eruptions of the Inyo volcanic chain are the most prominent surficial evidence of an active magmatic system in Long Valley.

The hydrothermal system of Long Valley caldera has varied through time (Bailey and others, 1976; Sorey and others, 1978). From 300,000 to 130,000 years ago the caldera supported an intense hydrothermal system which produced widespread hydrothermal alteration in and around the resurgent dome. The current hydrothermal system has probably been active for only the last 40,000 yrs. (Sorey, 1984). Most of the present surficial manifestations are found in the central portion of the caldera with as much as 80% of the current hydrothermal discharge occurring at Hot Creek on the southeastern edge of the resurgent dome (Sorey and others, 1978). Geochemical estimates of reservoir source temperatures range from 200°C to 280°C (Sorey and others, 1978; Fournier and others, 1979).

EARLY EXPLORATION

The first geothermal wells in the caldera were drilled in the 1960's around the hot springs and fumaroles at Casa Diablo (figure 2). These wells were generally less than 300 m deep and produced 170°C fluids at rates >60 kg/s from a shallow aquifer beneath Casa Diablo. By 1976 one deep well had been drilled east of the resurgent dome to a depth of 2.1 km. The maximum temperatures encountered were less than 80°C which did not encourage further exploration in the eastern caldera.

Unocal's early drilling efforts were directed toward assessing lease offerings on the caldera's resurgent dome. Two deep test wells were spud during the 1979 exploration season. One of these wells, Clay Pit-1, was drilled near the center of the resurgent dome (figure 2) to a depth of 1.85 km and encountered bottom hole temperatures of 148°C (figure 3). A second well, Mammoth-1, was drilled at Casa Diablo (figure 2) to a

depth of 1.6 km to test for a potential deep source of the hot springs. The temperature profile from this well revealed a complex aquifer system (figure 4). The maximum temperature was 169°C at 100 m, slightly lower than the productive aquifer at Casa Diablo. A deeper temperature peak occurs at 1 km within the Bishop Tuff; however, at 151°C it cannot be the deep source of the shallow production zone. Mammoth-1 also drilled 200 m into metamorphic basement rocks from 1.4 km to the well's total depth of 1.6 km. The temperature gradient in the lowest portion of the basement section was 9.1°C/km however the bottom hole temperature was only 100°C. The source of Casa Diablo's shallow production did not appear to be located directly beneath the surface springs.

RECENT EXPLORATION

Since 1979 Unocal's exploration efforts have concentrated on the western part of the caldera where data were sparse and no surface manifestations exist. A deep temperature gradient hole, designated 82-9, was drilled to 1.06 km near the Inyo Craters (figures 2 and 5) to evaluate new lease offerings in the western caldera moat. The bottom hole temperature in this well was 221°C, within the range of temperatures predicted for the ultimate source of the hydrothermal system of Long Valley.

Based on these results Unocal acquired leases in the western caldera and drilled a deep test well in 1985 in the western caldera moat (figure 2). That well, Inyo Domes Federal Unit 44-16, was drilled on the same site as 82-9 to a total depth of 1.8 km on the first penetration. A second penetration was attempted because of potential formation damage from mud drilling on the first hole. The side-track was drilled from 1 km to 1.68 km.

GEOLOGIC DATA

The geology of IDFU 44-16 is summarized in figure 6. This well drilled the same sequence of post caldera fill found in the 82-9 gradient hole and entered Bishop Tuff at a depth of 915 m. The well remained in Bishop Tuff for only 250 m and encountered a section of dacites and andesites from 1168 m to 1616 m. These rocks probably correlate with the pre-caldera volcanics of San Joaquin ridge on the west rim of the caldera (Bailey and others, 1976; Bailey and Koeppen, 1977). At a depth of 1616 m the well entered metamorphic basement. These rocks were calc-silicate hornfels similar to Paleozoic roof pendants exposed to the south and west in the Sierra Nevada.

Three cores were cut in the lower part of the well in the intervals from 1350 m to 1352 m, from 1596 m to 1603 m and from 1797 m to 1798 m. Analysis of the cores indicated none of the unfractured rock had permeabilities to air greater than .01 md. The maximum measured porosity was 10.5% in a fractured, argillicly altered andesite from 1599 m.

RESERVOIR DATA

Temperature data from IDFU 44-16 are also shown on figure 6. After attaining temperatures of 220°C at a depth of 1.1 km, the temperatures reverse by 93°C. The reversal occurs at the base of the Bishop Tuff at the contact with the underlying volcanics. In the lower portion of the well, beneath the Bishop Tuff, temperatures increase to 192°C and then reverse again to a bottom hole temperature of 181°C.

The pressure profile of the well (figure 7) suggests a water level at approximately 183 m. This is consistent with a relatively flat and deep water table inferred for the western caldera by Sorey and others (1978) and Farrar and others (1985) from water levels measured in shallow core holes.

The second penetration of IDFU 44-16 was completed with a slotted liner to total depth of 1687 m. Slotted intervals occur at 1012 m to 1073 m, 1101 m to 1336 m, 1364 m to 1437 m, 1465 m to 1490 m, and 1518 m to 1548 m. The perforation intervals were selected from a combination of drilling and well log data which suggested fractured or potentially permeable sections of the well. The perforations exposed the lower portion of Bishop Tuff, the hottest section of the wellbore and all of the potential reservoir rock below the Bishop Tuff.

Attempts were made to stimulate production on the second penetration of IDFU 44-16. The well was blown dry to a depth of 879 m through open-ended drill pipe and air was circulated continuously for 18 hrs in an attempt to lessen the hydrostatic head in the wellbore. During this time, the well flowed in a series of 20 minute to 60 minute slugs, but would not sustain the flow without stimulation. A total of approximately 2 wellbore volumes (~1000 bbls) was produced during the test attempts.

An injection test began immediately after the attempt at producing the well. In five hours, a total of 2830 bbls of water were pumped into the wellbore at zero wellhead pressures. Evaluation of pressure recovery after injection indicated a permeability of 20,000 md ft for the reservoir section exposed by the well. Temperature and pressure data from the injection test (figure 8) indicate the highest permeabilities probably occur at the base of the Bishop Tuff.

INTERPRETATION

IDFU 44-16 established the existence of the

western ring fracture system at least as far east as the Inyo Craters. The rocks in the lower section of the wellbore represent pre-caldera basement displaced at least 1.5 km down from the western caldera wall. Some of the displacement may be the result of pre-caldera faulting. IDFU 44-16 encountered only 250 m of Bishop Tuff while Mammoth-1 drilled through 862 m and Clay Pit-1 drilled through 1085 m. Evidently the Bishop Tuff draped over some pre-existing topography before foundering to its current level during caldera subsidence.

IDFU 44-16 established that permeability exists in the deep intracaldera fill of Long Valley. Permeability in the upper part of the well is apparently related to stratigraphic changes and the hottest part of the well is confined to the Bishop Tuff. Temperature reversals in the upper part of the well occur in the most permeable zone at the contact with the pre-caldera volcanics underlying the Bishop Tuff. In contrast, permeability in the lower section of the wellbore appears to be related to fracturing. Core analysis indicates the unfractured pre-caldera rocks are virtually impermeable yet some hydrothermal circulation must occur in the pre-caldera volcanics since the temperatures in that section reach 192°C (figure 6) and temperatures after injection indicate fluid losses in that part of the wellbore (figure 8). Mud log data indicates that fluid entries, gas kicks and temperature increases logged during drilling all occurred in discrete zones in the lower part of the wellbore and do not have an apparent relationship to stratigraphic changes in the pre-caldera volcanics.

The temperature regime in IDFU 44-16 is the result of outflow from a deep convecting geothermal system rather than upflow within the system. Isotopic data (Sorey and others, 1978; Fournier and Truesdell, 1979; Farrar and others, 1985) suggest the principal cold water recharge to the caldera occurs on the western caldera rim with discharge occurring at lower elevations to the east. In a manner similar to hydrologic models suggested by Blackwell (1985) the temperature peaks and reversals in IDFU 44-16 can be interpreted as evidence of warm thermal water floating over deeper colder recharge water from the caldera's western wall. The basement section of IDFU 44-16 shows some evidence of deep heating since the bottom hole temperature is 181°C, the highest in the caldera. Temperature reversals in the impermeable metamorphic basement rocks underlying the pre-caldera volcanics are probably related to deep cold water influx along a complex of pre-caldera or ring fracture faults. Through pre-caldera volcanics and into metamorphic basement rocks there is no evidence in the temperature profile of IDFU 44-16 for a deep upwelling hydrothermal system beneath the Bishop Tuff in this part of the western caldera moat.

ACKNOWLEDGEMENTS

I would like to thank Unocal's Geothermal Division for their permission to publish this manuscript. Cal Strobel deserves credit for much of the pressure transient analysis presented here. I am indebted to Foy Bailey, Mike Sorey and David Blackwell for many beneficial discussions which increased my understanding of Long Valley caldera.

REFERENCES

Bailey, R.A. and Koeppen, R.P., "Preliminary Geologic Map of Long Valley Caldera, Mono County California," USGS Open File Map 77-468.

Bailey, R.A., Dalrymple, G.B. and Lamphere, M.A., 1976, "Volcanism, Structure and Geochronology of Long Valley Caldera, Mono County, California," JGR, V 81, N 5.

Blackwell, D.D., 1984, "A Transient Model of the Geothermal System of Long Valley Caldera, California", USGS Open File Report 84-939.

Farrar, C.D., Sorey, M.L., Roistaezer, S.A., Janik, C.J., Mariner, R.H., Winnet, T.L. and Clark, M.D., 1985, "Hydrologic and Geochemical Monitoring in Long Valley Caldera, Mono County, California, 1982-1984," USGS Report Water Resources Investigations Report 85-4183.

Fournier, R.O., Sorey, M.L., Mariner, R.H., and Truesdell, R.H., 1979, "Chemical and Isotopic Prediction of Aquifer Temperatures in the Geothermal System at Long Valley, California," Journal of Volcanology and Geothermal Research, N 5.

Muffler, L.J.P. and Williams, D.L., 1976, "Geothermal Investigations of the U.S. Geological Survey in Long Valley, California, 1972-1973," JGR, V 81, N 5.

Muffler, L.J.P., 1978, "Assessment of Geothermal Resources of the United States-1978," USGS Circular 790.

Sorey, M.L., Lewis, R.E. and Omstead, F.H., 1978, "The Hydrothermal System of Long Valley Caldera, California," USGS Prof. Paper 1044-A.

Sorey, M.L., 1984, "Evolution and Present State of the Hydrothermal System in Long Valley Caldera," USGS Open File Report 84-939.

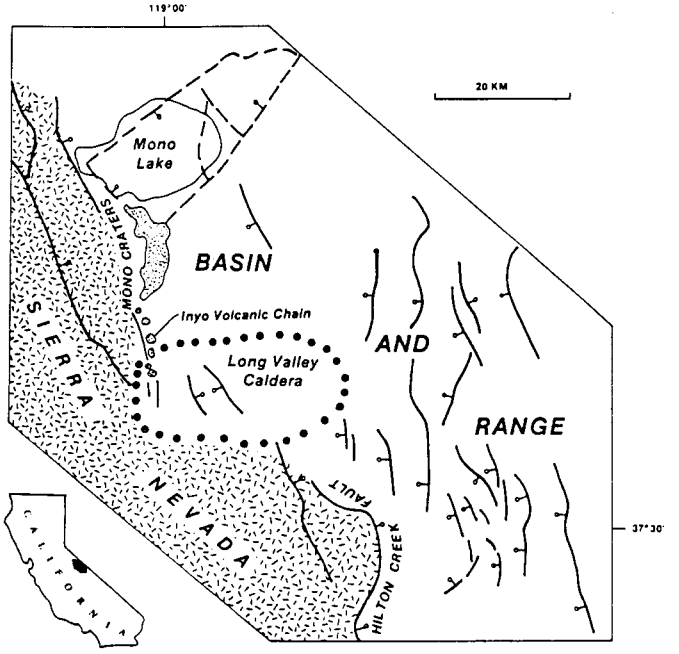


Figure 1. Index map and generalized geology of the Long Valley region

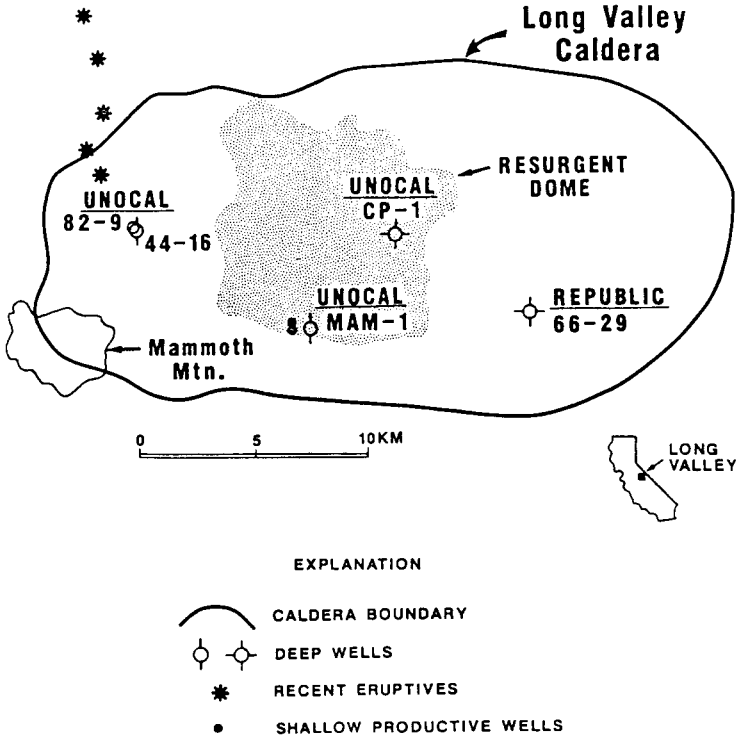


Figure 2. Generalized geology of Long Valley caldera

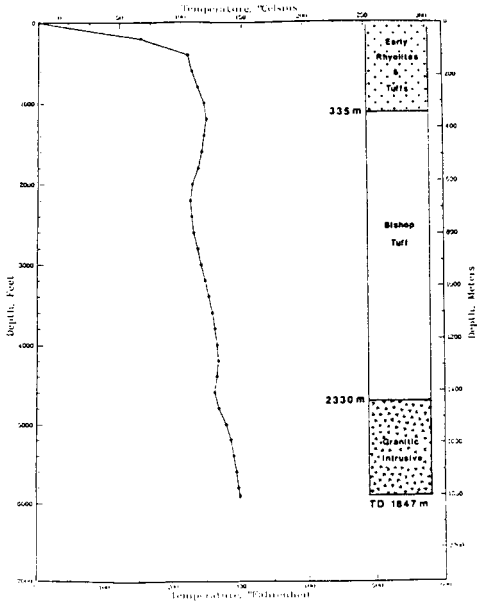


Figure 3. Clay Pit 1 temperature data

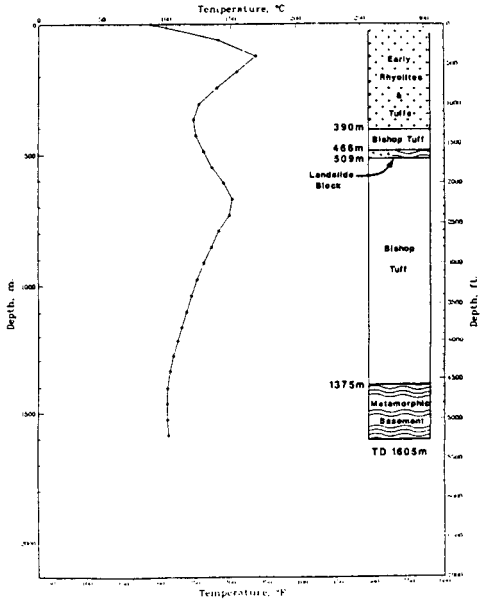


Figure 4. Mammoth 1 temperture data

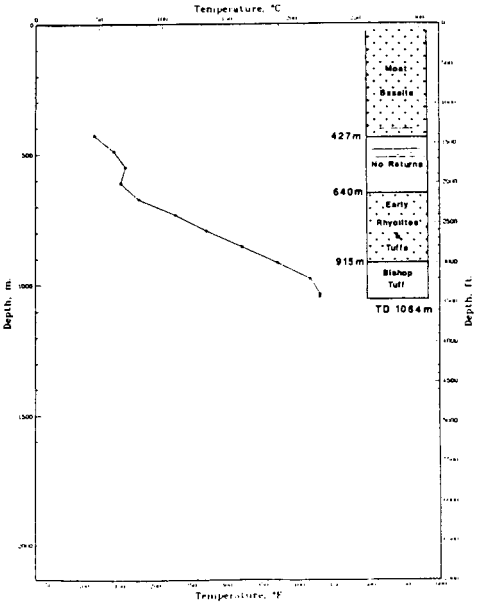


Figure 5. 82-9 temperature data

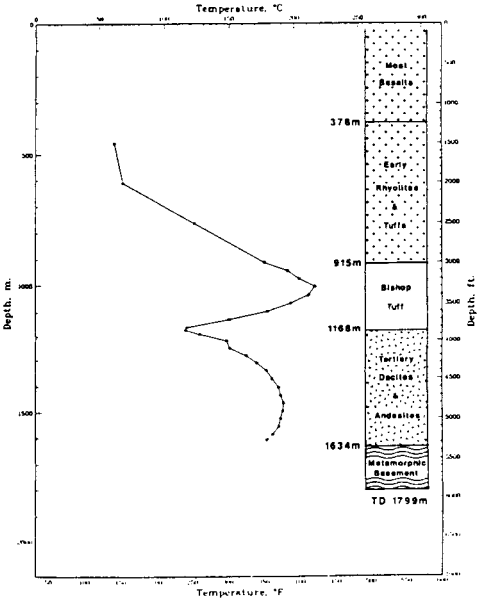


Figure 6. IDFU 44-16 temperature data

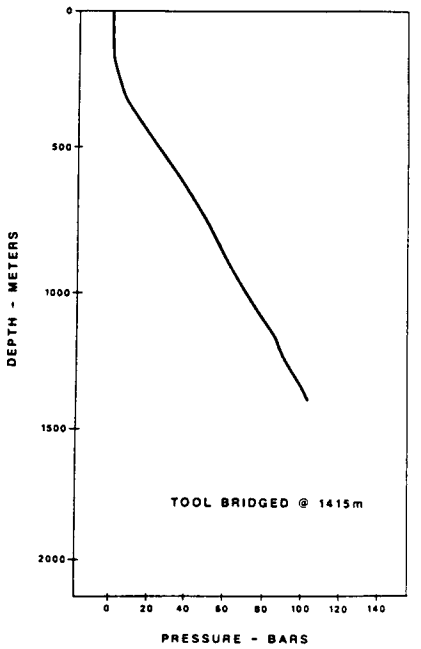


Figure 7. IDFU 44-16 subsurface pressure survey

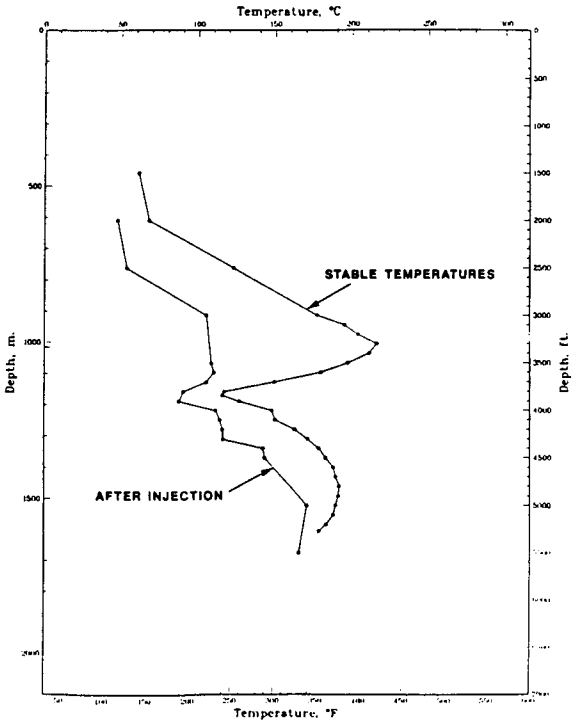


Figure 8. IDFU 44-16 temperatures before and after injection test

PROCEEDINGS, Twelfth Workshop on Geothermal Reservoir Engineering
Stanford University, Stanford, California, January 20-22, 1987
SGP-TR-109

GEOTHERMAL WELL STIMULATED USING HIGH ENERGY GAS FRACTURING

T. Y. Chu, R. D. Jacobson, N. Warpinski
Sandia National Laboratories
Albuquerque, New Mexico 87185

Henry Mohaupt
Servo-Dynamics, Inc.
Santa Barbara, California 93110

ABSTRACT

This paper reports the result of an experimental study of the High Energy Gas Fracturing (HEGF) technique for geothermal well stimulation. These experiments demonstrated that multiple fractures could be created to link a water-filled borehole with other fractures. The resulting fracture network and fracture interconnections were characterized by flow tests as well as mine back. Commercial oil field fracturing tools were used successfully in these experiments.

INTRODUCTION

Drilling is often a substantial fraction of the overall cost of a geothermal well. It may, therefore, be more economical to stimulate an under-productive well instead of redrilling a new well. Sandia National Laboratories, with funding from the U. S. Department of Energy has conducted studies on the use of High Energy Gas Fracturing (HEGF) techniques for geothermal well stimulation. By HEGF, we refer to any of the experimental and commercial techniques for inducing multiple, radial fractures in a wellbore using rapid pressure loading with propellants or explosives. A HEGF tool was originally developed at Sandia as a well stimulation technique for gas wells [2,3]. The geothermal applications represent an extension of this technology from gas filled to water filled boreholes.

Most HEGF techniques use propellants to pressurize a wellbore. With the right pressurization rate, they can produce multiple radial fractures emanating from a wellbore with typical fracture length up to 10 meters. Radial fractures in the non-hydraulic-fracture directions are most desirable for geothermal well stimulation since they are most likely to intersect the existing production fractures which typically run parallel to the hydraulic-fracture direction. While no detailed mappings are available to determine fracture spacings in a production field, field data show that typically production fracture spacings should be in the range of one to tens of meters. At the Geysers, production wells are known to be drilled as close as 3 meters from non-productive wells. HEGF will certainly be useful for fields where fracture spacing falls in the 1-10 meter range. Additionally, in our own study, [5], computer modeling of HEGF shows that HEGF is superior to hydraulic fracturing in correcting near wellbore damage.

The present study is a joint project between Sandia National Laboratories and Servo-Dyanmics, Inc. We are interested in evaluating the performance of commercial oil field fracturing tools for geothermal well stimulation. These tests were conducted in G-Tunnel, Rainier mesa, at DOE's Nevada Test Site (NTS). G tunnel is a tunnel system that is driven more than a mile into volcanic tuffs at a depth of about 425 m (1400 ft). It is ideal for fracturing experiments because it provides an in situ medium with appropriate boundary conditions (an isotropic stress field, no free surfaces) yet still allows detailed examination of the created fractures through mine back.

In a previous series of experiments in horizontal boreholes, we demonstrated the feasibility of producing multiple fractures in water filled boreholes [1,4]. However, because the tools used were relatively short, there were large end effects and multiple fractures were only observed in a portion of the test zone. Therefore, the present series of experiments were carried out in vertical boreholes using longer tools.

EXPERIMENTAL DESIGN AND PROCEDURE

The current series of tests were conducted in peralkaline ash fall tuffs of Tunnel Bed 5 of the Indian Trail Formation, which is approximately 30 m (100 ft) thick at the test location. Properties of these peralkaline tuffs are shown in Table I.

This work was supported by the U. S. Department of Energy at Sandia National Laboratories under Contract DE-AC-04-76DP00789.

They are usually soft, low modulus, low permeability and high porosity rocks and, as such, are well suited for mineback experiments since they allow for easy excavation with a continuous mining machine. The in situ stresses have been measured in the vicinity of these tests yielding an overburden stress of about 7 MPa (1000 psi) and horizontal stresses of about 3.4 MPa (500 psi) and 5.5 MPa (800 psi). The maximum horizontal stress (hydraulic-fracture) direction is S30°W.

Five vertical holes were cored into the the test drift. They are number 1 through 5. The layout of the hole pattern is shown in Figure 1. Because we were interested in observing fracture intersections and borehole to borehole interconnections, the borehole patterns were designed to facilitate the formation of fracture intersections.

Two holes (2 and 5) were placed along the hydraulic-fracture direction 4.5 meters (15 ft.) apart. Two more were located between 2 and 5, on either side of the line connecting the two, 2.4 meters (8 ft.) apart. A practice hole, hole 1, was located 3.0 meters (10 ft) down from hole 2, in the main drift direction (N42°W). The practice hole (1) was 17.4 meters (57 ft.) TD; the four test holes were 12.3 meters (42 ft) TD. The vertical displacement lessens the possible influence of practice shot in hole 1 on the rest of the tests. All holes, except hole 2 were open holes 9.60 cm (3.78 in.) in diameter. Hole 2 was cased with N80 casing and perforated, with 1.5 cm (0.6 in.) diameter perforation, 8 perf/ft with 90° phasing. Two sets of perforations were in line with the hydraulic-fracture direction, the other two perpendicular to it. Thus, hole 2 was designed to create fractures along the line connecting holes 2 and 5 and fractures perpendicular to this line. With this arrangement, we enhanced the probability of fractures from holes 3 and 4 intersecting the fractures from hole 2.

The experimental assembly consists of the propellant tool, the pressure transducer assembly, a rubber wiper above it and a cable tube. All the propellant tools used were 3.7 meters (12 ft.) in length. The Servo-Dynamics tools, trademark StressFrac tools, were used in holes 1-4; these are one piece solid propellants with a thin aluminum skin. There were three liner ignitors parallel to the axis of the tool. The reason for using three ignitors instead of one as in oil field tools was to insure ignition and to provide a way to control initial burning rates. Two sizes of StressFrac tools, one 6.4 cm. (2.5 in.) diameter with 16.6 Kgs (36.6 lbs) of propellant and one 7.6 cm (3.0 in.) diameter with 26.2 kgs (55.7 lbs) of propellant, were used. The Sandia tool was used in hole 5. This tool uses a 3 in. PVC tubing (8.26 cm, 3.25 in. I.D.; 8.89 cm, 3.50 in. O.D.) filled with a 50/50 mixture of M30A and M30B artillery propellant pellets; a RIP ignitor runs down the axis of the tool. The top of each tool is connected to the pressure transducer assembly with a 138 MPa (20k psi) pressure transducer to record the pressure/time history during the test and a crush gauge to record maximum pressure.

The tools were installed 0.3 meters (1 ft) above the bottom of the borehole. Upon installation of the tool, a sand tamp was formed above the wiper to within 15 cm of the collar to contain the gas pressure during the experiment. The test zone defined by the bottom of the sand tamp and the hole bottom was typically 4.4 meters (14.5 ft). Fifteen centimeters of a 50/50 mix of sand and sulfate-based cement at the collar insured containment of the stemming.

Core samples obtained during drilling were examined for existing fractures before the experiments. Some healed fractures were found, but there were no open fractures observed. Before each test, a TV log and a constant pressure permeability test were performed. During the test, pressure history and peak pressure were measured. Observations were also made of borehole-fracture interaction through video camera recordings. Before each shot, all the holes were filled with water. If interconnections were made during the shot between the test hole and any particular hole, water would be ejected from that particular hole, see for example Figure 2. Following each test, a TV log was used to examine the fracture patterns, Figure 3, and a constant flow test was performed to obtain the effective permeability of the borehole. Dyed water of different colors was used in the flow test to mark the fractures. In cases where borehole ejection occurred, permeabilities of holes other than the test hole were also measured after a shot to determine the effect of the shot on neighboring holes.

At the conclusion of all the shots, the test bed was mined back to examine the fractures in detail. To prevent the near wellbore fracture patterns from being damaged during mining, the patterns were potted in place by filling the borehole with grout. The grout was sufficiently fluid to also fill the near wellbore fractures. Mine back was accomplished by excavating a drift 38 feet below the test drift in the N11°E direction; centerline of the drift passed 0.76 meters to the right of hole 5 and 0.76 meters to the left of hole 2, Figure 1. The mineback drift was 3.7 meters (12 ft) by 3.7 meters (12 ft).

Each successive face corresponds to a vertical cross-section of the test bed, exposing the last 31 meters (10 ft) of the test zone and 0.6 meters (2 ft) beyond the bottom of the boreholes. Since the miner cuts typically a horizontal trough 0.5 meters high by 3.7 meters long by 0.5 meters deep, at each cut a strip of the "horizontal" section is also revealed.

RESULTS

The present test series is designated as GTSF86 and each test is identified by the hole number following the GTSF86 designation. The results of each shot are discussed in the sequence that the shots were made because the fracture patterns are significantly influenced by the fractures already existing at the time of the shot. Detailed fracture mapping is still under way at the present time. A composite schematic of the fracture network in the test zone is shown in Figure 4. TV logs show that in all the tests, fractures actually start to appear at about 2 meters above the test zone first in the hydraulic-fracture direction only. In cases where multiple fractures exist, the first occurrences were usually very near the top of the test zone; fracture width at the wellbore continues to increase downhole until the middle of the test zone.

EXPERIMENT GTSF-1

This was a practice test to help define the type of tool and pressurization rate that would be needed for the other holes. A StressFrac slow burning 6.4 cm diameter tool was used. The maximum pressure as recorded by the pressure transducer was 34.3 MPa (4970 psi); the value given by the maximum pressure crush gauge was 35.2 MPa (5100 psi). This close agreement is typical for all the shots; therefore, for subsequent shots only the valve obtained by the pressure transducer will be reported. The average pressurization rate, defined as the ratio of the maximum pressure to the pressure rise time (the time required to reach the peak pressure), was 9KPa/μs (1.3 psi/μs).

Hole 1 is outside of the mine back zone; no information on the fracture pattern is available. The TV log shows that the main fracture to be in the hydraulic-fracture direction with intermittent sections showing fracture initiation in the non-hydraulic direction. The fracture width at the wellbore was as wide as 4 centimeters.

EXPERIMENT GTSF-2

The second shot of the series was in hole 2, the cased/perforated hole, with an identical tool to the one used in hole 1. A peak pressure of 104 MPa (15,000 psi), was reached at an average pressurization rate of 110 Kpa/μs (16 psi/μs).

As designed, the shot produced fractures in the two principal stress directions, see Figure 4. The hydraulic fractures are the most prominent. The southern branch is fully exposed with a length at least 7 meters long. The northern branch should be of comparable length. In the direction perpendicular to the hydraulic fracture to the west, there is a short fracture of about 0.5 meters. The casing was found to be split on the east side along the perforation around 11 meters from the collar (the hole is 12.8 m TD) for about 0.5 meters. The split is as wide as 5 centimeters. Correspondingly, near the casing split the fracture going east of hole 2 is also quite wide, with a fracture aperture of about 0.6 centimeters wide as far as 0.5 meters away from the hole. The east-going fracture has not been mined back fully, but it appears to be turning south, possibly toward the hydraulic-fracture direction. The edge of this fracture can be traced at least as far as 3 meters along the east rib (sidewall) of the mine back drift.

On a more local scale, there appear to be two sets of fractures out of each perforation, one vertical and one horizontal. The horizontal fractures usually do not extend more than 0.3 meters beyond the borehole; the vertical one is distinct for each perforation. Due to a slight misalignment in the perforation shot, every other perforation is displaced from the neighboring one. Up to about one foot away, the edge of the fracture has the appearance of a sine wave with trough and valley corresponding to the perforation locations. These individual fractures eventually merge into a single fracture away from the hole.

EXPERIMENT GTSF-4

Hole 4 was shot with a 7.6 cm diameter StressFrac tool. A peak pressure of 10 MPa (10,150 psi), was reached at an average pressurization rate of 350 KPa/μs (51 psi/μs). During the test, water ejection was observed out of holes 2 and 5.

As many as six major fractures grow out of the borehole, Figure 4. A TV log shows that the fractures are about 5 to 7 centimeters wide near the borehole. Near the middle of the test zone, the circular borehole geometry is replaced by a star pattern (similar to Figure 3). The enlargement is not due to plastic deformation corresponding to borehole crushing rather, it appears to be caused by rock pieces detaching from the borehole as a result of fine fracturing near the borehole. This star pattern at the borehole is also typical of other holes with multiple fractures. Of the six fractures, two are in the hydraulic-fracture

direction, two toward the west, and two toward the east. One of the east running fractures intersects the hydraulic-fracture from hole 2. In this case, the advance of the fracture has been arrested at the intersection, Figure 5. This fracture intersection is the cause of water ejection at hole 2. There does not appear to be any direct link between holes 4 and 5 in the mine back zone. A TV log of hole 5 after the shot in hole 4 indicated a small localized fracture at about 9 meters corresponding to a healed fracture observed in the core samples of hole 5. Apparently, this fracture was reopened and caused the ejection out of hole 5.

EXPERIMENT GTSF-5

Following hole 4, hole 5 was shot with the Sandia tool. The peak pressure was 69.6 MPa (10,100 psi), 65.5 MPa (9500 psi) crush gauge; the pressurization rate was 33 KPa/μs (4.8 psi/μs). Water ejection occurred at holes 2 and 4.

Again there are as many as six fractures extending out of the borehole, Figure 4. The non-hydraulic fractures do not extend as far as those out of hole 4. Two of the fractures going east intersect the hydraulic fracture from hole 2. The northern branch of the hydraulic fracture from hole 5 runs very close to the southern branch of the hydraulic fracture from 2; at some depths (not throughout the entire depth of the test zone) they are probably merged. The southern branch of the hydraulic fracture runs into the left rib. Where it enters the rib, the wall simply slabs off revealing the fracture surface for a one meter length over the height of the drift. The multi-colored surface of the fracture is a vivid example of the hole to hole interconnection through a fracture network. During mine back, pieces of PVC from the propellant canister were found trapped in the fractures as far as 5 meters from the borehole. Since the PVC tube wall has an original thickness of 3 mm, the fracture aperture during the formation of the fracture is at least that wide.

EXPERIMENT GTSF-3

The last shot was done in hole 3 using a fast burning, 6.4 cm StressFrac tool, resulting in a peak pressure of 79.3 MPa (11,500 psi), 65.5 MPa (9500 psi) by crush gauge. The pressurization rate was 172 KPa/μs (25 psi/μs). Water ejection was observed at hole 2.

The shot results in multiple fractures, Figures 4 and Figure 5. The fractures in the non-hydraulic-fracture direction extend 1 meter or less from the borehole except the one perpendicular to the hydraulic-fracture direction going east. That particular fracture has not been fully excavated, but it appears to be turning south toward the hydraulic-fracture direction. The edge of the fracture is visible along the right rib of the drift for about 2 meters. The southern branch of the hydraulic fracture extends at least 3.7 meters. The northern branch intersected the non-hydraulic fracture going east from hole 2. In this case, the hydraulic fracture did not stop at the intersection, it went through the existing fracture out of hole 2. This hole 3 to hole 2 interconnection was the most productive fracture interconnection of the entire series (more in the next section).

FLOW TESTS

The pre-shot permeability of each borehole was measured using a constant pressure injection. The post-shot permeability was measured using a constant flow rate test. In both cases, the shut-in data were found to give the most consistent results. The results of the permeability tests are summarized in Table II. Generally, the primary effect of a shot is to increase the permeability of the test hole. While typical pre-shot permeabilities are in the range of 0.4-0.7 md, post-shot effective permeability ranges between 80 to 170 md. The shots also have secondary effects, i.e. effects on neighboring holes. For example after the shot in hole 4, the effective permeability of hole 5 increased to 2.0 md due to the interconnection between hole 4 and 5. Secondary effects are not always positive; effective permeability of holes 2 and 4 both show a decrease as a result of shots in neighboring holes, Table II.

The fracture network grew with each shot. Production was observed out of neighboring holes during permeability flow tests for later shots. Fracture aperture was estimated using production data from flow test of hole 3. During the last ten minutes of the test the average driving pressure was 1.3 MPa (190 psi); a steady production rate of 4.2ℓ/min (1.1 gpm) was observed out of hole 2. Using a fracture length of 3.5 meters consistent with the mineback result and a fracture height of 4.6 meters (essentially the entire test zone), the permeability aperture width product was calculated to be 0.04 darcy-meter. Assuming the fracture to be a parallel plate channel, the average fracture aperture for the hole 3 to hole 2 interconnection was then estimated to be approximately 0.1 mm (4 mils). This is considerably smaller than the estimated aperture width of greater than 3 mm at the formation of the fracture. Ash fall tuff is relative soft and may have poor self-propping properties. The actual fracture width observed during mine back varied from several centimeters to submillimeters.

CONCLUDING REMARKS

The present series of tests demonstrated conclusively that it is possible to create multiple fractures in water filled boreholes. It is useful to note that multiple fractures were obtained with average pressurization rates ranging from 33 KPa/μs to 350 KPa/μs. The fact that the operating range spans one order of magnitude in the pressurization rate means that the method is practical for field applications. The experiments also demonstrated that fracture interconnections can be made.

These tests have been conducted in ash fall tuffs which are not the typical geothermal reservoir rock, but proper application of rock mechanics principles allows these results to be extrapolated to other rock types. For example, energy considerations lead to the deduction that the fracture length is proportional to the square root of Young's modulus [4]. Greater lengths are expected in higher modulus formations because the crack is narrower and the gas volume can create more length. Thus, granites or basalts should have greater fracture lengths. On the other hand, length is obviously inversely proportional to the in situ stress level since any pressure below the minimum stress cannot do any useful work. A considerable amount of energy may be needed in pressurizing up to the in situ stress level.

Multiple fracture initiation also depends on the rock type and stress levels. We should expect that the pressure loading rate required for multiple fracturing will be

$$\frac{dp}{dt} \propto \frac{\sigma_{Hmax} - \sigma_{Hmin}}{D} V_p ,$$

where σ_{Hmax} and σ_{Hmin} are the maximum and minimum principal in situ stresses perpendicular to the axis of the hole, V_p is the compressional wave velocity of the rock and D is the borehole diameter. High velocity rocks, such as granite, will require faster load rates, as will formations with large horizontal stress differences. Such design calculations as these should always be considered when a new rock type is to be fractured.

Because the fracture aperture was found to be as wide as 3 mm during the shot, it will be useful, in the future, to test shots loaded with proppants. If the fractures can be propped near the borehole, it might then be useful to use multiple shots to achieve fracture extension. Finally, for actual applications, it will be necessary to develop high temperature tools. While the propellant in the StressFrac tools might be stable up to 650°F, high temperature ignition systems need to be developed.

REFERENCES

1. Chu, T. Y., Cuderman, J. F, Jung, J., and Jacobson, R. D., (1986) "Permeability Enhancement Using High Energy Gas Fracturing," Proceedings, Eleventh Workshop on Geothermal Reservoir Engineering, Stanford University.

2. Cuderman, J. F. (1984) "High Energy Gas Fracturing Development--Final Report to Gas Research Institute, SAND84-0247, Sandia National Laboratories, Albuquerque, NM.

3. Cuderman, J. F., and Northrop, D. A. (1984) "A Propellant-Based Technology for Multiple Fracturing Wellbores to Enhance Gas Recovery: Application and Results in Devonian Shale. "SPE/DOE/-GRI 12838, Unconventional Gas Recovery Symposium." Pittsburgh, PA.

4. Cuderman, J. F., Chu, T. Y., Jung, J. and Jacobson, R. D., (1985) "High Energy Gas Fracturing Experiments in Liquid Boreholes--Potential Geothermal application," SAND85-2809, Sandia National Laboratories, Albuquerque, NM.

5. Glowka, D. A. (1985) "Effects of Artificial Fracture Geometry on Geothermal Well Production, "Geothermal Resources Council Transactions, Vol 9.

TABLE I

Peralkaline ash-fall tuff properties

Bulk Density	1.8± 0.1 gm/cc
Porosity	40 ± 5 %
Water Saturation	90 ± 5 %
Young's Modulus	2-3 GPa; 0.3-0.4x10^{6}psi
Poisson's Ratio	0.15
Compressive Strength (unconfined)	14 MPa; 2x10^{3}psi
Tensile Strength (unconfined)	0.7 MPa; 100 psi
Permeability	0.1 - 2 md
Compressional Wave Velocity	1500-2500 m/sec
Shear Wave Velocity	900-1500 m/sec

EFFECTIVE BOREHOLE PERMEABILITY, md

TEST SEQUENCE	HOLE # 1	2	3	4	5
PRE-TEST	0.4	2.0	0.4	0.7	0.5
1	78				
2		172			
4				161	2.0
5				69	79
3		142	149		

Table II

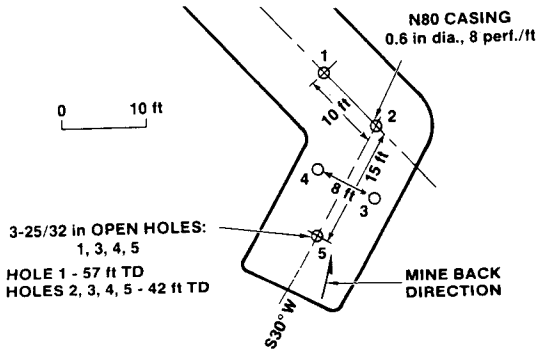


Figure 1. Test Layout



Figure 2. Water Ejection out of Hole 2 due to shot in Hole 3



Figure 3. Multiple Fracture Pattern of Hole 3

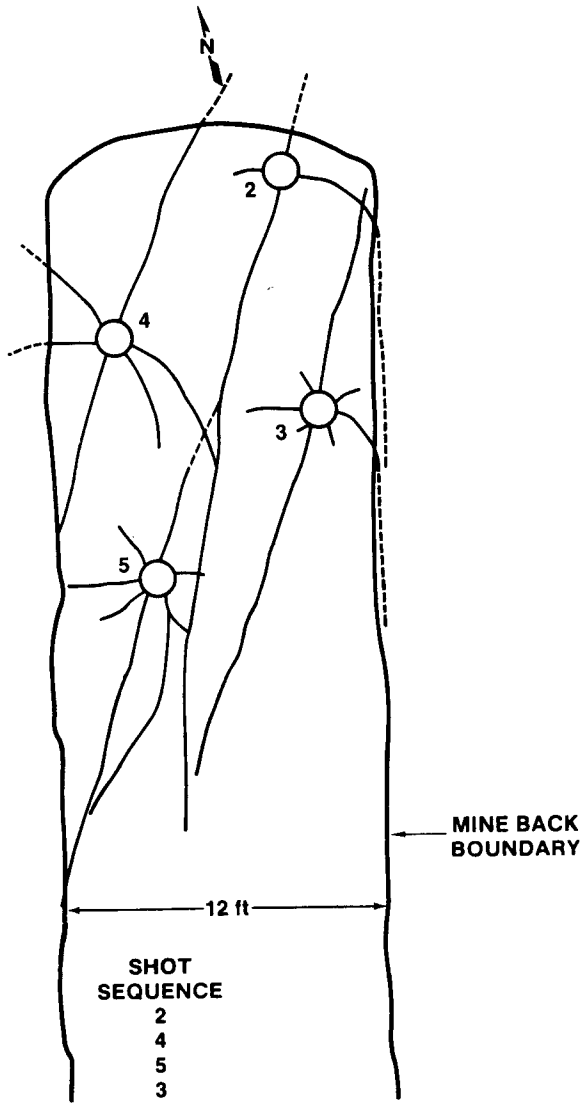


Figure 4. Schematic of Fracture Network

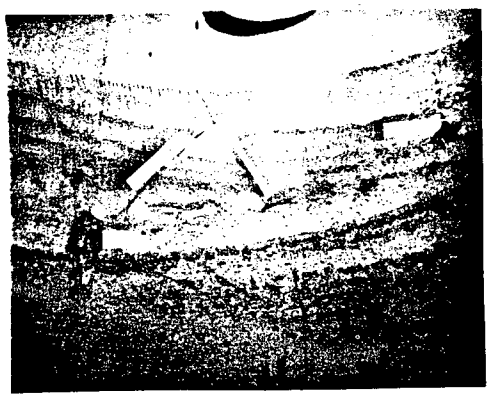


Figure 5. Fractures from Holes 2, 3, 4

PROCEEDINGS, Twelfth Workshop on Geothermal Reservoir Engineering
Stanford University, Stanford, California, January 20-22, 1987
SGP-TR-109

THE ELECTROKINETIC MECHANISM OF HYDROTHERMAL-CIRCULATION-RELATED AND PRODUCTION-INDUCED SELF-POTENTIALS

T. Ishido, T. Kikuchi, and M. Sugihara

Geological Survey of Japan

ABSTRACT

Self-potential (SP) surveys were carried out on a number of geothermal areas in Japan during the last decade. In most cases SP anomalies of positive polarity are found to overlie high temperature upflow zones. Streaming potential generated by hydrothermal circulation (Ishido, 1981) is considered to be the most likely cause of the observed positive anomalies. Repeated surveys conducted on the Nigorikawa caldera in Japan detected a change in SP induced by production of geothermal fluids. The observed change is dipolar in waveform and can also be attributed to an electrokinetic mechanism.

INTRODUCTION

Self-potential (SP) anomalies of widely varing amplitude, polarity, and spatial extent have been reported from several geothermal areas (Zohdy et al., 1973; Zablocki, 1976; Anderson and Johnson, 1976; Corwin and Hoover, 1979). The various mechanisms involved in producing these surface potentials have not been positively identified; however, an electrokinetic process related to the upward movement of pore fluids is believed to have caused the anomalies of positive polarity observed in Hawaii (Zablocki, 1976), Yellowstone (Zohdy et al., 1973), and Long Valley (Anderson and Johnson, 1976).

Quantitative modeling of the potential generating mechanism for hydrothermal circulation was done by Ishido (1981). His modeling is based on realistic values of the electrokinetic coupling coefficients for crustal rock-water systems estimated from experimental results (Ishido and Mizutani, 1981; Ishido et al., 1983). In this paper, the modeling presented by Ishido (1981) will be explained briefly, and some examples from recent self-potential surveys done in Japan will be given. Following the discussion of the SP anomalies under natural state conditions, a change in SP induced by production of geothermal fluids will be described.

STREAMING POTENTIAL ASSOCIATED WITH HYDROTHERMAL CIRCULATION

The flow of a fluid through a porous medium may generate an electric potential gradient (called the electrokinetic or streaming potential) along the flow path by the interaction of the moving pore fluid with the electrical double layer at the pore surface, a process known as electrokinetic coupling. The phenomenological equations describing electrokinetic coupling in a porous medium are given by Ishido and Mizutani (1981) on the basis of the capillary model:

$$\vec{I} = -\eta t^{-2}\sigma\cdot\nabla\phi + \eta t^{-2}(\varepsilon\zeta/\mu)(\nabla P - \rho\vec{g}) \quad (1)$$

$$\vec{J} = \eta t^{-2}(\varepsilon\zeta/\mu)\nabla\phi - (k/\mu)(\nabla P - \rho\vec{g}) \quad (2)$$

where $\vec{I}$ is the electric current density, $\vec{J}$ is the fluid volume flow flux; ϕ is the electric potential, P is the pore pressure; $\vec{g}$ is the acceleration of gravity; ρ, ε, and μ are the density, dielectric constant, and viscosity of the pore fluid, respectively; η, t, and k are the porosity, tortuosity, and permeability of the porous medium, respectively; $\sigma = \sigma_f + m^{-1}\sigma_s$ (σ_f, pore fluid electrical conductivity; σ_s, surface electrical conductivity; and m, hydraulic radius); and ζ is the zeta potential, the potential across the electrical double layer.

Neglecting the first term in the right-hand side of (2)(this term can be neglected safely for geologic materials) and substituting (2) into (1) yields:

$$\vec{I} = -\eta t^{-2}\sigma\{\nabla\phi + C(\mu/k)\vec{J}\} \quad (3)$$

where C ($= \varepsilon\zeta/\sigma\mu$) is called the streaming potential coefficient. If C is negative (positive), the positive (negative) charge is carried by the fluid flow $\vec{J}$. In the absence of current sources, $\nabla\vec{I} = 0$; and for homogeneous regions, by using (3):

$$\nabla^2\phi = -C(\mu/k)\nabla\vec{J} \quad (4)$$

Considering thermally driven convection in single-phase (liquid) systems, $\nabla\vec{J} = 0$(Boussinesq approximation), we get,

$$\nabla^2\phi = 0 \quad (5)$$

Sources for ϕ therefore can only occur at boundaries. Continuity of normal current flow requires

$$\hat{n}\cdot\vec{I}_1 = \hat{n}\cdot\vec{I}_2 \qquad (6)$$

where $\hat{n}$ is the unit vector normal to the boundary.

When a hydrothermal convection cell is confined to depth and no fluid flow intersects the surface, no surface electric potential anomaly will appear for a uniform half space, since the solution of (5) without any sources for ϕ must be zero throughout the half space. This is not the case, however, for inhomogeneous media (where there are boundaries between regions of differing physical properties such as C) since electric charge can be accumulated by fluid flow at the boundaries.

The streaming potential coefficient C in the earth is expected to be inhomogeneous rather than homogeneous. Figure 1 shows that C for the crustal rock-water system is very sensitive to the chemical composition of the pore water and to the temperature of the system (Ishido et al., 1983). (The polarity of C's shown in figure 1 is negative except for those shown by broken lines.) This implies that C is inhomogeneous in a hydrothermal convection cell, in which there is a large temperature change.

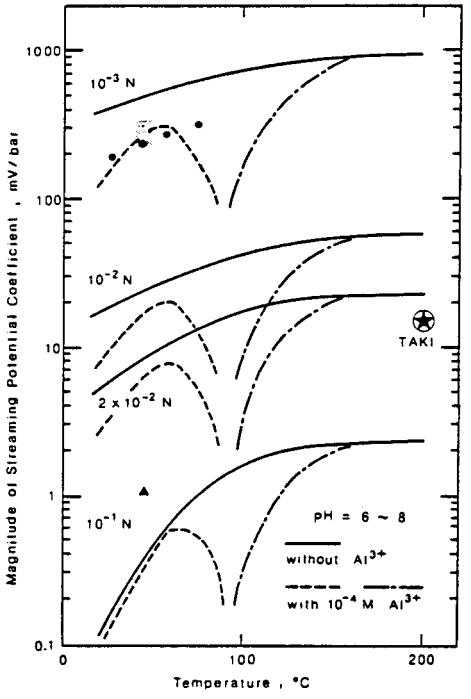


Fig. 1 The magnitudes of streaming potential coefficients of crustal rock-water systems as a function of temperature in 10^{-3}, 10^{-2}, 2×10^{-2} and 10^{-1} mol/l NaCl electrolytes (liquid phase) with and without 10^{-4} mol/l Al^{3+}. Also shown is the value of C obtained in the Takinoue geothermal field (TAKI). (After Ishido et al., 1983.)

By using the values of C estimated from the experiments (Ishido and Mizutani, 1981; Ishido et al., 1983), Ishido (1981) did quantitative modeling of electric potentials generated by hydrothermal circulation through a electrokinetic coupling. Equation (5) was solved numerically with boundary condition (6). In one of the models (Figure 2), a half space below the surface was divided into two regions: the first characterized by temperature above 150°C and the other characterized by lower temperatures. Physical properties of the higher and lower temperature regions are assumed to be those at 200° and 100°C, respectively. Considering the crustal rock-water system, the water chemistry of which is: pH = 7, 0.02 mol/l NaCl, 10^{-5} mol/l Al^{3+}, Ishido (1981) estimated the values of C as -35 and 0 mV/bar for the higher and lower temperature regions respectively (see also Ishido and Mizutani, 1981). As shown in figure 2, positive electric potential appears around the portion of the higher-lower temperature boundary intersected by the outward fluid flow from the higher temperature region.

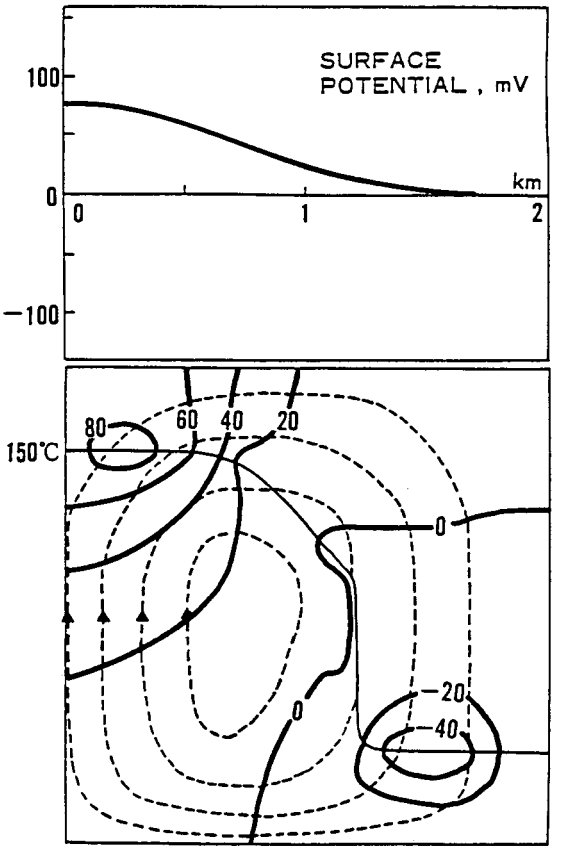


Fig. 2 The lower diagram shows the electric potential distribution (solid lines, in mV) generated by hydrothermal circulation (stream lines are shown by broken lines). The whole region is 2x2 Km^2 and divided into two regions by 150 °C isotherm. The upper diagram shows the SP distribution on the earth's surface. (after Ishido, 1981)

The accumulation of positive charge at this portion of the boundary is caused by fluid flow carrying positive charge ($C < 0$) and no charge ($C = 0$) in the higher and the lower temperature regions, respectively.

Ishido (1981) has shown that an observable self-potential anomaly, 10-100 mV in magnitude, can appear on the surface, if the following conditions are satisfied: (1) the circulating fluid is an aqueous solution of neutral pH($\geq$ 4) and moderate concentration of dissolved salt ($\lesssim$ 0.1 mol/l), and (2) the fluid flow rate ranges from 10^{-8} to 10^{-7} m/s. The polarity of the anomaly over a hot zone is always positive whether or not the fluid flow (with nonzero C) intersects the surface; this is mainly because C is negative ($\zeta < 0$) and larger in magnitude under high temperature conditions.

RESULTS OF RECENT SP SURVEYS IN JAPAN

Self-potential (SP) surveys were conducted on five geothermal areas by the Geological Survey of Japan (GSJ) and on two areas by the New Energy Development Organization (NEDO) during the last decade in Japan. Each survey covers an area of 50-100 Km^2 with survey lines of about 100 Km in total length. SP anomalies of various types have been recorded through these surveys, and obvious anomalies of positive polarity are found in five different areas: the Kussharo and Nigorikawa calderas, and the Sengan, Okuaizu and Hohi geothermal areas. In most cases, the correlation between the anomaly of positive polarity and the high temperature upflow zone is evident. Two examples are described here.

Okuaizu geothermal field

The Okuaizu geothermal field is located in Fukushima prefecture on the Japanese island of Honshu. In the area of about 70 km^2, NEDO has completed geological, geochemical, and geophysical explorations including an SP survey, and has drilled 7 1000-1500 m depth wells and 6 ~400 m depth heat holes during 1982-1984. Following NEDO's survey, Okuaizu Geothermal Co., Ltd. (OAG) conducted an exploratory well drilling program in the area.

The area of investigation has a mean elevation of approximately 300-500 m above sea level and is dominated by 729 m Mt. Yuno (Yuno-take). The temperature distribution at -500 m ASL (that is, 500 m below sea level) is shown in figure 3. The high temperature zone is located around wells OA-4 and 6. (The highest temperature observed is 286°C at -1120 m ASL in OA-6.) Well OA-4 was discharged for a month in 1984 and pressure transient tests were carried out (Ishido, 1985).

Also shown in figure 3 is the result of the SP survey; the positive anomaly of about 100 mV overlies the shaded area shown in figure 3. It should be noticed that the northern part of the area of positive anomaly coincides well with that of high temperature and of high productivity wells drilled by OAG (location of OAG's wells is not shown in figure 3).

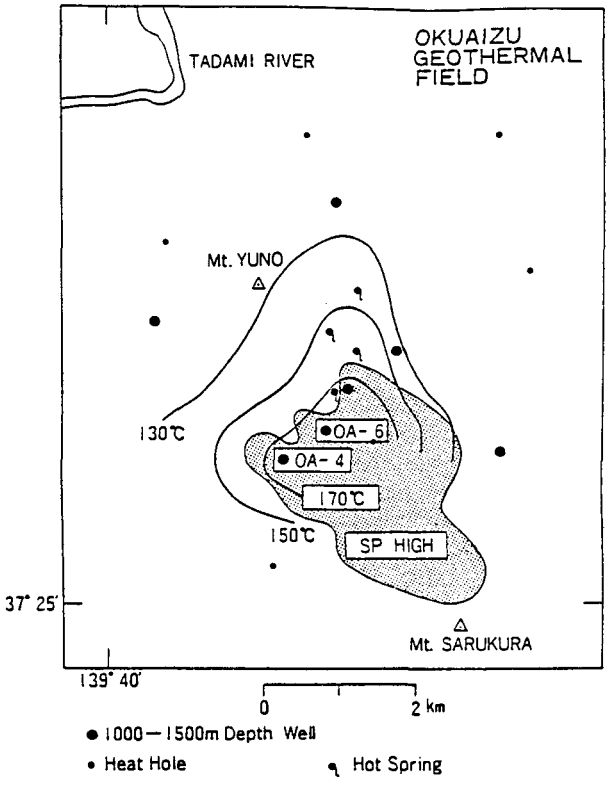


Fig. 3 Geothermal features and location of wells in the Okuaizu field. SP anomaly of positive polarity (~100 mV) overlies the shaded area.

Mt. Yake Volcano area

Mt. Yake (Yake-yama), located in the Sengan geothermal area, northern Honshu, is an active volcano and has many thermal manifestations such as fumaroles, hot springs and alteration zones. Under a joint program, GSJ and/or NEDO have been conducting geological, geochemical, and geophysical surveys and well drilling in the Sengan geothermal area. SP surveys in the Mt. Yake area have been carried out by GSJ since 1979. Exploration efforts were also undertaken by a private developer in the area; Mitsubishi Metal Corporation (MMC) has been running a 10 MW geothermal power plant at Ohnuma since 1974 and conducting an exploratory well drilling program in the Sumikawa field since 1981.

Surface rocks in the area shown in figure 4 are mostly andesitic lavas from Mt. Yake, 1366 m in elevation. The elevations of the fumaroles and hot springs shown in figure 4 are generally from 700 to 1100 m except for the fumaroles near the volcano summit and for the bicarbonate hot springs to the north (520 m). The most remarkable feature of the thermal waters of the area is their compositional variety. Waters discharged from production wells in the Ohnuma field and from exploratory wells in the Sumikawa field have neutral pH

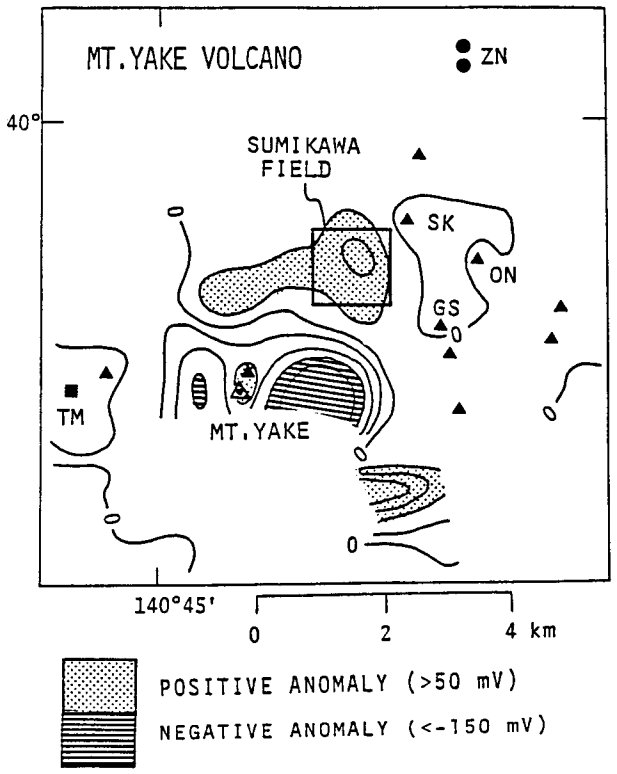


Fig. 4 Self-potential distribution in the Mt. Yake area. Contour interval is 50 mV. Areas with fumaroles and/or steam-heated sulfate type springs are shown as triangles (SK, Sumikawa; ON, Ohnuma; GS, Goshogake). Areas with chloride-bicarbonate type thermal water discharge are shown as solid circles (ZN, Zenikawa). Tamagawa (TM) hot springs area is shown by a solid square.

and total dissolved salt contents of about 2000 ppm on the average (Sakai and Mori, 1981).

The results of the SP surveys are shown in figure 4. Anomalies of positive polarity appear in three areas: at the volcano summit, and on the northern and southeastern flanks of Mt. Yake. The positive anomaly to the north of Mt. Yake overlies the Sumikawa field, where the subsurface temperature is higher than the surroundings (over 250°C at the sea level) and a vapor dominated zone is found at depths of 400-600 m ASL (Kubota, 1985). Considering the chemistry of the subsurface waters in the Sumikawa field, we believe that the subsurface upflow carries enough electric charge (C is large enough) to produce the observed SP anomaly.

Exploration data is not sufficient to characterize the geothermal activity in the area of the positive anomaly southeast of Mt. Yake. We also do not have enough data on the volcano summit area; however, the positive anomaly over 200 mV in amplitude and 500 m in width seems to be associated with the fumaroles there. (To discuss SP anomalies associated with fumaroles, we need more data on the streaming potential generated by the flow of two-phase mixtures of water and steam. Study on this problem is being carried out by Marsden and Tyran (1986).)

As shown in figure 4, there is no obvious anomaly overlying the areas with fumaroles and hot springs except the volcano summit. This is thought to be due to the thermal waters in the areas giving very small C under near surface condition and generating no observable anomaly with their discharge from the surface.

There are two obvious anomalies of negative polarity on the eastern and western flanks of Mt. Yake. The downflow of meteoric waters can generate such negative anomalies through electrokinetic coupling (Ishido, 1981). We do not, however, have enough data for further discussion.

SP CHANGE INDUCED BY PRODUCTION OF GEOTHERMAL FLUIDS

When a sink or source of fluid is created in a reservior as a result of production or injection of geothermal fluids, a surface electric potential anomaly can be produced through electrokinetic coupling if the following coditions are satisfied. The conditions have been derived for electrokinetic effects represented by (1) and (2) without bouyancy terms: there is a boundary separating regions of

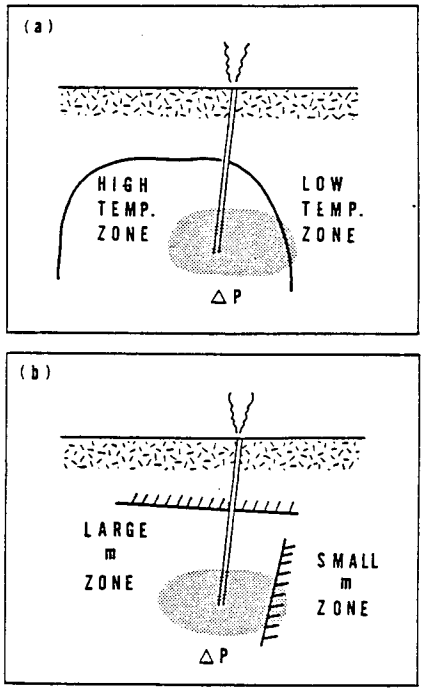


Fig. 5 Models for production-induced SP change. (a) High-low temperature boundary, or (b) large-small hydraulic radius (m) boundary acts as a boundary between regions of differing streaming potential coefficient.

differing streaming potential coefficient C and there is a component of pressure gradient parallel to this boundary (Nourbehecht, 1963; Fitterman, 1978).

A high-low temperature boundary, a boundary between regions of different pore water chemistry, or a contact of different rocks is considered as a candidate for a boundary between regions of differing C in a geothermal reservoir (figure 5). As shown in figure 1, the value of C depends largely on the temperature of the system; therefore, a high-low temperature boundary surrounding a reservoir acts as a boundary between regions of differing C (figure 5(a)). When two kinds of rocks come into contact with each other and other parameters such as pore water chemistry are homogeneous, no major deviations in C are expected for crustal rocks (Ishido and Mizutani, 1981). However, if the value of hydraulic radius (m) of the pores and the cracks varies significantly across the boundary, a large difference in C can appear (Ishido and Mizutani, 1981). A large-small hydraulic radius boundary, therefore, can be a boundary between regions of differing C (figure 5(b)).

When a pressure change induced by production and/or injection of fluids propagates to a boundary between regions of differing C in a reservoir (figure 5), an electric potential anomaly appears on the surface through electrokinetic coupling. We can model the potential generating mechanism quantitatively using the formulation derived by Nourbehecht (1963), Fitterman (1978), and Fitterman (1979). If the boundary is nearly vertical, the anomaly will be dipolar in waveform (Fitterman, 1979).

Production-induced electric potential observed at Nigorikawa

The Nigorikawa caldera is located in the southern part of the Hokkaido island, Japan. The diameter of the caldera is about 3 km and fumaroles and hot springs are distributed in the northern half of the caldera floor. The thermal waters are neutral and contain much HCO_3^- (500-1000 ppm). The concentration of NaCl ranges from 10^{-3} to 10^{-1} mol/l. The Mori geothermal power plant (50 MW) has been built and in operation since 1982. SP surveys were conducted by GSJ three times: in 1978 and 1981 (before plant startup) and in 1984 after the operation of the power plant began.

The result of the 1981 SP survey is shown in figure 6(a); SP is high inside the caldera compared to the surrounding area and anomalies of positive polarity overlie the northern area of hot springs. The results obtained from 1978 survey shows almost the same potential distribution as the 1981 result in the caldera. The SP distribution observed in 1984, however, is significantly different from that in 1981. The difference between the 1981 and 1984 SP distribution is shown in figure 6(b). The dipolar change in SP appears over the main zone of fluid production. The observed change is thought to be generated by the production (and reinjection) of geothermal fluids through electrokinetic coupling. Quantitative modeling of the induced SP change is proceeding on the basis of a formulation similar to that given by Fitterman (1979).

CONCLUSIONS

The correlation between positive SP anomalies and high temperature upflow zones has been confirmed for several geothermal areas in Japan. Quantitative modeling of the electrokinetic effects by Ishido (1981) shows that streaming potential generated by hydrothermal circulation is the most likely cause of the observed positive anomalies. The hydrothermal-circulation-related anomaly may or may not be

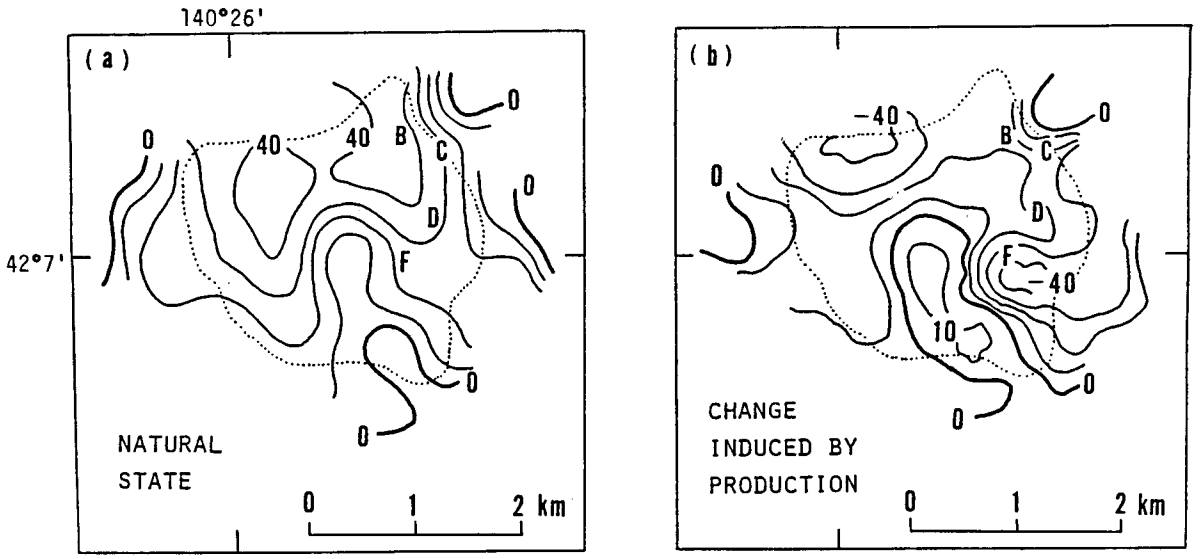


Fig. 6 (a) Self-potential distribution in the Nigorikawa caldera, Japan observed in 1981.
(b) Change in SP induced by production of geothermal fluids. Contour interval is 10 mV.
The edge of the caldera floor is shown by dotted lines. The well sites are shown as B - F.

observable depending upon conditions such as the temperature, the chemical composition of the pore water, the flow rate, and the geometry of the hydrothermal convection cell.

In the neighborhood of an operating geothermal power plant, there is the possibility of the development of production-induced SP change through electrokinetic coupling. The observed change at the Nigorikawa caldera in Japan can be modeled quantitatively using the formulation of Fitterman (1979).

ACKNOWLEDGMENTS

This work was supported by the MITI's "Sunshine" project under the direction of the Geological Survey of Japan, Geothermal Research Department. We thank K. Ogawa and K. Kimbara for their constant encouragement. K. Baba is greatly acknowledged for his guidance during the early stage of this work.

REFERENCES

Anderson, L. A. and Johnson, G. R. (1976), "Application of the Self-Potential Method to Geothermal Exploration in Long Valley, California," J. Geophys. Res., 81, 1527-1532.

Corwin, R. F. and Hoover, D. B. (1979), "The Self-Potential Method in Geothermal Exploration," Geophysics, 44, 226-245.

Fitterman, D. V. (1978), "Electrokinetic and Magnetic Anomalies Associated with Dilatant Regions in a Layered Earth," J. Geophys. Res., 83, 5923-5928.

Fitterman, D. V. (1979), "Calculations of Self-Potential Anomalies Near Vertical Contacts," Geophysics, 44, 195-205.

Ishido, T. (1981), "Streaming Potential Associated with Hydrothermal Convection in the Crust: A Possible Mechanism of Self-Potential Anomalies in Geothermal Areas," J. Geotherm. Res. Soc. Jpn., 3, 87-100 (in Japanese).

Ishido, T. and Mizutani, H. (1981), "Experimental and Theoretical Basis of Electrokinetic Phenomena in Rock-Water Systems and Its Applications to Geophysics," J. Geophys. Res., 86, 1763-1775.

Ishido, T., Mizutani, H. and Baba, K. (1983), "Streaming Potential Observations, Using Geothermal Wells and In Situ Electrokinetic Coupling Coefficients Under High Temperature," Tectonophysics, 91, 89-104.

Ishido, T. (1985), "Pressure Transient Tests at the Okuaizu Geothermal Field in Japan," Geothermal Resources Council, Transactions, Vol. 9 - Part II, 521-526.

Kubota, Y. (1985), "Conceptual Model of the North Hachimantai-Yakeyama Geothermal Area," J. Geotherm. Res. Soc. Jpn., 7, 231-245 (in Japanese).

Marsden, Jr., S. S. and Tyran, C. K. (1986), "The Streaming Potential Generated by Flow of Wet Steam in Capillary Tubes," Proceedings of the 11th Workshop on Geothermal Reservoir Engineering, Stanford University.

Nourbehecht, B. (1963), "Irreversible Thermodynamic Effects in Inhomogeneous Media and Their Applications in Certain Geoelectric Problems," Ph.D. Thesis, M.I.T.

Sakai, S. and Mori, H. (1981), "Ohnuma Geothermal Field," in Field Excursion Guide to Geothermal Fields of Tohoku and Kyushu, Volcanological Soc. Jpn., pp. 21-29.

Zablocki, C. J. (1976), "Mapping Thermal Anomalies on an Active Volcano by the Self-Potential Method, Kilauea, Hawaii," in Proc. 2nd U. N. Sympos. on the Devel. and Use of Geothermal Resources, Vol. 2, pp. 1299-1309.

Zohdy, A. A. R., Anderson, L. A. and Muffler, L. J. P. (1973), "Resistivity, Self-Potential, and Induced-Polarization Surveys of a Vapor-Dominated Geothermal System," Geophysics, 38, 1130-1144.

PROCEEDINGS, Twelfth Workshop on Geothermal Reservoir Engineering
Stanford University, Stanford, California, January 20-22, 1987
SGP-TR-109

VAPOR-DOMINATED ZONES WITHIN HYDROTHERMAL CONVECTION SYSTEMS

S. E. Ingebritsen

U. S. Geological Survey, Menlo Park, CA 94025

ABSTRACT

Three conceptual models are presented to illustrate the range of natural hydrothermal convection systems in which vapor-dominated conditions are found. Numerical simulation is used to test the feasibility of these models and to demonstrate geologically plausible evolutionary pathways for each model.

INTRODUCTION

How vapor-dominated zones evolve and how they behave in the natural state is not well understood, partly because of their scarcity and partly because of the difficulty of quantitatively describing two-phase systems. The goal of this study was to simulate the behavior of three model systems that represent the range of hydrothermal convection systems within which vapor-dominated conditions are found (fig. 1) and to quantitatively investigate the conditions that allow each system to evolve.

For the purposes of this study, vapor-dominated zones are considered to be those in which the mass flux of vapor is somewhat greater than the liquid flux ($|q_s/q_w| > 1$) and relative permeability to steam is much greater than relative permeability to water ($k_{rs}/k_{rw} >> 1$). A criterion based only on the vertical pressure gradient would not include the third conceptual model (fig. 1).

The conceptual models range from a system with an extensive vapor-dominated zone that is generally underpressured with respect to the local hydrostatic pressure (fig. 1 - Model I) to a system that includes a relatively thin vapor-dominated zone at pressures above local hydrostatic (fig. 1 - Model III). Although each model has unique features, they have some characteristics in common. They each involve phase separation at pressures significantly greater than atmospheric and include zones in which vapor is by far the more mobile phase (relative to liquid water). Each is associated with fumaroles and steam-heated low-chloride acid-sulfate springs, as a result of the phase separation. The vapor-dominated zones in Models II and III are both "parasitic" to relatively voluminous throughflows of liquid that also feed high-chloride thermal springs at lower elevations.

Most natural systems are significantly more complex than the models shown in figure 1, and some might be better represented as a combination of the models. Active systems such as The Geysers, Larderello (Italy), Kamojang (Indonesia), and Matsukawa (Japan) are generally similar to Model I. A relatively large number of high-temperature systems in regions of topographic relief are similar to either Model II or Model III (Ingebritsen, 1986); however, in most cases the thickness and pressure distribution within the vapor-dominated zone are unknown. Sumikawa, Japan (Y. Kubota, written commun., 1986) may be similar to Model II. Mud Volcanoes, Yellowstone and Rotorua, New Zealand (B. Simpson, oral commun., 1986) may be similar to Model III.

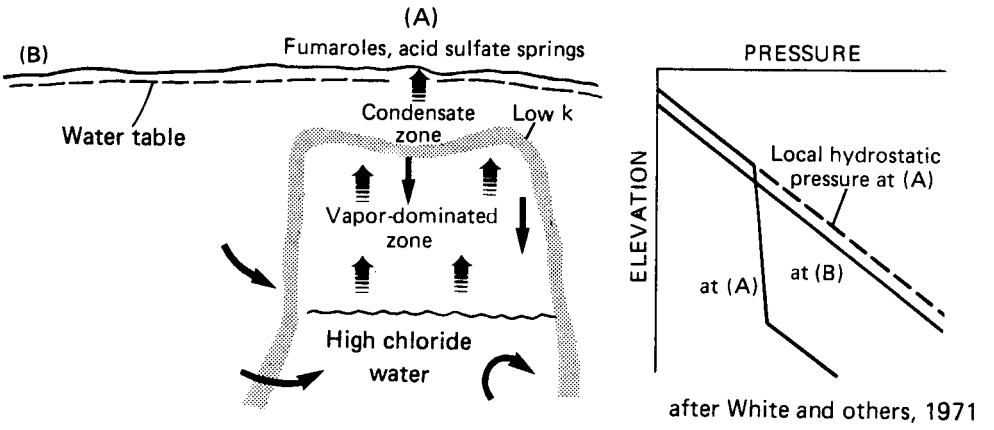
NUMERICAL SIMULATION

The conceptual models shown in figure 1 were simulated using a modified version of the GEOTHER code described by Faust and Mercer (1979a, 1979b; Mercer and Faust, 1979). This code simulates three-dimensional single- and two-phase heat and mass transport in a porous medium. Modifications to the original GEOTHER code and the limitations of the code with respect to the natural systems modeled are described by Ingebritsen (1986).

MODEL I

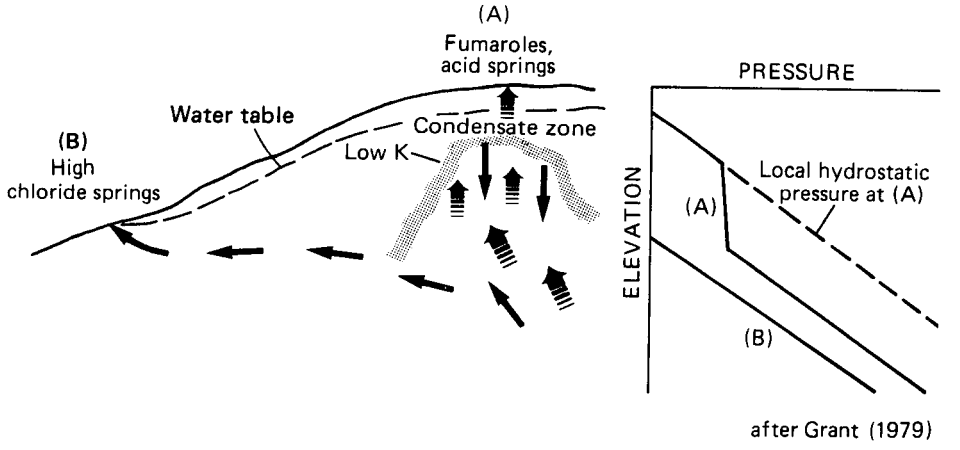
Within the extensive vapor-dominated zone in Model I (fig. 1; White and others, 1971) the vertical

MODEL I



after White and others, 1971

MODEL II



after Grant (1979)

MODEL III

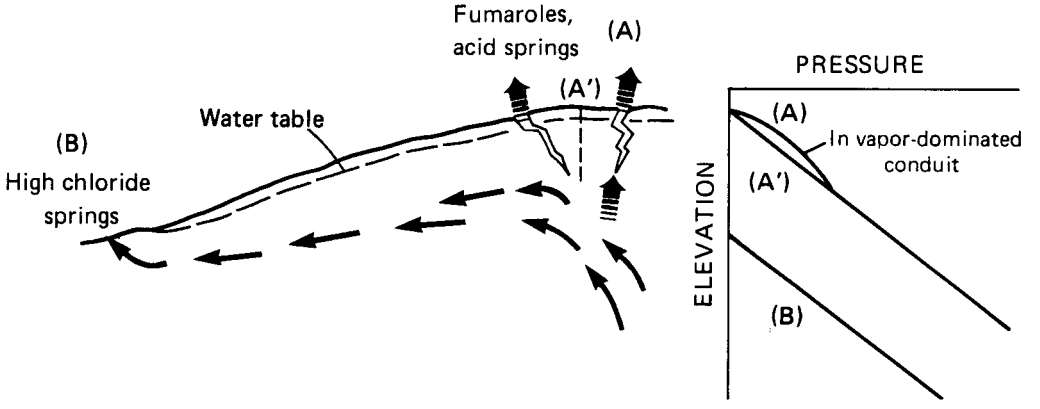


Figure 1. Conceptual models of three hydrothermal convection systems that include vapor-dominated zones. Broken arrows represent steam, solid arrows liquid water.

pressure gradient is somewhat above vaporstatic. There is steam/liquid counterflow within the vapor-dominated zone, as a fraction of the rising steam condenses and flows back down in narrower channels and pore spaces. The vapor-dominated zone is generally underpressured with respect to local hydrostatic pressures (fig. 1), so, to exist, it must be isolated from surrounding nonthermal flow systems by low-permeability barriers.

The vapor-dominated zone is overlain by a condensate zone that is liquid saturated, or nearly so (fig. 1). The vapor-dominated zone is presumably underlain by a zone of high-chloride liquid, but there is no evidence for voluminous liquid throughflow.

Geometric model

Model I is represented geometrically as a two-dimensional vertical cross section, with no boundaries closed to mass or energy (fig. 2a). The land surface is treated as a uniform constant pressure/enthalpy boundary, at a pressure of 1 bar and an enthalpy equivalent to 15°C. The system is flanked by nonthermal flow systems - also represented by constant pressure/enthalpy boundaries - but buffered to some extent by low-permeability barriers (k_l). The lower boundary is a controlled flux boundary. Some of the numerical simulations involved only conductive heat flux (q_h) at this boundary, and some involved a mass inflow (M) as well as conduction.

This geometric model represents the vapor-dominated zone as an open system. Previous quantitative analyses of such large-scale vapor-dominated zones have involved models with closed boundaries (Pruess and Truesdell, 1980; Pruess and others, 1983; Pruess, 1985) and/or dealt with less global representations of the system (Schubert and Straus, 1979, 1980; Straus and Schubert, 1981; Pruess, 1985).

The series of numerical experiments carried out for Model I involved variations in the lower boundary condition, the geometry of the low-permeability aureole (k_l), and the permeabilities k_h and k_l (fig. 2a). Initial conditions for all of the simulations were a hydrostatic pressure distribution and a low-temperature conductive temperature regime (the same conditions that were maintained at the lateral boundaries throughout the simulations). Total simulation times ranged from 10,000 to 40,000 years.

Results

A vapor-dominated zone such as the one in Model I can evolve within low-permeability barriers without changes in boundary conditions or rock properties, given an adequate supply of heat. The evolution of the system is more rapid in "decreasing recharge" cases that involve a relatively high initial fluid throughflow rate that diminishes through time. White and others (1971) suggested that a likely mechanism for decreasing recharge at depth is loss of permeability due to deposition of carbonates and/or $CaSO_4$, which decrease in solubility with temperature.

The factors most critical to the evolution of systems like Model I are (1) an intense heat source and (2) low-permeability barriers ($\lesssim 10^{-12}$ cm^2) capable of buffering a vapor-dominated zone both vertically and laterally. Since liquid throughflow is limited, the magnitude of the required heat input implies magmatic temperatures within a few kilometers below the vapor-dominated zone.

Given an adequate supply of heat and the appropriate permeability structure, a vapor-dominated zone will begin to develop immediately below a caprock and thicken downward. A permeability contrast at the top of the vapor-dominated zone is critical, because permeability within the vapor-dominated zone must be relatively high ($\gtrsim 10^{-11}$ cm^2). The vapor-dominated zone will continue to thicken as long as the mass of steam leaving the vapor-dominated zone exceeds the mass of liquid inflow. The equilibrium thickness of the vapor-dominated zone is affected by the heat input rate and the permeability of the low-permeability barriers that isolate the vapor-dominated zone laterally. Other factors being equal, a higher heat input rate and less permeable lateral barriers will lead to a thicker vapor-dominated zone. Within the simple geometric model used, vapor-dominated zone pressures vary regularly with depth to the caprock, and are also affected by the geometry of the low-permeability aureole. They are not limited by the pressure of maximum enthalpy of saturated steam (~30.6 bars).

MODELS II AND III

Models II and III (fig. 1) both represent systems that have fumaroles and steam-heated discharge at relatively high elevations and high-chloride springs at relatively low elevations. However, there are basic differences in terms of the nature and

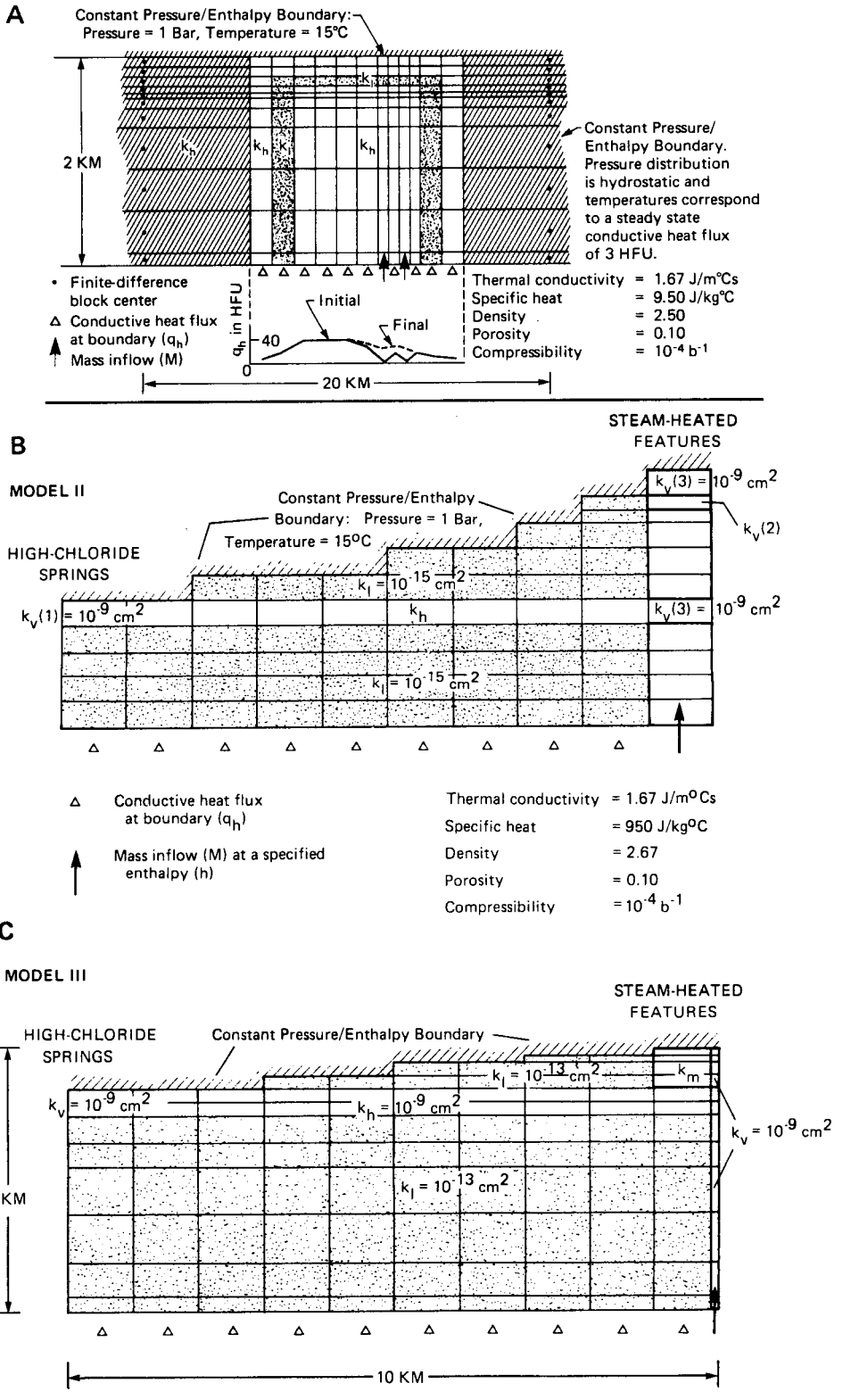


Figure 2 (a) Geometric model used in numerical simulations of Model I.
(b) Geometric models used in numerical simulations of Models II and III.

extent of vapor-dominated conditions.

These systems are distinct from Model I in that the vapor-dominated zones are relatively small and there is a significant throughflow of high-chloride liquid. The elevation difference between the steam-heated features and the high-chloride springs is essential to drive the systems, whereas in Model 1 fluid circulation is controlled largely by density differences.

In Model II, like Model I, phase separation occurs at pressures well below local hydrostatic, the pressure gradient within the vapor-dominated zone is near-vaporstatic, and a low-permeability aureole is required to buffer the vapor-dominated zone from surrounding nonthermal groundwater systems (fig. 1). In Model III, phase separation takes place at pressures close to local hydrostatic pressure (fig. 1), so the overall pressure gradient within the vapor-dominated conduit must be near-hydrostatic. It tends to be somewhat less than hydrostatic immediately above the area of phase separation and above hydrostatic near the land surface, due to expansion of the rising steam (fig. 1). Pressures in the vapor-dominated conduits are somewhat greater than pressures in the surrounding liquid saturated medium, so that low-permeability barriers are not necessarily required. Relative to Model II, high-chloride water is close to the land surface beneath the steam-heated features.

Geometric models

The geometric models shown in figure 2b and 2c were used to represent Models II and III. Both geometric models are two-dimensional vertical cross-sections with sloping upper boundaries. The land surface is treated as a constant pressure/enthalpy boundary and the lower boundary is a controlled flux boundary. Permeability in the patterned regions (k_1) is low enough that fluid circulation within the models is essentially confined to the vertical conduits along the sides (k_v, and k_v and k_m in Model III) and to the lateral conduit (k_h). Fluid circulation is driven by a mass inflow (M) at the lower right, and discharge occurs at the upper right and left sides of the models. A conductive heat flux of 2 HFU is specified along the base of the models, except in the upflow zone.

The values of permeability and other rock properties shown in figures 2b and 2c were used in all of the simulations, and were held constant throughout each simulation. Numerical experiments carried out within these geometric models involved variations in the mass inflow rate M, in the enthalpy of the mass inflow, in k_h and $k_v(2)$ (Model II), and in k_m (Model III). The width of the vertical conduit on the right hand side was also varied in Model III. Initial conditions for all of the simulations were a hydrostatic pressure distribution and a low-temperature conductive temperature regime corresponding to a uniform heat flow of 2 HFU. The simulations were continued until pressures and temperatures in the vertical and lateral conduits became relatively stable (temperatures changing less than 1°C per 1,000 years). In general, the simulations required 10,000 to 20,000 years to reach this "quasi-steady-state" condition.

Results

Several conditions are necessary for the evolution of the vapor-dominated zone in Model II, including (1) topographic relief; (2) a period of convective heating within an upflow zone followed by (3) some change in hydrologic or geologic conditions that initiates drainage of liquid from portions of the upflow zone; and (4) low-permeability barriers that inhibit the movement of cold water into the evolving vapor-dominated zone (see Ingebritsen and Sorey, 1985).

The conditions specified at the lower boundary in simulations of Model II are less restrictive than those required for the vapor-dominated zone in Model I, which involved a high rate of conductive heat input that implied an underlying magmatic heat source. The upflow or lateral flow of thermal fluid that feeds the vapor-dominated zone in Model II can capture heat flow over a relatively large area.

The thickness of the vapor-dominated zone in Model II is controlled by the permeability structure; that is, by the depths to the caprock (fig. 2b - $k_v(2)$) and to the lateral conduit. Pressures within the vapor-dominated zone are constrained by the liquid-saturated thickness above the base of the caprock, and are also affected by any parameters that influence the rate of steam upflow from the area of phase separation.

Simulations of Model III demonstrated that the vapor-dominated zone in this model can evolve relatively rapidly without changes in rock properties or boundary conditions, given circumstances that allow for a high rate of steam upflow from the area of phase separation. The system evolves similarly to Model II. However, there is no period of drainage of liquid; the steam quality of

the discharge at the land surface simply increases as the liquid saturation in the area of phase separation decreases.

Near the land surface the pressure gradient within the vapor-dominated zone in Model III is greater than hydrostatic (fig. 1), so no caprock is needed. The only requirement is that vertical permeability within the vapor-dominated zone be 1 to 2 orders of magnitude greater than the horizontal permeability into the surrounding rocks - a condition that is likely to be found in many fractured rocks.

Though the systems represented by Models II and III appear identical at the land surface, drilling in the area of steam-heated features might distinguish between the two models. Unless fluid temperatures are unusually high, the vapor-dominated zone in Model III must be relatively thin, since boiling and phase separation takes place at near-hydrostatic pressures. A thick vapor-dominated zone and/or pressures much less than local hydrostatic would suggest a system like Model II. The models might be distinguished without drilling by their response to stress. For example, the lack of a caprock in Model III implies that the steam-heated discharge will be more responsive to pressure changes at depth, such as those caused by fluid withdrawal.

Vapor-dominated conditions like those in Model III may be found locally in systems similar to Models I and II. Surface features provide evidence for vapor-dominated conduits through the condensate zones at such systems. If pressures at the top of the underlying vapor-dominated zones are near local hydrostatic, the vapor-dominated "fracture zone" in Model III is a reasonable analog for these conduits.

ACKNOWLEDGEMENTS

This is essentially an extended abstract of my Ph.D. thesis, and I would like to thank my committee: Irwin Remson, John Bredehoeft, Roland Horne, Ron Lyon, Mike Sorey, and Don White. My thesis work also benefitted greatly from discussions with Jon Gudmundsson, Karsten Pruess, and Terry Keith. Mike Sorey and Barbara Simpson reviewed this manuscript, and Rebecca Munn did the typing.

REFERENCES CITED

Faust, C.R., and Mercer, J.W., 1979a, Geothermal reservoir simulation (:) 1. Mathematical models for liquid- and vapor-dominated hydrothermal systems: Water Resources Research, 15, p. 23-30.

Faust, C.R., and Mercer, J.W., 1979b, Geothermal reservoir simulation (:) 2. Numerical solution techniques for liquid- and vapor-dominated hydrothermal systems: Water Resources Research, 15, p. 31-46.

Grant, M.A., 1979, Interpretation of downhole pressure measurments at Baca: Proc. Fifth Workshop on Geothermal Reservoir Engineering, Stanford Univ., Stanford, p. 261-268.

Ingebritsen, S.E., 1986, Vapor-dominated zones within hydrothermal convection systems (:) evolution and natural state: Ph.D. thesis, Stanford University, 179 p.

Ingebritsen, S.E., and Sorey, M.L., 1985, A quantitative analysis of the Lassen hydrothermal system, north-central California: Water Resources Research, 21, p. 853-868.

Mercer, J.W., and Faust, C.R., 1979, Geothermal reservoir simulation (:) 3. Application of liquid- and vapor-dominated hydrothermal modeling techniques to Wairekei, New Zealand: Water Resources Research, 15, p. 653-671.

Pruess, K, 1985, A quantitative model of vapor-dominated geothermal reservoirs as heat pipes in fractured porous rock, Geothermal Resources Council Transactions, 9, p. 353-361.

Pruess, K., and Truesdell, A.H., 1980, A numerical simulation of the natural evolution of vapor-dominated hydrothermal systems: Proc. Sixth Workshop on Geothermal Reservoir Engineering, Stanford Univ., Stanford, p. 194-203.

Pruess, K., Weres, O., and Schroeder, R., 1983, Distributed parameter modeling of a producing vapor-dominated geothermal reservoir (:) Serrazzano, Italy: Water Resources Research, 19, p. 1219-1230.

Schubert, Gerald, and J.M. Straus, 1979, Steam-water counterflow in porous media: Journal of Geophysical Research, 84, p. 1621-1628.

Schubert, Gerald, and J.M. Straus, 1980, Gravitational stability of water over steam in vapor-dominated geothermal systems: Journal of Geophysical Research, 85, p. 6505-6512.

Straus, J.M., and Schubert, Gerald, 1981, One-dimensional model of vapor-dominated geothermal systems: Journal of Geophysical Research, 86, p. 9433-9438.

White, D.E., Muffler, L.J.P., and Truesdell, A.H., 1971, Vapor-dominated hydrothermal systems compared with hot-water systems: Economic Geology, 66, p. 75-97.

PROCEEDINGS, Twelfth Workshop on Geothermal Reservoir Engineering
Stanford University, Stanford, California, January 20-22, 1987
SGP-TR-109

BLEEDING CHARACTERISTICS OF GEOTHERMAL WELLS

Russell James and Tom Gould

D.S.I.R., Wairakei, New Zealand

ABSTRACT

Discharging small flows (order of 1 t/h) from wells is known as bleeding and is to relieve the build-up of gas pressure at the wellhead and to arrest corrosion in the bore.

First tests over a range of bleeding flows indicate it as a fruitful subject for study in that temperature and pressure measurements at the wellhead can indicate the well enthalpy and the non-condensible gas content of the production system.

Because of environmental restrictions on testing with large discharges in the future, bleeding may soon be the only valid alternative for proving a well's potential.

INTRODUCTION

The production output curve of geothermal wells is familiar to test engineers and its typical shape is shown on Figure 1 as that part AB of the whole curve ABC. The underlying significance which can be drawn from the various shapes that AB can take has been studied, James (1980a), and the mathematics of the curve examined, James (1984). No work has been attempted, however, into studying that part of the generalised curve shown as BC on Figure 1 for deep power-production wells. A recent work, Siitonen (1986), concerns this aspect, however, in testing shallow wells (down to 150 m) at Rotorua, which are used for heating buildings; a simulator has also been employed to establish full output curves, Freeston and Hadgu (1986) in Tibet and Rotorua. These have been studied principally because the Rotorua wells function over the BC region of the curve (which is the reverse of how powerful wells operate) in that more bleeding increases both flow and wellhead pressure. Hence for the powerful wells there has been little or no incentive to study the BC region except to be aware that it exists: this is because no useful result could be seen to accrue from any work undertaken. Although, of course, bleeding of wells is a common and recommended procedure as a steady state condition of wells which have not yet been coupled to a power project, and which if left completely closed would develop corrosion within the casing. This corrosion can be caused by trickle-down condensate in the presence of carbon dioxide and hydrogen sulphide gas, within the top vapour-filled reaches of the well. A steady bleeding reduces this hazard and also eliminates the possibility of dangerous gas build-up at the wellhead which can lead to explosive rupture of the main stop valve as has happened at well BR25 Broadlands, New Zealand and also at Dieng No. 2, Indonesia.

The direct correlation of wellhead pressure and flowrate of a bleeding discharge is no doubt due to the increased heat loss per unit mass flowing when this is of the order of 1 t/h. This heat is lost to the water table, or lower-temperature fluids surrounding the well nearer the ground surface, and increases when flow is reduced, resulting in a lower wellhead pressure. This effect is negligible when wells are operating along AB as here flows generally exceed 100 t/h even at point B, the so-called location of MDP (Maximum Discharging-Pressure) whose importance has been emphasized in a previous work, James (1980b).

REASON FOR THE WORK

Merely the incentive due to our ignorance of how that part of the output curve functions. It seemed easy to test, and if nothing of interest emerged, this minor project could be quietly abandoned.

TEST FACILITY

Broadlands well BR1 was available with a good bleeding range suitable for the present work. As a production well it was poor and had therefore been rejected for incorporation into the forthcoming power project; it was, however, performing useful service for a series of metallurgical experiments. During an interlude between these latter tests, the well was available for the present study.

TEST PROCEDURE

A 10.7 mm diameter lip pressure pipe was attached to the throttle valve (as shown in Figure 2) which was adjusted to give a steady bleeding discharge. This took 24 hours to stablise after which, lip pressure P_c, wellhead pressure P_w and wellhead temperature t_w were noted. Also the discharge was by-passed into the simple drum calorimeter into order to determine flowrate and enthalpy. Results are shown on Table 1. The range of wellhead pressures obtained by this means was from 14.2 bar with the throttle valve wide-open to 5.6 bar when nearly closed; presumably the range could have been extended by employing a lip pressure pipe of larger diameter and hence raising the wellhead pressure further, but sufficient data was collected during this early investigation to keep us fully occupied in interpretation. Besides, greater flows would have required a larger calorimeter which was not currently available.

Table 1: Test results, gas concentration, enthalpy and flow.

P_w Bar	t_w °C	Gas / Gasteam	P_c Bar	h_o kJ/kg	W kg/s
5.6	63	0.983	-	-	-
6.0	87	0.956	-	-	-
6.3	94	0.943	-	-	-
7.2	122	0.854	-	-	-
7.6	132	0.8	1.15	554.9	0.20
7.7	130	0.818	1.2	546.3	0.213
7.8	132	0.807	1.25	554.9	0.218
8.0	136	0.781	1.35	572	0.226
8.8	145	0.728	1.8	610.6	0.28
9.2	148	0.715	2.9	623.6	0.429
9.5	151	0.69	3.1	636.5	0.448
9.8	155	0.657	3.5	653.8	0.489
11.2	167	0.551	5.25	706	0.662
12.5	174	0.5	7.25	736.8	0.862
14.2	186	0.353	9.18	789.8	1.00

CALCULATIONS

From test values of P_w and t_w the gas/steam mass ratio m can be determined from the following equation:

$$m = \frac{(P_w - P)\, V_g}{R(273.15 + t_w)} \qquad (1)$$

where P and V_g are the saturated vapour pressure and specific volume of saturated steam at temperature t_w. The gas constant R is evaluated from (a) the Universal Gas Constant 1.9858 cal/mol K, (b) Joule's Equivalent 4.1868 J/cal, (c) Gravitational Constant 9.8066 m/s^2, (d) The molecular weight of 44 for carbon dioxide which is the principal geothermal gas.

$$R = \frac{1.9858\ (4.1868)\ 9.8066}{44} = 1.853 \qquad (2)$$

The gas concentration in the gasteam mixture (water not included) is calculated from m as:

$$\text{gas/gasteam} = \frac{m}{m + 1} \qquad (3)$$

and results on Table 1 are plotted against wellhead pressure on Figure 3 where a straight line is obtained. The extrapolation of this line to zero gas gives a maximum wellhead pressure of about 19 bar, while for a gas/gasteam ratio of 0.1, a wellhead pressure of 17.5 bar is obtained. Downhole measurements on this well give a water phase below the casing at 227.3°C which from James (1980b) would be consistent with a maximum wellhead pressure under discharge, of 18.36 bar which would be in agreement with about 4% gas in the gasteam mixture of Figure 3. If this well is typical of bleeding conditions, it appears that an estimate can be made of the likely MDP (Maximum Discharging-Pressure) and hence of the well enthalpy merely by taking some values over a range of bleeding pressures (most production wells at Broadlands are in the range 2 to 6% gas). It would be useful, however, especially for new geothermal fields, to be able to estimate the gas concentration in the gasteam mixture at MDP from simple test results on bleeding as undertaken in this work. It should be noted that a knowledge of gas/steam or gas/gasteam ratio gives no information on the proportion of water present, which may be large or small.

The wellhead temperature t_w can be used to determine the enthalpy of single-phase liquid water h_f from Steam Tables of Keenan et al. (1969), and is shown plotted as a straight line on Figure 4 together with actual test results derived when the lip pressure pipe is discharged into the calorimeter. For wellhead temperatures exceeding 100°C, the enthalpy agrees well with that of the straight line, indicating that there is a negligible quantity of gasteam present and that enthalpy can be estimated as that of liquid water at the wellhead temperature. Hence, in Table 1, flowrate can be calculated from values of P_c and h_o according to the formula below from James (1987):

$$W = 1.6234\ \frac{d_c^2\ P_c^{0.96}}{h_o^{1.102}} \qquad (4)$$

For the lip pressure discharge pipe diameter of 10.7 mm, this simplifies to

$$W = 185.86\ \frac{P_c^{0.96}}{h_o^{1.102}} \qquad (5)$$

Therefore the lip pressure can be used to determine enthalpy without the requirement of a calorimeter, although whether this applies to all bleeding (high power) wells can only be confirmed by similar experiments on other boreholes.

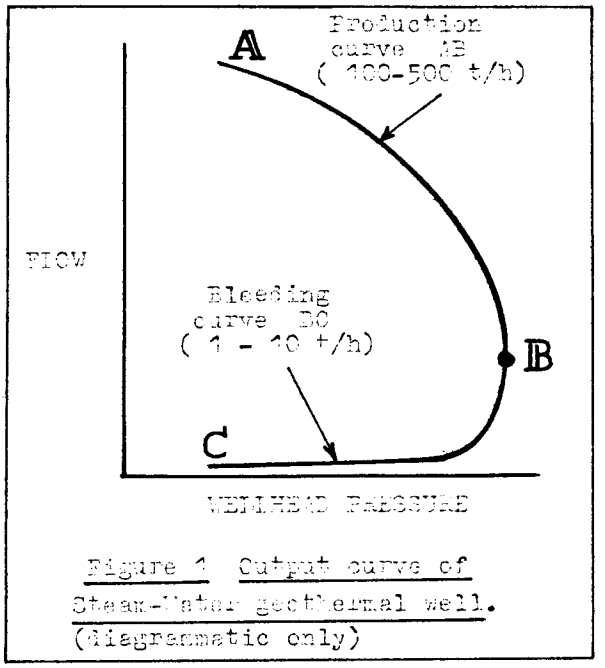


Figure 1 Output curve of Steam-Water geothermal well. (diagrammatic only)

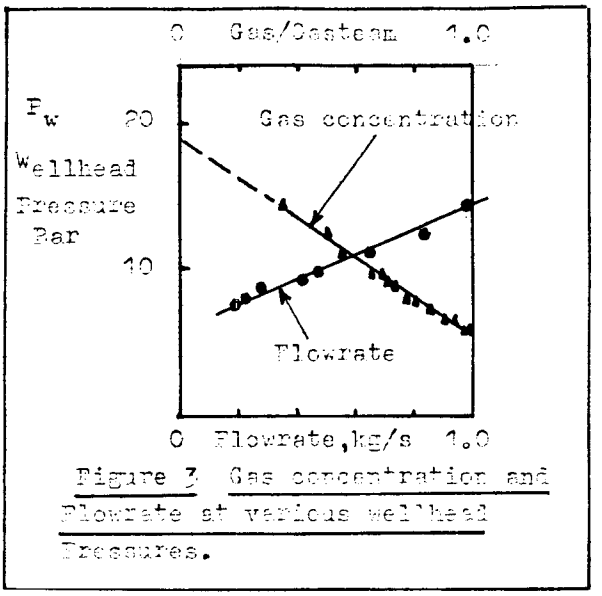


Figure 3 Gas concentration and Flowrate at various wellhead Pressures.

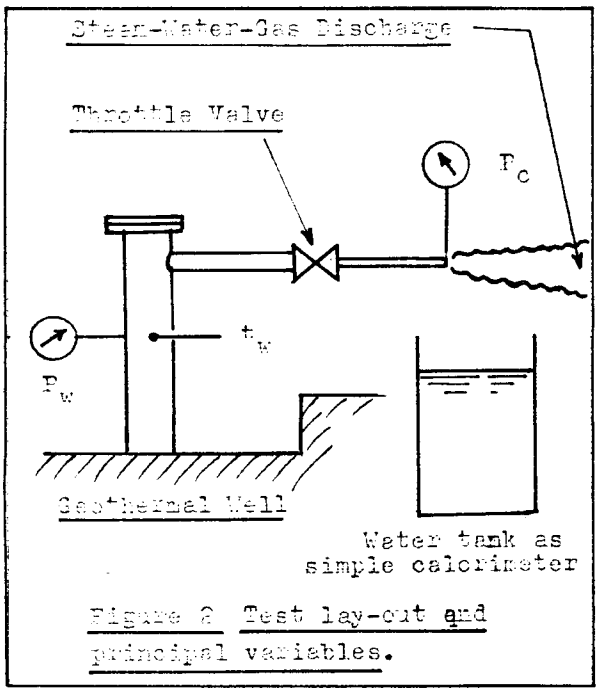


Figure 2 Test lay-out and principal variables.

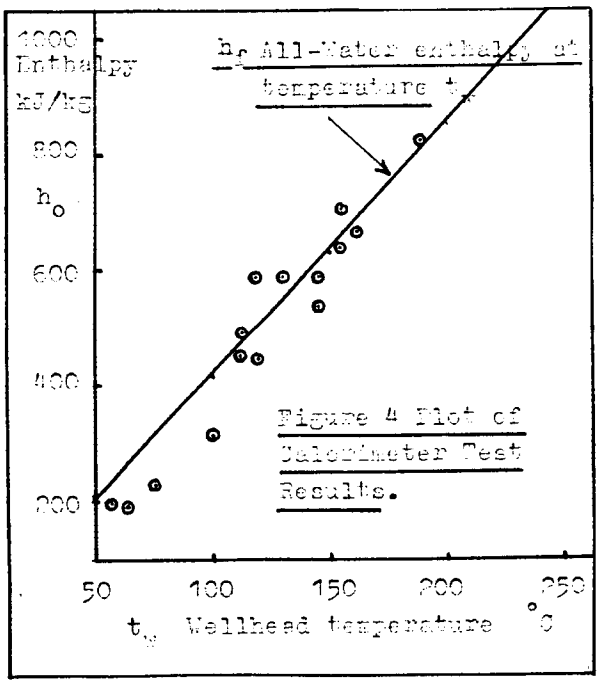


Figure 4 Plot of Calorimeter Test Results.

As lip pressures exceed atmospheric pressure only above wellhead pressures of about 7.5 bar, relevant values of P_c, h_g and W are not shown for lower pressures on Table 1.

GAS BUBBLE VELOCITY

The terminal vertical velocity of rising air bubbles in stagnant water is about 0.3 m/s, Wallis (1969), but this is for water at 20°C. As terminal velocity is inversely proportional to water viscosity which is 0.15 centipoise at 186°C compared with 1.0 centipoise at 20°C, we expect air bubbles (and similarly carbon dioxide bubbles) to rise at about 0.3/0.15 = 2.0 m/s in well water at 186°C.

From Table 1, at 186°C, the flowrate was 1.0 kg/s, hence the vertical velocity in 0.2 m diameter well casing for water of specific volume 1.1357 l/kg is:

Vertical water velocity =

$$\frac{(1.0)\ 1.1357}{(1000)\ \frac{\pi}{4}\ (0.2)^2} = 0.036 \text{ m/s}$$

Therefore at the low upward velocity of well water when bleeding at rates of the order of 1 kg/s (3.6 t/h), the bubble rise velocity is more than 50 times that of the water.

It appears likely, therefore, that over the range of discharges usual when bleeding a well, the non-condensible gas flow is relatively constant. This is confirmed by the common geothermal field experience of a steady gas build-up at wellheads even when total flow is halted by closure of the main stop valve (or comparable throttle valve).

If this is assumed, and employing mass distribution coefficients of carbon dioxide in steam and water, Ellis and Mahon (1977), together with equation (1), the percentage mass concentration of carbon dioxide in total flow, at bleeding wellhead pressures of 8.0 and 14.2 bar (from Table 1), is estimated to be 0.7% and 0.16% respectively.

CONCLUSIONS

This is only the first study (as far as we know) on bleeding of wells drilled for electric power development, which are relatively deep and of a temperature exceeding 200°C. Whether the results are symptomatic of the genre or untypical is impossible to determine without undertaking similar tests on a variety of wells.

REFERENCES

Ellis, A.J. and Mahon, W.A.J. (1977): Chemistry of Geothermal Systems. Academic Press, New York, U.S.A.

Freeston, D.H. and Hadgu, T. (1986): Calculation of Output Characteristics of Shallow Wells. Proc. 8th New Zealand Geothermal Workshop, Univ. of Auckland, Auckland, New Zealand.

James, R. (1980a): Deductions of the Character of Steam-Water wells from the Shape of the Output Curve. Proc. New Zealand Geothermal Workshop, Univ. of Auckland, Auckland, New Zealand.

James, R. (1980b): Significance of the Maximum Discharging-Pressure of Geothermal Wells. Proc. 6th Workshop Geothermal Reservoir Engineering, Stanford Univ., Stanford, Calif., U.S.A.

James, R. (1984): Successful Prediction of Mokai 5 Discharge. Geothermal Energy, 12, 2, p. 7.

Keenan, A.H., et al (1969): Steam Tables, Wiley, New York, U.S.A.

Siitonen, H.J. (1986): Output Tests of Shallow Rotorua Wells. Proc. N.Z. Geothermal Workshop, Univ. of Auckland, Auckland, New Zealand.

PROCEEDINGS, Twelfth Workshop on Geothermal Reservoir Engineering
Stanford University, Stanford, California, January 20-22, 1987
SGP-TR-109

DISCHARGING THROUGH AN ORIFICE DETERMINES STEAM-WATER ENTHALPY

Russell James

D.S.I.R., Wairakei, New Zealand.

ABSTRACT

A wide range of steam-water mixtures was discharged to the atmosphere through a 10.7 mm diameter orifice which was sharp-edged with a minuscule throat pressure tapping. The ratio of throat pressure to up-steam pressure was found sensitive to dryness fraction over the whole range studied from 0.03 to 1.0.

The technique (employing large orifices) has the potential of identifying the unknown enthalpy of geothermal wells discharging large flows.

Contrariwise, a nozzle (rounded entry orifice) was found remarkably insensitive over most of the dryness range and hence is useless for such determinations; however, it can be used to measure the flow-rate when enthalpy is known.

INTRODUCTION

What is the minimum wellhead equipment which will permit the evaluation of a steam-water discharge into its components of flow, enthalpy and (say) electric power potential? According to James (1970), an atmospheric separator is sufficient to accomplish this when lip pressure and reject water flow are measured. However, many wells - and especially isolated ones - are first discharged with no introduced equipment except the necessary discharge pipe vertically erected and bolted to the wellhead valve. Under this condition, it is still possible to estimate the power potential, James (1975), with an accuracy sufficiently good for most practical purposes. It is even possible to sometimes get an accurate figure for the enthalpy of flow from hot water reservoirs when the well is discharging under conditions of the highest possible wellhead pressure, James (1980a), and the lip pressure then employed to evaluate the other parameters.

The importance of enthalpy is such that it would be of considerable value if a technique could be developed to measure it directly from the discharge. An attempt to do just this was undertaken by James and others (1980b) who compared different approaches so as to find the most promising for further development. The methods tested included laser beam, hot-wire anemometer, pitot tube and digital thermometer.

The best tested proved to be a hydraulic analogue of the hot-wire anemometer, but had the disadvantage of interposing a small diameter pipe across the discharge near the sonic location which would result in its rapid erosion. It would be of advantage, therefore, to evolve an approach which avoided such interpositions especially when used on initial discharges which often eject rock fragments as well as steam-water mixtures at speeds up to 0.5 km/s.

To accomplish this, it was decided to study the effect of discharging steam-water mixtures through a nozzle in the expectation that the ratio of throat pressure to up-stream pressure would be related to the flowing enthalpy. (Up-stream pressure in this context is that of a vessel to which the nozzle is attached and whose dimensions are large compared with that of the nozzle's throat.) Experiments in the past have determined that this ratio is about 0.55 for superheated steam and 0.58 for moist steam, Potter (1959), hence it was thought likely that the ratio would increase further with steam wetness and provide a method of estimating the enthalpy of flow.

EXPERIMENTAL FACILITY

A geothermal well was used as the source of the steam and hot water which were individually piped to a small pressure vessel of 100 mm dia. The non-condensible gas content of the steam at the wellhead separator pressure of 10.75 bar was 2.5 wt% and steam and water enthalpies were 2781 and 777 kJ/kg respectively, at the same temperature of 183°C. By employing control and metering valves for the separate phases, any desired proportion of steam and water could be mixed in the vessel and then discharged through the nozzle whose throat diameter was 10.7 mm. Because of the pulsations inherent in the flow of steam-water mixtures, glycerine-damped pressure gauges were mandatory with needle valves between the gauges and the pressure locations; these were necessary to reduce the amplitude of the needle swing to readable values. The dimensions of the nozzle are

shown on Figure 1 with P_m as the manifold vessel pressure, and P_c as a critical throat pressure, in consistent units. Critical flow is a term generally used about compressible fluids which have attained the speed of sound (Mach 1) and which for steam is about 500 m/s. Because of the large difference in cross sectional area of the manifold to the throat together with the former's higher pressure, the velocity within the manifold is only 3.3 m/s for critical flow of steam through the nozzle. Therefore, the pressure-drop along the manifold is negligible and the location of the manifold pressure tapping relatively unimportant.

In the case of steam-water mixtures, sonic velocity is significantly less than that of dry steam and the steam content of the manifold fluid much less than that at the throat being at a higher pressure and identical stagnation enthalpy, hence the velocity in the manifold is much less than that of the comparable steam flow. This confirms the relative unimportance of manifold pressure tapping location compared with the geometry of the throat pressure tapping which as seen on Figure 1 is given with some precision as it was suspected that its location would be critical in both senses of the word. The same argument applies to the orifice of later tests which is also shown on Figure 1.

NOZZLE TEST RESULTS

These are shown plotted on Figure 2 and within the limits of accuracy expected of field testing, agree well with the condition of dry steam flow giving a ratio at $x_m = 1.0$ of about 0.56 compared with published values of 0.58. There is not much change in this ratio even when the dryness has decreased to a half at $x_m = 0.5$ and even over most of the remaining dryness range the curve is fairly shallow and makes the nozzle an unexciting prospect for determining the dryness fraction within the manifold (and therefore the enthalpy of flow).

A cheerful aspect of these results however is that the nozzle can be used as a flow metering device if the dryness fraction at the manifold pressure is in fact known and it is wished to determine the flow-rate to the atmosphere or into a low-pressure vessel (pressure less than the nozzle throat pressure). In this case, the shallowness of the experimental curve is an advantage in estimating the value of P_c which can then be used in the formula given by James (1966) in the metric form and for a 1.0 mm tapping.

$$w = 1.6234 \frac{d_c^2 \; P_c^{0.96}}{h_o^{1.102}} \qquad (1)$$

w Flow of mixture, kg/s
d_c Nozzle diameter, mm
P_c Throat pressure, bar
h_o Specific stagnation enthalpy (enthalpy of steam or steam-water mixture in manifold at pressure P_m and dryness fraction x_m), kJ/kg.

This result should have widespread use in permitting calculation of the flow of steam-water mixtures through nozzles from vessels of known pressure and enthalpy (or dryness) in a similar manner to the classical method for dry or superheated steam, Potter (1959).

Although this was an unexpected bonus, it merely compensated for the failure to develop a method of directly determining enthalpy in which the nozzle had appeared the most promising candidate. At this point therefore, other devices had to be considered.

ORIFICE TEST RESULTS

Short tubes were tried and these appeared to have merit but only if very short. It was finally decided to take the shortest possible tube and hence the final design was in effect a sharp-edged orifice being a plate of 2 mm thickness with a pressure tapping hole of 1.0 mm diameter drilled within it as shown in Figure 1 where the orifice diameter was 10.7 mm as for the nozzle throat.

The experimental results are shown on Figure 2 together with that of the nozzle and it is clear that the pressure ratio is now much more sensitive to dryness fraction over the whole range tested, namely 0.03 to 1.0 and can be used to determine it with far greater precision.

Small wetnesses in steam are notoriously difficult to estimate, but the orifice appears to have the capability of evaluating these as easily as for higher wetnesses, as the curve is of constant slope over a dryness range of 0.1 to 1.0 (wetness 0.9 to zero).

Although as has been mentioned, the throat pressure of the nozzle can be used to calculate flows from vessels at known enthalpies and pressures, it does not appear that the orifice pressure P_c can be so employed as it is not at all certain if it functions under conditions of critical flow at Mach 1. At a given flow and enthalpy, it gives a much lower ratio; for dry steam the nozzle gives 0.56 whereas the orifice gives 0.16 for example. Perhaps the true critical pressure exists in the orifice a little upsteam of the pressure within the plate. The present test series has not studied these interesting aspects as they are perhaps irrelevant to the purposes of this investigation which was to discover the simplest promising technique (a strictly ad hoc approach or perhaps even a minimalist one).

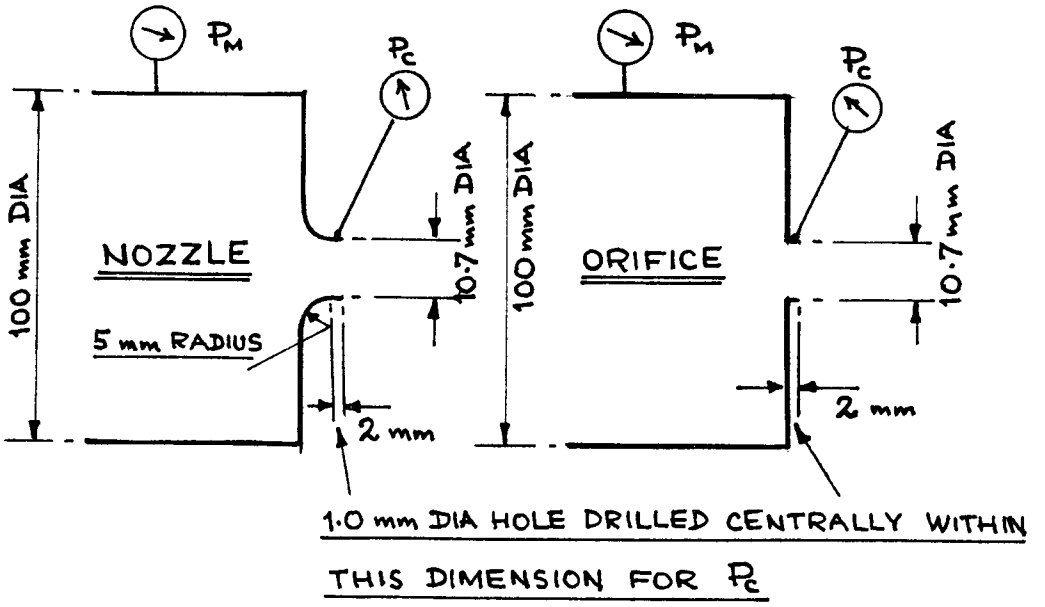


FIGURE 1 GEOMETRIC SHAPE OF NOZZLE AND ORIFICE

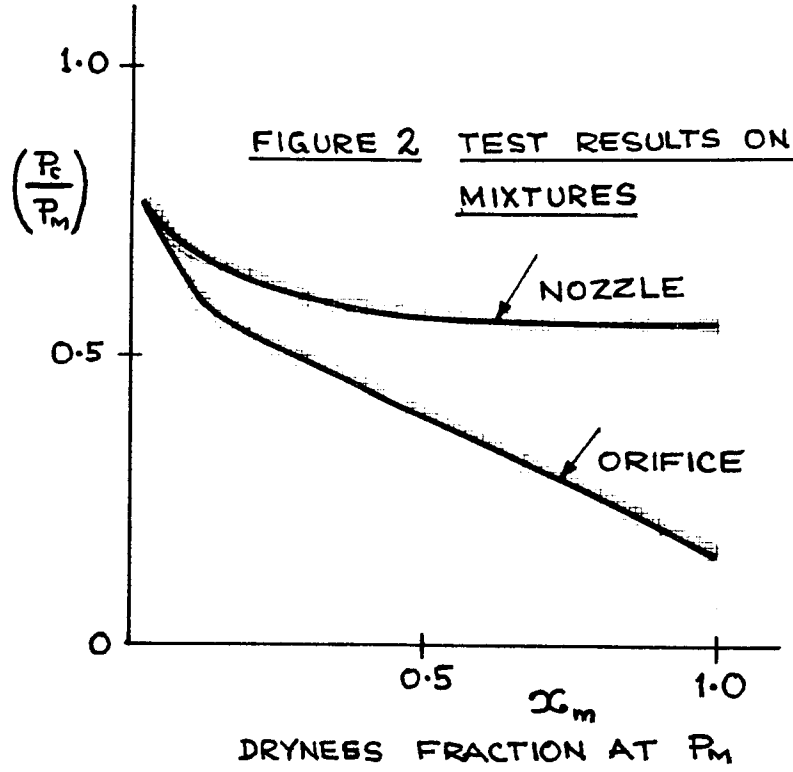


FIGURE 2 TEST RESULTS ON STEAM-WATER MIXTURES

From the viewpoint of geothermal wells, the orifice approach is not an ideal solution to the problem posed, as even for a relatively small output well, an orifice of 100 mm diameter would be required discharging from a manifold vessel of 1.0 m diameter and at least 1.0 m long; for powerful wells these dimensions would have to be doubled giving a vessel of not inconsiderable weight to be bolted to the wellhead. In practice, the orifice plate would have to be of stainless steel as although erosion could not be detected over weeks of testing, it is anticipated that standby corrosion would deteriorate the thin plate and its pressure tapping geometry. (Erosion is severe, however of objects which penetrate the flow for a significant period of time.)

If tests on large sized orifices confirm these results, then the example following may be typical of values obtained on actual wells which discharge steam-water mixtures of high enthalpy.

ILLUSTRATIVE EXAMPLE

Discharge through a 1.0 m diameter manifold and 100 mm diameter orifice gives a manifold pressure of 15 bar and orifice throat pressure of 6 bar. Estimate the enthalpy of discharge, and flow-rate.

$$\frac{P_c}{P_m} = \frac{6}{15} = 0.4$$

From Figure 2 for the orifice, $x_m = 0.485$

Enthalpy $h_o = h_f + x_m h_{fg}$ (2)

$h_o = 844.89 + (0.485)\ 1947.3 = 1789.3$ kJ/kg

where 844.89 and 1947.3 are the sensible and latent heats of steam at 15 bar from steam tables, Keenan and others (1969).

For a nozzle of throat diameter 100 mm and identical manifold pressure and dryness fraction of $x_m = 0.485$,

$$\frac{P_c}{P_m} = \frac{P_c}{15} = 0.57$$

Hence nozzle $P_c = 15\ (0.57) = 8.55$ bar
From equation (1)

$$w = 1.6234\ \frac{(100)^2\ (8.55)^{0.96}}{(1789.3)^{1.102}} = 33.16 \text{ kg/s} \quad (119.38 \text{ t/h})$$

A good high-enthalpy well of standard casing can possibly discharge up to 400 tonnes/hour, hence an orifice of 200 mm diameter would be required to cover a full range of outputs.

CONCLUSIONS

For discharging mixtures at known enthalpy to the atmosphere, the nozzle appears to be a useful instrument to determine flow-rate but is relatively insensitive to enthalpy. However, the orifice has reverse characteristics in that it is sensitive to enthalpy and can be used to evaluate this important parameter while incapable of estimating flow-rate. The overall accuracy of the orifice as a geothermal field device can probably only be evaluated in the last analysis by field tests on fully sized diameters of 100 and 200 mm. However, the results on even the small instrument reported here show no inherent problems are anticipated.

The orifice may also have wide application in its ability to determine small wetnesses carried by nearly dry steam in conventional steam engineering.

REFERENCES

James, R. (1966): Measurement of Steam-Water mixtures discharging at the speed of sound to the atmosphere. New Zealand Engng 21, (10), p. 437.

James, R. (1970): Factors controlling Borehole Performance. Geothermics Special Issue, 2, 2, Pt 2, p. 1502.

James, R. (1975): Rapid Estimation of Electric Power Potential of Discharging Geothermal Wells. Proc. 2nd U.N. Symp. Develop. and Use of Geothermal Resources, San Francisco, U.S.A.

James, R. (1980a): Significance of the Maximum Discharging-Pressure of Geothermal Wells. Proc. 6th Workshop Geothermal Reservoir Engineering, Stanford Univ., Stanford, Calif., U.S.A.

James, R., McDowell, G., Barnes, T., Syms, M. (1980b): Study of Sonic Steam-Water Mixtures by Laser-beam, Hot wire Anemometer, Pitot Tube and Digital Thermometer. Proc. 4th New Zealand Geothermal Workshop, Auckland Univ., Auckland, New Zealand.

Keenan, J.H., et al (1969): Steam Tables, Wiley, New York, U.S.A.

Potter, P.J. (1959): Power Plant Theory and Design. Ronald Press, New York, U.S.A.

PROCEEDINGS, Twelfth Workshop on Geothermal Reservoir Engineering
Stanford University, Stanford, California, January 20-22, 1987
SGP-TR-109

FRACTURE DETECTION IN GEOTHERMAL WELLS DRILLED IN VOLCANIC ROCKS

By: Mauro Gonfalini — AGIP Milan, Italy
Walter Chelini — AGIP Milan, Italy
Etienne Cheruvier — SCHLUMBERGER London, GB
Jean Suau — SCHLUMBERGER Milan, Italy
Werner Klopf — SCHLUMBERGER Milan, Italy

ABSTRACT

The Phlegrean Fields, close to Naples, are the site of important geothermal activity. The formations are volcanic and mostly tuffites. They are originally very tight but the geothermal alteration locally produces fractures with large increase in permeability. The lack of geological markers makes well-to-well correlation quite difficult. Thus the local detection of fractured zones in each well is very important for the evaluation of its potential.
The Mofete 8 D well is a typical example. A rather complete logging program was run for fracture detection. Standard methods turned out to be disappointing. However several non-standard detectors were found to be very consistent and, later on, in excellent agreement with the analysis of cuttings. They are derived from the Dual Laterolog, the SP, the Temperature log and, most particularly, the Acoustic Waveforms from the Long Spacing Sonic.
The Dual Laterolog and the Temperature Log indicate invasion by fresh and cold mud filtrate; the SP behaves as in a typical Sand-Shale sequence. Sonic Waveforms were first analyzed by a purely empirical method derived from consistent log patterns.
A practical algorithm compares the total energy measured in each of the two fixed time windows located the one before, the other after the fluid arrivals. The altered zones (i.e. fractured and permeable) are clearly shown by a complete reversal of the relative energy of these two windows.
A more scientific method was then applied to the Waveforms; it is based on both logging experiments and physical considerations. The energy carried by the tube wave is separated by a frequency discrimination: it correlates very well with formation alteration, thus also with the other indicators including the empirical Waveform method. It should have two advantages:

- It should permit at least a semi quantitative permeability evaluation
- It seems to be promising in other formations: non-volcanic geothermal wells and even hydrocarbon-bearing rocks.

INTRODUCTION

The Phlegrean Fields are a quaternary volcanic complex located in Southern Italy, west of Naples. This area has been known for geothermal activity even before the Roman Empire. From 1939 to 1953 SAFEN* carried out an exploration program particularly in the Mofete area, a very interesting zone for geothermal application. In 1978 AGIP, in a Joint venture with ENEL** resumed geothermal exploration by drilling new and deeper wells. The results indicated the presence of a water-dominated field with three main reservoirs (2). A very low permeability of the volcanic rocks is the main problem: the potential of this geothermal field is directly dependent on the presence of active fractures. Thus their detection usually by means of wireline logging is a key to the evaluation of the reservoir. The Mofete 8 D well was drilled in 1982 to explore a strongly altered and fractured area.

GEOLOGICAL SETTING

The Phlegrean Fields volcanic complex is located in the Upper Pliocene Graben structure of the Campanian plain (fig.1). It is on the margin of the Appennine mountains and was probably developped after the opening of the Tyrrhenian basin. The Phlegrean Fields are a sequence of dominantly pyroclastic eruptive centers in a regional caldera approximately 13 Km in diameter and created by paroxistic eruption of the Campanian Ignimbrite about 35,000 years ago (8). Very recently (June 1982 to December 1984),

the Phlegrean Fields were submitted to a tectonic uplift of about 1.8 m and to intense seismicity (1); this indicates permanent underground activity due to magmatic and phreato-magmatic phenomena.
Four main stages of volcanic activity can be recognized in this area (8):

1 - a pre-caldera, mostly submarine, activity culminating with the eruption of the Campanian Ignimbrite (50000 to 35000 years ago)
2 - a post-caldera, mostly submarine, activity (35000 to 10500 years ago)
3 - an early subaerial activity (10500 to 8000 years ago)
4 - a late subaerial activity (-4500 years to present); the latest recorded activity was the Monte Nuovo eruption, 1538 AD.

The subsurface, as recognized by the wells already drilled, consists in volcanic and volcano-sedimentary rocks. The lithologic sequence, with corresponding thickness from top to bottom is the following:

1 - Yellow Tuffs: 180 m to 590 m
2 - Tuffites and interbedded subaerial tuff: 500 m to 800 m
3 - Trachytic latitic lava domes: 250 m to 500 m
4 - Volcano sedimentary complex: 500 m to 600 m
5 - Thermometamorphic rocks may be intersected at the bottom of the deeper wells.

Unfortunately there are no clear marker beds; therefore correlation between wells is extremely difficult.
Alteration minerals present in these rocks are typical of a high temperature geothermal environment (9), (4). The mineralogy of the wells drilled in the Mofete area permits to distinguish four main zones: a-argillic, b-illite-chlorite, c-calc-aluminum silicate and d-thermometamorphic zone.
The well Mofete 8 D is 907 m deep and reaches only the first two formations (2 and 8, fig.2); from the point of view of alteration minerals, only the first three types (a, b and c, fig.3) are represented.

STRATIGRAPHIC AND HYDROTHERMAL CHARACTERISTICS OF MOFETE 8 D

All rocks crossed by the well are of volcanic origin and mainly pyroclastic. The lithological sequence is as follows:

1 - 60 m to 280 m: Yellow tuffs and chaotic tuffs dating from the latest part of post-caldera activity and the last two periods (1 and 9: subaerial activity)
2 - 280 m to 890 m: chaotic tuffites with lime-argillic matrix and thin layers of interbedded subaerial tuffs; these are products of caldera filling
3 - 890 to 907 m: Trachytic lava flow of original (non altered) mineralogy.

The alteration is mainly due to the solution and deposition of new minerals caused by circulation of hydrothermal fluids. The formation of these hydrothermal minerals is controlled by: temperature, permeability, fluid composition and texture. Permeability is an essential factor since most mineralogical changes are not isochemical: in order to start an exchange of constituents there must be open fluid channels in the rock; further alteration often enlarges them, thus increases permeability. From the point of view of this hydrothermal minerals, several zones can be defined:

1 - an argillic zone characterized by the presence of montmorillonite, zeolites and smectites in general. This zone should end at 100 m
2 - an illite-chlorite zone where, in addition to these two dominant minerals, sericite is also found. On the contrary, the percentage of smectites and zeolites is much lower. This zone ends at about 500 m.
3 - at this depth a calc-aluminum combination appears. It is produced by precipitation of silica-quartz, adularia, epidote and pyrite. This mineralogical association is particularly abundant in the lower part of this well. In the calc-aluminum zone one can observe remarkable variations in the abundance of hydrothermal minerals: this is due to the presence of active fractures allowing easy flow of geothermal fluids.
Three main zones of strong alteration are evident in this zone: around 700 m, from 780 m to 840 m and from 870 m to 890 m.

LOGGING PROGRAM

The target of the well was to intersect, at shallow depth, a zone of expected high secondary permeability due to fracture.
In this part of geothermal reservoir, the fracturing is generally provided by a fault system which can be located by surface evidences and geophysical surveys. The fault system was supposed to be in connection with the most

superficial acquifer tapped by other wells drilled in the Mofete Field (2). The formation temperature was supposed to be of the order of 230 - 250° C, and the formation water salinity of the order of 35,000 ppm (NaCl) at reservoir conditions.
After completion and testing (fig.3), the well was considered productive in the interval here analysed.
Under those conditions a rather complete set of logs was run (fig.3), including a Natural Gamma Ray Spectometry Survey, and an HDT service, to improve the usual log interpretation both for lithology and fracture detection.
As it has been reported in many geothermal field studies (7), Density and Neutron logs are not only affected by porosity changes, but also by the presence of hydrothermal alteration products.
Unfortunately, due to the hostile conditions of the wells drilled in the Mofete Field, such as temperature and hole rugosity, tools which carry a radioactive source were deleted from the logging program after few experiences.
So there is no information from such a combination of logs to define porosity and hydrothermal alteration minerals distribution.

COMMENTS ON LOGS AND THEIR RELATIONSHIP WITH HYDROTHERMAL ALTERATION MINERALS

Usually the GR is a very important log to define lithology in these volcanosedimentary sequences (5), but in case of the Mofete 8 well, the extreme homogeneity of the drilled terrains (fig.3), the interpretation of the Natural Gamma Ray Spectometry Survey does not add information compared to the standard GR log (fig.5).
A FIL (Fracture Identification Log) program, run on the HDT data, was considered not very useful to define the main fractured zones, because only scattered anomalies, probably due to different discontinuities mainly due to the hole rugosity, were detected.
At this stage a qualitative analysis of different patterns on the Acoustic Waveform recording from the SLS, gave rise to a less conventional approach for fracture detection. The information derived from this new kind of approach was of course compared with more conventional fracture detection techniques based on logs such as Dual Laterolog, SP and Temperature.
The peculiar patterns recognized on the Acoustic Waveform recording in different zones are clearly shown in fig.4 where, according to the transit time of different kind of waves, compressional and shear amplitudes are sometimes very well defined when mud and tube-wave are strongly attenuated, but in other zones the exactly inverse phenomenon is present.
Those patterns were, as a first step, correlated to a different behaviour of the DT curve, which shows a slight decrease in readings probably related to a lower porosity in a fairly homogeneous lithology (tuffs and tuffites rarely interbedded with trachilatitic lava flows) as in fig.4.
A detailed mineralogical analysis of cuttings, collected with a sample rate of 5 m per sample, in the interval from 650 to 907 m, was carried out to delineate the distribution of the most important hydrothermal alteration minerals.
This distribution seems to be strongly related to the different behaviour of different kind of waves as described before.
It is possible to differentiate three zones with different distribution of minerals within the interval of interest from top (663 m) to bottom (907 m) as shown in fig.4 and subsequents.
It is necessary to explain that the discrepancy in depth between the boundaries defined by means of logs and those defined by the analysis of the cuttings is largely due to the very poor vertical resolution of the latter. It has been reported (5) that in such lithologies, if a cutting sampling rate of 5 m per cutting is used, this discrepancy could be more than 10 m.
The first zone (A zone), is characterised by the presence of a variable but important volume of hydrothermal alteration minerals, which are mainly constituted by calcite, phyllosilicates (such as illite-sericite and chlorite), albite and adularia and as index mineralogical phase, calc-aluminum silicates (such as epidote).
Silica is fairly diffused and mainly distributed in veins.
Those minerals are diffused both in veins and in microfractures, as well as in the "matrix" itself.
From the petrographycal analysis in the A zone the microfractures seem to be widely diffused.
These zones are distributed in the interval of interest, but the amount of such hydrothermal alteration products is very important (up to 50% of the total volume) between 790 m and 800 m and 870 m to 890 m.
A second type of zone (B zone), is characterised both by the presence of

abundant argillaceous minerals and silica, and by a significant reduction of fracturing.
These zones are well defined in the following interval: 715-740m, 830-850 m, 890-900 m.
The third type of zone (C zone) is constituted by unalterated and unfractured lava beds, between 900 and 907 m.
It has been widely documented that the presence of hydrothermal alteration minerals in this reservoir is due to the possibility of geothermal fluids to move within the formations mainly through microfractures and, only in the second place, through primary permeable levels (3).
The SP log behaves like in a shaly-sand sequence, showing permeability in a wide extension of the analysed interval. A broad positive deflection, present between 838-858 m and 887 m to bottom, shows that the permeability is strongly reduced here; those zones broadly correspond to zones classified as B as far as the hydrothermal alteration is concerned (fig.5).
To make this relationship more evident, an empirical treshold was set on the SP curve and a different shading was applied for positive or negative excursions (fig.5).
By the use of a technique based on a calculation of the second derivative of the SP curve it is possible to define the boundary between levels of different concavities and, according to the value and sign of the second derivative, zones with different permeability (fig.5) (10).
The separation between resistivity curves from a Dual Laterolog is related to the invasion of the formation by fresh mud filtrate. This invasion is mainly due to the presence of microfractures. This high porosity formations (up to 40%) have very low initial permeability (from 0 to few tens of MD). Knowing the average salinity of the formation water, which is of the order of 35,000 ppm (NaCl), and the mud filtrate salinity, which is something like 5,000 ppm (NaCl), the zones, showing a separation between LLD and LLS readings with LLS resistivity higher than LLD one, are supposed to be invaded and thus permeable.
Where the resistivity readings of the two different devices are practically of the same value, the formation is free of invasion and those zones are to be considered as impermeable.
The zones where the invasion is present are generally in correlation with the zones classified as type A, those where the invasion is not present are broadly related with the zones classified as B or C (fig.4 and 5).
Two different temperature profiles recorded at different times indicate a broad invasion by cold mud, and particularly in two wide zones between 760-840 m and 860-890 m the separation is rather high, showing an increase in permeability. These two zones broadly correspond again to the zones classified as A.

TIME DOMAIN WAVEFORM ANALYSIS

To make evident with a more quantitative approach the different behaviour of the Acoustic Waves in zones characterised by a different distribution of hydrothermal alteration minerals, an empirical time window technique was applied.
The recording with a spacing (between transmitter and receiver) of 10' was selected.
Two different time windows of different lenght were selected in a fixed position in time in such a way that the first one includes only formation waves (compressional and shear together) and the second one fluid and borehole controlled waves.
The length of the second window is twice the length of the first.
A display of the amplitude integration measured in the two different windows is shown in fig.6.
These values are very high, as far as the first window is considered, in case of the A zone, and very low in case of B and C zones.
A complete reversal is observed for the curve representing the energy measured by the second window i.e. corresponding to mud and tube wave.
It has been suggested that a drastic tube wave amplitude reduction is a diagnostic feature in vicinity of fractured zones (6), such as in the A zones, where the amplitude integration reaches the lower values.
On the contrary a strong build up in amplitude of the tube waves should be related to the less fractured zones like the B and C zones are.
The propagation modes seem to contain also information about the interaction between the borehole fluid and the borehole elasticity which may be related to the formation permeability.
The complete reverse behaviour of the "formational waves" (as compressional and shear waves can be considered) adds new information about the rigidity of the formation itself. It seems reasonable to think that the hydrothermally altered formations are more rigid than the other ones, either because they were so before alteration, or because

the thermal and chemical processes helped to make them more rigid, thus its elasticity is reduced. On the contrary a rock, which is unfractured and contains authigenic clay minerals and silica seems to become more plastic and more attenuative to compressional and shear waves.
The higher activity of the integrated amplitude curve measured in the first window seems to be related to a locally non homogeneous distribution of the hydrothermal alteration minerals and thus a local change in permeability.
To summarize the information given by each single curve, a ratio between the two curves was calculated and displayed in fig.6 in a logarithmic scale.
A qualitative permeability related information is readily available when a treshold is applied.
The lower values compared to the treshold level are shown in black and these values are related to higher permeability levels as in A zones.
The higher values compared to the treshold level are left in white and are related to less permeable levels like in B and C zones.
Fig.6 displays the results of the interpretation carried out as discussed before. It is surprising that practically all the logs, if used like a permeability indicator, are in good agreement to discriminate zones of different distribution of hydrothermal alteration mineral and different elasticity of the formation.
Only the second derivative of a temperature profile (also tried to improve the sensibility of this permeability related indicator), does not seem a satisfactory medium to discriminate the main invaded zones but local changes in the formation behaviour may affect the variability of the curve.

FREQUENCY DOMAIN WAVEFORM ANALYSIS

The above dual window filtering technique is a phenomenological approach based on empirical observations in time domain only.
The behaviour of the signal picked by the first time window (early arrivals), namely the increase of the compressional energy in front of altered zone is reminiscent of what can be observed in some types of sedimentary rocks (i.e. fractured zones in a tight carbonate matrix).
This may be explained by the fact that the lithology supporting open fractures must be more rigid, less plastic than the one which is not fractured.
Regarding the lateral arrivals (picked by the second window), the decrease of the acoustic amplitude in front of the same altered zones is similar to what we observe with the Stoneley wave energy in front of permeable and/or fractured zones in sedimentary rocks.
Production tests confirm the hydraulic transmissibility which is thought to be responsible for alteration of the flowing zones.
Stoneley waves arrive late (indeed they are bound by borehole acoustics to arrive after the expected mud p-wave arrival time) and the frequencies carrying the energy which is sensitive to permeability/fluid mobility characteristics are rather low compared to the relatively higher frequency compressional and shear waves.
Spectral analysis of the composite full sonic waveforms reveals low frequency bands separated from the rest of the spectrum. Application of the inverse of the Fourier transform shows that most of the acoustic anergy carried by the lower frequencies arrives late, i.e. within the second time window.
Fig.6 displays the log obtained when extracting the energy carried by the 1-6 Khz band. It is very interesting to note the straight correlation with second window amplitude integration and the other logs when used like alteration/permeability indicators.
The experimental technique here described seems to be worth for detection of the most probable zones of fluid production in future geothermal wells of the field, or in similar situations.
A future step will be the study of the relationship between permeability measurement from cores and the value of the energy carried by Stoneley waves, to try to define directly a relative value of permeability from the waveform analysis.

ACKNOWLEDGEMENTS

The authors wish to thank the management of AGIP for the permission to publish this paper. They extend their appreciation to the SCHLUMBERGER staff who cooperated in this work.

SAFEN * : Società autonoma forze Endogene Napoletane.

ENEL ** : Ente Nazionale Energia Elettrica.

REFERENCES

(1) BERRINO, G.; CORRADO, G.; LUONGO, G.; TORO, B. (1985), "GROUND DEFORMATION AND GRAVITY CHANGES" ACCOMPANYING THE 1982 POZZUOLI UPLIFT, BULL.VOLC. (in press).

(2) CARELLA, R.; GUGLIELMETTI, M. (1983) "MULTIPLE RESERVOIRS IN THE MOFETE FIELDS, NAPLES, ITALY", NINTH WORKSHOP ON GEOTHERMAL RESERVOIR ENGINEERING. STANFORD UNIVERSITY, CALIFORNIA, Dec. 13-15.

(3) CHELINI, W. (1984), "ALCUNI ASPETTI GEOLOGICO-PETROGRAFICI SUL SISTEMA GEOTERMICO FLEGREO", RENDICONTI DELLA SOCIETA' ITALIANA DI MINERALOGIA E PETROLOGIA, VOL.39, 1984, p.387.

(4) ELDERS, W.A.; HOAGLAND, J.R.; WILLIAM, A.E. (1981), "THE DISTRIBUTION OF HYDROTHERMAL MINERAL ZONES IN THE CERRO PRIETO GEOTHERMAL FIELD OF BAJA CALIFORNIA", GEOTHERMICS, 10, 245-253.

(5) GONFALINI, M.; CHELINI, W. (1983), "STUDIO DEI LOGS REGISTRATI NEL POZZO GEOTERMICO LOCOLA 1", PERMESSO LAGO DI PATRIA (NA), AGIP Internal Report.

(6) PAILLET, F.L. (1980), "ACOUSTIC PROPAGATION IN THE VICINITY OF FRACTURES WHICH INTERSECT A FLUID-FILLED BOREHOLE", SPWLA TWENTY FIRST ANNUAL LOGGING SYMPOSIUM, 1980, p.1.

(7) RIGBY, F.A. (1980), "FRACTURE IDENTIFICATION IN AN IGNEOUS GEOTHERMAL RESERVOIR SURPRISE VALLEY, CALIFORNIA", SPWLA TWENTY FIRST ANNUAL LOGGING SYMPOSIUM, 1980, p.1.

(8) ROSI, M; SBRANA, A; PRINCIPE, C. (1983), "THE PHLEGREAN FIELDS: STRUCTURAL EVOLUTION, VOLCANIC HISTORY AND ERUPTIVE MECHANISM" IN M.F. SHERIDAN AND F.BARBERI ED. "EXPLOSIVE VOLCANISM" JOUR. OF VOLC. GEOTH.RES., 17, 273-288.

(9) STEINER, A. (1977) "THE WAIKAREI GEOTHERMAL AREA, NORTH ISLAND, NEW ZELAND", N. Z. GEOL.SURVEY BULL., 90, 1-136.

(10) SUAU, J. "at al" (1984) "INTERPRETATION OF VERY THIN GAS SANDS IN ITALY", SPWLA TWENTY FIFTH ANNUAL LOGGING SYMPOSIUM, 1984, p.1.

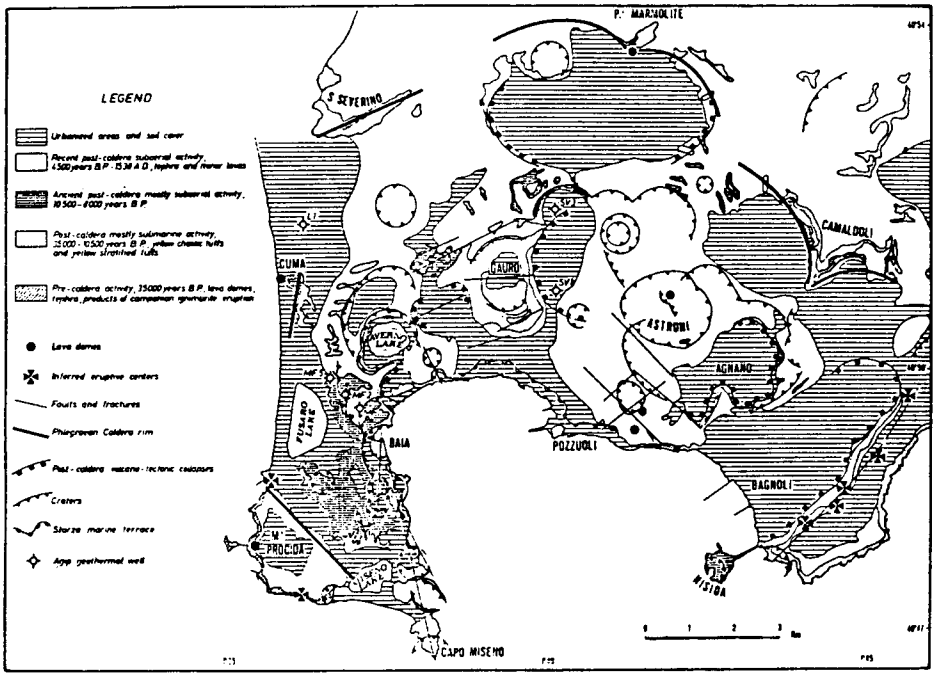


FIG 1 - PHLEGREAN FIELD VOLCANIC COMPLEX

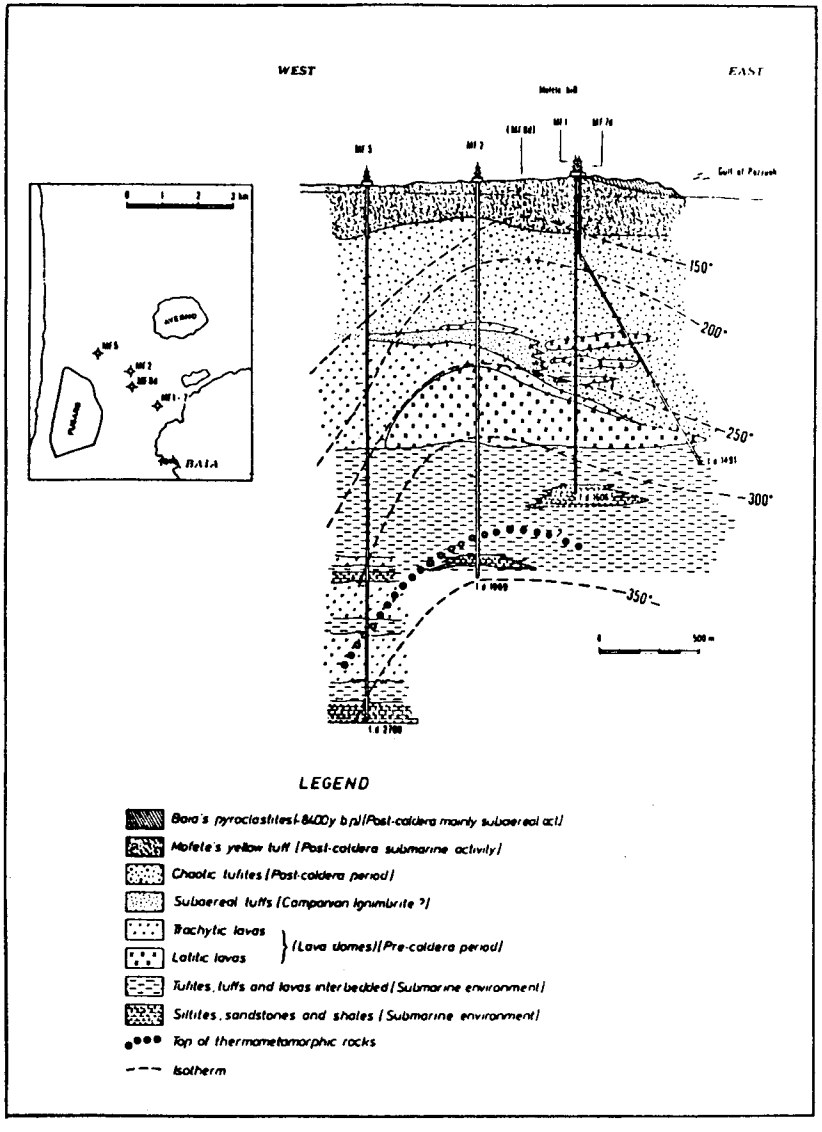


FIG. 2 - CROSS SECTION IN THE WESTERN PART OF PHLEGRAEAN FIELDS

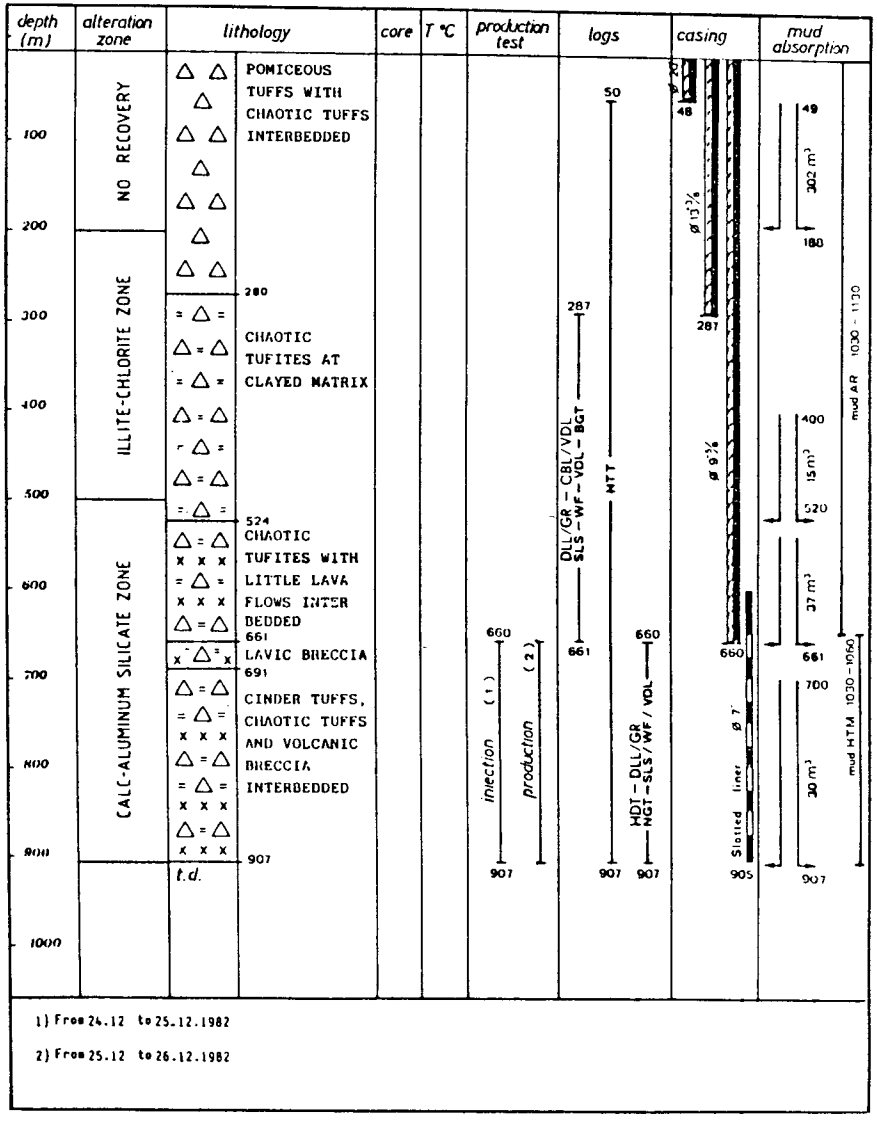


FIG. 3 - WELL MOFETE 8D, SUMMARIZED COMPOSITE LOG

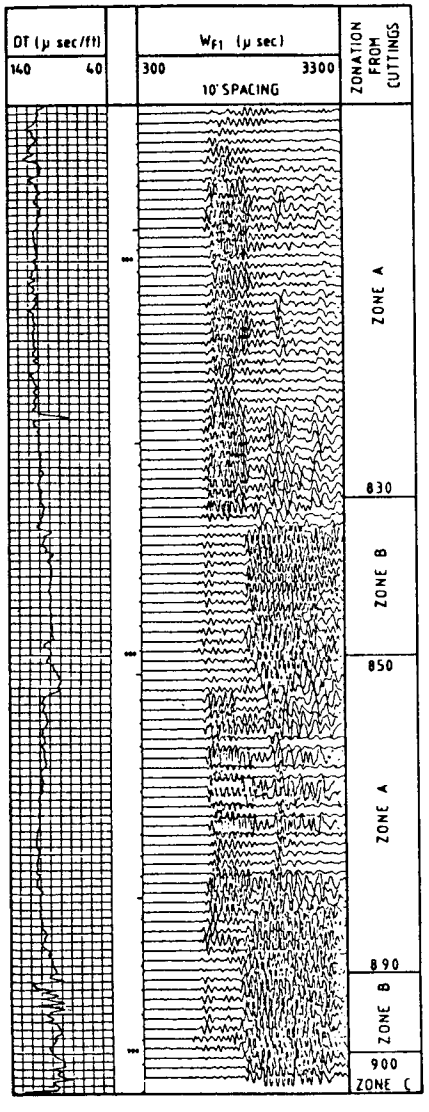


FIG. 4 - WELL MOFETE 8D, CORRELATION BETWEEN WAVE FORMS RECORDING FROM SLS (10' SPACING) AND MINERALOGY

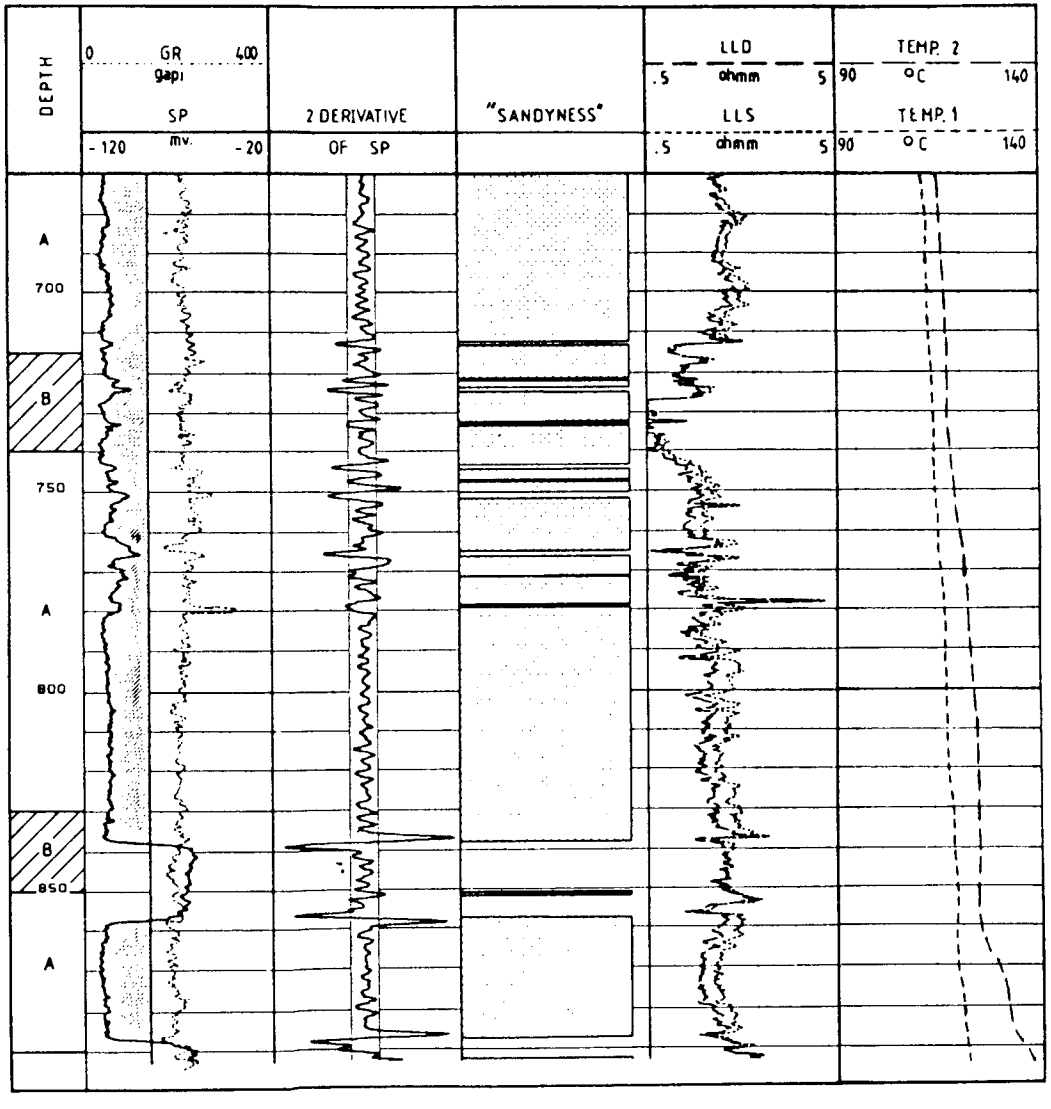


FIG. 5 – WELL MOFETE 8D, WELL LOG DATA AND DERIVED INFORMATION Vs. DEPTH

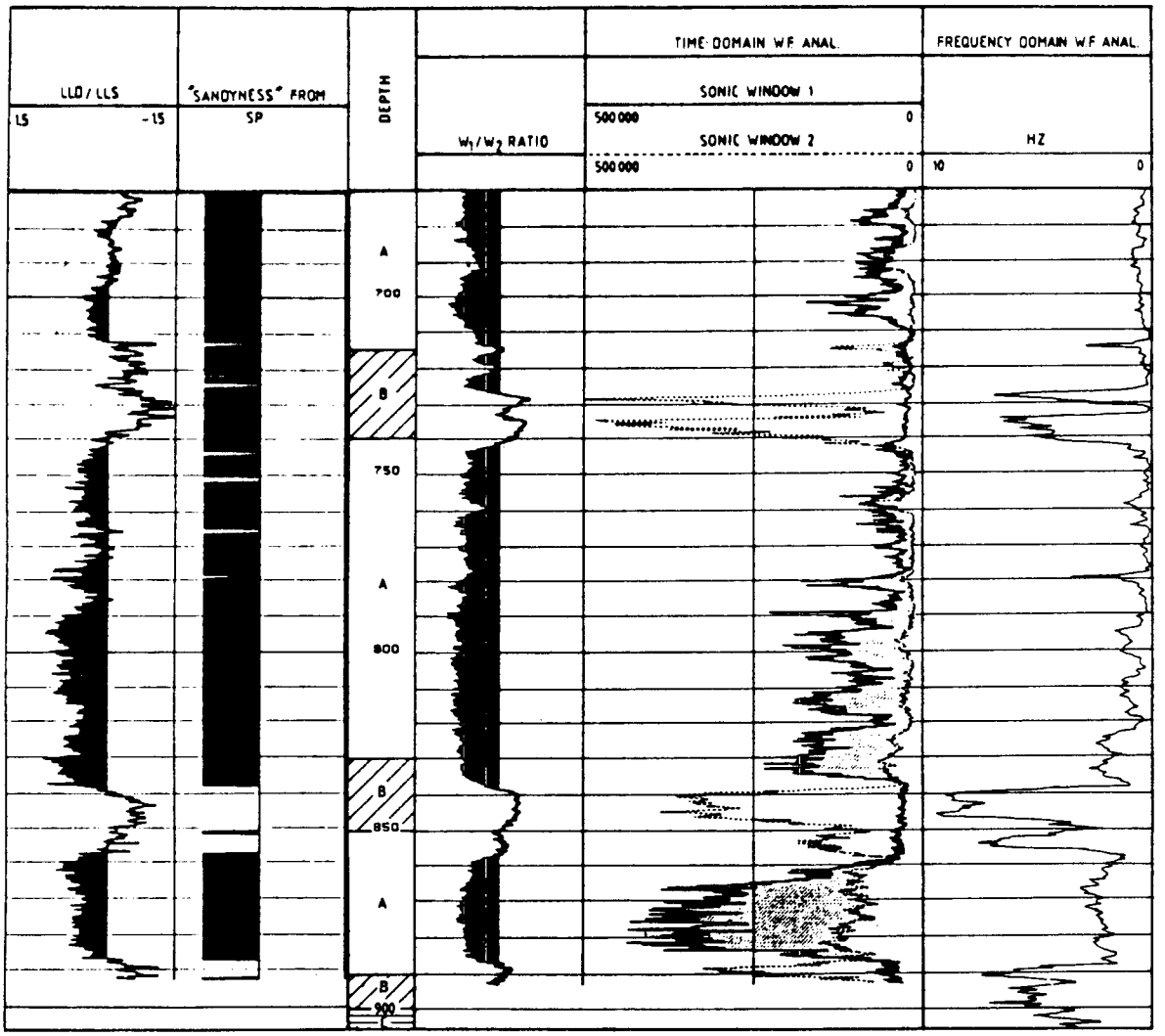


FIG. 6 - WELL MOFETE 8 D - COMPARISON BETWEEN RESULTS OF TIME DOMAIN / FREQUENCY DOMAIN WAVE FORM ANALYSIS AND OTHER PERMEABILITY RELATED RESULTS

PROCEEDINGS, Twelfth Workshop on Geothermal Reservoir Engineering
Stanford University, Stanford, California, January 20-22, 1987
SGP-TR-109

ANALYSIS OF TRANSIENT PRESSURE TESTS FOR OLKARIA EXPLORATION WELLS

CHARLES B. HAUKWA

KENYA POWER AND LIGHTING CO. LTD.
OLKARIA GEOTHERMAL PROJECT
P.O. BOX 785, NAIVASHA, KENYA

ABSTRACT

Analysis of transient pressure tests for Olkaria West wells shows that both infinite acting and double porosity models can be used to analyse the well behaviour and infer reservoir properties from fall-off steps of long enough duration, in wells where no siginificant thermal recovery occurs. The double porosity model gives better estimates of reservoir properties than the infinite acting model, for long fall-off steps in wells intercepting fractures. Semilog methods give fairly good estimates of reservoir transmissivity for the long fall-off steps but are highly inaccurate when used independently, especially for the short fall-off steps conducted in most of the wells. Double porosity models can also be used for recovery test analyses where two phase transients are not siginificant.

INTRODUCTION

In order to delineate the Olkaria geothermal field and define a new area for development nine wells have been drilled to the north and west of the present field (Fig. 1), referred to as Olkaria West. The pressure/temperature distribution from drilled wells indicates a large extension of the present field northwards with uplow around 702, large central cold zone associated with Ololbutot fault and separate field to west with an uplow to the west of 301, 303 area (Fig. 1). Transient pressure tests consisting of injection and fall-off steps during well completion tests have been carried out for all the wells. Recovery tests following discharge have also been done for some wells. Normally these tests have as a routine been analysed by Horner methods. Because of the short duration of the tests, selection of the proper slope for semilog lines is not easy. Tests for OW 101 to 501 were re-analysed using the curve match for infinite acting reservoir, semilog methods and using a computer fit to analytical models, for infinite acting reservoir, double porosity system and uniform flux vertical fracture. Since then further recovery data for OW 301 and completion tests on OW 701, 702 and 303 have become available.

These analytical models have been used in the analysis of recovery data from Krafla Wells by Sigurdsson et al (1985) which showed good fits to measured data, but gave generally lower transmissivities than initially estimated from the injection tests at well completion. The analytical models have also been used in interpretation of interference tests at Ngahwa geothermal field in New Zealand in which it was found that the reservoir response to production/injection was better modelled with double porosity systems that with infinite acting system McGuiness (1984).

In the infinite acting reservoir and double porosity models computer fit of field data, initial guess values of reservoir parameters from the type curve match were used. The programme then adjusted these figures for a best fit to measured data in a series of interation steps.

Injection/Fall-off Tests

Table 1 summarises the results of the transient analysis of the fall-off and injection steps using type curve match, semilog methods, analytical infinite acting and double porosity models. The injection and fall-off steps for wells 101 to 201 were of short duration typically 40-50 minutes, making reliable estimates of wellbore and reservoir properties difficult especially using the semilog methods. The transmissivity is 4.8-8.0 x 10^{-8} m^3/Pas for OW 101. Transmissivity for OW 201 is 1.8-2.0 x 10^{-8} m^3/Pas, (with the double porosity model giving the better fit (Fig. 2b), indicating large fracture permeability with no restriction to fluid flow in fractures.

Injection and fall-off tests for OW 301 were influenced by large thermal recovery with no conclusive results. Two injection and fall-off steps were conducted for OW 401. The fall-off steps lasted over 2 hours and give transmissivity in the range 1.8-4.3 x 10^{-3}/Pas. In the first step no semilog line develops (Fig. 3) making determination of transmissivity by semilog method inaccurate. In the 2nd step (Fig 4) all methods give fairly close estimates of transmissivity.

Two long injection/fall-off steps were conducted in well 501, the fall-off steps lasting 5 and 8 hours, conducted at 1400 and 1300 m depth. All the methods gave similar transmissivities of 0.4-0.7 x 10^{-8} m^3/Pas for the first step and 0.8-1.2 x 10^{-8} m^3/Pas for the repeat step. The double porosity model (Fig. 5) gave near perfect fit to measured data and all methods indicated negative skin showing the effect of the fracture intercepted at 1390 metres. They also indicate high wellbore storage with very low formation storage.

No transient tests were taken in OW 601 due to lack of permeability. Both transient injection and fall-off steps were taken for OW 701 and were analysed using only type curve and semilog methods. Type curve and semilog analysis of fall-off show a high transmissivity of 5.7-6.3 x 10^{-3} m^3/Pas with high well bore storage and zero skin. The injection steps show higher variation between semilog and type curve match with transmissivity of 4.7-10.5 x 10^{-8} m^3/Pas and correspondingly higher Kh when cold water viscosity is used. Similar analysis for OW 702 shows a transmissivity in the range of 0.8-1.2 x 10^{-8} m^3/Pas, but this well is completely plugged by the stuck drill string from the original depth of 1744 m to 840 metres and similar tests on OW 303 yielded no reliable data as little pressure change occurred downhole with injection of up to 35 l/s water.

Recovery/Drawdown

Recovery tests have been carried out in wells 101, 201 and 301. Pressure during flow for OW 101 indicates a drawdown of 30.0 bar at 1000m, but on shut in pressure recovers rapidly showing a small radius of influence. The transmissivity from drawdown is 0.5 x 10^{-8} m^3/Pas using a radius of 50 metres. The gas content of the discharge is 0.44% (mainly CO_2). Therefore, the large drawdown may be due to formation scale deposits which makes estimation of transmissivity erroneous (Petty, 1983). Taking into account the gas partial pressure, (Sutton, 1976) the minimum pressure for single phase conditions in the reservoir is 50.4 bar, showing that recovery is influenced by two phase conditions for the first two hours, hence no good fit is obtained using analytical models. Semilog methods (Fig 6) indicate a transmissivity of 17.9 x 10^{-8} m^3/Pas.

Similar analysis for OW 201 taking into account the gas content indicate two phase conditions are present for only 20 minutes, with the drawdown during discharge equivalent to 5.0-10^{-8} m^3/Pas. No good fit was obtained using the type curve or analytical infinite acting model. A good fit was obtained using the double porosity model (Fig. 7) and together with semilog methods give a transmissivity of 11.2-16.4 x 10^{-8} m^3/Pas, with high formation storage and a large positive skin.

Recovery tests on OW 301 indicate a very high transmissivity of 28.2 x 10^{-8} m^3/Pas from the type curve match (Fig. 8) with zero skin and very high formation storage. The semilog methods give higher transmissivity of 33.8-37.5 x 10^{-8} m^3/Pas. Results of the type curve match are influenced by lack of early time shut in data as a flowing profile could not be taken.

A recent flowing pressure survey of OW 401 indicates a drawdown of 35.5 at 1100 metres equivalent to a transmissivity of 0.7 x 10^{-8} m^3/Pas, but could also be influenced by scale deposits. A shut in test is yet to be conducted.

CONCLUSION

From the analyses presented, type curve match, analytical infinite acting, double porosity and semilog methods can be used to infer reservoir properties from long fall-off/injection steps, with no siginificant thermal recovery. Double porosity model gives a better estimate for wells intercepting fracture and only semilog methods can be used for recovery tests where large two phase transients occur. The average transmissivity of wells located within the Olkaria fault zone is high but compares with that obtained from the history match for the best wells in Olkaria East (KPC 1984), with recovery tests indicating higher transmissivities. The average output of Olkaria West wells is high with low discharge enthalpy, but the output does not directly correllate with transmissivity because of varying discharge enthalpy.

ACKNOWLEDGEMENTS

Many thanks go to the staff of UNU Iceland and in particular Omar Sigurdsson for critically evaluating the work presented in this paper. My thanks also go to the Kenya Power Company for permission to publish the data.

REFERENCES

1. KPC, : Completion tests, heating, discharge and shut in tests of wells 101, 201, 301, 401, 501, 701, 702 and 303. (Unpublished reports).

2. KPC, (1984) : History match and performance prediction for Olkaria geothermal field, by G.S. Bodvarsson.

3. McGuinnes, M.J.(1984) : Recent interference tests at Ngahwa and Ohaaki. Proceedings of the New Zealand geothermal Workshop (1984).

4. Petty, S. (1983) : Effective of scaling on downhole pressure transient data, 9th Workshop on GRE, Stanford University (Dec.1983).

REFERENCES (Contd.)

5. Sigurdsson, Omar et al (1985) : Pressure buildup monitoring of the Krafla geothermal field Iceland. 10th Workshop on GRE Stanford University (Jan. 1985).

6. Sutton, F.M. (1976) : Pressure - Temperature curves for a two phase mixture of water and carbon dioxide. New Zealand Journal of Science, 1976 Vol. 19.

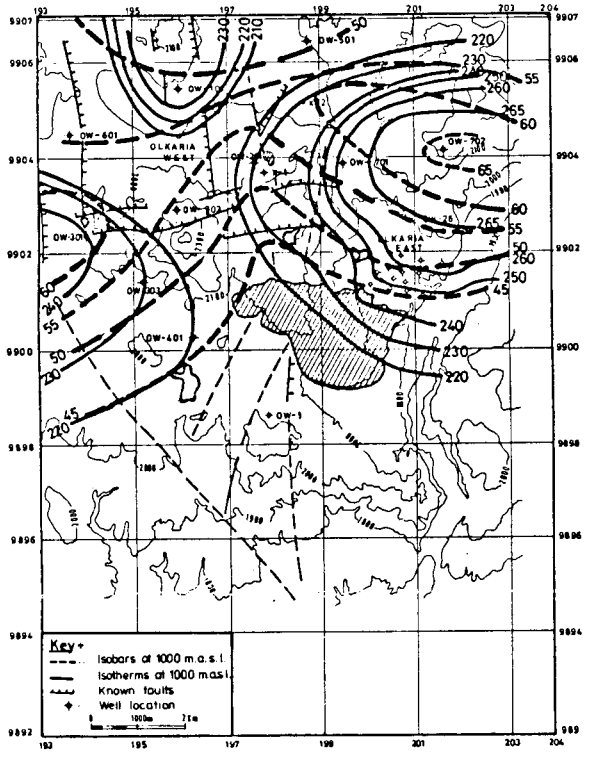


Fig:- 1. OLKARIA GEOTHERMAL FIELD

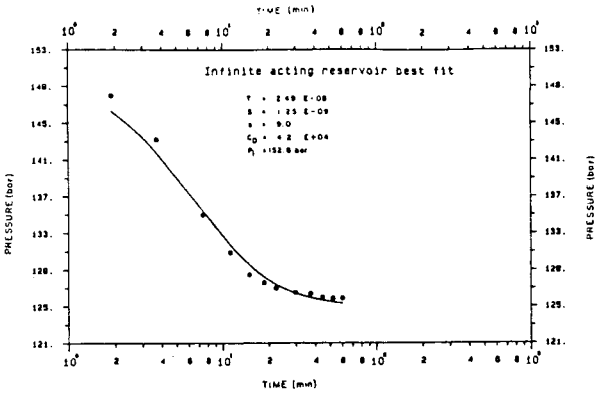


Fig. 2(a) Analytical infinite acting reservoir fit of pressure fall-off at 1900 m in well 201.

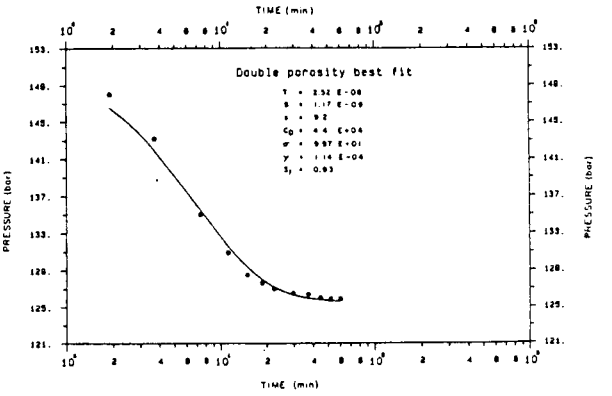


Fig. 2(b) Analytical double porosity fit of pressure fall-off at 1900 m in well 201.

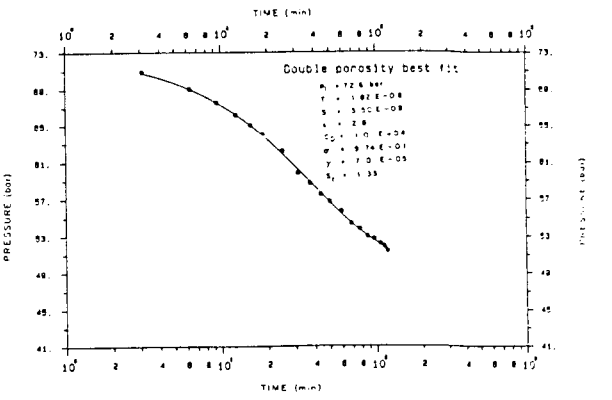


Fig. 3 Analytical double porosity fit of pressure fall-off at 1100 m in well 401.

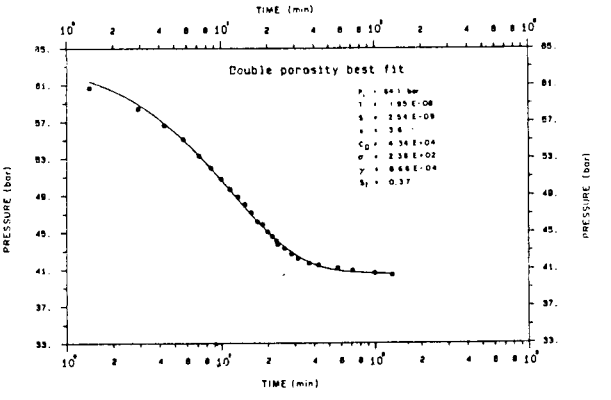


Fig. 4 Analytical double porosity fit of pressure fall-off at 1000 m in well 401.

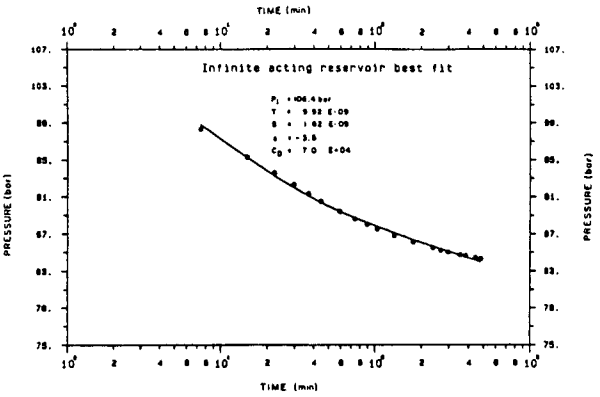


Fig.5(a) Analytical infinite acting reservoir fit of pressure fall-off at 1300 m in well 501.

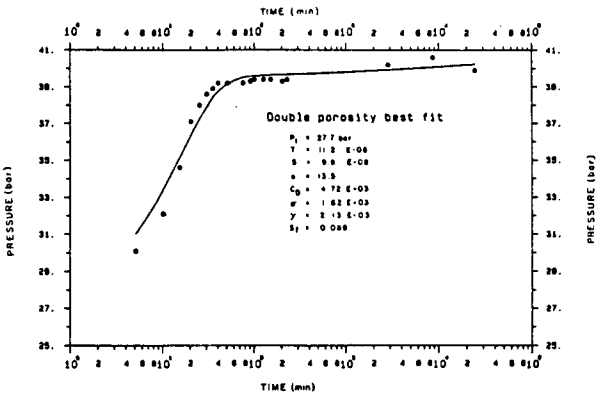


Fig. 7(a) Analytical double porosity fit of pressure recovery at 1000 m in well 201.

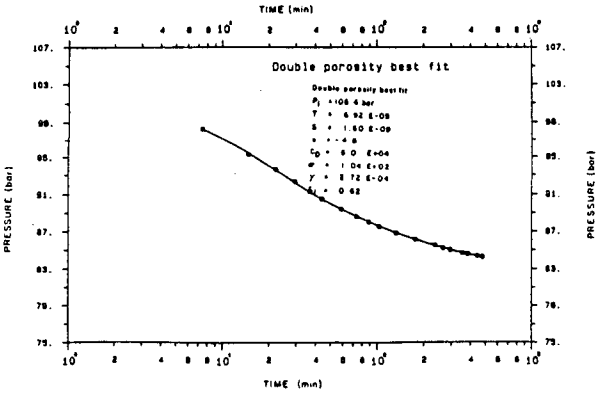


Fig. 5(b) Analytical double porosity fit of pressure fall-off at 1300 m in well 501.

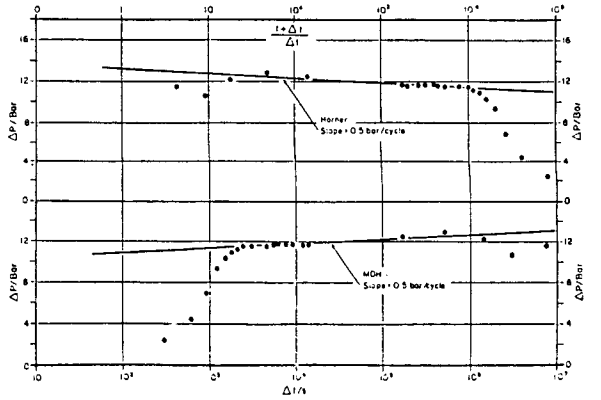


Fig.7(b) Semilog plot of pressure recovery at 1000 m in well 201.

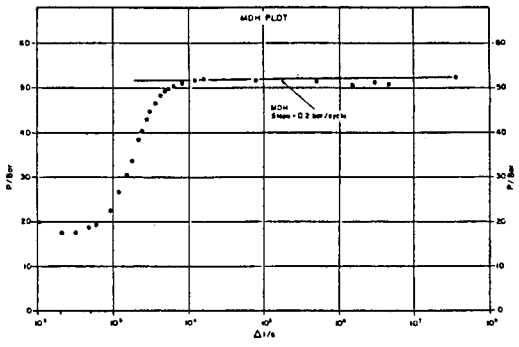


Fig. 6 MDH plot of pressure recovery at 1000 m in well 101.

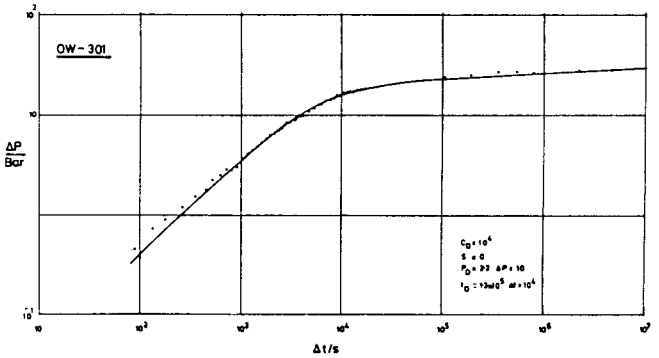


FIG.8 PRESSURE RECOVERY AT 1100 METRES

TABLE 1 (a): Summary of Exploration Wells Data

Well No.	Transmissivity m^3/Pas/10^{-8} from Injectivity	Injection step	Fall-off step	Recovery	Productivity	Discharge WHP Bar	Enthalpy KJ/kg	Mass Kg/s
101	5.5	-	5.0	17.9	0.5	6.0	1085	16.0
201	1.8	-	2.2	14.0	5.0	4.5	1085	34.2
301	>4.8	-	-	33.2	-	6.6	1600	27.9
401	>0.97	-	2.2	-	0.7	4.7	1050	21.0
501	>0.84	-	0.85	-	-	-	-	-
701	-	7.3	6.0	-	-	9.4	1490	27.7
702	-	0.7	0.9			1.8	?	>3.0
303	>8.0	-	-					

TABLE 1(b): Results of transient pressure analyses, well 101

Type of test	Type of analyses	T/E-08 m3/Pas	S/E-08 m/Pa	CD	s
Injectivity	Injectivity Index	5.5	-	-	-
Fall-off at 1200 m	Analytical infinite acting	4.8	0.60	1.2E+4	-3.0
	Analytical double porosity	4.8	0.69	1.1E+4	-3.0
	Type curve	8.0	1.00	1.0E+4	0
	MDH	4.2			
	Horner	3.7			
	KPC (Horner)	3.6			
Drawdown at 1000 m	Productivity Index	0.5			
	MDH	17.9			
Recovery at 1000 m	Horner	17.9			
	KPC (Horner)	0.02			

TABLE 1(c): Results of transient pressure analyses, well 201

Type of test	Type of analyses	T/E-8 m3/Pas	S/E-8 m/Pa	CD	s
Injectivity	Injectivity Index	1.83	-	-	-
Fall-off at 1900 m	Analytical infinite acting	2.2	2.7	1.3E+3	10
	Analytical double porosity	2.6	2.3	2.3E+3	13
	Type curve	4.0	0.06	1.0E+5	20
	MDH	2.1			
	Horner	2.2			
	KPC (Horner)	0.17			
Drawdown at 1000 m	Poductivity Index	5.0	-	-	-
Recovery at 1000 m	Analytical double porosity	11.2	9.9	4.7E+3	13.5
	MDH	16.4			
	Horner	16.4			
	KPC (Horner)	12.9			

TABLE 1(d): Results of transient pressure analyses, well 301

Injectivity	Injectivity Index >4.8				
Fall-off at 1000 m	MDH/Horner	No straight line			
Recovery at 1000 m	Type curve	28.2	187 x 10-8	104	0
	Horner	33.8			
	MDH	37.3			

TABLE 1(e): Results of transient pressure analyses, well 401

Type of test	Type of analyses	T/E-8 m3/Pas	S/E-8 m/Pa	CD	s
Injectivity	Injectivity Index	>.97			
Fall-off at 1000 m	Analytical infinite acting	2.6	0.71	1.5E+4	6.6
	Analytical double porosity	1.9	0.25	4.3E+4	3.6
	Type curve	2.3	1.0	1.0E+4	5.0
	MDH	2.0			
	Horner	1.5			
	KPC (Horner)	0.33			
Fall-off at 1100 m	Analytical infinite acting	2.4	1.7	1.5E+4	5.5
	Analytical double porosity	1.8	3.5	4.3E+4	2.8
	Type curve	4.3	0.59	1.0E+5	5.0
	MDH	0.41			
	Horner	0.35			
	KPC (Horner)	0.31			
Drawdown at 1100 m	Productivity Index	0.7			

TABLE 1(f): Results of transient pressure analyses, well 501

Type of test	Type of analyses	T/E-8 m3/Pas	S/E-8 m/Pa	CD	s
Injectivity	Injectivity Index	0.84-4.0			
Fall-off at 1300 m	Analytical infinite acting	0.99	0.18	7.0E+4	-3.5
	Analytical double porosity	0.69	0.16	6.0E+4	-4.6
	Type curve	0.75	0.08	1.0E+5	-5.0
	MDH	1.18			
	Horner	0.79			
	KPC (Horner)	0.78			
Fall-off at 1400 m	Analytical infinite acting	0.45	0.17	4.7E+4	-4.2
	Analytical double porosity	0.44	0.14	6.0E+4	-4.3
	Type curve	0.39	0.07	1.0E+5	-5.0
	MDH	0.70			
	Horner	0.54			
	KPC (Horner)	0.45			

Table 1g Results of transient pressure analyses Well 701

TEST	TYPE OF ANALYSIS	$T/10^{-8}$ M^3/Pas	$S/10^{-8}$ M/Pa	CD	S	Kh d-m
2nd Injection step	Type curve match	8.0	2.46	10^4	0	14.4
"	MDH	4.7	-	-	-	8.5
3rd injection step	Type curve match	10.5	10.0	10^3	0	18.9
"	MDH	6.0	-	-		10.8
Fall-off step	Type curve match	6.3	1.0	10^4	5	6.3
	MDH	5.9	-	-	-	5.9
	Horner	5.7	-	-	-	5.7

TABLE 1(h) : Results of transient pressure analyses, Well 702

TEST	TYPE OF ANALYSES	$T/10^{-8}$ m^3/Pas	$S/10^{-8}$ m/Pa	CD	S	Kh d-m
First Fall-off Step	MDH	0.79	-	-	-	0.96
	Type curve match	0.79	0.068	10^5	0	0.96
First Injection step	MDH	0.58	-	-	-	1.28
	Type curve match	0.82	0.064	10^5	0	1.82
2nd Injection step	MDH	No semilog straight line				
	Type curve match	- No match				
2nd fall-off step	MDH	0.74	-	-	-	0.91
	Type curve match	1.21	0.086	10^5	0	1.48

PROCEEDINGS, Twelfth Workshop on Geothermal Reservoir Engineering
Stanford University, Stanford, California, January 20-22, 1987
SGP-TR-109

GAS GEOCHEMISTRY OF THE DOGGER GEOTHERMAL AQUIFER (PARIS BASIN, FRANCE)

A. Criaud*, C. Fouillac*, B. Marty**, M. Brach*, and H.F. Wei***

* Institut Mixte de Recherches Géothermiques (BRGM-AFME)
BP 6009 - 45060 Orléans CEDEX, FRANCE
** M.A.G.I.E., Université Paris VI, 75252 Paris CEDEX 05, FRANCE
*** Ecole des Mines, Fontainbleau, FRANCE

ABSTRACT

The low enthalpy program developped in the Paris Basin provides the opportunity for studying the gas geochemistry of the calcareous aquifer of the Dogger. Hydrocarbons and CO_2 are mainly biogenic, He displays high concentrations. He, Ar and N_2 have multiple origins (radioactive decay, atmospheric migration, biochemical processes). The distribution of the gases in the zones of the basin varies in relation to the general chemistry, sedimentology and hydrodynamics. The gas geothermometers do not apply to this environment but useful estimations of the redox potential of the fluid can be derived from CO_2/CH_4 and N_2/NH_4^+ ratios. H_2 and H_2S are involved in corrosion processes and scaling in the pipes.

INTRODUCTION

Gas geochemistry has been used extensively for reservoir engineering purposes in high enthalpy geothermal environments (amongst others, Arnorsson and Gunnlaugsson, 1985; D'Amore and Panichi, 1980; Giggenbach, 1980), but has been less often used in low enthalpy geothermal reservoirs.

The Dogger sedimentary aquifer mainly consists of carbonate facies. It has been exploited for geothermal purposes since 1970. The salinity of the fluids varies from 6.5 to 35 g/l and the downhole temperatures at depths ranging from 1600 to 1850 m are between 47 and 85 °C (Rojas et al., this volume).

The chemistry of this reservoir was shown to be very complex by Bastide (1985) and Criaud et al. (1986). The heterogeneities observed in chemical and isotope compositions are presently best explained by the evolution of paleoseawater which has undergone partial evaporation, diagenesis and mixing phenomena involving several components having variable temperature and mineralization. The combination of different studies (isotopes, conservative elements, water-rock interaction processes) allows the distinction of several areas with various fluid evolutions, bacterial reduction (Fouillac et al., 1986) mixing processes, rock interactions (Rojas et al., this volume).

We present some preliminary results concerning the gas chemistry of the reservoir. The gas analyses all display typical compositions of the natural gas generally found in sedimentary rocks, with hydrocarbons, including methane, of which the concentration is as much as 50% of the gas content, the remainder, includes nitrogen, CO_2 and rare gases.

The aim of this study is: (1) To provide a complete set of gas data at a regional scale; (2) To use this tool for a better comprehension of the origin and circulation of fluids in the Paris Basin.

Among the various gases we will distinguish the inert species (rare gases, N_2) and the components undergoing chemical reactions (CO_2, H_2). CO_2, CH_4, to a certain extent H_2S, H_2 and N_2 can be used for redox considerations and thermodynamics.

SAMPLING AND ANALYTICAL PROCEDURES

All the gases were sampled at the wellheads either at the end of the drilling tests (artesian flow) or later during production (all wells equiped with pumps). A line of the fluid under pressure is taken from the main pipe and diverted to a Pyrex glass degassing system operating at atmospheric pressure. After purging, "free gas" was collected in a glass container with two vacuum stopcocks. A flask under vacuum closed by a teflon stopcock was half filled with the separated liquid phase, thus containing the dissolved gases and microbubbles of free gas.

During these operations the flow rate was kept constant and the gas/liquid ratio (GLR) was measured with a reproducibility of 6-7%. Important variations were sometimes observed when sampling at different times. These variations are attributed to changes in working conditions, sampling pressure, temperature or the presence of water vapor giving rise to an overestimated gas/liquid ratio, or a combination of these processes. The GLR were used to recalculate the total

gas content (free + dissolved) of the fluid.

The gas analyses were performed by gas chromatography except for a few recent He results determined in the field by mass spectrometry (Marty et al., in prep.). The gas analyses for free and dissolved gases are given in tables 1 and 2.

A notable oxygen content of 0.1 to 5% is present in some of the samples, and is hardly compatible with the reduced character of the water which contains dissolved hydrogen sulphide and displays low redox potentials. Only a few ppb of dissolved O_2 was detected onsite by the colorimetric method. The real concentration may be much lower. We conclude that the oxygen originated outside the Dogger aquifer and could result from air contamination during sampling or analytical procedures. Consequently, before interpretation, the "true" O_2 content was assumed to be zero, N_2 and Ar were corrected correspondingly, the effect being negligible for other gases.

GENERAL PATTERNS OF GAS DISTRIBUTION

In order to classify the zones of the aquifer, the results were reported on figure 1 according to the major components (N_2, CO_2, hydrocarbons). Despite a wide range it is clear that the southernmost samples are enriched in methane and other light hydrocarbons, while the proportion of nitrogen increases in the Seine-St-Denis areas and in samples from the border of the basin.

CO_2 is directly involved in equilibrium with minerals such as calcite and dolomite but the calculated partial pressure varies within the basin (Bastide, 1985). No relation was found between the total CO_2 content and the temperature or salinity. However, the concentration of methane is related to the temperature (Fig. 2) within the basin.

INERT GASES

The samples present very high helium concentrations (0.5-1.5%) when compared to the air content (5.24 ppm) and magmatic gases (a few ppm). Similar high He contents are found in some sedimentary basin gas reservoirs (e.g. the Texas Panhandle, Zartman et al., 1961) and result from the accumulation of ^4He produced from the decay of U+Th over a long period. Several attempts to date underground fluids have been successful, providing that reservoir parameters such as porosity, U+Th contents of wall rocks are known (e.g. Marine, 1979). In the case of the Dogger, these parameters are presently poorly constrained and any quantitative dating attempt would be unrealistic. The high He concentrations nevertheless indicate that the fluids are old, and part of them may be contemporaneous with the sedimentary wall rocks. Alternatively, part of the helium may result from the migration of He from deeper strata, and accumulation in the Dogger aquifer. Dating methods, including the use of Rn will be discussed elsewhere.

When plotted on a N_2-Ar-He diagram (not given here) all samples can be interpreted as resulting from mixing between the following components:

(1) An atmospheric component as defined by negligible He contents, and a N_2/Ar ratio between 83.6 and 40 (but the latter corresponds to either air mixing or limited outgassing of the fluid; the lower limit of N_2/Ar=40 corresponds to the solubility ratio of air gases, when outgassing occurs at a steady rate).
(2) A radiogenic component defined as having a He/Ar ratio of between 2 and 4, and corresponding to a chondritic composition for the parents U+Th and K.

Other information can be gained when considering absolute abundances. The calculated total N_2 content exceeds by about a factor of 10 the ASW concentration, which shows that part of the nitrogen present results from biogenic processes. This is also reflected in the N_2/Ar ratio which exceeds the air value in some cases. Unfortunately non-radiogenic rare gas data are not available and the biogenic N_2 addition cannot be quantified. The He/N_2 ratio is fairly constant, around 0.02, and indicates that ^4He production and N_2 addition occurred at similar rates for the different study areas.

The contour tracing He contents over the Paris Basin area (Fig. 3) are consistent with the general flow pattern derived from hydrodynamic studies and reveals a south-southeast trending gradient also indicated by other chemical parameters. The more evolved waters (high sulphide content) of Seine-St-Denis and north of the basin show an increase in the He content. In accord with this hypothesis, some recharge is thought to occur at the southeast border of the basin (Morvan area). Surprisingly, the He content is negatively correlated with the downhole temperature. A single heat flux model radiogenic input correlation, as is generally inferred, is clearly not applicable in this case. A detailed study of the production and mixing strata could clear up this inversion problem.

The picture derived from inert gases is consistent with the chemistry of the reservoir, which indicates mixing involving paleoseawater, recent fluids and diagenetic processes.

GAS GEOTHERMOMETRY

In geothermal environments the composition of the gas phase is frequently controlled by a chemical equilibrium so temperatures can be derived from gas analysis. When applying the formula of D'Amore and Panichi (1980) a great uncertainty is introduced if the hydrogen or hydrogen sulphide percentage (not always satisfactorily determined for this study) is overestimated. Nevertheless, comparisons between calculated and measured temperatures always lead to much higher estimated temperatures (100-150 °C) than downhole measurements. Evidently the Fischer-Tropsch reaction cannot explain the concentrations of methane found in this sedimentary environment, and H_2S, H_2 and CO_2, partly biogenic, are not fixed through equilibrium with mineral buffers. Corrosion may produce noticeable amounts of H_2, as proved by the variations at different sampling times, and H_2S is involved in iron sulphide scaling.

Likewise, the gas geothermometers of Arnorsson and Gunnlaugsson (1985) do not apply to this type of geothermal environment and because of the organic processes responsible for the occurrence of CO_2 there is no relationship between total CO_2 and temperature.

REDOX CONDITIONS IN THE RESERVOIR

Oxidation-reduction reactions are biochemically mediated in the waters studied, so that we may assume a partial redox equilibrium even at these moderate temperatures. We have shown (IMRG annual report, 1985) that the platinum electrode only provides, in this particular case, a measurement of pH_2S and is not related to the "true" redox potential. CH_4/CO_2, N_2/NH_4^+, H_2 or H_2S/SO_4^{2-} can thus be used to estimate a redox potential according to the reactions:

(1) $CO_2° + 8H^+ + 8e^- = CH_4° + 2H_2O$
(2) $N_2° + 8H^+ + 6e^- = 2NH_4^+$
(3) $2H^+ + 2e^- = H_2°$
(4) $H_2S° + 4H_2O = SO_4^{2-} + 10H^+ + 8e^-$

The pH of the reservoir was computed from surface pH and chemistry, then $(H_2S)°$ and $(CO_2)°$ were calculated. The sulphate and NH_4^+ concentrations at wellheads were respectively between 600 to 1200, and 18 to 36 mg/l and assumed to be the same in the reservoir. The total sulphide content varies from less than 0.1 mg/l to 100 mg/l. Activities were used instead of concentrations because of the mineralization.

The results of the calculations are summarized below (expressed in mV/NHE). Despite an uncertainty estimated to be at least 15%, an increase of the potentials with temperature is generally observed for the CO_2/CH_4, N_2/NH_4^+ and H_2 pairs.

	Minimum	Maximum
Pt electrode	-175	+ 67
$H_2S°/SO_4$	-250	-190
CO_2/CH_4	-315	-250
N_2/NH_4^+	-320	-240
H_2/H^+	-420	-350

The differences could be explained by a non-global redox equilibrium in the reservoir. As explained earlier, H_2 and H_2S are suspected to participate in the corrosion and scaling mechanisms (Fouillac et al., 1986). Moreover it is not known whether HS^-/SO_4^{2-} could have achieved equilibrium at these relatively low temperatures, so the CO_2/CH_4 value is probably the more reliable and in accordance with the N_2/NH_4^+ calculated potentials.

This method provides an accurate value of the redox potential, which is fairly constant at a regional scale, and has been used successfully for calculations to predict the deposition of corrosion products. The observed mineral phases correspond to the minerals found theoretically close to equilibrium with the fluids. The corrosion properties and scaling tendencies of the water from the Dogger aquifer are important parameters for reservoir engineering considerations.

CONCLUSIONS

The gas contents display large variations at a regional scale that reflect the evolution of the fluids during diagenesis, aging and mixing phenomena. The geographic trends are comparable to that observed from the chemistry of the water to the northwest.

The high helium contents show evidence for an old component attributed to paleoseawater. The helium concentration contours are consistent with the general hydrodynamics in the basin, with a recent recharge in the south-southeast margin of the basin.

The gas geothermometers used in geothermics do not apply to this sedimentary environment, most of the reactive gases resulting from biochemical processes.

The redox potential of the reservoir was estimated using CO_2 and CH_4 concentrations. This value, instead of a direct measurement of the potential, was proved to be useful for the characterization of the corrosion and scaling potential which play a major role in reservoir engineering of the Dogger aquifer. At the present time further investigations are needed to find out if the H_2 could be used as an aid in the early detection of corrosion processes.

ACKNOWLEDGEMENTS

This work was carried out under contract no. EN360046S (CG) Commission of the European Communities and received financial support from the BRGM AND AFME.

REFERENCES

Arnorsson, S. and Gunnlaugsson, E. (1985), "New gas geothermometers for geothermal exploration - calibration and application," Geochimica et Cosmochimica Acta, 49, p. 1307-1325.

Marine, I.W. (1979), "The use of naturally occurring helium to estimate groundwater velocities for studies of geologic storage of radioactive waste," Water Res. Res., 15 (5), p. 1130-1136.

Bastide, J.P. (1985), "Etude geochimique de la nappe du Dogger du Bassin Parisien," 3rd cycle thesis, University of Paris VII, 152 p.

Criaud, A., Fouillac, C. and Brach, M. (1986), "Chemical evolution of the fluids from the Dogger aquifer," Proceedings of workshop on geochemistry, CEC Contractors, Anvers, 5/11/86.

D'Amore, F. and Panichi, C. (1980), "Evaluation of deep temperatures of hydrothermal systems by a new gas geothermometer," Geochimica et Cosmochimica Acta, 44, p. 549-556.

Fouillac, C. and Criaud, A. (1986), "Corrosion potential of the fluids from the Dogger aquifer," Proceedings of Workshop CEC "Corrosion et entartrage dans les systèmes geothermaux," 17-18/11/86, Orléans, France, (in press).

Fouillac, C. and Criaud, A., Czernechowski, I. and Menjoz, A. (1986), "Sulphide scaling mechanism in the Dogger aquifer - theoretical description,"Proceedings of Workshop CEC "Corrosion et entartrage dans les systèmes geothermaux,"17-18/11/86, Orléans, France, (in press).

Giggenbach, W.F. (1980), "Geothermal gas equilibria," Geochimica et Cosmochimica Acta, 44, p. 549-556.

Institut Mixte de Recherches Géothermiques, "Rapport annuel 1985 (BRGM/AFME),".

Marty, B., Brach, M., Criaud, A., Fouillac, C. and Vuataz, F.D., "Analyse in situ de l'helium dans les fluides d'interêt géothermique par spectrométrie de masse. Exemple du Cezallier (Massif Central, France)," Compte Rendus de l'Academie des Sciences (in prep.).

Rojas, J., Menjoz, A. Martin, J.C., Criaud, A. and Fouillac, C. (1987), "Development and exploration of low enthalpy geothermal systems: example of the "Dogger" in the Paris Basin, France," this volume.

Zartman, R.E., Wasserburg, G.J. and Reynolds, I.W. (1961), "Helium, Argon and Carbon in some natural gases," Journal of Geophysical Research, 66 (1).

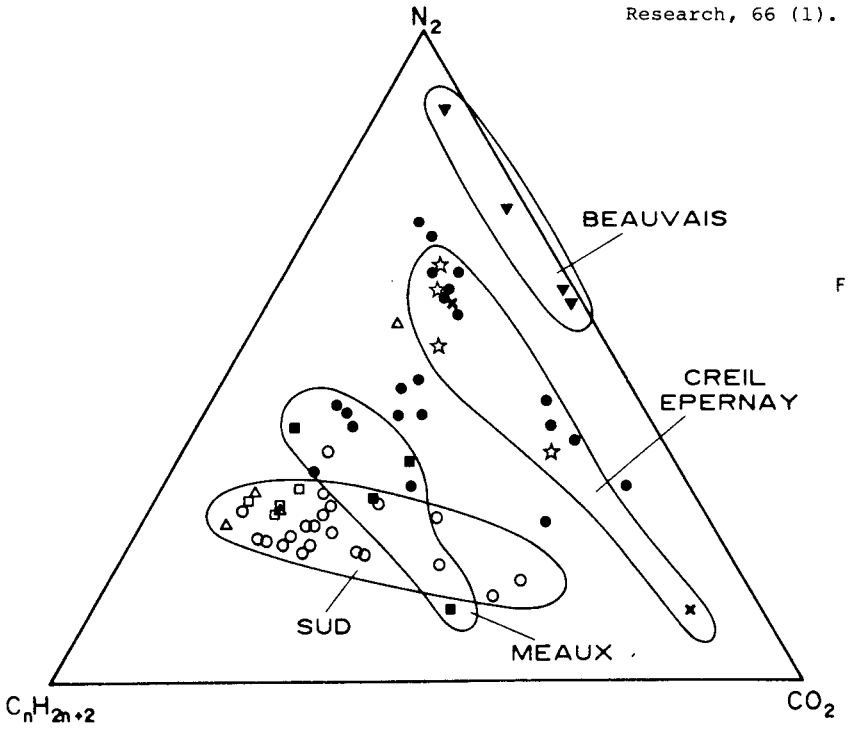


Figure 1 : Diagram CO_2 - N_2 - hydrocarbons

	ACHERES	ALFORT-VILLE	AULNAY 1	AULNAY 3	AULNAY 3	BEAUVAIS 1	BEAUVAIS 1	BEAUVAIS 2	BLANC MESNIL	BLANC MESNIL	BLANC MESNIL	BLANC MESNIL 2	BONDY 2	BONNEUIL 1	BONNEUIL 2
Well	GACH	GAL1	GAY1	GAY3	GAY3	GBVS1	GBVS1	GBVS2	GBXN1	GBXN1	GBXN1	GBXN2	GBO2	GBL1	GBL2
GLR	0,229	0,55		0,087	0,087							0,034	0,099	0,178	0,086
date	11 85	12 3 85	18 6 82	12 8 83		19 5 81	20 7 83	20 5 81	26 12 82	26 12 82	20 11 84	23 11 82	11 85	20 2 85	
CO2 %	17,2	11,6	22,1	48,47	24,5	38,3	9	38,3	12,2	43,6	21,6	19	19,8	20,1	22,3
N2 %	53,7	29,1	58,3	37,28	53,3	58,7	86	58,7	48,3	37,65	56,5	63,3	38,7	23,2	24,9
O2 %	0,77	1,22	0,1	0,54	0,005	1	0,05	0	0,16	0,62	0,3	3,26	0,45	0,24	0,18
Ar %	0,46	0,27	0,4		0,39		0,5		0,34		0,4	0,56		0,21	0,19
He %	1,3	0,56	1,1		1,1	1,4	1,7	1,4	0,96		1,03	0,97	0,78	0,51	0,49
H2 %	0,017	0,41	<0,002		0,8	0,5	0,26	0,5	26		0,18	1	0,002	0,86	0,88
H2S %	2,4	<0,01	2,3	3,03	1,9		<0,01	0,29		4,62	0,96	1,73	2,2		0,001
CH4 %	19,3	49,1	15,8	10,29	15,5	0,8	2,6	0,96	11,2	10,5	17,4	10,5	33	47,6	45,4
C2H6 %	4,6	3,4	0,7	0,36	1,1	0,1	0,16	0,02	0,78	0,29	0,67	0,5	4,2	3,17	3,1
C3H8 %	0,03	2,2	0,08					0,01					0,5		
C4H10 %	0,05	1,1	0,1										0,4		
C5H12 %	0,1	0,6	0,02										0,1		
C6H14 %	0,09	0,3	0,02										0,1		
TDS (g/l)	12,2	19,4	14,3	24,9	25	23,8	23,8	23,8	26,5	26,5	28,06	28,1	17	22,1	24,35
Temp (°C)	60	72	71,6	70,7	70,7	47,3	47,3	47,3	67,5	67,5	67,5	65,6	65,1	79,3	79,7

	CACHAN SUD 1	CACHAN NORD 1	CACHAN NORD 2	CHATENAY MALABRY	CHAMPIGNY 1	CHAMPIGNY 1	CHAMPIGNY 2	CHEVILLY LARUE 1	CLICHY 1	CLICHY 2	COULOMMIERS 1	COURNEUVE NORD 2	CREIL 4 GTH 4	CREIL 5 PLATEAU	CREIL 6 PLATEAU
Well	GCDS1	GCDN1	GCDN2	GCTM1	GCHM1	GCHM1	GCHM2	GCHL1	GCL1	GCL2	GCO1	GLCN2	CREIL4	CREIL5	CREIL6
GLR	0,14	0,09	0,17	0,147	0,093	0,2		0,146			0,221	0,05		0,055	
date	1984	1984	1984	10 85	9 2 85	22 10 86	25 3 85	23 10 86	19 4 84	12 81	10 83	4 82	18 2 82	6 9 82	11 10 82
CO2 %	30,62	42,1	51,6	17,7	28,9	23,9	20,1	20,7	17,7	25,8	28,6	57,42	15,9	18,5	25
N2 %	21,3	18,9	13,9	22,2	23,9	26,6	27,6	22,2	33,5	28	27,7	29,76	65,6	58,5	50
O2 %	0,54	0,45	0,29	0,06	<0,06	0,054	0,05	0,044	1,15	1	0,35	0,51	3,9	2,3	0,07
Ar %				0,24	0,17	0,2	0,21	0,22	0,32	0,3	0,21		0,8	0,42	0,35
He %		0,38	0,43	0,52	0,53	0,52	0,64	0,45	0,43	1,3	0,46		0,9	0,84	1,06
H2 %				0,001	0,87	0,55	0,71	<0,000	0,03	0,5	0,47		0,004	0,56	0,27
H2S %	0			0,023	0,01	<0,001	0,001	<0,001	1,13		0,01	4,45		2,37	2,93
CH4 %	45,2	35,1	31,9	51,7	39,4	42	43,9	49,1	39,3	21	36,9	7,43	11,3	12,9	18,2
C2H6 %	1,73	2,02	1,45	3,3	2,72	3,21	3,3	3,48	3,23	9		0,21	1,8	1,97	2,5
C3H8 %	0,48	0,71	0,58	2,1		1,58		2,01	1,49					0,025	0,04
C4H10 %	0,06	0,08	0,17	1,2		0,78		1,2	0,61					0,004	0,005
C5H12 %				0,7		0,34		0,59						0,002	0,002
C6H14 %				0,3		0,2		0,32							
TDS (g/l)	17	16,4	17,7	13,8	25,3	25,3	25,6	16,9	19,4	19,4	33,75	22,8	28	28,9	28,2
Temp (°C)	71	65	69,5	67	78,2	78,2	73,9	75,4	70,8	70,4	85,4	58,4	58	58,6	56,4

	CRETEIL 1	CRETEIL 2	LA CELLE ST CLOUD	EPERNAY 1	EVRY 1	FONTAINE-BLEAU 1	FONTAINE-BLEAU 1	FONTAINE-BLEAU 2	GARGES LES GONESSE 1	GARGES LES GONESSE 2	LESL'HAY LES ROSES 2	MEAUX 1 COLLINET	MEAUX 6 BEAUVAL	MEAUX 7 BEAUVAL	LE MEE SUR SEINE
Well	GCRT1	GCRT2	GLC1	GEPE1	GEV1	GFO1	GFO1	GFO1	GGAR2	GGAR2	GHLR2	GMX1	GMX6	GMX7	GLMS1
GLR	0,15	0,125	0,141	0,026	0,068	0,05	0,099		0,09	0,09	0,157	0,1	0,12		0,14
date	29 11 84	27 12 84	11 85	26 7 83	11 11 81	17 11 83	21 10 86	5 3 82	29 5 83	29 5 83					21 5 85
CO2 %	24,3	21,9	14,6	22,9	8,3	15,7	11,1	18	48,2	12	29,5	3,09	26,9	11,9	12,7
N2 %	22,8	24,2	27	54,3	40,9	25,4	42,3	22,5	39,44	61	24,3	61,9	26,8	39,8	28,4
O2 %	0,24	0,34	0,05	<0,015	6	0,36	6,78	0,5	0,62	0,02	1,72	4,41	0,16	1,29	0,09
Ar %	0,21	0,21	0,26		0,6	0,31	0,52	0,3					0,2	0,3	0,2
He %	0,38	0,4	0,64		0,13	0,94	0,62	0,7		0,97	0,48	0,64	0,4	0,55	0,64
H2 %	0,73	0,57	0,0003		0,024	0,001	0,005	1		0,77		0,76	1,9	1,28	0,003
H2S %	<0,009	<0,009	0,23	4,7		0,91	0,41		3,67		0,01		<0,001	0,001	0,15
CH4 %	45,2	46,1	50,5	13,4	35	48,8	33,7	50,5	7,88	13,2	41,7	26,9	39,5	40,1	47,8
C2H6 %	3	3	3,1	3,3	5	2,9	2,07	3,2	0,16	0,51	1,85	1,25		2,54	3
C3H8 %			2			1,8	1,13	1,8			0,61				2,8
C4H10 %			1				0,67	1			0,19				2,2
C5H12 %			0,4				0,33				0,08				1,4
C6H14 %			0,2				0,2								0,6
TDS (g/l)	23,5	23	11,1	8,8	10,4	6,5	6,5	7,3	30,4	30,4	16,2	30,1	33	35	12,95
Temp (°C)	79	77,9	62	58	71,8	74,2	74,2	73,2	65,5	65,5	74,1	79,3	78	78,1	73

	MONTGERON 1	ORLY I 1	ORLY II 3	RIS ORANGIS	SEVRAN 1	SEVRAN 2	SUCY EN BRIE	TREMBLAY 1	TREMBLAY 2	VAUX LE PENIL	VIGNEUX 2	VILLENEUVE LA GARENNE	VILLETTE 2	VILLETTE 1
Well	GMO1	GOR1	GOR3	GRO1	GSA1	GSA2	GSUC1	GTRE1	GTRE2	GVLP2	GVS2	GVG1	GLAV2	GLAV1
GLR	0,163	0,17	0,12	0,155	0,04		0,333	0,089				0,055	0,093	0,15
date			23 10 86				11 85	31 5 83	8 7 83	10 85			17 11 83	
CO2 %	17,2	22,1	20,4	17,3	25,6	21,7	17,3	27,6	24,7	10,8	52,7	15,43	17	15,6
N2 %	22,2	18,9	21,6	29	40,7	43,6	35,5	41,3	44,8	26,8	15	67,3	38,4	39,3
O2 %	0,1	0,11	0,014	0,12	0,04	0,78	5,4	0,63	0,3	1,1	0,07	1,14	0,068	0,02
Ar %	0,25	0,24	0,23	0,24	0,3	0,4	0,33	0,34	0,35	0,27	0,13	0,5	0,35	0,64
He %	0,59	0,33	0,47	0,73	0,8	0,58	0,38	0,66	0,79	0,71	0,3	0,89	0,87	0,97
H2 %	0,004	0,76	0,017	0,0007	0,6	0,0029	0,48	0,59	0,3	0,004	2,97	0,0176	0,43	1,04
H2S %	0,006	0,01	<0,001	<0,01	0,01	3	0,001	0,01		0,25	0,003	0,96	0,94	1,3
CH4 %	52	49,4	49,8	47,2	28,7	27,3	35,3	26,1	23,7	53	24,5	13,9	32,1	33,1
C2H6 %	3,3	4	3,43	2,8	3,4		2,6	2,15	1,84	3,2	2,1	0,49	4,6	4,4
C3H8 %	2,1		2		0,3		1,5			2,1	1,03			
C4H10 %	1,2		1,14		0,3		0,7			1,2	0,6			
C5H12 %	0,7		0,61		0,1		0,5			0,7	0,31			
C6H14 %	0,4		0,31							0,4				
TDS (g/l)	11,55	16,9	15,2	9,8	20,95		26	26,1	25,7	12,5	13,7	25,7	17,8	18
Temp (°C)	72,5	76	76,9	72,2	69	70,7	78,2	73,9	74,2	71,9	73,5	57,5	56,9	57,3

Table 1 : Analysis of free gases in volume %.

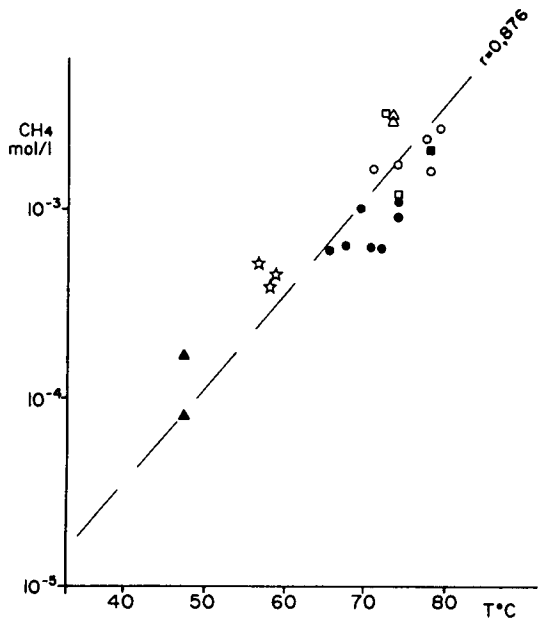


Figure 2 : Correlation between CH_4 content and downhole temperature.

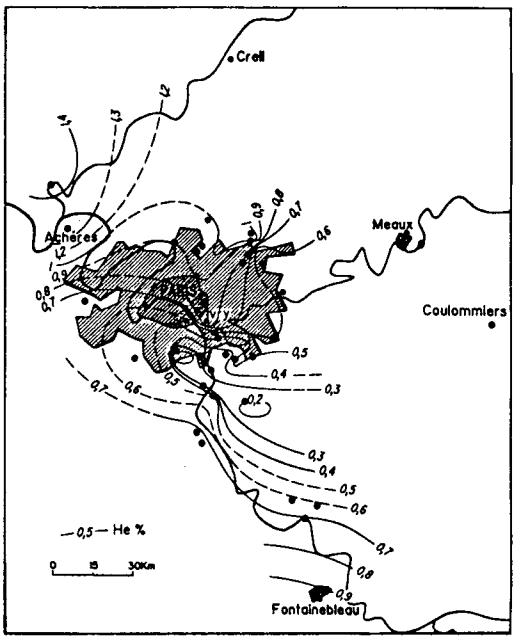


Figure 3 : Helium concentrations measured at the head of the geothermal wells. Relative percentages instead of absolute concentrations were used because of the uncertainties on GLR and missing data.

date	GAY1 18 6 82	GAY3 12 8 83	GBVS1 20 7 83	GBMM2 23 11 82	GCHM1 9 2 85	GCHM2 25 3 85	GCL1 19 4 84	GCRE4 18 2 82	GCRE5 6 9 82	GCRE6 11 10 82	GCRT1 29 11 84
CO2 10-2	1,08	0,909	0,985	1,25	1,05	0,926	0,85	0,863	1,1	1	1,045
N2 10-3	2,35	2,72	5,72	2,53	1,05	1,42	1,3	1,77	1,43	1,09	1,35
Ar 10-4	0,39	0,233	0,37	0,23	0,06	0,09	0,1	0,17	0,108	0,1	0,136
He 10-5	4,33	4,38	10,6	4,6	1,85	2,36	1,59	2,67	2,22	2,61	2,14
H2 10-5	12	4	1,54	4,93	3,36	2,76	11,6	3,92	1,57	7,2	4,4
CH4 10-4	6,05	6,31	1,75	6,03	16	17,7	16,1	6,3	4,69	5,45	28,1
C2H6 10-5	2,97	4,5	1,12	2,85	11,3	13,3	13,4		6,8	7,34	19
>C3H8 10-6	8,02			0,36			153		1,06	1,24	
TDS(g/l)	26,6	25	23,8	28,1	25,3	19,4	19,4	28	28,8	28,2	23,5
Temp (°C)	71,6	70,7	47,3	65,6	78,2	70,8	70,8	58	58,6	56,4	19

date	GCRT2 27 12 84	GFO1 17 11 83	GGAR2 29 5 83	GLAV1 30 1 83	GLAV2 17 11 83	GLMS1 19 2 82	GLMS2 10 5 85	GMX6 8 82	GRO1 23 10 85	GSA1 30 5 82	GTRE2 8 7 83	GTRE1 31 5 83
CO2 10-2	9,5	0,895	1,2	0,9	0,9	0,9	1,02	1,02	1,097	1,2	1,02	0,799
N2 10-3	1,21	0,62	2,72	1,73	1,75	1,18	1,64	1,38	1,83	5,24	1,94	1,69
Ar 10-4	0,122	0,082		0,269	0,176	0,131	0,156	0,192	0,158	0,48	0,19	0,114
He 10-5	1,97	2	4,19	3,5	3,4	2,7	3,5	2,05	4,3	2,6	2,9	2,6
H2 10-5	2,9		3,5	3,7	1,9			9,9		2,6	1,1	2,5
CH4 10-4	24,4	12	6,4	14,5	14,9	31,7	29	21,1	33,4	10,1	9	11,5
C2H6 10-5	16,1	6,9	2,4	19,7	21,6	21,2	17,9	11,3	19,4	11,9	7	9,2
>C3H8 10-6		42,5				238	389			31,5		
TDS(g/l)	23	6,5	30,5	18	17,8	12,95	13	33	9,8	20,9	25,7	26,1
Temp (°C)	77,9	74,2	67,7	57,3	56,9	73	72	78	72,2	69	74,2	73,9

Table 2 : Total gas (dissolved + free) contents of the fluids expressed in moles/l

PROCEEDINGS, Twelfth Workshop on Geothermal Reservoir Engineering
Stanford University, Stanford, California, January 20-22, 1987
SGP-TR-109

A PRACTICAL APPROACH TO PRODUCING VAPOR-DOMINATED RESERVOIRS

Mark K. Kumataka

Santa Fe Minerals, Inc.
13455 Noel Rd., Suite 1100
Dallas, TX 75240-6620

Abstract

This paper presents arguments for initially producing Geysers steam wells at wellhead pressures in excess of 200 psig instead of the normal practice of producing at minimum wellhead pressures. A conceptual model is presented which defines a flow equilibrium resulting from a "constant pressure source" whose location is a function of the withdrawal rate from the reservoir. Based on this model, it is argued that producing at elevated wellhead pressures is equal to producing at minimum wellhead pressures, assuming the mass withdrawal is the same. Additional benefits of producing at elevated wellhead pressures are discussed and include minimizing casing and reservoir rock thermal transients and scaling and bridging of the wellbore.

SFGI's experience has been favorable but due to a very high capacity factor and very few outages, a comparison of performance of other areas of The Geysers is inconclusive.

Introduction

Santa Fe Minerals, Inc. (SFMI, formerly Occidental Geothermal, Inc.) operates an 80 MW (net) power plant and attendant steam field at The Geysers in Northern California. The first well on the lease was spud on February 16, 1980 and the project began commercial operation on April 10, 1984. SFMI's experience in producing this lease has evolved an operational philosophy of maintaining wellhead pressures in excess of 200 psig. This philosophy appears to deviate from other operator's practices of producing at minimum flowing wellhead pressures typically in the range of 125 to 150 psig. SFMI was afforded the opportunity of producing at elevated wellhead pressures because of the development of an excess steam deliverability in anticipation of an early high decline rate typical of Geysers wells during the first few months of production.

SFMI also believed there were additional benefits of initially operating wells at higher wellhead pressures which included minimizing casing and reservoir rock thermal transients and scaling of the wellbore and nearby reservoir. This paper discusses the production of steam wells at elevated wellhead pressures by presenting a conceptual model of the reservoir, the production dynamics of the model, analysis of wellbore and inflow performance relationships, and qualitatively discussing mechanical and heat transfer aspects of the wellbore and reservoir during production.

Geysers Conceptual Reservoir Model

A conceptual model of The Geysers reservoir is shown in Figure 1. The major components of the model are a shallow steam zone at the top, a main steam zone in the middle, and a steam generation source at the bottom. The shallow steam zone is connected to the main steam zone by a flow path with length x, and the steam generation source is connected to the main steam zone by a flow path with variable length y, which is a function of Q_5. The system is initially at equilibrium, but this does not necessarily mean the shallow steam zone is in equilibrium with the main steam zone. The two zones may be so poorly connected that the shallow steam zone could have an equilibrium pressure and temperature substantially lower than the main steam zone due to heat loss to the surface and buildup of non-condensible gases. The shallow steam zone could also initially have been perched water or a non-condensible gas zone with the wellbore acting as a flow path between the two zones. An example of a shallow steam zone is the Thermal Shallow Reservoir presented by Mogen and Maney (1985).

The steam generation source in this conceptual model is depicted as being below the main steam zone because we have defined a flow path from the steam generation source to the main steam zone that is a function of the withdrawal rate. In actuality, the steam generation source is integral to the main steam zone and

The inflow performance curves were based on the deliverability equation presented by Rawlins and Schellhardt (1936):

$$Q_t = C(P^2_{static} - P^2_{flow})^{0.75}$$

This equation is used assuming surface conditions and maximum steam flowrates (at 110 psig) of 100,000 lbs./hr.(curve A), 150,000 lbs./hr. (curve B), and 200,000 lbs./hr. (curve C).

The results are shown in Figure 3 and are what would be expected. At high flowrates the wellbore is the limiting factor and there is very little change in flowing bottomhole pressure. At low flows, the reservoir is the limiting factor. This would indicate that maintaining elevated producing wellhead pressures on high productivity wells does not measurably change the bottomhole flowing pressure and the only reason to produce these wells at elevated wellhead pressures would be to minimize thermal effects. In the case of a well whose inflow performance matches curve A (100,000 lbs./hr.), there is a substantial change in the bottomhole flowing pressure. However, this theoretical curve was determined assuming constant enthalpy without considering the superheating of the steam as it travels in the reservoir to the wellbore. In the reservoir, this lower pressure and therefore temperature would cause higher heat transfer rates between the reservoir rock and the steam. This could possibly increase the specific volume of steam to such an extent that the mass flow is decreased resulting in a flattening of curve A at lower wellhead pressures. This phenomena has actually occurred in a few wells during short term flow tests but only when flowing wellhead pressures have been below 100 psig. Producing these lower productivity wells at elevated wellhead pressures minimizes the possibility of the specific volume change becoming the limiting factor for flow from the reservoir.

The analysis of the wellbore and inflow performance relationship should be performed on individual wells to determine actual bottomhole flowing conditions. The wellbore profile presented is restrictive due to the depth of the production and not typical of the majority of the wells in the Geysers.

Additional Benefits of Operational Philosophy

Prior to start up a production review was performed on The Geysers open file wells to analyze their initial production performance. The wellbore mechanical aspects of production with respect to temperature changes and casing problems was also analyzed to determine if we could improve steam well performance.

A problem in The Geysers that could be minimized by producing wells at higher wellhead pressures is casing failures resulting from thermal contraction and expansion of the casing occuring every time a well was flowed and then shut-in. For example, by keeping a minimum wellhead pressure at 200 psig instead of 150 psig the decrease in temperature difference between producing and shut-in is 22.4% (assuming a maximum wellhead pressure of 470 psig). This is a significant improvement and should substantially decrease the risk of casing problems.

In the review of The Geysers wells, there appeared to be a significant amount of scaling in the bottom portion of the casing and bridging of the open hole which required cleaning out in the first year of production. To reduce these problems it was reasoned that the departure from initial reservoir equilibrium conditions needs to be minimized and that producing superheated steam near the wellbore may not be advantageous because of the chemical changes occuring in the steam during production and shut-in conditions. This is very important with regard to our model because the shallow steam zone increases the possibility of such problems. As an example, if the initial pressure and temperature of the shallow steam zone is substantially lower than the shut-in pressure and temperature of the main steam zone, the shallow steam zone acts as a heat sink condensing steam flowing from the main steam zone. The steam that has entered the shallow steam zone may be subjected to a drastically different geochemical environment because of the conditions that initially existed in the shallow steam zone. When the well is returned to production the condensed steam in the shallow zone is flashed or is produced as a liquid if there is not enough heat or time available. Although the actual causes of scaling in the wellbore are not well understood, by maintaining higher wellhead pressures these affects should be minimized.

The two remaining reasons for operating at higher flowing wellhead pressures are to create a more uniform pressure drawdown of the reservoir and to eliminate transmission of pipeline pressure and temperature spikes from being transmitted down the wellbore during a power plant outage.

most probably exists as a complex combination of insitu liquid water in the main steam zone fracture or matrix volume, a deeper liquid layer, meteoric recharge, injected steam condensate, or possibly even a deeper steam zone.

Production Dynamics

The production dynamics of this model are consistent with the dynamics of vapor-dominated systems presented by Truesdell and White (1973), with the added constraint that the steam generation source rate (Q_5) seeks to maintain an equilibrium flow equal to production from the main steam zone ($Q_3 + Q_4$). This constraint requires the reservoir to have a constant pressure boundary. A constant pressure boundary, in the petroleum engineering sense, is probably an incorrect term for a vapor-dominated geothermal reservoir. Instead, we should consider a "constant pressure source" that is moving in the reservoir. This "constant pressure source" appears more reasonable because the steam and liquid water in the reservoir will always seek a thermodynamic equilibrium which is very close to initial condition equilibrium. This is because the reservoir rock temperature is always at or near initial condition temperature (ignoring cooling of the rock due to cold water injection). At the "constant pressure source," the generation of steam is the mechanism available to the system for attaining an equilibrium. Also, if we assume instantaneous equilibrium, the constant pressure source is stationary as long as there is any liquid water available which can be converted to steam.

This model of a moving "constant pressure source" could be another possible explanation for the pressure history of Cobb Mountain No. 1 presented by Lipman, et. al. (1978). A "constant pressure source" which has moved further away from a well due to increased production would cause the experienced initial static pressure decline and stabilization of pressure of Cobb Mountain No. 1, if Q_5 reached a flow equilibrium with $Q_3 + Q_4$. This was hinted at by Grant et. al. (1982) but was not discussed in any detail.

The above discussion assumes $Q_3 + Q_4$ does not exceed the maximum steam generation rate (Q_5) which would be reasonable in a reservoir initially at or near thermodynamic equilibrium due to high initial liquid saturation. In a reservoir or portion of a reservoir that has experienced pressure depletion, the steam generation source has already migrated some distance away and $Q_3 + Q_4$ might exceed the maximum Q_5 rate forcing the flow equilibrium to equal the maximum Q_5 rate. This is likely to happen with increasing production from the shallow zone because of the fixed distance x and decreasing pressure in the main steam zone. An example of this occurring in The Geysers is the Thermal Shallow Reservoir (Mogen and Maney 1985).

This tendency towards a flow equilibrium and a "constant pressure source" are the basic arguments that lead us to the conclusion that producing wells at elevated wellhead pressures is equal to producing wells at minimum wellhead pressures. A power plant requires a certain mass flowrate and producing wells at minimum wellhead pressures will increase the volumetric flowrate but will not change the mass withdrawal from the reservoir. As long as the mass flowrates out of the reservoir are equal, there should be no difference in the location of the "constant pressure source".

However, the possibility exists that by producing at elevated wellhead pressures we can improve steam recovery. In the case of producing at minimum wellhead pressure, it would appear that a higher proportion of steam would be produced from the matrix near the wellbore because of the higher differential temperature available to vaporize liquid water in the near wellbore matrix. If this is the case, producing at elevated wellhead pressures may actually increase drainage radius because of the decreased production from the near wellbore and there would be a change in the location of the constant pressure source. This effect is not obvious and needs to be studied further.

Also, in an area that is in equilibrium at initial conditions, producing at elevated wellhead pressures minimizes the pressure and temperature changes in the reservoir near the wellbore, which should allow the reservoir to reach a flow equilibrium more rapidly.

Wellbore Versus Inflow Performance Considerations

From the perspective of individual wellbores, it appears that some wells may benefit from the philosophy of producing at elevated wellhead pressures more than others. Wellbore and inflow performance curves were developed to determine if this is the case. The wellbore performance, assuming the idealized wellbore shown in Figure 2, was determined using the following equation of vertical flow of gas derived by R. V. Smith (1950):

$$Q_1 = 393.7 \left[\frac{d^5}{G T_a Z_a f X} \left(P_2^2 - e^s P_1^2\right) \frac{S}{e^s - 1} \right]^{0.5}$$

Operational Experience

SFGI's experience of operating wells at greater than 200 psig flowing wellhead pressures has been favorable. To date, wells have experienced no noticeable bridging or scaling problems, and the stabilized lease decline is consistent with other operators. One of the results of this operational philosophy was our wells did not experience the high decline typical of a Geysers well in the first few months of production. Instead, a moderate decline rate was spread out over a longer period of time, with the decline rate slowly leveling out to a typical Geysers decline rate. This type of performance is typical of curtailed conditions. Also, our production forecast has been more predictable because of the minimal amount of downhole problems. This is a very important consideration when there is no capability of transferring steam from other power plant areas.

The design of the power plant has allowed us to run at very high capacity factors and outages that would thermally cycle the well's casing and wellbore have been minimal. Due to this sharp reduction in outages with respect to other steam field operators experience, it is difficult to determine whether maintaining higher wellhead pressures or our minimum outage record has been the reason for the favorable performance. A longer production history is required to provide a definitive comparison.

A possible drawback to this operational philosophy is that due to higher wellbore heat losses and less superheating of the steam in the reservoir, the water production to the surface is higher than would be expected from wells produced at minimum wellhead pressures. This higher water production may or may not be a negative aspect because of the trend of desuperheating steam prior to entering the steam turbines.

The philosophy of operating wells at a minimum 200 psig wellhead pressure is constantly being reviewed and will definitely be evolving in the near future. The next step will be to determine at what minimum wellhead pressure we should operate at with regard to the declining average reservoir pressure and the change in the well deliverability at these lower reservoir pressures.

Conclusions

An operational philosophy of maintaining flowing wellhead pressures in excess of 200 psig has been implemented on SFGI's lease. Based on the conceptual model presented, this philosophy should be equal to operating wells at minimum wellhead pressures because there is no difference in net mass withdrawal. Maintaining flowing wellhead pressures above 200 psig should minimize casing failures, and may minimize wellbore scaling and bridging problems. SFMI's operational experience is favorable but due to very high capacity factors and very few outages, a comparison of performance of other areas of The Geysers is inconclusive. We are continuing to expand on our operational philosophy to optimize our production with respect to the decreasing reservoir pressure to determine if and when we should begin producing at wellhead pressures below 200 psig.

References

Grant, M.A. , Donaldson, I.G., and Bixley, P.F., Geothermal Reservoir Engineering, Academic Press 1982, pp. 217-218

Lipman, S.C., Strobel, C.J. and Gulati, M.S., "Reservoir Performance of the Geysers Field", Geothermics, Vol. 7, 1978, pp. 209-219.

Mogen, P.G. and Maney, J., "The Thermal 15 Relief Well," Proceedings for the Tenth Workshop on Geothermal Reservoir Engineering, Stanford, California, January 22-24, 1985.

Rawlins, E.L., and M.A. Schellhardt: Back-Pressure Data on Natural Gas Wells and Their Application to Production Practices, U.S. Bureau of Mines Monograph 7, 1936

Smith, R.V.:Determining Friction Factors for Measuring Productivity of Gas Wells, Trans. AIME, 189: 73 (1950)

Truesdell, A.H., and White, D.E., (1973), "Production of Superheated Steam from Vapor-Dominated Geothermal Reservoirs", Geothermics Vol. 2, Nos. 3-4, pp. 154-173.

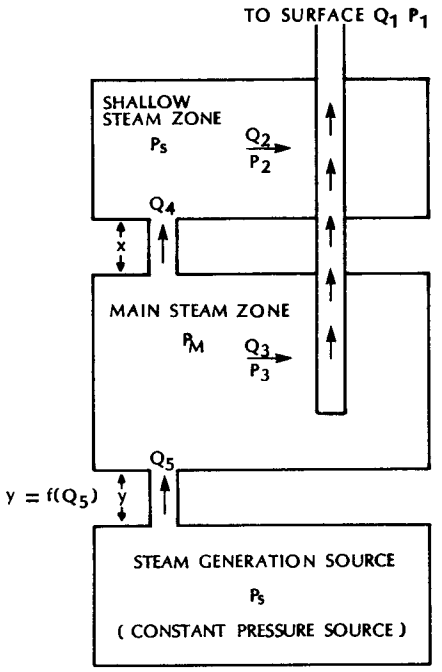


Figure 1.
Geysers Conceptual Reservoir Model

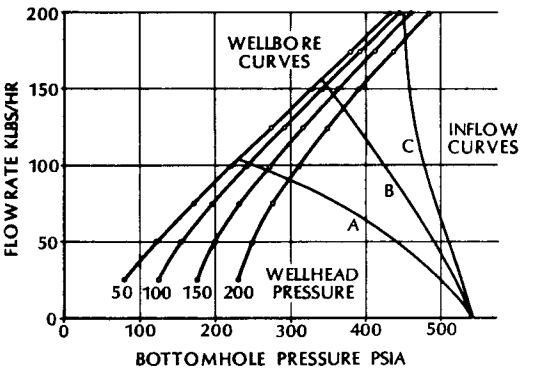


Figure 3.
Wellbore vs. Inflow Performance Relationship

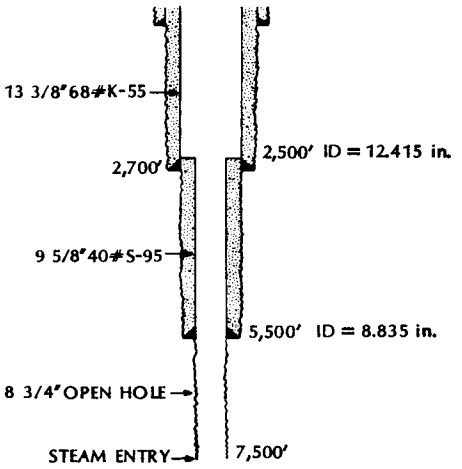


Figure 2.
Wellbore Profile

PROCEEDINGS, Twelfth Workshop on Geothermal Reservoir Engineering
Stanford University, Stanford, California, January 20-22, 1987
SGP-TR-109

GEOTHERMAL ENERGY - AN EMERGING RESOURCE

Dr. John R. Berg

U.S. Department of Energy

It is a pleasure to address the geothermal reservoir engineering community tonight. Although I will not be able to attend all of the technical sessions, I am pleased to discuss the issues with which I am most familiar -- the Department of Energy's overall energy policy, the role of alternative energy resources within the policy framework, and, specifically, our expectations for geothermal energy.

While our expectations are high for geothermal energy, based upon current geothermal industry performance, they are realistic. Your industry is to be congratulated on its farsighted decision to open a number of reservoirs to development with small "ice-breaker" plants during this period of grace in the long-term outlook for energy supply and cost. In recognition that the current over-supply of oil and electric power in geothermal areas and bargain oil prices are very likely to be transitory, your industry is preparing itself to be ready to serve an expanded energy market at prices that should reward your current wisdom.

The Department is delighted that you have embarked on this course. It is our contention that, sooner or later, OPEC to some extent will succeed in determining the prices and quantities of petroleum supplies. Since our economic prosperity and national security depend on a constant flow of reasonably priced energy from reliable suppliers, and that oil is a finite resource, our concern is that undue complacency in any quarter of the energy market is a challenge to our future.

Estimates from the Department of Energy, the Energy Information Administration, the National Petroleum Council, and the American Petroleum Institute all show that rising consumption and lower domestic energy production could push U.S. oil imports up sharply by the mid-1990's. Other nations are experiencing similar trends, and it is entirely possible that the Persian Gulf will once again be supplying half of the world's oil in the next 10 years.

That is virtually the same situation the world faced in the 1970's -- a time when market manipulations by a single set of energy suppliers nearly tripled the price of oil. The future formula could be a similar one: increased consumption and decreased domestic production added to increased imports ultimately adding up to out-of-control price spirals and renewed dependence on insecure and volatile foreign sources of oil. We cannot afford to let this happen again. Energy is too vital a component of our national security to allow a new cycle of overdependence on foreign sources, supply shortages, and rapid price increases.

This administration is dedicated to that goal. Our ideal is an economically efficient, flexible energy system which avoids undue dependence on any single source of supply. This means the development of an adequate technology base for all sources of energy, from conventional sources such as our domestic fossil fuels, to nuclear, to every form of renewable energy which, through research, continued technological advances, and market expansion, stands an excellent chance of being cost-competitive in the future. With every small improvement in the new technologies, with every new facility that opens, the prospect of our developing and conserving domestic sources of energy and avoiding undue dependence on any one source is enhanced.

The Department of Energy projections suggest that supplies from alternative technologies will continue to increase throughout the rest of this century and may represent more than 13 percent of domestic energy supply by the year 2010. In fact, on a percentage basis, geothermal energy is currently the fastest growing source of new energy supplies. Clearly, we need to continue public and private efforts to make alternative technologies more efficient, more reliable, less expensive, and readily available. We need to work for the day when these technologies are no longer "alternative," but a normal part of daily life.

The Department of Energy is committed to supporting technological innovation. Our own research program concentrates on high potential projects that are too risky and expensive for private industry to pursue alone. We are emphasizing basic and fundamental research which will expand the frontiers of our scientific and technological knowledge. For it is through research that we will make the technological break-throughs which will enable

alternate sources of energy to be cost-competitive and provide the building blocks for innovation in all available energy resources.

I would like to emphasize that the involvement of private industry is fundamental to federal research, and we are inviting industry to participate in our research program through cost-shared projects. We also encourage geothermal industry representatives, both potential users and producers, to participate in our program planning activities and to let us know what is relevant, needed, and important.

We see cost-sharing as a means of multiplying government and private capital, as the best means of initiating technical transfer, and as a means of ensuring that work being done is both meaningful and effective. We, DOE, cannot take the product of the research to the marketplace where the public will benefit from the investment, but the private sector, sharing in the program, can. The geothermal community has an excellent record in this regard, both in participation in cooperative R&D projects and in its willingness to consult with and advise the Department on optimum R&D planning. The Department's Geothermal Technology Division recently compiled a list of over 30 cooperative ventures with industry and the public sector. These range from use of industry facilities for testing DOE-developed materials and technology to the large Heber Binary Plant Project in which industry and public agencies invested over $60 million. Government/industry cooperation also extends well beyond these structured arrangements to include more informal cooperation in the field.

In addition to cooperating in the development and testing of technology, the U.S. geothermal community -- industry and the laboratories and universities that implement large portions of the R&D program -- is also generous with its time and expertise in consulting with the Department. This workshop is only one example of the opportunities made available each year for interchange among all parties concerned. The Electric Power Research Institute and Geothermal Resources Council annual meetings also afford opportunities to meet both formally and informally to discuss technology needs and priorities. Industry also makes itself available for service on several invaluable technology review panels on which I am sure many of you serve. These include the Lawrence Berkeley Laboratory review panel on geothermal reservoir engineering and the Sandia review panel on wellbore technology.

In addition, industry and the research institutions, including the U.S. Geological Survey, join in the annual program review of the Geothermal Technology Division to offer advice and counsel. Their participation was formalized during last October's review at Los Alamos where attendees were assigned to panels to evaluate priorities in hydrothermal R&D and in development of technology for utilization of the advanced geothermal resources. These groups contributed two days of their time to this productive effort. In addition, industry suggested the possibility of contributing $3.5 million per year for five years for cost-sharing with the Department in the development and testing of hydrothermal reservoir technology and drilling research.

As most of you know, this contribution can be made in several ways. One of these is the cost-shared development of DOE-funded technology, such as the borehole televiewer, through the Geothermal Drilling Organization. This arrangement expedites the availability of technology that does not attract equipment supplier interest due to the very limited market involved. DOE and industry are 50-50 partners in supporting this effort. A Geothermal Technology Organization is now being formed to apply a similar approach to reservoir technology and geothermal energy conversion systems.

Another cooperative mechanism involves joint field projects for which industry absorbs the cost of the logistical and operational aspects and DOE provides the scientific input and technology transfer. A project of this type might involve, for example, industry furnishing drilling cores, cuttings, and geophysical well logs for analysis and reservoir modeling under DOE funding. We believe that a combination of these approaches will result in the greatest contribution to the progress of geothermal technology.

In that connection, the Department has sought the counsel of the National Academy of Sciences in evaluating the whole range of mechanisms available for DOE/industry cooperative R&D ventures. The Academy study is currently underway, and it will report its recommendations to us in the near future.

Thus far, I have only addressed the Department's participation in developing a technology base for geothermal power generation. I would like to add that we have also used the authority given to us by Congress under the Geothermal Loan Guaranty Program to assist developers of new geothermal projects which met the requirements of the Loan Guaranty Act, such as the funding of construction of the Northern California Power Agency's first plant at The Geysers. NCPA was able to repay this loan 24 years early and to move on to construction of its second plant. Another very promising 30 MWe project by ORMESA is currently underway at East Mesa which was also made possible by a loan guaranty. In addition, similar support permitted early development of commercial establishments for using geothermal energy. These include the Geothermal Food Processors' onion drying plant in Nevada and the Oregon Trail Mushroom's establishment at Vale, Oregon. Both of these highly successful operations serve as models for other commercial geothermal enterprises to come.

All of the efforts of the geothermal community that I have enumerated here contribute substantially to the realization of the Department's goal of achieving a mixed and balanced resource base for this country. If we can achieve this goal, we may never again have to face the economic and energy chaos we experienced a decade ago.

What do we expect of geothermal energy in the future? The fifth National Energy Policy Plan, or NEPP V, published in 1985, projects that the annual geothermal input to the electricity grid will double between 1984 and 1990 and double again by the year 2000 to 0.68 quads, representing about 8300 MWe on line. The sixth NEPP is currently in preparation, and while I cannot second guess the statistics it will contain, I believe that the industry performance noted earlier will support an increase in these numbers.

Since the data were gathered for NEPP V, power plant development has occurred or is planned for a number of liquid-dominated reservoirs that are estimated by the U.S. Geological Survey to have the capacity to produce several thousand megawatts for a lifetime of 30 years. The performance and behavior of these fields are being tested and evaluated now with small facilities. If an energy shortfall occurs in the 1990's, as has been predicted by some experts, your industry will be ready to meet the challenge with larger capacities. Most of the effort to characterize these reservoirs will be behind you, and you can gear up quickly as demand requires.

Your ability to cope expeditiously with an energy shortage is enhanced by the short lead times for construction of geothermal power plants once the capability of the reservoir is known. I don't need to remind this audience of the brief construction schedules for the first round of hot water plants or of plants at The Geysers brought on-line ahead of schedule. The Department commends your decision to pursue the longer-term field effort now when there is low demand for your product. You have recognized that you cannot take 10 to 15 years to find new energy sources, develop them, and bring the energy to market overnight. It just cannot be done, and you are building your future competitive position at this moment.

All of you here this evening are contributing in one way or another to the preparations for a substantial geothermal contribution to our energy security. We are grateful to you for the wisdom, foresight, and leadership that you are demonstrating in this effort.

Keep up the good work.

Participants List

Anil Ambastha
Petroleum Engineering Department
Stanford University
Stanford, CA 94305

David N. Anderson
Geothermal Resources Council
P.O. Box 1350
Davis, CA 95617
(916) 758-2360

Paul Atkinson
Unocal Geothermal Division
2099 Range Avenue
Santa Rosa, CA 95402
(707) 542-9543

Ralph Aviles
Unocal Geothermal Division
2099 Range Avenue
Santa Rosa, CA 95402
(707) 542-9543

Kenzo Baba
Sumiko Consultants Co., Ltd.
16-9, Kabuki-cho 2-chome Shinjuku-ku,
Tokyo 160 Japan
03-205-6031

E. L. Baldwin
Baldwin Engineering, Inc.
13612 Midway Road, #490
Dallas, TX 75244
(214) 980-0784

Michael L. Barnes
Unocal Geothermal
Imperial District
P.O. Box 1805
Indio, CA 92201
(619) 342-4723

Anthony S. Batchelor
Geoscience, Ltd.
P.O. Box 36
Falmouth, Cornwall TR11 3DU
England
011-44-326-76868

Joseph J. Beall
Geysers Geothermal
1160 No. Dutton Ave., #200
Santa Rosa, CA 95401
(707) 598-2725

Sally Benson
Earth Sciences
Lawrence Berkeley Laboratory
Building 50E
Berkeley, CA 94720
(415) 486-6760

John Berg
U.S. Department of Energy
Washington, D.C.

Grimur Bjornsson
Lawrence Berkeley Laboratory
1 Cyclotron Road
Berkeley, CA 94720
(415) 486-7045

Robert E. Blackett
Meridian Corporation
5113 Leesburg Pike, Suite 700
Falls Church, VA 22041
(703) 998-0922

John M. Bodell
Philippine Geothermal, Inc.
Metrobank Plaza, 1st Floor
P.O. Box 7336 Airport
Metromanila, Philippines
Philippines, Manila 817-8876

G. Bodvarsson
Earth Sciences Division
Lawrence Berkeley Laboratory
Building 50E
Berkeley, CA 94720

W. T. Box, Jr.
Geysers Geothermal Company
P.O. Box 11279
Santa Rosa, CA 95401
(707) 823-1678

W. E. Brigham
Petroleum Engineering Department
Stanford University
Stanford, CA 94305
(415) 723-0611

Kevin L. Brown
Geothermal Research Centre, DSIR
Private Bag
Taupo, New Zealand
(303) 236-1568

Mike Bryan
Unocal Geothermal Division
2099 Range Avenue
Santa Rosa, CA 95402
(707) 542-9543

Myron Burr
Unocal Geothermal Division
2099 Range Avenue
Santa Rosa, CA 95402
(707) 542-9543

Raffaele Cataldi
ENEL
via Andrea Pisano c/o UNG
56100 Pisa, Italy
(050) 533.26

Ken Chan
BLM
2800 Cottage Way
Sacramento, CA 95825
(916) 978-4735

Bill Christensen
Unocal Geothermal Division
2099 Range Avenue
Santa Rosa, CA 95402
(707) 542-9543

T. Y. Chu
Division 6242
Sandia National Laboratories
P.O. Box 5800
Albuquerque, NM 87185
4-3953

Jim Combs
Geothermal Resources Int'l, Inc.
1825 S. Grant Street, Suite 900
San Mateo, CA 94402
(415) 349-3232

Simon Cordova
Calif. Div. of Oil and Gas
1419 Ninth St., Room 1310
Sacramento, CA 95814
(916) 445-9686

John Counsil
Engineering Consultant
1148 Shadyoak Place
Santa Rosa, CA 95404
(707) 538-2288

Charlene L. Crockett
Geysers Geothermal Company
1160 No. Dutton, Suite 200
Santa Rosa, CA 95401
(707) 578-2727

Robert G. Daniel
Unocal Geothermal Division
1450 Guerneville Road
Santa Rosa, CA 95401
(707) 542-9543

Bill Dugan
Dresser Atlas
2421-A Portola Drive
Ventura, CA 93003
(805) 642-7774

Andy Drenick
GEO Operator Corp.
1330 No. Dutton Ave., Suite A
Santa Rosa, CA 95401
(707) 523-4272

Einar T. Eliasson
Nat'l Energy Authority of Iceland
Grensasvegur 9, 108 Reykjavik
Iceland
354-1-83600, Ext. 199

Steven L. Enedy
No. Calif. Power Agency
P.O. Box 425, 101 Grant Ave.
Healdsburg, CA 95448
(707) 987-3101

Christy Craig
Calif. Div. of Oil and Gas
485-B Broadway
El Centro, CA 92243
(619) 353-9900, 344-9757

Franco D'Amore
Int'l Inst. for Geoth. Res., CNR
Piazza Solferino 2
Pisa 56100, Pisa, Italy
(050) 41503, 46069

Ronald C. Dick
R.C. Dick Geothermal Corp.
22 Mitchell Blvd.
San Rafael, CA 94903
(415) 499-1444

J.C. Dunn
Division 6242
Sandia National Laboratories
P.O. Box 5800
Albuquerque, NM 87185
844-4715

Herman Dykstra
Consultant
4180 Treat Blvd., Suite I
Concord, CA 94518
(415) 676-7464

Kathleen Enedy
Geysers Geothermal Company
P.O. Box 11279
Santa Rosa, CA 95406
(707) 578-2710

Daniel J. Entingh
Meridian Corporation
5113 Leesburg Pike, Suite 700
Falls Church, VA 22041
(703) 998-0922

I. Ershaghi
State Lands Commission
245 W. Broadway
Long Beach, CA 90802
(213) 590-5246

David D. Faulder
Chevron Geothermal
595 Market Street
San Francisco, CA 94105
(415) 894-9592

Robert O. Fournier
U.S. Geological Survey
M/S 910
345 Middlefield Road
Menlo Park, CA 94025
(415) 323-8111

Scott Gaulke
U.C. Berkeley
Lawrence Berkeley Lab., 50E
1 Cyclotron Road
Berkeley, CA 94720
(415) 486-4952

Keshav Goyal
Thermal Power Company
2333 Mendocino Ave., #120
Santa Rosa, CA 95401
(707) 576-1362

Andrew S.P. Green
CSM, Geothermal Energy Proj.
Rosemanowes Quarry, Herniss,
Penryn, Cornwall, TR10 9DU
England
0209-860141

Richard Gunderson
Unocal Geothermal Division
1450 Guerneville Road
Santa Rosa, CA 95401
(707) 542-9543

John Farison
Unocal Geothermal Division
2099 Range Avenue
Santa Rosa, CA 95402
(707) 542-9543

Dan Fisher
Unocal Geothermal Division
2099 Range Avenue
Santa Rosa, CA 95402
(707) 542-9543

Fikry Garas
Taylor Woodroe Group
345 Ruislip Road
Southall, Middlesex, England
01-575-4505

Colin B. Goranson
Berkeley Group, Inc.
1330 Broadway, Suite 1450
Oakland, CA 94612
(415) 465-1744

Eduardo Granados
GeothermEx, Inc.
5221 Centrol #201
Richmond, CA 84804
527-9876

Mohinder Gulati
Unocal Geothermal Division
2099 Range Avenue
Santa Rosa, CA 95402
(707) 542-9543

Robert Habel
Calif. Div. of Oil and Gas
1416 Ninth St., Room 1310
Sacramento, CA 95814
(916) 323-1786

Jill Haizlip
GEO Operator Corporation
1330 No. Dutton Ave., Suite A
Santa Rosa, CA 95401
(707) 523-4272

Robert Hendron
Los Alamos National Laboratory
M/S J979
Los Alamos, NM 87545
(505) 667-3185

Viet T. Hoang
Chevron Resources Company
P.O. Box 7147
San Francisco, CA 94120
(415) 894-4141

Roland N. Horne
Petroleum Engineering Department
Stanford University
Stanford, CA 94305
(415) 723-9595

Eduardo Iglesias
IIE
APDO Postal 475
Cuernavaca, Mor., Mexico
(73) 14-3811, Ext. 3210

Tsuneo Ishido
Geological Survey of Japan
1-1-3 Higashi, Yatabe
Ibaraki, 305 Japan
(0298) 54-3736

Dawn Janney
Naval Weapons Center
Geothermal Program Office
Code 2606
Naval Weapons Center
China Lake, CA 93555-6001
(619) 9390 3411, Ext. 233

Jeffrey Hebein
Diamond Shamrock Thermal Power Co.
3333 Mendocino Aave., Suite 120
Santa Rosa, CA 95401
(707) 576-1398

Paul N. Hirtz
Thermochem. Inc.
6119 Old Redwood Highway, Suite A-2
Santa Rosa, CA 95401
(707) 575-1310

Susan F. Hodgson
Calif Div. of Oil and Gas
1416 Ninth Street, Room 1310
Sacramento, CA 95814
(916) 445-9686

Lawrence Hull
Idaho National Eng. Lab.
P.O. Box 1625
Idaho Falls, ID 83415
(208) 526-1627

Steve Ingebritsen
U.S. Geological Survey
345 Middlefield Road
Menlo Park, CA 94025
(415) 323-8111, Ext. 2631

Earl James
Chevron Geothermal
151 Taurus Avenue
Oakland, CA 94611
(415) 894-2889

Ibrahim Kocabas
Petroleum Engineering Department
Stanford University
Stanford, CA 94305

Robert L. Kohlbush
U.S. Dept. of the Interior
Bureau of Land Management
800 Truxtun, Room 311
Bakersfield, CA 93301
(805) 861-4012

Paul Kruger
Civil Engineering Department
Stanford University
Stanford, CA 94305
(415) 723-4123

Al Lewis
State Department of Water Resources
Energy Division
P.O. Box 388
Sacramento, CA 95802

Stephen C. Lipman
Unocal Geothermal Division
1201 W. Fifth Street
P.O. Box 7600
Los Angeles, CA 90051
(213) 977-7677

Jim Lovekin
Petroleum Engineering Department
Stanford University
Stanford, CA 94305

Jeralyn Luetkehans
Petroleum Engineering Department
Stanford University
Stanford, CA 94305

Luis Macias-Chapa
The University of Tulsa
600 So. College Ave.
Tulsa, OK 74104
(918) 592-6000

Tom MacPhee
GEO Operator Corp.
1330 No. Dutton Ave., Suite A
Santa Rosa, CA 95401
(707) 523-4272

Mark A. Magers
Unocal, Geothermal Division
1201 W. Fifth Street, Room M33
Los Angeles, CA 90017
(213) 977-6958

R. L. Makin
Taylor Woodroe Group
345 Ruislip Road
Southall Middlesex, England
01-575-4255

S. S. Marsden, Jr.
Petroleum Engineering Department
Stanford University
Stanford, CA 94305
(415) 723-3570

Brad Martin
Unocal Geothermal Division
2099 Range Avenue
Santa Rosa, CA 95402
(707) 542-9543

Jean-Claude Martin
BRGM, IMRG
Orleans, France

Ross A. McCartney
Geoscience, Ltd.
P.O. Box 36
Falmouth, Cornwall TR11 3DU
England
011-44-326-76868

Craig J. McClanahan
Unocal
376 So. Valencia
Brea, CA 92621
(714) 528-7201, Ext. 2549

Bob McEwen
PG&E
77 Beale St.
San Francisco, CA 94106
(415) 972-4554

Gregory M. McFadden
Unocal Geothermal
Imperial District
P.O. Box 1805
Indio, CA 92201
(619) 344-7170

Mark J. McGuinness
DSIR New Zealand
P.O. Box 1335
Wellington, New Zealand
(415) 486-5837 (LBL)

Glenn Melosh
Unocal Geothermal Division
1450 Guerneville Road
Santa Rosa, CA 95401
(707) 542-9543

Will Menninger
Box 6571
Stanford University
Stanford, CA 94305

Anthony J. Menzies
GeothermEx, Inc.
5221 Central Ave., Suite 201
Richmond, CA
(415) 799-3077

Donald E. Michels
Don Michels Associates
P.O. Box 895
Whittier, CA 90608
(213) 698-5728

F. G. Miller
Petroleum Engineering Department
Stanford University
Stanford, CA 94305
(415) 723-2938

Richard J. Miller
Cascadia Pacific Corp.
1000 E. Walnut Ave., #237
Pasadena, CA 91106
(818) 795-3214

Richard A. Miram
PG&E
77 Beale Street
San Francisco, CA 94106
(415) 972-3397

Srikanta Mishra
Petroleum Engineering Department
Stanford University
Stanford, CA 94305

John E. Mock
U.S. Department of Energy
1000 Independence Ave., SW
Washington, D.C. 20585

Allen Moench
U.S. Geological Survey
345 Middlefield Road
Menlo Park, CA 94025

Phil Mogen
Unocal Geothermal Division
2099 Range Avenue
Santa Rosa, CA 95402
(707) 542-9543

Rafael Molinar
CFE
Volta 655, Box 58-I
Morelia, Mexico
451-436 49

Martin W. Molloy
U.S. Department of Energy
1333 Broadway
Oakland, CA 94612
(415) 273-7945

Joseph N. Moore
Univ. of Utah Res. Inst.
Earth Science Laboratory
391 Chipeta Way, Suite A
Salt Lake City, Utah 84108
(801) 524-3428

Kent S. Murray
CSUS/CEC
1516 Ninth Street
Sacramento, CA 95814
(916) 324-3474, 278-7200

Larry E. Murray
Unocal
P.O. Box 76
Brea, CA 92621
(714) 528-7201

Manuel Nathenson
U.S. Geological Survey
345 Middlefield Road, M/S 910
Menlo Park, CA 94025
(415) 323-8111, Ext. 4153

David Nieva
IIE
APDO Postal 1612
Cuernavaca, Mor. 62000
(73) 12-86-97

Alfonso Ortega
Geothermal Research Div. 6242
Sandia National Laboratories
Albuquerque, NM 87185
(505) 844-3952

Jaime Ortiz
CFE
Melchor Ocampo 35
Cd. Hidalgo, Mich.
(725) 40944

Roger Parker
Camborne School of Mines
HDR Geothermal Energy Project
Rosemanowes Quarry, Herness,
Penryn, Cornwall TR10 9DU UK
0209-861013

Susan Petty
Mesquite Group
P.O. Box 1283
Fullerton, CA 92632
(714) 738-8224

Al Pingol
Unocal Geothermal Division
2099 Range Avenue
Santa Rosa, CA 95402
(707) 542-9543

Susan Prestwich
U.S. Department of Energy
785 DOE Place
Idaho Falls, ID 83402
(208) 526-1147

John W. Pritchett
S-Cubed
P.O. Box 1620
La Jolla, CA 92038
(619) 453-0060

Karsten Pruess
Earth Sciences Division
Lawrence Berkeley Laboratory
Building 50E
Berkeley, CA 94720
(415) 486-6732

Robert Prucha
Earth Sciences Division
Lawrence Berkeley Laboratory
Building 50E
Berkeley, CA 94720
(415) 486-6110

Stephen Pye
Unocal
1201 W. Fifth Street
Los Angeles, CA 90017
(213) 977-6262

Peter M. Pyle
BGI
1330 Broadway, #1450
Oakland, CA 94612
(415) 465-1744

Gregory Raasch
Unocal Geothermal Division
2099 Range Avenue
Santa Rosa, CA 95402
(707) 542-9543

Henry J. Ramey, Jr.
Petroleum Engineering Department
Stanford University
Stanford, CA 94305
(415) 723-1774

Jetzabeth Ramirez
University of Mexico
Division de Estudios de Posgrado
Facultad de Ingenieria
Universidad Nacional Autonoma de Mexico
04510 Mexico, D.F.
(525) 5508712

Marshall Reed
DOE Geothermal Division
DOE, CE-342
Washington, D.C. 20585
(202) 586-8076

Ken Reidel
Unocal Geothermal Division
2099 Range Avenue
Santa Rosa, CA 95402
(707) 542-9543

Joel Renner
INEL
Box 1625
Idaho Falls, ID 83415
(208) 526-9824

Mark Ripperda
Earth Sciences Division
Lawrence Berkeley Laboratory
Building 50E
Berkeley, CA 94720
(415) 486-5875

Jesus Rivera
Petroleum Engineering Department
Stanford University
Stanford, CA 94305
(415) 723-1218

Bruce Robinson
Los Alamos National Lab.
M/S J981
Los Alamos, NM 87545
(505) 455-3608

Joel Robinson
Unocal Geothermal Division
2099 Range Avenue
Santa Rosa, CA 95402
(707) 542-9543

Ray V. Rothermel
Board of Equalization
State of California
P.O. Box 1799
Sacramento, CA 95816
(916) 445-4982

David Sanchez
Calif. Div. of Oil and Gas
50D Street, Room 300
Santa Rosa, CA 95404
(707) 576-2385

Douglas Sheppard
DSIR, New Zealand
Chemistry Division DSIR
Private Bag
New Zealand

Ronald C. Schroeder
Berkeley Group Inc.
1330 Broadway, Suite 1450
Oakland, CA 94612
(415) 465-1744

Warren Smith
Unocal Geothermal Division
2099 Range Avenue
Santa Rosa, CA 95402
(707) 542-9543

Amanda Spencer
Earth Sciences Division
Lawrence Berkeley Laboratory
Building 50E
Berkeley, CA 94720
(415) 486-7312

Don Ross
Bureau of Land Management
311 Federal Building
800 Truxton Avenue
Bakersfield, CA 93301
(805) 861-4179

Abraham Sageev
Petroleum Engineering Department
Stanford University
Stanford, CA 94305
(415) 723-9476

Sam Sarem
Unocal Science and Technology
P.O. Box 76
Brea, CA 92621
(714) 528-7201

Hiroshi Shigeno
U.S. Geological Survey
Geological Survey of Japan
345 Middlefield Road, M/S 910
Menlo Park, CA 94025
(415) 323-8111, Ext. 2162

Barbara Simpson
N.Z. Geological Survey
P.O. Box 499
Rotorua, NZ
(073) 80059

Mike Sorey
U.S. Geological Survey
345 Middlefield Road
Menlo Park, CA 94025
(415) 323-8111

Kenneth F. Stelling
Calif. Div. of Oil and Gas
50 "D" Street, Room 300
Santa Rosa, CA 95404
(707) 576-2385

Susan Stiger
EG&G
P.O. Box 1625
Idaho Falls, ID 83415
(208) 526-0457

Mary K. Stroh-Twichell
Geysers Geothermal Company
1160 No. Dutton, Suite 200
P.O. Box 11279
Santa Rosa, CA 95406-11279
(707) 578-2728

Chandler A. Swanberg
GEO Operator Corporation
1825 So. Grant St., Suite 900
San Mateo, CA 94402
(415) 349-3232

Jefferson W. Tester
MIT
Department of Chem. Engring 66-305
Cambridge, MA 02139
(617) 253-4598

W. M. Thompson
State Lands Commission
Suite 425
245 W. Broadway
Long Beach, CA 90802
(213) 590-5243

Alfred H. Truesdell
U.S. Geological Survey
345 Middlefield Road
Menlo Park, CA 94025
(415) 323-8111

Raymond H. Wallace, Jr.
U.S. Geological Survey
1000 Independence Ave., SW
Washington, D.C. 20585
(202) 252-8082

Calvin Strobel
Unocal Geothermal Division
2099 Range Avenue
Santa Rosa, CA 95402
(707) 542-9543

Gene Suemnicht
Unocal Geothermal Division
1450 Guerneville Road
Santa Rosa, CA 95401
(707) 542-9543

R. J. Taylor
Energy Tech. Support Unit
U.K.
0235 834621, Ext. 3541

Richard Thomas
Calif. Div. of Oil and Gas
1416 Ninth St., Room 1310
Sacramento, CA 95814
(916) 323-1787

R. K. Traeger
Sandia National Labs
Department 6240
Albuquerque, NM 87185
(505) 844-2155

Al Viesca
Unocal Geothermal Division
2099 Range Avenue
Santa Rosa, CA 95402
(707) 542-9543

Mark Walters
GEO Operator Corp.
1573 Manzanita Avenue
Santa Rosa, CA 95404
(707) 523-4272

Ken Williamson
Unocal Geothermal Division
2099 Range Avenue
Santa Rosa, CA 95402
(707) 542-9543

Ted E. Wilmsen
Thermal Power Company
3333 Mendocino Ave., Suite 120
Santa Rosa, CA 95401
(707) 527-8947

Phillip M. Wright
Univ. of Utah Res. Inst.
391 Chipeta Way, Suite C
Salt Lake City, UT 84108
(801) 524-3422

Adadu Yemane
Unocal Geothermal Division
2099 Range Avenue
Santa Rosa, CA 95402
(707) 542-9543

SUBJECT INDEX VOLUMES 1-12

Acid stimulation: IX 421

Acoustic emission: IX 403

Acoustic logging: XI 283

Adsorption: X 247

Ahuachapan field: IX 97; XI 217

Air-steam-water systems: IX 351

Alaska: VI 66; VIII 25, 31; X 227

Albano field: IX 17

Alfina field: I 93

Amiata field: IX 17

Aquifer:
    contamination: IX 351
    Free surface: IX 351
    infinite: XII 109
    geopressured-geothermal: VIII 261
    linear: X 97

Aquitaine basin: IX 5

Autoclave test facilities: IX 415

Axial splitting: IX 381

Azores: VIII 73

Baca field: VI 28; VII 47, 53; VIII 91, 97; IX 145; XI 7

Back-pressure turbines: IX 275

Barometric pressure: XI 15

Basalt: VIII 189

Bejing field: IX 127

Beowaw field: IX 421; XII 159

Berea sandstone: VIII 197, 205

Bleeding: XII 297

Boise KGRA: III 130

Boiling processes: IX 231

Borehole televiewer: X 13

Bottle Rock (The Geysers): IX 135

Bottom-hole pressure: IX 289, 291

Brady hot springs: IV 218

Breakthrough time: XI 93

Brines: II 176; VII 61; VIII 309, 329,
    reinjection: IV 42; XII 57
    scaling: IV 42
    thermodynamic properties: II 247

Brittle-ductile transition: IX 381

Broadlands field: IV 139, 332; V 37, 313; VI 28, 238; VIII 127, 183; IX 107; X 189

Bubble flow: XI 277

Build-up tests: IX 403

Bulalo field: IV 228; V 255

Calcite: IX 317; X 247

Calcium: IX 317; X 37

California: I 52, 74, 84, 89, 135, 143, 146, 153; II 9, 16, 30, 39, 61, 75, 116, 126, 143, 159, 324; III 18, 61,107, 116, 145, 178, 209; IV 96, 106, 118, 300; V 83, 131, 139, 189, 211; VI 13, 279, 303, 344, 351, 361; VII 161; VIII 31, 39, 45, 177, 295; IX 5, 157, 205, 299, 311, 365, 409; X 89, 123, 129, 133, 141, 195, 247, 297; XI 29, 43, 141, 197, 251; XII 23, 29, 37, 241, 267, 273, 327

Campi Flegrei Caldera: IX 17, 53

Canada: X 253

Capillary pressure effects: IX 351, 443

Carbon dioxide: X 233, 273

Carbon monoxide: XII 247

Casa Diablo: X 297

Cascade volcanic belt: X 253

Castelnuovo: VIII 323; IX 17, 221

Casing corrosion: X 189

Cell boundaries: X 89

Cements:
    testing: VI 126

Cerro Prieto: IV 5; V 44, 55, 228; VI 121, 130, 258, 344; VII 23, 29, 35; VIII 49, 161; VIII 171, 197, 205, 231; IX 81, 247, 291, 357, 427; X 73, 301; XI 7, 51, 127; XII 153

Chemical analysis: V 139

Chemical tracers: VIII 289

China: IX 127

Chingshin field: V 64, 96, 277; IX 193

Chingshui field: IX 193

Choking: IX 279

Chloride concentration studies: IV 239

Chloride tracer: X 265

Circulation: X 195

Cold water injection: VII 175; VIII 279; IX 339; XI 161

Comision Federal de Electricidad (CFE) research: VIII 49; IX 81

Composite reservoir: VIII 103

Compressibility: VIII 197; IX 279, 381; XII 119

Computer codes: V 147, 169, 222, 195
FRACSL: X 287, 293
FRIP: IX 387
GEOCOM: IX 409
NSCGREATS: VIII 149
liquid-dominated systems: V 199

Computerized well test analysis: IX 199

Conceptual model: X 29, 279; XI 65, 109, 197

Confining pressure: IX 427

Contamination of aquifers: IX 351

Continuum model: VII 157

Convection: VIII 5

Cool downflows: XI 169

Cooling effects: IX 351; X 73, 195

Corrosion: X 189; XI 1; XII 321

Coso field: VIII 45

Coso Hot Springs: IV 118; XII 37

Costa Rica: VII 13; X 37

Costs: IX 409; X 31; XII 21

Crack-like reservoirs: IX 403

Cracks: IX 415, 449

Critical flow slip model: VIII 143

Decline curve: X 105, 163; XII 23, 29

Deliverability: X 31, 97, 105

Denmark: IX 5

Depletion analysis: XII 103

Desert Peak: IX 151

Dilatancy: IX 381

Discrete fracture model: VII 157

Dispersion: VII 103; VIII 283; IX 253, 311, 373; X 259, 287

Dogger reservoir: XII 203, 321

Double porosity: VIII 115, 219; IX 175, 181; X 163, 293; XII 125, 315

Doublet systems: IX 331

Downhole instruments: XI 231

Downhole pressure transient data: IX 217

Drawdown: IX 261; X 45; XI 77, 149; XII 37

Drift velocity: X 287

Drill cores: XII 195
data acquisition systems: II 46

Drilling mud: VIII 205

Dry steam: X 23, 65; XI 225

Dual permeability: X 293; XI 71, 77; XII 139

Ducts: IX 279

Earth tides: XI 15

East Africa: I 113

East Brawley: VIII 39

East Mesa: IX 299, 311; X 247, 287; XII 233

East Mesa field: I 23, 52, 146; II 9, 39, 75

Electric Power Research Institute (EPRI) VII 21

Electrical potential: IX 421

Electrokinetic mechanism: XII 285

Ellidaar field: IX 37; X 279

El Salvador: VII 13; IX 97; XI 217

England: VIII 237; IX 387; XI 35; XII 131

Enthalpy data: VII 143, 151; VIII 127, IX 253, 345, 357; X 133, 241, 273; XII 208, 301

Environmental effects: VIII 329

Epidote: IX 269

Europe: IX 5

Expansion: IX 427

Exploration: IX 167; XII 273, 315

Explosive fracturing: IX 409

Explosive stimulation: VIII 237

FRACSL code: X 287, 293

Falloff data: X 151

Fault-charged systems: VII 161

Fenton Hill: II 188; IV 244, 249, 256; VI 272, 367; VII 97; VIII 249, 269; IX 397; XI 189; XII 7, 163

Ferrara: IX 17

Field development: XII 159, 163, 173, 181, 189, 195, 203

Field studies: XI 175, 183, 189

Fieldwide gradients: XII 241

Fissured reservoirs: IX 175

Flashing: VIII 143; IX 253, 279, 449; X 37

Flow and gas extraction model: VII 133

Flow data analysis: VII 47, 131; VIII 119, 133, 175; IX 199, 205, 345, 443; X 227

Flow, interporosity: X 163

Flowmeter: IX 205

Flow modeling: XI 77

Flowrate analysis: IX 345, 443

Flowrate decline: XII 23, 29

Flowrate prediction: IX 305, 365, 373

Flow test: XII 163

Flow velocity: XI 231

Fluid and heat model: VII 151; VIII 219

Fluid behavior: VIII 225

Fluid depletion: VIII 177; XI 161

Fluid flow: VII 151; VIII 211, 219; X 37
  measuring methods: III 198; VI 126

Fluid migration: VIII 161; XI 71

Fluid reserves: X 113

Fossil-liquid-dominated system: XI 203

Fracture:
  detection: X 13; XI 65, 207; XII 305
  explosive: IX 409
  gas: XI 245
  ladders: VIII 139
  mechanics: IX 415
  modeling: XI 72
  networks: VIII 285; X 287, 293
  skin: IX 175; XII 125
  stimulation: VII 53; IX 409
  widths: IX 323

Fractured reservoirs: II 16, 21, 34, 168; V 293; VII 151, 169; VIII 97, 111, 115, 119, 143, 219, 275; IX 135, 151, 299, 305, 311, 323, 331, 373; X 145, 259; XI 35, 43, 51, 59, 65, 71, 77, 85, 149; XII 7, 213, 219, 233

  flow models: I 45; VI 178
  heat transfer: V 175
  permeability: V 103

Fractures:
  deformation: I 37

Fracturing pressure: IX 397, 409

France: IX 5; XII 203, 321

Fujian: IX 127

Fumarole steam: IX 231

GEOCOM model: IX 409

Gabbro zone: X 97

Galzignano: IX 17

Garibaldi volcanic belt: X 253

Gas:
  composition: IX 221
  concentration: IX 247
  correction: VIII 133
  fracturing: XII 279
  geochemistry: XII 321
  geothermometers: IX 231; XII 247, 321
  noncondensable: X 37

Gas-steam ratio: VIII 323

Gas-water ratio: VIII 261

Generating capacity: IX 157

Geochemistry: XII 241, 247, 253, 261

Geologic cross-sections: XI 251

Geological model: VIII 231

Geologic structures: I 37; III 209,
geothermal exploration: I 113
mathematical models: III 214

Geologic surveys:
Alaskan sites: VIII 31
Cerro Prieto: VIII 49
Imperial Valley: VIII 39
Los Humeros: VIII 19
Pilgrim Springs: VIII 25
Sarukawa: X 207

Geophysical surveys: I 52; III 18, 36, 61, 70; VI 328, 338
evaluation: V 115

Geopressured-geothermal aquifer: VIII 261

Geopressured systems: I 130, 146; VI 76, 84, 98, 105
geologic faults: III 209
geothermal wells: IV 280
ground subsidence: IV 280
mathematical models: II 299
sandstones: IV 280
simulation: II 299; V 159

Geoscience: XI 135, 141, 149; XII 267, 273, 279, 285

Geothermal energy:
research programs: I 23, 198, 199, 219; III 192; IV 15; V 5; VI 150
resource assessment: VI 3
resource development: IV 5

Geothermal exploration: III 130; VI 338, 361

Geothermal fields:
geologic faults: II 46
geologic structure: II 46; VI 21
heat flow: II 30
mathematical models: IV 36
recharge: II 40, 150, 159, 339; V 55; VI 21
reinjection: II 8, 46, 98, 116, 181; IV 322; V 26, 37
rock-fluid interactions: II 34
tracer techniques: IV 249; VI 344
well temperature: II 290; VI 272, 279, 297, 316, 328

Geothermal fluids: V 278
chemical analysis: II 30, 116; VI 21,
chemical composition: IV 96; V 262 VI 279
geochemistry: VI 84, 367
plugging: III 163; IV 275
reinjection: IV 294; V 355
scaling: I 185; IV 42
thermodynamic properties: I 247; II 247; IV 294
transport: V 329
water chemistry: VI 98

Geothermal power plants: I 117, 153; II 9, 116
economics: I 153
performance: I 135
steam separators: I 135

Geothermal reserves: IX 193

Geothermal resources:
brines: I 135
economic analysis: II 150, III 158; VI 3, 238
economics: I 161, 167
geothermal fluids: I 113
management: II 181; V 5
remote sensing: II 30
reservoir engineering: IV 234
resource assessment: II 12; III 145; VI 238
resource development: VI 13, 34; I 41, 374, 380
resource potential: III 3, 9, 70, 96, 107
risk assessment: VI 374, 380
temperature surveys: II 30, 40; VI 28

Geothermal space heating: II 181

Geothermal systems:
convection: I 206, 213; II 236, 251, 339; IV 300
flow models: I 26, 42, 45, 52, 62, 201, 213, 267; II 193, 200, 229; III 188, 209; IV 286, 300, 308; V 11; VI 194, 218, 322
fluid injection: VI 98, 204
heat extraction: II 46, 181, 188, 200; VI 264, 272
homogeneous: XI 85
heat transfer: I 50, 52, 249; II 46, 222, 236, 251, 263, 268; IV 112, 286, 300; IV 308; VI 243
hydrodynamics: IV 146, 160
mass transfer: II 268; IV 286, 300, 308
mathematical models: I 26, 65, 146, 242, 247, 267; II 46, 126, 193, 263, 268, 308, 324; III 203, 214; IV 36, 286, 300, 308, 194, 213, 264
natural convection: VI 194
reinjection: I 62
reservoir engineering: I 146; II 3, 6, 9; IV 36; V 5; VI 66, 253
rock-fluid interactions: I 240, IV 275; VI 322
simulation: I 130, 198, 201, 225, 232, 247; II 116, 159, 222, 308, 310, 178, 185, 188; IV 308, 332; VI 188; III 178, 185, 188; IV 308, 332; VI 188, 204, 213, 253
thermodynamic properties: VI 213
two-phase flow: I 42; III 185, 192;

IV 308; VI 28, 49, 170, 288
vapor pressure: IV 60
water chemistry: IV 42, 275, 294

Geothermal wells:
enthalpy: VI 224
explosive stimulation: I 192; II 213, 219
field tests: II 109, 176; IV 96
flow models: V 322; VI 130, 159, 188
flow rate: VI 139
fluid withdrawal: VI 139
hydraulic fracturing: I 174, 178, 180; II 188, 198, 200; III 36; VI 272, 303
mathematical models: VI 130, 159
measuring instruments: II 101, 109, 176; VI 126
performance: VI 218
plugging: III 163; IV 106
pressure measurement: IV 96
sampling: VI 84
scale control: I 185
sonic logging: IV 256
temperature measurement: II 136; IV 96
testing: I 69, 74, 77, 93, 101, 117, 124; II 21, 75, 85, 98, 116, 143, 168; III 64, 96, 116, 125, 130, 138, 145, 172; IV 106, 112, 118, 133, 139, 146, 153, 160, 165, 176, 188, 201, 207, 213, 218, 322; V 11, 44, 55, 64, 77, 83, 90, 115; VI 322, 76, 105, 145, 150, 159, 170, 288
transients: I 93, 124; III 172; VI 159, 170
two-phase flow: I 77; II 21; III 198
well logging: I 74; II 21, 66; III 36, 70, 81; V 282, 316; VI 258, 279, 303, 310
well pressure: I 157; VI 28, 145, 150

Geothermometry: II 34; VI 367, 351; IX 231

Germany: IX 5

Geysers: I 84, 89, 153; II 16, 30, 61, 143; III 18, 61; IV 96, 106, 201; V 83, 127, 175, 302; VI 13, 279, 344, 351, 361; VIII 177, 295; IX 135, 409; X 89, 105, 123, 129, 133, 141; XI 29, 43, 197, 251; XII 23, 29, 241, 327

Goddard Springs: VIII 31

Granite: VII 127, 133; IX 387

Gravity change/subsidence ratio: VIII 177

Greece: IX 73

Ground subsidence: I 65

Groundwater: XI 135

Guangdong: IX 127

Gulf coast, U.S.: VI 84

Hatchobaru; IX 115; X 79

Hawaii: I 219; II 109; III 138; IV 133, 201; VIII 155, 309; X 65, 201; XI 1; XII 13

Heat:
conduction: X 195
extraction: VII 169; VIII 255; X 73
flow: VII 151; VIII 211, 219, 225; XII 89
sweep analysis: XII 97
sweep model: X 73
transfer: VII 151; X 151; XII 13
transmission model: VIII 269

Heat transfer: III 49; XI 175

Heber field: I 74, 135; II 9, 126; IX 157; XII 257

Hengill geothermal area: X 23

High-energy gas fracturing: XI 245

High-temperature logging: VII 115

History matching: X 97

Hoki: X 79

Hot-dry-rock reservoirs: VII 97; VIII 237, 249, 269; IX 5, 387, 397; IX 403; XI 35, 59, 189

Hot-dry-rock systems: I 174, 258; II 188, 193, 198, 200, 213; III 49; V 103; VI 272, 303, 367; XII 7, 131, 163
fluid flow: IV 244, 249, 256, 264
fracture properties: IV 244, 249, 256, 264, 270
growth: IV 270
heat extraction: IV 244
resource assessment: III 3

Hot springs: IX 365; X 123

Hot spring monitoring: XI 141

Hot-water reservoirs: IX 291

Hot-water systems: VI 351
economics: III 158
reservoir engineering: VI 3

Hydraulic conductivity: X 287; XI 71

Hydraulic fracturing: IX 397, 409, 415; XI 189

Hydraulic injections: IX 387

Hydraulic modeling: XI 35

Hydrogeologic model: VIII 171

Hydrogen sulfides:
renewal: I 153

Hydroisotopic studies: XI 175

Hydrologic flow: XI 231

Hydrology: VIII 67, 275, 285

Hydrothermal alteration: II 34; III 361; IX 145, 269; X 253

Hydrothermal convection systems: VIII 5; XII 291

Hydrothermal systems: VIII 5, 19, 25, 31, 39, 45; IX 135, 145, 151, 157; X 89

Hydrothermal systems:
ground subsidence: II 310
mathematical models: I 126, 161; VI 21, 69
simulation: V 147, 159, 212

Iceland: IV 153; V 169, 329; VI 49; VII 13, 61, 71, 139; VIII 111, 189, 211; IX 37, 345; X 23, 45, 177, 279; XI 7, 109; XII 67

Idaho: I 117, 124; II 75, 168; III 125, 130; V 26, 120, 183; VI 115; VIII 275, 279; IX 299, 311; X 287; XI 71, 77

Imperial Valley: III 107; VIII 39, 197; IX 5, 205, 409

Indium chelated tracers: XI 103

Industry advisory panel: X 5

Infinite acting model: XII 315

Inhibitor degradation rate: IX 317

Injected fluid monitoring: X 297

Injection-backflow tracer tests: IX 299, 305, 311; X 247

Injection depth: IX 339

Injection intervals: XI 207

Injection studies: XI 167

Injection tests: VII 71, 77, 175; VIII 73, 97, 103, 111, 249, 275, 279, 283; IX 299, 305; X 195

Injection wells: XII 37, 57
performance: V 255
plugging: III 163
testing: V 26, 37; VI 115

Injectivity-productivity estimation: XI 23

Interference testing: IX 151, 187, 193; XI 15; XII 173

Isothermal flow systems: XI 135

Isotopic studies: VIII 45, 309, 323; IX 253; X 253; XII 241, 253

Italy: I 37, 93, 101; II 21, 40, 150; IV 201, 165; III 214; V 90, 197, 212, 262; VI 21, 351; VII 13, 77, 85, 91; VIII 295, 315, 323; IX 5, 17, 53, 221, 247; XI 161; XII 87, 241, 247, 305

Ixtlan de los Hervores: IX 81

Japan: III 70; VII 13, 103, 115; VIII 149, 155; IX 115, 403; X 79; X 207; XII 285

Kakkonda: IX 115; IX 403

Kawerau field: VI 170; VIII 183; XII 173

Kenya: IX 65; XII 315

Kilauea volcano: VIII 309; X 65, 201

Kilauea Iki lava lake: XII 13

Kirishima field: VIII 149

Kizildere field: X 53

Klamath Falls: IX 187, 331; XII 77

Krafla field: V 169; VI 49; VII 71, VIII 211; IX 37, 211, 345; X 177; XI 7

La Primavera: VI 328; IX 81, 87; XII 97

Land leasing
legal aspects: I 153

Lardarello field: I 37; II 21, 40, 150; III 214; V 90, 212, 262; VI 21, 351; VII 77, 85, 91; VIII 295, 315, 323; IX 5, 17, 221, 247; X 113, 273; XI 161; XII 87, 241, 247

Lassen hydrothermal system: IX 365; XI 141

Latera field: IX 5, 17

Laugarnes field: IX 37

Lawrence Berkeley Laboratory: IX 205, 443; XI 65

Lawrence Berkeley Laboratory numerical simulator: VIII 255; IX 157

Leyte: IX 121

Linear acquifer: X 97

Linear boundary detection: XI 15

Linear elastic fracture mechanics: IX 415

Linear water influx: XII 109

Lip-pressure method: VIII 133

Liquid-dominated system: X 189; XI 197, 217; XII 103

Liquid-phase heterogeneity: IX 253

Log-log type curve: X 163

Logging: XII 305

Longevity: IX 157

Long Valley: II 324; XII 273

Los Alamos: VIII 249, 269; XI 59

Los Azufres field: IV 176; VII 41, 143; IX 81, 253, 269, 275, 285; X 213, 219, 233, 241, 265; XI 51, 237; XII 57, 181, 189, 195, 253

Los Humeros field: VIII 19; IX 81; XII 97

Los Negritos: IX 81

Louisiana: VI 76; VIII 261

Low-temperature reservoirs: VII 109

Lumped double porosity: VIII 189

Lumped parameter model: VII 23; X 45, 97

Magma energy extraction: XII 13

Mak-Ban field: VI 34

Makushin volcano: VIII 31; IX 167; X 227

Mammoth-Pacific power plant: X 297

Maritaro: IX 269

Mathematical models
comparative evaluations: VI 121
wellbore: VI 130

Matrix diffusion: IX 323

Matrix-dominated reservoirs: IX 299

Matrix thermal expansion: IX 427

Matsukawa: IX 115

Maturing geothermal fields: XI 161, 169

Meager Creek: X 253

Measurement technology: XII 131, 139, 147, 153

Methane: VII 133

Mexico: IV 5, 239, 176; V 44, 55, 228; VI 60, 130, 258, 328, 344; VII 13, 23, 29, 35, 41, 53; VIII 19, 49, 161, 171, 197, 231; IX 81, 87, 253, 269, 275, 285, 357, 427; X 73, 213, 219, 233, 241, 265, 273, 301; XI 7, 51, 127, 237; XII 57, 97, 153, 189, 195, 253

Microcracking: IX 381

Milos Island: IX 73

Mineral alteration zones: IX 269; XII 305

Mineralogy: IX 269; X 89, 253

Mineral precipitation: X 247

Miravalles field: X 37

Mist flow: XI 277

Modeling: XI 109, 117, 127, 283; XII 57, 67, 77, 119, 219, 229, 247, 267, 293, 315, 327

Mofete: IX 5, 17, 53

Mokai field: IX 107; X 29

Momotombo: III 96

Monroe field: V 115

Monte Amiata: IX 5, 17

Mori: IX 115

Mountain Home field: V 183

Mountainous terrain: XI 135

Moving front: VIII 103

Mud contamination: VIII 205

Multi-component modeling: X 279

Multiple feed wells: XI 23

Multiple interacting continua (MINC): VIII 219

NSCGREATS model: VIII 149

Namafjall field: VI 49; IX 37

Natural gas wells: III 29

Nesjavellir field: IX 37; X 23; XI 109

Nevada: IV 218; V 329; IX 151, 421; XII 159, 279

New Mexico: II 88; V 103, 238; VI 28, 272, 367; VII 97; VIII 91, 97, 249; IX 145, 397; XI 59, 189; XII 7, 163

New Zealand: I 126; II 40, 308, 310; III 185; IV 36, 139, 217, 332; V 37, 199, 205, 302, 309; VI 28, 41, 126, 139, 145, 170, 238; VII 13; VIII 67, 111, 127, 133, 183; IX 107, 323; X 31, 189; XI 15, 169, 217, 271; XII 173, 261, 297, 301

Ngawha field: V 309; VIII 133; IX 107; XII 261

Nicaragua: III 96; VII 13

Niland field: I 135, 143; II 9

Nigorikawa: IX 403; XII 285

Noncondensible gases: X 113, 233

Nonisothermal injection: VIII 103; IX 211; X 151; XI 59

Nozzle test: XII 301

Numerical simulation: XII 13, 89, 291

Ohaaki field: XI 15

Ohtake: X 79

Okoy field: VI 69

Olkaria: IX 65; XII 315

One-dimensional sweep model: VIII 255

Onikobe: IX 115

Onuma: IX 115

Open heat exchanger: XII 14

Optimization: X 31

Oregon: IX 187, 331; XII 77

Orifice test: XII 301

Orthogonal fracture junctions: IX 373

Otake: IX 115

Output curve: X 37

Overexploitation: IX 97

Oxidation reduction: XII 321

Packer seats: XI 207

Paragenesis: IX 269

Parallel fractures model: XII 229

Paris basin: IX 5; XII 203, 321

Pauzhetka field: X 57; XI 175

Permeability: VII 121, 127; VIII 111, 127, 205, 211, 261; IX 145, 239, 299, 345, 387, 443; X 301; XI 66, 223, 245, 283; XII 57, 89, 267

Permeability-thickness ratio: VIII 261

Petrochemistry: VIII 39

Petrophysical properties: XI 51

Petrothermal energy: IX 381, 387, 397, 403, 409, 415

Phase separation: IX 253

Phase studies:
aqueous solutions: IV 66

Phase trapping: IX 443

Philippines: IV 228; V 255; VI 34, 69; IX 121

Phlaegrean fields (Mofete): IX 5, 17; XII 305

Pilgrim Springs field: VIII 25
flow models: II 229; VI 218
two-phase flow: IV 66

Plastic flow: IX 381

Porosity logging: VIII 189

Porosity prediction: IX 305

Porosity-thickness product: IX 193

Porous media: IX 443; X 287, 293; XI 85, 223, 283

Potassium concentration studies: IV 239

Power costs: XI 217

Power generation: VII 35, 21; IX 81, 275; X 53, 219, 227; XI 169, 215, 217

Pressure build-up tests: IX 193; X 177; XII 45, 189, 297

Pressure depletion calculations: XII 103

Pressure drawdown: X 97, 233

Pressure drop: XI 277

Pressure measurements: V 96, 103; VIII 67, 91, 103, 119, 279; IX 199; X 241

Pressure prediction: IX 351

Pressure profiles: XI 187

Pressure-temperature-spinner tool: XI 198

Pressurized tests: X 169; XI 59

Pressure transient analysis: VII 161; IX 387; X 133, 151, 163; XI 7, 93; XII 49

Production data: IX 345; X 57; XII 23

Production engineering: X 183, 189, 195

Production/injection ratio: IX 339

Productivity index: IX 289, 291

Productivity (inferred): IX 211

Proximity functions: VIII 219

Pseudo-steady state flow: IX 175, 181

Puhagan field: IX 121

Puna: X 65, 201; XI 1

Pyrite: IX 269

p/Z analysis: X 97

Quartz precipitation: IX 239

Quasi-three-dimensional model: VIII 225

Radial dispersion: XII 125

Radial flow: IX 449

Radicondoli: IX 17

Radon: VII 133; VIII 315; IX 261
- simulation model: IX 261
- transport: IX 261

Radon 222:
- diffusion: V 302
- monitoring: II 61; V 309; VI 344
- tracer studies: IV 201

Raft River: VIII 275, 279; IX 299, 311, 77; XII 213

Raft River field: I 117, 124; II 75, 168; III 125; V 26, 120; VI 115, 159

Rate-pressure doublet: XII 49

Rate testing: VIII 73, 119; X 163

Reactive-solute transport: IX 239

Recharge (natural): IX 221, 351, 357; X 73

Redondo Creek: VIII 91, 97; IX 145

Reinjection: VII 41, 77, 85; VIII 49, 275, 279, 289; IX 17, 97, 121, 339; X 259, 265; XI 85, 93, 97, 103, 267

Relative permeability: IX 443

Remote sensing: X 13

Research programs:
- DOE: VIII 1, 49; IX 1
- EPRI: VII 21
- International cooperation: VII 13, 29; VIII 49; IX 1
- University: VII 5; VIII 255
- U.S.: VII 7, 11

Reservoir:
- behavior: VII 143; XI 35
- boundaries: X 89
- decay: X 213
- evaluation: X 201, 207, 213, 219, 227
- longevity: VII 161
- performance study: X 207
- scale: IX 217
- simulation: VIII 137
- sizing: XI 149
- temperature: XI 267
- vapor-dominated: XI 161

Reservoir chemistry: VII 91, 127, 133, 143; VIII 45, 295, 309, 315, 323, 329; IX 65, 221, 231, 239, 247, 253, 261, 269; X 113, 133, 233, 241, 247, 253, 259, 265

Reservoir engineering: III 87; IV 36; VII 1, 5, 7, 11, 13, 21, 161; VIII 25, 49, 171, 231, 275; IX 17, 107, 121, 415; X 1, 5, 13, 97, 207, 273; XI 1; XII 1, 21, 119

Reservoir modeling: XII 67, 77, 89, 97, 103, 109, 119, 125

Reservoir physics: VII 115, 121, 139, 143; VIII 19, 49, 161, 171, 177, 183, 189, 197, 205; IX 421, 427, 443, 449; X 293, 297, 301, 307; XI 217, 223, 225, 231, 237, 245

Reservoir rock:
- permeability: I 26, 192; II 16, 34, 188, 198; III 24, 172,192; IV 50; VI 218, 224, 288, 297, 316, 361
- plugging: II 34
- rock mechanics: II 263

Reservoir Technology Program: XII 1

Resistivity monitoring: VIII 161, 189; IX 421; X 45

Resistivity-porosity relationship: VIII 189

Resource assessment: VII 109; VIII 1, 31

Resource development: VII 23, 29, 35, 41, 47, 53, 61, 71, 77, 85, 91; VIII 1, 49,

67, 73; IX 5, 17, 37, 53, 65, 73, 81, 87, 97, 107, 115, 121, 127; X 23, 31, 37, 45, 53, 57, 65, 73, 79

Reykjanes field: VII 61; IX 37; X 45

Ribiera Grande field: VIII 73

Rift zone: X 65

Rock failure: IX 381

Roosevelt KGRA: I 77; III 89

Rosemanowes Quarry: XII 131

Rotorua field: IX 107

Rotorua monitoring program: XI 271

Rotarua-Whakarewarewa Field: VI 41

Rotary drilling: II 3

Salton Sea area: X 195

Salton Sea field: III 145, 178; V 120; XII 1

San Donato: IX 17

Sandstone: VIII 197, 205; IX 427; X 287

San Miguel Island: VIII 73

San Vito: IX 5

Sarukawa waterflood project: X 207

Scale inhibitor: IX 317

Scaling: VI 130; XI 207; XII 321

Scaling effects: IX 217, 277, 449; X 37

Sedimentary rocks: IX 427

Seismicity: II 101

Seismic monitoring: XII 7

Seismic study: X 297; XII 131

Self-potential surveys: XII 285

Seltjarnarnes field: IX 37; XII 67

Semilog methods: XII 315

Sensitivity analysis: XII 139

Serrazzano Field: IV 201; V 169

Shear failure: IX 383, 397

Silica: X 247, 279; XI 1, 259

Simulation: VIII 115, 149, 211, 219, 225, 231, 255, 261; IX 261, 351, 357, 365, 373; X 105, 151, 195, 273, 279, 287; XI 117

Single borehole system: XI 215

Sitka: VIII 31

Skin: X 169

Slug flow: XI 277

Slug test: IX 181; X 169

Sodium concentration studies: IV 239

Solute breakthrough: VIII 285

Solute transport: IX 305; X 287

Southern Negros: IX 121

Soviet Union: XI 175

Spinner measurements: IX 199, 205

Stanford Geothermal Program: VIII 255; IX 199

Stanford hydrothermal model: VII 169

Steam:
- condensation: IX 231
- excess: X 233
- flow model: VII 179
- quality: IX 231
- reservoirs: IX 285
- upflow: XII 253

Step-rate injection tests: VIII 103

Stimulation: VIII 237; XI 35

Stochastic fracture distributions: VIII 219; XI 71

Storage capacity: X 169

Stratigraphy: IX 145

Streaming potential: XI 225; XII 147, 285

Stress: IX 387, 397, 415, 427

Streamtube model: VIII 143

Subsidence: VIII 177, 183

Suginoi: IX 115

Sulfate discharge: XI 143

Summer Bay: VIII 31

Surface electrical potential: IX 421

Surprise Valley: VI 303

Svartsengi field: IX 37

Sweet Lake aquifer: VIII 261

Tainjin field: IX 127

Taiwan: V 64, 96, 249; VII 13; IX 193

Tauhara field: VIII 67

Tectonics: VIII 39

Tejamaniles: IX 269

Temperature:
  cycling: IX 427
  distribution: IX 339; XII 219
  drop model: X 183
  monitoring: X 265
  reversals: X 31

Temperature gradients:
  mathematical models: V 337, 343

Temperature measurement: III 55, 89, 107

Tenakee Springs: VIII 31

Test well: IX 167

Texas: II 299; IV 280; VI 76, 105

Thermal:
  breakthrough: XII 97
  conductivity: VIII 214
  degradation: IX 351
  expansion: VIII 197; IX 427
  landslide: X 123
  shallow reservoir: X 129, 133, 141
  water discharge: XI 141

Thermodynamic behavior: X 213, 241

Thermohydrodynamic model: X 57

Tibet: IX 127

Tiwi field: VI 34

Tongonan field: IX 121

Torre Alfina: IX 5, 17

Torvaliga: IX 17

Tracer:
  breakthrough times: XII 49, 213
  chelated indium: XI 103
  chemically reactive: XII 219
  dispersivity: X 259; XII 125
  flow: XII 213, 219, 229, 233
  fluorescein: XI 97
  hydrocarbon: XI 97
  injection-backflow tests: XII 233
  inert and reacting: XI 149
  recovery: IX 299, 305, 311
  retention: VIII 289
  rhodamine: XI 97

Tracer tests: VII 41, 85, 103, 135; VIII 289; IX 261, 323, 331; X 133, 247, 265; XI 39, 77, 93, 97, 103, 189

Transient flow: IX 175, 181; XI 277

Transient pressure: XII 315

Transmissivity: VIII 279; IX 211; X 23; XII 315

Travale: IX 5, 17

Travale KGRA: I 101; IV 165

Triangular probability: X 31

Tritium: VIII 323

Turbogenerators: IX 275

Two-phase flow: VII 175; VIII 91, 127, 133, 137, 143, 149, 155; IX 283, 443; X 23, 65, 183, 227, 241; XI 7, 183, 223, 277

Two-phase flow:
  monitoring: III 43

Unalaska Island: VIII 31; IX 167; X 227

United Kingdom: VIII 237; IX 5, 387

U.S. Department of Energy (DOE)
  research: VIII 1, 9; IX 1; X 1; XII 1, 333

U.S. Geological Survey: VII 11

USSR: VIII 329; X 57

Utah: I 77; III 89; V 115; XI 97

Valles Caldera: V 238; VI 272; IX 145, 397

Valve closure: IX 403

Vapor-dominated system: VI 194; VIII 295, 315; IX 247, 261; X 89, 97, 105, 113, 65, 227, 273; XI 117; XII 89, 291, 327
  bottom hole pressure: V 127
  two-dimensional calculations: VI 194

Vapor separation: IX 253

Vertical flow model: VIII 155; XI 237

Vertical steam wells: IX 285

Vicenza: IX 17

Viscosity: IX 211, 443

Volcanic regions: XII 305
heat transfer: VI 243

Volcanoes: IX 17
Garibaldi belt: X 253

Kilauea: VIII 309; X 65, 201
Makushin: VIII 31; IX 167; X 227

Wairakei: II 40, 308, 310; III 185; IV 36, 217; V 199, 205, 302, 309; VI 121, 126, 139, 145, 28, 41, 238, 253

Wairakei field: VIII 67, 183; IX 107, 323; XI 169, 217; XII 301

Water influx: X 45, 97

Water-rock reaction: IX 317

Water reservoirs:
hydrodynamics: IV 146

Well:
completion: X 37
discharge: VII 61
drilling: VII 35; VIII 25; X 31
stimulation: VII 53; VIII 237; IX 17; IX 121; XII 279

Wellbore:
heat transmission code: VIII 269
scale: IX 217; X 37
simulation: VIII 137

Wellbore simulator: XI 277

Wellhead power plant start-up: X 219

Wellhead pressure: IX 285, 291. XII 327

Well logging: VII 29, 115; VIII 161, 171, 177, 183, 189, 197, 205, 237; IX 205; X 13, 189; XI 197, 207, 215, 207, 283

Well siting: VII 161

Well testing: VIII 73, 91, 97, 103, 111, 115, 119, 137, 261; IX 17, 53, 73, 167, 175, 181, 187, 193, 199, 205, 211, 217; X 145, 151, 163, 169, 177; XI 7, 15, 23, 29; XII 37, 45, 49, 57

Wet steam: XI 225

Whakarewarewa springs: XI 271

Wyoming: VI 28

X-ray diffraction: IX 269

Yangbajain field: IX 127

Yunnan: IX 127

Yellowstone: VI 28

AUTHOR INDEX VOLUMES 1-12

Aamont, R.L.: II 188

Abe, H.: I 180; II 200, IX 403, 415

Abou-Sayed, A.S.: V 26

Abriola, L.: V 175

Abril, A.: VII 29; VIII 231

Adams, M.C.: IX 299; X 247, 253; XI 97

Adams, R.H.: III 96

Aguilar, R.G.: VI 367; XII 163

Ahmed, U.: V 26

Ahn, J.H.: XI 97

Albright, J.N.: IV 256

Allegrini, G.: VII 77; VIII 231

Allen, C.A.: III 125

Allis, R.G.: VIII 67, 177, 183

Allman, D.W.: XI 77

Alonso-E., H.A.: IV 5; V 228; IX 81

Ambastha, A.K.: XI 183, 227; XII 109

Andrade, M.: VIII 261

Ansari, J.: VIII 31

Antonelli, G.: V 147

Aragon, A.: X 219, 241; XII 97

Archambeau, C.: II 263

Arce, G.N.: VIII 31

Arellano, V.: VII 29; IX 291, 357; X 241, 301; XI 237; XII 57

Arenas, A.: VIII 205

Arnorsson, S.: IX 65, 321

Asseus, G.E.: II 268

Atherton, R.W.: I 267

Atkinson, P.G.: II 46; III 29, 64; V 257

Axelsson, G.: VIII 189

Ayatollahi, M.S.: IV 264

Ayuso, M.A.: XII 153

Banerdt, M.: VII 133

Barelli, A.: I 93, 101; IV 165, V 11

Baria, R.: XII 131

Barkman, J.H.: II 116; III 116

Barnes, H.L.: I 185; II 176

Barr, H.: X 31

Barragan, R.M.: IX 253; X 219, 265; XII 253

Bartz, D.: IV 50

Batchelor, A.S.: VIII 237; XI 35

Bayar, M.: XII 213

Bazant, Z.P.: I 232; IV 270

Benoit, W.R.: IX 151

Bentley, H.: XI 97

Benson, S.: VII 71, 161; VIII 103, IX 187, 205; XII 57, 77

Berg, J.R.: XII 333

Bermejo M., F.: VII 25; VIII 197; IX 427

Bertrami, R.: IX 221

Bickham, R.E.: V 316

Birdsell, A.: XII 163

Bixley, P.F.: V 37; VI 126, 238; VIII 133; IX 107; X 189; XI 169

Bjornsson, S.: IX 65; XI 109

Blackett, R.E.: XII 1

Blair, C.K.: V 115; VI 98

Bloomster, C.H.: I 167

Bodvarsson, G.: I 45; II 52; III 203; IV 146, 153, 160; V 64, 329; VI 338; VII 139

Bodvarsson, G.S.: VII 71, 161; VIII 161, 211; IX 157, 211, 345, 351, 443; X 105, 151, 279; XI 7, 109, 127; XII 23, 67

Boehm, R.F.: XII 13

Bories, S.: I 247; IV 66

Box, W.T.: XII 241

Brach, M.: XII 321

Breitenbach, K.A.: VIII 289

Brigham, W.E.: I 26; IV 165; V 212; VI 297, 150; X 97

Brown, D.W.: II 188; VIII 249

Brown, G.L.: IX 409

Brown, L.S.: VI 279

Brown, S.: V 183, 343

Brownell, D.H.: II 310; IV 280

Bunyak, M.J.: VII 53

Burnell, J.G.: XII 173

Burns, K.L.: XI 207

Burr, M.: XI 29

Byerlee, J.D.: II 198; IV 50; VII 127

Cabrera, J.: X 265

Calamai, A.: IX 17

Calore, C.: VI 21; VII 85, 91; VIII 295; IX 221, 247; X 273; XI 161; XII 89

Campbell, D.A.: II 116; III 116; IX 167; X 227

Cappetti, G.: VII 77; XII 89

Capuano, R.M.: VIII 275; IX 299

Carella, R.: IX 53

Carrigan, C.R.: XI 231

Castaneda, M.: VII 29; VIII 231; IX 357

Castanier, L.M.: IV 66; VII 23

Cataldi, R.: IX 17

Cathelineau, M.: IX 269

Cederberg, G.: IV 201

Celati, R.: I 37, 101, 242; II 21, 150; VI 21; VII 77, 91; VIII 295; IX 221, 247; X 273; XI 161; XII 89

Chang, C.R.Y.: V 64, 96, 249, 337

Chang, S.P.: II 193

Champman, D.S.: V 115

Chavez, P.: XI 207

Chelini, W: XII 305

Chen, B: II 109; III 138; IV 133; X 201; XI 1

Cheng, P.: I 219; II 236; V 192, 322; VI 243

Cheruvier, E.: XII 305

Chiang, C.Y.: V 337; IX 193

Chiang, S.C.: V 249

Chiu, T.L.: IX 193

Chrysikopoulos, C.: XI 103

Chu, T.Y.: XI 245; XII 279

Cillerai, V: II 21

Cinco, H.: IV 165

Clemo, T.M.: X 287; XI 71; XII 139

Cofo, J.: X 73

Conche, B.: XI 283

Contreras, E.: VIII 197; IX 427; X 307; XI 51; XII 195

Corona, A.: X 265

Counce, D.A.: VI 367; XII 163

Counsil, J.: III 192; IV 60

Cox, B.L.: X 151; XI 7

Criaud, A.: XII 203, 321

Crosby, G.: III 89

Cuderman, J.F.: XI 245

Cuella, G.: IX 97

Culver, G.C.: IX 331

Daggett, J.S.: XII 57

D'Amore, F.: V 262; VI 21, 351; VII 91; VIII 295, 315; IX 221, 247; X 113, 273; XII 241, 247

Danesh, A.: IV 60

DaPrat, G.: VIII 119; X 163

Dash, Z.V.: VII 97; VIII 269; IX 397; XI 59, 207

Dee, J.F.: X 97

Delaney, P.T.: IX 239

de las Alas, V.F.: IV 228

Denlinger, R.: VI 178

DeVilgiss, J.: IV 84

Dibble, W.E.: VI 316

Dickinson, D.A.: IX 279

Dominguez A.B.: IV 5; V 228; VII 35; IX 87; XII 195

Donaldson, I.G.: IV 36; V 222; VI 41; VII 1

Dorfman, M.H.: I 130; II 299; VI 105; VIII 261

Dougherty, D.E.: VIII 115

Downs, W.F.: II 34, 176; VIII 275; IX 311

Dreesen, D.S.: XI 207

Drenick, A.: XI 197

Duda, L.E.: X 195

Duffield, W.A.: VII 11

Dundurs, J.: I 178

Dunn, J.C.: XI 231; XII 13

Dvorov, I.M.: VIII 329

Dvorov, V.I.: VIII 329

Dykstra, H.: III 96; VI 13

Eaton, R.R.: VI 218

Economides, M.: IV 165; V 83, 127; VI 66; VIII 25, 31; IX 73, 167; X 227

Ehlig-Economides, C.: IV 60, 188; VI 66; VIII 25; IX 73

Eliasson, E.T.: VIII 211

Eliasson, J.: VI 288

Enedy, S.: XII 29

Engi, D.: IX 421

Entingh, D.: XII 21

Epperson, I.J.: XII 159, 267

Ershaghi, I.: V 282; VI 258

Esquer, C.A.: IX 357; X 73

Fallon, J.B.: VIII 91

Fancelli, R.: XII 247

Fandriana, L.: V 183

Farrell, W.E.: X 79

Faust, C.R.: I 198; II 308; III 185; IV 275

Fehlberg, E.L.: I 84; II 16; V 83

Ferguson, J.H.: XI 149; XII 219

Ferriz, H.: VIII 19

Fisher, H.N.: V 103

Forster, C.: XI 135

Fossum, M.P.: VIII 289

Fouillac, C.: XII 203, 321

Fournier, R.O.: VIII 45

Fradkin, L.J.: V 199

Frimannsson, H.: IX 65

Frye, G.: I 89; II 30; IV 96

Fujinaga, Y.: VI 188; X 207

Gale, R.O.: IV 139

Gallardo, M.: XII 181

Garcia, A.: XII 195

Garfias, A.: IX 253, 269; X 233, 241, 265

Garg, S.K.: I 65; II 310; III 178; IV 217, 280; V 195; VI 76; VII 47, 175; VIII 97; X 79

Gentner, R.: XII 37

Ghaemian, S.: VI 258

Gilardi, J.: X 259

Giovannoni, A.: VII 77

Glover, R.B.: VIII 127

Gobran, B.D.: VI 279, 297; VII 121

Golabi, K.: II 181; III 158; VI 374, 380

Goldman, D.: II 168; III 130

Goldstein, N.E.: VIII 161; X 13; XI 65

Gonfalini, M.: XII 305

Gonzalez, A.: VI 60

Gonzalez, J.: X 233

Goranson, C.: III 116; IV 118; IX 205

Gould, T.L.: I 146; XII 297

Goyal, K.P.: III 209; IV 300; V 205; VI 130; IX 151

Graj, A.N.: IV 15

Granados, E.E.: X 37; XII 37

Grant, M.A.: IV 78, 139; V 37, 242; VI 170, 28; VIII 111, 127, 133; IX 107; X 31; XI 271

Gray, W.G.: II 222

Green, A.S.P.: XII 131

Greenfield, R.J.: IV 275

Grisgsby, O.C.: IV 249; VI 367

Gringarten, A.C.: I 113

Gudmundsson, J.S.: VII 61; VIII 143; IX 331, X 45; XI 183, 217, 277; XII 189

Guevara, M.: VIII 205

Guglielminetti, M.: IX 53

Guillot, A.: IX 199

Gulati, M.S.: I 69; V 238

Gunnarson, A.: XI 109

Gunnarsson, G.: VI 288

Gunnlaugsson, E.: IX 231; XI 109

Haas, J.L.: II 247

Halfman, S.E.: VIII 171; XI 127

Haizlip, J.R.: XII 241

Halldorsson, G.K.: VII 71

Hammond, D.E.: VII 133

Handy, L.L.: V 282

Haney, J.: IV 118

Hanson, J.M.: II 46; IV 160; V 120

Hanson, M.E.: I 192

Harban, D.C.: I 77

Hardee, H.C.: XI 231

Harrar, J.E. VI 98

Harrison, R.F.: IV 272; V 115

Hart, C.M.: IX 421

Hauksson, T.: VII 61

Haukwa, C.B.: XII 315

Hebein, J.J.: IX 135; X 89; XI 43, 251

Hendron, R.H.: XII 7

Herkelrath, W.N.: III 43; IV 54; VI 322; VII 179

Hernandez, L.: X 73

Hickox, C.E.: XII 13

Hinrichs, T.C.: I 143

Hirakawa, S.: III 70; IV 234; VI 188; VII 115; VIII 225; IX 115; X 207

Hiriart, G.: VII 41; IX 275; X 213

Hite, J.R.: II 16

Hoang, V.T.: VIII 137; XII 159, 267

Holcomb, D.: II 263

Horii, H.: IX 381

Horne, R.N.: III 192; IV 138; VI 150; VII 5, 103; VIII 143, 289; IX 199, 323, 331; X 259; XII 233

Hosca, H.: XI 85

Howard, J.H.: III 9; IV 15; V 5; VI 3

Hsieh, C.H.: III 192; IV 60

Hsieh, P.A.: X 169

Hulen, J.B.: IX 145

Hull, L.C.: VIII 285; IX 305, 311; X 293; XII 139

Hunsbedt, A.: II 213; III 49; V 293; VI 264; VII 169; VIII 255; X 73

Ichikawa, M.: VIII 225

Iglesias, E.: XI 51, 237; XII 57, 195

Ingebritsen, S.E.: IX 365; XI 117; XII 291

Inglesias, E.R.: VI 84; VII 41; VIII 197, 205; IX 291; X 241, 265, 301

Iovenitti, J.L.: XI 65

Iregui, R.: II 213; III 49

Isherwood, W.: III 18

Ishido, T.: X 79; XII 285

Isokrari, O.F.: I 130; II 299

Izaguirre, O.: IX 269

Izquierdo, G.: VIII 205

Jackson, P.B.: IX 331

Jacobson, R.D.: XI 245; XII 279

James, E.D.: XII 159, 267

James, R.: I 52; III 198; V 355; VI 139, 145; VIII 133; IX 449; XI 259, 267; XII 297, 301

Jamieson, I.: III 61

Jensen, C.L.: IX 323

Jig, H.: IV 84

Johnson, S.E.: IX 331

Jones, A.H.: V 26

Jones, T.: VI 328

Jung, J.: XI 245

Juprasest, S.: V 183

Kanaori, Y.: XII 163

Karasaki, K.: VIII 219; X 145

Karmarkar, M.: IV 207; V 322

Kasameyer, P.W.: I 249; II 290; III 163; X 297

Kassoy, D.R.: I 23; II 263; III 209; IV 300

Keer, L.M.: I 180; II 200

Keith, L.A.: IX 239

Kelkar, S.: XI 59, 207

Kelsey, F.J.: II 251

Keskinen, M.: VIII 39

Keys, W.S.: II 66

Kihara, D.: II 109; III 138; IV 133

Kikuchi, T.: XII 285

Killup, M.W.: VIII 127

King, M.S.: X 307

Kingston, R.: IX 121

Kiryukhin, A.V.: X 57; XI 175

Kjaran, S.P.: VI 288

Klein, C.W.: X 37

Klopf, W.: XII 305

Knapp, R.M.: I 130; II 299

Kocabas, I.: XII 233

Kolar, J.: XI 207

Koslow, K.N.: VIII 285; IX 305

Kristmannsdottir, H.: XII 67

Kruger, P.: I 169; II 61, 213; III 49, 192; IV 201; V 327; VI 264, 344; VII 1; VIII 255, 315; IX 261; X 73, 219; XI 103; XII 97, 181

Kuide, X.: IX 127

Kumataka, M.K.: XII 327

Kunze, J.F.: I 117; II 168; III 125, 130; VIII 25

Kuo, T.M.C.: V 139

Kuwada, J.T.: I 157

Lai, C.H.: X 279

Lam, S.T.: VIII 255; X 73; XII 97

Laredo, F.: IX 253, 253

Lawton, R.G.: II 188

Leaver, J.D.: IX 107; XI 15, 23

Lebreton, F.: XI 283

Levy, S.S.: XI 207

Li, T.M.C.: II 34

Lin, J.J.: V 249

Lipman, S.C.: II 6

Lippmann, M.J.: IV 5; V 228; VI 130; VII 35; VIII 49, 171; IX 87, 157; XI 127

Liguori, P.E.: V 147

Lockett, G.E.: XI 215

Lockner, D.: II 198; IV 50

Lofgren, B.: VIII 25

Lombard, G.L.: I 135

London, A.L.: II 213; III 49

Long, J.C.S.: X 145

Lowell, M.G.: I 117

Maas, J.P.: IX 151

MacDonald, R.C.: VI 105

Macias-Chapa, L.: V 302; IV 201; XII 119

Maeder, P.F.: IX 279

Maes, M.E.: II 219

Maini, T.: I 258

Manetti, G.: I 93, 101, 242; II 150; IX 17

Maney, J.: X 141

Mangold, D.C.: VII 161

Mann, L.: I 74

Mannon, L.S.: III 29

Manon, A.: IV 5

Marconcini, R.: II 21, 150

Marcou, J.A.: XI 217

Marquez, R.: VIII 231; IX 357; X 73

Marsden, S.S., Jr.: XI 225; XII 147

Martin, J.C.: I 42; II 251; IV 42

Martinez, A.: X 265

Marty, B.: XII 321

Mateen, K.: IX 181

Mathews, M.: VI 303

Mathias, K.E.: II 39

Matsunaga, I.: XII 163

Matthiasson, J.: IX 65

Mazor, E.: III 55

McAtee, R.E.: VIII 275

McCoy, R.L.: VII 29

McEdwards, D.G.: II 75; III 116

McGuinnes, M.J.: XII 173

McKee, C.R.: I 192

McNitt, J.R.: X 37

Meidav, T.: I 52; II 126

Menjoz, A.: XII 203

Menninger, W.: XI 93; XII 49

Menzies, A.J.: VIII 143; XII 37

Mercado, S.: VI 60

Mercer, J.W.: I 198; II 308; III 185; IV 275

Messer, P.H.: II 136; IV 228; V 255

Mete, L.: VIII 73

Michels, D.E.: IX 317; X 183

Miller, C.W.: VI 130, 159

Miller, F.G.: II 3; IV 165; VI 150; VII 13

Miller, J.D.: IX 373; XI 77

Miller, L.G.: II 168

Miranda, C.: X 219, 241, 265; XII 181

Mishra, S.: XII 45

Miyoshi, M.: VI 188

Mlodinow, L.D.: III 172

Mock, J.E.: X 1; XII 1

Moench, A.F.: II 229; III 64; IV 54, 112; V 90; VI 178, 322; VII 179; IX 175; X 169; XII 125

Mogen, P.: X 141

Mohaupt, H.: XII 279

Molinar, R.: V 228; IX 291; X 219, 301; XII 97

Moore, D.: VI 361

Moore, D.E.: VII 127; IX 239

Moore, J.N.: X 253; XI 97

Morris, C.W.: VII 53; X 227

Morris, H.E.: IX 421

Morrow, C.A.: VII 127

Morse, J.G.: III 145

Muffler, L.J.P.: III 3

Mura, T.: I 180; II 200

Murakami, K.: X 79

Murphy, H.D.: I 174; II 188; IV 244; VI 272; VII 97; IX 397

Murphy, W.: VI 328

Nair, K.: VI 380

Nakanishi, S.: X 79

Nakatsuka, K.: IX 403

Narasimhan, T.N.: I 124; II 75; III 116; V 205

Nathenson, M.: I 50; II 40; IV 96

Nelson, D.V.: V 293; VI 264

Nelson, L.B.: III 130

Nemet-Nasser, S.: I 232; IX 381

Neri, G.: I 37, 101, 242; II 21, 150; V 90, 229; IX 17, 97

Netherton, R.: III 163; VI 98

Nguyen, V.V.: VI 213

Nielson, D.: IX 145

Nieva, D.: IX 253, 269; X 233, 265; XII 253

Niitsuma, H.: IX 403

Nikitopoulos, D.E.: IX 279

Noble, J.E.: IV 15

Noto, P.: VII 85

Nugent, J.M.: I 135

Nur, A.: IV 84; VI 316; VI 328

Nuti, S.: VII 85

Ohkuma, H.: VIII 261

Ohtsubo, H.: I 232

Okandan, E.: IX 339; X 53; XI 85; XII 213

Okazaki, J.: V 139

Oliver, R.: VIII 205; IX 269

Olhoeft, G.R.: V 282

Olsen, G.: X 45

O'Neill, K.: II 222

Ortega, A.: XII 13

Ortiz, J.: X 219; XII 181, 253

Ortiz-Ramirez, J.: XI 237; XII 57

O'Sullivan, M.J.: IV 332; VI 204, 224; IX 107

Owen, L.B.: III 163; VI 98

Palmason, G.: IX 37

Parlaktuna, M.: IX 339

Perusini, P.: I 37

Peters, E.: VIII 261

Petty, S.: VI 115; IX 217

Pinder, G.F.: I 199; II 222; III 188; IV 286; V 175; VI 213; VII 157; VIII 115

Pine, R.J.: IX 387

Piwinskii, A.J. & Netherton, R.: III 21

Pohoiki, H.I.: IV 201

Polat, T.: X 53

Portugal, E.: XII 253

Potter, J.M.: VI 316

Potter, R.M.: II 188; III 36; VI 272

Potter, R.W.: II 247; III 55

Pritchett, J.W.: I 201; II 310; III 178; V 159, 195; IV 217; VII 175; X 79

Prucha, R.H.: XII 77

Pruess, K.: IV 308; V 169; VI 194, 204; VII 151; VIII 161, 211, 219, 255; IX 345, 443; X 113, 273; XI 109, 161, 223; XII 89

Qilong, Y.: IX 127

Quijano, L.: IX 253; XII 253

Raasch, G.D.: VI 34; X 129

Rago, F.: VIII 261

Ramey, H.J., Jr.: II 3; III 49, 192; IV 1, 60, 165; V 64, 175; VI 150, 297; VII 13; IX 181; X 163; XI 15; XII 45, 119

Ramirez, J.S.: XII 229

Randall, G.S.: IV 272

Razo, A. XI 51

Reda, D.C.: VI 218

Reed, M.: IV 3; VII 109; X 1

Reeder, J.W.: VIII 31

Rex, R.W.: II 116

Rice, L.F.: II 159; IV 217; V 195

Rigby, F.A.: VI 310

Rimstidt, J.D.: I 185; II 176

Rinehart, J.S.: II 263

Riney, T.D.: III 178; IV 280; V 195; VII 47; VIII 97

Ripperda, M.: XII 23

Ritz, C.L.: VII 19

Rivera-Rodriguez, J.: VIII 73; IX 97; XII 229

Roberts, V.W.: II 9; VII 21

Robinson, B.A.: XI 149, 189; XII 163, 219

Rodriguez, F.: VII 103; XII 229

Rodriguez, J.: IV 176

Rojas, J.: XI 283; XII 203

Rosa, A.: IX 199

Rosser, J.R.: IX 151

Rothstein, S.: VI 380

Roux, B.: V 343

Rudisill, J.M.: IV 218

Russell, B.F.: IX 311

Safai, N.M.: III 188

Sageev, A.: VI 297; X 163; XI 15, 93; XII 49, 109

Saltuklaroglu, M.: IV 176; V 44, 55; VII 143

Samaniego-V, F.: IX 97

Sammis, C.G.: I 240; II 34; VII 133

Samundsson, K.: IX 65

Sanchez, E.: X 213

Sanchez-Upton, P.: XII 189

Santoyo, E.: XII 253

Santoyo, S.: VIII 205

Sanyal, S.K.: I 52; II 126; III 81; V 183, 316, 343; VI 279; X 37; XII 37

Saracco, L.: XII 247

Scherer, C.R.: I 161; II 181; III 158

Schroeder, R.C.: I 249; II 85, 290; III 116; IV 118, 308; V 169; IV 5; V 228; XII 103

Schultz, A.: IV 165

Schwarz, W.J.: III 9; IV 15; V 5

Seki, A.: IV 133; X 201; XI 1

Semprini, L.: IV 201; V 302; VI 344; VIII 315; IX 261; X 219

Sengul, M.: II 126

Sepehrnoori, K.: VIII 261

Shapiro, A.: V 175; VII 157

Sharme, D.: I 258

Shen, H.W.: I 213

Shen, K.Y.: V 96

Sheppard, D.S.: XII 261

Sigúrdsson, O.: VII 71; VIII 189; IX 211; X 177

Sill, W.: VIII 275

Sioshansi, F.: VI 380

Skiba, P.A.: VIII 279

Smith, A.T.: X 297

Smith, E.W.: VI 69

Smith, J.L.: II 116

Smith, L.: XI 135

Solbau, R.D.: IX 205

Sorey, M.L.: I 225; II 324; V 199, 222; VI 253; VII 109; VIII 5; IX 365; XI 141

Speliotis, G.: IX 73

Spencer, A.L.: XII 67

Spivak, A.: II 159

Squarci, P.: VI 21

Squerci, P.: I 37

Stauder, J.J. X 253

Stefansson, V.: VI 49; VII 71; VIII 189, 211; IX 37, 65, 211, 345; X 23, 177; XI 109

Steingrimsson, B.: VI 49; X 177

Sternfeld, J.: VIII 39

Stieltjes, L.: I 113

Stoker, R.C.: I 117; II 168; III 125, 130

Strobel, C.J.: II 143; IV 106

Suau, J.: XII 305

Suemnicht, G.: XII 273

Sugihara, M.: XII 285

Sugine, S.: XII 37

Sugrobov, V.M.: X 57; XI 175

Summers, R.: II 198

Svanbjornsson, A.: IX 65

Sveinbjornsdottir, A.E.: XII 67

Swenson, L.W., Jr.: VII 169

Syms, M. C.: VI 126

Syms, P. H.: VI 126

Tachimori, M.: VIII 149, 155

Takahashi, H.: IX 403, 415

Takahashi, P.: II 109; III 138; X 201; XI 1

Takanohashi, M.: IX 403

Tansev, E.: III 107; IV 213

Tester, J.W.: II 188; IV 249; V 103; VI 272; XI 149; XII 219

Thomas, D.M.: VIII 309

Thompson, J.M.: VIII 45

Thorhallsson, S.: IX 37; X 45

Thorson, L.: III 163

Thorsteinsson, T.: IX 37

Todd, M.C.: IV 275

Tomasson, J.: VII 61

Toms, R.S.H.: VIII 1; IX 1

Traeger, R.K.: XII 21

Truesdell, A.H.: III 55; IV 96, 239, V 262, 277; VI 21, 194, 351; XII 241, 247

Trujillo, P.E.: VI 367; XII 163

Tsang, C.F.: I 62; II 75, 85; III 172; IV 322; VI 224; VII 7; IX 443

Tsang, Y.W.: IV 322

Tsao, L.: IV 294

Tulinius, H.: XII 67

Tyran, C.K.: XI 225

Ucok, H.: V 282

Ungemach, P.: IX 5

Veggeberg, S.: XI 97

Verma, A.K.: VI 243; IX 443; XI 223

Verma, M.: XII 253

Verma, S.: X 219, 265

Vides-R., A.: IX 97

Voss, C.I.: IV 286

Vrouzi, F.: IX 73

Warpinski, N.: XII 279

Warren, G.: II 61

Wasserman, M.L.: III 107

Watson, A.: IX 121

Wei, H.F.: XII 321

Weertman, J.: II 193

Wegner, R.E.: II 251

Wells, L.E.: V 373

Wemple, R.P.: XII 13

Weres, O.: III 214; IV 294

Wescott, E.: VI 60

Westwood, J.D.: VII 23

Wheatall, M.W.: XII 147

Whitehead, N.E.: V 309

Wilson, D.M.: X 189

Wilt, M.J.: VIII 161

Witherspoon, P.A.: I 62, 124; IV 5; V 228; VII 7; IX 443; X 105, 145, 279; XII 77

Woitke, L.J.: I 153

Wolgemuth, K.M.: V 26

Wooding, R.A.: I 126, 206; II 339

Woodruff, J.: XI 1

Wright, P.M.: IX 299

Wu, T.M.: V 249

Wu, T.S.: IX 193

Yamaguchi, S.: VII 115; X 207

Yee, A.: IV 294

Yoshimura, T.: X 79

Yuen, P.: III 138; IV 133

Zais, E.: III 85; IV 153; V 190; VI 121

Zebib, A.: II 263

Zelwer, R.: VIII 171

Zerzan, J.: IV 308

Zyvoloski, G.A.: IV 332; VIII 269; XI 59